



UNIVERSITY OF
BIRMINGHAM

Lead-Free Pyroelectric Materials for Environmentally Friendly Solid-State Cooling Systems

By

Hojat Pooladvand

A Thesis Submitted to the University of Birmingham

for the degree of

DOCTOR OF PHILOSOPHY

School of Metallurgy and Materials
College of Engineering and Physical Sciences

The University of Birmingham

September 2017

UNIVERSITY OF
BIRMINGHAM

University of Birmingham Research Archive

e-theses repository

This unpublished thesis/dissertation is copyright of the author and/or third parties. The intellectual property rights of the author or third parties in respect of this work are as defined by The Copyright Designs and Patents Act 1988 or as modified by any successor legislation.

Any use made of information contained in this thesis/dissertation must be in accordance with that legislation and must be properly acknowledged. Further distribution or reproduction in any format is prohibited without the permission of the copyright holder.

Abstract

Due to the detrimental environmental problems caused by common cooling systems that rely on compressed air and cooling gas (freon), researchers have started developing different types of cooling systems. One of the newest methods uses electrocaloric materials to make a cooling system. The electrocaloric effect (ECE) is the reverse of pyroelectricity, which means that the ability of the dielectric materials to change their temperature under an applied electric field. If they have been put through a cycle in adiabatic and isothermal conditions; this can create cooling. All of the ferroelectric materials are pyroelectric materials and are economical for mass production. From an economic and environmental view, two ferroelectric materials were selected for this project: BCZT ($\text{Ba}_{0.85}\text{Ca}_{0.15}\text{Ti}_{0.9}\text{Zr}_{0.1}\text{O}_3$) as a normal ferroelectric and BNT – BT (94 mol% $\text{Bi}_{0.5}\text{Na}_{0.5}\text{TiO}_3$ – 6 mol% BaTiO_3) as a relaxor ferroelectric. These compounds were prepared by the solid-state method, calcined, pressed, sintered and optimised to make bulk ceramics. The relative density, relative permittivity at room temperature and its temperature dependence, d_{33} , grain size, and k_p of all of the samples were measured. BCZT was calcined at 1250°C and sintered at 1400°C, 1425°C, 1450°C, 1475°C, and 1500°C. BNKT ($\text{Bi}_{0.50}(\text{Na}_{0.82}\text{K}_{0.18})_{0.50}\text{TiO}_3$) as a relaxor ferroelectric was added to the BCZT compound as a normal ferroelectric in 1 wt%, 3 wt%, and 5 wt% to investigate the mixture of a normal and relaxor ferroelectric and the samples were sintered at 1250°C, 1300°C, 1350°C, 1400°C, 1450°C and 1500°C. On the BNT-BT compound, the effect of the BF (BiFeO_3) was investigated at 0.025, 0.05mol%, 0.075mol% and 0.1mol%. Also, the effect of the deficiency in BNT-BT was investigated as a common problem in the process of BNT-BT to investigate the effect of deficiency in BNT-BT on the ECE.

Both direct and indirect methods were selected to measure the ECE. The device for direct method measurement was designed and fabricated, and the ECE of all of the prepared samples were measured with both methods.

The results for BCZT show the best properties with a relative density of 96.1%, the grain size of 32µm, piezoelectric charge coefficient (d_{33}) of 410 pC/N, and electromechanical coupling factor (k_p) of 46% for samples sintered at 1450°C. The highest ECE ($\Delta T= 0.97$) measured by an indirect method was achieved for BCZT sintered at 1450°C. The result of the direct method was around 70% of indirect method. ECE was decreased by the addition of additives BNKT to BCZT due to the diversion of the MPB.

The best properties for BNT-BT were found for materials sintered at 1125°C with a relative density of 97%, the grain size of 3.2 μ m, d_{33} of 165 pC/N and k_p of 47%. BNT-BT shows high ECE $\Delta T = -2.91$ and -2.1°C for samples sintered at 1125 and 1150°C respectively measured under 50 kV/cm which, due to the two step calcination process, is higher than previous reports. The results of the direct method were around 75% of the indirect method. Also, the addition of additives decreased the ECE of pure BNT- BT and non-stoichiometric BNT-BT (0.94(Bi_{0.45.5}Na_{0.47.5}Ti_{0.94}O_{2.82})-0.06BT) shows an ECE $\Delta T = -1.65$ at -10°C under 50 kV/cm, due to a lower relative density in comparison with pure BNT-BT.

**To My Father, Mother,
Sister and Brother**

Acknowledgments

I would like to express my deepest sincere appreciation to my supervisors, Professor Tim. W. Button and Professor Rex Harris for their valuable advices, suggestions, guidance, patience and constructive critics through the completion of my thesis work. Without their constant encouragement and support, this work would not have been possible and accomplished.

A very especial thank to Dr. Hana Hughes, Mr. Carl Meggs and Mr. Frank Biddlestone who has been supporting me all this time with his technical expertise. It is always a great feeling to have a knowledgeable and helpful person like you.

A very especial thank to proofreading international company for proof reading of my thesis.

My sincerest thanks are extended to all my friends in our group. Thanks for my constant support and contributions.

A very special note of appreciation to my supportive and understanding family members (Karim, Nahid, Nassim, and Nima), thanks for supporting me with all your love during the days of intensive work.

List of Publication and conferences

Yang Bai, Ales Matousek, Pavel Tofel, Bo Nan, Vijay Bijalwan, Michael Kral, **Hojat Pooladvand**, Hana Hughes and Tim W. Button Phase Transitions and Dielectric, Ferroelectric and Piezoelectric Properties of $\text{Bi}_{0.5}(\text{Na}_{0.82}\text{K}_{0.18})_{0.5}\text{TiO}_3$ - Doped $(\text{Ba}_{0.85}\text{Ca}_{0.15})(\text{Zr}_{0.1}\text{Ti}_{0.9})\text{O}_3$ Ceramics, IEEE International Symposium (ISAF/ISIF/PFM), 2015, 268-271

Hojat Pooladvand, Carl Meggs, Rex Harris, Vijay Bijalwan, Yang Bai, Hana Hughes and Tim Button, BCZT as an electrocaloric material for future solid state cooling systems, Materials and Structures for Energy Harvesting conference, June 2016, Brno, Czech republic

Hojat Pooladvand, Carl Meggs, Rex Harris, Vijay Bijalwan, Yang Bai, Hana Hughes and Tim Button, BCZT as an electrocaloric material for future solid state cooling systems, Energy harvesting conference, May 2016, London

Hojat Pooladvand, Carl Meggs, Rex Harris, Vijay Bijalwan, Yang Bai, Hana Hughes and Tim Button, BCZT as an electrocaloric material for future solid state cooling systems, IEEE International Symposium, (ISAF/ISIF/PFM), August 2016, Darmstadt, Germany

TABLE OF CONTENT

ABSTRACT	I
ACKNOWLEDGMENTS.....	IV
List of Publication and conferences.....	V
LIST OF FIGURES.....	IX
LIST OF TABLES.....	XV
NOMENCLATURE.....	XVI
CHAPTER 1 INTRODUCTION.....	1
1.1 Introduction	2
CHAPTER 2 LITERATURE REVIEW	4
2.1 Pyroelectric materials	5
2.1.1 Piezoelectric, pyroelectric, and ferroelectric materials	5
2.1.1.1 Lead-based ferroelectric materials	9
2.1.1.2 Lead-free ferroelectric materials	10
2.1.1.2.1 BT: BaTiO ₃	10
2.1.1.2.2 Bismuth-ferrite or BF: BiFeO ₃ and related materials	15
2.1.1.2.3 BNT: Bi _{0.5} Na _{0.5} TiO ₃	16
2.2 Environmentally friendly solid-state cooling systems	23
2.2.1 Magnetocaloric solid-state cooling systems	23
2.2.2 Thermoelectric solid-state cooling systems	23
2.2.3 Electrocaloric solid-state cooling systems	23
2.3 Pyroelectric (electrocaloric) Materials for Environmentally Friendly Solid-State Cooling Systems	27
2.3.1 The properties needed for the ECE in ceramic materials	27
2.3.1.1 Ferroelectric properties	28
2.3.1.2 The order of phase transition	29
2.3.1.3 Dielectric strength	29
2.3.1.4 Electrical Conductivity	30
2.3.1.5 Relaxor ferroelectrics	30
2.3.1.6 ECE in temperature ranges	31
2.3.1.7 The invariant critical point (ICP) and line of critical end points (LCEP)	32
2.3.2 Measurement of the electrocaloric effect	32
2.3.3 Lead-free electrocaloric ceramic materials	36
2.3.3.1 Single crystal materials	36
2.3.3.2 Bulk ceramics with a thickness greater than 100µm	36
2.3.3.2.1 BNT-based bulk ceramics	37
2.3.3.2.2 BT, BZT, and BCZT bulk ceramics	41
2.3.3.3 Thin- and thick-film ceramics	44
2.4 Summary	45
2.5 The aim of this project	Error! Bookmark not defined.

CHAPTER 3 EXPERIMENTAL PROCEDURES	48
3.1 Introduction	49
3.2 Mixing materials	49
3.3 Calcination	51
3.4 Characterisation and analysis of the materials	52
3.5 Forming (pressing)	52
3.6 Sintering	52
3.7 Density and dimensions	53
3.8 Cleaning the samples and preparing for applying the electrode	53
3.9 Poling the samples	54
3.10 Polishing and SEM	54
3.11 Piezoelectric properties	54
3.12 ECE indirect measurement	57
3.13 Direct measuring method	57
3.14 Measurement errors, repeatability, and reproducibility	63
CHAPTER 4 FABRICATION, CHARACTERISATION, AND OPTIMISATION OF THE CERAMICS	65
4.1 The fabrication and characterisation of the materials	66
4.2 Fabrication of $0.5((\text{Ba}_{0.7}\text{Ca}_{0.3})\text{TiO}_3)-0.5(\text{Ba}(\text{Zr}_{0.2}\text{Ti}_{0.8})\text{O}_3)$ or $\text{Ba}_{0.85}\text{Ca}_{0.15}(\text{Zr}_{0.10}\text{Ti}_{0.90})\text{O}_3$	66
4.2.1 The effect of $\text{Bi}_{0.50}(\text{Na}_{0.82}\text{K}_{0.18})_{0.50}\text{TiO}_3$ on $\text{Ba}_{0.85}\text{Ca}_{0.15}(\text{Zr}_{0.10}\text{Ti}_{0.90})\text{O}_3$	77
4.2.1.1 BCZT-1, 3, and 5% BNKT	78
4.3 Fabrication of BNT-BT ($0.94\text{Bi}_{0.5}\text{Na}_{0.5}\text{TiO}_3-0.06\text{BaTiO}_3$)	101
4.3.1 $((1-x)0.94\text{BNT}-0.06\text{BT})-x\text{BF}$ or (BNT-BT-BF)	115
4.3.2 Deficiency in the BNT-BT system	124
4.4 Summary	128
CHAPTER 5 ELECTROCALORIC MEASUREMENTS	130
5.1 Measuring the electrocaloric effect (ECE)	131
5.1.1 The indirect method used to measure the ECE	131
5.1.1.1 The indirect measurement of ECE of BCZT-based materials	133

5.1.1.2 Using the indirect method to measure the ECE of pure BCZT	137
5.1.1.3 Using the indirect method to measure the ECE of BCZT-1% BNKT	139
5.1.1.4 Using the indirect method to measure the ECE of BCZT-3% BNKT	143
5.1.1.5 Using the indirect method to measure the ECE of BCZT-5% BNKT	146
5.1.2 Using the direct method to measure the ECE of BCZT-based materials	149
5.1.2.1 Pure BCZT	149
5.1.2.2 BCZT-BNKT	151
5.1.2.2.1 The ECE direct measurement of BCZT-1%BNKT	151
5.1.2.2.2 BCZT-3%BNKT	154
5.1.2.2.3 BCZT-5%BNKT	156
5.1.2.3 ECE comparison of BCZT- and BCZT-based ceramics	159
5.1.3 Indirect ECE measurements of BNT-BT based materials	164
5.1.3.1 Indirect ECE measurement of pure BNT-BT	164
5.1.3.2 The indirect ECE measurements of BNT-BT-BF	171
5.1.3.3 The indirect ECE measurement of BNT-BT deficient samples	177
5.1.4 The direct ECE measurement of BNT-BT-based materials	178
5.1.4.1 The direct ECE measurement of pure BNT-BT	178
5.1.4.2 The direct ECE measurement of BNT-BT-BF	185
5.1.4.3 The direct ECE measurement of BNT-BT deficient samples	190
5.1.4.4 ECE comparison of BNT-BT-based ceramics	191
5.2 The comparison between ECE and relative density	131
CHAPTER 6 CONCLUSIONS.....	199
CHAPTER 7 FUTURE WORK AND RECOMMENDATIONS	206
REFERENCES.....	209
APPENDIX I.....	222
APPENDIX II	229

LIST OF FIGURES

Figure 2-1: The classification of crystals with piezoelectric, pyroelectric, and ferroelectric effects.....	7
Figure 2-2: Cubic perovskite unit cell. A-site cations are grey, the B-site cation is green, and oxygen is red.....	8
Figure 2-3: A phase diagram of PZT with MPB, between the rhombohedral and tetragonal phases.	9
Figure 2-4: Polymorphic Phase Transition in BT single crystals, observed through changes in the unit cell parameters, spontaneous polarisation, and dielectric constant.....	10
Figure 2-5: Phase diagram of $x\text{BaZrO}_3-(1-x)\text{BaTiO}_3$ ceramics with $0 < x < 0.2$	11
Figure 2-6: Phase diagrams of BZT-BCT; A is the first one reported by Liu et al. [15], which shows the rhombohedral and tetragonal phases, and B is the revised diagram of BZT-BCT, as reported by Keeble et al, which shows the orthorhombic phase, between the rhombohedral and tetragonal phases.	14
Figure 2-7: Schematic of BNT formation mechanisms: the diffusion of TiO_2 and Na_2CO_3 into Bi_2O_3 and the transformation of Bi_2O_3 into BNT	16
Figure 2-8: The perovskite structure of BNT: Bi and Na at the A site, Ti at the B site	17
Figure 2-9: The binary phase diagram of BNT-BT. It has a curved MPB between the rhombohedral and tetragonal phases	19
Figure 2-10: A schematic illustration of an electrocaloric cooling system, in comparison to a vapour compressor. It has four stages: adiabatic polarisation; isoelectric enthalpic transfer; adiabatic depolarisation; and isoelectric entropic transfer	25
Figure 2-11: T-S diagram for a second-order transition (left), in which the entropy changes continuously, and a first-order transition, in which it does not (right)	29
Figure 2-12: Schematic hysteresis loops for: (A) normal ferroelectric; (B) paraelectric or dipolar glass or relaxor ferroelectrics; (C) anti-ferroelectrics; and (D) dielectric materials.	31
Figure 2-13: The schematic of ICP and LCEP. The ICP shows the coexistence of several phases at one point, while the LCEP displays the line between two critical points in the electric field-temperature-composition plots of the materials	32
Figure 3-1: Summary of the experimental procedures	50
Figure 3-2: The temperature profile for the calcination of the powders	52
Figure 3-3: The sintering profile plot for the green pellets	53
Figure 3-4: Impedance and phase plots of a typical piezoelectric sample showing how to measure the resonant and anti-resonant frequencies. a) The log of impedance at a range of the frequencies; b) the phase response corresponding to plot a; c) the log of the first impedance peak; and d) the phase response corresponding to plot c, which rises to a maximum value roughly at the centre of the resonance.	56
Figure 3-5: The measurement apparatus constructed for direct temperature reading to measure the ECE, with all parts, and a close view from the sample in the middle of probes.	60
Figure 3-6: Schematic of the application and removal of the electric field on the sample	61
Figure 3-7: Photograph and schematic diagram of the ECE direct reading measurement equipment. .	62
Figure 3-8: Schematic of the change in sample temperature with time on the application and removal of the electric field on the sample	62
Figure 3-9: Calibration of the resistance of the thermistor versus the temperature between -50 and 150°C	63
Figure 4-1 The XRD patterns of BZT, calcined at 1250°C for two hours,.....	66
Figure 4-2: The XRD patterns of BT, calcined at 1100°C for two hours.....	67

Figure 4-3 The XRD patterns of BCT, calcined at 1250°C for two hours.....	68
Figure 4-4: The XRD patterns of firstly, BCZT 1: Calcined BCZT from BZT and BCT calcined at 1250°C for two hours and secondly, BCZT 2: calcined BCZT from raw materials at 1250°C for two hours and BCZT3: BCZT2 sintered at 1450°C for two hours.	69
Figure 4-5: SEM micrographs of the BCZT samples, sintered at A) 1400°C, B) 1425°C, C) 1450°C, D) 1475°C, and E) 1500°C for two hrs (see the appendix for a low magnification photo).....	70
Figure 4-6: Variation in the relative density as a function of the sintering temperature for BCZT	71
Figure 4-7: The variation in grain size as a function of the sintering temperature for BCZT	71
Figure 4-8: The variation of relative permittivity of unpoled samples as a function of sintering temperature for BCZT, measured at room temperature.	72
Figure 4-9: The variation of d_{33} as a function of sintering temperature for BCZT, measured at room temperature.....	72
Figure 4-10: The variation of k_p as a function of sintering temperature for BCZT, measured at room temperature.....	73
Figure 4-11: The temperature dependence of relative permittivity (ϵ_r) and dielectric loss ($\tan\delta$) of unpoled samples at 100 Hz, 1 kHz, 10 kHz, 100 kHz, and 1 MHz for BCZT sintered samples at A) 1400, B) 1425, C) 1450, D) 1475, and E) 1500°C for two hours.....	76
Figure 4-12: The XRD patterns of A) calcined BNKT powder, B) calcined BCZT powder, and BCZT-1% BNKT mixtures sintered for four hours at C) 1250°C, D) 1350°C, E) 1450°C, and F) 1500°C for four hours respectively.....	79
Figure 4-13: The XRD patterns of calcined BCZT powder, and BCZT- 1%BNKT sintered at 1250°C, 1350°C, 1450°C, and 1500°C for four hours for values of 2θ around A) $=38.5^\circ$ for (111) and B) $=45^\circ$ for (200).....	80
Figure 4-14: The XRD patterns of A) calcined BNKT powder, B) calcined BCZT powder, and BCZT-3% BNKT sintered at C) 1250°C, D) 1350°C, E) 1450°C, and F) 1500°C, sintered for four hours.....	81
Figure 4-15: The XRD patterns of calcined BCZT powder, and BCZT-3% BNKT at sintered at 1250°C, 1350°C, 1450°C, and 1500°C for four hours at around 2θ A) $=38.5^\circ$ for (111) and B) $=45^\circ$ for (200).	82
Figure 4-16: The XRD patterns of A) calcined BNKT powder, B) calcined BCZT powder, BCZT-5% BNKT sineterd at C) 1250°C, D) 1350°C, E) 1450°C, and F) 1500°C for four hours.....	83
Figure 4-17: The XRD patterns of calcined BCZT powder, and BCZT-5% BNKT sintered at 1250°C, 1350°C, 1450°C, and 1500°C for four hours at around 2θ A) $=38.5^\circ$ for (111) and B) $=45^\circ$ for (200).	84
Figure 4-18: SEM micrograph of the BCZT-1% BNKT samples sintered at A) 1250°C, B) 1350°C, C) 1450°C, and D) 1500°C (see the appendix for a low magnification photo).....	85
Figure 4-19: SEM micrograph of the BCZT-3% BNKT samples sintered at A) 1250°C, B) 1350°C, C) 1450°C, and D) 1500°C (see the appendix for a low magnification photo).....	86
Figure 4-20: SEM micrograph of the BCZT-5% BNKT samples sintered A) 1250, B) 1350°C, C) 1450°C, and D) 1500°C (see the appendix for a low magnification photo).	86
Figure 4-21: The variation of relative density as a function of the sintering temperature for BCZT-1, 3, and 5% BNKT.....	87
Figure 4-22: The variation of grains size as a function of sintering temperature for BCZT-1, 3, and 5% BNKT.....	88
Figure 4-23: The variation of relative permittivity of unpoled samples as a function of the sintering temperature for BCZT-1, 3, and 5% BNKT measured at RT.	89

Figure 4-24: The variation of d_{33} as a function of the sintering temperature for BCZT-1, 3, and 5% BNKT.....	90
Figure 4-25: The variation of k_p as a function of the sintering temperature for BCZT-1, 2, and 5% BNKT.....	91
Figure 4-26: The temperature dependence of relative permittivity (ϵ_r) and dielectric loss ($\tan\delta$) of unpoled samples at 100 Hz, 1 kHz, 10 kHz, 100 kHz, and 1 MHz for BCZT-1% BNKT samples sintered at A) 1250, B) 1350, C) 1450, and D) 1500°C for four hours.....	94
Figure 4-27: The temperature dependence of relative permittivity (ϵ_r) and dielectric loss ($\tan\delta$) of unpoled samples at 100 Hz, 1 kHz, 10 kHz, 100 kHz, and 1 MHz for BCZT-3% BNKT sintered samples at A) 1250, B) 1350, C) 1450, and D) 1500°C for four hours.....	96
Figure 4-28: The temperature dependence of relative permittivity (ϵ_r) and dielectric loss ($\tan\delta$) of unpoled samples at 100 Hz, 1 kHz, 10 kHz, 100 kHz, and 1 MHz for BCZT-5% BNKT sintered samples at A) 1250, B) 1350, C) 1450, and D) 1500°C for four hours.....	99
Figure 4-29: The XRD patterns of A) BNT-BT formed from the raw materials and calcined at 850°C for two hours, and B) BNT-BT formed from separate BNT and BT and subsequently calcined together at 850°C for two hours.	101
Figure 4-30: The XRD patterns of BT, calcined at 1100°C for two hours.	102
Figure 4-31: The XRD patterns of A) BNT: the blue line (bottom) – mixed by the wet method and calcined at 850°C for two hours; B) BNT: the red line – mixed by the dry method and calcined at 800°C for two hours; C) BNT: the green line – mixed by the dry method and calcined at 825°C for two hours; and D) BNT: the purple line – mixed by the dry method and calcined at 850°C for two hours.	103
Figure 4-32: Phase relations in the system $\text{Bi}_2\text{O}_3\text{-Na}_2\text{O-TiO}_2$ at 1000°C [68].....	104
Figure 4-33: The XRD patterns of: A) BNT: the black line, calcined at 800°C; B) BNT: the red line, calcined at 825°C; and C) BNT: the blue line, calcined at 850°C for five hours, produced by the dry powder method.....	105
Figure 4-34: The XRD patterns of A) 0.94BNT-0.6BT calcined at 850°C; B) 875°C; C) 900°C; D) 950°C; E) 1000°C; F) 1050°C; G) 1100°C; and H) 1150°C, for five hours.	105
Figure 4-35: SEM micrograph of the 0.94BNT-0.6BT samples sintered a) 1100°C; B) 1125°C; C) 1150°C; D) 1175°C; and E) 1200°C (see the appendix for a low magnification photo).	107
Figure 4-36: The variation of relative density as a function of the sintering temperature for 0.94BNT-0.6BT.....	108
Figure 4-37: The variation of grain size as a function of sintering temperature for 0.94BNT-0.6BT.	109
Figure 4-38: The variation of relative permittivity of unpoled samples measured at room temperature as a function of sintering temperature for 0.94BNT-0.6BT at RT.....	109
Figure 4-39: The variation of d_{33} as a function of the sintering temperature for 0.94BNT-0.6BT.....	110
Figure 4-40: The variation of k_p as a function of the sintering temperature for 0.94BNT-0.6BT.....	111
Figure 4-41: The temperature dependence of relative permittivity (ϵ_r) and dielectric loss ($\tan\delta$) of unpoled samples at 100 Hz, 1 kHz, 10 kHz, 100 kHz, and 1 MHz for 0.94BNT-0.06BT samples sintered at A) 1100, B) 1125, C)1150, D) 1175, and E)1200°C for two hours.	114
Figure 4-42: The XRD Patterns of BF powder calcined at 850°C for 5hours.....	115
Figure 4-43: The XRD Patterns of (0.94BNT-0.06BT)-x BF sintered at 1125°C for x values of A) 0.000, B) 0.025, C) 0.050, D) 0.075 and E) 0.100 BF.....	116
Figure 4-44: The XRD patterns of (0.94BNT-0.06BT)-x BF sintered at 1125°C at around $2\theta =$ A) 40° for (111) and B) 46.5° for (200).....	117

Figure 4-45: SEM micrographs of the (0.94BNT-0.06BT)-x BF samples sintered at 1125 °C for x values of A) 0.00, B) 0.025, C) 0.050, D) 0.075, and E) 0.10 (see the appendix for a low magnification images).....	118
Figure 4-46: The variation of relative density as a function of (0.94BNT-0.06BT)-x BF for samples sintered at 1125°C.....	119
Figure 4-47: The variation of grain size as a function of (0.94BNT-0.06BT)-x BF for samples sintered at 1125°C.....	119
Figure 4-48: The variation of relative permittivity of unpoled samples measured at room temperature as a function of x in (0.94BNT-0.06BT)-x BF for samples sintered at 1125°C.	120
Figure 4-49: The variation of d_{33} as a function of (0.94BNT-0.06BT)-x BF for samples sintered at 1125°C.	121
Figure 4-50: The variation of k_p as a function of (0.94BNT-0.06BT)-x BF for samples sintered at 1125°C.	121
Figure 4-51: The temperature dependence of relative permittivity (ϵ_r) and dielectric loss ($\tan\delta$) of unpoled samples at 100 Hz, 1 kHz, 10 kHz, 100 kHz, and 1 MHz for (0.94BNT-0.06BT)-x BF sintered samples for A) x=0.025, B) x=0.05, C) x=0.075, and D) x=0.1 sintered at 1125°C for two hours.....	124
Figure 4-52: The XRD patterns of A) $\text{Bi}_{0.5}\text{Na}_{0.5}\text{TiO}_3$ and B) $\text{Bi}_{0.455}\text{Na}_{0.475}\text{Ti}_{0.94}\text{O}_{2.82}$ samples, calcined at 850°C for five hours.	125
Figure 4-53: The XRD patterns of A) $0.94\text{B}_{0.5}\text{N}_{0.5}\text{TiO}_3\text{-}0.06\text{BaTiO}_3$ and B) $\text{Bi}_{0.455}\text{N}_{0.475}\text{Ti}_{0.94}\text{O}_{2.82}\text{-}0.06\text{BT}$ deficient samples, sintered at 1125°C for two hours.	126
Figure 4-54: SEM micrograph of A) $0.94\text{B}_{0.5}\text{N}_{0.5}\text{TiO}_3\text{-}0.06\text{BaTiO}_3$ and B) $\text{Bi}_{0.455}\text{N}_{0.475}\text{Ti}_{0.94}\text{O}_{2.82}\text{-}0.06\text{BT}$ samples sintered at 1125 °C (see the appendix for a low magnification photo).	126
Figure 4-55: The temperature dependence of relative permittivity (ϵ_r) and dielectric loss ($\tan\delta$) of unpoled sample at 100 Hz, 1 kHz, 10 kHz, 100 kHz, and 1 MHz for $0.94(\text{Bi}_{0.455}\text{Na}_{0.475}\text{Ti}_{0.94}\text{O}_{2.82})\text{-}0.06\text{BT}$ sample sintered at 1125°C for two hours.....	127
Figure 5-1: The heat capacity of A) $\text{Ba}_{0.85}\text{Ca}_{0.15}\text{Zr}_{0.1}\text{Ti}_{0.9}\text{O}_3$ and $0.94(\text{Bi}_{0.5}\text{Na}_{0.5}\text{TiO}_3\text{-}0.06(\text{BaTiO}_3))$ prepared by solid state method and sintered at 1450 and 1125°C respectively.....	132
Figure 5-2: Polarisation-hysteresis loops of BCZT sintered at 1400°C, measures at temperatures from -30 to 150°C.	134
Figure 5-3: The extracted polarisation versus temperature data from Figure 5-2 for a range of electric fields for BCZT sintered at 1400°C.	135
Figure 5-4: The pyroelectric coefficient as a function of temperature for BCZT sintered at 1400°C, and for different values of applied electric field.....	135
Figure 5-5: The ECE of BCZT sintered at 1400°C as a function of measurement temperature and for various applied electric field values.	136
Figure 5-6: The ECE figure of merit as a function of temperature of pure BCZT sintered at 1400°C, and for a range of applied electric field values.	137
Figure 5-7: The ECE of BCZT sintered at 1450°C as a function of measurement temperature and for various applied electric field values. (Pure BCZT sintered at 1400, 1425, 1475, and 1500°C in appendix II).....	138
Figure 5-8: The ECE figure of merit as a function of temperature of pure BCZT sintered at 1450°C, and for a range of applied electric field values. (Pure BCZT sintered at 1400, 1425, 1475, and 1500°C in appendix II)	139
Figure 5-9: The ECE as a function of temperature and applied electric field for BCZT-1% BNKT ceramics sintered at A) 1250, B) 1350, C) 1450, and D) 1500°C.(The ECE figure of merit as a	

function of temperature and applied electric field for BCZT-1% BNKT ceramics sintered at A) 1250, B) 1350, C) 1450, and D) 1500°C in Appendix II)	142
Figure 5-10: The ECE as a function of temperature and applied electric field for BCZT-3% BNKT ceramics sintered at A) 1250, B) 1350, C) 1450, and D) 1500°C.(The ECE figure of merit as a function of temperature and applied electric field for BCZT-3% BNKT ceramics sintered at A) 1250, B) 1350, C) 1450, and D) 1500°C in Appendix II)	145
Figure 5-11: Polarisation-hysteresis loops of BCZT-3% BNKT, sintered at 1350°C and measured from -30 to 150°C.....	146
Figure 5-12: The ECE as a function of temperature and applied electric field for BCZT-5% BNKT ceramics sintered at A) 1250, B) 1350, C) 1450, and D) 1500°C.(The ECE figure of merit as a function of temperature and applied electric field for BCZT-5% BNKT ceramics sintered at A) 1250, B) 1350, C) 1450, and D) 1500°C in Appendix II)	148
Figure 5-13: The ECE of the pure BCZT sintered at 1450°C measured between -30 and 125°C, using the direct method. (Pure BCZT sintered at 1400, 1425, 1475, and 1500°C in Appendix II).....	150
Figure 5-14: The ECE figure of merit of pure BCZT sintered at 1450°C and measured between -30 and 125°C (Pure BCZT sintered at 1400, 1425, 1475, and 1500°C in Appendix II).	151
Figure 5-15: The ECE of the BCZT-1%BNKT sintered at A) 1250, B) 1350, C) 1450, and D) 1500°C measured between -30 and 125°C and at 10, 20, and 30 kV/cm.....	153
Figure 5-16: The ECE of the BCZT-3%BNKT sintered at A) 1250, B) 1350, C) 1450, and D) 1500°C measured between -30 and 125°C and at 10, 20, and 30 kV/cm.....	156
Figure 5-17: The ECE of the BCZT-5% BNKT sintered at A) 1250, B) 1350, C) 1450, and D) 1500°C measured between -30 and 125°C and at 10, 20, and 30 kV/cm by a direct method.	158
Figure 5-18: The ECE of BNT-BT sintered at A) 1100, B) 1125, C) 1150, D) 1175, and E) 1200°C measured between -30 and 140°C by the indirect method.....	168
Figure 5-19: The polarisation-hysteresis loops of BNT-BT sintered at 1150°C measured from -30 to 150°C.	168
Figure 5-20: The ECE figures of merit of the BNT-BT samples sintered at A) 1100, B) 1125, C) 1150, D) 1175, and E) 1200°C measured between -30 and 140°C by the indirect method.	171
Figure 5-21: The ECE of the (1-x) BNT-BT-x BF samples for x A) 0.025, B) 0.05, C) 0.075, and D) 0.1 measured between -30 and 140°C by the indirect method.....	174
Figure 5-22: The ECE figures of merit of the (1-x) BNT-BT-x BF samples for x A) 0.025, B) 0.05, C) 0.075, and D) 0.1 measured between -30 and 140°C by the indirect method.	176
Figure 5-23: The ECE of the BNT-BT deficient samples sintered at 1125°C measured between -30 and 140°C by the indirect method.	177
Figure 5-24: The ECE figure of merit of the BNT-BT deficient samples sintered at 1125°C measured between -30 and 140°C by the indirect method.	178
Figure 5-25: The ECE of the pure BNT-BT sintered at A) 1100, B) 1125, C) 1150, D) 1175, and E) 1200°C measured between -30 and 125°C by the direct method.	182
Figure 5-26: The ECE figure of merit of the pure BNT-BT sintered at A) 1100, B) 1125, C) 1150, D) 1175, and E) 1200°C measured between -30 and 125°C by the direct method.	185
Figure 5-27: The ECE of the (1-x) BNT-BT-x BF for x A) 0.025, B) 0.05, C) 0.075, and D) 0.1 measured between -30 and 125°C by the direct method.....	187
Figure 5-28: The ECE figure of merit of (1-x) BNT-BT-x BF for x A) 0.025, B) 0.05, C) 0.075, and D) 0.1 measured between -30 and 125°C by the direct method.....	189
Figure 5-29: The ECE of BNT-BT deficient samples measured between -30 and 125°C by the direct method.....	190

Figure 5-30: The ECE figure of merit of BNT-BT deficient samples measured between -30 to 125°C by the direct method.	191
Figure 5-31: the comparison between ECE and relative density for all samples including BCZT, BCZT-BNKT, BNT-BT, BNT-BT-BF and BNT-BT with deficiency.....	195
Figure 5-32: the comparison between ECE and polarisation for all samples including BCZT, BCZT-BNKT, BNT-BT, BNT-BT-BF and BNT-BT with deficiency.....	196
Figure 5-33: the comparison between ECE and d_{33} for all samples including BCZT, BCZT-BNKT, BNT-BT, BNT-BT-BF and BNT-BT with deficiency.....	196
Figure 5-34: A comparison between ECE and relative density for BCZT, BCZT-1, 3 and 5%BNKT (ECE extracted of 30 kV/cm electric field for comparison).....	197
Figure 5-35: The comparison between ECE and relative density for BNT-BT.....	198

LIST OF TABLES

Table 2-1: Summary of BT properties at room temperature.....	11
Table 2-2: A summary of the 50BZT-50BCT properties, based on references.	14
Table 2-3: A summary of the BF properties taken from the literature, and near MPB with BT.....	15
Table 2-4: A summary of the BNT properties, and BNT with deficiency. A deficiency in BNT structure can change its properties.	17
Table 2-5: Summary of the properties of BNT-BT, prepared with different methods. The processing of the raw materials can affect the final properties.	21
Table 2-6: Summary of the ECE of BNT-based materials; with measurement and preparation method. The results show that the method of preparation affects the ECE.	39
Table 2-7: Summary of the ECE of BCZT-based materials; with measurement and preparation method. The results show that the method of preparation affects the ECE, and there are some differences in the ECE when measured by different methods.	43
Table 2-8: Summary of the ECE of thin films of BNT- BT by the indirect method, and BT by the indirect and DSC methods.	45
Table. 3-1: List of raw materials.....	51
Table 3-2: The calcination temperature of the powders.....	51
Table 3-3: The selected sintering temperatures for the green pellets	53
Table 4-1: Summary of the properties of BCZT sintered at different temperatures	77
Table 4-2: Summary of the properties of BCZT and BCZT-1, 3, and 5% BNKT	100
Table 4-3: The effect of the sintering temperature on the properties of 0.94BNT-0.06BT.	115
Table 4-4: Summary of the properties of (1-x) (0.94BNT-0.06BT)-x BF for x=0, 0.025, 0.05, 0.075, and 0.1.	124
Table 4-5: Summary of the properties of $0.94\text{B}_{0.5}\text{N}_{0.5}\text{TiO}_3\text{-}0.06\text{BaTiO}_3$, compared to $0.94(\text{Bi}_{0.45.5}\text{Na}_{0.47.5}\text{Ti}_{0.94}\text{O}_{2.82})\text{-}0.06\text{BT}$	127
Table 5-1: A summary of the ECE of BCZT- and BCZT-based materials using the direct and indirect methods.....	162
Table 5-2: A summary of the ECE of BNT-BT and BNT-BT-based materials using the direct and indirect methods.	194

Nomenclature

Symbol	Definition	Symbol	Definition
AFE	Anti - ferroelectric	KNN	$K_{(1-x)}Na_xNbO_3$
Au	Gold	KN	$KNbO_3$
Ba	Barium	LCEP	Line of critical end points
BCT	$BaCaTiO_3$	MLC	Capacitors or multilayers capacitors
BCZT	$Ba_{0.85}Ca_{0.15}Ti_{0.9}Zr_{0.1}O_3$	MPB	Morphotropic phase boundary
BF	$BiFeO_3$	Na	Sodium
Bi	Bismuth	O	Oxygen
BNT	$Bi_{0.5}Na_{0.5}TiO_3$	P	Polarization $\mu C/cm^2$
BNKT	$Bi_{0.50}(Na_{0.82}K_{0.18})_{0.50}TiO_3$	P_r	Remnant polarization $\mu C/cm^2$
BT	$BaTiO_3$	p_i	Pyroelectric coefficient $C/m^2.K^1$
BZT	$BaZrTiO_3$	PPT	Polymorphic phase transition
Ca	Calcium	PMN - PT	$0.75Pb(Mg_{1/3}Nb_{2/3})O_3 - 0.25PbTiO_3$
C_p (s)	Specific heat capacity of the specimen, J/(g*K)	PZT	Lead- zirconate-titanate
C_p (st)	Specific heat capacity of the sapphire standard, J/(g*K)	Q	Heat J
D	Electric displacement C/m^2	RC	Refrigerant capacity
d_{33}	Piezoelectric constant pC/N	S	Strain
DSC	Differential scanning calorimetry	T	Temperature °C
E	Electric field kV/cm	T_c	Curie temperature °C
EC	Electrocaloric	Ti	Titanium
ECE	Electrocaloric effect K or °C	V	Voltage V
EC materials	Electrocaloric materials	XRD	X-ray diffraction
f_r	Resonance frequency Hz	Z	Impedance Ω
f_a	Anti - resonance frequency Hz	Zr	Zirconium
FE	Ferroelectric	σ_j	Applied stress N/m^2
ICP	Invariant critical point	ρ	Density g/cm^3
IM	Indirect method	ϵ_r or $\epsilon_{33}^T/\epsilon_0$	Relative permittivity
K	Potassium		
k_p	Electromechanical coupling factor %		

Chapter 1

Introduction

1.1 Introduction

In recent years science and technology has been grown rapidly in many fields. However, these improvements have led to increased usage of non-environmental friendly materials and increased emissions of greenhouse gases. One of these technologies is cooling systems based on the compression of gases such as Freon, which are ubiquitous but suffer from environmental problems. Environmental agencies and government organizations have started to address this problem by encouraging replacement of these materials [1]. Therefore, research is focusing on the development of alternative cooling technologies: potential candidates include systems based on thermoelectric, magnetocaloric and electrocaloric effects. The development of cooling systems based on thermoelectric materials, also known as Peltier cooling systems, are now available commercially, although the efficiency of this technology is quite low (around 10%) [2], and is therefore not attractive as a replacement for the compressed gas systems which typically have efficiencies of 40-50% [2]. A lot of research has been carried out on magnetocaloric cooling systems with efficiencies of around 60-70% being reported [2]. In spite of such high efficiencies, magnetocaloric materials and the necessary magnetic field are expensive due to the need to use rare earth materials [3]. One of the newest methods is the use of electrocaloric materials to make a cooling system with the same and sometimes higher efficiency than magnetocaloric cooling systems. Such materials can be used in refrigeration applications instead of gas evaporation, including micro and nano-technology electronic devices. The electrocaloric effect concerns the ability of a material to change temperature in response to an applied electric field and can be considered as the reverse of the pyroelectric effect. As such, the search for suitable materials has concentrated on those exhibiting pyroelectric behaviour, and in particular, those which are ferroelectric, since all ferroelectric materials are pyroelectric and, from a commercial perspective, usually easier for production. Electrocaloric materials can be used in cooling systems utilizing adiabatic and isothermal conditions. Ferroelectric materials based on lead zirconate titanate (PZT) have been ubiquitous for many years in sensing and actuating applications. However, the high content of lead, which can be harmful to both the environment and humans, has recently driven legislation and research to find lead-free replacements. So, similar to greenhouses gases, the European Parliament has adopted directives “Waste Electrical and Electronic Equipment” (WEEE) and “Restriction of the use of certain Hazardous Substances in electrical and electronic equipment” (RoHS) in order to prevent, reuse, or recycle waste electrical and electronic equipment and to protect human

health and environment by the substitution of hazardous substances by safe or safer materials” [2-6].

This thesis begins with the literature review chapter. The first part, briefly explains about piezoelectric, pyroelectric (electrocaloric), ferroelectric and lead-free ferroelectric materials and then focuses on the selected materials for this project. This is followed by an explanation about the type of the new cooling systems and their positive and negative points. After that, the key properties of electrocaloric materials are explained including materials that have been selected for further study. The different methods are discussed for measuring electrocaloric effect (ECE). Existing methods can be divided into two main categories: direct and indirect method. Based on the existing facilities, one indirect method was selected to measure ECE and for direct measurements, an experimental device was designed and fabricated. The ECE of selected materials were extracted and are discussed from the literature review and at the end, the discussion leads to the aim of this project. In the experimental chapter, the fabrication and characterisation procedures used in the work are explained. This is followed by piezoelectric and ferroelectric measurements; ECE measurements; and the design of the direct reading apparatus. The fourth and fifth chapters are results and discussion. This starts with confirmation of the procedure and optimization by property measurements. ECE was measured and the results discussed for all the samples. The effect of additives was also investigated. The sixth chapter is conclusions, followed by the seventh chapter describing future work and recommendations.

Chapter

2 Literature

Review

2.1 Pyroelectric materials

2.1.1 Piezoelectric, pyroelectric, and ferroelectric materials

Some materials show changes in their dimensions when an electric field is applied to them, and some show an electric polarisation when stress is applied. These materials are known as piezoelectric materials. They can exhibit direct or indirect effects. The direct effect can be seen in the materials when they are affected by stress and show electric polarisation, while the indirect effect can be seen in the materials when they are affected by electric fields and generate strain.

The direct piezoelectric effect can be described by the following equation:

$$D_i = d_{ijk} \sigma_{jk} + \epsilon_{kl} E_k \quad (2-1)$$

(Where D_i is electric displacement, d_{ij} is the piezoelectric charge coefficient, and σ_j is applied stress, ϵ_{kl} is permittivity and E is electric field.)

The indirect piezoelectric effect can be described by the following equation:

$$S_{ij} = d_{kij} E_k + s_{ijkl} \sigma_{kl} \quad (2-2)$$

(Where S_i is the electric field-induced strain, E_j is the applied electric field, and d_{ij} is the piezoelectric charge coefficient, s is compliance and σ is stress.)

Pyroelectricity is the ability of dielectric materials (polar materials) to generate an electric field due to the development of polarisation when their temperature changes (the direct effect), or when they change their temperature due to an applied electric field, which is the so-called electrocaloric effect (indirect effect). In cooling systems, this can be used by a cycle including changing the entropy in isothermal conditions, and changing the temperature in adiabatic conditions.

In polar materials, the dielectric displacement is given by:

$$D = \epsilon_0 E + P \quad (2-3)$$

(Where D is the electric displacement, ϵ_0 is the permittivity of the free spaces, E is the electric field, and P is polarisation.)

$$\text{Therefore: } \frac{\partial D}{\partial T} = \frac{\partial P}{\partial T} + E \frac{\partial \epsilon}{\partial T} \text{ or } P_g = p_i + E \frac{\partial \epsilon}{\partial T} \quad (2-4)$$

(Where P_g is the generalised pyroelectric coefficient and p_i is true pyroelectric coefficient.)

The temperature coefficient of the permittivity of ferroelectric materials is high, so the magnitude of p_i and $E \frac{\partial \epsilon}{\partial T}$ are comparable to each other.

Pyroelectric materials are polar materials, so are piezoelectric as well. For pyroelectric materials under stress, the thermal expansion due to the changing temperature can cause a strain, and affect the surface charges of pyroelectric materials and therefore their pyroelectricity. In this way, the pyroelectric coefficient at constant stress can be calculated by the following two-part equation:

$$P = P_g + d_{ijk} c_{jklm} \alpha_{lm} \quad (2-5)$$

(Where P is the whole and P_g is the primary pyroelectric coefficient, as explained above, and for the secondary pyroelectric coefficient: d_{ijk} is the piezoelectric strain tensor under a constant stress, c_{jklm} is the elastic stiffness tensor under constant stress and an electric field, and α_{lm} the thermal expansion tensor under a constant electric field.)

The secondary pyroelectric coefficient can be as high as the primary pyroelectric coefficient in some piezoelectric materials, and especially in thin films. More explanation can be found in section 2.3.1.5.

Ferroelectric materials show both piezoelectric and pyroelectric properties, and are also able to change their polarisation direction through the application of an electric field. The best way to categorise piezoelectric, pyroelectric, and ferroelectric materials is through the symmetry of their crystal classes (there are seven crystal systems and 32 crystal classes). Twenty-one of them have a structure with no centre of symmetry, which in principle can show the piezoelectric effect. One of these exhibits symmetrical characteristics in another way, and so is not piezoelectric; ten are pyroelectric and polar materials, in which a change in temperature causes a change in their polarisation; and the rest do not show spontaneous polarisation. Some of the polar materials can change the direction of polarisation due to an electric field or mechanical stresses, and these are known as ferroelectric materials. Figure 2-1 provides a summary of the above description [7-9]. Ceramics materials can be formed in single-crystal or polycrystalline forms. Single crystals are difficult to form and are expensive; from a commercial viewpoint, polycrystalline materials are more viable for mass-production. From this perspective, only ferroelectric materials can be used as polycrystalline piezoelectric and pyroelectric materials because their polarisation can be aligned through the application of electric fields [10].

All ferroelectric materials are pyroelectric and piezoelectric but the opposite is not the case, so explaining the nature of ferroelectric materials also covers piezoelectric and pyroelectric materials. The general characteristics that usually investigate for ferroelectric, piezoelectric and pyroelectric materials can be summarised as follows [10, 11]:

- 1- The crystal structure, such as a perovskite structure
- 2- A morphotropic phase boundary (MPB)
- 3- An electronic structure of the atoms and ions (polarisability)

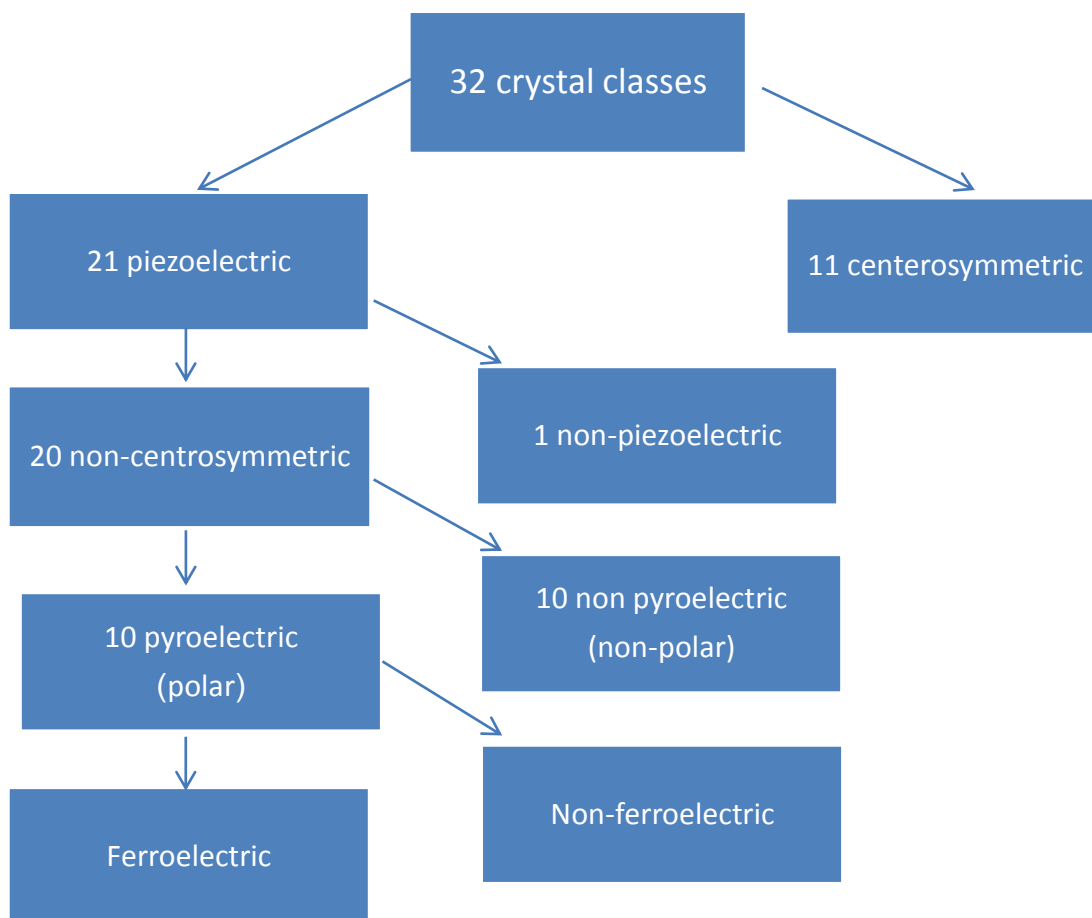


Figure 2-1: The classification of crystals with piezoelectric, pyroelectric, and ferroelectric effects [9].

The crystal structures of ferroelectric materials

The main crystal structures for ferroelectric materials can be divided into four categories, as follows [10, 12]:

- 1- A perovskite structure, with the chemical composition ABO_3
- 2- A bismuth-layer structure (BLS – a variation of the perovskite structure) with the chemical composition $Bi_2A_{x-1}B_xO_{3x+3}$
- 3- A $LiNbO_3$ structure, with the same chemical composition as perovskite
- 4- A potassium tungsten bronze structure, with the chemical composition $A_xB_2O_6$

The majority of research in this area has focused on perovskite structures. For this reason, we explain about this structure in more detail [7-9]. A perovskite structure has the chemical composition ABO_3 , with a cubic unit cell, a large cation A in the corner, a smaller cation B in the centre of the structure, and oxygen at the centre of the faces, as can be seen in Figure 2-2. Based on the ionic radii, cations can be located at the A or B sites, and some can be found at both sites. Smaller cations occupy the octahedral holes, so tilting it can result in ferroelectricity properties.

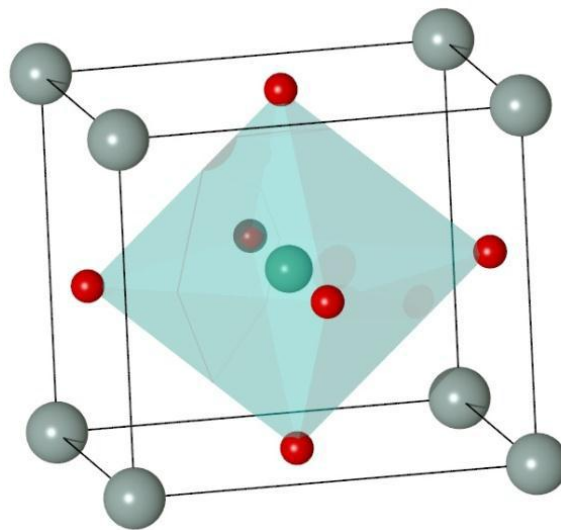


Figure 2-2: Cubic perovskite unit cell. A-site cations are grey, the B-site cation is green, and oxygen is red [13].

A morphotropic phase boundary (MPB)

An MPB is a change in regions of different symmetries with composition dependence. The most famous compound with an MPB is PZT ($PbZr_xTi_{(1-x)}O_3$ ($0 < x < 1$)) (Figure 2-3). Large d_{33} can be seen near these boundaries due to the mixture of phases and a flattening of the energy barrier between two different symmetries [10, 11, 14].

The electronic structure of ferroelectric materials

Another important issue in ferroelectric materials is the electronic structure of the elements that constitute the ferroelectric materials. The number of electrons in the outer layer, the polarisability of the ions, and the tendency to form chemical bonds by the hybridisation of electronic orbitals are the main factors of a ferroelectric material. For example, Pb and Bi have high polarisability and a lone electron pair in the outer shell [10].

2.1.1.1 Lead-based ferroelectric materials

The best known compound that is a ferroelectric material is $\text{PbZr}_x\text{Ti}_{(1-x)}\text{O}_3$ ($0 < x < 1$), which shows high piezoelectric properties, piezoelectric charge coefficient ($d_{33} = 500\text{-}600$ pC/N), and electromechanical coupling coefficients (50-60%) near the MPB at around $x=0.48$ -0.52. PZT is a solid solution of PbZrTiO_3 and PbTiO_3 (Figure 2-3). It has a perovskite structure with MPB and a good electronic structure for a combination in which Pb occupies the corner of the perovskite structure and Zr or Ti occupies the body-centred positions. The main problem with this compound is that it contains more than 60% Pb, which is toxic and therefore far from being environmentally friendly if used in a cooling system. For this reason, we focus on explaining lead-free materials [11, 13, 14].

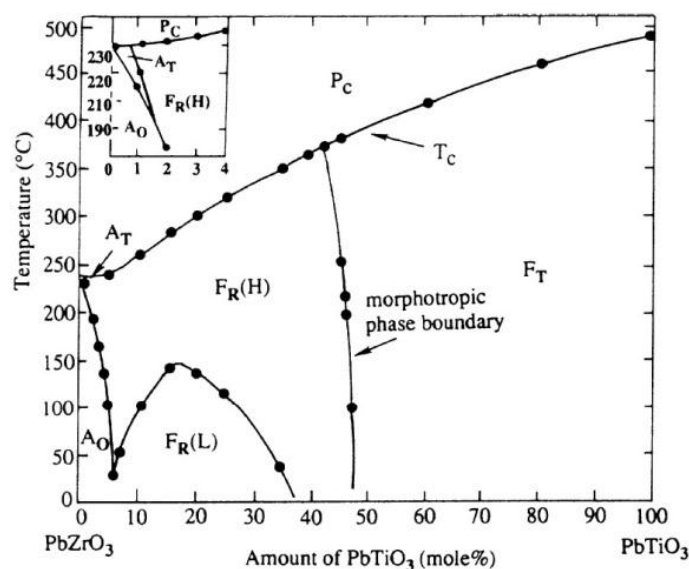


Figure 2-3: A phase diagram of PZT with MPB, between the rhombohedral and tetragonal phases [7].

2.1.1.2 Lead-free ferroelectric materials

In recent years, many researchers have sought to find a suitable replacement for PZT, and good progress has been made, with the best candidates being based on BaTiO_3 (BT), BiFeO_3 (BF), $\text{Bi}_{0.5}\text{Na}_{0.5}\text{TiO}_3$ (BNT), and related materials [10, 11, 14, 15]:

2.1.1.2.1 BT: BaTiO_3

BT was developed for the first time in the 1940s and 1950s. It has a perovskite structure, with a Curie temperature of 130°C . Below -80°C BT is rhombohedral, above -80°C it becomes orthorhombic, then it becomes tetragonal at around 0°C , while above 130°C it is cubic. It has a piezoelectric constant of 191pC/N , but high relative permittivity (1680), which makes it able to be used for capacitors or multilayer capacitors (MLC). It has a polymorphic phase transition (PPT), as illustrated in Figure 2-4; its characteristics are outlined in Table 2-1 [7, 11, 16]. Some additives such as LiF usually decrease BT's sintering temperature, without any effect on the dielectric properties [17].

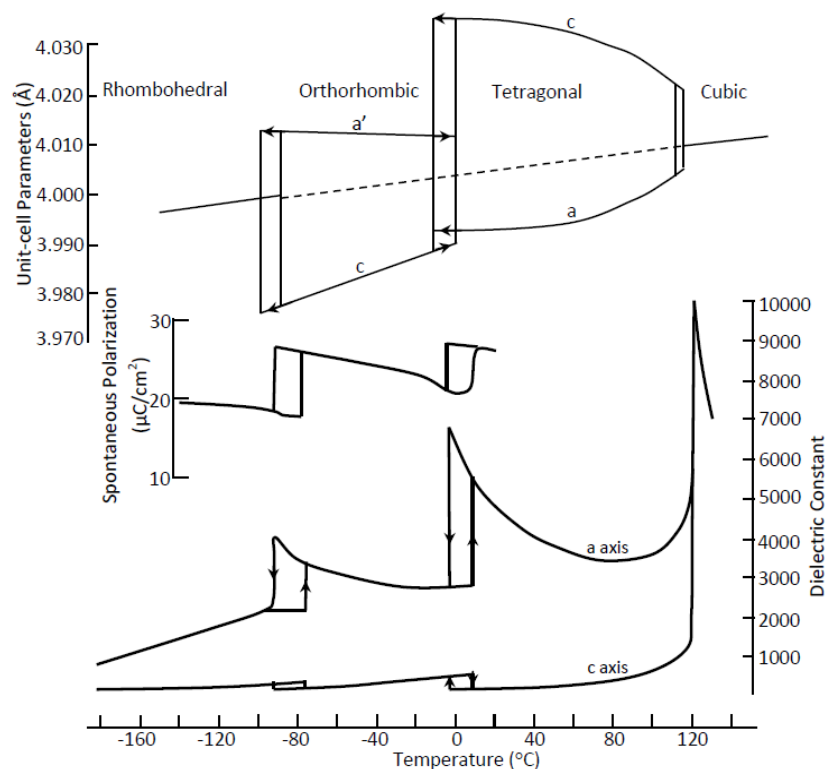


Figure 2-4: Polymorphic Phase Transition in BT single crystals, observed through changes in the unit cell parameters, spontaneous polarisation, and dielectric constant [7, 11].

Table 2-1: Summary of BT properties at room temperature [11].

Material	d_{33} pC/N	$(\epsilon_{33}^T/\epsilon_0)$	k_p %
BaTiO ₃ (ceramic)	191	1680	29
BaTiO ₃ (single crystal)			
Parallel [001]	125	-	-
Parallel [111]	203		
At high field	295		

2.1.1.2.1.1 Barium-calcium-titanate: $(\text{Ba}_{(1-x)}\text{Ca}_x)\text{Ti}_x\text{O}_3$ BCT

One of the additives that has been studied for BT, is calcium. Ca can be a substitute for Ba in A sites of the perovskite structure. The addition of 20%mol of Ca increases the Curie temperature from 130°C to around 170°C [18]. The addition of 20%mol Ca causes the orthorhombic and rhombohedral phase transition to take place at lower temperatures, and adding more Ca (30%mol) leads to the disappearance of these phases and shifts them to a tetragonal phase. The addition of Ca decreases the dielectric constant (from 1680 to around 1000 at RT) due to the non-ferroelectric nature of CaTiO₃.

2.1.1.2.1.2 Barium-titanate-zirconate: $\text{Ba}(\text{Ti}_{(1-x)}\text{Zr}_x)\text{O}_3$ (BZT)

One compound that has been studied in BT is Barium-zirconate (BaZrO₃). The addition of BaZrO₃ decreases the Curie temperature (Figure 2-5), makes a diffuse phase transition in BT, and leads to relaxor behaviour at around 0.29mol of addition. Furthermore, zirconium (Zr) is more stable than titanium (Ti) in the B site, which has led to its use in applications such as capacitors. The transformation of the tetragonal, orthorhombic, and rhombohedral phases are influenced by the doping, with the tetragonal and orthorhombic phases not extending beyond 10-15% mol of Zr, as can be seen in Figure 2-5 [19-22].

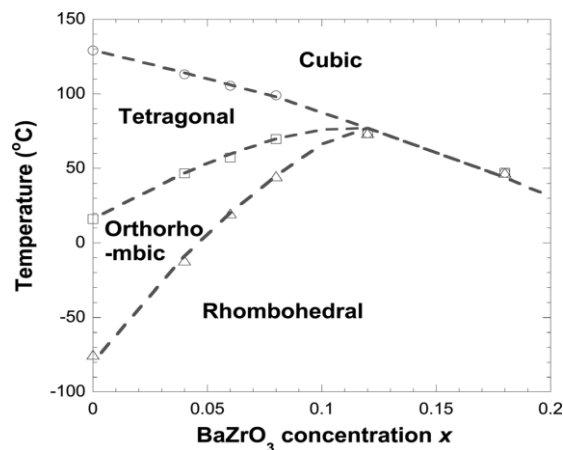


Figure 2-5: Phase diagram of $x\text{BaZrO}_3-(1-x)\text{BaTiO}_3$ ceramics with $0 < x < 0.2$ [20].

Adding only 0.06%mol of Zr increases the piezoelectric constant to 420 from 193pC/N for BT, and the coupling factor from 29% to 49%. The point (Figure 2-5) at which cubic, tetragonal, orthorhombic, and rhombohedral (or in general several phases) are coexistent is called the invariant critical point (ICP) [20, 22].

2.1.1.2.1.3 BCZT

One of the most recent lead-free piezoelectric and ferroelectric compositions that has been found is a solid solution of x Ba $(\text{Ti}_{0.8}\text{Zr}_{0.2})\text{O}_3$ -(1- x) $(\text{Ba}_{0.7}\text{Ca}_{0.3})\text{TiO}_3$, which can be abbreviated as BZT-BCT or BCZT. This shows large piezoelectric properties that are comparable with PZT, and in some parts better than it. One of the weaknesses of this compound is a low Curie temperature ($T_c=100^\circ\text{C}$) compared to PZT ($T_c=240$ to 450°C), but in thermal camera, door sensors and light detectors which use pyroelectric coefficient (higher pyroelectric coefficient can be seen near Curie temperature), this can be a positive point. The best properties such as d_{33} and dielectric constants have been achieved at the 50BZT-50BCT composition, as can be seen in Table 2-2 [15, 23-29]. This composition has $d_{31}=200$ pC/N at room temperature [30]. The high piezoelectric properties can be attributed to a triple point in this compound, and instabilities of the structure at both R-T and T-C transitions. In situ X-ray diffraction measurements during electric field application studies have shown that there are nanodomains at 50BZT-50BCT that possess low domain wall energy, a low-energy barrier between the two ferroelectric phases, and elastic softening [31-34]. In fact, based on the diagram phase (Figure 2-6-A), when the amount of the tetragonal phase decreases, the domain wall motion will increase until the MPB. Near the MPB, the domain wall motion upon application of an electric field that is much easier due to symmetry mismatch of the octahedral tilting between TiO_6 and ZrO_6 , which makes a random local strain and so a high d_{33} [35-39].

The piezoelectric coefficient (d_{33}) is related to the intrinsic and extrinsic piezoelectric contribution [40]: the intrinsic contribution depends on lattice deformation, and the extrinsic on the domain wall motion or inter-phase boundaries (reversible or irreversible). In 50BZT-50BCT, 80% of d_{33} is extrinsic, of which most is related to the domain wall motion. Achieving such a high d_{33} is difficult due to the high sensitivity of the compound to fabrication parameters such as the sintering temperature and particle size of the raw materials [41, 42]. Other parameters which have been shown to affect d_{33} are calcination temperature, grain boundaries, and the grain size of sintered samples, which for the compound, atomic

arrangement of grain boundaries becoming more similar to grain at 1250-1300°C for the calcination temperature due to a decrease in internal stress and continually crossing domains forming grain boundaries. The optimised temperature for the sintering of this sample is around 1450°C, which leads to optimised density and a grain size of around 32 μ m; a higher grain size makes domain wall motion easier [43].

There are some discussions [44] about the phase transformation of 50BZT-50BCT from around -10°C to room temperature, which are rhombohedral-tetragonal or rhombohedral-orthorhombic-tetragonal (Figure 2-6). The evidence shows that [24] if there is an orthorhombic phase at RT, it cannot be detected by XRD due to the small amount, but Raman spectroscopy or Synchrotron Radiation proves the orthorhombic variety [45]. Kebble et al. [46] believe that the transformation from rhombohedral to tetragonal cannot happen directly due to the absence of a group-subgroup relationship, and that an intermediate phase (orthorhombic) is needed. They did their experiment on x BZT- (100-x) BCT for x=20, 32, 40 and 50 and from 80K to 450K. They used high resolution powder diffraction experiments at synchrotron source that is more powerful than conventional X-ray tubes with high brilliance and many orders of magnitude. In addition, the difference between the strain forces of the tetragonal and rhombohedral phases is quite high, which makes an intermediate phase necessary. In this case, the d_{33} is higher at the phase boundary of tetragonal and orthorhombic phases, and the tetragonal-orthorhombic phase boundary has a lower storage modulus (which makes a mechanically softer state, and therefore higher elastic compliance) and lowers internal friction, as opposed to the rhombohedral-orthorhombic phases, which cause higher d_{33} . BCZT displays normal piezoelectric behaviour, and does not show any frequency dependence for permittivity at different temperatures. When Zr replaces Ti at B-site in BZT at a level higher than 0.25%, it changes from normal piezoelectric behaviour to relaxor, but the amount of substitution of Zr at the B-site in 50BZT-50BCT is around 10%, but BCZT displays relaxor behaviour at a low sintering temperature because it causes a small grain size, with a greater amount of pores in the microstructure [43].

One of the problems with 50BZT-50BCT is that it is only suitable for a narrow range of temperatures. If it is heated above the Curie temperature and cooled again, the piezoelectric properties will be affected, due to changes in the amount of ferroelectric phases; this is because the nucleation of the tetragonal phase during cooling will completely prevent the formation of a rhombohedral phase in the cooling process [36]. In the phase diagram of this compound, the MPB has a significant curvature and not similar to PZT, which makes it

sensitive to any changes in both composition and temperature. Another problem is that its piezoelectric properties decrease under compressive stress, which is higher for the rhombohedral part in comparison to the tetragonal area, while this is very difficult for PZT [47]. The best ferroelectric and piezoelectric properties can be found in the [001] and [111] direction, respectively [37].

Table 2-2: A summary of the 50BZT-50BCT properties, based on references [15, 42, 43, 48, 49].

Material	d_{33} pC/N	$(\epsilon_{33}^T/\epsilon_0)$	k_p %	P_r $\mu\text{C}/\text{cm}^2$	E_c kV/cm	T_c $^\circ\text{C}$
50BZT - 50BCT	450 - 620	2500-3060	48-57	14-16	1.8-2.2	90-105

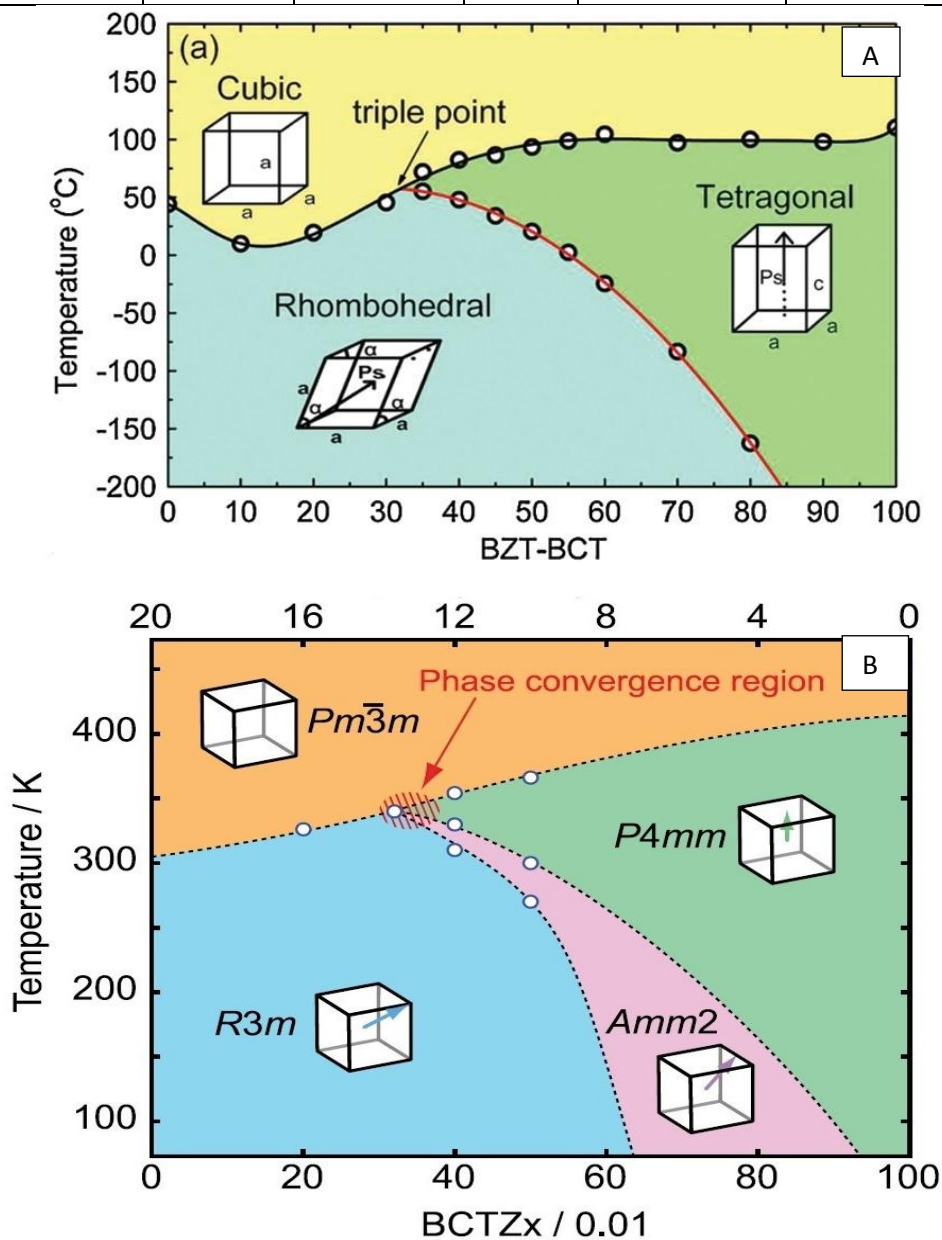


Figure 2-6: Phase diagrams of BZT-BCT; A is the first one reported by Liu et al. [15], which shows the rhombohedral and tetragonal phases, and B is the revised diagram of BZT-BCT, as reported by Keeble et al. [46], which shows the orthorhombic phase, between the rhombohedral and tetragonal phases.

BCZT exhibits a large pyroelectric coefficient of $17.17 \times 10^{-4} \text{ C/m}^2 \cdot \text{K}^{-1}$ at 300 K [50]. Some additives, like Li and Y_2O_3 , can decrease the sintering temperature from 1450 to around 1350°C without a big effect on the piezoelectric properties, (for example, d_{33} of 0.5wt%Li for BCZT decreases to 560 pC/N [51-53]).

Furthermore, the effect of BCZT on the other ferroelectric compositions like $\text{Bi}_{0.51} (\text{Na}_{0.82} \text{K}_{0.18})_{0.5} \text{TiO}_3$ with the goal of reaching higher properties has been investigated, and an additional 0.02mol% of BCZT can increase the d_{33} of BNKT from around 100 pC/N to around 206 pC/N [54].

The effect of Mn on the 50BZT-50BCT composition has been investigated; by adding this additive, the d_{33} goes down, and the compound shows relaxor behaviour [55].

In a similar composition $(\text{Ba} (\text{Ti}_{0.8} \text{Hf}_{0.2}) \text{O}_3 - (\text{Ba}_{0.7} \text{Ca}_{0.3}) \text{TiO}_3)$ and BCT-BTS), an MPB was found with high piezoelectric and ferroelectric properties, but Sr and Hf are both more expensive than Zr, and the properties are a bit lower than BCT-BZT [10, 56].

2.1.1.2.2 Bismuth-ferrite or BF: BiFeO_3 and related materials

BiFeO_3 is one interesting compound that possesses both ferroelectric and ferromagnetic properties. In this compound, Bi occupies the A-site and Fe the B-site in the perovskite structure, and spontaneous polarisation can be achieved by the electric and magnetic fields. It can then form a rhombohedral phase in bulk samples, and monoclinic for thin films. A substitution of 14mol% samarium makes a MPB with BF; a summary of its properties can be seen in Table 2-3 [11, 57, 58].

Table 2-3: A summary of the BF properties taken from the literature, and near MPB with BT [11, 59].

Material	d_{33} pC/N	$(\epsilon_{33}^T/\epsilon_0)$	k_p %	P_r $\mu\text{C}/\text{cm}^2$	E_c kV/cm	T_c $^\circ\text{C}$
BiFeO_3	15-60	30	-	-	-	-
BiFeO_3 thin film	70	-	-	50-60	-	-
BiFeO_3 single crystal	-	-	-	100	12	870
BiFeO_3 ceramic	50-60	-	-	40	-	-
$\text{Bi}_{0.86}\text{Sm}_{0.14}\text{FeO}_3$	110	-	-	70	-	-
0.75 BF -0.25 BT	116	557		22.9	39.3	619
0.67 BF -0.33 BT	70	750		15.2	20.7	605

One of the substitutions that has been investigated for BF is BT. For compositions $(1-x)BF - xBT$ the structure is tetragonal for $x=0.92-1$, cubic for $x=0.33-0.92$, and rhombohedral for $x=0-0.33$. Adding BT increases the dielectric constant of BF ($x=0-0.33$), the low-field d_{33} decreases, and the high-field d_{33} increases [59].

2.1.1.2.3 BNT: $\text{Bi}_{0.5}\text{Na}_{0.5}\text{TiO}_3$

BNT was reported for the first time in the 1960s and has been developed by researchers in the past two decades. Like other compositions, the calcination of BNT depends on the particle size of the raw materials; a small particle size leads to a lower calcination temperature and, in general, better properties. Methods such as sol-gel, citrate, and various solid-state methods have been employed to calcine the BNT. Aksel et al. [60] studied the formation process of BNT and found that due to the similarity of its structure at high temperatures (a Cubic body centred structure at 500°C) to perovskite structures, bismuth oxide is the host structure in this process. Figure 2-7 shows a schematic of the transformation of the raw materials (TiO_2 , Bi_2O_3 , and Na_2CO_3 using solid-state methods) to BNT. The formation of BNT starts at 500°C and finishes at around $700-850^\circ\text{C}$ (depending on the processing conditions and the particle size of the raw materials).

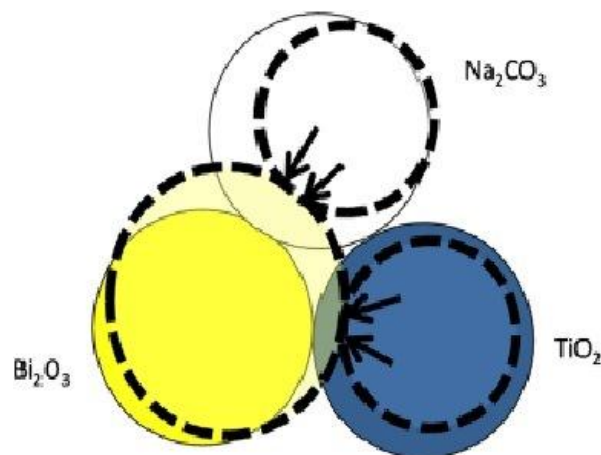


Figure 2-7: Schematic of BNT formation mechanisms: the diffusion of TiO_2 and Na_2CO_3 into Bi_2O_3 and the transformation of Bi_2O_3 into BNT [60].

BNT is rhombohedral at room temperature, transforms to a tetragonal phase at about 200°C , and changes to the cubic phase at about 540°C . Between 200°C and 320°C , BNT exhibits anti-ferroelectric characteristics, and is not yet understood. Some researchers believe that there is an intermediate anti-ferroelectric phase, while others believe that such a phase is not

completely anti-ferroelectric. In addition, some researchers believe that the rhombohedral phase changes to orthorhombic and after that, changes to tetragonal at 320°C. Tu et al. and Aksel et al. [61, 62] have stated that there is a coexistence of rhombohedral and tetragonal forms at around 250-310°C, and found that the formation of nanoscale regions disrupt the long-range ferroelectric order. Beanland et al. and Dorcet et al. [63, 64] believe that the rhombohedral and tetragonal phases coexist at room temperature. However, all researchers have the same view about the transformation at 200°C, which is the temperature at which BNT transfers from a polarised to a depolarised state, which is known as the depolarisation temperature (T_d) [11, 60, 61, 63, 65-73]. Figure 2-8 details the pseudo-cubic perovskite structure of BNT, which shows that Bi and Na randomly occupy A sites, while Ti occupies B sites. Its characteristics are outlined in Table 2-4.

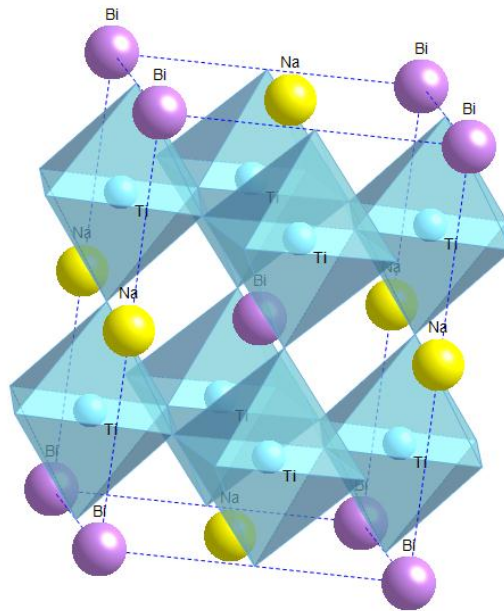


Figure 2-8: The perovskite structure of BNT: Bi and Na at the A site, Ti at the B site [11].

Table 2-4: A summary of the BNT properties, and BNT with deficiency. A deficiency in BNT structure can change its properties.

Material	d_{33} pC/N	$(\epsilon_{33}^T/\epsilon_0)$	k_p %	P_r $\mu\text{C}/\text{cm}^2$	E_c kV/cm	T_c °C
$\text{Bi}_{0.5}\text{Na}_{0.5}\text{TiO}_3$ [11]	72.9	343	16.8	-	73	325
$\text{Bi}_{0.5}\text{Na}_{0.5}\text{TiO}_3$ [68]	82	-	-	39	62	320
$\text{Bi}_{0.485}\text{Na}_{0.5}\text{TiO}_{2.993}$ [68]	88	-	-	29	67	330
$\text{Bi}_{0.47}\text{Na}_{0.5}\text{TiO}_{2.85}$ [68]	97	-	-	34	74	335

The low melting point of Bi_2O_3 (825°C) and Na_2O (1132°C) can make non-stoichiometry in BNT at the A sites (such as a deficiency or excess in Na and Bi). This affects the properties of BNT, especially a deficiency of Bi, which changes the crystal structure from rhombohedral to cubic. The deficiency of Bi causes the poling of the bulk samples to become more difficult, and any excess of Bi decreases d_{33} to around 60 from 78 pC/N [68, 73-75]. A deficiency in Na causes another phase ($\text{Na}_{0.47}\text{Bi}_{0.5}\text{TiO}_{2.85}$) with cubic symmetry and affects the properties. In addition, it is believed that the formation of $\text{Bi}_{0.5}\text{Na}_{0.5}\text{TiO}_3$ starts from the reaction of $\text{Bi}_{0.5}\text{Na}_{0.47}\text{TiO}_{2.85}$ and sodium [68]. One method to compensate the A-site vacancy due to evaporation is the addition of some additives such Li, which can be substituted in the A or B sites [76].

2.1.1.2.3.1 BNT-BT: $\text{Bi}_{0.5}\text{Na}_{0.5}\text{TiO}_3$ - BaTiO_3

$\text{Bi}_{0.5}\text{Na}_{0.5}\text{TiO}_3$ - BaTiO_3 is one of the main binary systems that has been researched; an MPB was found at 6-7 mol% of BT between rhombohedral-tetragonal phases; the stability of these phases depends on the oxygen octahedral rotation [66, 69, 77-80]. The coexistence of the tetragonal and rhombohedral phases can be observed until 15 mol% BT, but the best properties are to be found at 6-7 mol% BT. It has been proposed that this is due to the maximum domain texture of the tetragonal and rhombohedral phases, and optimum domain reorientation by applying an electric field, which also shows that the rhombohedral phase fraction alone is not the dominant factor in the enhancement of properties [81, 82]. In fact, by adding BT to BNT: the size of the tetragonal phase field increases; the size of the polar nano-regions decreases; the anti-ferroelectric phase that exists at room temperature decreases; and, through an enhancement in temperature, polarisation extension causes electrically induced strain [83, 84]. Furthermore, the constriction in P-E loops at high temperature reveals the existence of another phase (AFE), which is non- or weakly polar. This has been observed by Raman spectrometry, as well as TEM, which shows the transformation of the ferroelectric tetragonal phase into the anti-ferroelectric tetragonal phase. The transformation is still unclear and there are some discussion about it and it can be transformation of the ferroelectric tetragonal phase into the relaxor phase [85, 86]. The binary diagram of BNT-BT can be seen in Figure 2-9 and the piezoelectric properties of BNT-BT in Table 2-5. As can be seen in Figure 2-9, the MPB is dependent on temperature, which leads to a curved shape.

The piezoelectric properties of BNT-BT, like other materials, are much higher in single crystals than ceramics; for example, the d_{33} in single crystals is about 360 pC/N, in

comparison with 120 pC/N in ceramics, due to the domain-switching behaviour of grains with different orientations, which results in an internal stress in ceramics. An additional 0.5mol% of Mn increases the d_{33} in 92.5BNT-7.5BT from 185 pC/N to 190 pC/N in ceramics and in single crystals from 280 pC/N to 483 pC/N, due to a reduction in the leakage current density. A 93.5BNT-6.5BT single crystal shows a small signal piezoelectric result (d_{33}) as high as 4600pm/V in the $\langle 111 \rangle$ direction. Ge et al. [84] have studied 0.944BNT-0.056BT single crystals and measured piezoelectric coefficients as high as 2500pm/V in the $\langle 001 \rangle$ direction at 130°C. They believe that this high piezoelectric coefficient is a result of polarisation rotation and extension between a polar pseudo cubic with slight tetragonal distortion, and a polar tetragonal one with a large tetragonal distortion. Ge et al. measured the strain of 0.944BNT-0.056BT single crystals under an electric field at different temperatures, and found that a high strain of 0.6% can be achieved at 130 °C under 20 kV/cm [87-96].

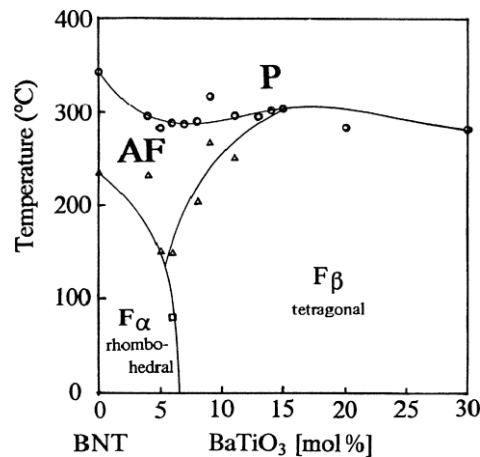


Figure 2-9: The binary phase diagram of BNT-BT. It has a curved MPB between the rhombohedral and tetragonal phases [14].

Piezoelectric properties are anisotropic and depend on crystallographic orientation; for example, in the BNT-BT system if an electric field is applied in [001], the structure changes from pseudo-cubic to tetragonal and, if the field is applied in [111], structural changes from pseudo-cubic to rhombohedral are observed, while the d_{33} is higher in the [001] direction. BNT-BT shows relaxor behaviour (the long-range order disappears, and only PNR remains), and the trend is to make a long-range order decrease through an enhancement in temperature. Relaxor behaviour around 70 to 120°C means that field-induced strain is recoverable at these temperatures. Relaxor behaviour can be divided into two types: ergodic and non-ergodic; when polar nano-regions are mobile at a high temperature, they show ergodic behaviour, but at a lower temperature, when their dynamics become slow, they show non-ergodic behaviour. The transformation of normal ferroelectric behaviour into a relaxor ferroelectric is a second-

degree transition. The dependence of relaxor materials on the frequency depends on the value of the maximum electric field relative to the poling electric fields, and if they are close to each other, the relaxor behaviour will decrease. However, the kinetics of the field-induced phase transition are slow for the relaxor, compared to a normal ferroelectric [97-108]. The depolarisation temperature in BNT-based materials is lower than for the ferroelectric to anti-ferroelectric transformation, which can be explained by minimising elastic energy due to internal stress; i.e., when the temperature increases, the domain wall and vector rotation become a bit easier, which causes depolarisation to happen at a lower temperature than for ferroelectric to anti-ferroelectric. This depolarisation is caused by an octahedral tilting [87]. Xu et al. [109] have investigated the electrical properties of (1-x) BNT-xBT (x=0-0.12). They were prepared by the citrate method, calcined at 600°C, and sintered at 1150°C. The obtained particle size was around 100nm, due to the citrate method. XRD patterns show coexistence of the tetragonal and rhombohedral phases at x=0.4-0.8, which shows a MPB in BNT-BT. They believe that due to the existence of MPB in 0.94BNT-0.06BT and the tetragonal and rhombohedral phases, it can show the best results of piezoelectric and ferroelectric properties, as outlined in Table 2-5.

Yan et al. [110] used the reactive-templated grain growth method to fabricate 0.94BNT-0.06BT with $\langle 001 \rangle$ texture, and they increased the properties of this composition, as shown in Table 2-5. The MPB is different for BNT-BT in poled and unpoled samples. In unpoled samples, the MPB divides the ferroelectric and anti-ferroelectric relaxor phases from each other, for X=0.7 -0.9. The poling process causes anti-ferroelectric to change to ferroelectric (for these compositions) [111].

Guo et al. [112, 113] have studied the anti-ferroelectric phase and pyroelectricity in (1-x)BNT-xBT for x=0.6-0.8, and also by changing the ratio of Bi and Na (Bi/Na) from 1 to a higher amount. The materials that change FE to AFE can potentially be used in high-energy storage capacitors, high-strain actuators, uncooled pyroelectric sensors, explosive electrical transducers, and for electrical refrigeration. They have found that by increasing the molar ratio of Bi/Na, the depolarisation temperature decreases, and the pyroelectric coefficient increases and then decreases. The authors reported a pyroelectric coefficient of $32.70 \times 10^{-4} \text{ C}/(\text{m}^2 \cdot \text{K})$ for $0.94 \text{ Na}_{45.5} \text{ Bi}_{47.5} \text{ Ti}_{94} - 0.06 \text{ BT}$ at 64°C. In addition, Sun. et al reported the largest amount of pyroelectricity in the $\langle 111 \rangle$ direction in 0.946 BNT-0.054BT single crystals as high as $5.88 \times 10^{-4} \text{ C}/(\text{m}^2 \cdot \text{K})$ [114]. The anti-ferroelectric phase is in place at room

temperature, which changes to the ferroelectric phase by applying an electric field and going back to anti-ferroelectric phase by removing an electric field, but an excess of Bi or a deficiency of Na results in stability of this phase in the ferroelectric state by removing the electric field. In general, this shows that the source of anti-ferroelectric phase is elongation along $\langle 001 \rangle$. This compound shows relaxor behaviour with a high electrostriction coefficient, which is comparable with Pb-based ferroelectric materials.

Table 2-5: Summary of the properties of BNT-BT, prepared with different methods. The processing of the raw materials can affect the final properties.

Material	d_{33} pC/N	$(\epsilon_{33}^T / \epsilon_0)$	k_p %	P_r $\mu\text{C} / \text{cm}^2$	E_c kV/cm	T_c °C	Preparing the raw materials
0.94 Bi _{0.5} Na _{0.5} TiO ₃ – 0.06 BaTiO ₃ [11]	125	580	-	20	-	288	Solid-state
0.96 Bi _{0.5} Na _{0.5} TiO ₃ – 0.04 BaTiO ₃ [21][12]	120	550	26	36	65		citrate
0.94 Bi _{0.5} Na _{0.5} TiO ₃ – 0.06 BaTiO ₃ [109]	180	600	28	37.1	42.7		citrate
0.92 Bi _{0.5} Na _{0.5} TiO ₃ – 0.08 BaTiO ₃ [109]	165	1100	20	30	36		citrate
0.88 Bi _{0.5} Na _{0.5} TiO ₃ – 0.12 BaTiO ₃ [109]	140	720	16	27.5	47		citrate
0.94 Bi _{0.5} Na _{0.5} TiO ₃ – 0.06 BaTiO ₃ [110]	241	1500	41.2	-	-	265	Reactive –templated grain growth
0.946 Bi _{0.5} Na _{0.5} TiO ₃ – 0.054 BaTiO ₃ [95]	280	-	-	16.44	32.7	-	Single Crystal- top-seeded solution growth
0.93 Bi _{0.5} Na _{0.5} TiO ₃ – 0.054 BaTiO ₃ -0.014 Mn[95]	483	-	-	45.3	29.1	-	Single Crystal- top-seeded solution growth

One factor that can affect the properties of the sintered materials is the sintering temperature [115-117]. Liu et al. have studied the effect of sintering temperature (1100, 1120, 1140, 1160, and 1180°C) on BNT-BT thick films prepared by screen printing, and found that the best sintering temperature is 1160°C, which shows the highest relative density (98%), the highest d_{33} (122 pC/N), and the highest polarisation, of 26.3 $\mu\text{C}/\text{cm}^2$. Lidjici et al. [116] studied the effect of sintering temperature on the BNT-BT bulk samples. They found that the best sintering temperature is 1200°C, with the d_{33} as high as 155 pC/N. BT can make a MPB with

(1-x) B (Zr_{0.05}Ti_{0.95}) O_{3-x}BT at x=0.07, but in general, the properties do not increase and the main difference with BNT-BT is the depolarisation temperature, which decreases to 50°C. The addition of up to 30%mol BNT to BT enhances the tetragonal phase of the composition [118, 119].

2.1.1.2.3.2 BNT-BT-BF: Bi_{0.5}Na_{0.5}TiO₃-BaTiO₃-BiFeO₃

One of the compounds that has been subject of a great deal of research for a BNT base material is (1-x) (BNT-BT)-xBF. Chen et al. investigated the dielectric and ferroelectric properties for 0.01, 0.03, and 0.07%mol of BF, and the effect of sintering atmosphere for 0.05%mol BF [120, 121]. They found that the addition of BF to BNT-BT can increase the density by substituting the heavier element Fe for Ti at the B site. Increasing the amount of BF and using N₂ for the sintering atmosphere causes a decrease in the amount of tetragonal phase. BF increases the grain size up to 0.03%, but after that BF goes to the phase boundary and prevents the growth of the grain. In addition, in the N₂ sintering atmosphere, grain size is higher than in the O₂ sintering atmosphere due to a higher concentration of oxygen vacancies. BF has a high Curie temperature, at around 800°C, and for this reason, it increases the T_m (temperature of the maximum relative permittivity) to a higher temperature, decreases the relative permittivity, and broadens the permittivity peaks around the T_m. P_r has been increased from 12 to 17 μ C/cm² at 0.03%mol of BF (which has the highest grain size) and after that, goes to around 4 μ C/cm² for 0.07%mol of BF. These authors found that at a lower grain size, the coupling is stronger between domain walls, and grain boundaries cause a decrease in domain wall mobility. The addition of more than 0.03%mol BF affects the structure by substituting Ti for Fe, which leads to oxygen vacancies, and makes changing polarisation harder.

2.2 Environmentally friendly solid-state cooling systems

There are a variety of ways to make a cooling system. The most common is based on vapour compression and cooling gas, however it has several problems: it has low energy efficiency, and is environmentally harmful. The Freon gas in common cooling systems has a detrimental effect on the ozone layer and plays a role in global warming. Also, advances in the electronic industry have taken place, particularly in the microelectronic industry, which require small cooling systems. In addition, gasses have a lower energy density due to their lower mass in comparison to liquid and solid materials and, for this reason, in recent years, other alternative methods and technologies have been investigated. These new ways use solid-state cooling systems, and the promising technologies are based on magnetocaloric, thermoelectric (the Peltier effect), and electrocaloric materials, with the main challengers being magnetocaloric and electrocaloric materials. The efficiency of the vapour compression cooling system is around 40-50%, while that of the thermoelectric cooling system is around 10%, and there are a lack of known materials that can be used in this system. The efficiency of the magnetocaloric and electrocaloric cooling systems is around 60-70%, which makes them suitable for further investigation [2-6].

2.2.1 Magnetocaloric solid-state cooling systems

Magnetocaloric materials bring about a temperature change by the application of a magnetic field under adiabatic and isothermal conditions. However, there are some issues: the high cost of the permanent magnets as the field source, and magnetic materials that are rare-earth materials. These are disadvantages in comparison to electrocaloric systems [3, 122].

2.2.2 Thermoelectric solid-state cooling systems

Thermoelectric materials become hot on one side and cold on the other when an electric field is applied. The efficiency of these materials is low, they are expensive to use, and they require a DC current. This type of cooling system is the so-called Peltier cooling system [123, 124].

2.2.3 Electrocaloric solid-state cooling systems

The electrocaloric effect (ECE) is when a temperature variation results in a change in polarisation. In a cooling system, this effect is used in both adiabatic and isothermal conditions: under adiabatic conditions (where the total entropy is constant), when an electric field is applied to an electrocaloric material, the disordered dipoles – which are randomly

oriented – start to be oriented in the direction of the applied field. To keep the total entropy constant (which shows the amount of order), the temperature of the electrocaloric material starts to increase. Under isothermal conditions, when an electric field is applied, entropy starts to increase in order to keep the temperature constant. The opposite of the above process can be observed when the electric field is removed and so to keep the total entropy constant due to the dipole disordering, the temperature of the material decreases. In the isothermal condition, when an electric field is applied, to keep the temperature constant, entropy starts to increase and, when the electric field is removed, to keep the temperature constant, entropy starts to decrease. This is the ECE; materials with this ability are known as electrocaloric materials, their ability shows as ΔT , and the use of this effect under adiabatic and isothermal conditions makes the cooling system [3, 5, 125-127].

However, this explanation is not always correct and for some materials, the reverse effect is observed (for example, $\text{Bi}_{0.5}\text{Na}_{0.5}\text{TiO}_3$ (BNT)); i.e., applying the electric field causes a reduction in the temperature of the material. For this reason, it is better to say that the electrocaloric effect is a change in temperature, or a change in entropy during the application or withdrawal of an electric field in adiabatic or isothermal conditions [23]. Caloric effects can also be observed by magnetic field (as explained before), hydrostatic pressure (barocaloric effect), and uniaxial stress (elastocaloric effect) stimuli. Using a combination of effects at the same time can increase the power of cooling systems [128, 129].

The term “electrocaloric solid state cooling system” means trying to use electrocaloric materials for fridges and other applications instead of vapour compression [5]. Electrocaloric materials have shown great potential for cooling systems and in recent years, a lot of researchers have worked on this issue [130, 131]. The entropy change in solid materials is 6-8 times higher than in gases per unit volume.; a value of $\Delta T = 2^\circ\text{C}$ can lead to a Carnot efficiency of 0.6 [132]. Sinyavsky et al. [69] have reported that a ΔT value of 3K at 20-300K could be practical for electrocaloric refrigerator applications.

Changes in the temperature of the material below the depolarisation temperature is related to irreversible field-induced phase transitions (for depoled samples), reversible electrocaloric ordering, and domain reorientation-related hysteresis, while above the depolarisation temperature, it is only related to reversible electrocaloric ordaining and domain reorientation. In other words, it is related to entropy change, lattice elastic energy, and electric polarisation energy, which other factors such as lattice deformation and dipole reorientation enhance

[132-135]. Material entropy change is related to changes in polarisation, phonons, and electron fluctuations [136]. The rate of the applied electric field affects the heat flow; i.e., a higher rate of application of the electric field increases the heat flow [135, 137]. In addition, ΔT depends on the type of electric field (AC or DC); in the AC electric field, the resonance frequency of materials affects the electrocaloric effect [138]. Bai et al. [139] investigated the effect of grain size on ECE, and found that increasing the grain size increases the ECE due to the weaker ferroelectricity of the grain boundaries, which reduces with an increase in grain size. The schematic of this effect in comparison with vapour compressors can be seen in Figure 2-10.

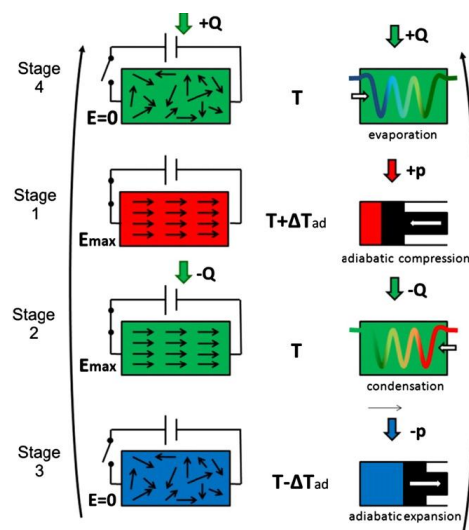


Figure 2-10: A schematic illustration of an electrocaloric cooling system, in comparison to a vapour compressor. It has four stages: adiabatic polarisation; isoelectric enthalpic transfer; adiabatic depolarisation; and isoelectric entropic transfer [5].

As can be seen in Figure 2-10, the process can be divided into four stages for comparison with vapour compression, as follows [4, 5]:

- 1- Adiabatic polarisation: In the first stage, applying the electric field leads to an increase in the material temperature and an alignment in the dipoles; this is similar to the pressure of the gas in the vapour compressor.
- 2- Isoelectric enthalpic transfer: In this stage, the materials exchange heat with the environment to change their temperature to the environmental temperature by keeping the electric field constant.
- 3- Adiabatic depolarisation: In this stage, by removing an electric field, the material temperature decreases and causes the dipoles to lose their order, and be ready to absorb the heat of the hot part.

- 4- Isoelectric entropic transfer: In this stage, the temperature of the materials increases in contact with the heat sink, and it causes a reduction in the heat sink's temperature.

Sinyavsky et al. [69] state that if the ΔT of the electrocaloric materials equals 3K at 20-300K, it has a practical application as an electrocaloric refrigerator. In addition, Qian et al. and Liu et al. [19, 140] studied EC materials under 200V, which most voltages of cooling systems use, and found that a high ECE at room temperature can be applied for a wide range of cooling systems, under a low electric field.

2.3 Pyroelectric (electrocaloric) Materials for Environmentally Friendly Solid-State Cooling Systems

Ceramics and polymers, or a composite of them, can be used in solid-state cooling systems in single crystal, bulk, and thin-film forms. The ECE was first discovered in 1930 with Rochelle salt, but the ΔT was too low to use for any application until 2006, when Mischenko et al. discovered a much larger ECE ($\Delta T=12K$) in PZT thin films [141]. The ECE is an intrinsic property and the form of EC materials can increase the ability of materials to withstand higher electric fields. For this reason, in this project, the ECE has been investigated with regard to bulk materials.

In this section firstly, the required properties are explained for their electrocaloric effect on the materials. Then, the different methods of measurement of the ECE are reviewed and, finally, materials which exhibit these properties are described.

2.3.1 The properties needed for the ECE in ceramic materials

The properties that are needed for a material to show a strong electrocaloric effect can be divided as follows:

- 1- Ferroelectric properties
- 2- First order of phase transition
- 3- High dielectric strength
- 4- Low electrical conductivity
- 5- Relaxor ferroelectric properties
- 6- ECE in the temperature range of interest
- 7- Invariant critical point (ICP) and line of critical end point (LCEP)

A material that has a high ECE should be ferroelectric, and the highest electrocaloric effect can be seen near the Curie temperature (T_C) or the depolarisation temperature (T_d); the depolarisation temperature is defined as a sudden reduction of remnant polarisation, which puts ΔS into the highest mode. This means that the highest entropy can be seen in the change from a ferroelectric to a paraelectric phase or from a ferroelectric to an anti-ferroelectric phase. The $\Delta T/\Delta E$ is considered a figure of merit for the electrocaloric effect, and $\Delta T \cdot \Delta S$ for the refrigerant capacity (RC). Some characteristics of materials can affect the electrocaloric effect, such as the polarisation switching time, the polarisation value, the behaviour of the

polarisation changes by an electric field, the fabrication and processing of the raw materials and methods of formation such as bulk or thin films. Generally higher ΔT values can be observed in thin films, but the heat absorption capacity is higher for bulk ceramics. Bulk electrocaloric materials cannot withstand large changes in the electric field, which can cause a fracture in the materials due to the electromechanical or chemical degradation of the compound [3, 5, 142-147]. Using Equation 2-6 Valant et al. [142] have calculated the Q (heat) for bulk and thin-film materials ($\Delta T = 1K$ for bulk material and $\Delta T = 10K$ for thin films, with the same surface, but 1mm thickness for bulk and $1\mu m$ for thin films) and found that the heat absorption for thin films is only 0.1% of the bulk sample.

$$Q = M.C.\Delta T = C. \rho. V. \Delta T \quad (2-6)$$

where M: mass, C: specific heat, ρ = density and V= volume

2.3.1.1 Ferroelectric properties

The general properties of ferroelectric materials and the reasons for using them were explained in section 2.1.1, and the properties of ferroelectric materials for ECE are explained in this section. Ferroelectric materials that have multiple phase transitions (such as MPBs) show a higher ECE under high electric fields for use in cooling devices [148]. As explained previously, a high ECE takes place near the depolarisation or Curie temperature, and can be affected by the size of the electric field and the ferroelectric type (whether normal or relaxor). The electric field causes differences in phase transition, compared to the electric field-free version. In a low electric field, the highest ECE usually takes place around the Curie and depolarisation temperatures for both normal and relaxor ferroelectric materials, but in high electric fields for normal and relaxor materials, it can take place at temperatures higher than the Curie and depolarisation temperatures, which show as twin peaks in measurements of ΔT as a function of the temperature for the relaxor materials. It is worth noting that depolarisation or Curie temperatures in relaxor materials occur at a range of temperatures due to the impact of the interaction between long range order, polar nano regions, and electric fields [5, 90, 143, 149]. Another important factor in ferroelectric materials is the domain fragmentation during electric field cycling, which can affect their properties and usually, a reduction can be seen in relative permittivity and polarisation; it first increases in coercive electric fields, and then decreases [91]. Another factor is the sintering temperature of the

materials, which can affect the grain size and the remnant polarisation, which can affect the ECE [42].

2.3.1.2 The order of phase transition

The order of phase transition affects the electrocaloric effect. As can be seen in Figure 2-11, in a second-order phase transition (left), entropy changes continuously, which leads to small amounts of change in the entropy.

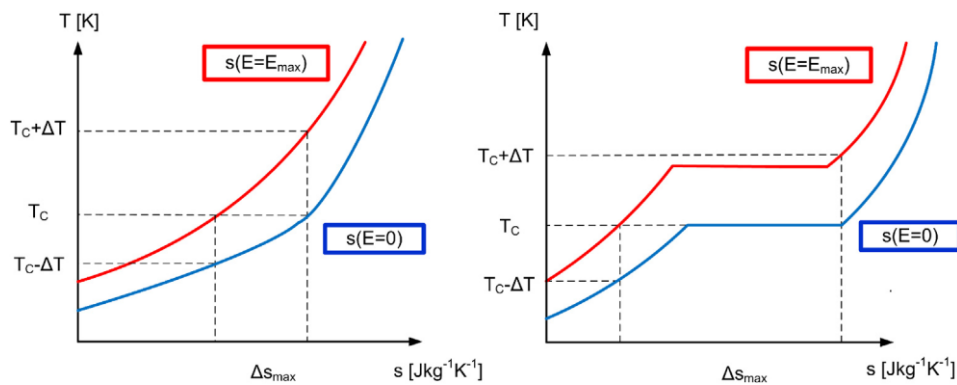


Figure 2-11: T-S diagram for a second-order transition (left), in which the entropy changes continuously, and a first-order transition, in which it does not (right)

On the other side of the diagram, in the first-order phase transition (right), changes in entropy are not continuous, which leads to more changes and an electrocaloric effect. A high electric field causes a phase transition from the first- to the second-order system. The behaviour of the dipoles and their ability to reorder under an electric field at, below and above the depolarisation temperatures leads to change in entropy and different ECE. In addition, near the MPB, ferroelectric materials show a better first-degree transition [103, 141, 150, 151]. Sebald et al. [125] have found a higher ECE in first-order transitions, when comparing 0.75Pb(Mg_{1/3}Nb_{2/3})O₃-0.25PbTiO₃ single crystals and bulk samples.

2.3.1.3 Dielectric strength

High dielectric strength is needed for a high electrocaloric effect. Dielectric strength is related to lattice vibration and electron-phonon scattering and porosity and is different for each material. The material shape and configuration formed affects the dielectric strength; a thin film can, due to its reduced defects, withstand a higher electric field and for this reason, they have higher temperature changes than bulk materials. Saturation takes place when all the dipoles are aligned along the field, but in bulk materials, a breakdown can occur in the materials at a lower electric field, which does not cause saturation [5, 142]. Other important factors in dielectric strength are thickness (Foelani and Minnaja relation: $E_b \propto h^{-n}$, E_b :

dielectric strength, n : fitting parameter and h : thickness), porosity, impurity phases, particle shape, particle size, grain boundaries, and so on. By adjusting process control or using glass-ceramic composites, the dielectric strength can be increased. It is worth noting that the shape of the sample, quality, size, and type of electrode [144], and so on can affect dielectric strength [142]. Liu et al. [152, 153] studied the effect of processing methods (spark plasma sintering) on BaSrTiO₃-based ceramics and found that by increasing density and decreasing particle size, higher electric fields can be applied to ceramics, which results in a higher ECE. They state that by adding Mn, oxygen vacancies – and therefore current leakage decreases, leading to a higher dielectric strength. Glass-ceramic composites are another method that increases the electric strength by decreasing the porosity. This method increases the electric strength for Ba_{0.5}Sr_{0.5}TiO₃ to 800kV/cm. Another method is to add a glassy phase to ceramic materials, which increases the electric strength; for example by adding 1% weight of BaO-B₂O₃-SiO₂ to BNT, increasing the electric strength from 500 to 600 kV/cm [154, 155].

2.3.1.4 Electrical Conductivity

Low electrical conductivity is another important factor for ECE. Conductivity can be a result of ionic or electronic processes, which causes leakage current and therefore joule heating. Some promising materials (ammonium- and glycine-based sulphates) have a high conductivity that cannot be used for this purpose. It can be reduced by a reduction in the measurement frequency, chemical substituents, and modifying microstructure [5, 143].

2.3.1.5 Relaxor ferroelectrics

The term relaxor ferroelectric means a material which exhibits diffuse phase transitions and high electrostriction. In other words, by increasing the frequency, the maximum relative permittivity of a relaxor material shifts to a higher temperature, without any microscopic symmetry change. It has been found that relaxor ferroelectric materials have a higher ECE because they have randomly distributed dipoles, without the application of an electric field. This causes the generation of a large field-induced polarisation, and its change with an electric field can lead to a high ECE. The high electrostriction in these materials can affect the secondary pyroelectric coefficient, and so the ECE. The long-range ferroelectric ordering in relaxor materials is disrupted by structure disorder, and can easily be switched by electric fields. In relaxor materials, the polar-nano regions have important roles in producing high ECE and at a range of temperatures. Lu et al. [156] studied ECE using the same base of materials, normal and relaxor ferroelectric, and found 50% higher ECE for relaxor materials.

For example, adding PMN-PNN as a relaxor ferroelectric to the PZT can increase the ECE. The coexistence of relaxor behaviour with the AFE phase increases the ECE, which can be observed in PMN-PZ or BNT-based compositions. The relaxor ferroelectric can be found in a ferroelectric material with the following characteristics [124, 134, 157-165]:

- 1- B site-disordering ferroelectric materials such as $\text{Ba}(\text{Zr}_x\text{Ti}_{1-x})\text{O}_3$. (This is related to the amount of x .)
- 2- A site-disordering ferroelectric materials such as BNT.
- 3- Tungsten-bronze structures.
- 4- Solid solutions between relaxor and normal ferroelectrics such as BNT-BT

The schematic of relaxor behaviour in comparison with normal, anti-ferroelectrics, and dielectric materials can be seen in Figure 2-12.[166].

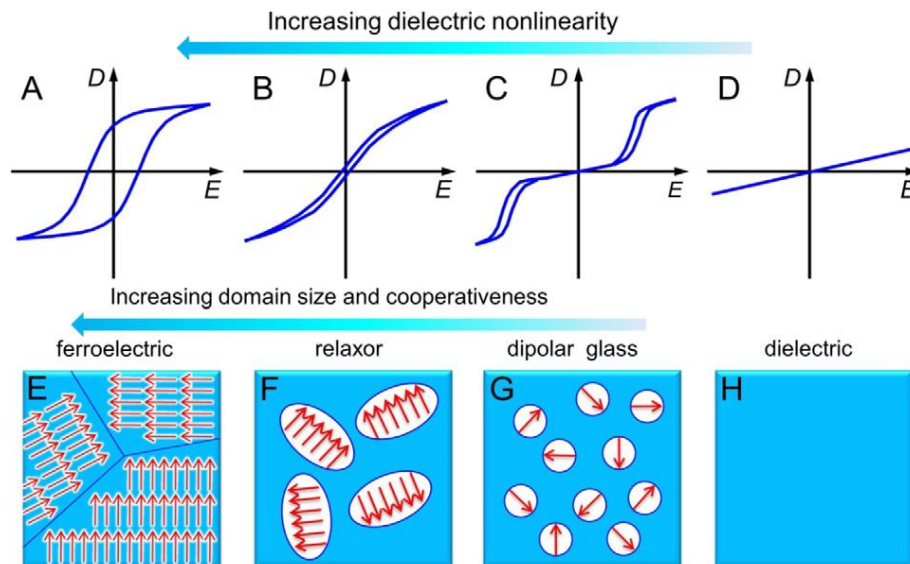


Figure 2-12: Schematic hysteresis loops for: (A) normal ferroelectric; (B) paraelectric or dipolar glass or relaxor ferroelectrics; (C) anti-ferroelectrics; and (D) dielectric materials.

The bottom panel illustrates the ferroelectric domain structures of: (E) normal ferroelectric; (F) relaxor ferroelectric; (G) dipolar; and (H) dielectric materials [166].

2.3.1.6 ECE in temperature ranges

Another important item to consider when creating an applicable ECE is finding a compound with a high ECE over a wide range. For example, for a refrigerator that works between the environment temperature and -10°C , a high ECE is needed in this temperature range. PMN-PT has ECE more than 1K at a range of temperature, which makes it applicable for devices, while $\text{PZ}_{0.95}\text{T}_{0.05}$ modified by MgO has a high pyroelectric coefficient at 24°C , which is only useful for uncooled infrared detectors such as night vision applications [142, 167-169]. As

explained previously, given a low electric field, the highest ECE can be seen near the Curie or depolarisation temperatures, but with a high electric field, it can be seen at a wide range, depending on the composition [160, 167].

2.3.1.7 The invariant critical point (ICP) and line of critical end points (LCEP)

The ICP shows the coexistence of several phases at one point (for example: BZT or $\text{BaSn}_x\text{Ti}_{(1-x)}\text{O}_3$ ($x=0.10-0.15$) [19, 170-172], while the LCEP shows the line between two critical points in the electric field-temperature-composition plots of the materials (Figure 2-13). Near these points, molar-specific heat and the number of equilibrium orientations of polar states is high, and entropy is higher; the energy barrier of the phase transition is lower, which leads to higher ECE. By increasing the number of phases near these points, ECE can be increased.

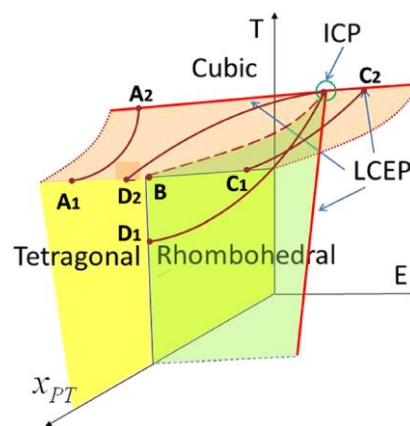


Figure 2-13: The schematic of ICP and LCEP. The ICP shows the coexistence of several phases at one point, while the LCEP displays the line between two critical points in the electric field-temperature-composition plots of the materials [170].

2.3.2 Measurement of the electrocaloric effect

There is no a standard way to measure the electrocaloric effect, and a variety of different methods have been used. The different techniques can be divided into two main categories, direct and indirect, as described in more detail below [2, 4, 5, 173-179]:

- 1- Direct methods: As the name implies, in these techniques, the key thermal parameters are measured directly as a function of the applied electric field, and they can be further divided as follows:

- 1-1- Reading the direct temperature: applying an electric field and read the temperature of the sample; it can also be done in silicone oil.
 - 1-2- Using differential scanning calorimetry (DSC): applying an electric field to samples in the isolated environment of DSC, and measuring endothermic and exothermic heat flows.
 - 1-3- Using adiabatic calorimetry: applying an electric field and reading the temperature of the sample in an isolated environment.
 - 1-4- Using scanning thermal microscopy.
 - 1-5- Using infra-red imaging: this can be done by capturing images as a function of time and heat flow.
- 2- Indirect methods: These techniques utilise the established theoretical concepts of the electronic, thermal, and dielectric behaviour of materials in order to calculate the EC parameters from other measured data, and are usually based on either Maxwell or Devonshire Landau analyses, as outlined below.

2-1- Ferroelectric hysteresis loops. Ferroelectric materials are typically characterised by Polarisation-Electric Field (P-E) loops measured as a function of temperature. These data can be used to calculate the electrocaloric effect, while the Maxwell equations can be used to demonstrate that the electrocaloric effect is the opposite of the pyroelectric effect. Measurements of the pyroelectric coefficient can be used to calculate the ECE in isothermal and adiabatic conditions, respectively, as shown below:

$$\left(\frac{\partial P}{\partial T}\right)_E = \left(\frac{\partial S}{\partial E}\right)_T \quad (2-7)$$

$$\Delta S = - \int_0^E \left(\frac{\partial P}{\partial T}\right)_E dE \quad (2-8)$$

$$\Delta T = - \frac{1}{\rho} \int_0^E \frac{T}{C} \left(\frac{\partial P}{\partial T}\right)_E dE \quad (2-9)$$

Where ρ is the density and C is the specific heat capacity. These equations indicate that a large pyroelectric coefficient is needed over a broad temperature range and electric field to achieve a large ΔT and ΔS [180]. A smaller, specific heat capacity leads to a higher ECE, but on the other hand, a smaller specific heat capacity leads to lower Q (heat). The specific heat

capacity is dependent on the temperature, but the application of an electric field decreases this [142, 157, 173, 181]. However, Starkov et al. [182] believe that the above equations are not valid for measurements of the dynamic polarisation, and need to be corrected.

2-2- Using Landau-Devonshire phenomenological theory: these equations calculate entropy, and after that, ECE [157, 173].

The theory explains that the Gibbs free energy of ferroelectric materials can be written as follows:

$$G = \frac{1}{2}\alpha P^2 + \frac{1}{4}\epsilon P^4 + \frac{1}{6}\zeta P^6 - EP \quad (2-10)$$

Where $\alpha = \beta (T-T_0)$ (2-11).

And, β , ζ and ϵ are temperature-independent phenomenological coefficients.

$$\left(\frac{dG}{dT}\right)_E = -\Delta S \quad (2-12)$$

Above the ferroelectric-to-paraelectric transition and under the influence of an applied electric field, entropy can be deduced from the following equation:

$$\Delta S = -\frac{1}{2}\beta P^2 \quad (2-13)$$

In an adiabatic condition, the temperature change is equal to:

$$\Delta T = -T\Delta S/C_E \quad (2-14)$$

Where C_E is the specific heat capacity.

The ECE can be written as follows:

$$\Delta T = -\frac{1}{2C_E}\beta TP^2 \quad (2-15)$$

Some researchers have studied the differences between these methods [148, 183, 184]. Ponomareva et al. [148] have used atomistic first-principles-based simulations for BST ($Ba_{0.5}Sr_{0.5}TiO_3$) to compare the direct and indirect methods, and have concluded that the results are the same. However, they state that the indirect method has some limitations due to the accuracy of the numerical integration of the Maxwell differential equation, and it cannot

measure the hysteresis effects usually observed on heating and cooling, or the effects of relative permittivity and polarisation or the variation in specific heats [145].

Sebald et al. [123, 185] looked at $0.75\text{Pb}(\text{Mg},\text{Nb})\text{O}_3\text{-}0.25\text{PbTiO}_3$ by indirect and DSC methods and obtained consistent results, except near the Curie temperature, when by increasing the electric field, one can increase the electrocaloric effect value measured by DSC. Bai et al. [184] also studied the difference between the measurements made by the DSC and indirect methods. It has been found that the direct method results in a higher value for ECE in BT thick films because the measurement also includes the effects of lattice deformation, which causes stronger polarisation, and also the use of ultrahigh electric fields, which can induce lattice elastic energy, both of which enhance the measured ECE. Smith et al. [33] measured the ECE on BT multilayer ceramic capacitor structures using both the direct infrared imager and indirect methods. The results show the same ECE values from both methods for the normal ferroelectric (BT). Wang et al. [186] looked at the ECE in $\text{B}_{0.98}\text{Ca}_{0.02}\text{Zr}_{0.085}\text{Ti}_{0.915}\text{O}_3$ using both indirect and direct methods, the latter using a homemade system. The ECE value measured using an indirect method was higher than that from the direct method, which the authors propose is due to losses from heat dissipation into the environment, and Joule heating in the direct measurement apparatus. Bai et al. [187] also compared two indirect methods for BT single-crystal materials. In low electric fields, both methods are consistent, that the Maxwell relationships are valid for ergodic (relating to systems for which each point can represent all the points of the system) systems and not for ferroelectric (FE) relaxors with a polar-glass nonergodic system. In addition, these equations have been defined for stress- and strain-free conditions, which are not available for high electric fields. Lu et al. [183] compared direct (direct reading) and indirect methods in relaxor ferroelectric polymers, finding that ECE values obtained via the direct method are higher than those from the indirect method. Narayan et al. [188] studied ECE in commercial BT multilayer capacitors using the direct (direct reading) and indirect methods. To measure the ECE, a low electric field was used, and the results from the two methods are consistent. Lu et al. [180] showed that for materials with a narrow hysteresis loop, both indirect and direct methods can be used to reach the same results and in another work, [157] they proposed that for relaxor ferroelectric materials, which are nonergodic in some temperature ranges, Maxwell relationships do not give the correct values.

In summary, the use of indirect methods (such as by using P-E loops) is experimentally less demanding, and can be conducted using standard facilities. The indirect method provides an

accurate response for low electric fields and ergodic systems, but is less accurate for nonergodic systems and high electric fields, or when a system is under stress and strain. It is advisable to use the direct method for relaxor materials that shows nonergodic behaviour in some temperature ranges, while the indirect method shows 50% higher ECE for these materials, as opposed to indirect methods. It is worth noting that the direct methods are quite hard to use because they require modifications to the standard experimental measurement systems to accommodate the additional variables of the electric field and/or temperature, or a completely new design.

2.3.3 Lead-free electrocaloric ceramic materials

Electrocaloric materials can be divided into four categories from the formation perspective, as described below:

- 1- Single crystals
- 2- Bulk ceramics with a thickness greater than 100 μm
- 3- Thick films ceramics with a thickness greater than 10 μm
- 4- Thin films ceramics with a thickness less than 10 μm

2.3.3.1 Single crystal materials

Single crystals are difficult to form and also expensive, so from the industrial point of view, are not suitable for mass production. The main factors involved in measuring ECE in single crystals are the direction of the electric field and crystal orientation. The results show that ECE is different for different directions in crystals [125]. Bai et al. [187] studied BT single crystals and by applying 10kV/cm for the electric field, obtained a result of $\Delta T = 1.6$ K; this resulted in a figure of merit of 0.16 K.cm/kV.

2.3.3.2 Bulk ceramics with a thickness greater than 100 μm

The applied electric field for bulk materials is, due to the weakness of dielectric strength, lower than for thin-film materials, which means that the ΔT is lower than for thin films. However, their heat capacities are much higher than thin films and in general, the figure of merit for both methods of formation are quite similar to each other.

2.3.3.2.1 BNT-based bulk ceramics

Table 2-6 shows a summary of ECE for BNT-based materials. Bai et al. [23] studied BNT and 0.92BNT-0.08BT. These compounds were made by the solid-state method, calcined at 850°C and sintered at 1120°C, with an indirect method used to measure the ECE. The measured ECE shows that the BNT ceramic has an abnormal ECE; i.e., the temperature of the ceramic decreases under an applied electric field, and is increased by removing the electric field. Around the phase transition from ferroelectric to anti-ferroelectric, in the anti-ferroelectric phase, there is a mixture of randomly oriented regions with ordered and disordered dipole, but they are in an antiparallel order, and the nonpolar regions prevent them from being oriented by applying an electric field, and make a macro domain state. Increasing the temperature destroys the ordered displacement of B site ions and the binding force becomes weak, which leads to nonpolar regions polarised and reoriented by the application of an electric field and causes an abnormal ECE. It is worth noting that this compound has a high $E_c=73$ kV/cm and in the bulk form, it is not possible to apply this high electric field, and the lower electric field cannot orient all the domains, leading to a rise in entropy. 0.92BNT-0.08BT shows a normal ECE for the low electric field and an abnormal ECE for a high electric field. An abnormal ECE of the BNT can increase the efficiency of the solid -state cooling system by using abnormal and normal EC materials at the same time. The abnormal or negative ECE has also been observed in other compounds, such as $(\text{Pb}_{0.97}\text{La}_{0.02})(\text{Zr}_{0.95}\text{Ti}_{0.05})\text{O}_3$ [189].

Zheng et al. [190] looked at $x\text{BNT}-(1-x)\text{BT}$ ($x=0, 0.05, 0.06, 0.1, 0.25, 0.3$) prepared by the citrate method, with 600°C for calcination, 1100°C for sintering, and an indirect method used to measure ECE. The highest ECE was found in BNT-0.3BT at 150°C, while 0.94BNT-0.06BT shows a high ECE at a range of temperatures (50-70°C), and it can be suitable for microelectronic devices that usually require cooling around these temperatures.

Jiang et al. [65] looked at $(1-x)\text{BNT}-x\text{KNbO}_3$ with $x=0.00, 0.04, 0.06, \text{ and } 0.08$. These compounds have been prepared by solid-state methods, sintered at 1150°C, and indirect methods are used to measure the ECE. P_r and E_c are decreased by increasing the KN content and for $x=0.08$, the ferroelectric properties become weak. In BNT, Na and Bi are at the A site, making the site disordered and causing a fluctuation in the charge, but the electric field can overcome this and form a long-range ferroelectric order. By adding the KN, the site disordering and charge fluctuation increase, so the T_d decreases. Abnormal behaviour was observed for $x=0.04$ and 0.06 at a low temperature, with normal behaviour at a high

temperature; most ECE was observed in the BNT-0.06KN, with $\Delta T = 1.73\text{K}$ under an electric field of 70kV/cm .

Zannen et al. [191] studied the effect of some rare earth elements such as Er, Nd, Dy, and Ho (1 wt.%) as dopants on BNT to investigate the ECE, and they reached a high ECE for Nd-BNT and a Dy-BNT as high as $\Delta T = 2.0\text{K}$. Cao et al. [192] studied the effect of SrTiO_3 on $(1-x)\text{BNT}-x\text{SrTiO}_3$ for $x=0.1, 0.25, 0.26,$ and 0.30 , prepared by solid-state methods. This addition decreases the depolarisation temperature to around $50\text{-}60^\circ\text{C}$, so the ECE of these compositions changes to room temperature. Cao et al. [193] investigated the ECE for the four compounds, based on BNTT: 1- BNT ($T_d=170^\circ\text{C}$), 2- $0.94\text{BNT}-0.06\text{BT}$ ($T_d=89^\circ\text{C}$), 3- $0.90\% \text{BNT}-0.05\text{KBT}-0.05\text{BT}$ ($T_d=78^\circ\text{C}$), and 4- $82\text{BNT}-0.18\text{KBT}$ ($T_d= 67^\circ\text{C}$) prepared by the sol-gel method, with 650°C used for calcination, 1150°C for sintering, and the ECE measured by the indirect method. They found that the coexistence of the ferroelectric and anti-ferroelectric phases can cause a high ECE and, that BNT absorbs heat during the application of the electric field and releases heat when the applied electric field is removed (abnormal behaviour), and is different compared to the other compounds. The highest ECE value was observed at $94\% \text{BNT}-6\% \text{BT}$ for $\Delta S = 2.20\text{ J}\cdot\text{K}^{-1}\cdot\text{kg}^{-1}$ and $\Delta T = 1.5\text{K}$ under an applied field of 50 kV/cm .

Uddin et al. [194] studied the ECE of $1-x(0.94\text{BNT}-0.06\text{BT})-x\text{BaSrTiO}_3$ for $x=0, 0.04, 0.06, 0.08,$ and 0.1 prepared by the sol-gel method, with 800°C for calcination and 1100°C for sintering. They found a negative ECE below the depolarisation temperature and a positive ECE above that for BNT-BT. Adding BST to BNT-BT causes the T_d to increase because the substitution of Ba and Sr ions for Na stabilised the octahedral oxygen and shifts the T_d to a higher temperature. Goupil et al. [195] studied the ECE for $0.82\text{BNT}-0.18\text{KBT}$ using the direct and indirect methods. This composition was prepared by the solid-state method and the ECE obtained from the indirect method was 0.57°C at 160°C , while the ECE measured by the direct method was 0.73°C , which shows the difference between these methods for a relaxor material. Tang et al. [196] looked at the effect of SrTiO_3 on $(0.935-x)\text{BNT}-0.065\text{BT}-x\text{SrTiO}_3$ for $x=0.02, 0.18,$ and 0.22 prepared by a solid state method. The depolarisation temperature decreases to around room temperature, and this was observed at a range of temperatures. Zheng et al. [197] studied the effect of BiFeO_3 on $(1-x) (0.96\text{BNT}-0.06\text{BT})-x\text{BF}$ for $x=0, 0.05, 0.1,$ and 0.15 prepared by the citrate method. They decreased the depolarisation temperature (105°C) to around room temperature. The best ECE was observed (-2.61K) for $x=0.1$ at 87°C . Li et al. [198] studied the effect of Li_2O_3 on $(1-x) (0.96\text{BNT}-0.06\text{BT})-x\text{Li}_2\text{O}_3$

for $x=0, 0.5, 1,$ and 1.5 wt%, prepared by the solid-state method. The depolarisation temperature was decreased to around room temperature, and the ECE of these compositions changed to room temperature from 96°C for pure BNT-BT to 37°C for BNT-BT- $1.5\text{wt}\%\text{Li}_2\text{O}_3$. The best ECE (-1.75 K) was observed for $x=0.05$ at 30°C .

Table 2-6: Summary of the ECE of BNT-based materials; with measurement and preparation method. The results show that the method of preparation affects the ECE.

Materials	$T_d^{\circ}\text{C}$	$T^{\circ}\text{C}$	ΔT_{max} K	ΔS J/K.kg	E_{max} kV/cm	$\frac{\Delta T}{\Delta E}$ K.cm/kV	Max ($\epsilon_{33}^T/\epsilon_0$)	Tan $\delta\%$	MD	PRM
BNT[23]	-	~ 140 *	-0.33^*	$\sim -$ 0.42^*	50	-0.0066^*	-	-	IM	Solid State
0.92BNT – 0.08BT[23]	-	$\sim 95^*$	$\sim 0.17^*$	$\sim 0.25^*$	40	0.00425^*	-	-	IM	Solid State
BNT[65]	182	20	-1.62	-	70	-0.023	380	2.5	IM	Solid State
0.96BNT – 0.04KN[65]	78	125	1.33	-	70	0.019	750	5.03	IM	Solid State
0.94BNT – 0.06KN[65]	35	76	1.73	-	70	0.025	1606	5.78	IM	Solid State
0.92BNT – 0.08KN[65]	-	70	0.23	-	70	0.003	1977	5.7	IM	Solid State
BNT[193]	-	50	-1.40^*	-2.0^*	50	-0.028	$\sim 3500^*$	~ 0.9	IM	Sol gel
0.82BNT – 0.18 KBT [195]	150	40- 160	0.73	-	22	0.033	~ 6000	-	DSC	Solid State
0.82BNT – 0.18 KBT [195]	150	40- 160	0.57	-	22	0.026	~ 6000	-	IM	Solid State
0.82BNT – 0.18 KBT[193]	67	80	1.06	1.62	50	0.0212	$\sim 3500^*$	~ 0.7 *	IM	Sol gel
0.94BNT – 0.06BT[193]	89	100	1.50	2.20	50	0.0300	$\sim 5000^*$	~ 0.7 *	IM	Sol gel
0.90BNT- 0.05KBT- 0.05BT[193]	78	90	0.99	1.47	50	0.0198	$\sim 6000^*$	~ 0.7 *	IM	Sol gel
BNT[190]	130	25- 200	-0.15	-	60	-0.0025^*	-	-	IM	Citrate
0.95BNT – 0.05BT[190]	< 150	200	$\sim -$ 1.25	-	60	-0.021^*	-	-	IM	Citrate
0.94BNT - 0.06BT[190]	< 150	50- 70	$\sim -$ 1	-	60	-0.017^*	-	-	IM	Citrate
0.9BNT – 0.1BT[190]	< 150	160	$\sim -$ 1	-	60	-0.017^*	-	-	IM	Citrate
0.75BNT – 0.25BT[190]	< 150	200	$\sim -$ 1.4	-	60	-0.023^*	-	-	IM	Citrate
0.70BNT – 0.30BT[190]	< 150	150	-2.1	-	60	-0.035^*	-	-	IM	Citrate
0.94BNT-0.06BT [194]	120	0 - 210	-2.1	-	70	0.030	5800	0.09	IM	Sol-gel
0.96(0.94BNT-0.06BT)- 0.4BST [194]	142	0 - 210	-2	-	70	0.0286	3000	0.1	IM	Sol-gel

Materials	T _d °C	T°C	ΔT _{max} K	ΔS J/K.kg	E _{max} kV/cm	$\frac{\Delta T}{\Delta E}$ K.cm/kV	Max ($\epsilon_{33}^T/\epsilon_0$)	Tan δ%	MD	PRM
0.94(0.94BNT-0.06BT) - 0.06BST [194]	160	0 - 210	-1.4	-	70	0.0200	4400	0.1	IM	Sol gel
0.92(0.94BNT-0.06BT)- 0.08BST [194]	200	0 - 210	-1.4	-	70	0.020	6000	0.1	IM	Sol gel
0.90(0.94BNT-0.06BT) - 0.10BST [194]	205	0 - 210	-1	-	70	0.014	3000	0.1	IM	Sol gel
0.915BNT-0.065BT- 0.02SrTiO ₃ [196]	70	0- 170	1.07	-	40	0.027	6000	0.1	IM	Solid State
0.915BNT-0.065BT- 0.02SrTiO ₃ [196]	40	25- 150	0.75	-	40	0.019	6000	0.1	IM	Solid State
0.915BNT-0.065BT- 0.02SrTiO ₃ [196]	0	0- 130	0.66	-	40	0.017	6000	0.1	IM	Solid State
0.94BNT-0.06BT [197]	105	30- 200	-1.55	-	60	0.025	6000	0.09	IM	Citrate
0.95(0.94BNT-0.06BT) - 0.05BF [197]	30	30- 200	-1.75	-	60	0.029	2500	0.1	IM	Citrate
0.85(0.94BNT-0.06BT) - 0.15BF [197]	30	30- 200	-1.1	-	60	0.018	1700	0.1	IM	Citrate
0.94BNT-0.06BT [198]	96	30- 160	-1.86	2.95	50	0.037	5000	0.7	IM	Solid State
0.95(0.94BNT-0.06BT) - 0.05La ₂ O ₃ [198]	87	30- 160	-2.61	3.96	50	0.052	4000	0.7	IM	Solid State
0.95(0.94BNT-0.06BT) -0.0 La ₂ O ₃ [198]	50	30- 160	-1.95	2.47	50	0.039	3000	0.9	IM	Solid State
0.95(0.94BNT-0.06BT) - 0.05 La ₂ O ₃ [198]	37	30- 160	-1.65	2.22	50	0.033	2500	0.5	IM	Solid State
0.9BNT-0.1SrTiO ₃ [192]	158	30	-0.62	1.1	50	0.012	2500	0.1	IM	Solid State
0.75BNT-0.25SrTiO ₃ [192]	58	60	1.64	2.5	50	0.033	5000	0.07	IM	Solid State
0.74BNT-0.26SrTiO ₃ [192]	48	50	1.52	2.25	50	0.030	6500	0.08	IM	Solid State
0.7BNT-0.3SrTiO ₃ [192]	-	30	0.35	0.6	50	0.007	5500	0.1	IM	Solid State

*: Calculated by Arthur: IM: indirect method; MD: measured method; PRM: preparing raw material method.

As can be seen in the table, the ECE was mostly measured by the indirect method for BNT-based materials. As explained previously, BNT-based materials show relaxor behaviour, so the indirect method does not appear to measure the real ECE. In addition, for the same composition (for example, 0.94BNT-0.06BT), the ECE was different using the same method. Many compounds have been investigated based on BNT, and most are near MPB due to the higher expected ECE. In this project, 0.94BNT-0.06BT was selected due to its high potential for ECE. Most of the achieved ECE are at a higher temperature than room temperature, which is not applicable for some applications such as fridges; they remain at one temperature, not a range of temperatures, which restricts their applications.

2.3.3.2.2 BT, BZT, and BCZT bulk ceramics

A summary of the ECE of BT, BZT, and BCZT can be seen in Table 2-7. Wang et al. [186] studied the ECE in BCZT ($\text{Ba}_{0.98}\text{Ca}_{0.02}(\text{Zr}_{0.085}\text{Ti}_{0.915})\text{O}_3$) prepared by the solid-state method, calcined at 1100°C and sintered at 1280°C. A high ECE ($\Delta T=2.33\text{K}$) was observed using the indirect method, but $\Delta T=0.6\text{K}$ was achieved by the direct method (a direct reading in non-adiabatic conditions) at 40kV/cm. Singh et al. [199] looked at the ECE in ($\text{Ba}_{1-x}\text{Ca}_x(\text{Zr}_{0.05}\text{Ti}_{0.95})\text{O}_3$) for $x=0.05, 0.08$ and 0.1 . An orthorhombic-to-tetragonal transformation takes place around these compositions, and they found that the best ECE is obtained by $x=0.08$, which indicates that polarisation flexibility causes a high ECE. Bai et al. [200] studied the ECE in $\text{Ba}_{0.97}\text{Ca}_{0.03}(\text{Zr}_{0.18}\text{Ti}_{0.82})\text{O}_3$, $\text{Ba}_{0.775}\text{Ca}_{0.225}(\text{Zr}_{0.05}\text{Ti}_{0.95})\text{O}_3$, $\text{Ba}_{0.79}\text{Ca}_{0.21}(\text{Zr}_{0.06}\text{Ti}_{0.94})\text{O}_3$, $\text{Ba}_{0.805}\text{Ca}_{0.195}(\text{Zr}_{0.07}\text{Ti}_{0.93})\text{O}_3$, $\text{Ba}_{0.85}\text{Ca}_{0.15}(\text{Zr}_{0.10}\text{Ti}_{0.90})\text{O}_3$, and $\text{Ba}_{0.91}\text{Ca}_{0.09}(\text{Zr}_{0.14}\text{Ti}_{0.86})\text{O}_3$. The best ECE was observed in the $\text{Ba}_{0.91}\text{Ca}_{0.09}(\text{Zr}_{0.14}\text{Ti}_{0.86})\text{O}_3$ with $\Delta T=0.3\text{K}$ under 20kV/cm, near the triple point with the tetragonal, rhombohedral, and cubic phases, and a composition with relaxor behaviour. The ECE is high at $\text{Ba}_{0.79}\text{Ca}_{0.21}(\text{Zr}_{0.06}\text{Ti}_{0.94})\text{O}_3$ but not at a range of temperature like $\text{Ba}_{0.91}\text{Ca}_{0.09}(\text{Zr}_{0.14}\text{Ti}_{0.86})\text{O}_3$. Singh et al. [201] studied a single crystal of $\text{Ba}_{0.835}\text{Ca}_{0.165}(\text{Zr}_{0.09}\text{Ti}_{0.91})\text{O}_3$, and a high ECE $\Delta T=0.46\text{K}$ was observed under 12kV/cm. Sanliyalp et al. [202] investigated $\text{Ba}_{0.895}\text{Ca}_{0.105}(\text{Zr}_{0.13}\text{Ti}_{0.87})\text{O}_3$ using the DSC as the direct and Maxwell relations as the indirect methods. This compound, prepared by the solid-state method, shows the ECE of the direct method ($\Delta T=0.33\text{K}$) and the indirect method ($\Delta T=0.23\text{K}$). The relaxor behaviour of this composition can cause the difference between these two methods. Kaddoussi et al. [203] and Qian et al. [19] looked at $\text{Ba}(\text{Ti}_{1-x}\text{Zr}_x)\text{O}_3$ ($x=0.1, 0.15, 0.20$ and 0.25) prepared by the solid-state method, calcined at 1100°C and sintered at 1360°C. The BZT at $x=0.2$ shows the highest ECE $\Delta T=4.5\text{K}$ under a 145 kV/cm electric field. Ye et al. [204] investigated a sintering aid (PbO and B_2O_3 for

1%wt) on the same composition by lowering the sintering temperature to 1200 °C, and reached the same ECE. The existence of an invariant critical point (ICP) with a four-phase existence, with more polar states and a low energy barrier between the phases, leads to higher changes in the entropy, and so a high ECE in this composition. Asbani et al. [205] studied the ECE on the $\text{Ba}_{0.8}\text{Ca}_{0.2}(\text{Zr}_x\text{Ti}_{1-x})\text{O}_3$ for $x=0, 0.02, 0.04, 0.06, 0.08$ and 0.1 prepared by the solid-state method. The best ECE $\Delta T=0.27$ K was observed at $x=0.04$ under a 7.95 kV/cm electric field. Patel et al. [206] investigated the ECE on the $\text{Ba}_{0.85}\text{Ca}_{0.15}(\text{Zr}_{0.1}\text{Ti}_{0.9})\text{O}_3$ prepared by the solid-state method, and the best results were observed at 93°C , with an ECE ($\Delta T=0.41$ K) under a 21.5 kV/cm electric field. In another paper, Patel et al. [207] studied the ECE on $\text{Ba}_{0.85}\text{Ca}_{0.15}(\text{Zr}_{0.1}\text{Ti}_{0.9-x}\text{Sn}_x)\text{O}_3$ for $x=0, 0.01, 0.02$ and 0.04 prepared by the solid-state method and measured by an indirect method. The best result ($\Delta T=0.39$ K) was observed under a 21 kV/cm electric field for $x=0$, $\Delta T=0.81$ K under a 32 kV/cm electric field for $x=0.01$, $\Delta T=0.84$ K under a 32 kV/cm electric field for $x=0.02$, and $\Delta T=0.45$ K under a 32 kV/cm electric field for $x=0.04$. The addition of Sn to BCZT decreases the highest ECE temperature to a lower temperature (from 100°C for $x=0$ to 70°C for $x=0.04$). Patel et al. [208] studied the ECE on the $\text{Ba}_{0.85}\text{Ca}_{0.15}(\text{Zr}_{0.1}\text{Ti}_{0.9-x}\text{Fe}_x)\text{O}_3$ for $x=0, 0.05, 0.1$, and 0.15 prepared by the solid-state method and measured by an indirect method. The best results ($\Delta T=0.4$ K) were observed under a 21.5 kV/cm electric field for $x=0$, $\Delta T=0.60$ K under a 33 kV/cm electric field for $x=0.05$, $\Delta T=0.86$ K under a 37 kV/cm electric field for $x=0.1$, and $\Delta T=0.54$ K under a 33 kV/cm electric field for $x=0.15$. The addition of Fe to BCZT decreases the highest ECE temperature to a lower temperature (from 97°C for $x=0$ to 70°C for $x=0.1$).

Kim et al. [209] looked at the ECE for $0.996(\text{Ba}_{0.85}\text{Ca}_{0.15}(\text{Zr}_{0.1}\text{Ti}_{0.9})\text{O}_3) 0.004\text{CuO}$, prepared by the solid-state method. The best results ($\Delta T=0.096$ K) were observed at 110°C under a 15.3 kV/cm electric field. Kaddoussi et al. [210] investigated the ECE for $(\text{Ba}_{1-x}\text{Ca}_x)(\text{Zr}_{0.1}\text{Ti}_{0.9})\text{O}_3$ for $x=0.05$, and 0.20 prepared by the solid-state method and measured by the indirect and direct methods. The best results ($\Delta T=0.2$ K) were observed under an 8 kV/cm electric field for $x=0.05$ by the indirect method, $\Delta T=0.25$ K under an 8 kV/cm electric field for $x=0.05$ by the direct method, and $\Delta T=0.09$ K under an 8 kV/cm electric field for $x=0.2$ by the direct method. Han et al. [211] studied the ECE of the $\text{Ba}_{0.96}\text{R}_{0.04}\text{TiO}_3$ for $\text{R}=\text{La, Ce, Nd, Sm, Eu, Gd, Dy, and Er}$ prepared by the solid-state method and measured by the indirect method. The best results ($\Delta T=1.04$ K) were observed under a 30 kV/cm electric field for $\text{R}=\text{Dy}$ and $\Delta T=0.92$ K, and 30 kV/cm electric field for $\text{R}=\text{Sm}$. The reduction in the ionic

radios of the additives increases the Curie temperature due to its effect on the rise in the tetragonality of the structure and expansion in the unit cell.

Table 2-7: Summary of the ECE of BCZT-based materials; with measurement and preparation method. The results show that the method of preparation affects the ECE, and there are some differences in the ECE when measured by different methods.

Materials	T _d °C	T °C	ΔT _{max} K	ΔS J/K.kg	E _{max} kV/cm	ΔT/ΔE K.cm/kV	(ε ₃₃ ^T / ε ₀)	Tan δ%	MD	PRM
Ba _{0.98} Ca _{0.02} (Zr _{0.085} Ti _{0.915})O ₃ [186]	-	28 - 105	2.33	-	40	0.058	-	-	IM	Solid State
Ba _{0.98} Ca _{0.02} (Zr _{0.085} Ti _{0.915})O ₃ [186]	-	28 - 125	0.6	-	40	0.015	-	-	Direct	Solid State
BaZr _{0.15} Ti _{0.85} O ₃	70	20- 50	4.2	7	150	0.028	12000	0.1	Direct	Solid State
BaZr _{0.2} Ti _{0.80} O ₃	30	20- 50	4.5	8	145	0.031	10000	0.1	Direct	Solid State
Ba _{0.95} Ca _{0.05} (Zr _{0.05} Ti _{0.95})O ₃ [199]	120	30- 150	0.31	-	15	0.0206	-	-	IM	Solid State
Ba _{0.92} Ca _{0.08} (Zr _{0.05} Ti _{0.95})O ₃ [199]	120	30- 150	0.38	-	15	0.0253	-	-	IM	Solid State
Ba _{0.9} Ca _{0.1} (Zr _{0.05} Ti _{0.95})O ₃ [199]	120	30- 150	0.23	-	15	0.0153	-	-	IM	Solid State
Ba _{0.97} Ca _{0.03} (Zr _{0.18} Ti _{0.82})O ₃ [200]	45	30- 90	0.125	-	20	0.00625	14000	-	IM	Solid State
Ba _{0.775} Ca _{0.225} (Zr _{0.05} Ti _{0.95})O ₃ [200]	60	30- 90	0.25	-	20	0.0125	11000	-	IM	Solid State
Ba _{0.79} Ca _{0.21} (Zr _{0.06} Ti _{0.94})O ₃ [200]	60	30- 90	0.30	-	20	0.015	10000	-	IM	Solid State
Ba _{0.805} Ca _{0.195} (Zr _{0.07} Ti _{0.93})O ₃ [200]	75	30- 90	0.27	-	20	0.0135	11000	-	IM	Solid State
Ba _{0.85} Ca _{0.15} (Zr _{0.10} Ti _{0.90})O ₃ [200]	90	30- 90	0.28	-	20	0.014	7000	-	IM	Solid State
Ba _{0.91} Ca _{0.09} (Zr _{0.14} Ti _{0.86})O ₃ [200]	100	30- 90	0.33	-	20	0.0165	8000	-	IM	Solid State
Ba _{0.835} Ca _{0.165} (Zr _{0.09} Ti _{0.91})O ₃ [201]	102	-30 - 120	0.46	-	12	0.0383	10000	0.12	IM	Single Crystal
BaZr _{0.1} Ti _{0.9} O ₃ [203]	100	0- 160	0.2	-	8.7	0.023	800	-	IM	Solid State
Ba _{0.895} Ca _{0.105} (Zr _{0.13} Ti _{0.87})O ₃ [202]	67	20- 100	0.23	-	20	0.115	12500	-	IM	Solid State
Ba _{0.895} Ca _{0.105} (Zr _{0.13} Ti _{0.87})O ₃ [202]	67	20- 100	0.23	-	20	0.0165	12500	-	DSC	Solid State
Ba _{0.8} Ca _{0.2} TiO ₃ [205]	127	25- 138	0.12	-	7.95	0.015	5000	-	IM	Solid State
Ba _{0.8} Ca _{0.2} (Zr _{0.04} Ti _{0.96})O ₃ [205]	123	25- 138	0.27	-	7.95	0.034	7000	-	IM	Solid State
Ba _{0.8} Ca _{0.2} (Zr _{0.08} Ti _{0.92})O ₃ [205]	67	52- 138	0.215	-	7.95	0.027	5000	-	IM	Solid State
Ba _{0.85} Ca _{0.15} (Zr _{0.10} Ti _{0.90})O ₃ [206]	93	25- 120	0.41	0.45	21.5	0.019	4500	-	IM	Solid State
Ba _{0.85} Ca _{0.15} (Zr _{0.10} Ti _{0.90})O ₃ [207]	-	100	0.39	0.45	21	0.018	-	-	IM	Solid State
Ba _{0.85} Ca _{0.15} (Zr _{0.10} Ti _{0.89} Sn _{0.01})O ₃ [207]	-	90	0.81	0.87	32	0.0253	-	-	IM	Solid State
Ba _{0.85} Ca _{0.15} (Zr _{0.10} Ti _{0.88} Sn _{0.02})O ₃ [207]	-	80	0.84	0.91	32	0.0262	-	-	IM	Solid State
Ba _{0.85} Ca _{0.15} (Zr _{0.10} Ti _{0.86} Sn _{0.04})O ₃ [207]	-	70	0.45	0.5	32	0.014	-	-	IM	Solid State

Materials	T _d °C	T °C	ΔT _{max} K	ΔS J/K.kg	E _{max} kV/cm	ΔT/ΔE K.cm/kV	(ε ₃₃ ^T / ε ₀)	Tan δ%	MD	PRM
0.996 (Ba _{0.85} Ca _{0.15} (Zr _{0.10} Ti _{0.90})O ₃)-0.004CuO [209]	105	110	0.096	-	15.3	0.006	-	-	IM	Solid State
Ba _{0.85} Ca _{0.15} (Zr _{0.10} Ti _{0.90})O ₃ [208]	-	97	0.4	0.45	21.5	0.018	-	-	IM	Solid State
Ba _{0.85} Ca _{0.15} (Zr _{0.10} Ti _{0.895} Fe _{0.005})O ₃ [208]	-	72	0.6	0.67	33	0.018	-	-	IM	Solid State
Ba _{0.85} Ca _{0.15} (Zr _{0.10} Ti _{0.89} Fe _{0.01})O ₃ [208]	-	72	0.86	0.97	37	0.023	-	-	IM	Solid State
Ba _{0.85} Ca _{0.15} (Zr _{0.10} Ti _{0.885} Fe _{0.015})O ₃ [208]	-	72	0.54	0.59	33	0.016	-	-	IM	Solid State
Ba _{0.95} Ca _{0.05} (Zr _{0.10} Ti _{0.90})O ₃ [210]	93	77- 110	0.2	-	8	0.025	10000	0.05	IM	Solid State
Ba _{0.95} Ca _{0.05} (Zr _{0.10} Ti _{0.90})O ₃ [210]	93	77- 110	0.24	-	8	0.030	10000	0.05	Direct	Solid State
Ba _{0.80} Ca _{0.20} (Zr _{0.10} Ti _{0.90})O ₃ [210]	100	77- 110	0.09	-	8	0.011	4000	0.05	IM	Solid State
Ba _{0.096} La _{0.04} TiO ₃ [211]	34	30- 160	0.68	-	30	0.022	8000	-	IM	Solid State
Ba _{0.096} Ce _{0.04} TiO ₃ [211]	44	30- 160	0.72	-	30	0.024	6000	-	IM	Solid State
Ba _{0.096} Nd _{0.04} TiO ₃ [211]	52	30- 160	0.79	-	30	0.026	6500	-	IM	Solid State
Ba _{0.096} Sm _{0.04} TiO ₃ [211]	70	30- 160	0.92	-	30	0.031	5800	-	IM	Solid State
Ba _{0.096} Eu _{0.04} TiO ₃ [211]	82	30- 160	0.89	-	30	0.029	5000	-	IM	Solid State
Ba _{0.096} Gd _{0.04} TiO ₃ [211]	94	30- 160	0.86	-	30	0.028	4500	-	IM	Solid State
Ba _{0.096} Dy _{0.04} TiO ₃ [211]	130	30- 160	1.04	-	30	0.035	4000	-	IM	Solid State

2.3.3.3 Thin- and thick-film ceramics

Table 2-8 shows the ECE of thin and thick films. The ECE is higher in thick and thin films compared to bulk materials of the same composition due to their resistance to the higher electric field, but the figures of merit are similar and heat capacity lower than bulk ceramics. For example, the ECE for PMN-PT thin film is about 14.5°C under a 60 kV/cm [212]. For BaZr_{0.2}Ti_{0.80}O₃, the figure of merit of 0.051 Kcm/kV is the same for both bulk and thin films [213]. Thin films are usually deposited on a substrate, so the Joule heating between the films and substrate leads to a decrease in the efficiency. Narayan et al. [174] measured the Joule heating between thin films and substrates, and found that it is negligible. Other factors such as the thermal stress between the films and substrate, the type of substrate, and the annealing temperature affect the ECE of thin films. In addition, a multilayer heterostructure configuration of a ferroelectric, paraelectric, or anti-ferroelectric enhances the pyroelectricity and ECE [214-217].

Zheng et al. [218] looked at (1-x) BNT-xBT (x=0, 0.1, 0.9, and 1.0) thin films prepared by the sol-gel method and crystallised at 850°C. The coexistence of the rhombohedral and tetragonal at 0.9BNT-0.1BT shows that the MPB is different in thin films of this composition. The highest ECE ($\Delta T=3$ K) was observed in this compound near the change from ferroelectric to anti-ferroelectric. Bai et al. [184] studied BT multilayer thick films prepared by the tape-casting method - 180 layers with a thickness of 1.4 μm . A high ECE ($\Delta T=4$ K) was observed at 80°C and under 352 kV/cm.

Compressive stress can be used to increase the ECE, especially in ultrathin films [128]. In ultrathin films (nanoscale) or nanoshells, the electric field and thickness of the film affects the ECE and through a rise, the maximum temperature of ECE shifts to a higher temperature [140, 219].

Table 2-8: Summary of the ECE of thin films of BNT- BT by the indirect method, and BT by the indirect and DSC methods.

Materials	T _d °C	T°°C	ΔT_{max} K	ΔS J/K.kg	E _{max} kV/cm	$\frac{\Delta T}{\Delta E}$ Kcm/kV	($\epsilon_{33}^T/\epsilon_0$)	Tan $\delta\%$	MD	PRM
0.90BNT – 0.10BT[218]	-	30-50	3	-	-	0.0058	-	-	IM	Sol Gel
BT[184]	-	80	4	-	352	0.011	-	-	DSC	Tape casting
BT[184]	-	80	0.68	-	176	0.0038	-	-	IM	Tape casting

2.4 Summary

There are a number of methods of cooling systems; the common system for cooling appliances is compressed air and cooling gas to generate cooling, but this method is not environmentally friendly and has other problems as well. Researchers have sought to find alternative methods to make an efficient cooling system, one of which is an electrocaloric solid cooling system: it is environmentally friendly, but still needs more research and investigation.

The materials that can be used in this technology are known for their ability to change their temperature due to the application of an electric field, and are known as electrocaloric materials, which in fact are pyroelectric materials. To enable mass production of such systems, ferroelectric materials are good options, and merit investigation with regard to which shows pyroelectricity as well, and for this reason, electrocaloric materials have been selected. Contemporary ferroelectric materials can be divided into lead-based and lead-free

types due to the toxicity of the lead, so an environmentally friendly cooling system requires environmentally friendly materials and for this reason, lead-free ferroelectric materials have been selected, and their ECE investigated. These materials are made in bulk, single crystal, and film formats, while also, the ECE is an intrinsic property for them, so in this project, the literature review has focused exclusively on bulk ceramics and the effect of factors such as electric fields and the ECE, investigating a range of temperatures. For these reasons, two of the compounds that show good potential for ECE are based on BNT-BT and BCZT, and all of the previous research done on this material has been collated and reviewed. The piezoelectric, pyroelectric, and ferroelectric properties of the selected materials have been investigated, based on the previous research. One of the weaknesses in measuring the ECE is that there is no standard cause of the differences in the results, so a number of methods have been employed to find this, but they depend on the type of ferroelectric materials (normal or relaxor) and the shape of the samples to ensure the appropriate method is selected. In general, the methods used can be divided into direct and indirect methods and in this project, one from each was selected to measure the ECE.

All the previous research regarding BNT-BT-based ceramics used indirect ways to measure the ECE, and each reached a different answer. There is, therefore, a need for more investigation to reveal a precise answer for this composition, and the EC for BNT-BT needs to be investigated via both methods. As for BNT-BT, there is little research into BCZT with the same composition that was selected for this project, and all the previously research on BCZT to measure the ECE has been done using indirect methods, resulting in different answers. Therefore, as has been done for BNT-BT, this composition needs to be investigated using both methods.

2.5 Project Aims

The overall aim of this project is to investigate and develop lead-free materials for electrocaloric applications. The objectives can be summarised as follows:

- 1- To fabricate BCZT powder and ceramics.
- 2- To fabricate BNT-BT powder and ceramics.
- 3- To optimise the fabrication of BCZT ceramics by characterising the physical, structural, microstructural, and functional properties of the material.
- 4- To optimise the fabrication of BNT-BT ceramics by characterising the physical, structural, microstructural, and functional properties of the material.
- 5- To compare the ECE in the BNT- BT and BCZT bulk ceramics via the direct and indirect methods.
- 6- To investigate the effect of BNKT on BCZT ceramics by characterising the physical, structural, microstructural, and functional properties of the material.
- 7- To investigate the effect of BF on BNT-BT ceramics by characterising the physical, structural, microstructural, and functional properties of the material.
- 8- To investigate any deficiencies of BNT-BT ceramics by characterising the physical, structural, microstructural, and functional properties of the material.
- 9- To compare the ECE in BNT-BT-based ceramics and BCZT-based ceramics via both direct and indirect methods.
- 10- One aim of this project is to investigate moving ECE closer to room temperature and increase the available range of temperatures.

Chapter

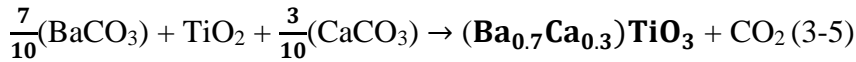
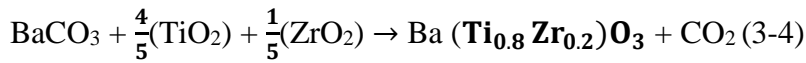
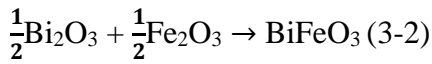
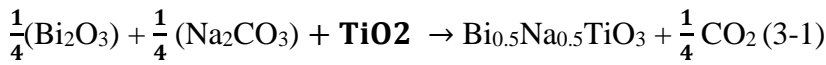
3 Experimental procedures

3.1 Introduction

Conventional solid-state methods for preparing materials have been used in this project, followed by uniaxial cold pressing for green body fabrication. Brief details of the experimental procedures are summarised in the schematic diagram shown in Figure 3-1, and summarised in the sections below.

3.2 Mixing materials

The selected raw materials are listed in Table. 3-1. In the first step, all the compounds were prepared separately and the required powder calculated, based on stoichiometric amounts of the constituents, based on the chemical reactions detailed below:



Using a precise balance (0.0001g), the required starting powders were weighed in their stoichiometric proportions to make the compositions listed in Table 3-2, and then placed in a 75ml (diameter of 3cm and height of 7cm) plastic bottle. Ethanol was added to powders at 80% of the total powder weight, together with zirconia milling balls (with a diameter of under 5mm) at 200% of the total powder weight. Then, they were ball-milled in a roller ball mill (Pascall Engineering, Sussex, UK) for 24 hours with speed of 90 rpm (r/min), and dried in an oven (WF60 laboratory oven, Lenton, UK) for another 24 hours at 80°C.

For the BNT, vibro-milling (Model M.18, Sweco Europe S.A., Belgium) with a 180watt motor was used to decrease the particle size (in a 75ml (diameter of 3cm and height of 7cm) plastic bottle) and enable a reduction of the calcination temperature. The particle size of the powders was analysed using a laser diffraction particle size analyser (Gracell, Sympatec, Bury, Germany).

Some of the BCZT powder was prepared at the Central European Institute of Technology (CEITEC) to investigate the effect of BNKT. In addition, the BNKT ($\text{Bi}_{0.50}(\text{Na}_{0.82}\text{K}_{0.18})_{0.50}\text{TiO}_3$) was prepared at CEITEC, and they were both used to fabricate BCZT-1, 3, and 5% BNKT samples. The same preparation route was used to prepare these BCZT and BNKT

samples. The calcination temperature was 1100°C for BCZT and 700°C for BNKT in air. The powders were prepared separately and then they were mixed based on the weight percentage.

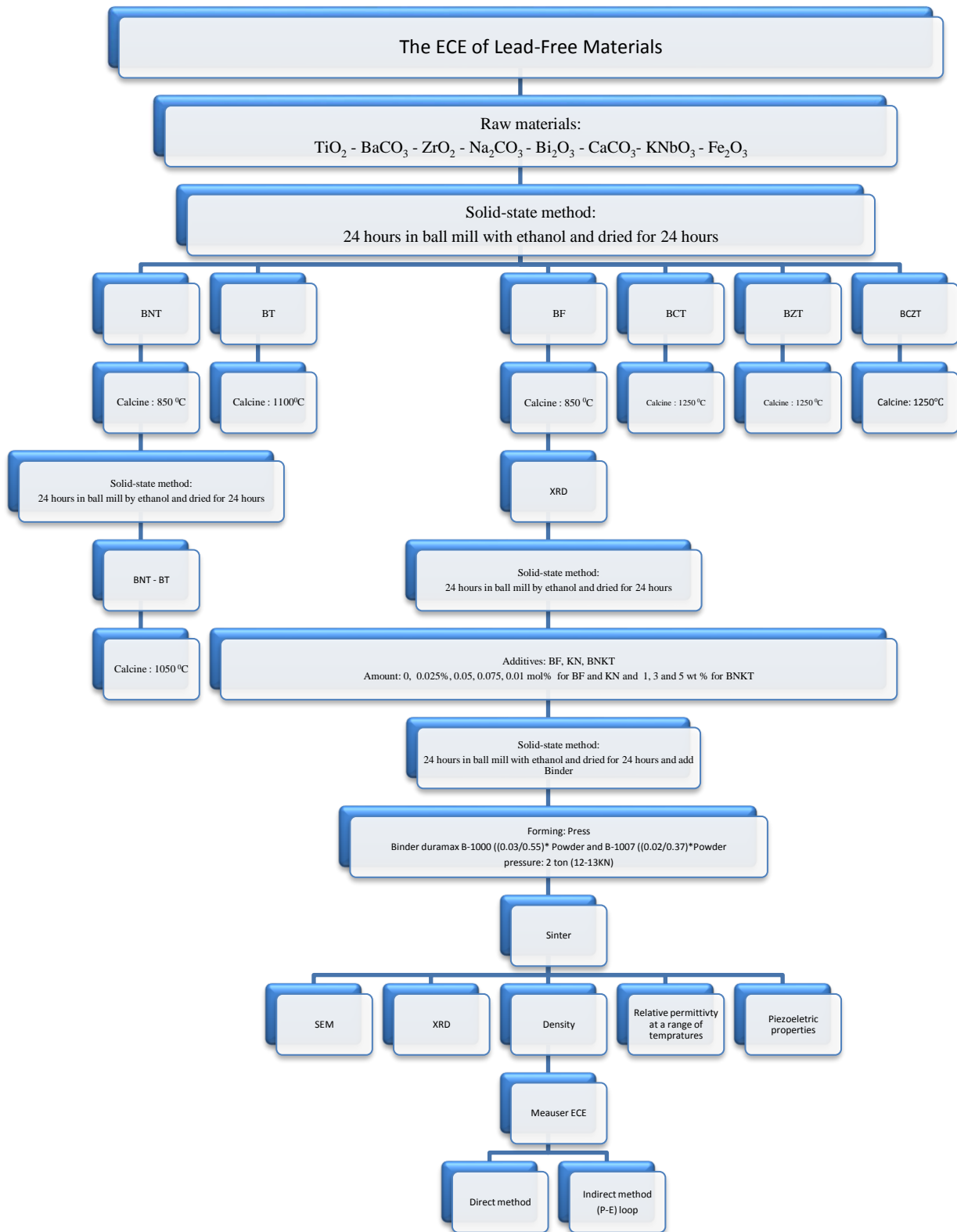


Figure 3-1: Summary of the experimental procedure

Table. 3-1: List of raw materials

Materials	Company	Country of Company	Purity	Code No
TiO ₂	Pi-Kem	UK	99.9	-
BaCO ₃	Dakram	UK	≥ 99.98%	-
ZrO ₂	Dakram	UK	≥ 99.5%	-
Na ₂ CO ₃	Sigma Aldrich	UK	≥ 99.5%	22358
Bi ₂ O ₃	Sigma Aldrich	UK	≥ 99.9%	223891
CaCO ₃	Dakram	UK	≥ 99.4%	2012/07427
Fe ₂ O ₃	Sigma Aldrich	UK	≥ 99%	310050
KNbO ₃	Treibacher Industrial	Austria	≥ 99%	-

3.3 Calcination

First of all, the calcination temperatures for various powder mixtures were chosen from the literature, as can be seen in Table 3-2. Two methods were selected to calcine BCZT; BCZT was calcined from calcined BCT and BZT, and BCZT was directly calcined from the raw materials. The same process was done for BNT-BT; BNT-BT was calcined from calcined BNT and BT, and BNT-BT was directly calcined from the raw materials.

Table 3-2: The calcination temperature of the powders

Powders	Calcination Temperature (°C)	References
Bi _{0.5} Na _{0.5} TiO ₃	800 - 825 - 850	[23, 75, 109]
BiFeO ₃	850	[57]
BaTiO ₃	1100	[16]
Ba (Ti _{0.8} Zr _{0.2})O ₃	1250	[20]
(Ba _{0.7} Ca _{0.3})TiO ₃	1250	[15]
BCZT	1250	[15, 50]
BNKT	700	CEITEC
BCZT	1100	CEITEC

The new zirconia crucibles (Almath-UK) were heated at 1400°C for two hours to remove any residue. After that, the powders were calcined according to the temperature profile, as shown in Figure 3-2.

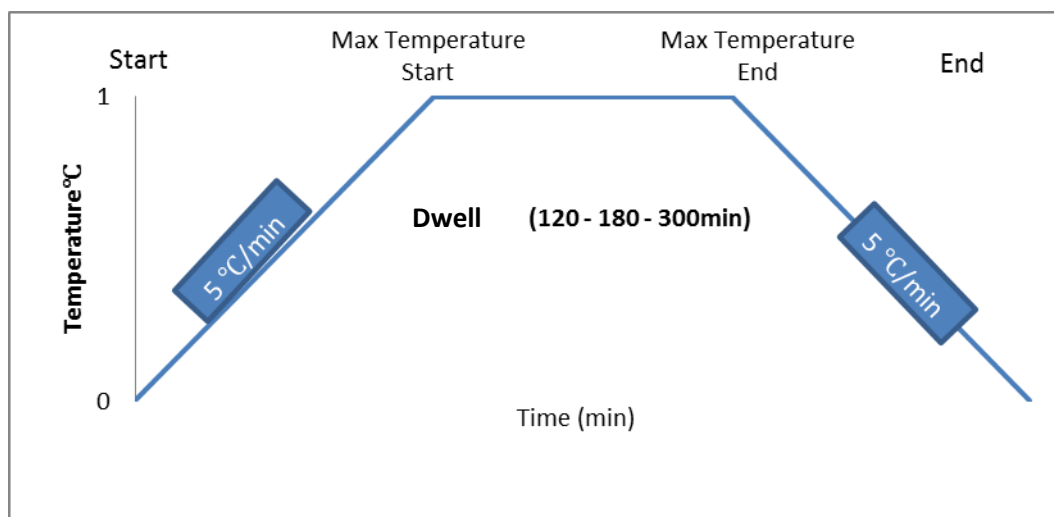


Figure 3-2: The temperature profile for the calcination of the powders

3.4 Characterisation and analysis of the materials

An X-ray diffractometer (EQUINOX 3000, INEL, France) with Cu-K α radiation, with a wavelength of 1.540560 and $2\theta=15-90^\circ$, was used to characterise the phases present in the materials. Match software was employed to analyse the peaks, with the help of the National Chemistry Database Service (ICDS) - <http://cds.rsc.org/>.

3.5 Forming (pressing)

Calcined powders were dry ball-milled for another 24 hours to obtain soft powders and after, poly vinyl acetate (PVA) binders B-1000 and B-1007 (Duramax, Chesham Chemicals Ltd., UK) were added. Then, they were mixed for another 20 minutes and dried for 24 hours.

The prepared powders were crushed by a pestle and mortar, sieved through a 300-micron mesh, and weighed (to around 0.4-0.6g) for pressing. The powders were then pressed into disks under 90 MPa, using a stainless steel die with a 13mm diameter.

3.6 Sintering

The prepared disks were placed on a zirconia substrate and put in a muffle furnace (Lenton, UK), heated at sintering temperatures according to the profile outlined in Figure 3-3, and were sintered at the temperatures shown in Table 3-3.

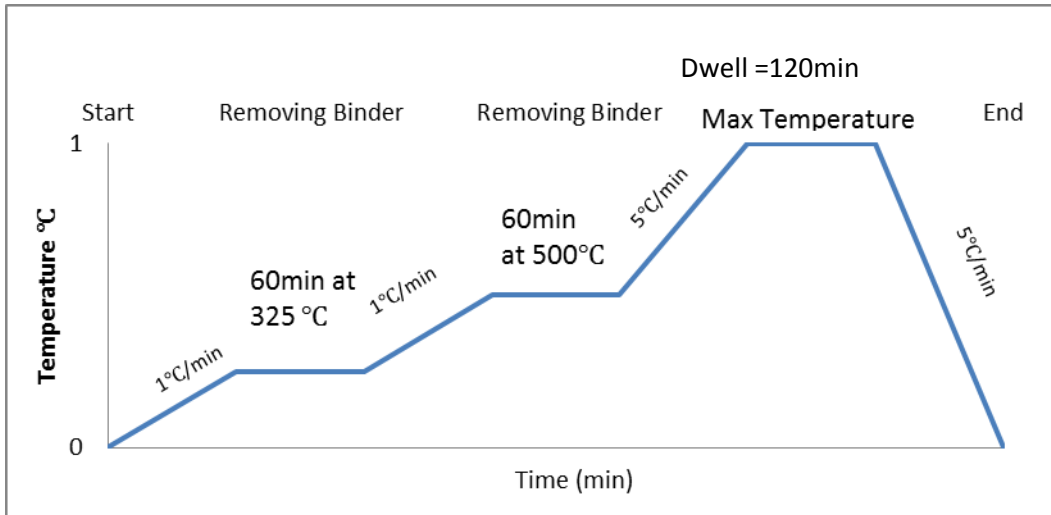


Figure 3-3: The sintering profile plot for the green pellets

Table 3-3: The selected sintering temperatures for the green pellets

Powders	Sintering Temperature (°C)	References
BNT-BT	1100, 1125, 1150, 1175, 1200	[23, 75, 109]
BNT-BT with deficient	1125	[112]
BCZT	1400, 1425, 1450, 1475, 1500	[15, 50]
BCZT-1, 3, 5%BNKT	1250, 1350, 1350, 1400, 1450, 1500	-
(1-x) BNT-BT-x BF	1125	[121]

3.7 Density and dimensions

The Archimedes method was employed to measure the density of the samples. In addition, dimensional measurements of the samples were carried out to 0.01mm using digital calipers and a micrometer.

3.8 Cleaning the samples and preparing for applying the electrode

After sintering, the samples were cleaned using ultrasonic vibration to remove any dust or impurity; after that, ethanol was added to remove any impurity of the surface. Then, plastic (PVC) self-adhesive tape was stuck onto the curved surface of the cylindrical samples in order to separate the two planar surfaces from each other, and thin layers of 80nm chromium (Cr) then 200nm gold (Au) electrodes sputtered on each side by a sputter coater (K575X, EMITECH, UK).

3.9 Poling the samples

The poling of the samples was done in silicone oil, using a homemade poling machine (power supply: Alpha III, Brandenburg, UK) at 25°C and 50°C, with an electric field of 2.5 and 3 kV/mm for 10-20 minutes, depending on the sample.

3.10 Polishing and SEM

The surface of samples were first polished using wet and dry paper (360 grit), followed by polishing with 9, 6, 3, and 1 micron liquids, respectively, for around 20 minutes for each part. The polished samples were thermally etched at 100°C lower than the sintering temperature for 10 minutes, using a heating and cooling rate of 10°C/min. The thermally etched samples were placed on SEM stubs with carbon sticky tape, after which a gold electrode was applied on the top of samples. The surface of the electrode samples was observed using a Jeol 6060 (the surface of the samples were just observed with SEM) at low magnification (around 3000), and ESEM for higher magnification. The average grain intercept (AGI) method was used to measure the grain size of the sintered samples.

3.11 Piezoelectric properties

The piezoelectric properties were characterised by an HP Agilent 4294A impedance analyser (Agilent Ltd, S Queens Ferry, UK), and d_{33} was measured by a YE2730A, Berlincourt d_{33} meter made in China.

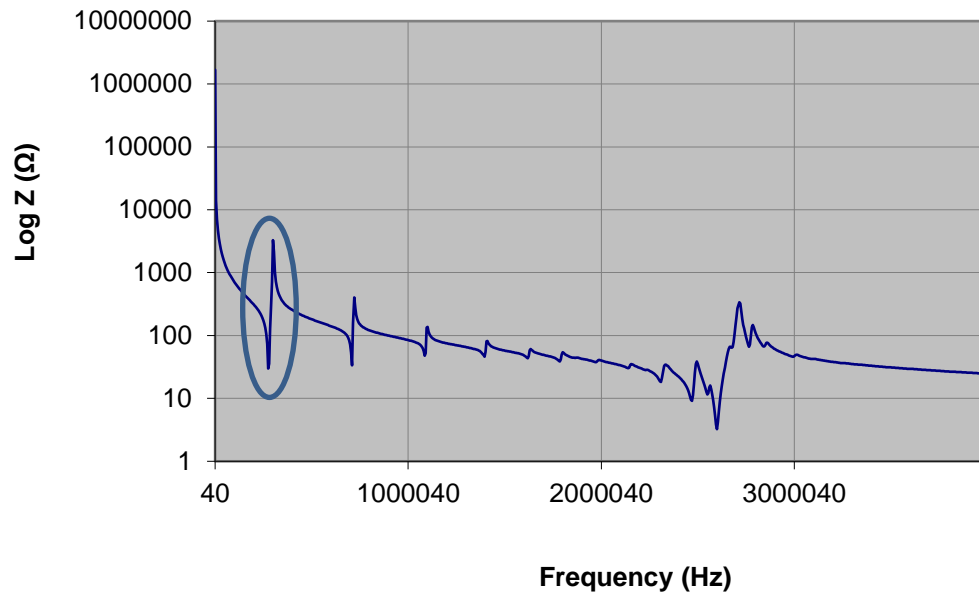
The planner electromechanical coupling factor (k_p) was determined by an impedance analyser (HP-4294A) based on the EN-50324-2 standard and the resonance-anti-resonance method [7].

Using this method, the log of impedance (Z) was measured as a function of frequency. The first peak is related to radial resonance; the frequency of the minimum of this peak (marked in Figure 3-4-A) is the resonance frequency (f_r), and the maximum is the anti-resonance frequency (f_a). The resonance at the lowest frequency is related to the motion of the biggest dimension of the sample, which in disk shape samples is in the radial direction. The deduced frequencies from the plots were inserted into the following equation, and the k_p of the samples were calculated according to Equation 3-6 [7]:

$$k_p \cong \sqrt{[(2.51 (f_a - f_r) / f_a) - ((f_a - f_r) / f_a)^2]} \quad (3-6)$$

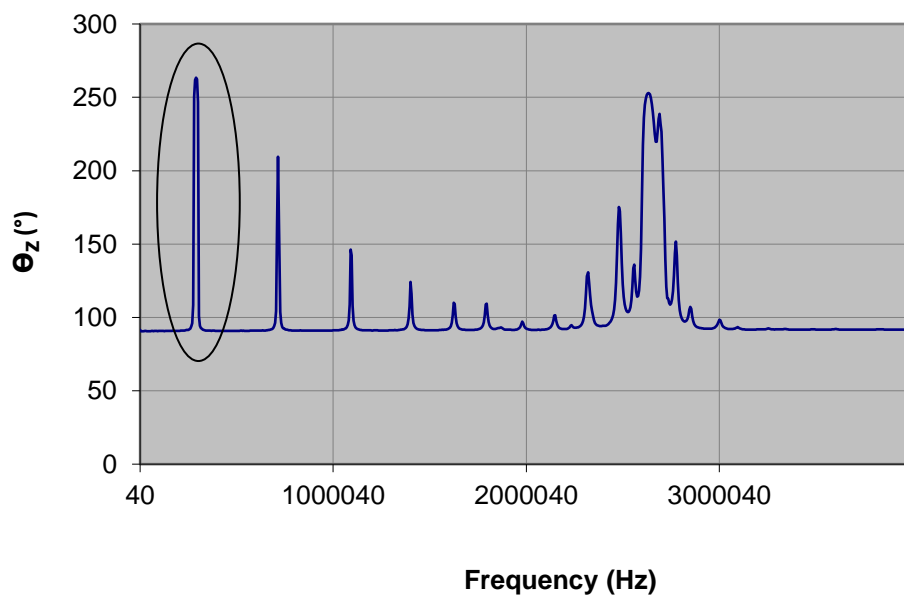
a

4294A TraceA



b

4294A TraceB



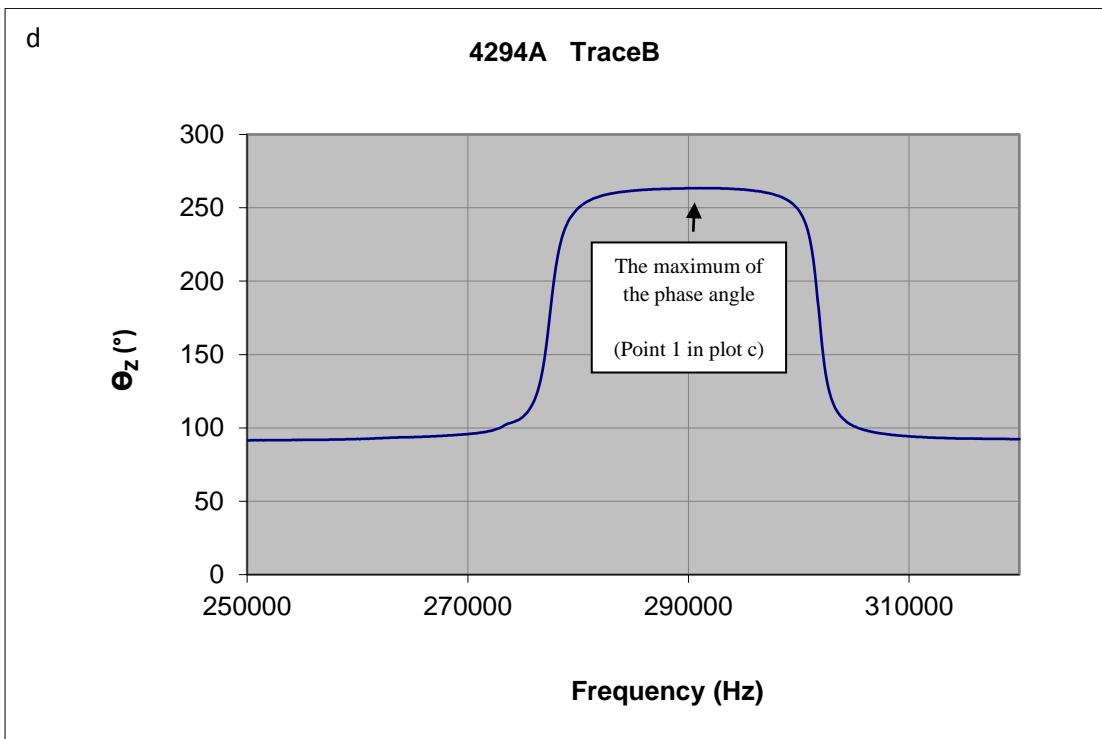
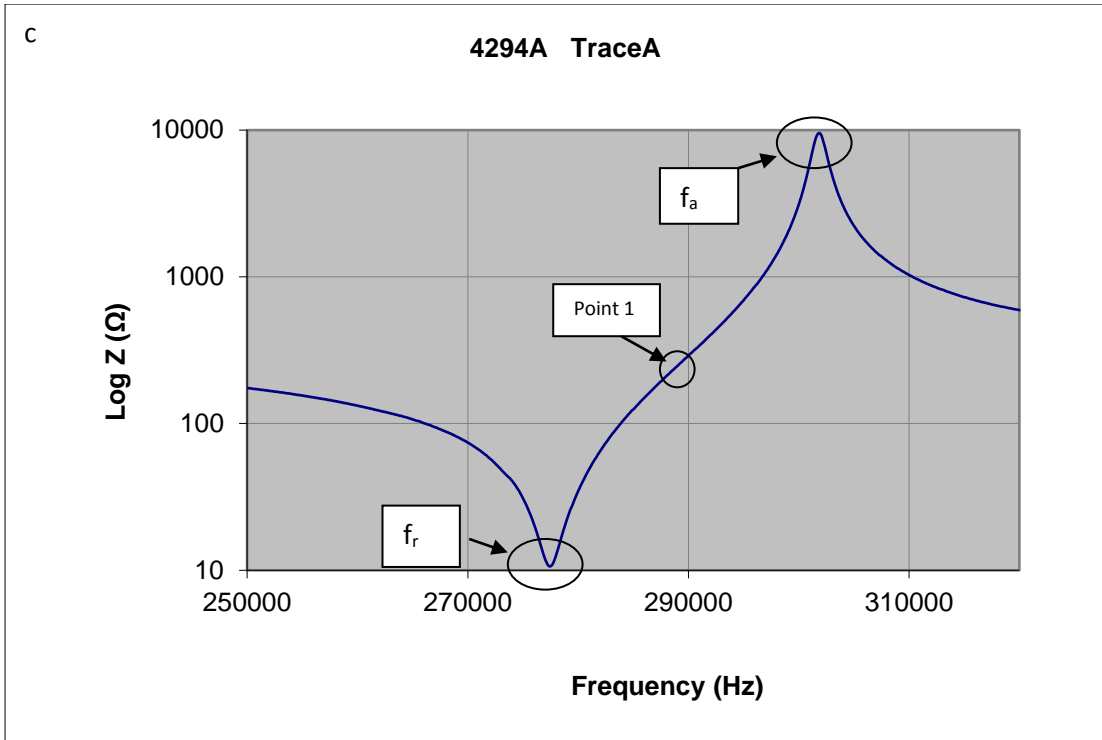


Figure 3-4: Impedance and phase plots of a typical piezoelectric sample showing how to measure the resonant and anti-resonant frequencies. a) The log of impedance at a range of the frequencies; b) the phase response corresponding to plot a; c) the log of the first impedance peak; and d) the phase response corresponding to plot c, which rises to a maximum value roughly at the centre of the resonance.

3.12 ECE indirect measurement

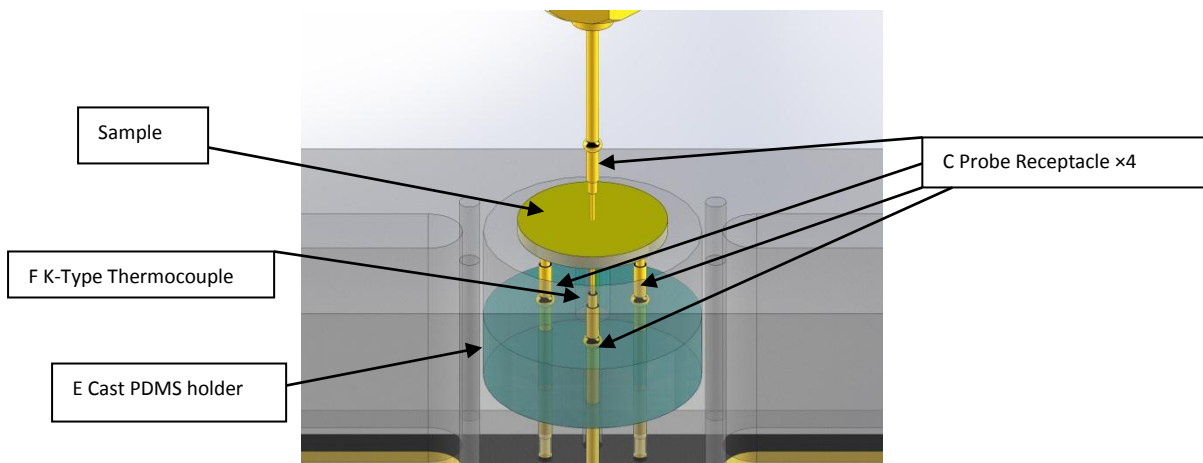
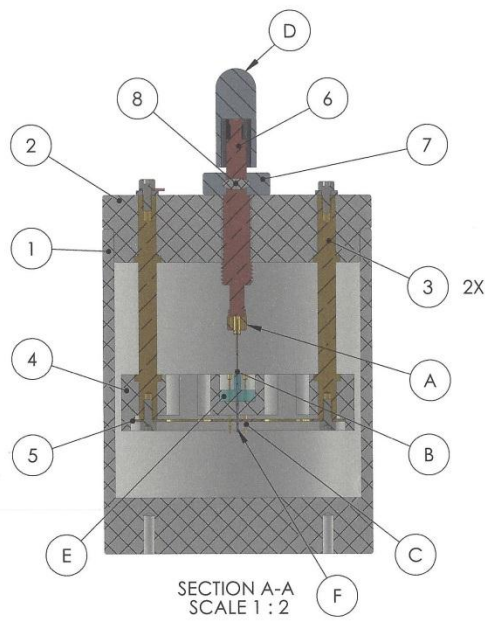
The ECE indirect measurement was performed by measuring polarisation-electric field loops at -30-150°C, with 10 °C increments. The other required data are heat capacity (measured by differential scanning calorimetry (DSC1, Mettler Toledo Co.USA)) and density, based on the equation 2-9 and the detail of experiment explained in section 5.1. Polarization-electric field measurements were carried out at the Central European Institute of Technology in Brno, Czech Republic, using the ferroelectric evaluating system AixPES, Aixacct (Advanced Customized Characterization Technology, Germany).

3.13 Direct measuring method

There are several ways of measuring ECE by the direct method, such as DSC, direct reading, and other methods, as explained in the literature review. All the methods are based on the fast-tracking of the temperature change in the materials. DSC can quickly measure the heat change in the materials, but there are some changes needed to the equipment, including the connection of a high voltage power supply and modification of the crucible to accept the samples. Scanning thermal microscopy has two types of temperature change detection: measuring it with a thermocouple or measuring the change in the resistance of detector and then calculate the temperature change. The temperature change is fast in the ferroelectric materials and the thermocouple has a high error rate, so a resistance based measurement is more accurate. The same measurement system is used for adiabatic calorimetry, and it can be done with a thermocouple or thermistor in a vacuum atmosphere, which entails design and manufacturing costs. Infra-red systems are based on pyroelectric materials and depend on the infra-red accuracy; they can measure the ECE in the materials. There are some limitations to the above measurement in this project, so the direct reading method was selected. This can be done in almost every lab with a minimum of facilities, and is cheaper than the other methods. The ECE measurement can be done based on thermistor or thermocouple systems; due to the faster tracking, the thermistor was selected for this project. The primary design was done in Solidworks software, and can be seen in Figure 3-5, and the device construction was undertaken by Carl Meggs in the School of Metallurgy and Materials, University of Birmingham. The basis of direct reading is similar to the poling machine for the ferroelectric materials; it has two electrodes that apply an electric field, with one pin and one plate used as electrodes. In this project, pins were used instead of a plate due to their lower heat conductivity, and the diameter of the pins was decreased to reduce heat conduction, which can affect the ECE. Three pins were placed at the bottom, which were inserted through a

PDMS (polydimethylsiloxane) holder to reduce heat conduction and protect the electrode, with one pin above of the sample. For the measurement of temperature, a precise thermocouple close to the sample is needed, so a thermocouple was held between the electrodes and inside the PDMS, less than 1mm from the sample to protect the thermocouple and prevent any short circuits. A K-type thermocouple or resistance temperature detector (RTD) is needed to measure the exact temperature of the environment and a negative temperature coefficient (NTC) thermistor (ATC SEMITEC LTD-axial glass-encapsulated diode style-104ATCDB-#P) in contact and at top of the sample measured the temperature of the sample. A base of PTFE (polytetrafluoroethylene (Teflon)) was selected for all the parts to help maintain a constant temperature inside the device, with two hollow brass supports where any wires (for example, for thermocouples) could be routed from the outside to the inside. The PTFE has two main parts, the base and the lid, and the top electrode pin is held in the lid. The inside of the device is filled with silicone oil to protect the sample from breakdown voltage, and minimise moisture ingress during storage. Figure 3-6 shows the thermistor attached to the sample, which monitors the difference between the resistance before and after applying and removing the electric field, giving the temperature gradient.

- 1 PTFE Base
- 2 PTFE Lid
- 3 Brass Support x2
- 4 PTFE Crossbeam
- 5 Connector Bar
- 6 Copper Electrode
- 7 Knurled Adjuster
- 8 PTFE Pin
- A SMA Connector
- B Spring Contact Probe x4
- C Probe Receptacle x4
- D Spark Plug Cap
- E Cast PDMS Holder
- F K-Type Thermocouple or RTD



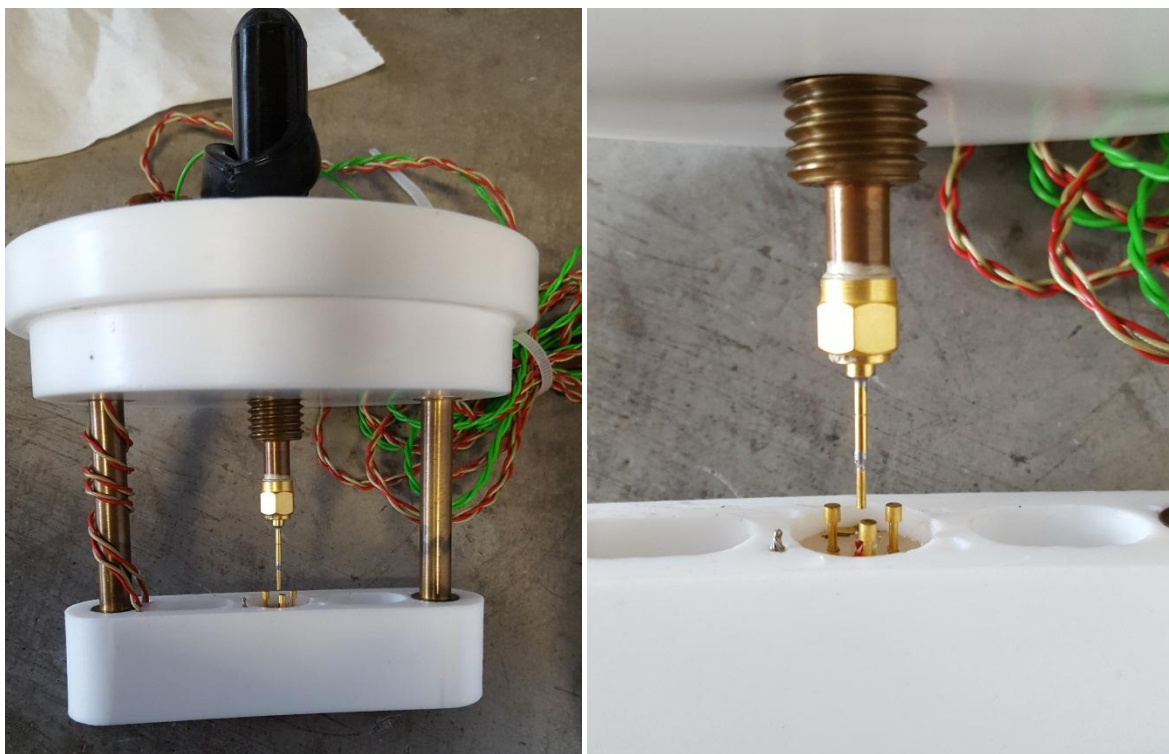
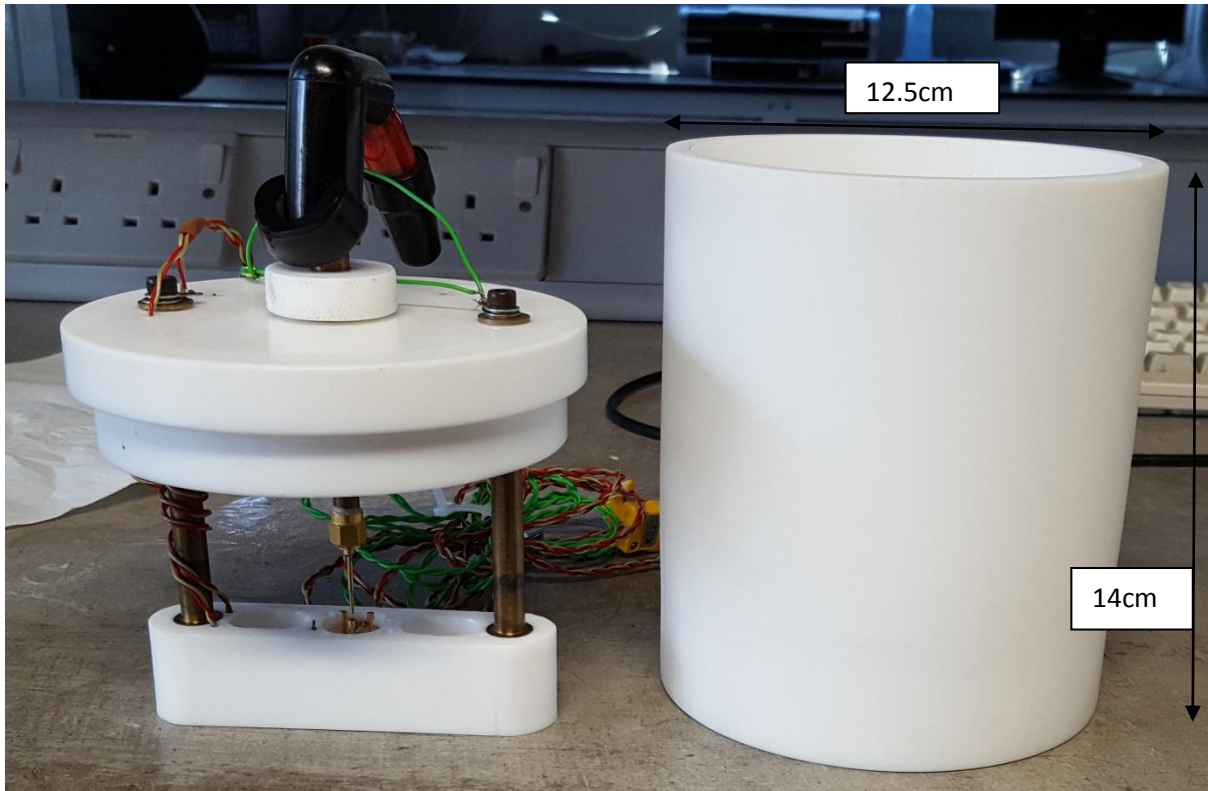


Figure 3-5: The measurement apparatus constructed for direct temperature reading to measure the ECE, with all parts, and a close view from the sample in the middle of probes.

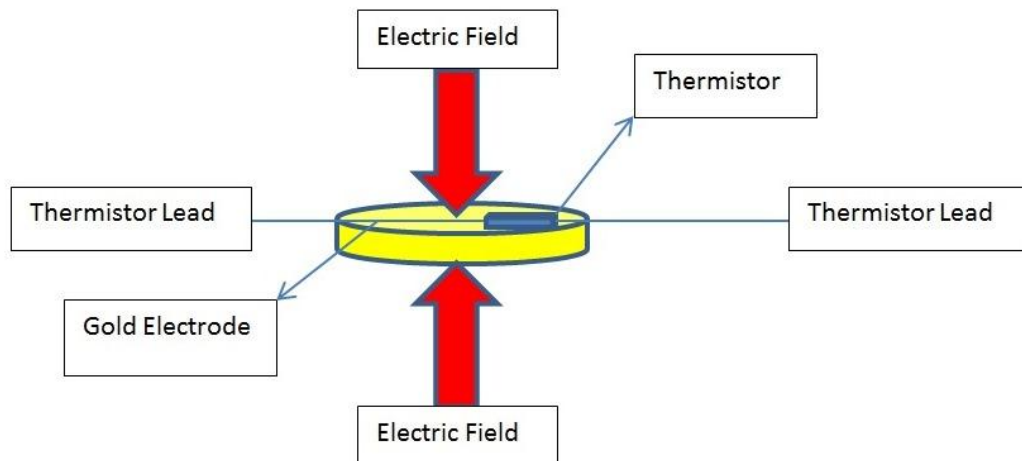


Figure 3-6: Schematic of the application and removal of the electric field on the sample

The resistance of the thermistor was measured using a digital multimeter, Keithley Instrumentation Company (2400). The direct temperature reading device was put in an environmental chamber (Tenney Company, TJR model) to make sure the temperature is constant and uniform in all the devices for two hours and each specific temperature, and a step size of 10°C was selected to measure the ECE from -30 to 125°C (Figure 3-7). The same was done for all of the samples. The electric field values of 1, 2, and 3 kV/mm were applied, in less than one second for each and after that, the temperature was recorded versus the time in order to obtain the thermal gradient ΔT . A total of 90 seconds were allowed until the sample temperature was the same as that of the environment. After that, the electric field was removed, which caused the temperature of the sample to decrease below that of the environment. Figure 3-8 shows the schematic of the application and removal of the electric field on the sample.

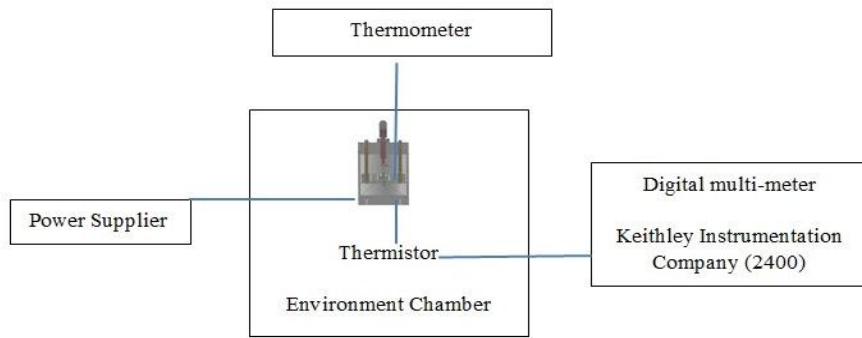
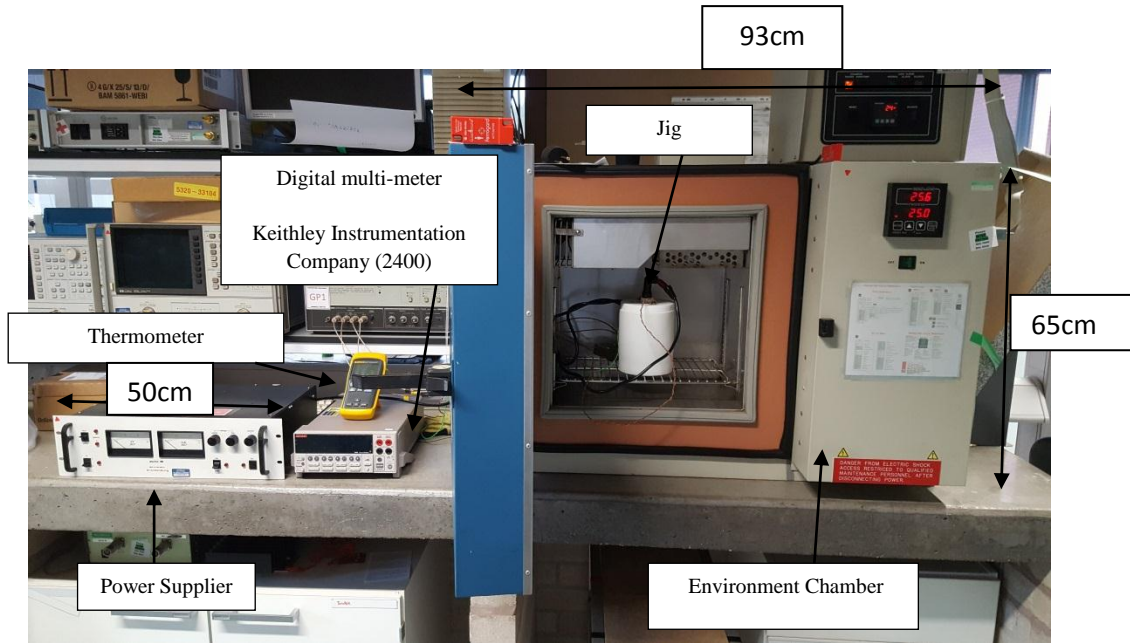


Figure 3-7: Photograph and schematic diagram of the ECE direct reading measurement equipment.

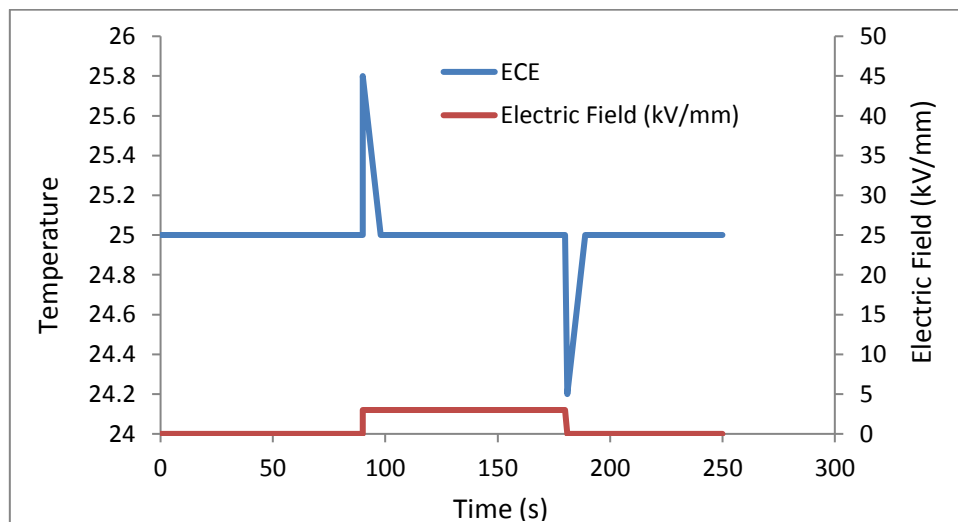


Figure 3-8: Schematic of the change in sample temperature with time on the application and removal of the electric field on the sample

Figure 3-9 shows the calibration of the resistance of the thermistor, versus the temperature between -50 and 150°C. A negative temperature coefficient (NTC) thermistor shows a reduction in the resistance with an increase in the temperature and, as can be seen, the resistance decreases with the rise in temperature. When the electric field was applied, a sharp reduction was seen in the resistance and it returned back to the primary resistance after around 90s. When the electric field was removed, a sharp rise was seen in the resistance, and again it returned back to the primary resistance after around 90s.

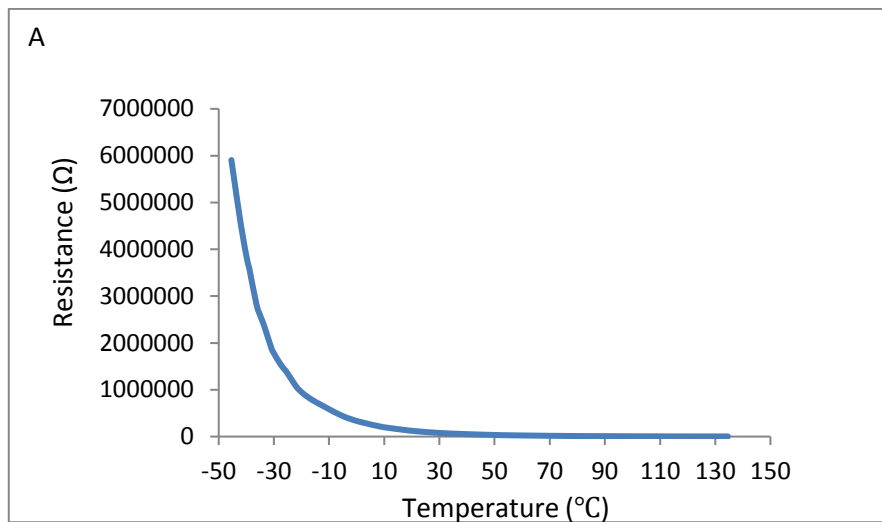


Figure 3-9: Calibration of the resistance of the thermistor versus the temperature between -50 and 150°C.

The resistance of the thermistor was measured for the experimental temperatures range, and the difference between the resistance of the sample without an electric field and under the electric field was calculated; based on the graph in Figure 3-9, the thermal gradient was calculated for all samples.

3.14 Measurement errors, repeatability, and reproducibility

Measurements of the relative density and piezoelectric properties were repeated three times on three different samples of the same composition to measure errors and check the repeatability of the experiments. This was done for relative density, k_p , d_{33} , and relative permittivity at room temperature. The grain size of the samples was measured for three areas of each sample. The measurement was done once for relative permittivity at a range of temperatures and indirect electrocaloric measurements, but the software measured them three

times and the average of the results was recorded in the thesis. Random samples were then selected and the experiments repeated to check their repeatability. A direct ECE measurement was done three times for each sample for any temperature and an average value was recorded. This was repeated for three samples to check the repeatability of the experiments. The entire process was repeated (i.e. powder mixing, calcination, sintering, XRD etc) and the property measurements, and then the ECE measurements, were done again to check reproducibility.

Chapter

4 Fabrication, characterisation, and optimisation of the ceramics

4.1 The fabrication and characterisation of the materials

The fabrication and characterisation of the materials to be investigated in this project will be described in the following sections. First, the calcination of the powders is described for BCZT and then, the optimisation of this composition is investigated.

4.2 Fabrication of $0.5((\text{Ba}_{0.7}\text{Ca}_{0.3})\text{TiO}_3)-0.5(\text{Ba}(\text{Zr}_{0.2}\text{Ti}_{0.8})\text{O}_3)$ or $\text{Ba}_{0.85}\text{Ca}_{0.15}(\text{Zr}_{0.10}\text{Ti}_{0.90})\text{O}_3$

Two methods were used to fabricate BCZT; firstly, preparing the BCT ($\text{Ba}_{0.7}\text{Ca}_{0.3}\text{TiO}_3$) and BZT ($\text{Ba}(\text{Zr}_{0.2}\text{Ti}_{0.8})\text{O}_3$) separately, mixing them together, and calcining at 1250°C for two hours, and secondly, mixing all of the raw materials at the same time, and calcining at 1250°C . The powders prepared using the solid-state method were calcined at 1250°C for BZT. Figure 4-1 shows the XRD patterns of BZT, with a small amount of ZrO_2 remaining. The ionic radius of Zr^{4+} is 0.72\AA , which is a slightly larger than Ti^{4+} (0.605\AA) [20], and causes an expansion of the BT lattice and a shift of the 2θ positions to a lower angle, in comparison with the BT, as shown in Figure 4-2. The splitting of peaks at around $2\theta=30, 56,$ and 75° , which shows that the tetragonal phase does not occur here, indicating a rhombohedral symmetry [20, 22].

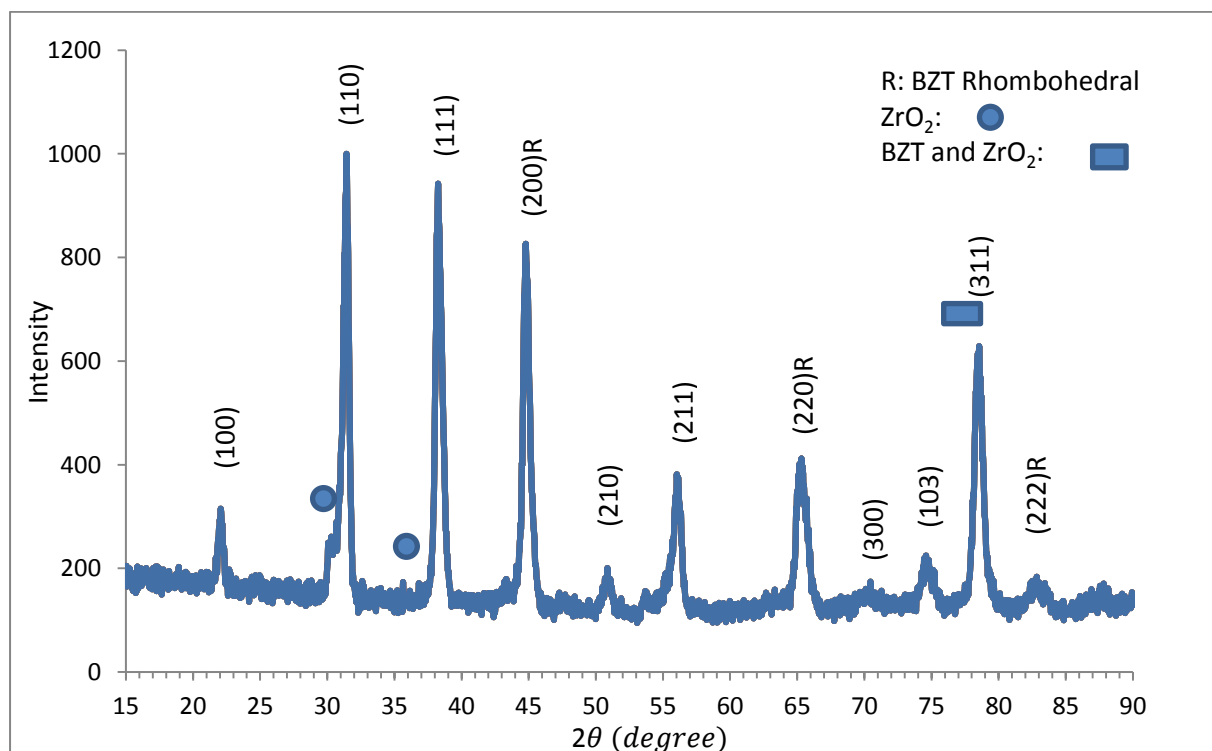


Figure 4-1 The XRD patterns of BZT, calcined at 1250°C for two hours,

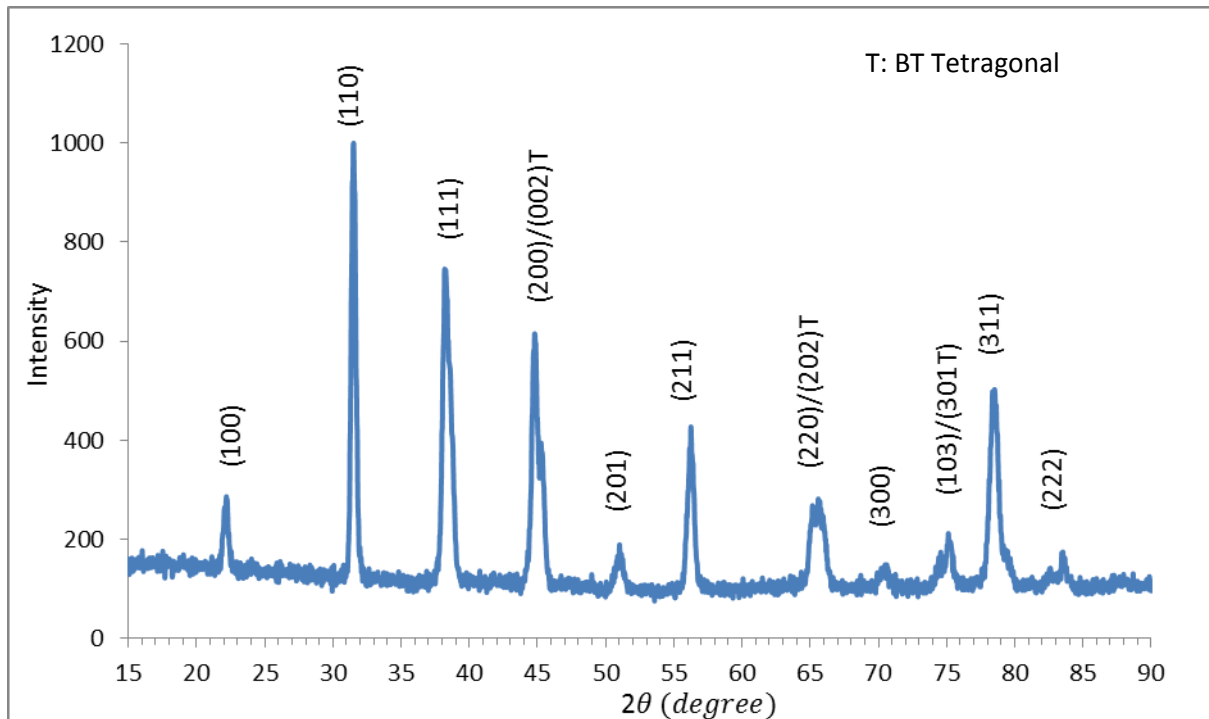


Figure 4-2: The XRD patterns of BT, calcined at 1100°C for two hours

To prepare BCT, the powders prepared by the solid-state method were also calcined at 1250°C. Figure 4-3 shows the XRD patterns of the calcined BCT. The XRD patterns show the perovskite structure, and the splitting of peaks at about $2\theta=45, 65,$ and 75° are indicative of the formation of a tetragonal structure, checked by the collection code 190928 at the ICDS. At this temperature, additional peaks due to CaTiO_3 phase can also be seen, indicating that this temperature is not high enough for the formation of BCT (in comparison to Figure 4-2), and a higher temperature is needed. However, after mixing the calcined BZT and BCT together, followed by further calcination at 1250°C, there were no secondary phases, as is shown in the XRD of BCZT in Figure 4-4. This demonstrates that the two-step calcination process allows more time for diffusion and homogeneity to occur.

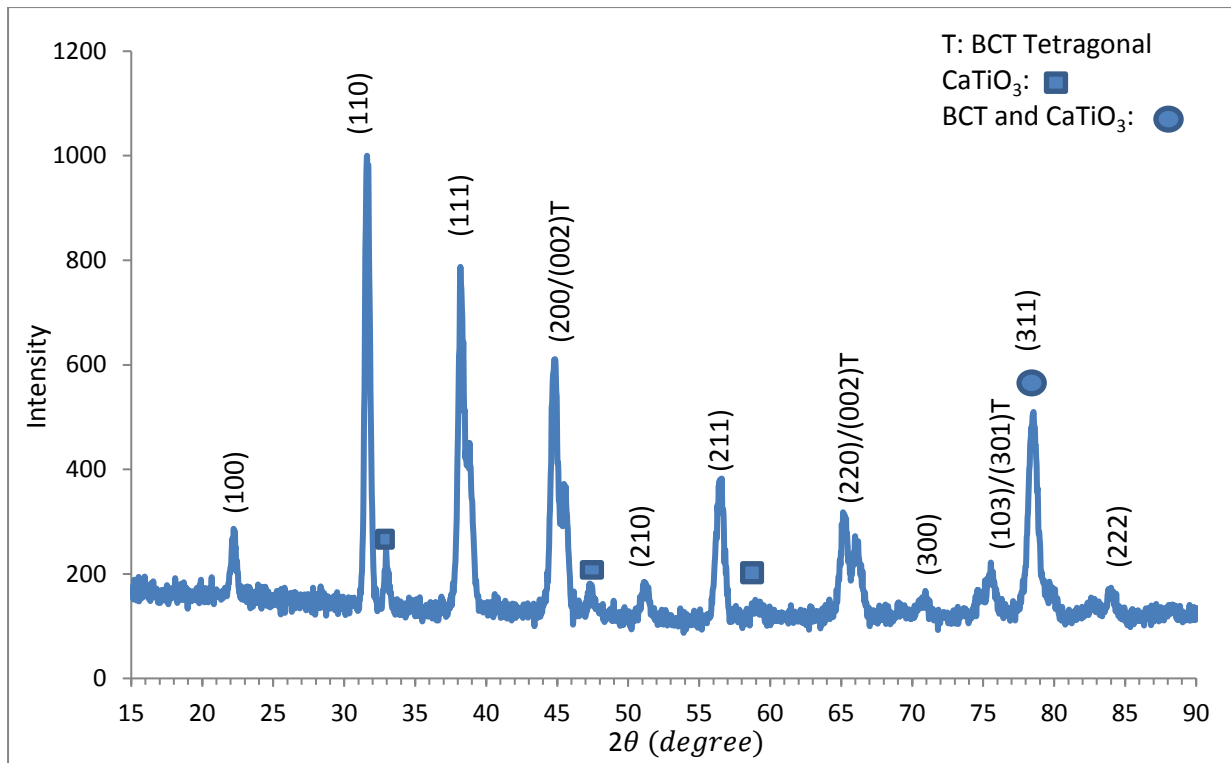


Figure 4-3 The XRD patterns of BCT, calcined at 1250°C for two hours.

Figure 4-4 shows the XRD patterns of BCZT for both methods of formation and also the sintered sample of the powder calcined directly from the raw materials (checked by the ICSD collection code: 187674 and 187675). There is no difference between the XRD patterns of samples produced by both fabrication methods and in general, the synthesis of BCZT directly from raw materials needs less time and heating, which makes it easier. In addition, some of the properties of samples from both methods, such as the d_{33} and relative permittivity, were measured and no difference was observed. For these reasons, the direct fabrication method (BCZT 2) was chosen for further work in this project.

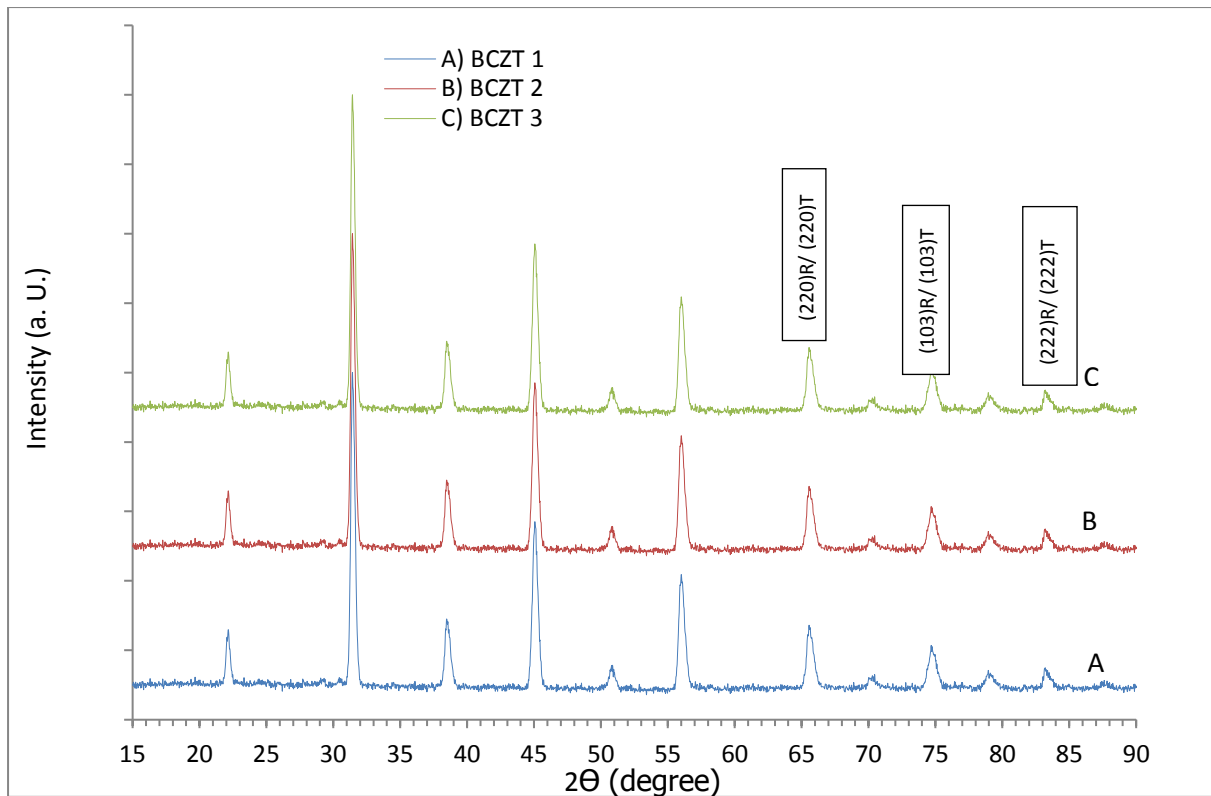


Figure 4-4: The XRD patterns of firstly, BCZT 1: Calcined BCZT from BZT and BCT calcined at 1250°C for two hours and secondly, BCZT 2: calcined BCZT from raw materials at 1250°C for two hours and BCZT3: BCZT2 sintered at 1450°C for two hours.

Figure 4-5 shows the SEM images of BCZT samples sintered at 1400, 1425, 1450, 1475, and 1500°C for two hrs. Figure 4-6 shows the effect of the sintering temperature on the relative density of the BCZT ceramics samples, and Figure 4-7 shows the effect of the sintering temperature on the grain size of the BCZT samples.

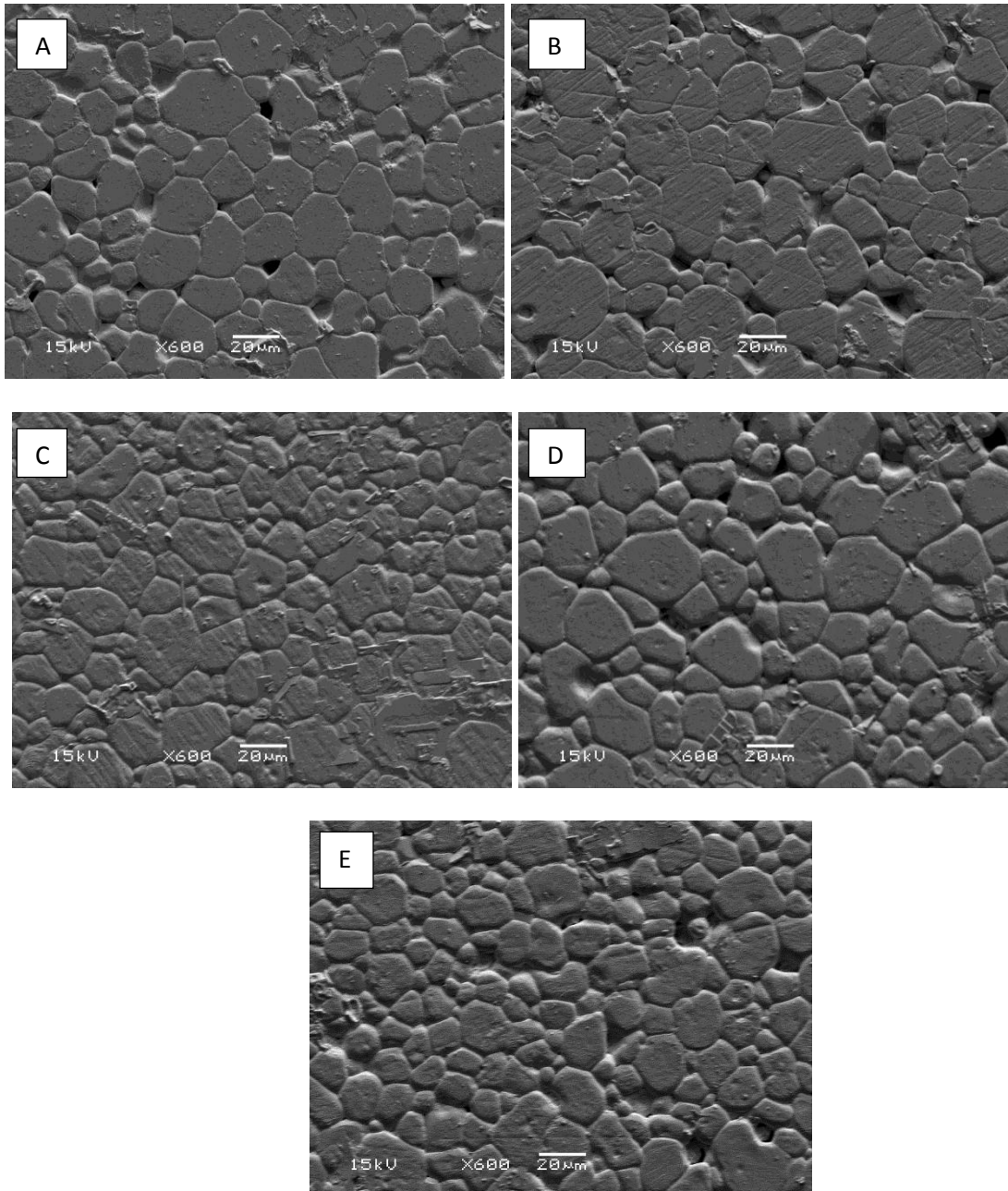


Figure 4-5: SEM micrographs of the BCZT samples, sintered at A) 1400°C, B) 1425°C, C) 1450°C, D) 1475°C, and E) 1500°C for two hrs (see the appendix for a low magnification photo).

It can be seen that the relative density increases as the sintering temperature increases from 1400°C to a maximum value of 96%, for the samples sintered at 1450°C. Any further increase in the sintering temperature results in a slight decrease in the relative density, to 94.5% at 1500°C. A comparison of the density with the SEM images show that for the samples sintered at 1400°C, there is a large number of intergranular pores, while the grain sizes are small, so it causes a relative density of around 92%. Through a rise in the sintering temperature, a reduction in the intergranular porosity and a corresponding increase in the grain size can be seen, resulting in an increased density. After that, in

spite of any increase in the grain size, the density decreases from 96% to 94.5%, which can be attributed to the volatilisation of some elements [43], or grain growth happens before the complete densification, which can then trap porosity. The volatilisation continues at a higher temperature and causes the density to decrease from 95.5% at 1475°C to 94.5% at 1500°C, as it can be seen in the SEM images. The relative density of all BCZT samples is higher than 90%, which is similar to previous research for sintering temperatures greater than 1400 °C [42, 43].

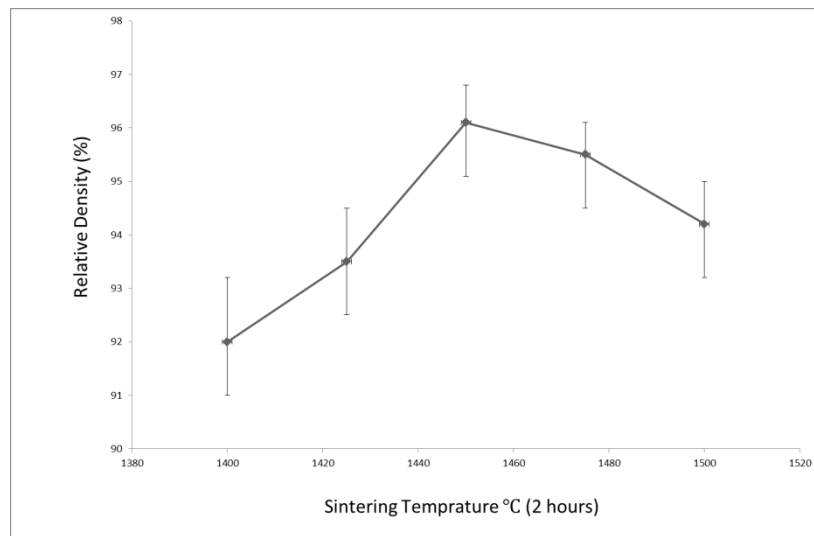


Figure 4-6: Variation in the relative density as a function of the sintering temperature for BCZT

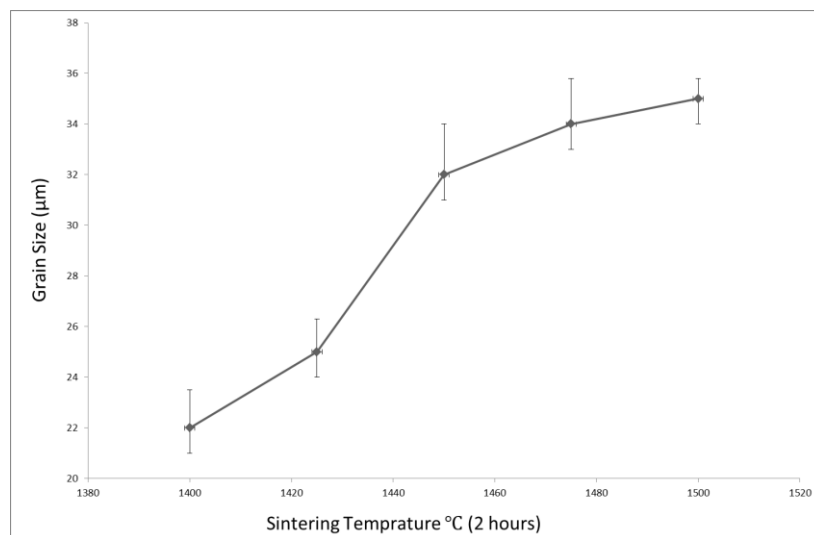


Figure 4-7: The variation in grain size as a function of the sintering temperature for BCZT

Figure 4-8 and Figure 4-9 show the relative permittivity of unpoled samples and d_{33} of the samples sintered at various temperatures. The d_{33} and relative permittivity both increase as the sintering temperature increases from 1400 to 1450°C, and then decrease slowly, as the

sintering temperature further increases from 1475 to 1500°C, following the same trend as the relative density.

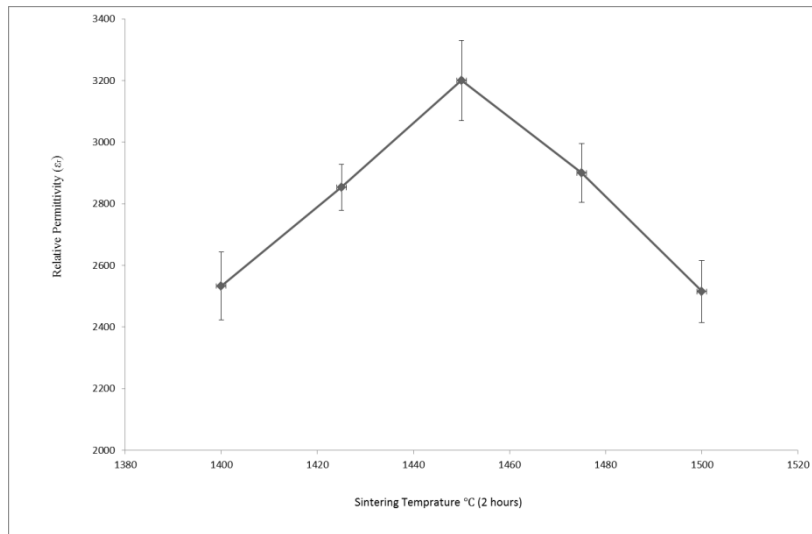


Figure 4-8: The variation of relative permittivity of unpoled samples as a function of sintering temperature for BCZT, measured at room temperature.

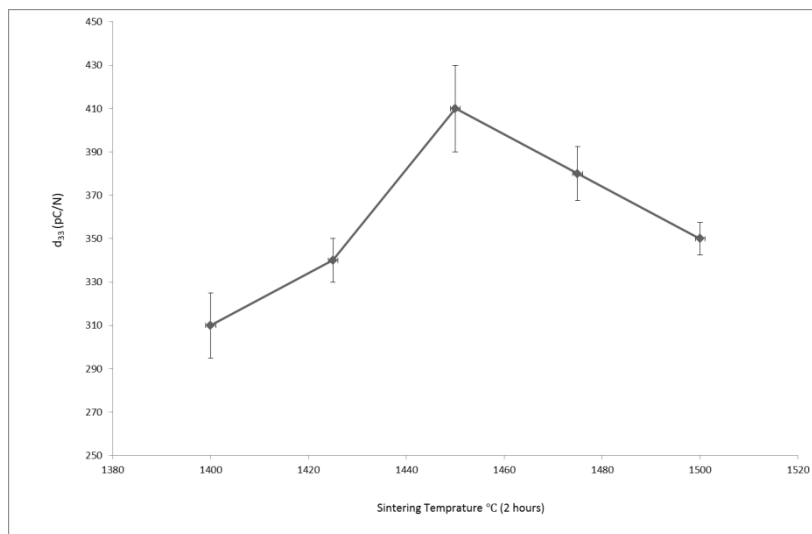


Figure 4-9: The variation of d_{33} as a function of sintering temperature for BCZT, measured at room temperature.

Figure 4-10 shows the variation of k_p as a function of sintering temperature for BCZT sintered at 1400, 1425, 1450, 1475, and 1500°C. The value of k_p is around 36% for BCZT sintered at 1400°C, and increases with increasing sintering temperature to reach a maximum value of 46%, for samples sintered at 1450°C. With a further increase in sintering temperature, the k_p decreases to a value of 42% for samples sintered at 1500°C. This trend is similar to those reported above for the d_{33} and relative density, with the properties maximised for the samples sintered at 1450°C. Any increase in the grain size leads to a rise in the d_{33} and relative

permittivity, but there is an optimal grain size and after that, both fall. The relationship is more similar to density; i.e., by an increase in the density, d_{33} and relative permittivity reach the highest value and after that, both decrease.

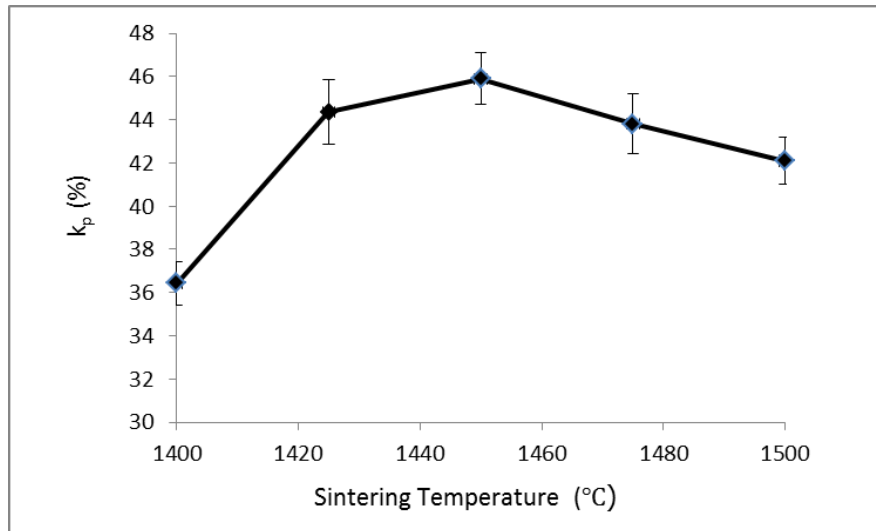
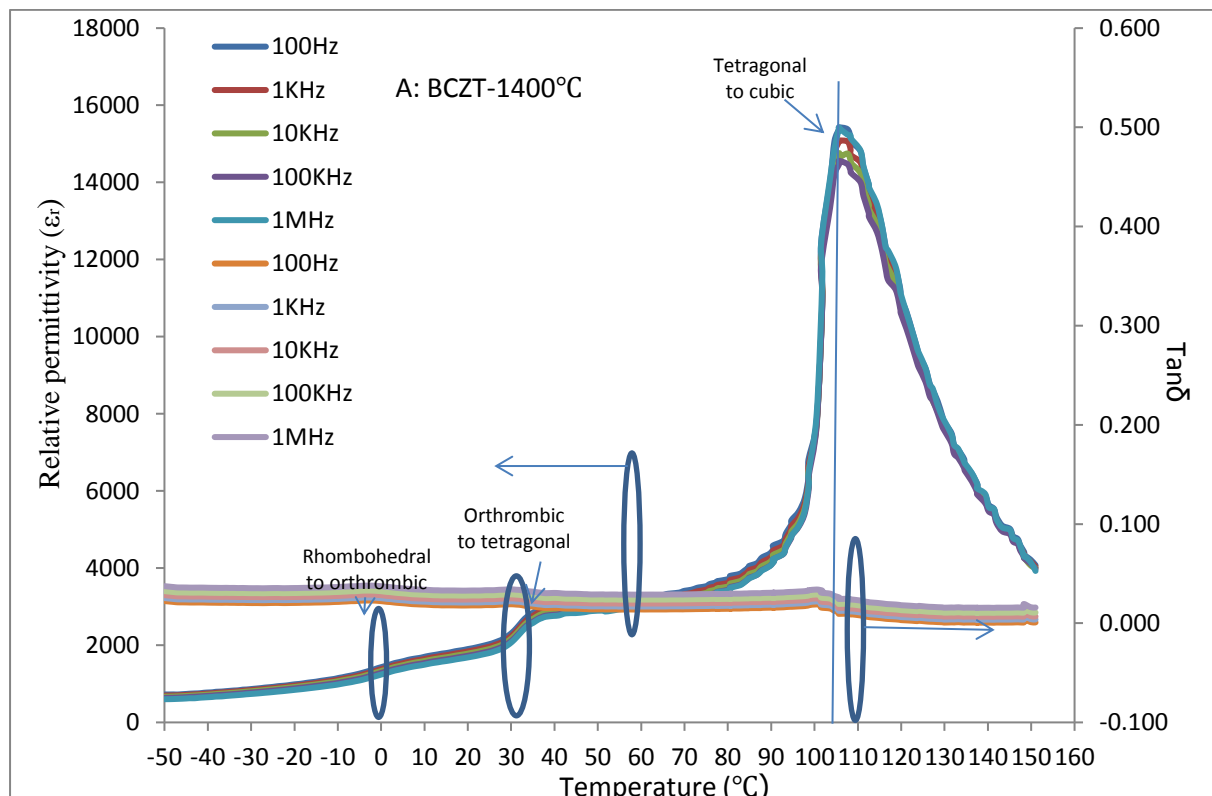
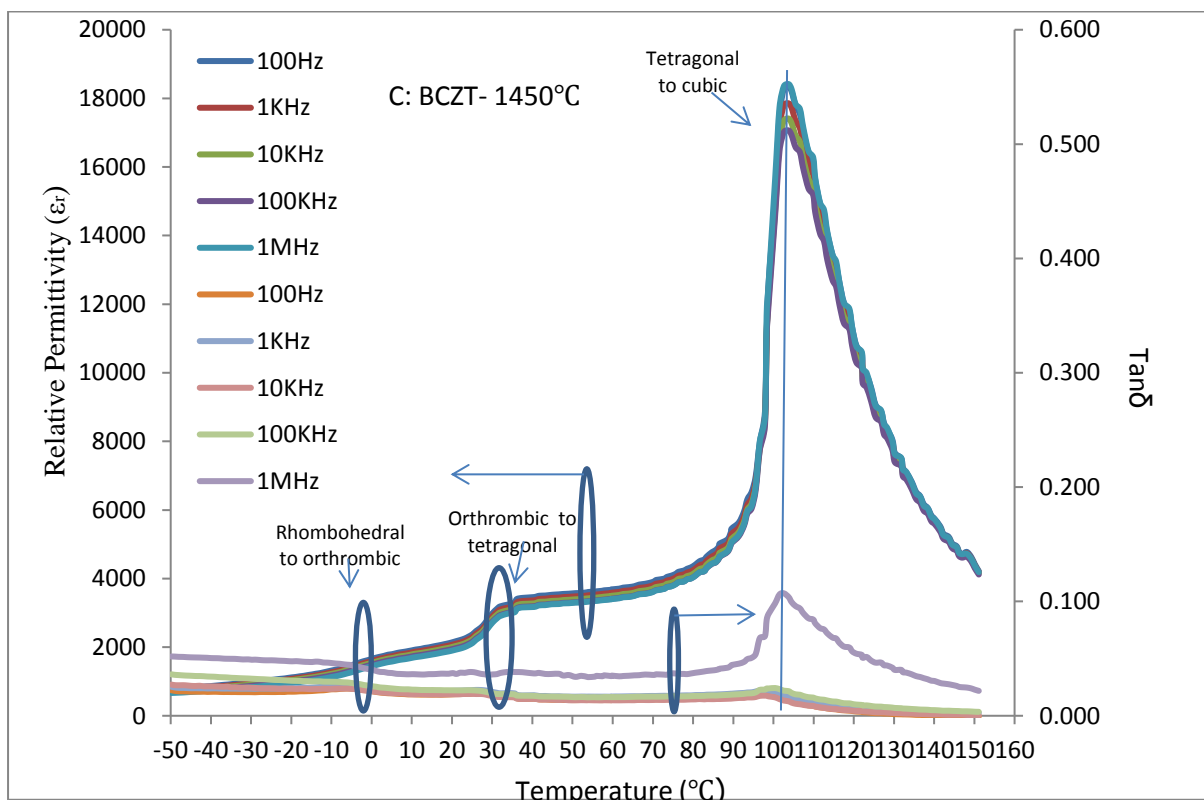
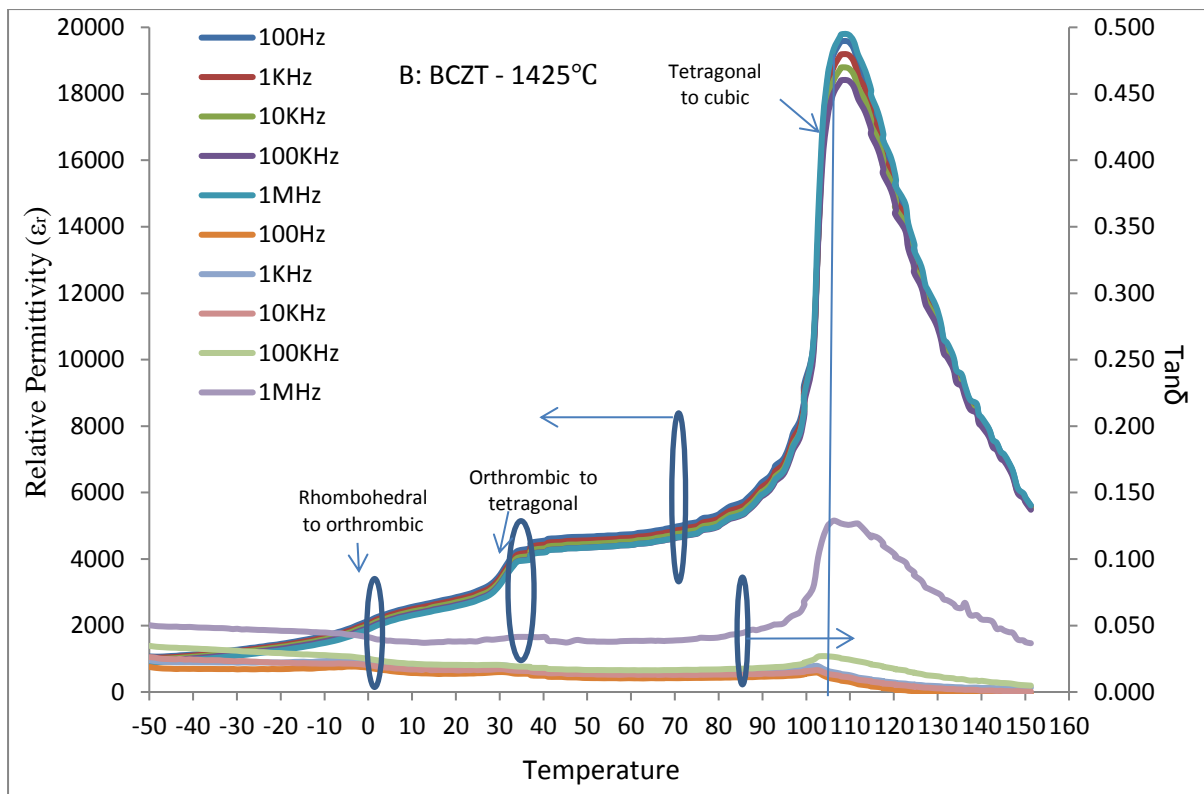


Figure 4-10: The variation of k_p as a function of sintering temperature for BCZT, measured at room temperature.

Figure 4-11 shows the temperature dependence of relative permittivity (ϵ_r) and dielectric loss ($\tan\delta$) of unpoled samples at five different frequencies (100Hz, 1 kHz, 10 kHz, 100 kHz, and 1 MHz) for BCZT samples sintered at 1400, 1425, 1450, 1475, and 1500°C for two hours; details of the plots have been summarised in Table 4-1. Their schematics are all similar, while there are three anomalies in each, which are related to the phase transformations. The relative permittivity slightly decreased with increases in the frequency from 100Hz to 1MHz, and the value of the dielectric loss is low (under 0.1) for all the samples and frequencies, and it is increased by increasing the frequency from 100Hz to 1MHz. There has been some discussion in the literature about BCZT structures at similar temperature ranges. In 2009, Liu et al. [15] reported high piezoelectric and ferroelectric properties such as a high $d_{33}=620$ pC/N and $E_c=2$ kV/mm in the $\text{Bi}_{0.85}\text{C}_{0.15}\text{Z}_{0.1}\text{T}_{0.9}\text{O}_3$ structure. They attributed the good properties to the coexistence of tetragonal and rhombohedral phases, or in other words, the existence of an MPB at room temperature for this composition, although the techniques used may not be sensitive to small amounts of other phases. Further research was done by Keeble et al. [46] on the BCZT structure via high-resolution powder diffraction beamlines and have found an orthorhombic intermediate phase between the tetragonal and rhombohedral phases.

One of the measurements that are sensitive to structural transformation is relative permittivity and dielectric loss, which can be measured at a range of temperatures; with peaks or discontinuities in these properties being observed at the phase transformation temperatures. It has been proven that at low temperatures from -50 to -4°C, the BCZT structure is rhombohedral [46]. The first peak can be seen at around -4°C, which can be attributed to the formation of the orthorhombic phase, and it continues until 4°C. This peak is quite small because polycrystalline materials usually show low latent heat; this is quite similar to second-order phase transformations and for this reason, is usually hard to observe. The transformation from rhombohedral to orthorhombic has taken place from -4 to 4°C, which can be attributed to the coexistence of both phases at a range of temperatures. The second peak starts from 24°C, which can be matched by the transformation from orthorhombic to tetragonal, and it continues to around 37°C, implying the coexistence of orthorhombic and tetragonal phases. There is no peak until around 90°C and after that, the permittivity goes sharply up to a maximum value, as is typical for normal ferroelectric behaviour. From around 95°C, the cubic phase starts to form until around 105°C, which shows the coexistence of the tetragonal and cubic phases and after that, only cubic phase exists, and there is a sharp reduction in relative permittivity.





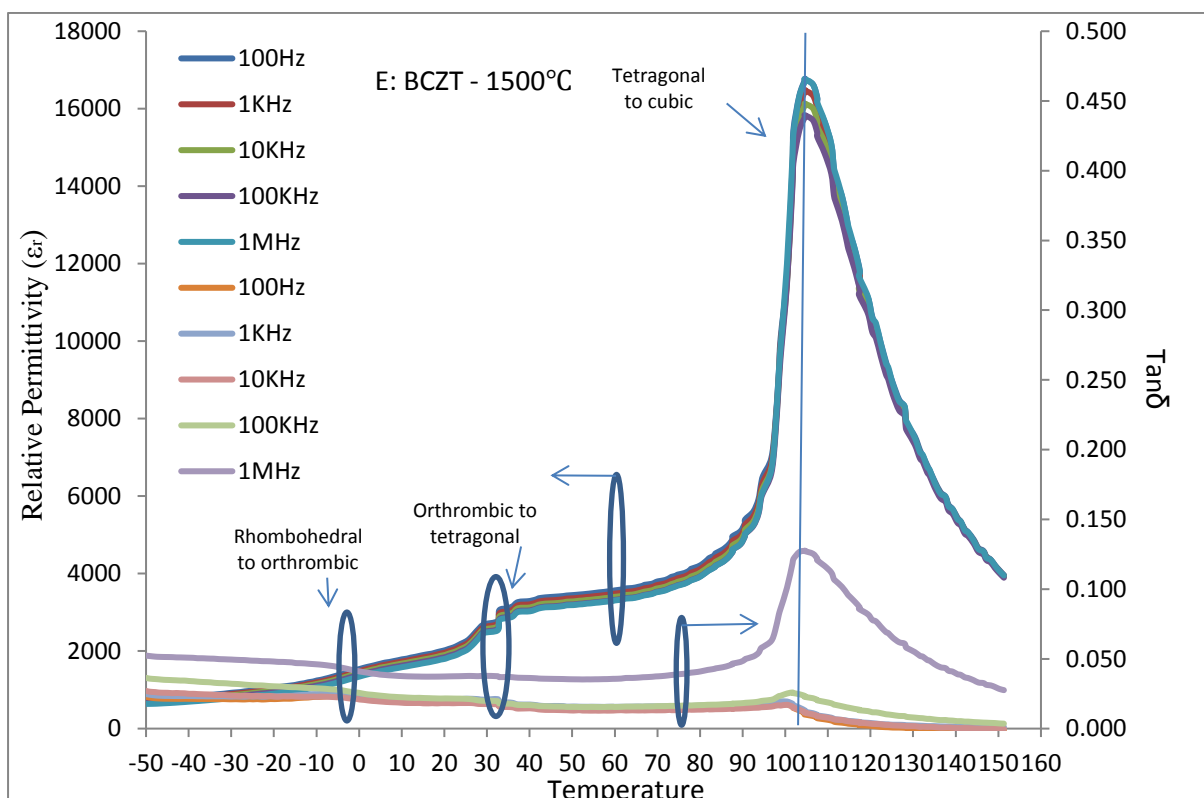
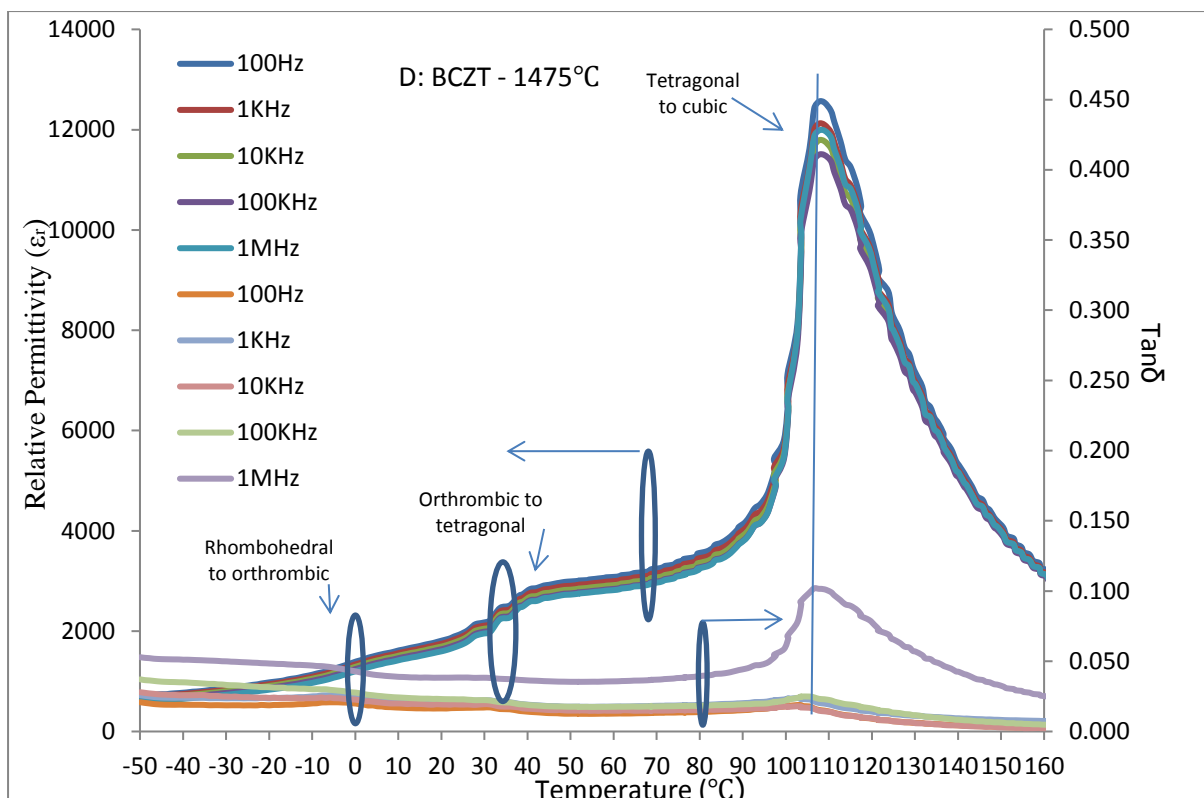


Figure 4-11: The temperature dependence of relative permittivity (ϵ_r) and dielectric loss ($\text{Tan}\delta$) of unpoled samples at 100 Hz, 1 kHz, 10 kHz, 100 kHz, and 1 MHz for BCZT sintered samples at A) 1400, B) 1425, C) 1450, D) 1475, and E) 1500°C for two hours.

The results of the BCZT-sintered samples are summarised in Table 4-1. The best results such as relative density and d_{33} can be seen at 1450°C. There are a number of different values of maximum relative permittivity for the samples sintered at different temperatures. The values increase from 1400°C to 1450°C and after that, decrease as the sintering temperature is increased to 1500°C. At higher sintering temperatures, in spite of the increased grain size, the porosity and associated space charges increase, which can lead to a reduction in the maximum relative permittivity.

Table 4-1: Summary of the properties of BCZT sintered at different temperatures

Sintering temperature (°C)	1400	1425	1450	1475	1500
Relative density%	92±0.6	93.5±0.5	96.1±0.3	95.5±0.3	94.2±0.4
d_{33} pC/N	310±15	340±10	410±20	380±13	350±8
RT ϵ_r	2533±110	2853±75	3200±130	2900±95	2515±100
Grain size (μm)	22±1.5	25±1.3	32±2	34±1.8	35±0.8
Max ϵ_r	15100	19200	17900	12100	16500
k_p (%)	36±1	44±1.5	46±1.2	43±1.4	42±1.1
Phase transition - rhombohedral to orthorhombic (°C)	-4 to 4.2	-3.8 to 4	-3.9 to 4.1	-3.8 to 4.1	-3.8 to 4.1
Phase transition- orthorhombic to tetragonal (°C)	23.1 to 35.7	24.1 to 37.1	24.1 to 37.5	23 to 37.8	23 to 37.3
Phase transition - tetragonal to cubic (°C)	96.4 to 105.7	94.7 to 108	94.6 to 104.2	94.1 to 107.7	96.7 to 105.5

4.2.1 The effect of $\text{Bi}_{0.50}(\text{Na}_{0.82}\text{K}_{0.18})_{0.50}\text{TiO}_3$ on $\text{Ba}_{0.85}\text{Ca}_{0.15}(\text{Zr}_{0.10}\text{Ti}_{0.90})\text{O}_3$

The effect of $\text{Bi}_{0.50}(\text{Na}_{0.82}\text{K}_{0.18})_{0.50}\text{TiO}_3$ (abbreviated BNKT) when added to BCZT has been investigated. BNKT (calcined at 700°C) and BCZT (calcined at 1100°C) were made in

CEITEC and then mixed and sintered in our lab. BNKT shows relaxor ferroelectric behaviour, with d_{33} = 80-120 pC/N, depolarisation temperature (T_d) of nearly 200 °C, and k_p values around 0.32 [220, 221]. The goals of the addition of BNKT to the BCZT can be defined as firstly, to investigate the effect of the addition of a material with relaxor behaviour on the properties of BCZT and secondly, to investigate the effect of this additive on the ECE of BCZT. Samples of BCZT were prepared with additions of 1, 3, and 5 wt% BNKT, and sintered at temperatures of 1250, 1300, 1350, 1400, 1450, and 1500°C for four hours.

4.2.1.1 BCZT-1, 3, and 5% BNKT

Figure 4-12, Figure 4-14, and Figure 4-16 show the XRD patterns for the powders of BNKT (calcined at 700°C) and BCZT (calcined at 1100°C), and BCZT-1, 3, and 5% BNKT samples respectively, sintered at 1250, 1350, 1450, and 1500°C for four hours. It can be seen in the XRD pattern of the BNKT powders (checked by the ICSD collection code: 98054) that there is another phase that can be attributed to the pyrochlore ($\text{Bi}_2\text{Ti}_2\text{O}_7$) phase, checked by the ICSD collection code: 99437. The pyrochlore phase forms during the calcination of the BNKT powders, but it disappears during the sintering process at a higher temperature. The BCZT calcined powder has been shown here for comparison with the samples of BNKT to investigate the effect of this additive on the XRD patterns (checked by the ICSD collection codes: 187674 and 187675). The BCZT powder was calcined at 1100°C (prepared in the CEITEC) and for this reason, there are some remains of ZrO_2 (checked by the ICSD collection code: 67004), which during the sintering process, diffuses into the perovskite structure. It can be seen that for the samples sintered at 1250, 1350, 1450, and 1500°C, the peaks slightly shift to lower angles, as the sintering temperature is increased (Figure 4-13, Figure 4-15, and Figure 4-17).

Bismuth (Bi^{3+} =0.096nm), sodium (Na^+ =0.095nm), and potassium (K^+ =0.133nm) can be substituted on the A site in the perovskite structure in place of barium (Ba^{2+} =0.135nm) and calcium (Ca^{2+} =0.099nm), while the B site can have as a substitute titanium (Ti^{4+} = 0.068) instead of zirconium (Zr^{4+} =0.079) [10]. In this case, due to the smaller ionic radius of the replacement ions, it would be expected that the XRD peaks shift to higher angles, but they have instead moved to lower angles. One possible reason for this might be firstly, the diffusion of bismuth, sodium, and potassium at the B site [10], which would lead to the peaks moving to lower angles, and secondly, BNKT did not diffuse into the BCZT structure and, has been held between the BCZT grains, and the peaks decrease to lower angles. The

possibility of the second reaction is higher than the first one, because due to the lower evaporation temperature of the BNKT, the relative density of BCZT-1, 3, and 5% BNKT (Figure 4-21) are decreased. As can be seen, this shift is higher for BCZT-1% BNKT at 1250°C and at 1350°C, and it then goes back, and again for 1450 and 1500°C, it goes to lower angles. The evaporation of BNKT is lower at low temperatures due to low evaporation of this composition (1200°C) [10], so can cause the peaks to go to lower angles at 1250°C. At 1350°C, more BNKT evaporation causes the peaks to shift to higher angles, and it seems that lower evaporation and growth of the remnant BNKT for 1450 and 1500°C causes the peaks to shift to lower angles again. In general, the amount of BNKT added below the amount which they can be detected by XRD. By increasing the amount of the BNKT, the XRD peaks slightly shift to higher angles. The existence of higher amounts of BNKT grains between BCZT grains can cause the XRD patterns to go to higher angles (more figures can be seen in the Appendix I).

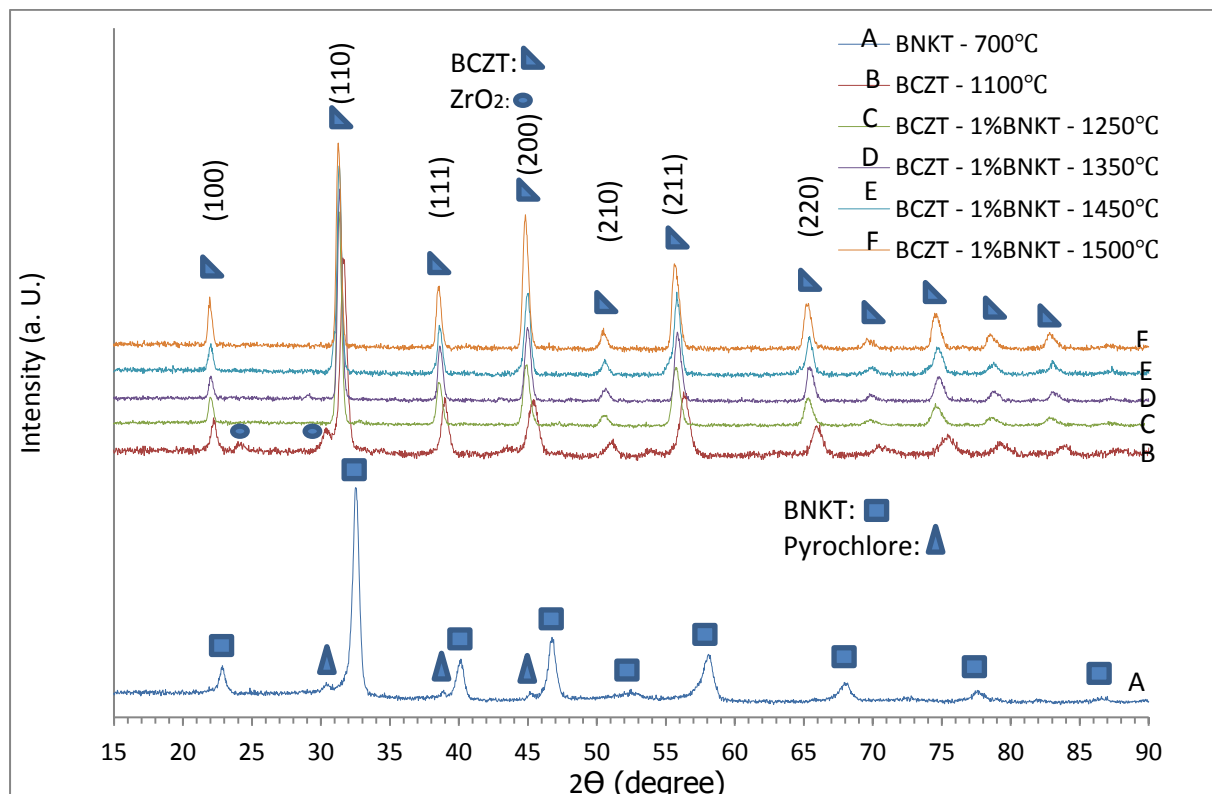


Figure 4-12: The XRD patterns of A) calcined BNKT powder, B) calcined BCZT powder, and BCZT-1% BNKT mixtures sintered for four hours at C) 1250°C, D) 1350°C, E) 1450°C, and F) 1500°C for four hours respectively.

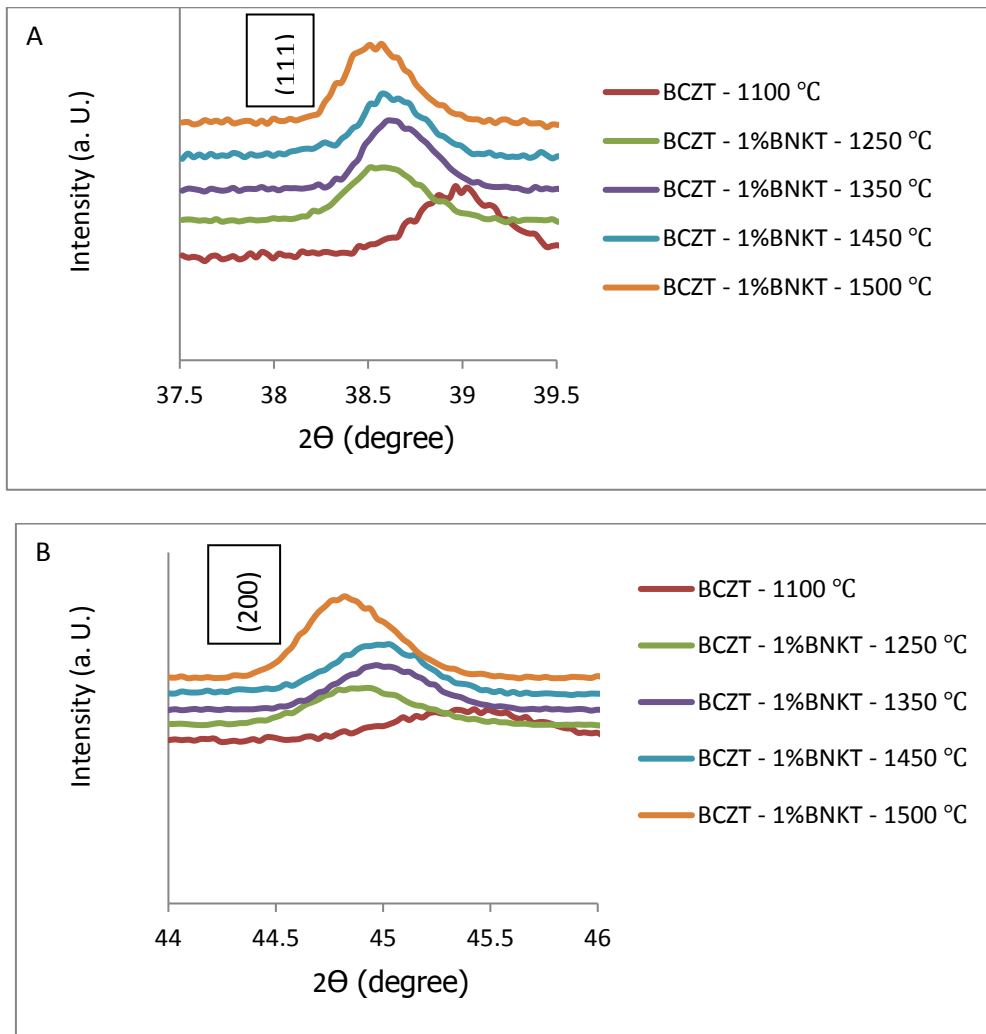


Figure 4-13: The XRD patterns of calcined BCZT powder, and BCZT- 1%BNKT sintered at 1250°C, 1350°C, 1450°C, and 1500°C for four hours for values of 2θ around A) =38.5° for (111) and B) =45° for (200).

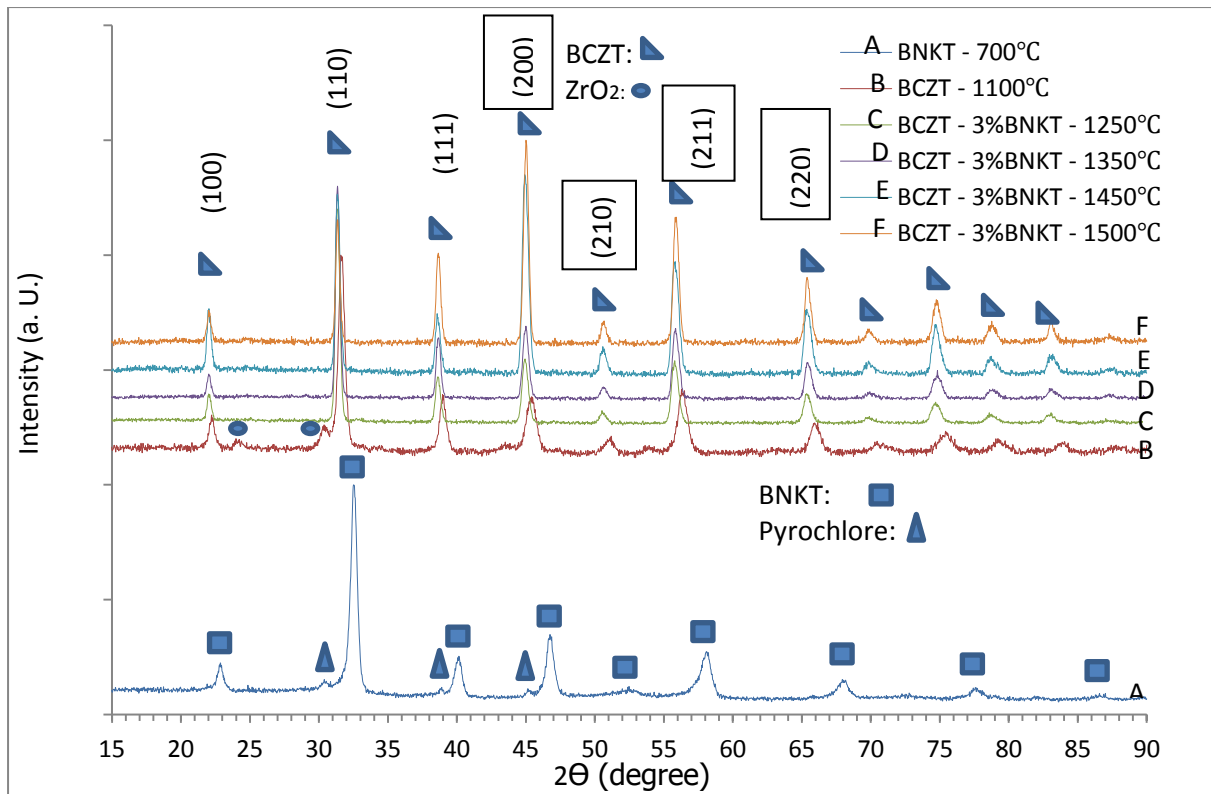


Figure 4-14: The XRD patterns of A) calcined BNKT powder, B) calcined BCZT powder, and BCZT-3% BNKT sintered at C) 1250°C, D) 1350°C, E) 1450°C, and F) 1500°C, sintered for four hours.

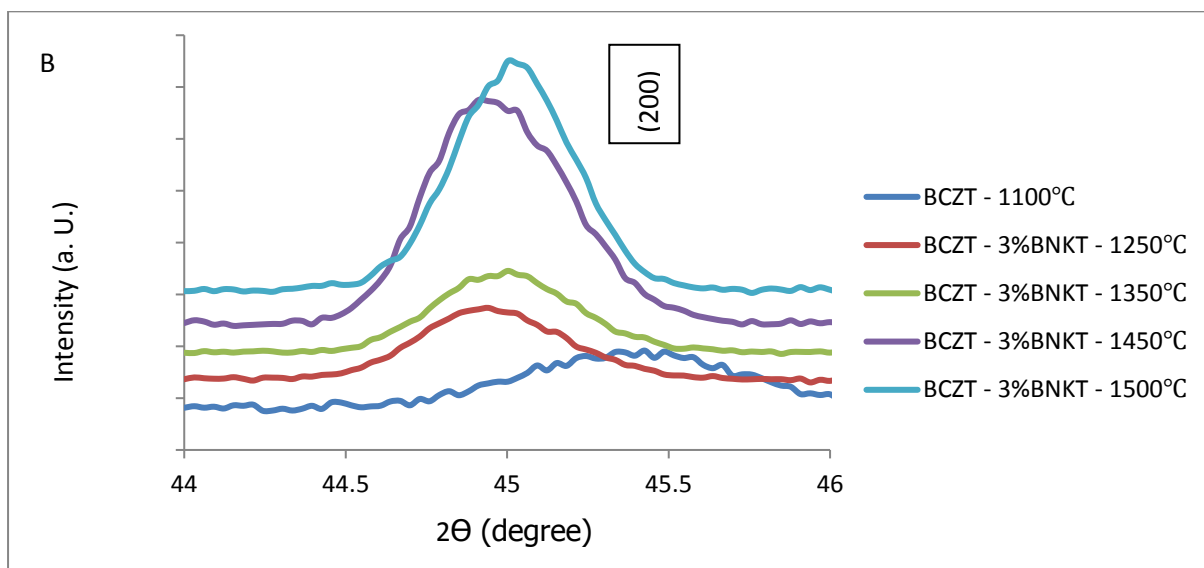
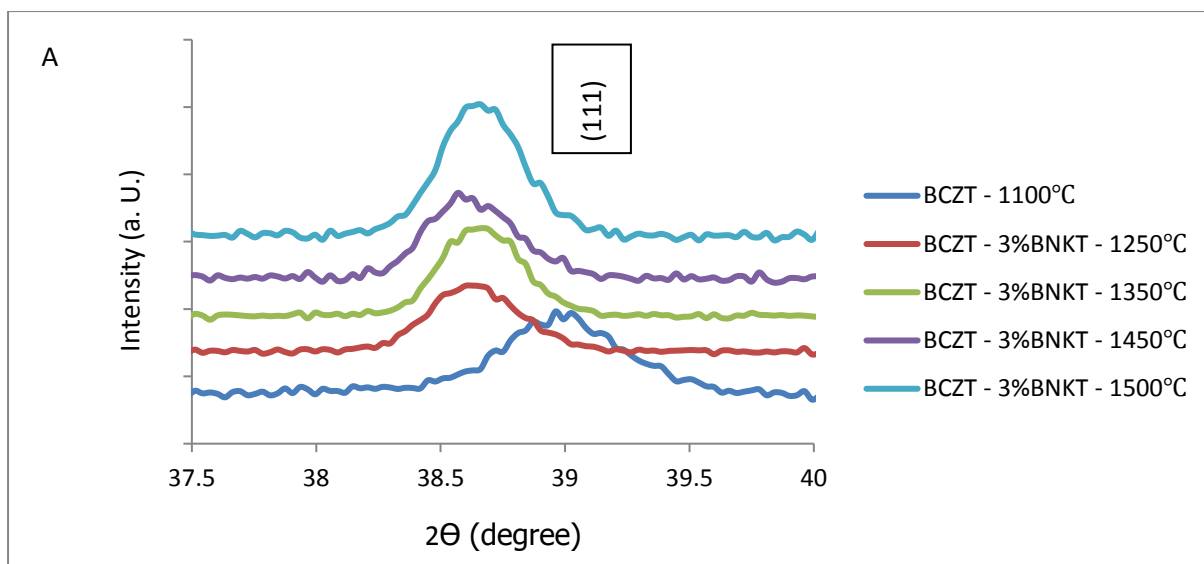


Figure 4-15: The XRD patterns of calcined BCZT powder, and BCZT-3% BNKT at sintered at 1250°C, 1350°C, 1450°C, and 1500°C for four hours at around 2θ A) $\approx 38.5^\circ$ for (111) and B) $\approx 45^\circ$ for (200).

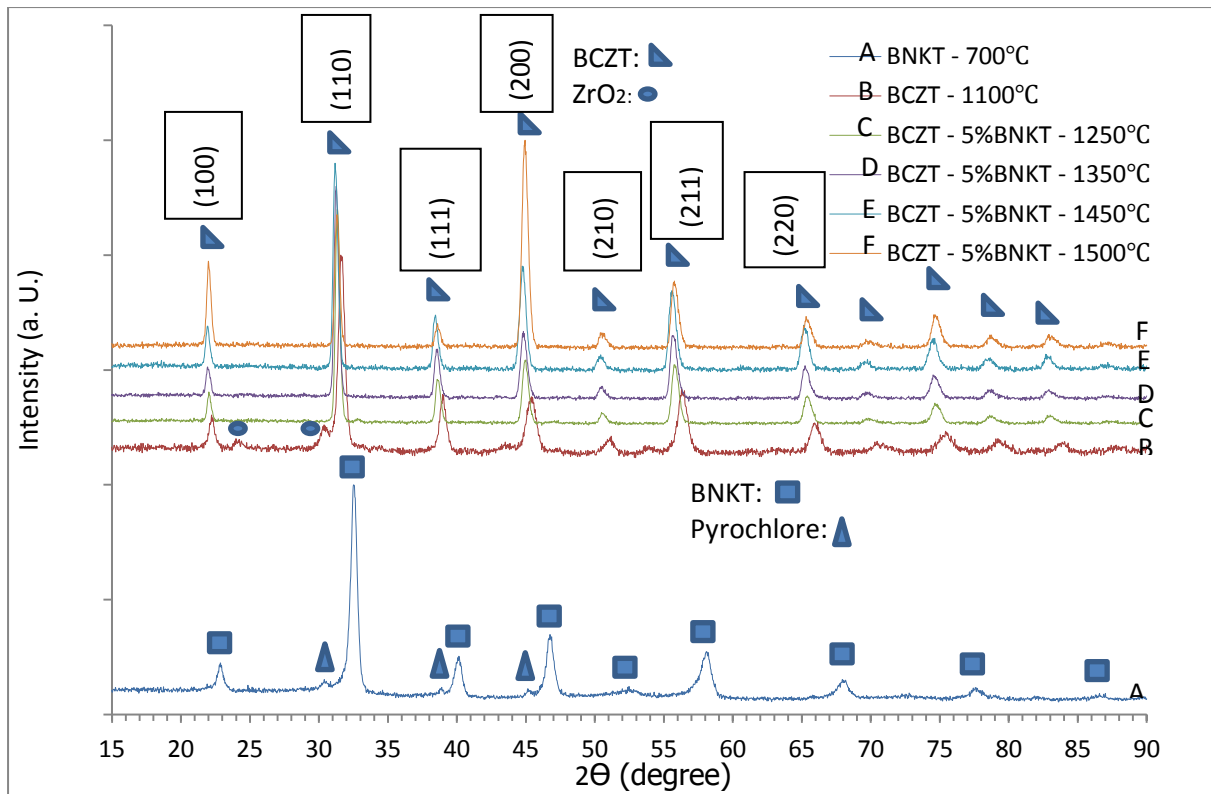


Figure 4-16: The XRD patterns of A) calcined BNKT powder, B) calcined BCZT powder, BCZT-5% BNKT sintered at C) 1250°C, D) 1350°C, E) 1450°C, and F) 1500°C for four hours.

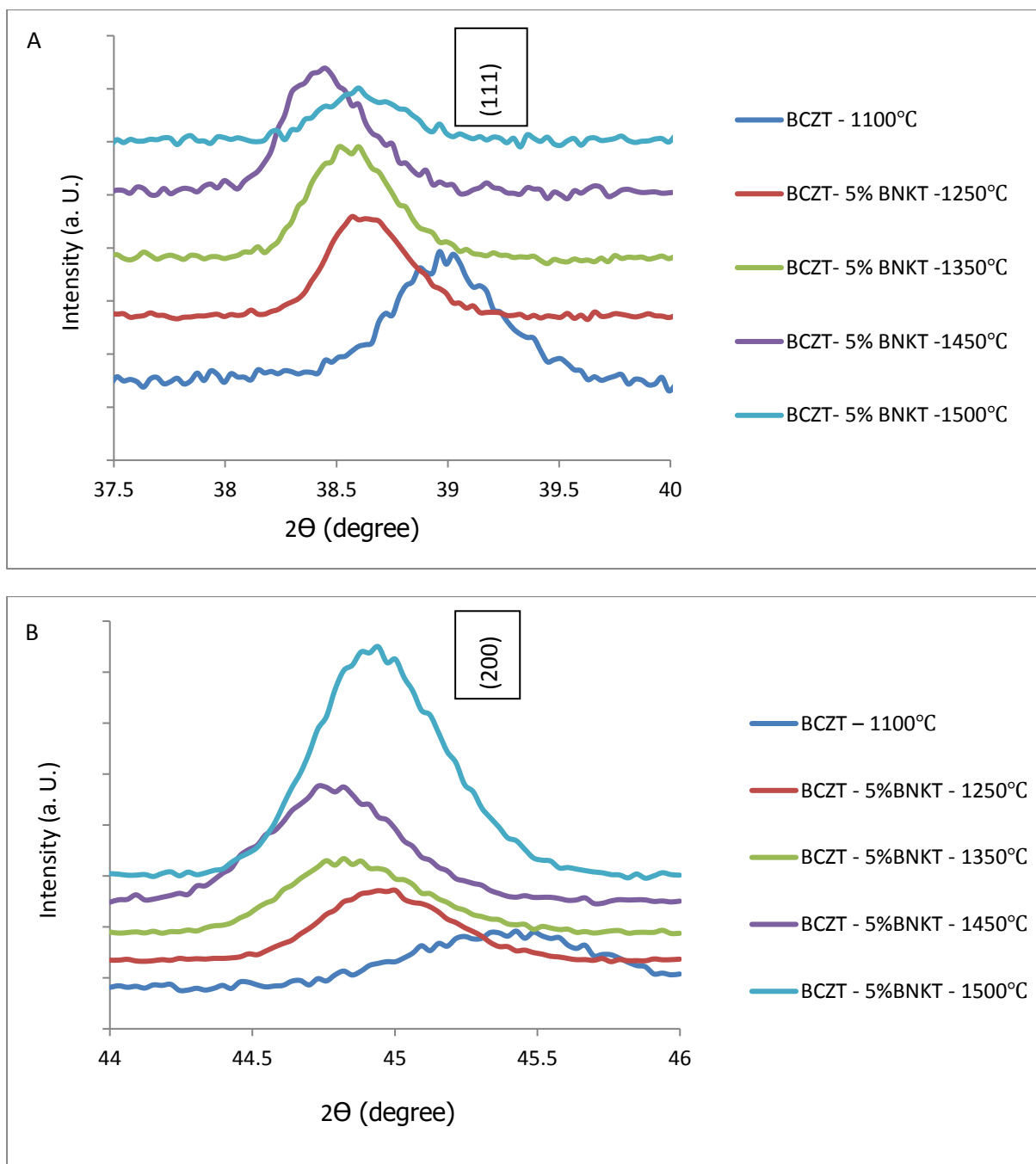


Figure 4-17: The XRD patterns of calcined BCZT powder, and BCZT-5% BNKT sintered at 1250°C, 1350°C, 1450°C, and 1500°C for four hours at around 2θ A) $\approx 38.5^\circ$ for (111) and B) $\approx 45^\circ$ for (200).

Two obvious effects of sintering temperature on the microstructure of the samples can be seen in Figure 4-18, Figure 4-19, and Figure 4-20; there are increases in the grain size and densification of the sample in the sintering process. As can be seen, from 1250 to 1500°C, there is a rise in the grain size of the sintered samples, as has been plotted in Figure 4-22. The samples sintered at 1250°C have a wide range of grain sizes, and the grain sizes of samples sintered at higher temperatures are much more homogeneous. The average particle size of calcined BCZT was around 2-3 μm , and for BNKT, was less than 1 μm (not shown here). This could be connected to the different particle sizes of the two component powders (BCZT and BNKT), and could be another reason for the existence of the BNKT and BCZT together, and BNKT not diffusing into BCZT.

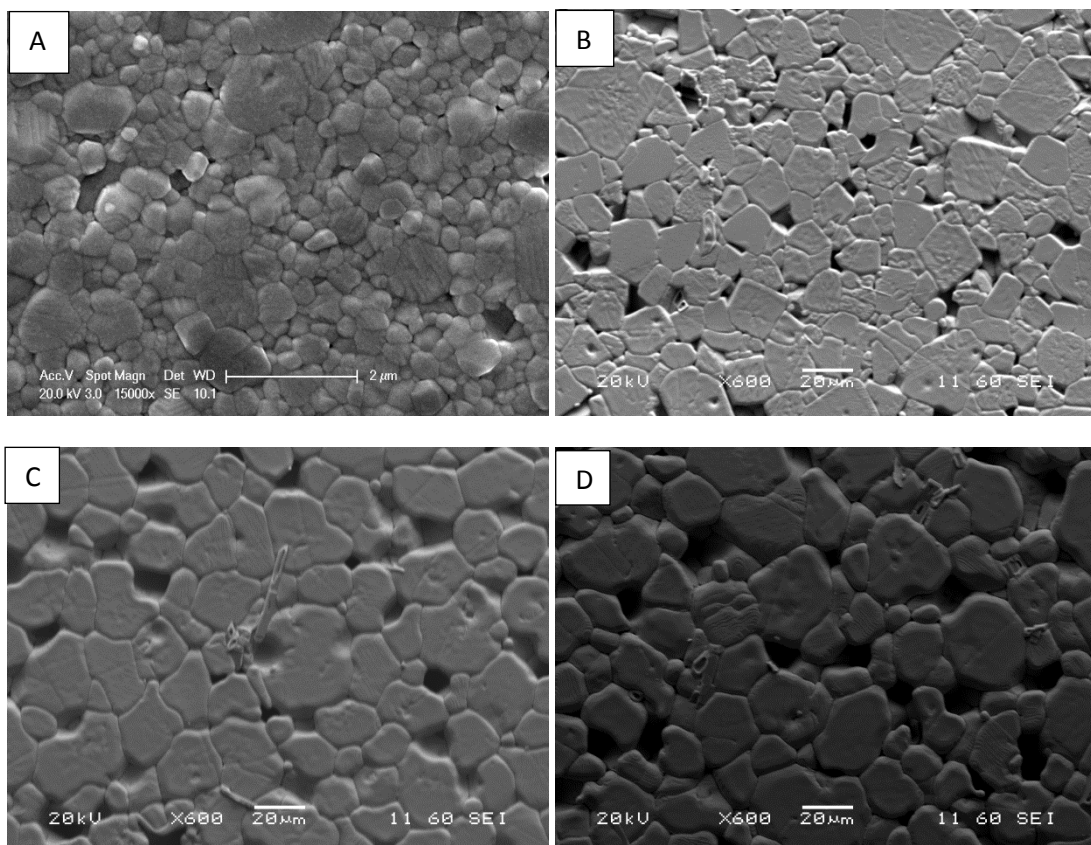


Figure 4-18: SEM micrograph of the BCZT-1% BNKT samples sintered at A) 1250°C, B) 1350°C, C) 1450°C, and D) 1500°C (see the appendix for a low magnification photo).

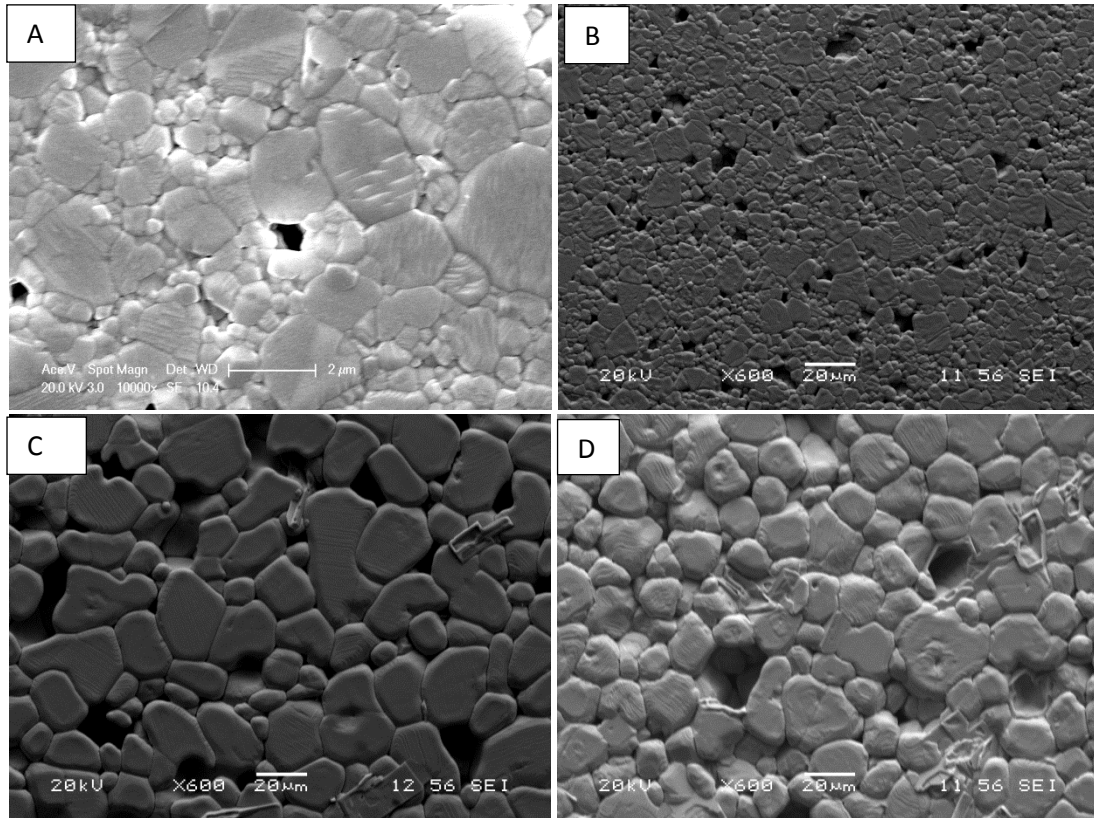


Figure 4-19: SEM micrograph of the BCZT-3% BNKT samples sintered at A) 1250°C, B) 1350°C, C) 1450°C, and D) 1500°C (see the appendix for a low magnification photo).

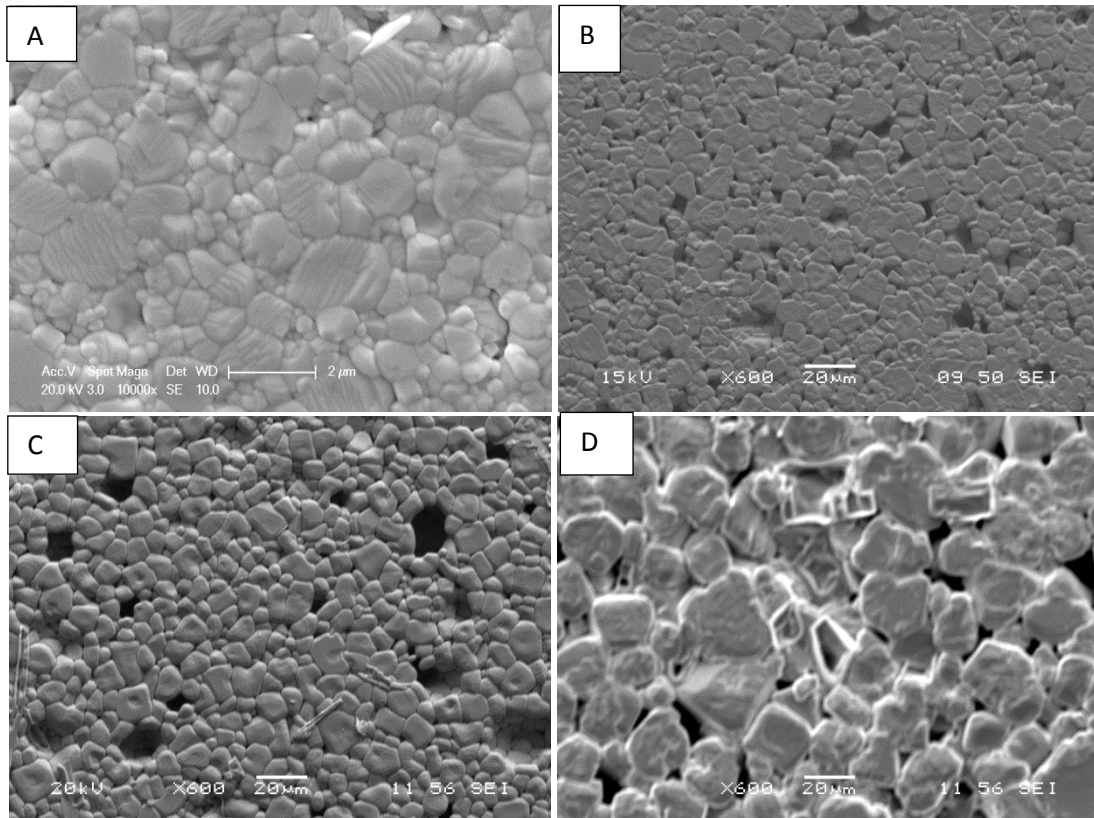


Figure 4-20: SEM micrograph of the BCZT-5% BNKT samples sintered A) 1250, B) 1350°C, C) 1450°C, and D) 1500°C (see the appendix for a low magnification photo).

Figure 4-21 shows the relative density of BCZT-1, 3, and 5% BNKT as a function of the sintering temperature. As can be seen for the BCZT-1% BNKT, the relative density increases to a maximum of around 96.5% for samples sintered at 1300°C, and then decreases to 93% for samples sintered at 1500°C. The relative density decrease observed for the sintering temperatures >1300°C is likely to be due to the evaporation of the BNKT. For BCZT-3%BNKT, the relative density increases to around 97% at 1300°C, similarly to BCZT-1%BNKT, and after that, it decreases to 92% at 1500°C. For BCZT-5% BNKT, the relative density is around 98% at 1250°C and after that, it decreases, to 88% at 1500°C. The plot shows that for this composition the relative density decreases continuously with increasing sintering temperature, indicating that the evaporation of BNKT increases with increasing sintering temperature, with the highest evaporation occurring between 1450 and 1500°C. All the samples have reached relative densities above 90%, except the BCZT-5% BNKT samples sintered at 1500°C, which due to the higher value of BNKT and high temperature can be attributed to the evaporation of the BNKT. In general, the relative density decreases with an increase in the temperature.

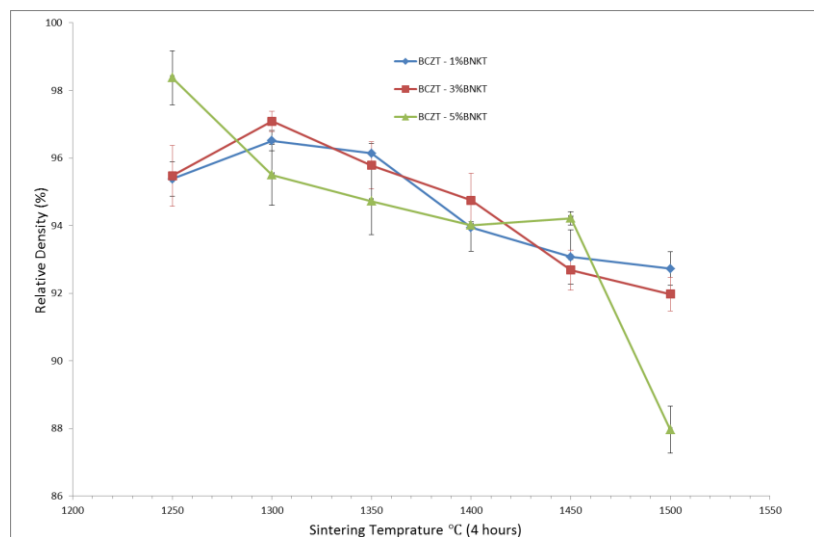


Figure 4-21: The variation of relative density as a function of the sintering temperature for BCZT-1, 3, and 5% BNKT.

Figure 4-22 shows the variation in grain size as a function of the sintering temperature for BCZT-1, 3, and 5% BNKT. As can be seen, the grain size increases as the sintering temperature increases, from 1250 to 1500°C. In comparison with pure BCZT, the grain size of BCZT-1% BNKT is slightly larger, which might be influenced by the evaporation of the BNKT. For BCZT-3%BNKT, from 1350°C to 1450°C, the grain size increases more sharply than 1250 to 1350°C. In comparison with pure BCZT and BCZT-1% BNKT, the grain size of BCZT-3% BNKT is slightly lower, which can be attributed to the interaction of BNKT and BCZT grains, which prevent the BCZT grains from growing. For BCZT-5% BNKT, from 1450°C to 1500°C, the grain size increases more sharply than 1250 to 1450°C. In comparison with pure BCZT and BCZT-1% and 3% BNKT, the grain size of BCZT-5% BNKT is slightly lower, which can be attributed to the interaction between the BNKT and BCZT grains, which prevents the BCZT grains from growing.

For all samples, the grain size is increased by an increase in the sintering temperature, but with an increase in the value of BNKT, a reduction in grain size can be observed, indicating that BNKT is somehow restricting the growth of the grains.

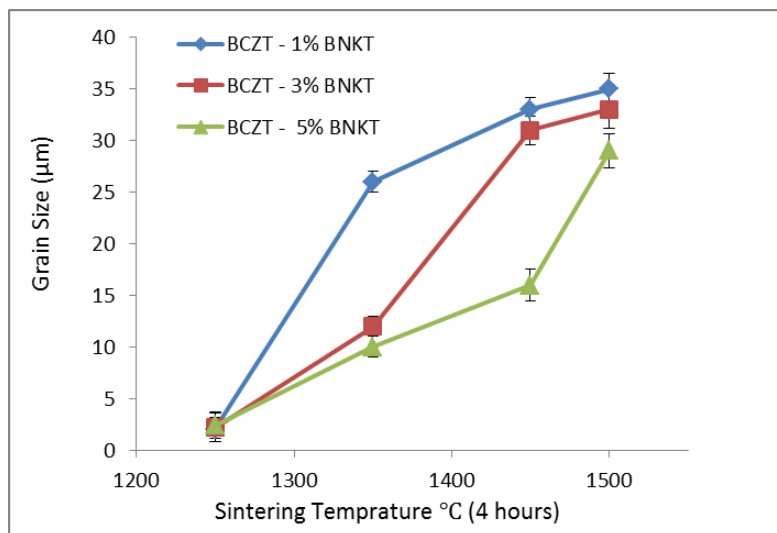


Figure 4-22: The variation of grains size as a function of sintering temperature for BCZT-1, 3, and 5% BNKT.

Figure 4-23 shows the variation of relative permittivity of unpoled samples measured at room temperature as a function of the sintering temperature for BCZT-1, 3, and 5% BNKT. The relative permittivity increases with increases in the sintering temperature for BCZT-1%

BNKT, which could be suitable for RT applications. To understand more about this, measuring the relative permittivity at a range of temperatures could be helpful to get to know the effect of the BNKT on the maximum permittivity of BCZT, and if the addition of BNKT causes the temperature of the peak to decrease to room temperature, this could lead to an increase in the RT relative permittivity. From 1300 to 1400°C, the relative permittivity increases with increasing sintering temperature for BCZT-3% BNKT and after that, slightly shifts to a lower value between 1450 and 1500°C, but is in general higher than for pure BCZT (3200). From 1250 to 1300°C, the relative permittivity increases through an increase in the sintering temperature for BCZT-5% BNKT and after that, slightly shifts to a lower value at 1450°C, before sharply decreasing at 1500°C. The shape of the graphs for different amounts of BNKT are quite different; there are peaks in the relative permittivity of 3 and 5% BNKT but for 1% BNKT, the relative permittivity is increased. The highest value can be seen for 5% BNKT, which when compared to the temperature dependence of the relative permittivity, may be caused by the vicinity of the maximum relative permittivity to room temperature.

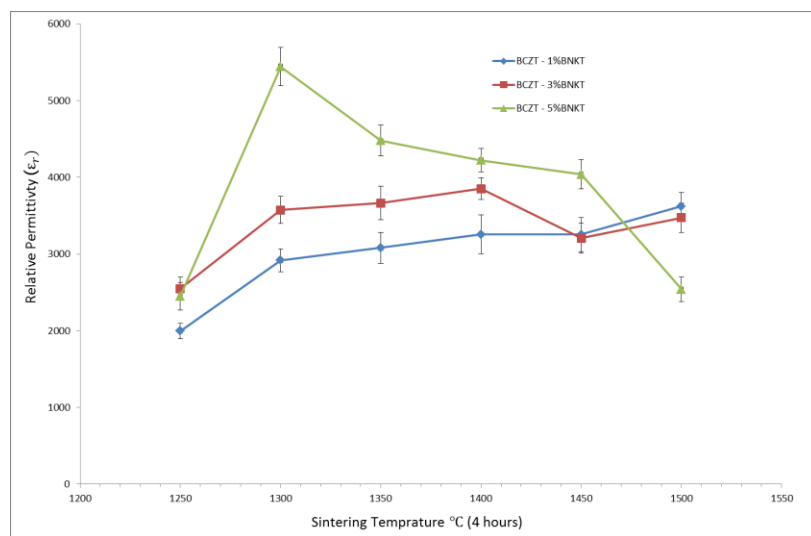


Figure 4-23: The variation of relative permittivity of unpoled samples as a function of the sintering temperature for BCZT-1, 3, and 5% BNKT measured at RT.

Figure 4-24 shows the variation of d_{33} as a function of sintering temperature for BCZT-1, 3, and 5 % BNKT. For BCZT-1% BNKT, the d_{33} increases with an increase in the sintering temperature, except for a slight decrease for the sample sintered at 1450°C. The d_{33} can be affected by a number of factors such as the grain size, relative density, and evaporation of BNKT. The interaction between these factors (especially relative density) could be a reason for the change in d_{33} at different temperatures. For BCZT-3% BNKT, the d_{33} increases with an increase in the sintering temperature, except around 1400°C, where it slightly decreases, and

again rises to 1500°C. For BCZT-5% BNKT, the d_{33} generally increases due to an increase in the sintering temperature. The d_{33} values increased with the sintering temperature for all of the samples, except for a reduction for BCZT – 1, 3, and 5% BNKT at 1450, 1400, and 1350°C, respectively, which can be attributed to reduction factors being more effective than increasing factors. An increase in the value of BNKT from 1% to 5% caused a reduction in the d_{33} .

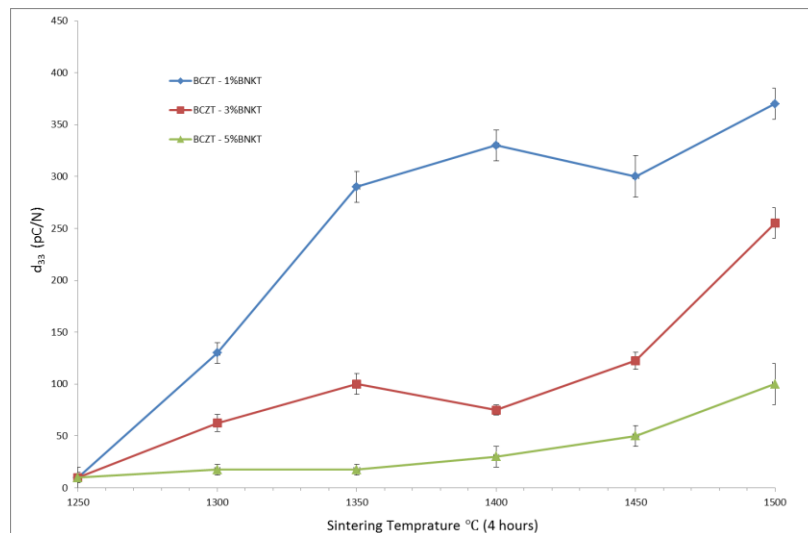


Figure 4-24: The variation of d_{33} as a function of the sintering temperature for BCZT-1, 3, and 5% BNKT.

Figure 4-25 shows the variation of k_p as a function of the sintering temperature for BCZT-1, 3, and 5% BNKT. For BCZT-1% BNKT, the value of k_p is around 17% for BCZT-1% BNKT sintered at 1250°C, and with increases in the sintering temperature, the value increases to a maximum of around 42% for the samples sintered at 1450°C, and then remains approximately constant. For BCZT-3% BNKT, the value of k_p is around 10% for samples sintered at 1250°C and by increasing the sintering temperature, the value increased to 18, 20, 26, and 24% at 1300, 1350, 1400, and 1450°C, respectively, and reached 43% at 1500°C. For BCZT-5% BNKT, the value of k_p is around 8% for BCZT-5% BNKT sintered at 1250°C and by increasing the sintering temperature, the value increased to 12, 17, 21, and 25% at 1300, 1350, 1400, and 1450°C, respectively, and the value reached 24% at 1500°C.

The k_p values have been increased by increasing the sintering temperature for all the samples, except slight reductions for BCZT-1 and 3% BNKT at 1500 and 1450°C, respectively. The k_p decreased from 1% to 5% BNKT addition to BCZT. It has been accepted that the d_{33} and k_p increases near the MPB and for pure BCZT, the MPB is between the orthorhombic and

tetragonal phases at RT. The addition of BNKT can cause structural change, which can be seen through shifts in the XRD patterns, and the structure goes farther from the MPB, and affects the d_{33} and k_p .

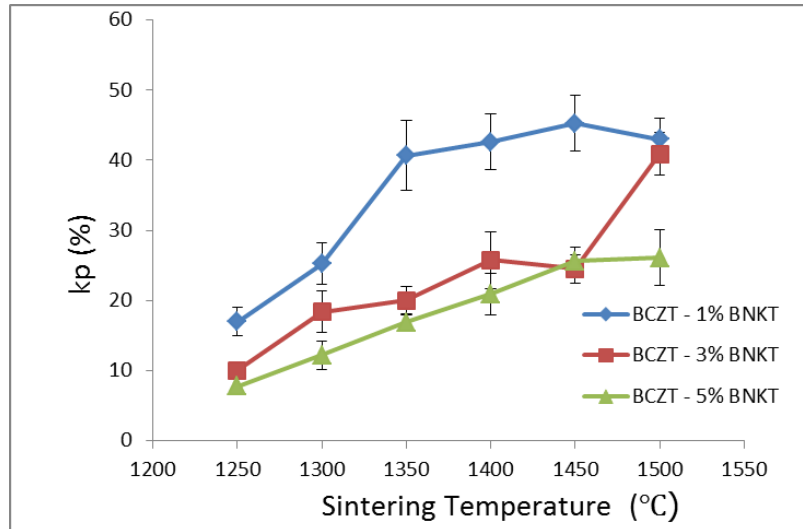
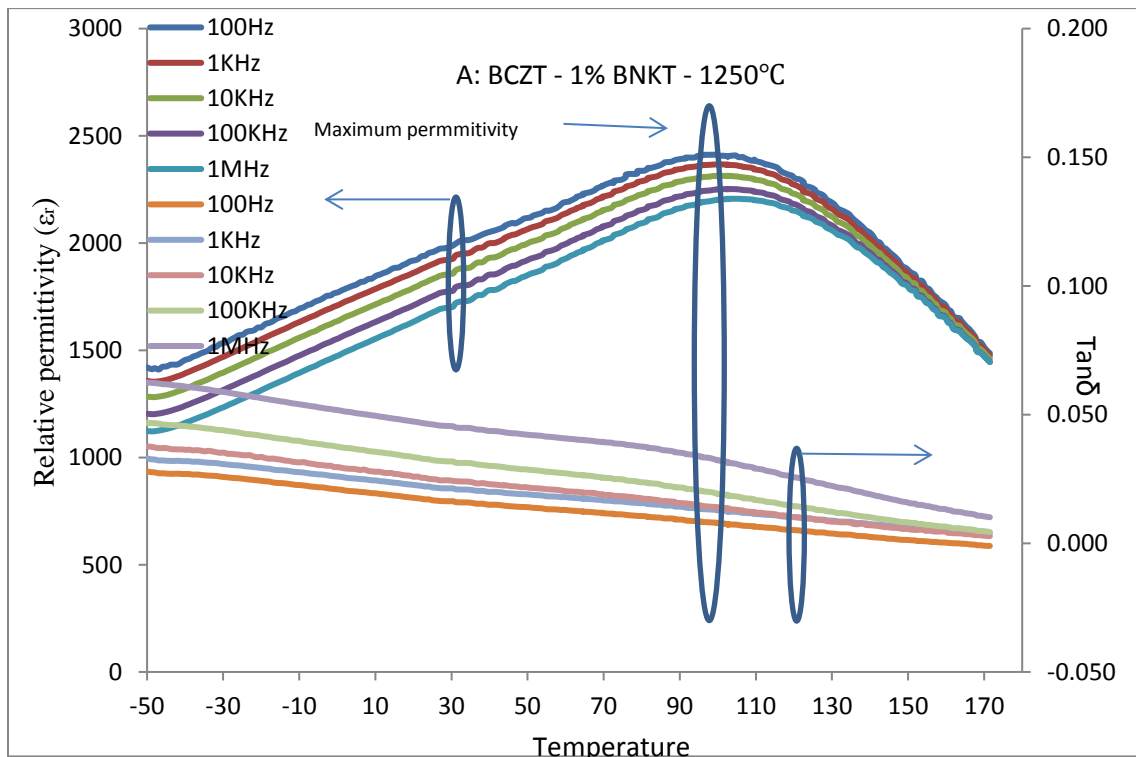


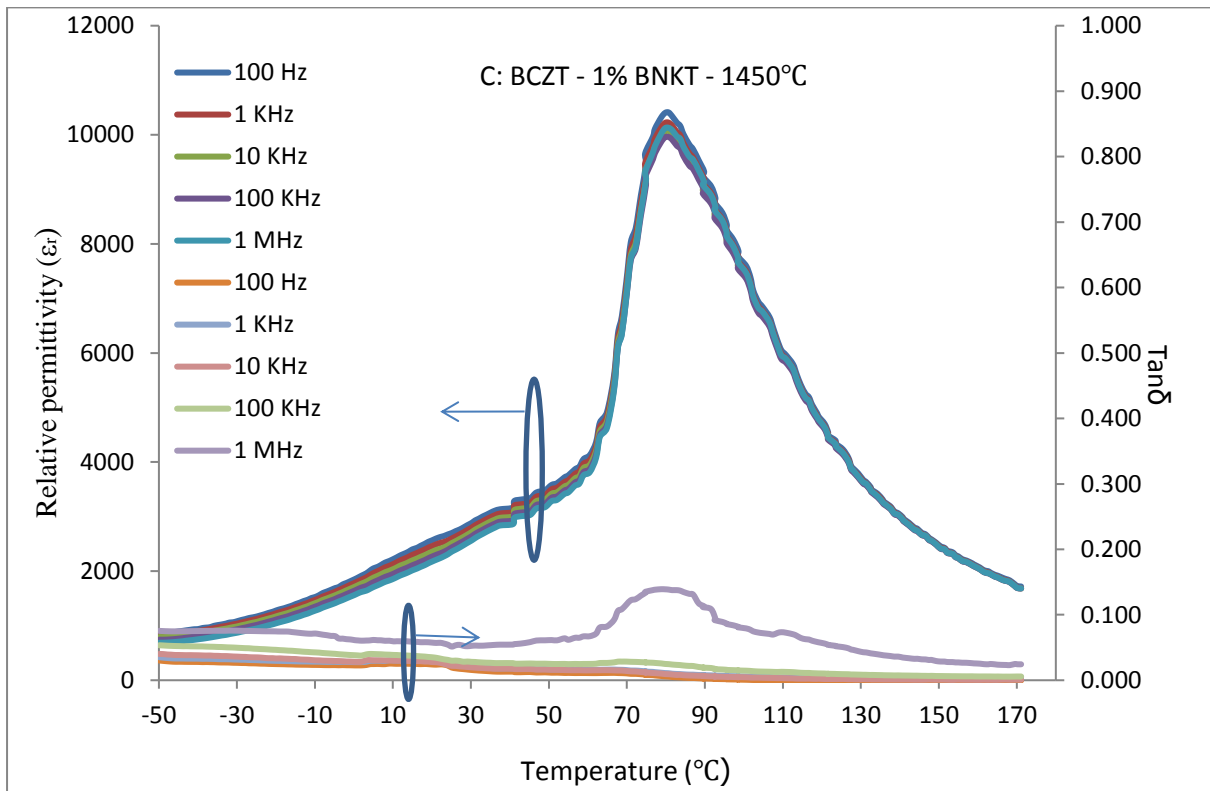
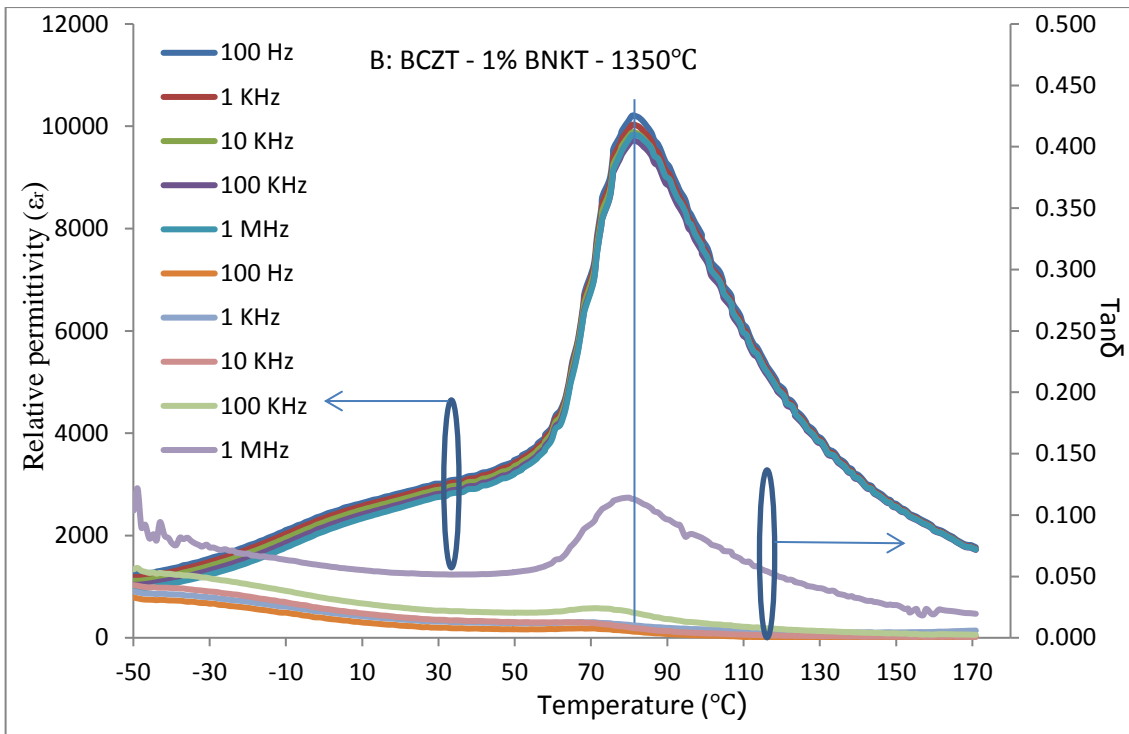
Figure 4-25: The variation of k_p as a function of the sintering temperature for BCZT-1, 2, and 5% BNKT.

Figure 4-26, Figure 4-27, and Figure 4-28 show the temperature dependence of relative permittivity (ϵ_r) and dielectric loss ($\tan\delta$) of unpoled samples at 100 Hz, 1 kHz, 10 kHz, 100 kHz, and 1 MHz for BCZT-1, 3, and 5% BNKT samples sintered at 1250, 1350, 1450, and 1500°C, respectively. The relative permittivity slightly decreased by increasing the frequency from 100Hz to 1MHz, and the value of the dielectric loss is low (under 0.1) for all the samples and frequencies, and it was increased by increasing the frequency from 100Hz to 1MHz.

There is a big difference in the shape and relative permittivity of BCZT-1% BNKT sintered at 1250°C, in comparison to other temperatures, and it shows to a slight extent the relaxor behaviour. At low sintering temperatures (between 1200 and 1300°C), BCZT has been shown to exhibit relaxor behaviour or diffuse phase transitions (the frequency dependence of relative permittivity) [43] due to smaller grain size, which leads to space charge effects and lower relative permittivity (around 2370 at 1 kHz). In addition, BNKT shows relaxor behaviour [222, 223] so in this case, relaxor behaviour for the BCZT-1% BNKT samples sintered at 1250°C is reasonable. For the BCZT-1% BNKT sample sintered at 1350°C, the temperature of the maximum relative permittivity is 81.4°C for 1

kHz, while the maximum relative permittivity is approximately 10028. The transformation from cubic to tetragonal and rhombohedral at the Curie temperature phases causes some stress in the structure, caused by the formation of the domains [43]. At a lower sintering temperature, the grain size of the sample is smaller and leads to a lower amount of the domains, in addition to smaller domains. Smaller domain size cannot release the stress, and so disrupts the structure and leads to lower relative permittivity. For the sample sintered at 1450°C, the maximum relative permittivity (10222 at 80.7°C) is slightly higher. Relative permittivity is increased by increasing the sintering temperature from 1350 to 1450°C, but for the 1500°C-sintered sample, the maximum relative permittivity is slightly lower (8903 at 78.7°C), which is due to the lower relative density and more porous microstructure as a consequence of possible evaporation losses.





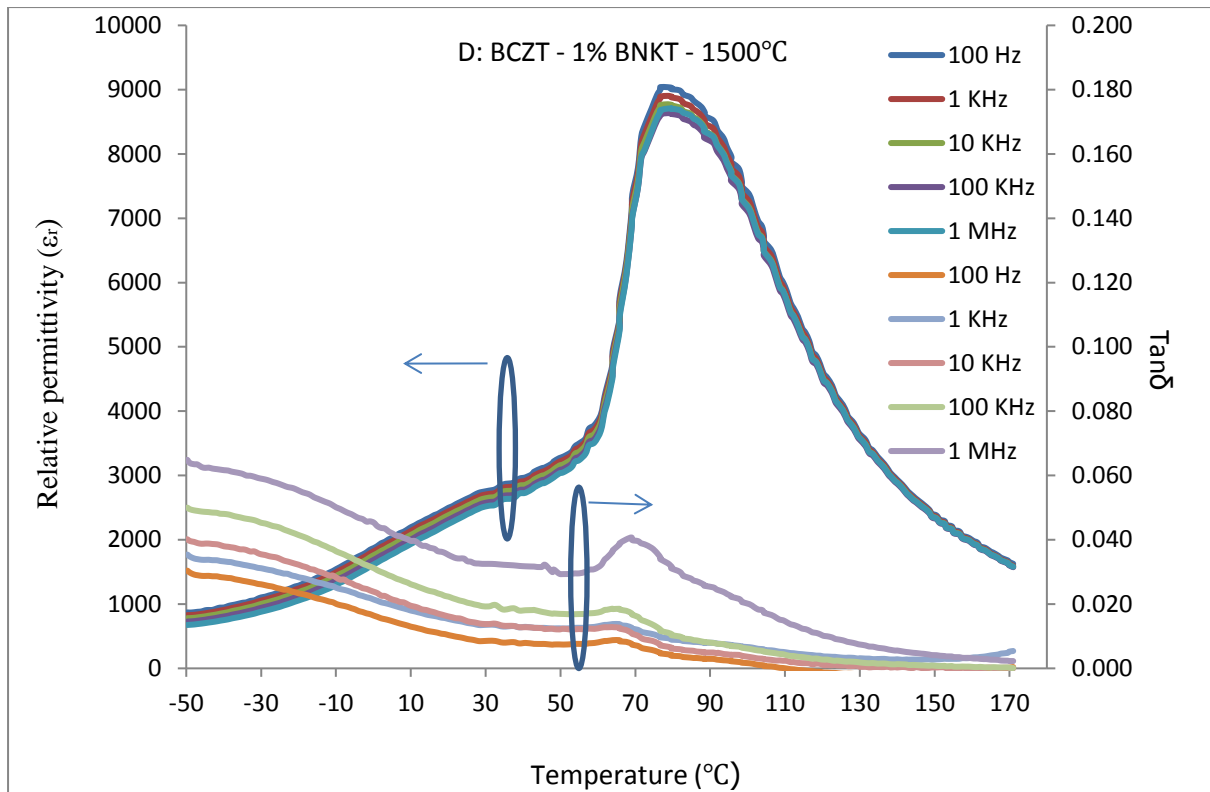
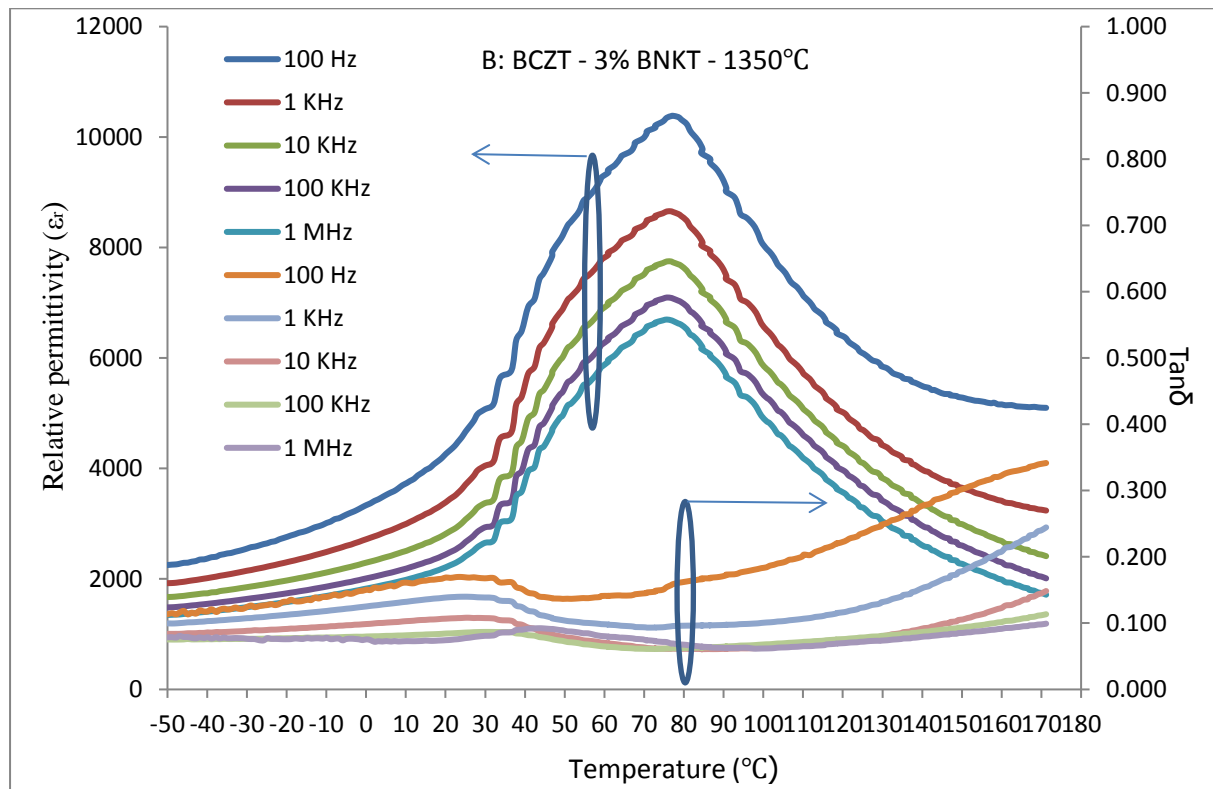
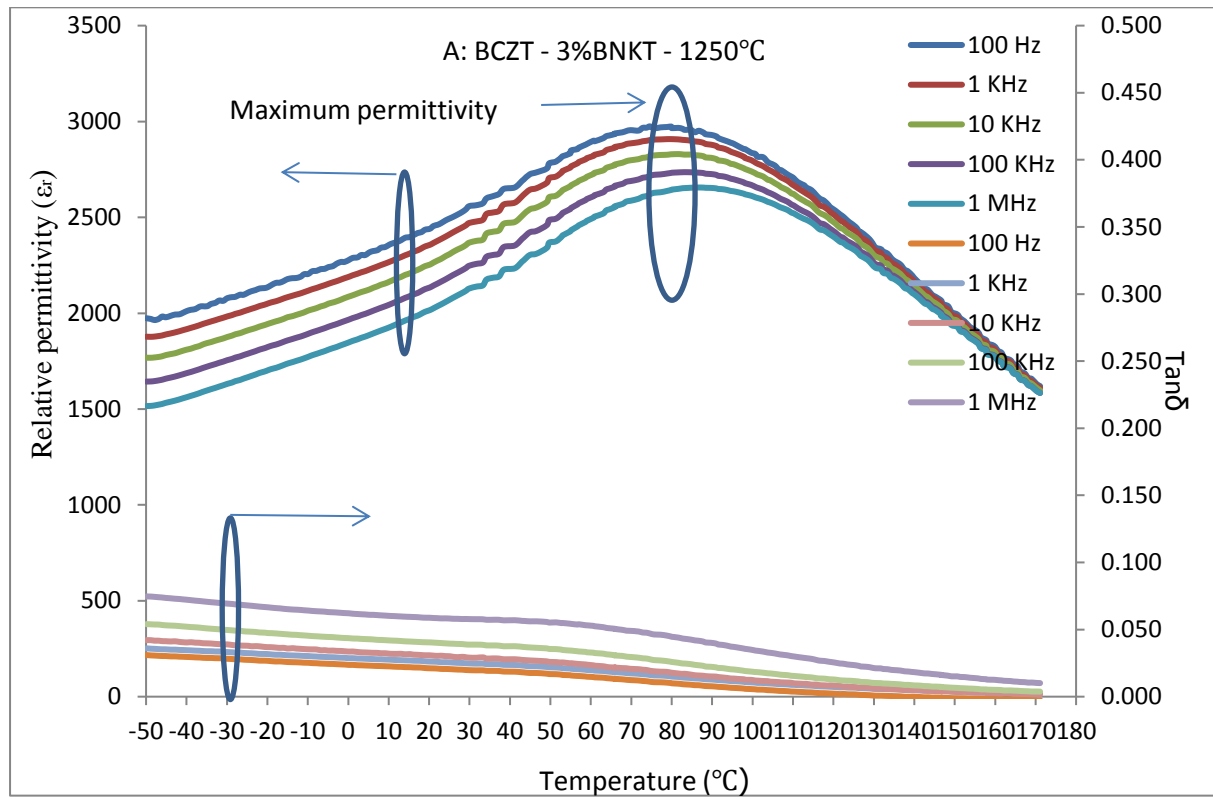


Figure 4-26: The temperature dependence of relative permittivity (ϵ_r) and dielectric loss ($\text{Tan}\delta$) of unpoled samples at 100 Hz, 1 kHz, 10 kHz, 100 kHz, and 1 MHz for BCZT-1% BNKT samples sintered at A) 1250, B) 1350, C) 1450, and D) 1500°C for four hours.

For the BCZT-3% BNKT samples, the value of the dielectric loss increases when the frequency is increased from 100Hz to 1MHz but remains low (under 0.1) for all samples and frequencies except those sintered at 1350 and 1450°C, which could be due to ionic conductivity [7]. BCZT-3% BNKT sintered at 1250°C is similar to BCZT-1% BNKT, and shows a slight amount of relaxor behaviour. At 1350°C, BCZT-3% BNKT still shows the relaxor behaviour, in comparison with BCZT-1% BNKT, due to the higher amount of BNKT and the relaxor behaviour of this material; it is reasonable for this composition to show relaxor behaviour at this temperature. The temperature of the maximum relative permittivity shifts to a slightly lower temperature, at 76.8°C for 1 kHz. The maximum relative permittivity is approximately 8665 and lower than the BCZT-1%BNKT due to the higher porosity in the BCZT-3% BNKT samples. For the samples sintered at 1450°C, normal behaviour can be observed, but at a temperature of around 120°C and at 100 Hz, there is an increase in the relative permittivity and dielectric loss. The maximum relative permittivity (7644 at 76.7°C for samples sintered at 1500°C) is lower than for

pure BCZT and slightly lower than for BCZT-1% BNKT due to the higher evaporation of BNKT.



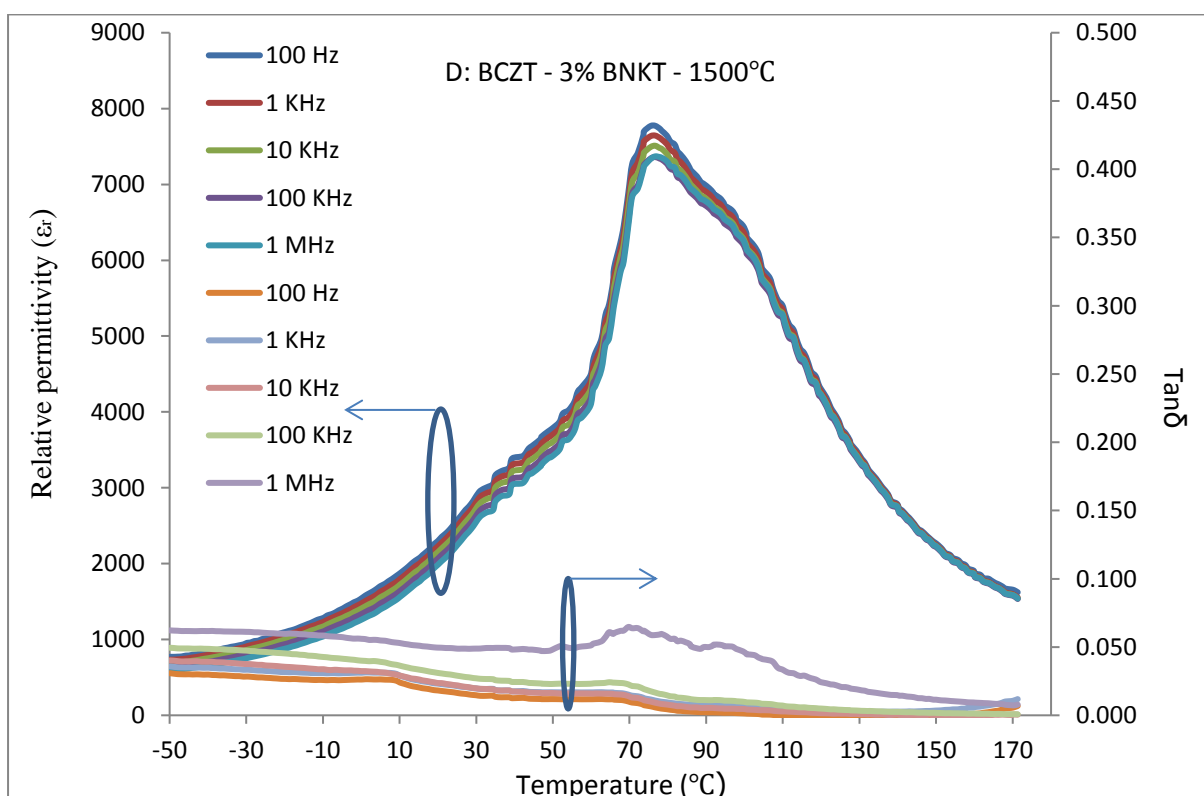
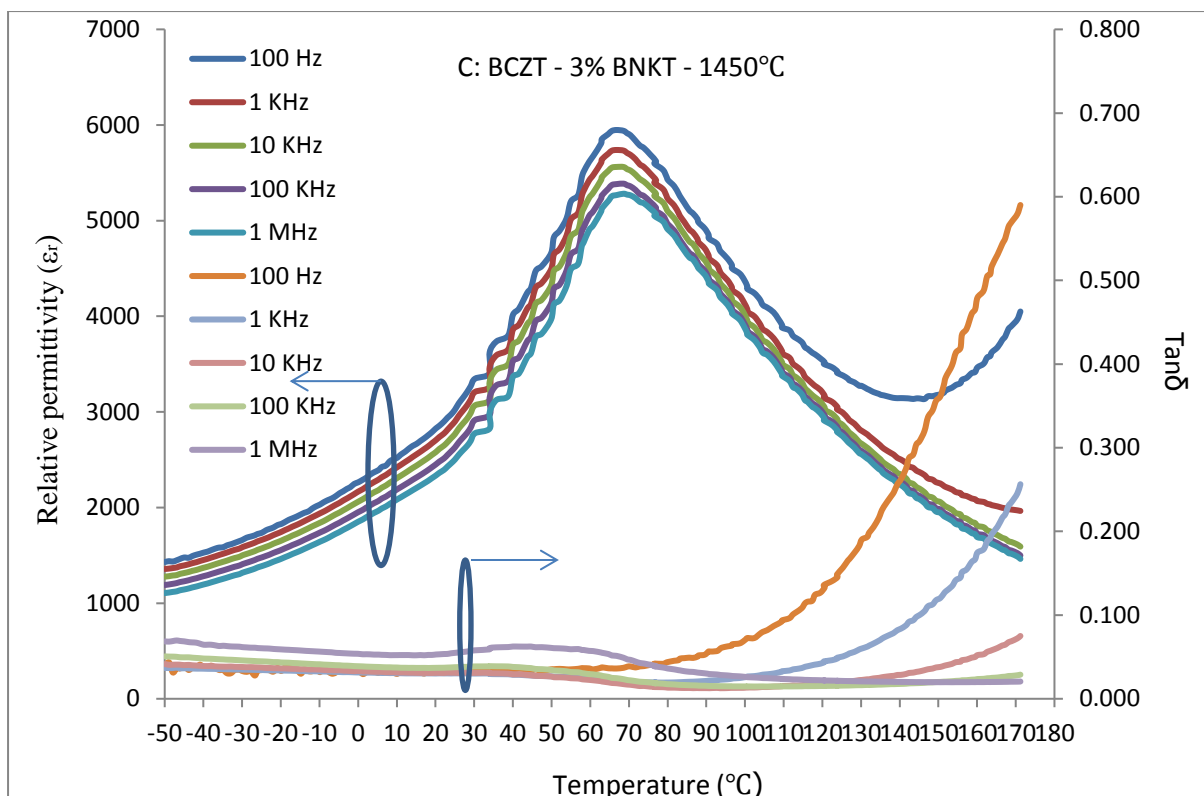
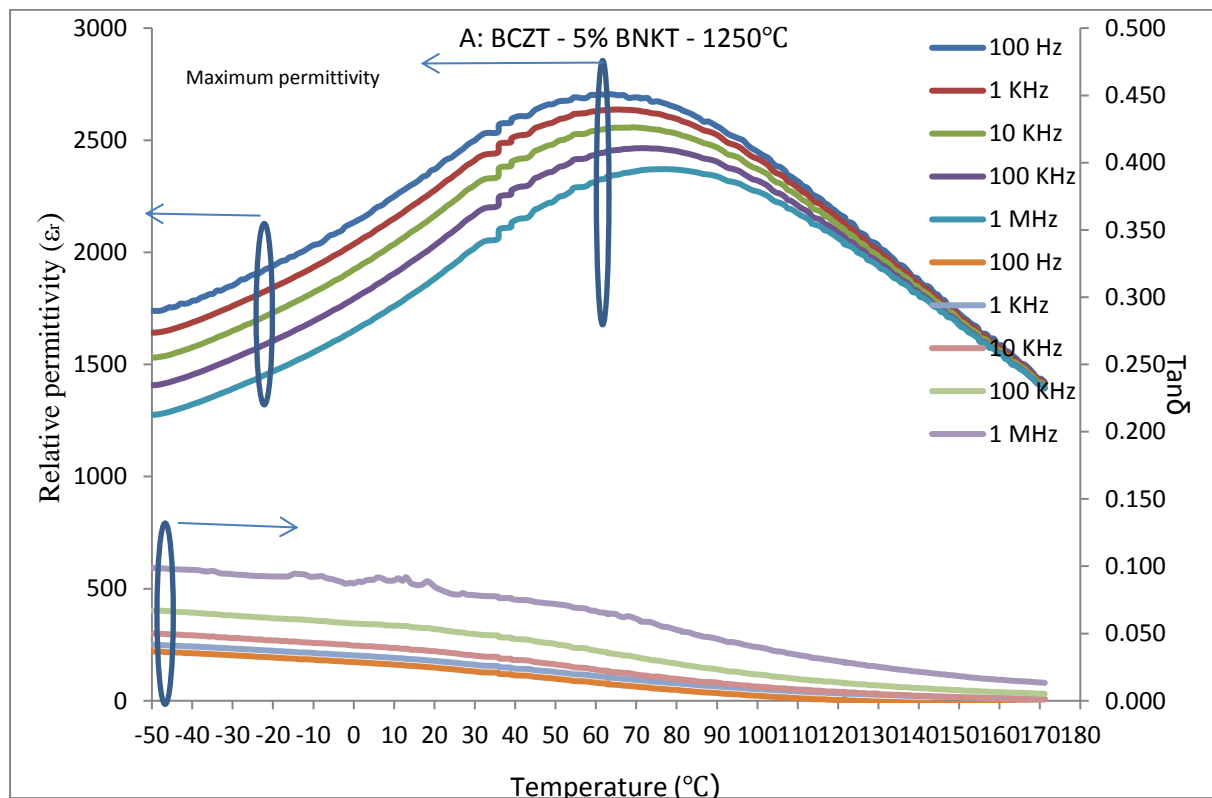
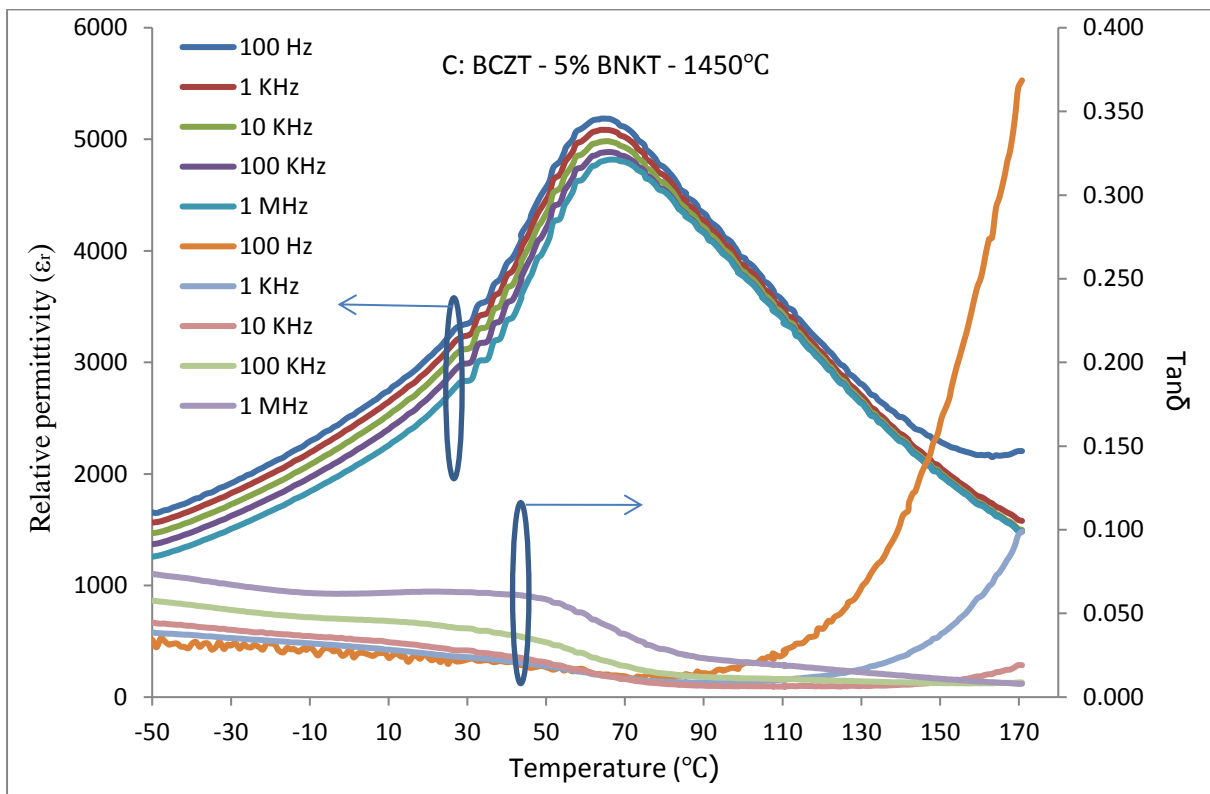
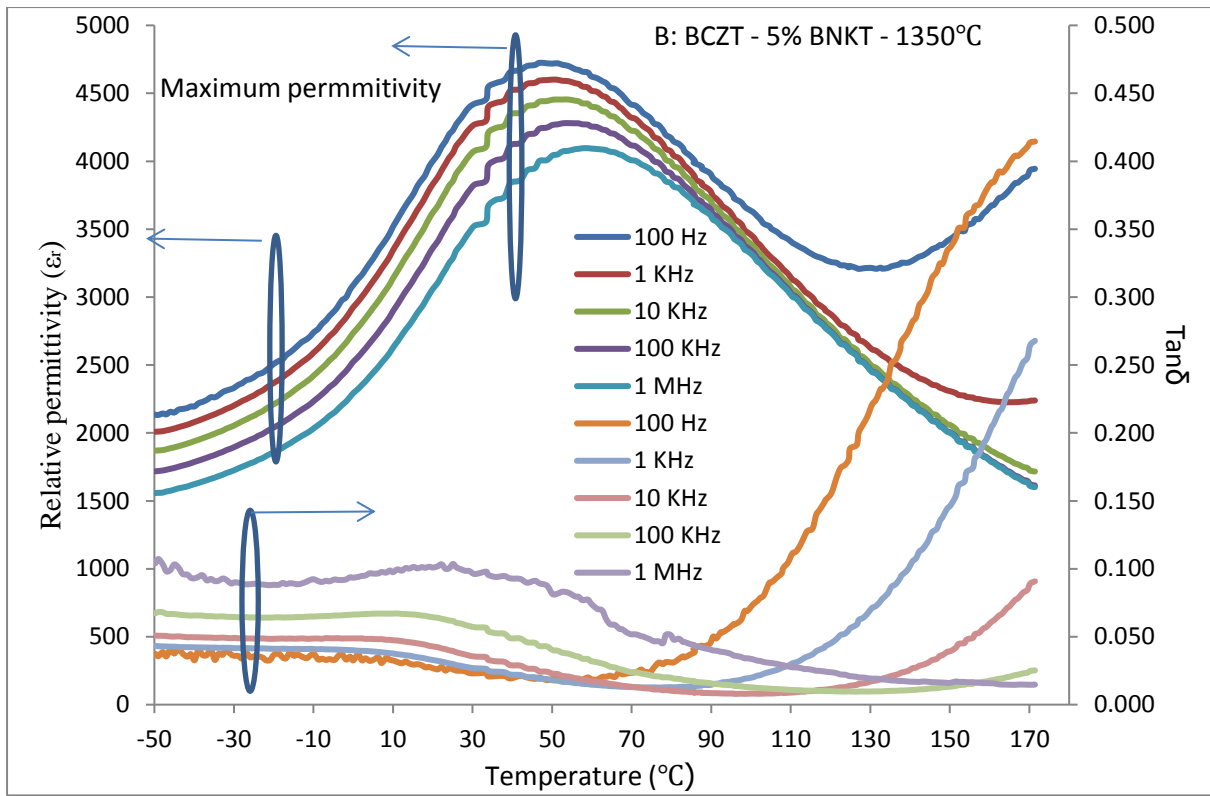


Figure 4-27: The temperature dependence of relative permittivity (ϵ_r) and dielectric loss ($\text{Tan}\delta$) of unpoled samples at 100 Hz, 1 kHz, 10 kHz, 100 kHz, and 1 MHz for BCZT-3% BNKT sintered samples at A) 1250, B) 1350, C) 1450, and D) 1500°C for four hours.

BCZT-5% BNKT samples sintered at 1250°C exhibit relaxor behaviour (Figure 4-28). When sintered at 1350°C, BCZT-5% BNKT still shows relaxor behaviour, which could be

due to a higher amount of BNKT. The temperature of the maximum permittivity slightly shifts to a lower temperature at 50.1°C for 1 kHz, and the maximum relative permittivity is approximately 4600. For the sintered samples at 1450°C, normal behaviour can be observed, but at a temperature of around 120°C and at 100 Hz, there is an increase in the relative permittivity and dielectric loss, which may be related to the ionic conductivity. The maximum relative permittivity is 4321 at 98.6°C for samples sintered at 1500°C.





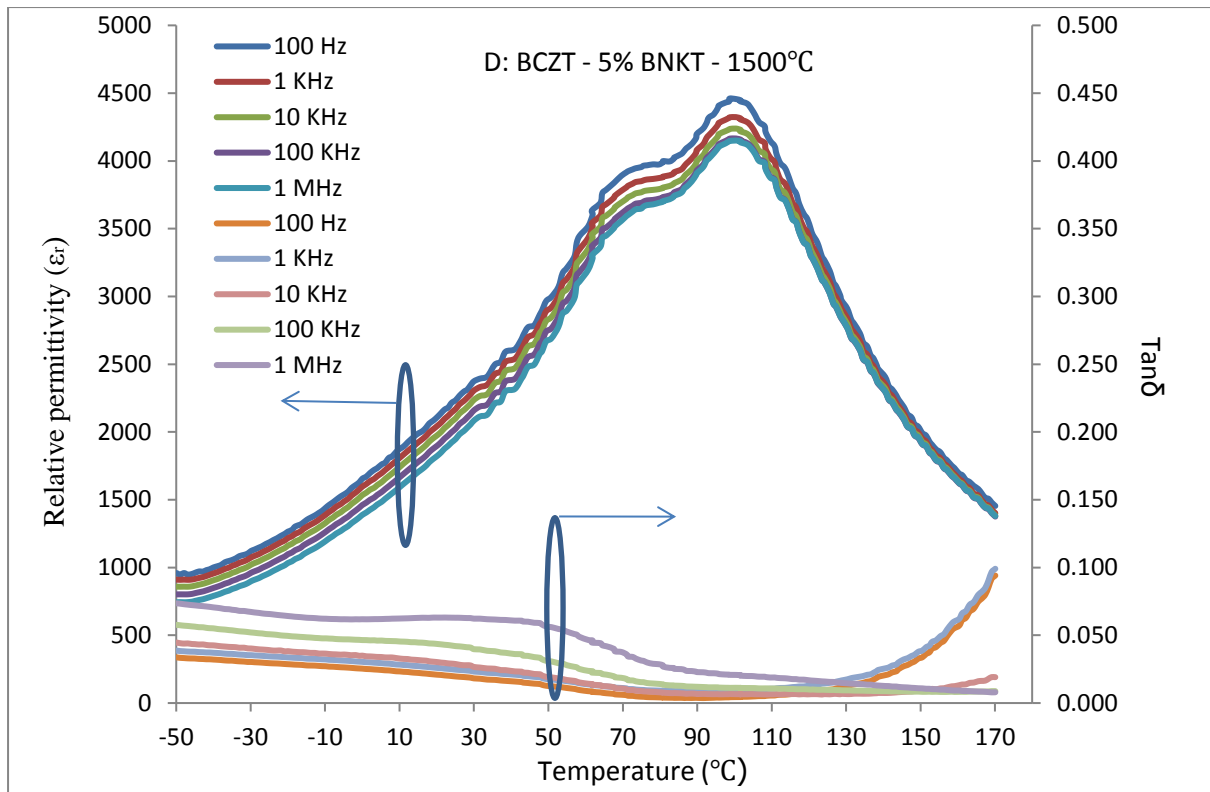


Figure 4-28: The temperature dependence of relative permittivity (ϵ_r) and dielectric loss ($\text{Tan}\delta$) of unpoled samples at 100 Hz, 1 kHz, 10 kHz, 100 kHz, and 1 MHz for BCZT-5% BNKT sintered samples at A) 1250, B) 1350, C) 1450, and D) 1500°C for four hours.

The properties of BCZT-1, 3, and 5% BNKT ceramics compared to pure BCZT are summarised in Table 4-2. The relative density does not vary much for the samples, and all of them are above 90%, except for the 5% BNKT at 1500°C, which is about 88%. For 1% BNKT sintered at 1500°C, the d_{33} is almost 90% pure BCZT at 1450°C, which implies that the addition of 1% BNKT does not have much effect on the structure of BCZT. The grain size of BCZT-1% BNKT is similar to BCZT, which could be the reason that the d_{33} of this sample is similar to pure BCZT, but a reduction in the grain size of BCZT-3 and 5% BNKT shows that BNKT decreases the grain growth of BCZT, and affects d_{33} . RT relative permittivity for the samples with BNKT is higher than BCZT, except for the high evaporation of BNKT at 1500°C for BCZT-5% BNKT and low relative density (88%). A comparison between the temperatures of the highest relative permittivity shows that another reason for the higher RT relative permittivity is the vicinity of RT to the maximum relative permittivity temperature. The addition of BNKT caused the maximum relative permittivity to decrease, compared to pure BCZT. Increasing the amount of BNKT caused the evaporation of this additive to

increase by increasing the sintering temperature and causing more porosity; as a result, there may be more space charges, which would decrease the maximum relative permittivity.

Table 4-2: Summary of the properties of BCZT and BCZT-1, 3, and 5% BNKT

Pure BCZT						
Sintering Temperature (°C)	1250	1300	1350	1400	1450	1500
Relative density%	-	-	-	92±1.2	96.1±0.7	94.2±0.8
d ₃₃ pC/N	-	-	-	310	410	350
RT ε _r	-	-	-	2533	3200	2515
Grain Size (μm)	-	-	-	22±1.5	32±2	35±0.8
Max ε _r	-	-	-	15100	17900	16500
k _p (%)	-	-	-	44	46	42
Curie temperature °C	-	-	-	103.5	102.5	102
BCZT – 1% BNKT						
Sintering Temperature (°C)	1250	1300	1350	1400	1450	1500
Relative density%	95±0.5	96±0.3	96±0.3	93±0.8	93±0.7	92±0.5
d ₃₃ pC/N	10±	130±10	290±15	330±15	300±20	370±15
RT ε _r	1998±100	2919±150	3080±200	3256±250	3253±220	3622±180
Grain Size (μm)	2±0.25	-	26±1	-	33±1.2	35±1.5
Max ε _r	2366	-	10028	-	10222	8903
k _p (%)	16±2	25±3	40±5	42±4	45±4	43±3
Curie temperature °C	98.8	-	81.4	-	80.7	78.7
BCZT – 3% BNKT						
Sintering Temperature (°C)	1250	1300	1350	1400	1450	1500
Relative density%	95±0.9	97±0.9	95±0.7	91±0.8	92±0.6	91±0.5
d ₃₃ pC/N	10±10	62.5±8	100±10	75±5	122.5±8	255±15
RT ε _r	2547±150	3575±180	3664±220	3852±250	3207±220	3473±180
Grain Size (μm)	2.2±0.4	-	12±1	-	31±1.4	33±1.8
Max ε _r	78.8	-	8655	-	5738	7644
k _p (%)	10±1	18±3	20±2	26±4	25±	41±3
Curie temperature °C	94.8	-	76.8	-	66.8	76.7
BCZT – 5% BNKT						
Sintering Temperature (°C)	1250	1300	1350	1400	1450	1500
Relative density%	98±0.8	95±0.9	94±1	94±0.1	94±0.2	87±0.7
d ₃₃ pC/N	5±5	17±5	17±5	30±10	50±10	100±20
RT ε _r	2450±180	5442±250	4477±200	4222±150	4039±190	2542±160
Grain Size (μm)	2.4±0.3	-	10±1	-	16±1.5	29±1.6
Max ε _r	2635	-	4600	-	5084	4321
k _p (%)	8±1	12±2	17±1	21±3	25±2	26±4
Curie temperature °C	63.1	-	50.1	-	64	98.6

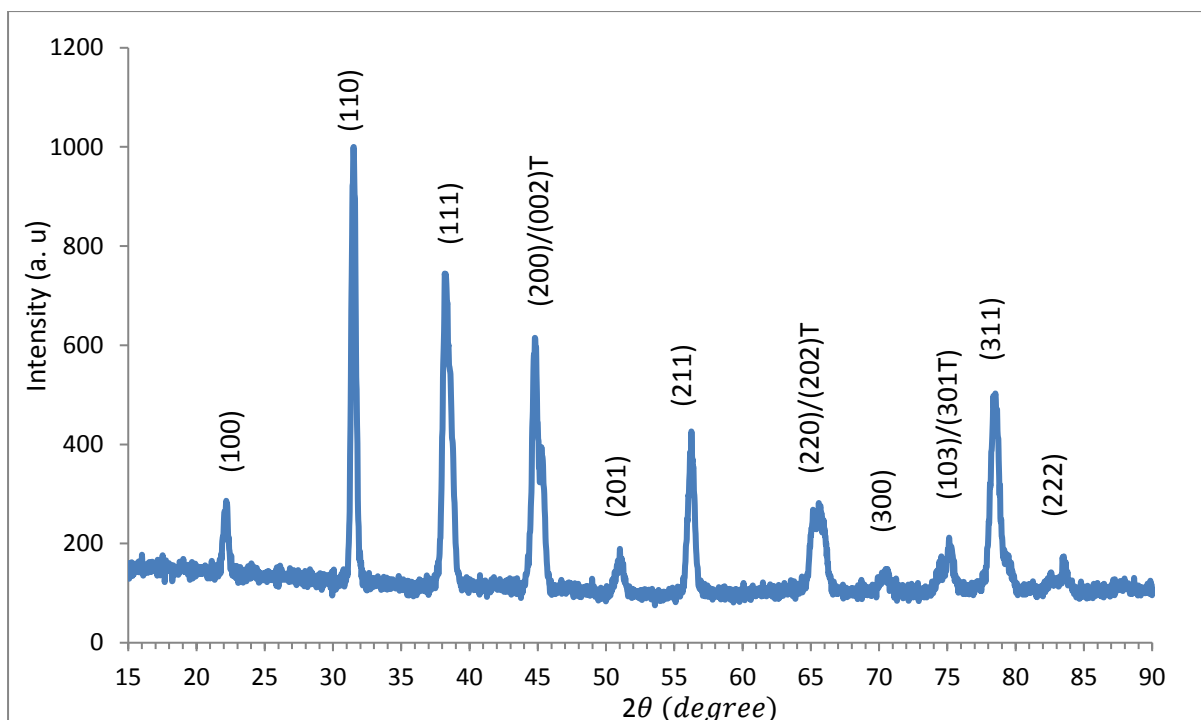


Figure 4-30: The XRD patterns of BT, calcined at 1100°C for two hours.

The XRD patterns show the perovskite structure, and the splitting of peaks at about $2\theta=45$, 65, and 75 degrees are indicative of the formation of tetragonal symmetry from the cubic structure below the Curie temperature. In addition, no impurity phases were detected, indicating a complete reaction of the raw material.

2- Fabrication of $\text{Bi}_{0.5}\text{Na}_{0.5}\text{TiO}_3$

Figure 4-31 shows the XRD patterns of BNT powder, calcined at different temperatures and using two fabrication methods. Figure 4-31-A shows BNT prepared by mixing the raw materials using solid state method, followed by calcination at 850°C (checked by the ICDS collection code: 154342). As can be seen, a pyrochlore phase can be observed for the samples prepared at this calcination temperature, and the relative peak intensities indicate that the phase content is quite large. The $\text{Bi}_2\text{Ti}_2\text{O}_7$ -pyrochlore phase is a low-temperature phase with a high dielectric constant [224], and is an intermediate phase that should be avoided by changing the experimental conditions in order to achieve a pure perovskite phase.

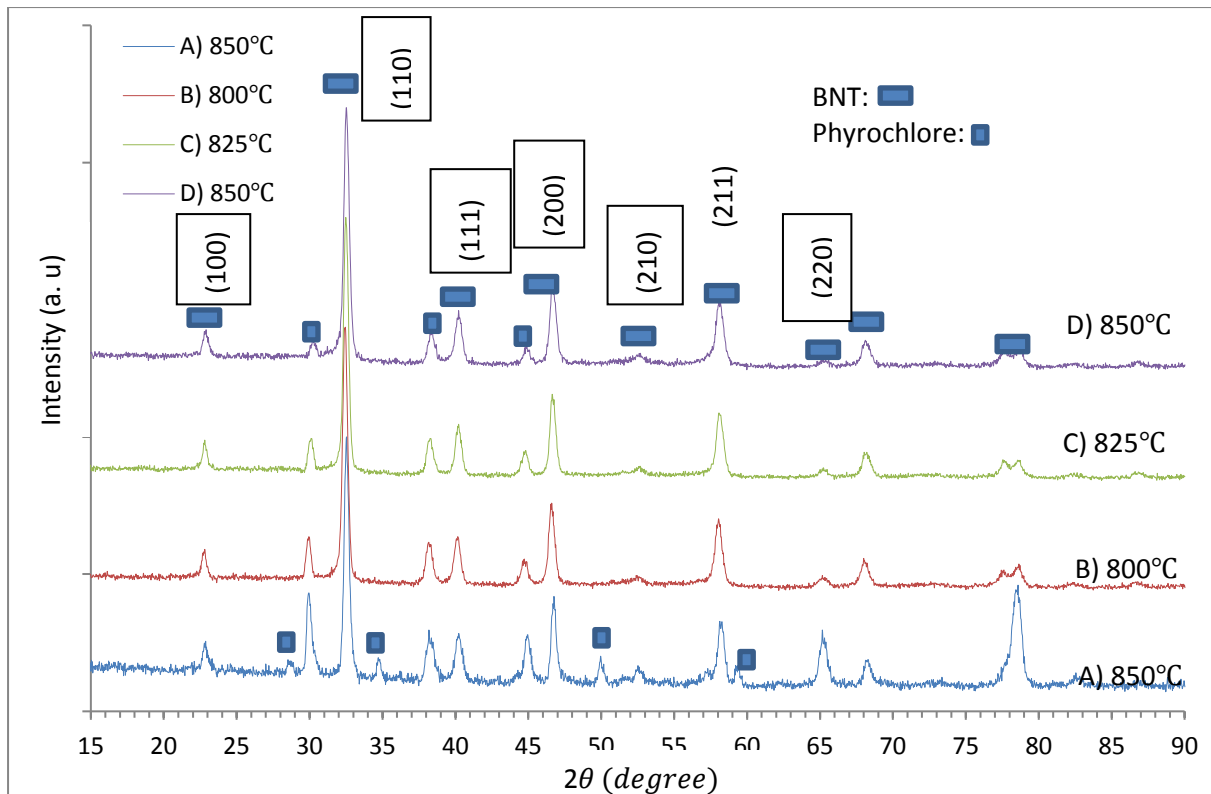


Figure 4-31: The XRD patterns of A) BNT: the blue line (bottom) – mixed by the wet method and calcined at 850°C for two hours; B) BNT: the red line – mixed by the dry method and calcined at 800°C for two hours; C) BNT: the green line – mixed by the dry method and calcined at 825°C for two hours; and D) BNT: the purple line – mixed by the dry method and calcined at 850°C for two hours.

It was observed that after calcination, the powder mixed via the wet method and calcined powder at 850°C appeared to have a large particle or agglomerate size, and that the particles were stuck together. There are two potential ways to solve this problem: firstly, to use dispersion and add it to the slurry, and secondly, to use another method, such as a dry method, to mix the powders. In this case, the dry method was chosen, so the raw materials were mixed in the vibro-milling machine; the average particle size achieved was under 0.8 μm (d_{50}). Figure 4-31 A, B, C, and D show the XRD patterns of the dry mixed powder calcined at 800, 825, and 850 °C for two hours. As can be seen, the pyrochlore phase is observed in all of them, but the amount – even for powders prepared by the dry method and calcined at 800°C – is lower than for the powder prepared by the wet method and calcined at 850°C. For this reason, the dry method was chosen to continue the project.

The calcination temperature for BNT should be kept as low as possible ($< 850^\circ\text{C}$) due to the low melting point of Bi_2O_3 at 825°C and Na_2O at 1132°C, which could cause evaporation of the Bi and Na and affect the ferroelectric properties of BNT [67]. However, as can be seen in Figure 4-31 (A), the pyrochlore phase is still present. This problem has been observed by

other groups [60] with the formation of pyrochlore or $\text{NaBiTi}_6\text{O}_{14}$ and TiO_2 during the calcination of BNT. One method to solve this problem is to use a two-step calcination procedure similar to that developed for lead magnesium niobate (PMN) [225]. This would involve mixing Na_2CO_3 and Bi_2O_3 as the first step to form NaBiO_2 . However, NaBiO_2 has a low melting temperature and evaporates at a low temperature, as can be seen in the phase diagram of the $\text{Bi}_2\text{O}_3\text{-Na}_2\text{O-TiO}_2$ system presented in Figure 4-32 [68, 168].

Therefore, an increase in calcination time was chosen to avoid the formation of the pyrochlore phase. To achieve this purpose, BNT was calcined at temperatures of 800, 825, and 850°C for five hours. The XRD patterns of the resulting powders are shown in Figure 4-33. As can be seen, the pyrochlore peaks start to disappear as the calcination temperature is increased from 800 to 850°C and at this temperature, only peaks from the BNT phase are observed. Based on the above results, the calcination temperature of BNT-BT should be between 850 and 1100°C. Thus, the BT and BNT powders from the previous steps were weighed and mixed, based on molar ratios, and calcined at a range of temperatures from 850 to 1150°C for five hours; the XRD patterns of the resulting powders are shown in Figure 4-34.

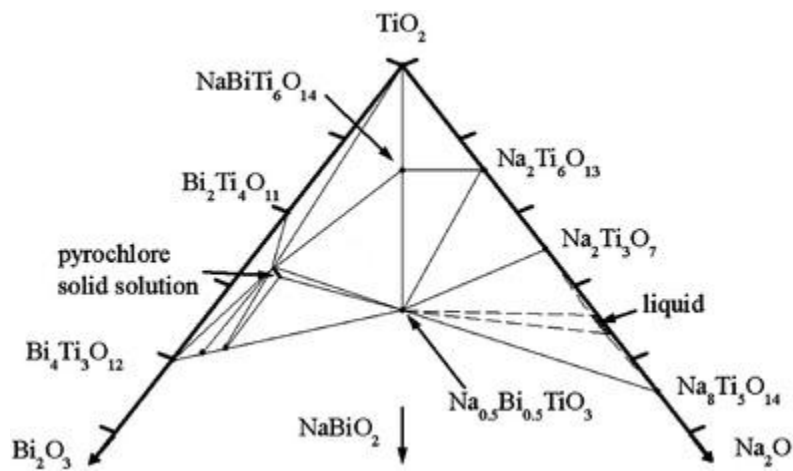


Figure 4-32: Phase relations in the system $\text{Bi}_2\text{O}_3\text{-Na}_2\text{O-TiO}_2$ at 1000°C [68]

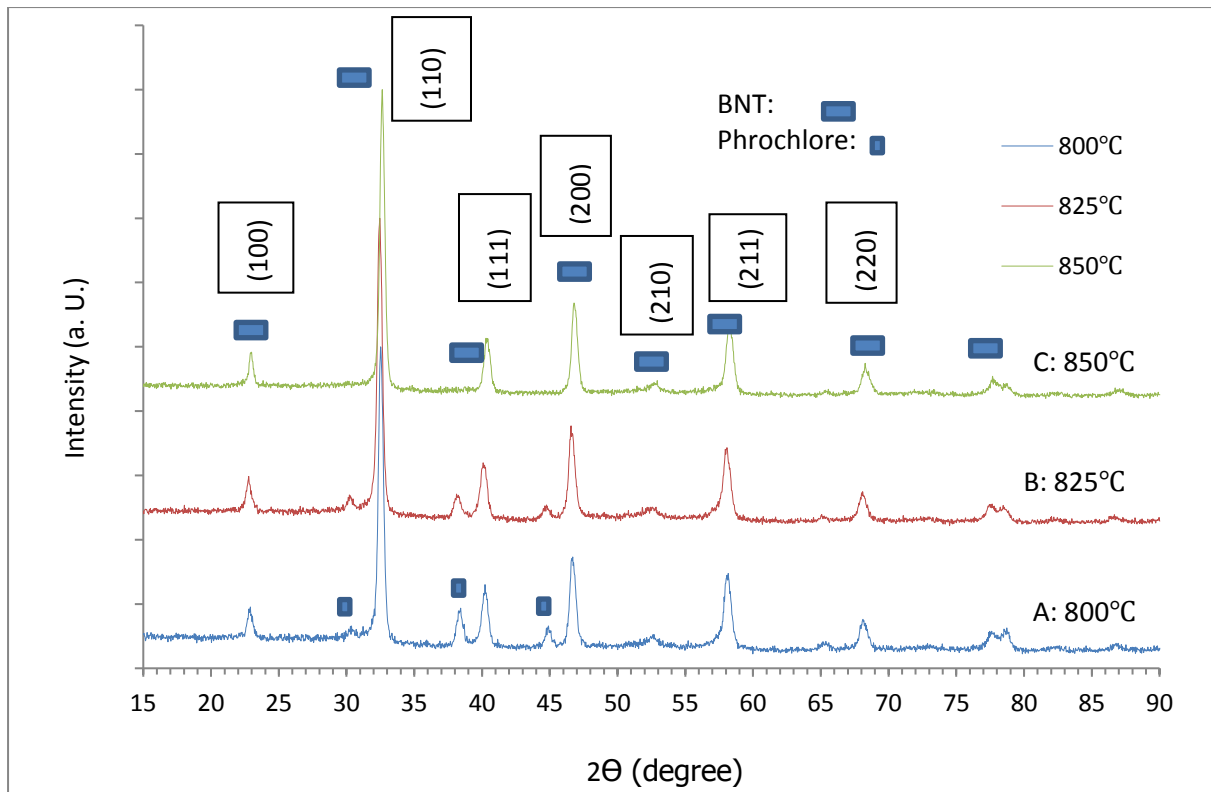


Figure 4-33: The XRD patterns of: A) BNT: the black line, calcined at 800°C; B) BNT: the red line, calcined at 825°C; and C) BNT: the blue line, calcined at 850°C for five hours, produced by the dry powder method..

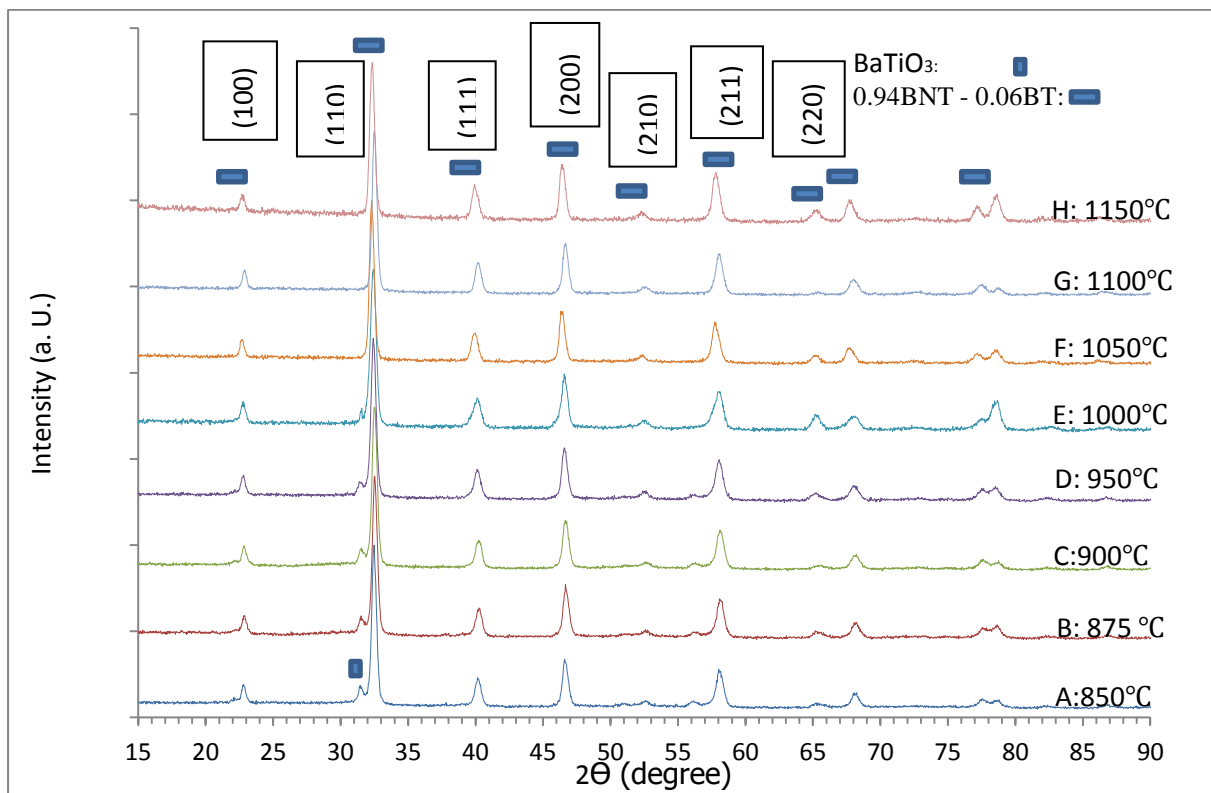


Figure 4-34: The XRD patterns of A) 0.94BNT-0.6BT calcined at 850°C; B) 875°C; C) 900°C; D) 950°C; E) 1000°C; F) 1050°C; G) 1100°C; and H) 1150°C, for five hours.

The results show that the BT phase remains until 1000°C and at 1050°C, BNT and BT form a pure perovskite structure; i.e., BT diffuses to the BNT structure, and no remaining BT phase is detected. The calcination temperature for pure BNT is 850°C, while for 0.94BNT-0.06BT it is 1050°C, and for pure BT it is 1100°C.

For sintering BNT-BT, ranges of temperature between 1100-1200°C were chosen with 25°C increments and after that, density, relative permittivity, d_{33} , and grain size using SEM were measured to optimise the sintering temperature for the composition.

Figure 4-35 shows the SEM images of BNT-BT samples sintered at 1100, 1125, 1150, 1175, and 1200°C for two hours. The sample sintered at 1100°C does not show a dense structure or grain growth in comparison to the other temperatures, due to the high intergranular pores, while for the sample sintered at 1125°C and other sintering temperatures, a reduction in the inter-grain porosity and increase in size can be observed along with the evaporation of the Bi and Na elements. Figure 4-36 shows the effect of the sintering temperature on the relative density of the BNT-BT ceramic samples.

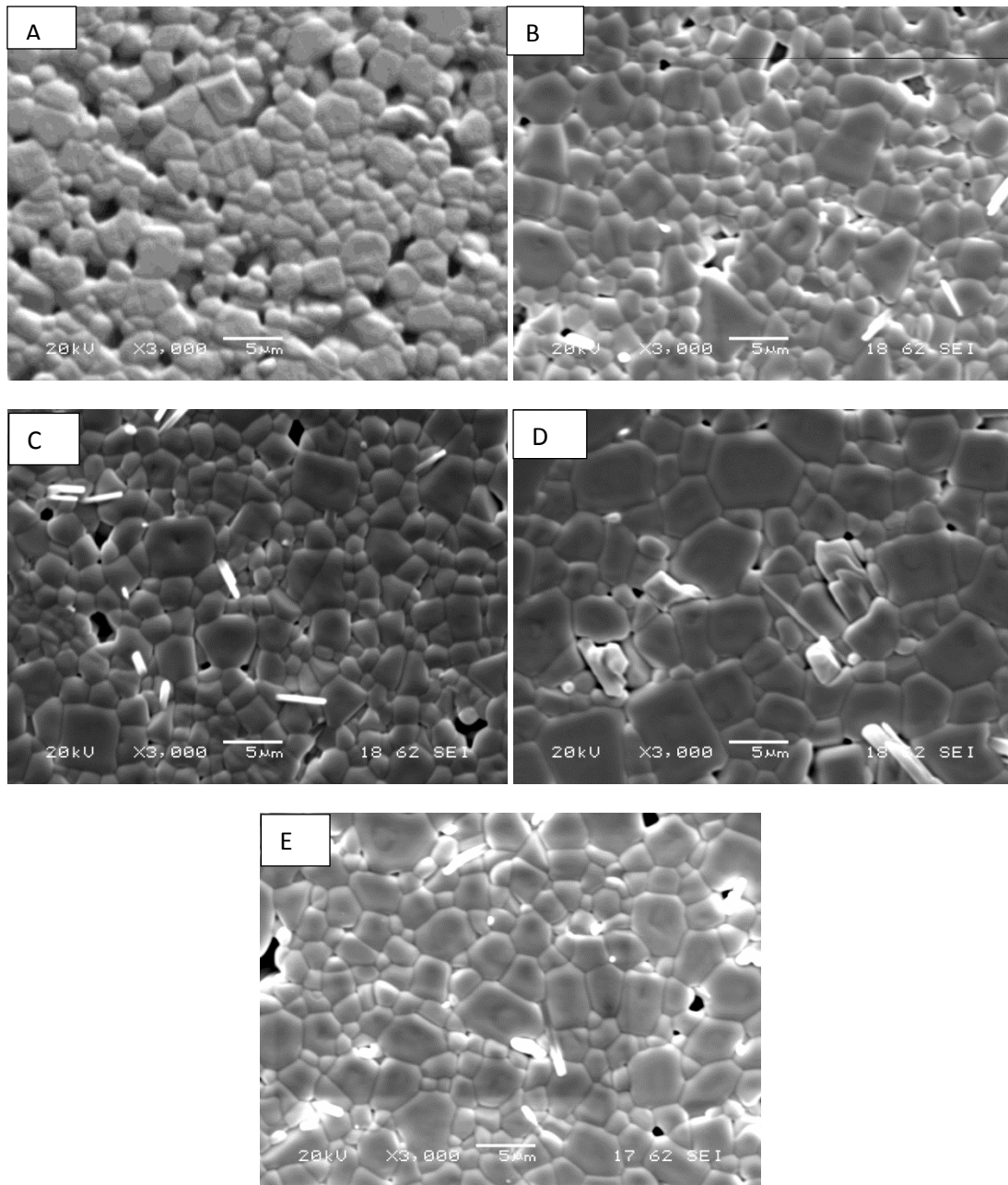


Figure 4-35: SEM micrograph of the 0.94BNT-0.6BT samples sintered a) 1100°C; B) 1125°C; C) 1150°C; D) 1175°C; and E) 1200°C (see the appendix for a low magnification photo).

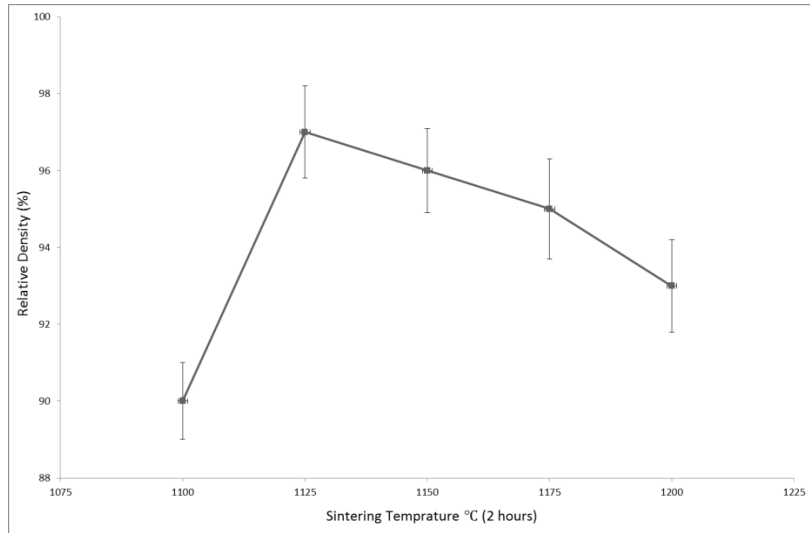


Figure 4-36: The variation of relative density as a function of the sintering temperature for 0.94BNT-0.6BT.

There is a large increase in the density from 1100°C to 1125°C, while relative density decreases from 98% to 92% at 1200°C. A comparison between the densities with SEM images shows that at 1100°C, the intergranular pores are large, which causes the relative density to be around 90%. With a rise in the sintering temperature, a reduction can be seen in the inter-grain by increasing the grain size, so a rise in the density can be seen. Then, in spite of the increase in grain size, the density decreases from 97% to 96%, which can be attributed to the volatilisation of Bi and Na. The volatilisation continues at higher temperatures and causes the density to decrease from 95% at 1175°C to 93% at 1200°C. Figure 4-37 shows the variation of grain size as a function of the sintering temperature for BNT-BT. As can be seen, from 1100 to 1200°C, there is a rise in the grain size starting from 2.5 μm to around 4 μm .

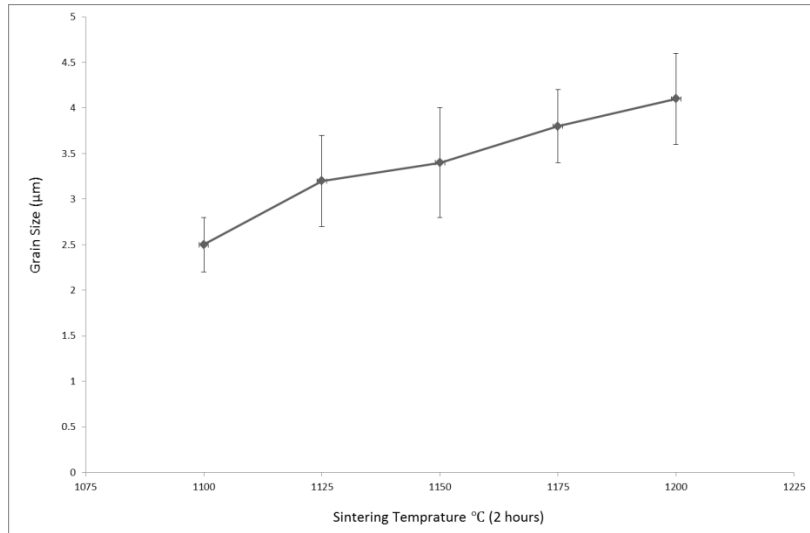


Figure 4-37: The variation of grain size as a function of sintering temperature for 0.94BNT-0.6BT.

Figure 4-38 shows the variation of relative permittivity of unpoled samples measured at room temperature as a function of the sintering temperature for BNT-BT. The relative permittivity starts at 950 for samples sintered at 1100°C, increases to around 1230 for samples sintered at 1125°C, and after that, slightly shifts to a lower value for higher sintering temperatures. Two main factors can affect the value of relative permittivity: firstly, a rise in the relative density, which shows the more dense structure, and secondly, evaporation of the Bi and Na elements, which by increasing the intergranular porosity, causes higher space charges, so the relative permittivity decreases. The variation in relative permittivity is similar to that of the relative density, which shows its effect on the properties of the compound.

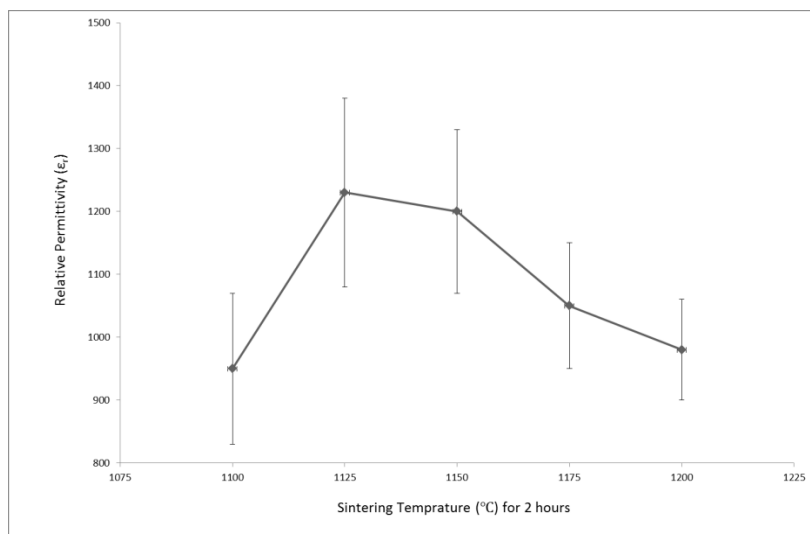


Figure 4-38: The variation of relative permittivity of unpoled samples measured at room temperature as a function of sintering temperature for 0.94BNT-0.6BT at RT.

Figure 4-39 shows the variation of d_{33} as a function of sintering temperature for BNT-BT and again, the variation is similar to the relative density. The d_{33} is around 115 pC/N for a sintering temperature of 1100°C and increases to a maximum of 165 pC/N for a sintering temperature of 1125°C, and decreases to 120 pC/N as the sintering temperature is increased to 1200°C.

Figure 4-40 shows the variation of k_p as a function of sintering temperature for BNT-BT at 1100, 1125, 1150, 1175, and 1200°C. The value of k_p is around 20% for BNT-BT sintered at 1100°C and by increases in the sintering temperature, it increases to 47, 49, 44, and 42% at 1125, 1150, 1175, and 1200°C, respectively. The highest amount of electromechanical coupling factor, or the transformation of mechanical energy to electrical (or vice versa), can be found at 1150°C. The reasons for the increase in the k_p can be the same as d_{33} ; i.e., by an increase in the grain size, the k_p is increased and after that, it decreases to lower values.

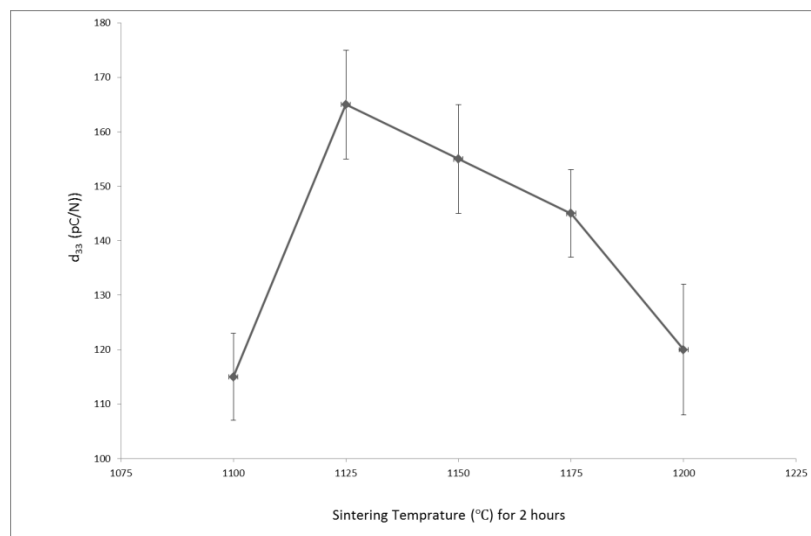


Figure 4-39: The variation of d_{33} as a function of the sintering temperature for 0.94BNT-0.6BT.

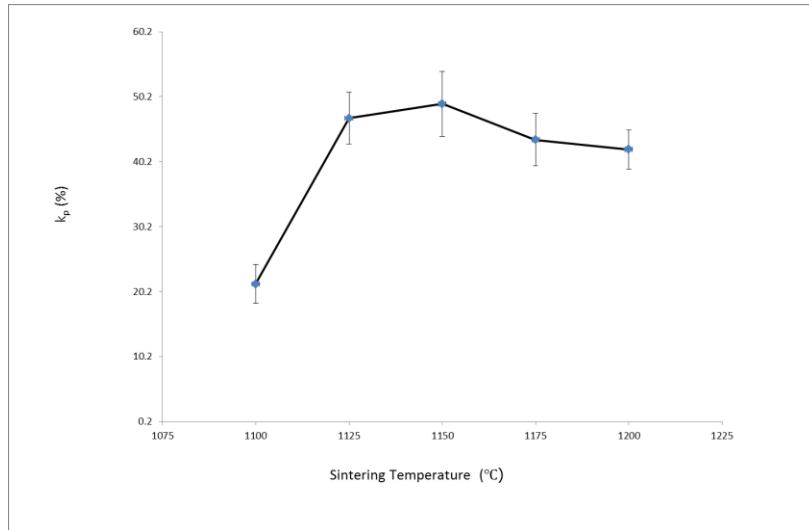
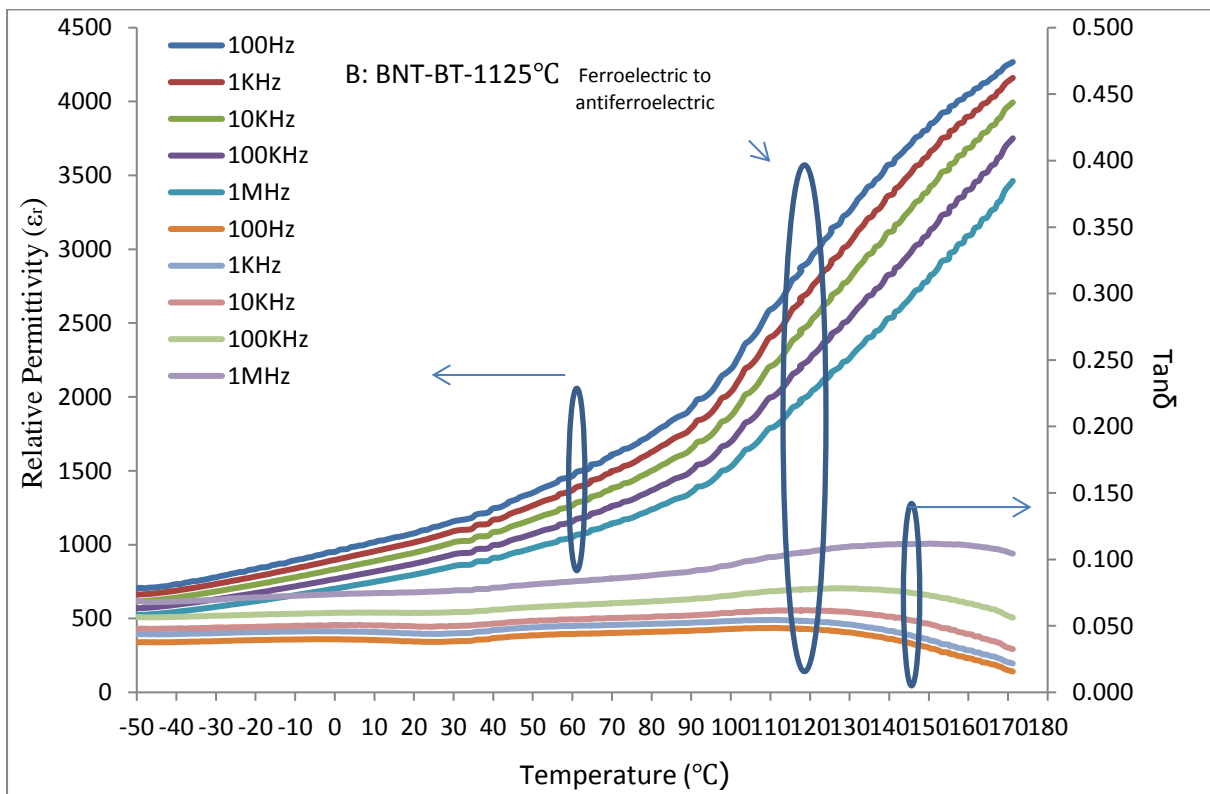
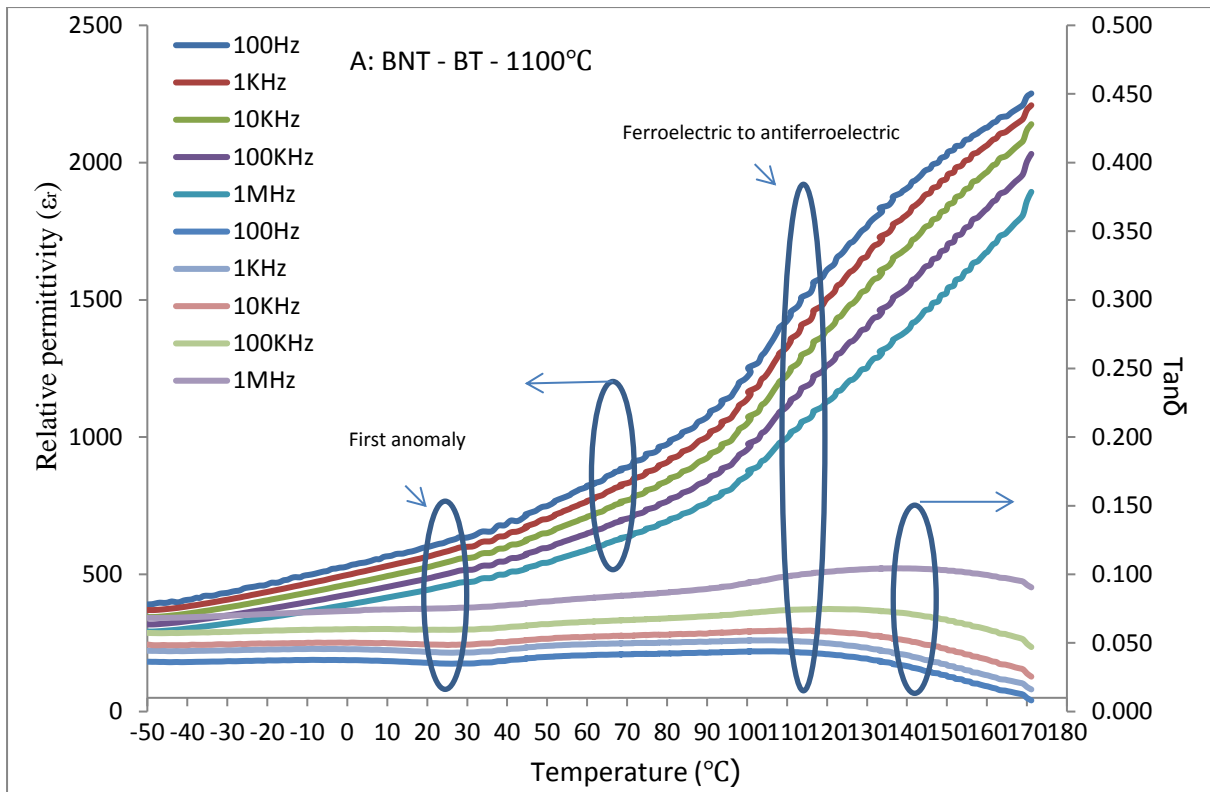
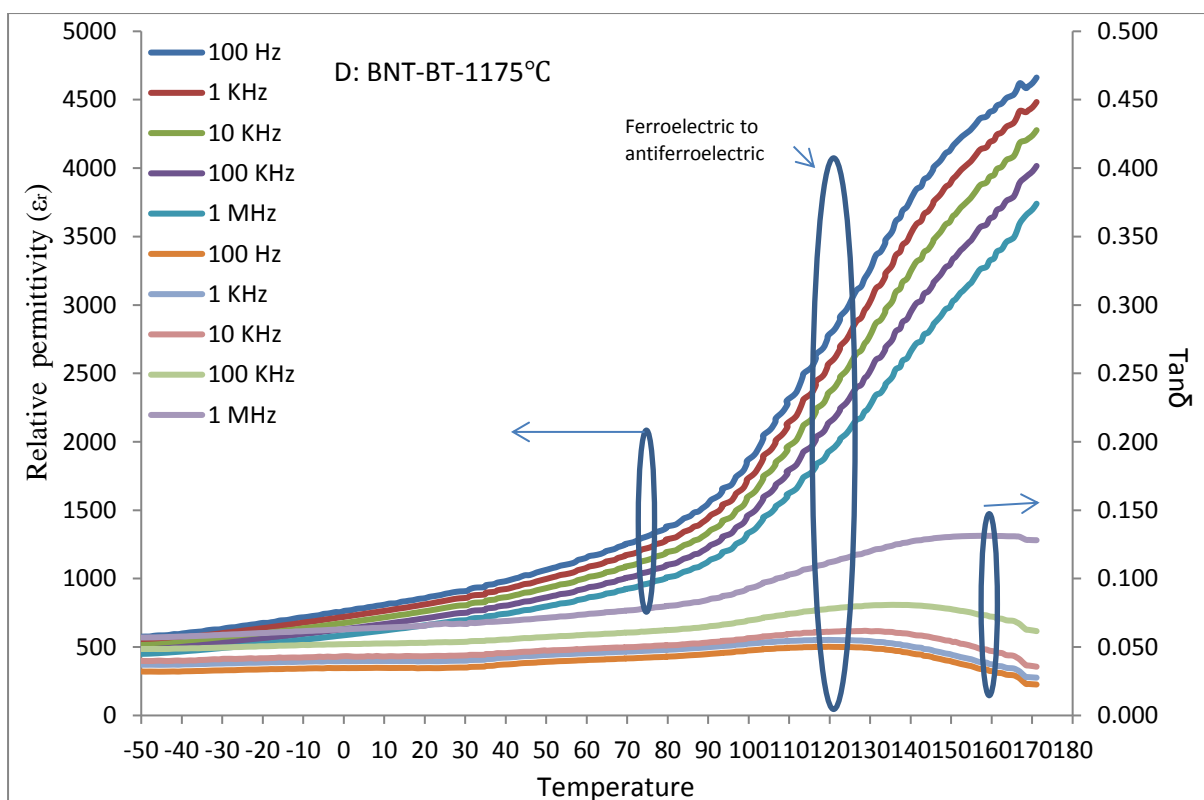
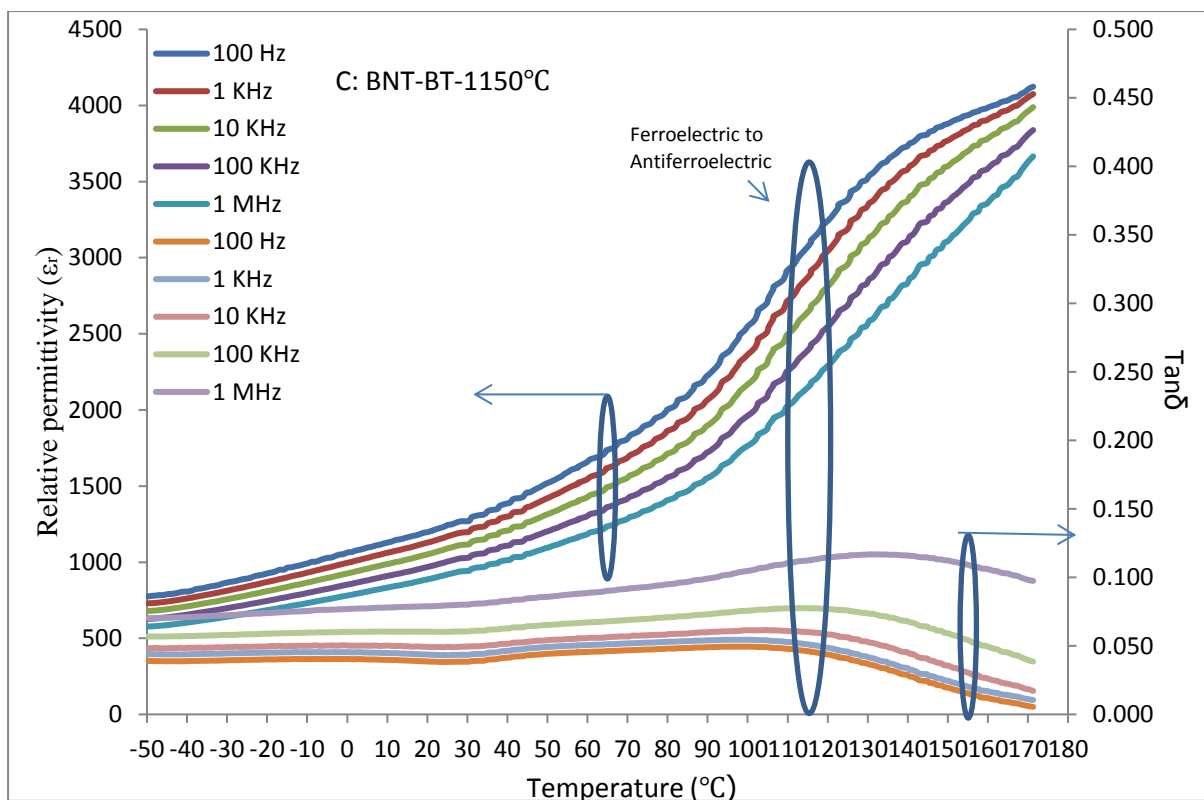


Figure 4-40: The variation of k_p as a function of the sintering temperature for 0.94BNT-0.6BT.

Figure 4-41 shows the temperature dependence of relative permittivity (ϵ_r) and dielectric loss ($\text{Tan}\delta$) of unpoled samples at 100 Hz, 1 kHz, 10 kHz, 100 kHz, and 1 MHz for BNT-BT sintered samples at 1100, 1125, 1150, 1175, and 1200°C, respectively. The relative permittivity slightly decreases when increasing the frequency from 100Hz to 1MHz, the value of the dielectric loss is low (under 0.15) for all the sample and frequencies, and it increases with increases in the frequency from 100Hz to 1MHz. There are two anomalies in the range of temperatures measured, the first around room temperature, and the second around 110-128°C. As explained in section 2.1.1.2.3.1, there is some discussion about the phases in BNT-BT at room temperature; firstly, the existence of the ferroelectric and anti-ferroelectric phase with tetragonal symmetry at room temperature and secondly, the existence of the ferroelectric phase only at room temperature. The possibility of the existence of the anti-ferroelectric phase has been proven by TEM, which takes the form of polar nano regions (PNR) at RT [66]. The first anomaly can be related to the formation of the PNR at room temperature, which then promotes the anti-ferroelectric behaviour at a higher temperature. The second anomaly is related to the ferroelectric-to-anti-ferroelectric transformation, which occurs from 110°C to around 128°C. The relative permittivity around this temperature for samples sintered at 1100°C is around 1000, while for samples sintered at 1125, 1150, 1175, and 1200°C the values are 2225, 2180, 2105, and 1980, respectively, due to the lower relative density, higher porosity and potentially the existence of space charges.





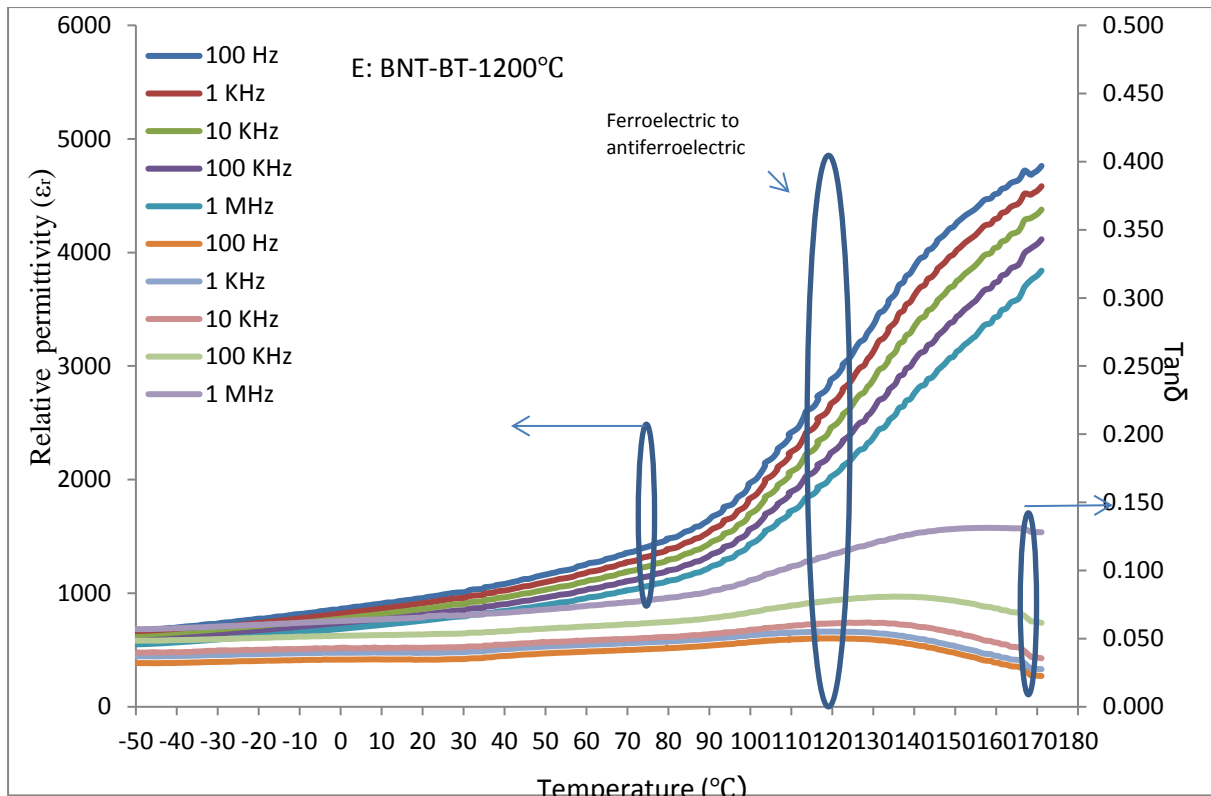


Figure 4-41: The temperature dependence of relative permittivity (ϵ_r) and dielectric loss ($\text{Tan}\delta$) of unpoled samples at 100 Hz, 1 kHz, 10 kHz, 100 kHz, and 1 MHz for 0.94BNT-0.06BT samples sintered at A) 1100, B) 1125, C) 1150, D) 1175, and E) 1200°C for two hours.

Table 4-3 shows a summary of the properties of the BNT-BT materials; as can be seen, the optimum properties are found at sintering temperatures of 1125 - 1150°C, which shows the highest relative density (97-97%). A comparison between this table and Table 2-5 shows that the d_{33} is increased using the solid method in this project. The increase from 120 to 165 pC/N can be attributed to the two-step calcination process and the calcination temperature. A calcination temperature of around 850 to 900°C and the one-step method is the usual solid-state method to prepare BNT-BT, which is different to the method that has been used in this project. A higher calcination temperature (1050°C) makes the atomic arrangement in the grain boundaries more similar to the grains that allow cross-domain access, rather than low a calcination temperature, because irregular grain boundaries can cause higher internal stresses [42, 43]. In addition, a higher calcination temperature can increase the relative density through a reduction in the intra granular porosity, which has a direct relation with its properties.

Table 4-3: The effect of the sintering temperature on the properties of 0.94BNT-0.06BT.

Sintering Temperature (°C)	1100	1125	1150	1175	1200
Relative density%	94	97	96	95	93
d_{33} pC/N	115	165	155	145	120
Relative permittivity at RT	950	1230	1200	1050	980
Grain Size (μm)	2.5 ± 0.5	3.2 ± 0.7	3.4 ± 0.6	3.8 ± 0.8	4.1 ± 0.5
Ferroelectric to Anti ferroelectric	110 -128	110-128	106-128	110-128	110-128
k_p (%)	20	47	49	44	42

4.3.1 ((1-x) 0.94BNT-0.06BT)-xBF) or (BNT-BT-BF)

BiFeO₃ (abbreviated BF) is one of the compositions whose effect was investigated on the BNT-BT properties. Firstly, BF was calcined at 850°C for five hours, and as can be seen in Figure 4-42, the XRD pattern shows the perovskite structure without any secondary phase, checked by collection code 157424 on the ICSD.

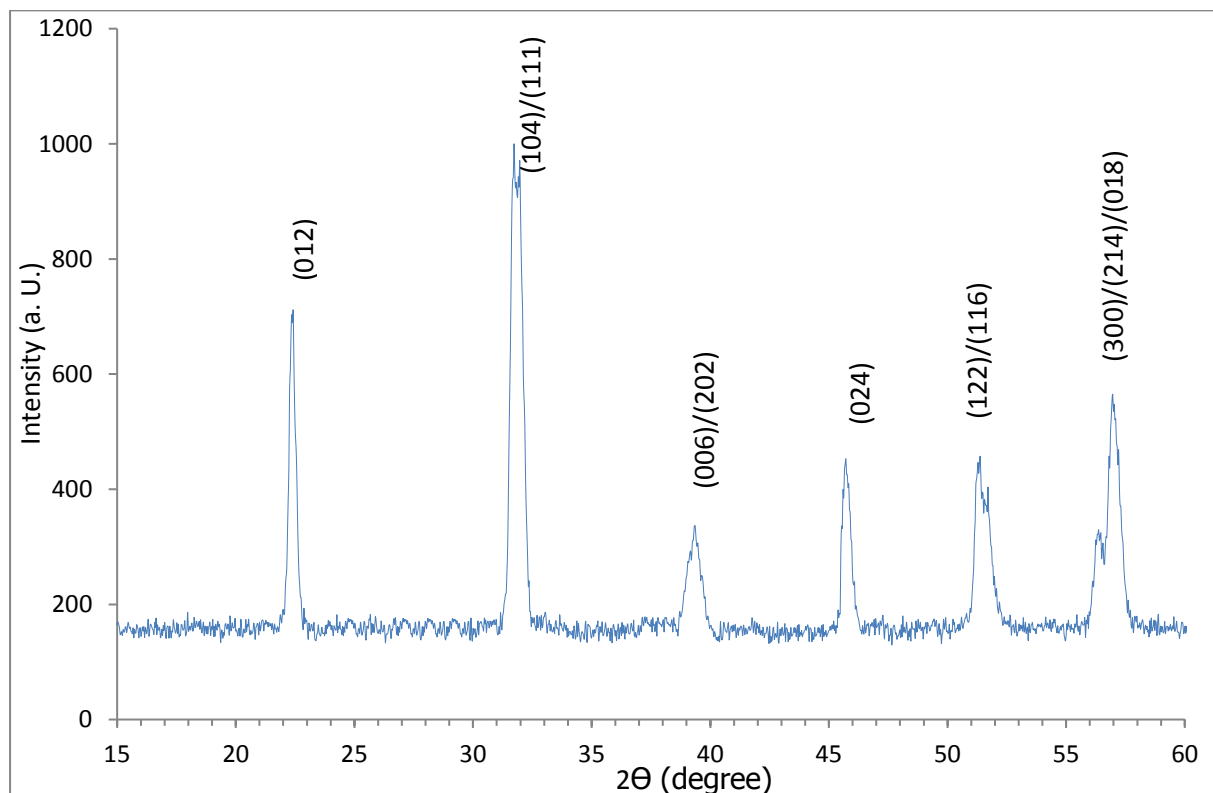


Figure 4-42: The XRD Patterns of BF powder calcined at 850°C for 5hours

BF was added as 0.025, 0.05, 0.075, and 0.01 mol% to BNT-BT (1-x) (0.94BNT-0.06BT)-xBF). Figure 4-43 shows the XRD patterns of the (1-x) BNT-BT-xBF for x=0.00, 0.025, 0.05, 0.075, and 0.1. As can be seen, the XRD patterns reveal that BF made a solid solution with

BNT-BT in the perovskite structure, without any secondary phase. However, the maximum BF addition is 1% and XRD may not be sensitive enough to detect the secondary phase. The addition of BF causes shifts in the XRD patterns, which confirms the substitution of BF in the BNT-BT perovskite structure; to show this more clearly, the XRD patterns were enlarged at around $2\theta = 40$ and 46.5 in Figure 4-44. The peaks shift to a lower angle with the addition of BF to 0.05 mol% and go to a higher angle at 0.075 and 0.1 mol% of BF.

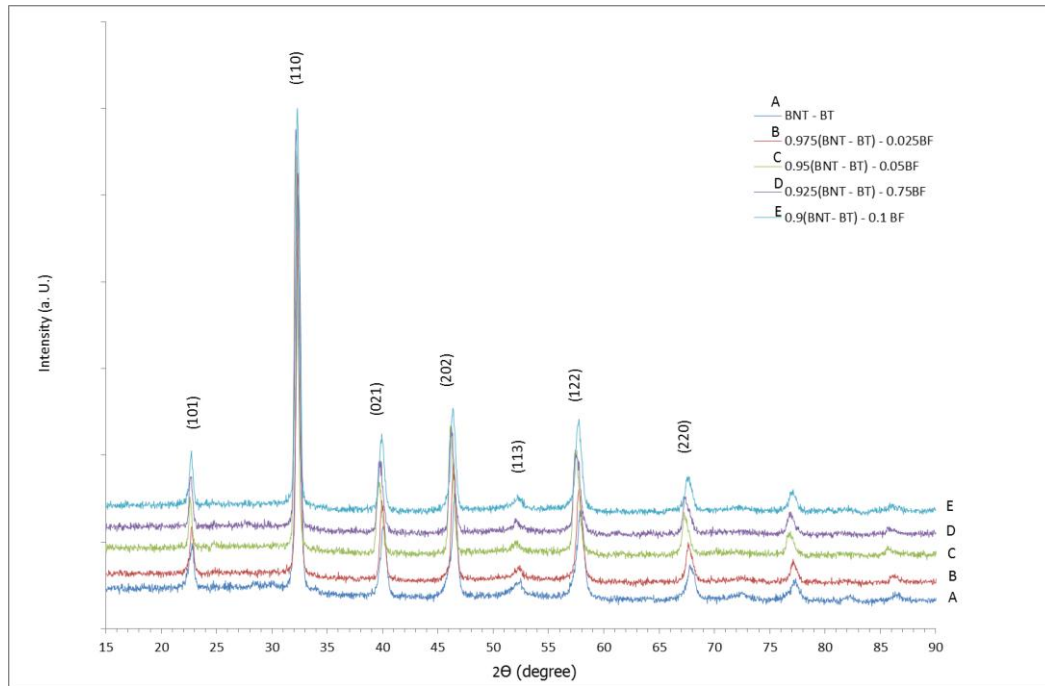


Figure 4-43: The XRD Patterns of (0.94BNT-0.06BT)-x BF sintered at 1125°C for x values of A) 0.000, B) 0.025, C) 0.050, D) 0.075 and E) 0.100 BF

Bismuth and iron in the BF can occupy the A and B sites in the perovskite structure; due to its higher ionic radius ($\text{Bi}^{3+} = 0.096$ nm), bismuth is usually the substitute in the A site, while iron, which has a similar ionic radius to titanium ($\text{Fe}^{3+} = 0.064$ and $\text{Ti}^{4+} = 0.068$ nm), is the replacement in the B site. The substitution of bismuth in the A site causes the peaks to shift to lower angles due to the expansion of the structure, and the Fe^{3+} substitution in B site can cause the peaks to shift to higher angles. So, an addition of BF to a 0.050 mol% amount made the angles to go to a lower degree, while higher than this amount, the peaks shift to a higher angle again.

Figure 4-45 shows the SEM images of (1-x) (0.94BNT-0.06BT)-xBF samples sintered at 1125°C. The SEM images reveal that the addition of BF decreases the densification of the sintered samples, which can contribute to the evaporation of more bismuth from the

composition. In addition, the grain size is increased by the addition of BF to the BNT-BT, and by an increase in the value of BF, promoting this grain growth.

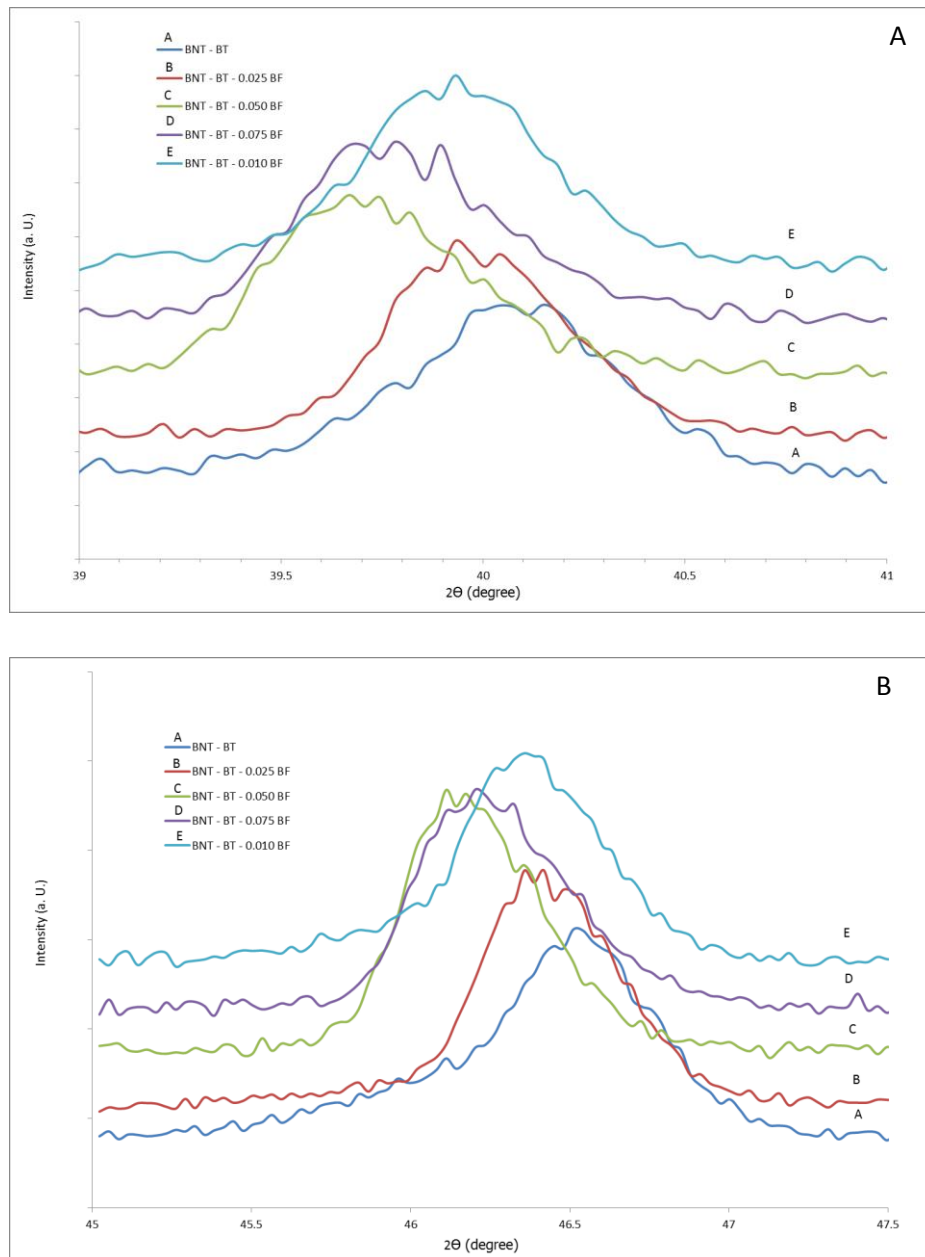


Figure 4-44: The XRD patterns of (0.94BNT-0.06BT)-x BF sintered at 1125°C at around $2\theta =$ A) 40° for (111) and B) 46.5° for (200).

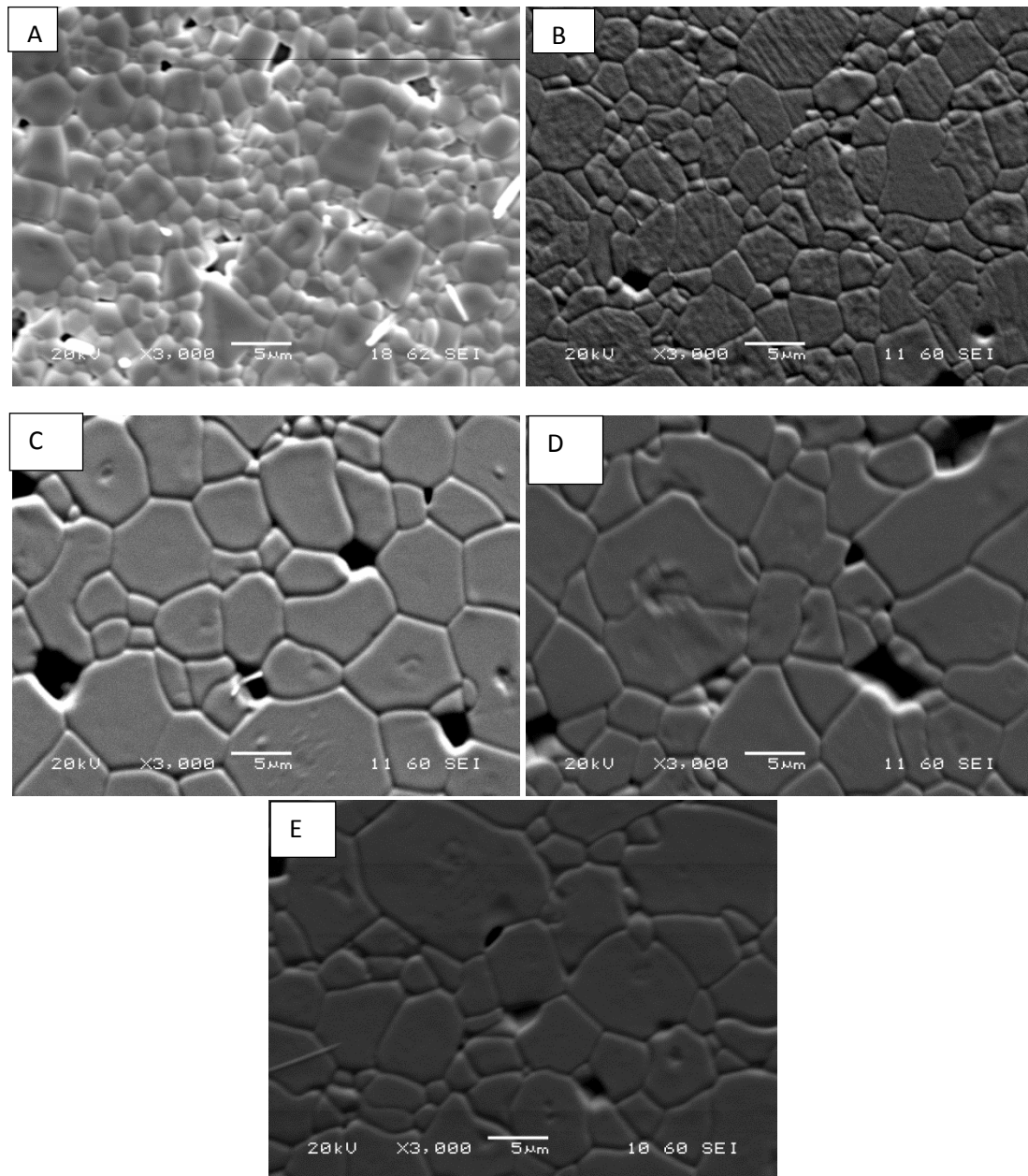


Figure 4-45: SEM micrographs of the (0.94BNT-0.06BT)-x BF samples sintered at 1125 °C for x values of A) 0.00, B) 0.025, C) 0.050, D) 0.075, and E) 0.10 (see the appendix for a low magnification images).

Figure 4-46 shows the variation in the relative density of $(1-x)(0.94\text{BNT}-0.06\text{BT})-x\text{BF}$ for $x=0, 0.025, 0.05, 0.075,$ and 0.1 . The relative density decreases with a rise in the amount of BF; it starts from 97% for pure BNT-BT and after that, it sharply decreases to 93% for $0.975(0.94\text{BNT}-0.06\text{BT})-0.025\text{BF}$ and then slightly decreases until around 92.5% for $0.9(0.94\text{BNT}-0.06\text{BT})-0.1\text{BF}$.

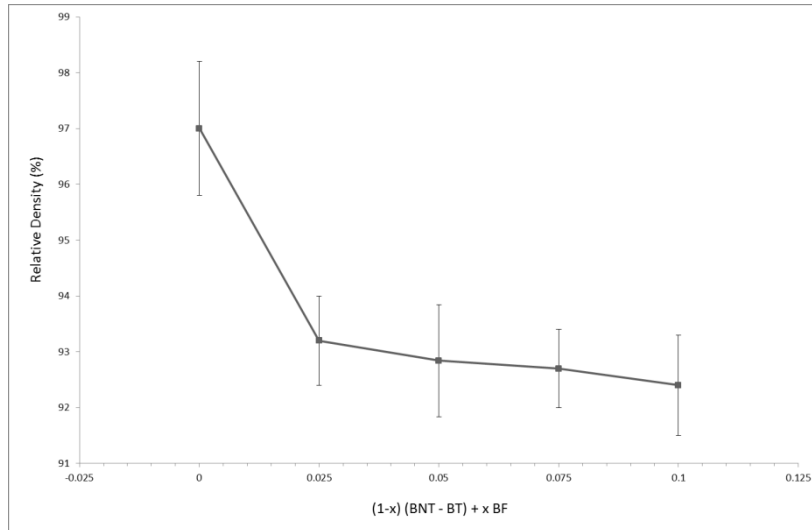


Figure 4-46: The variation of relative density as a function of (0.94BNT-0.06BT)-x BF for samples sintered at 1125°C.

Figure 4-47 shows the variation in grain size of (1-x) (0.94BNT-0.06BT)-xBF) for x=0, 0.025, 0.05, 0.075, and 0.1. The main effect is from x=0 to x=0.025, then the grain size is approximately constant. An increase in the amount of BF increases the grain size from around 3.2 μm for x=0 to around 6.5, 6.7, 7 and 7.2 μm for x=0.025, 0.05, 0.075 and 0.1 respectively.

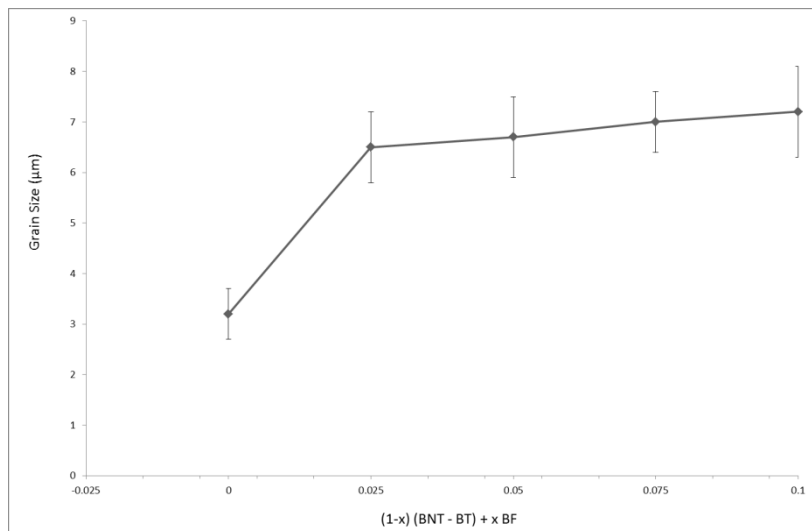


Figure 4-47: The variation of grain size as a function of (0.94BNT-0.06BT)-x BF for samples sintered at 1125°C.

Figure 4-48 shows the variation in relative permittivity of unpoled samples as a function of x in (1-x) (0.94BNT-0.06BT)-xBF) for samples sintered at 1125°C. The relative permittivity

is 1230 for $x=0$ and decreases continuously to 461 for $x=0.1$, and follows the trend of relative density.

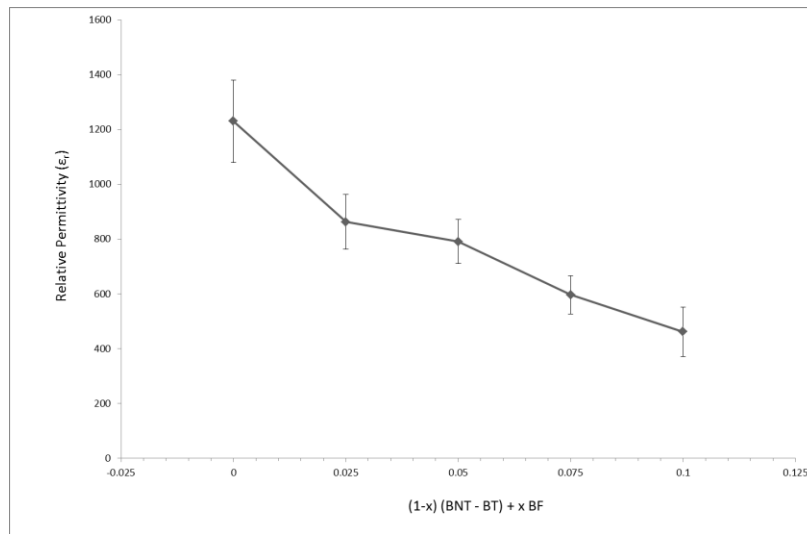


Figure 4-48: The variation of relative permittivity of unpoled samples measured at room temperature as a function of x in $(0.94\text{BNT}-0.06\text{BT})-x\text{BF}$ for samples sintered at 1125°C .

Figure 4-49 shows the variation of d_{33} as a function of x in $(1-x)(0.94\text{BNT}-0.06\text{BT})-x\text{BF}$ for samples sintered at 1125°C . The d_{33} was decreased by substituting BF into BNT-BT; while the value for pure BNT-BT is around 165 pC/N , it was decreased to 95 pC/N by adding 0.025 mol\% of BF. The rhombohedral and tetragonal forms coexist at MPB in BNT-BT, and the XRD patterns in Figure 4-43 show the pseudo cubic phase, but the shift in the XRD patterns can lead the structure of the compound far from the MPB [120], which affects the piezoelectric properties, and especially the d_{33} . Between $x=0.025$ and 0.075 mol\% BF, the d_{33} slightly decreases from 95 to 75 pC/N , and from 0.075 to 0.1 mol\% , it sharply decreases from 70 to 30 pC/N .

Figure 4-50 shows the variation of k_p as a function of $(1-x)(0.94\text{BNT}-0.06\text{BT})-x\text{BF}$ for samples sintered at 1125°C . The value of k_p is around 47% for the BNT-BT sintered at 1125°C and by the substitution of BF into BNT-BT, it decreases to 33 , 19 , 16 , and 14% for 0.025 , 0.050 , 0.075 , and 0.10 mol\% of BF, respectively. The highest value of the electromechanical coupling factor or the transformation of mechanical to electrical energy or vice versa can be found for pure BNT-BT. The reason for the reduction in the k_p can be the same as for the d_{33} ; i.e., with an increase in the value of BF, due to the reduction in relative density, the k_p is decreased to lower values.

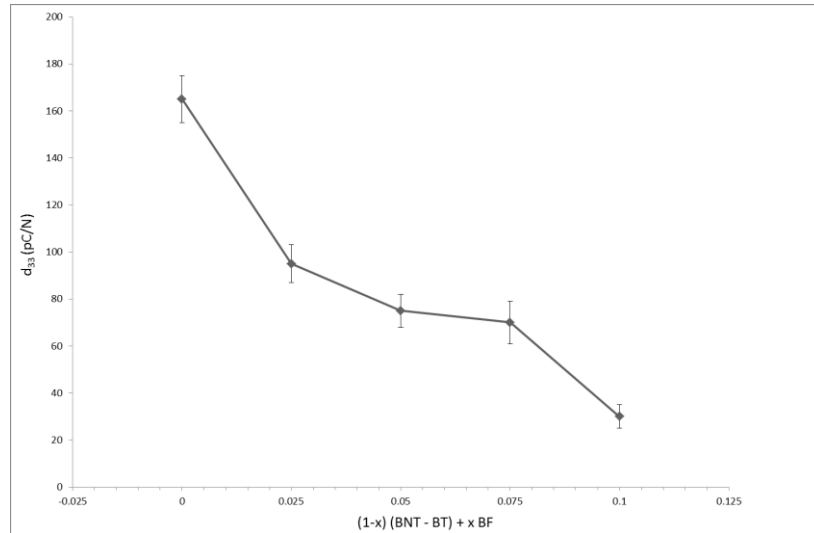


Figure 4-49: The variation of d_{33} as a function of (0.94BNT-0.06BT)-x BF for samples sintered at 1125°C.

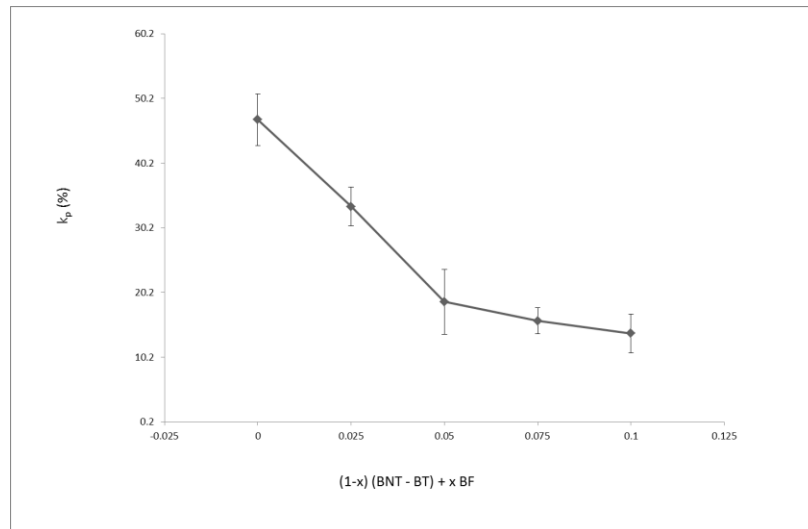
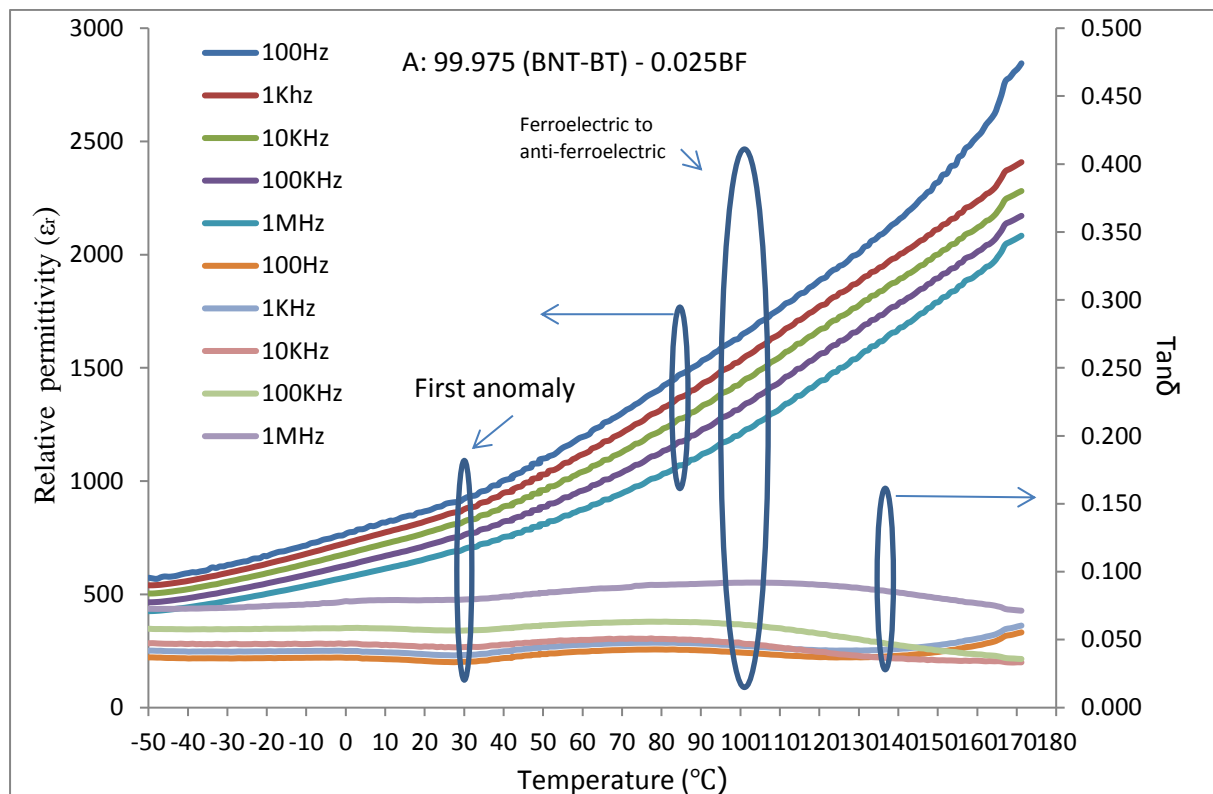
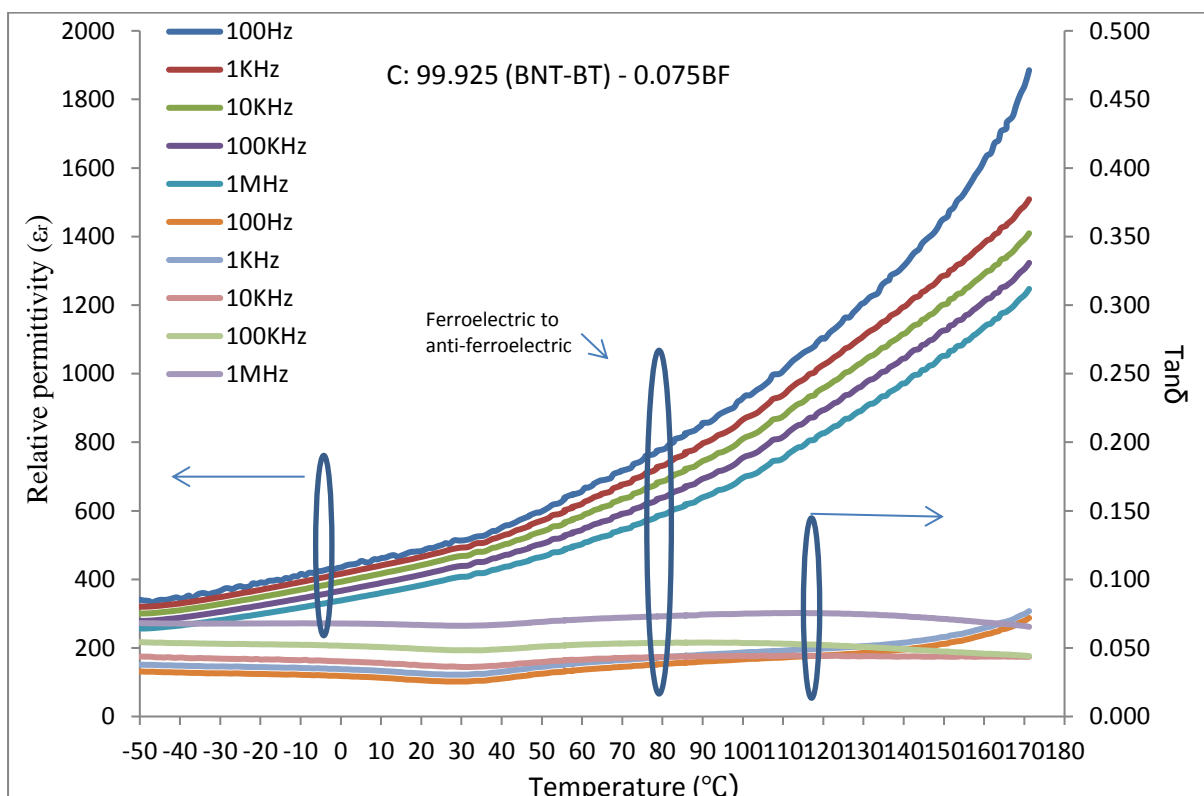
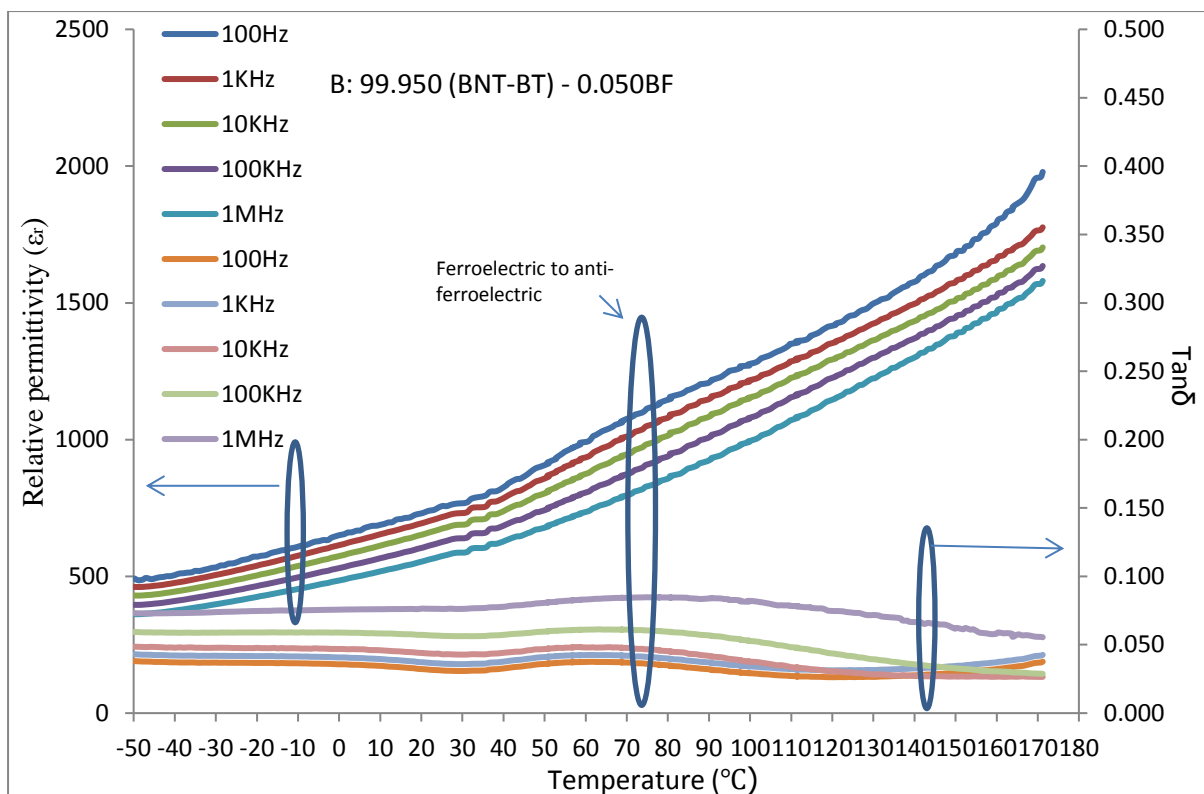


Figure 4-50: The variation of k_p as a function of (0.94BNT-0.06BT)-x BF for samples sintered at 1125°C.

Figure 4-51 shows the temperature dependence of relative permittivity (ϵ_r) and dielectric loss ($\text{Tan}\delta$) of unpoled samples at 100 Hz, 1 kHz, 10 kHz, 100 kHz, and 1 MHz for (1-x) (0.94BNT-0.06BT)-x BF samples at x=0.025, 0.05, 0.075, and 0.1 sintered at 1125°C for two hours. The relative permittivity slightly decreased with an increase in the frequency from 100Hz to 1MHz, while the value of the dielectric loss was low (under 0.1) for all the sample and frequencies, but it increased with an increase in the frequency from 100Hz to 1MHz. Two anomalies in the relative permittivity and dielectric loss are observed for all of the compositions; the first can be attributed to the formation of PNR, such as BNT-BT. The second can be attributed to the ferroelectric-to-anti-ferroelectric phase transformation; in comparison with pure BNT-BT (Figure 4-41), the substitution of BF into the structure results

in a decrease in the depolarisation temperature (T_d). Compared to BNT-BT, the shape of the temperature dependence of relative permittivity of BNT-BT-BF samples is more diffuse. The value of relative permittivity for all samples with BF substitutions are decreased, due to their higher porosity and space charges. The replacement of the Fe^{3+} at the B site (Ti^{4+}) would lead to the creation of oxygen vacancies, which increase the space charges and therefore decrease the relative permittivity. The thermally activated oxygen vacancies at high temperature and low frequencies could lead to the dispersion of the relative permittivity of these compositions at low frequencies. In general, compared to pure BNT-BT, it seems that oxygen vacancies cause the polar nano regions in these compositions to form at a lower temperature due to the easier transformation from the ferroelectric to the anti-ferroelectric phase.





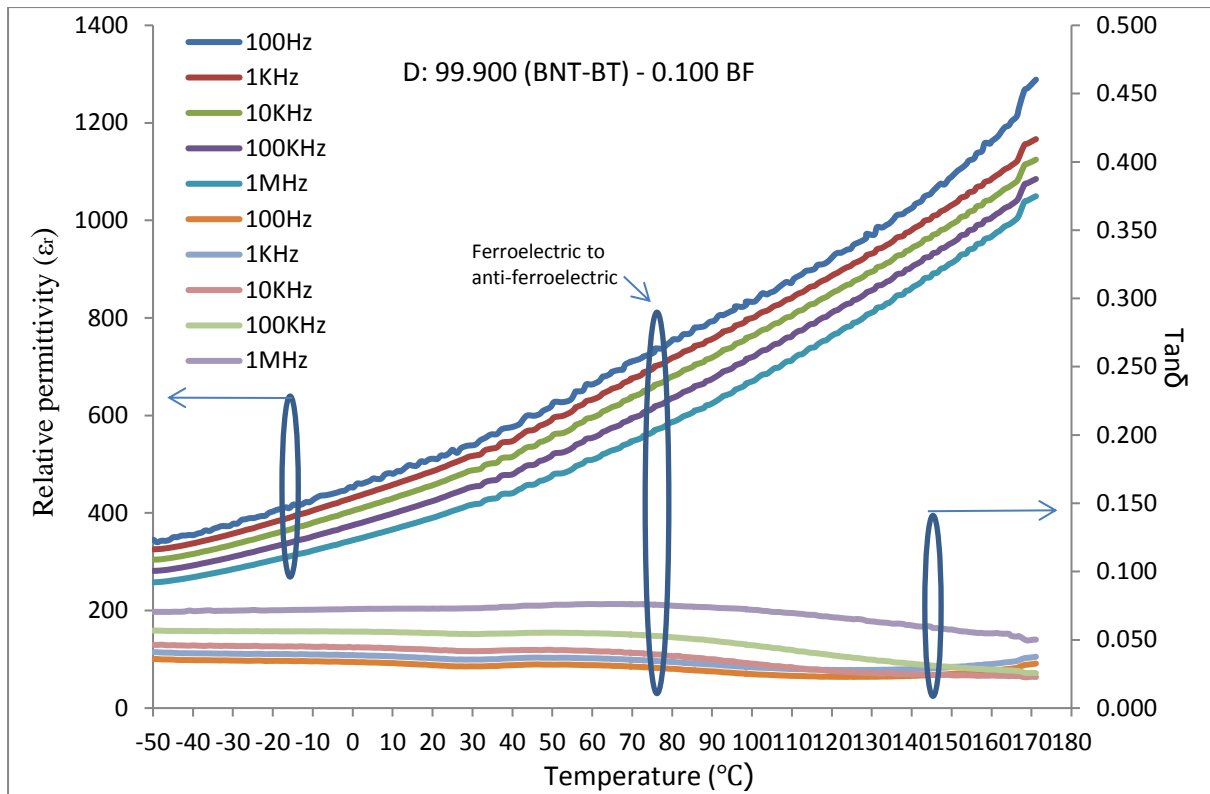


Figure 4-51: The temperature dependence of relative permittivity (ϵ_r) and dielectric loss ($\text{Tan}\delta$) of unpoled samples at 100 Hz, 1 kHz, 10 kHz, 100 kHz, and 1 MHz for $(0.94\text{BNT}-0.06\text{BT})-x\text{BF}$ sintered samples for A) $x=0.025$, B) $x=0.05$, C) $x=0.075$, and D) $x=0.1$ sintered at 1125°C for two hours.

Table 4-4 shows a summary of the properties of $(1-x) (0.94\text{BNT}-0.06\text{BT})-x\text{BF}$ for $x=0, 0.025, 0.05, 0.075$, and 0.1 .

Table 4-4: Summary of the properties of $(1-x) (0.94\text{BNT}-0.06\text{BT})-x\text{BF}$ for $x=0, 0.025, 0.05, 0.075$, and 0.1 .

Composition (x)	0.000	0.025	0.050	0.075	0.100
Relative density%	97 ± 1.2	93.2 ± 0.8	92.84 ± 1	92.7 ± 0.7	92.4 ± 0.9
d_{33} pC/N	165 ± 10	95 ± 8	75 ± 7	70 ± 9	30 ± 5
Relative Permittivity at RT	1230 ± 150	862 ± 100	790 ± 80	596 ± 70	461 ± 90
Grain Size (μm)	3.2 ± 0.5	6.5 ± 0.7	6.7 ± 0.8	7 ± 0.6	7.2 ± 0.9
Ferroelectric to Anti ferroelectric phase transformation temperature ($^\circ\text{C}$)	110-128	100	85	79	74
k_p (%)	47 ± 4	33 ± 3	19 ± 5	16 ± 2	14 ± 3

4.3.2 Deficiency in the BNT-BT system

As explained in 2.1.1.2.3.1, Gao et al. [112] investigated deficiencies in the BNT-BT structure and found that when the composition is $0.94(\text{Bi}_{0.45.5}\text{Na}_{0.47.5}\text{Ti}_{0.94}\text{O}_{2.82})-0.06\text{BT}$, pyroelectric behaviour is increased. In this project, this deficient compound has been prepared to enable a further experiment on the ECE. To do this, firstly two-step calcination

and the same route as pure BNT-BT has been employed to calcine the compound. Figure 4-52 shows the XRD patterns of BNT and BNT with deficiency powders calcined at 850°C. There are no secondary peaks indicative of the pyrochlore phase visible in the XRD patterns, which confirms that this route is appropriate for BNT deficient compositions as well. The XRD patterns shift to a higher angle compared to the pure BNT due to the lower amount of bismuth.

Figure 4-53 shows the XRD patterns of BNT-BT, compared to the BNT-BT deficient sample sintered at 1125°C for two hours. There is a shift to higher angles in the XRD patterns for the BNT-BT deficient sample, again due to lower value of the bismuth, while the obverse is not observed in the secondary phase.

Figure 4-54 shows the SEM images of the BNT-BT deficient sample in comparison with pure BNT-BT. As can be seen in the images, the grain size has decreased in the deficient material, but the deficient sample also looks more dense and more uniform grains.

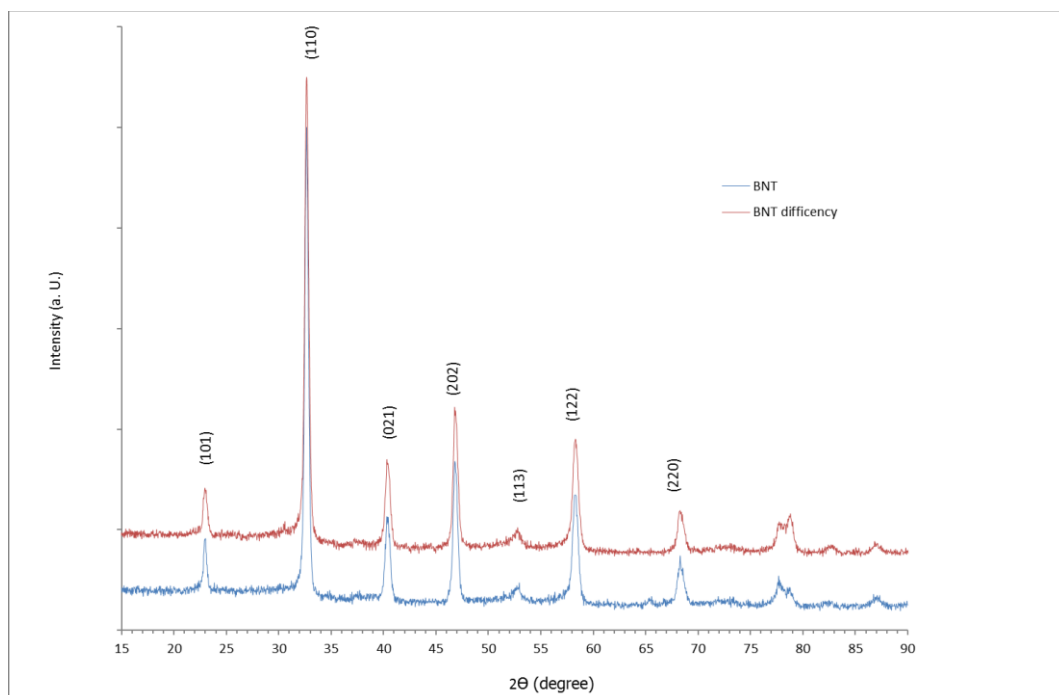


Figure 4-52: The XRD patterns of A) $\text{Bi}_{1.5}\text{Na}_{0.5}\text{TiO}_3$ and B) $\text{Bi}_{0.455}\text{Na}_{0.475}\text{Ti}_{0.94}\text{O}_{2.82}$ samples, calcined at 850°C for five hours.

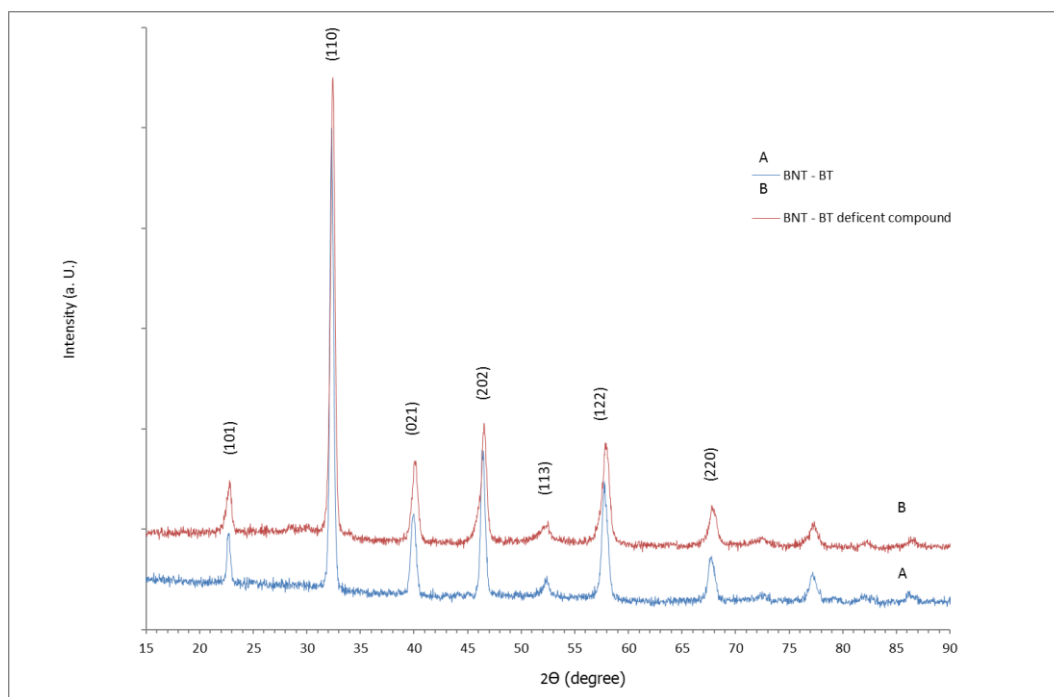


Figure 4-53: The XRD patterns of A) $0.94\text{Bi}_{0.5}\text{Na}_{0.5}\text{TiO}_3\text{-}0.06\text{BaTiO}_3$ and B) $\text{Bi}_{0.455}\text{Na}_{0.475}\text{Ti}_{0.94}\text{O}_{2.82}\text{-}0.06\text{BT}$ deficient samples, sintered at 1125°C for two hours.

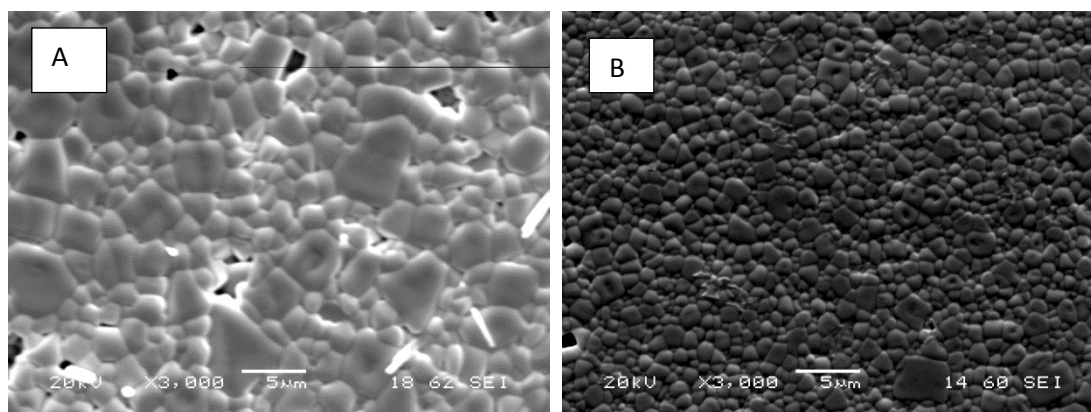


Figure 4-54: SEM micrograph of A) $0.94\text{Bi}_{0.5}\text{Na}_{0.5}\text{TiO}_3\text{-}0.06\text{BaTiO}_3$ and B) $\text{Bi}_{0.455}\text{Na}_{0.475}\text{Ti}_{0.94}\text{O}_{2.82}\text{-}0.06\text{BT}$ samples sintered at 1125°C (see the appendix for a low magnification photo).

Figure 4-55 shows the temperature dependence of relative permittivity (ϵ_r) and dielectric loss ($\text{Tan}\delta$) of unpoled sample at 100 Hz, 1 kHz, 10 kHz, 100 kHz, and 1 MHz for the $0.94(\text{Bi}_{0.455}\text{Na}_{0.475}\text{Ti}_{0.94}\text{O}_{2.82})\text{-}0.06\text{BT}$ samples sintered at 1125°C for two hours. The relative permittivity slightly decreased with increases in the frequency from 100Hz to 1MHz, while the value of the dielectric loss is low (under 0.1) for all the frequencies, and increased with an increase in the frequency from 100Hz to 1MHz. The anomaly in the figure can be attributed

to the ferroelectric-to-anti-ferroelectric phase change, and compared to pure BNT-BT (Figure 4-41), the depolarisation temperature (T_d) shifts to a lower temperature. In addition, the value of the relative permittivity is lower than BNT-BT, due to the lower relative density (94%) and more space charges.

Table 4-5 provides a summary of the properties of BNT-BT, compared to a deficiency in BNT-BT. The relative density of $0.94(\text{Bi}_{0.45.5}\text{Na}_{0.47.5}\text{Ti}_{0.94}\text{O}_{2.82})-0.06\text{BT}$ sample decreased, which caused the relative permittivity at RT to decrease as well. The piezoelectric coefficient (d_{33}) decreased from 165 to 70 pC/N, which was due to the lower grain size of the BNT-BT deficient samples (1.7 μm).

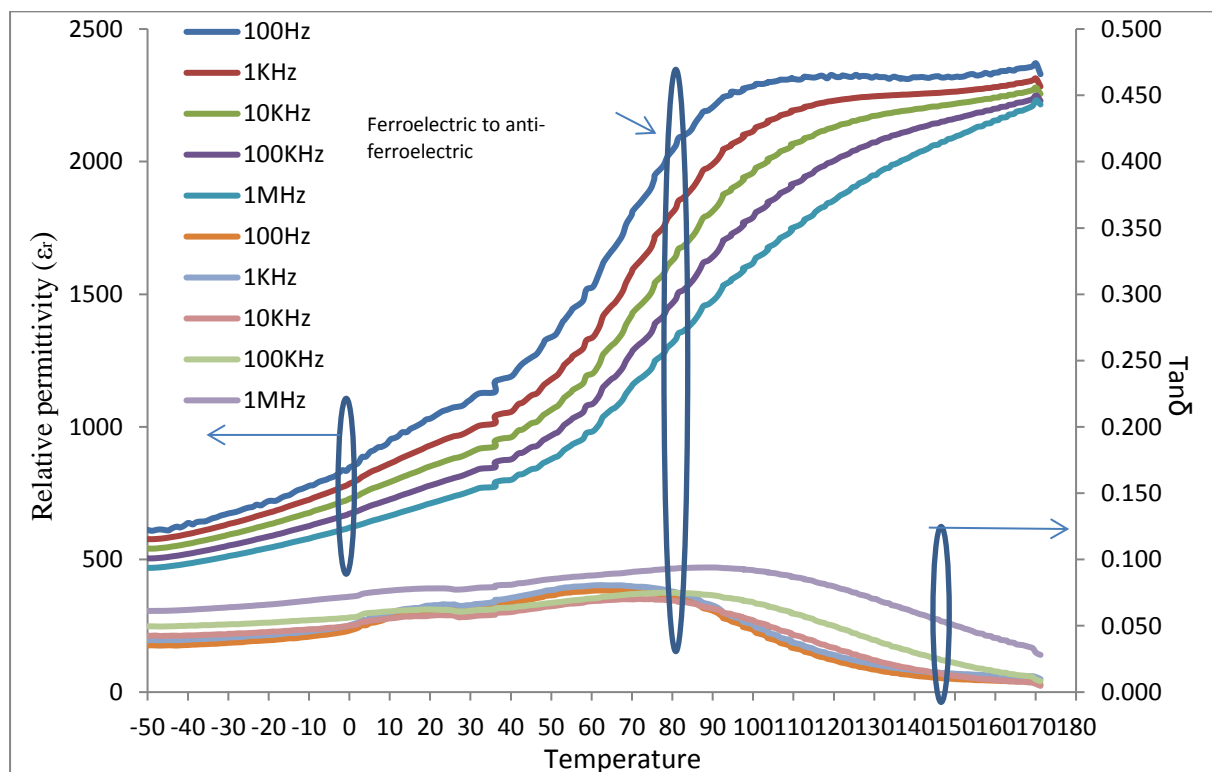


Figure 4-55: The temperature dependence of relative permittivity (ϵ_r) and dielectric loss ($\text{Tan}\delta$) of unpoled sample at 100 Hz, 1 kHz, 10 kHz, 100 kHz, and 1 MHz for $0.94(\text{Bi}_{0.45.5}\text{Na}_{0.47.5}\text{Ti}_{0.94}\text{O}_{2.82})-0.06\text{BT}$ sample sintered at 1125°C for two hours.

Table 4-5: Summary of the properties of $0.94\text{B}_{0.5}\text{N}_{0.5}\text{TiO}_3-0.06\text{BaTiO}_3$, compared to $0.94(\text{Bi}_{0.45.5}\text{Na}_{0.47.5}\text{Ti}_{0.94}\text{O}_{2.82})-0.06\text{BT}$.

Composition	Relative density%	d_{33} pC/N	Relative Permittivity at RT	Grain Size (μm)	k_p (%)	Ferroelectric to anti ferroelectric phase transformation temperature ($^{\circ}\text{C}$)
$0.94\text{B}_{0.5}\text{N}_{0.5}\text{TiO}_3-0.06\text{BaTiO}_3$	97 ± 1.2	165 ± 10	1230 ± 150	3.2 ± 0.5	47 ± 4	110
$0.94(\text{Bi}_{0.45.5}\text{Na}_{0.47.5}\text{Ti}_{0.94}\text{O}_{2.82})-0.06\text{BT}$	94.22 ± 1	70 ± 8	756 ± 100	1.7 ± 0.2	37 ± 3	82

4.4 Summary

The fabrication, characterisation, and optimisation of BCZT and BNT-BT powders and ceramics have been reported and discussed in this chapter. In addition, the effect of two additives to these materials was investigated; BNKT on BCZT, BF on BNKT, and a deficiency of BNT-BT. BCZT is one of the newest compounds of all the ferroelectric materials that have been investigated, and it shows good ferroelectric properties, and can be considered one of the candidates for replacement of PZT. This compound was calcined at 1250°C by mixing the raw materials using the solid-state method similar to most previous studies, and then sintered at temperatures between 1400 to 1500°C. Based on the literature review BCZT exhibits the best properties between 1400 and 1500°C. In this work XRD and SEM confirmed phase purity and densification of the samples, respectively. The best properties were observed for samples sintered at 1450°C with values of relative density = 96.1%, $d_{33} = 410$ pC/N, $k_p = 46\%$ and relative permittivity at RT = 3200 of, in agreement with the literature.

The effect of the addition of small amounts of BNKT on BCZT was investigated. No previous studies have been conducted regarding the addition of BNKT to BCZT. BCZT and BNKT were separately calcined at 1100 and 700°C, respectively, mixed together by the solid-state method, and then sintered at temperatures in the range 1250 to 1500°C. The properties were measured for these samples, and the results show that the addition of BNKT decreased the d_{33} of BCZT, probably due to the diversion of the MPB. The relative permittivity increased at RT and k_p decreased for 3 and 5wt% of BNKT, similarly to BCZT for 1wt% BNKT. Some of these compositions show relaxor behaviour (for example, BCZT-1%BNKT sintered at 1250°C), while others show normal ferroelectric behaviour (for example, BCZT-1%BNKT sintered at 1450°C)

BNT-BT was the next compound tested in this project, and first calcined at 850°C for two hours from raw materials, based on the literature review. Then, due to problems in the phase identification process, BNT and BT were separately calcined. Calcination was done at different temperatures and times to eliminate the formation of the pyrochlore phase in the formation of BNT. Phase pure BNT was formed after calcination at 850°C for five hours. Then, BNT was mixed with BT using the solid-state method and calcined at different temperatures. The results show that BNT-BT can form at 1050°C after five hours of calcination. The prepared powders were sintered at temperatures between 1100 to 1200°C and

the best properties were obtained for samples sintered at 1125°C , with relative density = 97%, $d_{33} = 165$ pC/N, , $k_p = 47$ % and of the relative permittivity at RT = 1230. The values for k_p and relative permittivity are similar to those in the literature, but in this project a higher d_{33} value has been obtained, possible due to the two-step calcination. Substitution of BF into BNT-BT resulted in a decrease in properties, but the temperature of the anti-ferroelectric-to-ferroelectric transformation phase decreased, which might be useful for ECE.

Deficiency is one of the problems to the BNT-BT process and it can decrease some of the properties of this compound, but it can be useful for other properties such as pyroelectricity. One compound with the deficiency and a high pyroelectric coefficient was selected based on the literature review, and fabricated using the same route as for pure BNT-BT, and the properties measured. The results show values of relative density = 94%, $d_{33} = 70$ pC/N, $k_p = 37$ %, relative permittivity at RT = 756, and a reduction in the temperature of ferroelectric-to-anti-ferroelectric transformation phase from 110 to 82°C.

All of these materials were investigated further to ascertain their suitability for ECE applications. These results are present and discussed in the next chapter.

Chapter

5

Electrocaloric measurements

5.1 Measuring the electrocaloric effect (ECE)

There are two main methods of measuring the ECE; the direct and indirect methods. In this project, a direct reading method and calculation from Maxwell relations as the indirect method have been chosen. As explained previously, there is no standard device to measure the ECE, so a new route was designed and manufactured for the direct method.

5.1.1 The indirect method used to measure the ECE

As explained in sections 2.3.2 and 3.12, using the polarisation-electric field at a range of temperatures and the Maxwell relation (2-9), the ECE can be deduced. To do this, it is necessary to measure the density and heat capacity of the materials to calculate the ECE.

The density of the materials was measured by the Archimedes method, and the heat capacity of the materials measured based on the ASTM E1269-11 and described in Section 3.12 The heat capacity of $\text{Ba}_{0.85}\text{Ca}_{0.15}\text{Zr}_{0.1}\text{Ti}_{0.9}\text{O}_3$ and $0.94(\text{Bi}_{0.5}\text{Na}_{0.5}\text{TiO}_3-0.06(\text{BaTiO}_3))$ (prepared by solid state method and sintered at 1450 and 1125°C respectively) are plotted in Figure 5-1. It is worth noting that the heat capacity of the materials under an applied electric field is different to the normal state and with a rise in the electric field due to the transformation of the first order of the phase to the second order, the dependence of the heat capacity decreases in temperature [181].

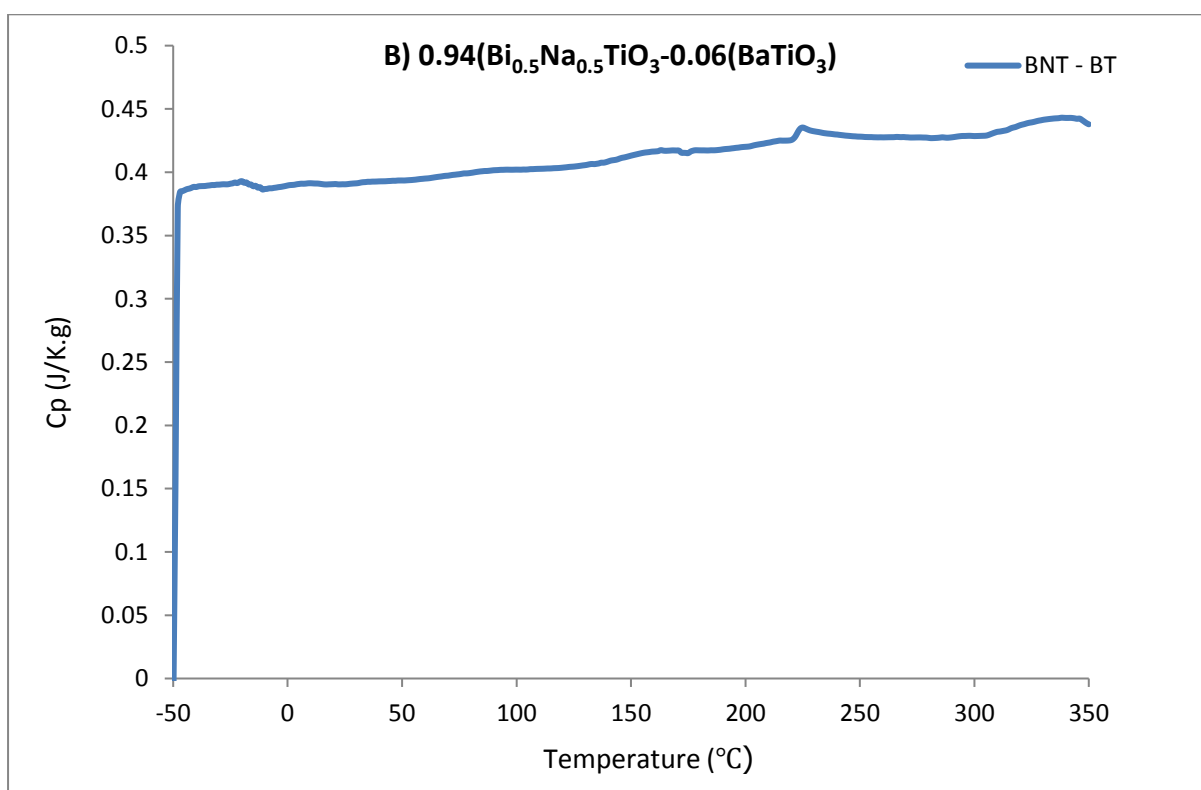
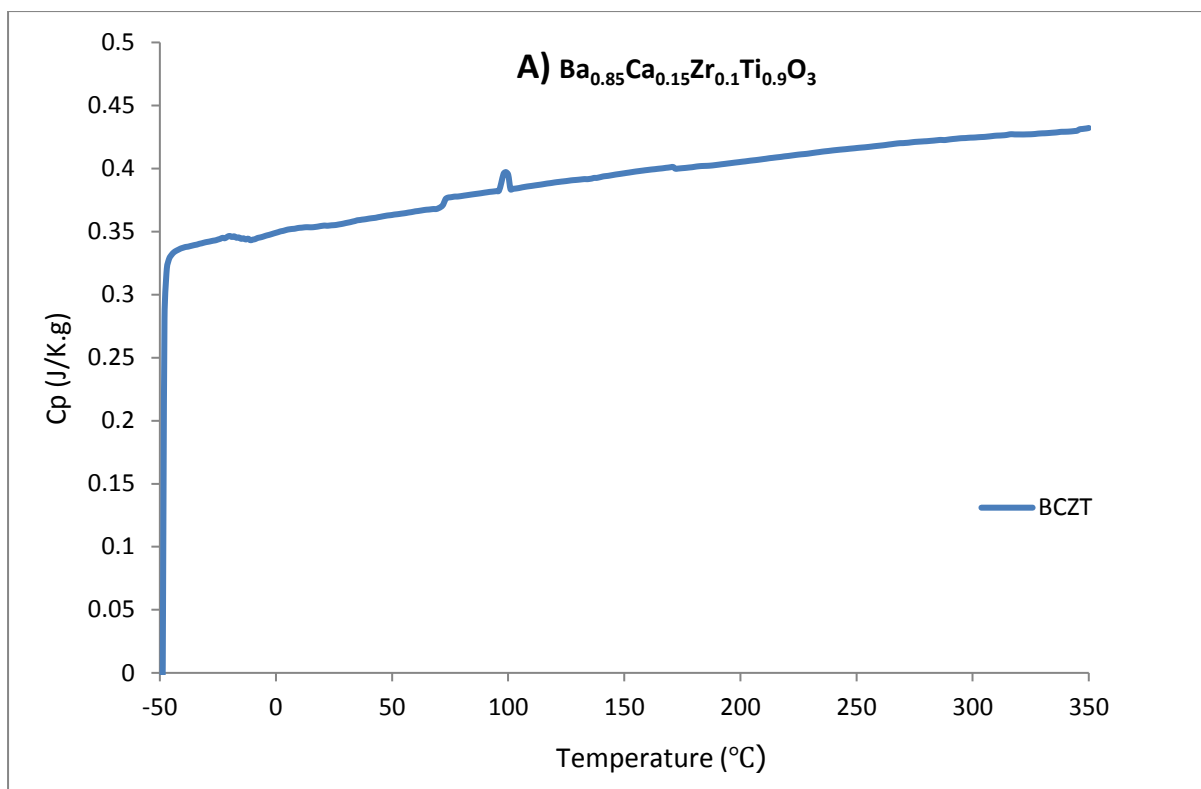


Figure 5-1: The heat capacity of A) $\text{Ba}_{0.85}\text{Ca}_{0.15}\text{Zr}_{0.1}\text{Ti}_{0.9}\text{O}_3$ and $0.94(\text{Bi}_{0.5}\text{Na}_{0.5}\text{TiO}_3-0.06(\text{BaTiO}_3))$ prepared by solid state method and sintered at 1450 and 1125°C respectively.

The heat capacity of BCZT starts from around 0.32 J/g. K at -50°C and increases to 0.42 at 350°C. To calculate a more precise ECE, the heat capacity at any given temperature was extracted from the measured dependence, and not treated as a constant. The same method was chosen for BNT-BT- and BNT-BT-based materials.

5.1.1.1 The indirect measurement of ECE of BCZT-based materials

Due to the long process of calculating the ECE by indirect methods, the principle is explained here for only BCZT samples sintered at 1400°C. The same method has been applied for other samples, including BCZT- and BCZT-based samples. It is worth noting that all of the calculations were done by Excel software.

In the first step, the polarisation-hysteresis loops were measured as explained in section 3.12 at temperatures between -30 to 150°C in 10°C increments, for each composition. Figure 5-2 shows the polarisation-hysteresis loops for pure BCZT sintered at 1400°C. The same process was done for the rest of the samples. For some of the samples, due to the breakdown during the measurement, the maximum applied electric field was decreased to 30 kV/cm, but a higher value of 50 kV/cm was employed for other samples.

Figure 5-2 shows well defined ferroelectric response at low temperatures, which decrease with increasing temperature for BCZT sintered at 1400°C. A small amount of hysteresis observed at the highest temperatures, even though these are well above the Curie temperature.

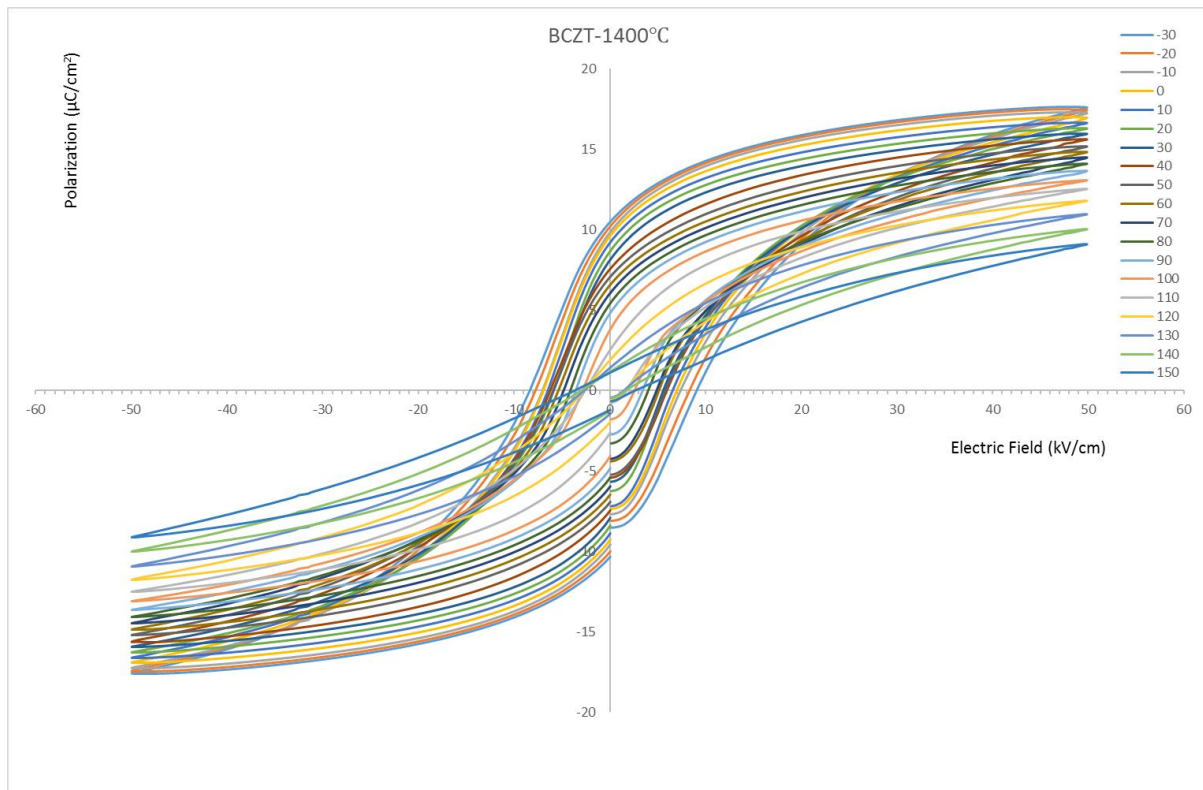


Figure 5-2: Polarisation-hysteresis loops of BCZT sintered at 1400°C, measured at temperatures from -30 to 150°C.

After that, the value of polarisation was extracted in the positive quadrant between P_r and P_{max} for different electric field values and for each measurement temperature.

Figure 5-3 shows these extracted polarisation data from the polarisation-electric field loops presented in Figure 5-2. The next step is the calculation of the pyroelectric coefficient, which is needed for the calculation of the ECE. The pyroelectric coefficient (p_i) dP/dT is the change of polarisation at a range of temperatures, and can be obtained by calculating the slope of the polarisation vs temperature plots (Figure 5-3) for each value of applied electric field and at a range of temperatures, and these data are shown in Figure 5-4 for the BCZT sample sintered at 1400°C. Based on this information, the ECE can be calculated by the Maxwell relation. The obtained results can be seen in Figure 5-5 (the ECE of BCZT sintered at 1400 °C between -30 to 140°C).

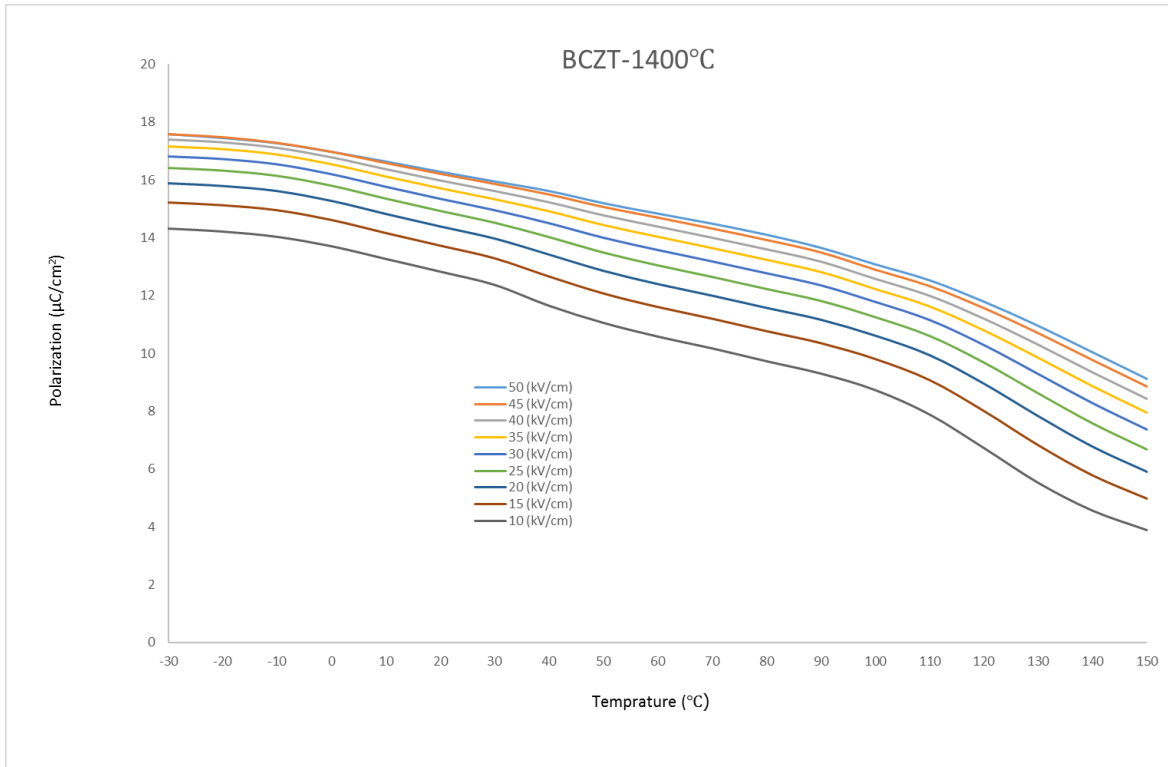


Figure 5-3: The extracted polarisation versus temperature data from Figure 5-2 for a range of electric fields for BCZT sintered at 1400°C.

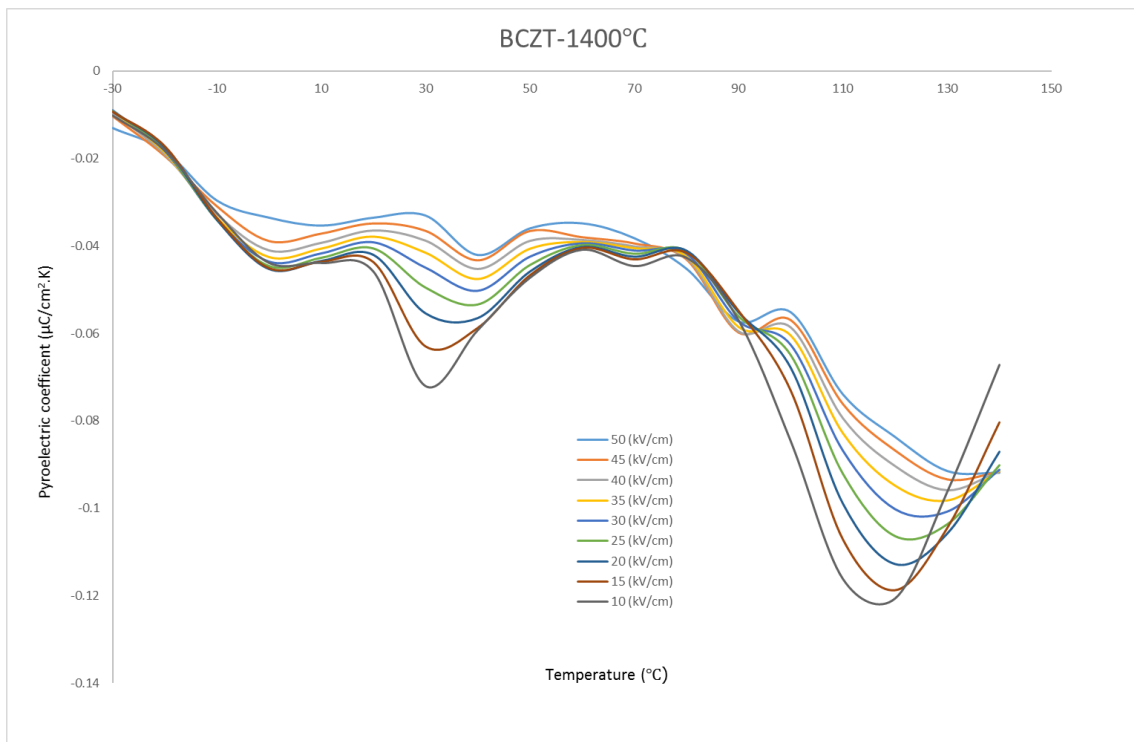


Figure 5-4: The pyroelectric coefficient as a function of temperature for BCZT sintered at 1400°C, and for different values of applied electric field.

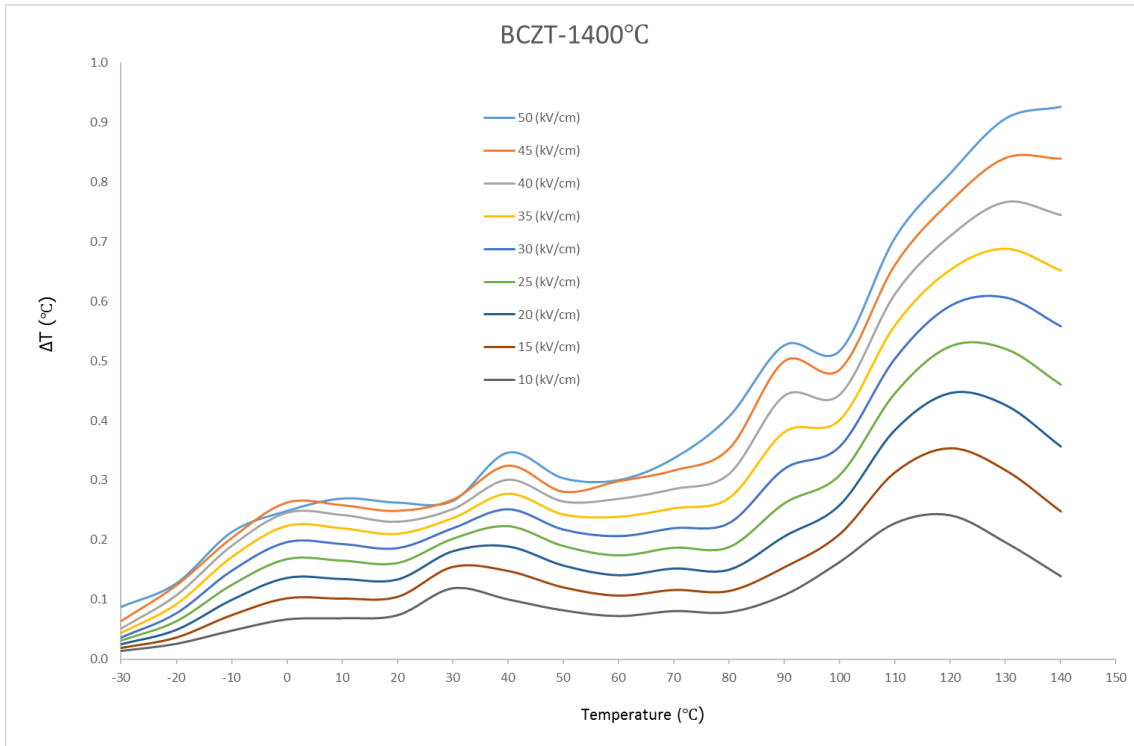


Figure 5-5: The ECE of BCZT sintered at 1400°C as a function of measurement temperature and for various applied electric field values.

The figure of the merit of the ECE, defined as the value of the ECE per unit of electric field applied, is the best way to compare the direct and indirect methods, and also the different compositions. For this reason, the figure of merit was calculated for all the samples, and to compare them to each other. Figure 5-6 shows the ECE figures of merit of pure BCZT sintered at 1400°C from -30 to 140°C.

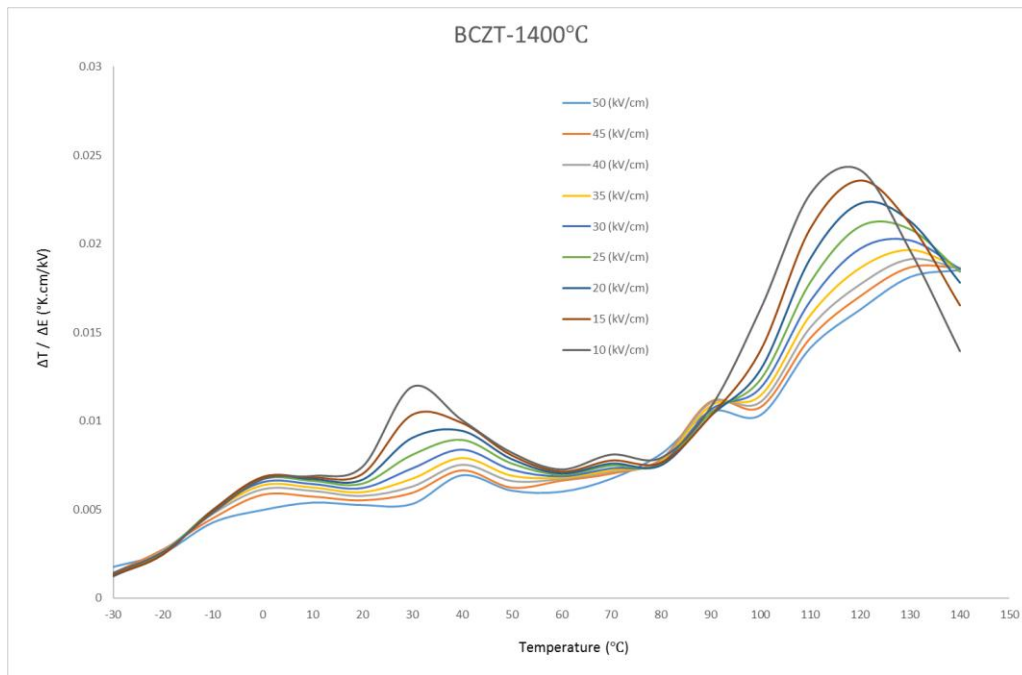


Figure 5-6: The ECE figure of merit as a function of temperature of pure BCZT sintered at 1400°C, and for a range of applied electric field values.

5.1.1.2 Using the indirect method to measure the ECE of pure BCZT

Figure 5-7 shows the ECE between -30 and 140°C of the pure BCZT sintered at temperature of 1450°C, measured by the indirect method. It can be seen that there are three anomalies for all of them; the first is around -10 to 10°C, which is related to the rhombohedral-orthorhombic phase transition and mirrors the transformation observed in the relative permittivity-temperature data (Figure 4-11) transformation. The second anomaly is to the orthorhombic-tetragonal phase transformation around 20 to 40°C; and the third one is related to the tetragonal-to-cubic phase transformation, around 100-130°C. There is another peak at around 90°C, but is only for the higher electric field values. Latent heat is normally released at the phase transformation, and so in the three-phase transformations of the BCZT structure, the ECE is higher compared to the temperatures away from these phase transformations. The highest value of ECE can be seen at the tetragonal-to-cubic phase transition due to the higher latent heat in this transformation.

The ECE for BCZT sintered at 1400°C is $\Delta T = 0.926^\circ\text{C}$ at 50 kV/cm and 140°C. The tetragonal-cubic transformation in the BCZT is around 104°C and the highest ECE is at around 140°C. The electric field can cause a change in the temperature of the phase transformation and shift it to a higher temperature, due to a rise in the polarisation caused by a rise in the electric field, and this shift goes to a higher temperature through a rise in the

temperature. The highest ECE is around 120°C for 10 kV/cm, and around 140 °C for 50°C kV/cm.

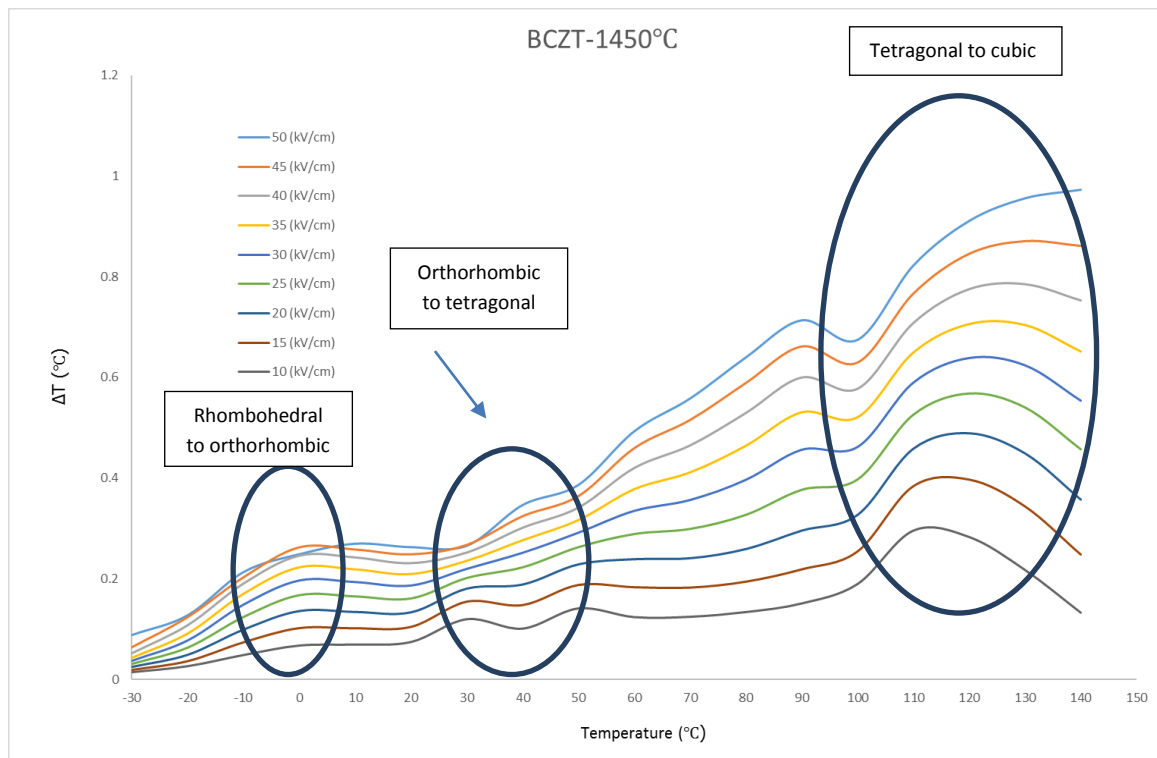


Figure 5-7: The ECE of BCZT sintered at 1450°C as a function of measurement temperature and for various applied electric field values. (Pure BCZT sintered at 1400, 1425, 1475, and 1500°C in appendix II)

Figure 5-8 shows the temperature dependence of the ECE figure of merit of pure BCZT sintered at 1450°C, for a range of applied electric field values. In general, three anomalies can be seen in each BCZT sample, which are similar to the ECE of these samples, and relate to phase transitions in the measurement temperature range. The highest figure of merit can be seen near the final phase transition from tetragonal to cubic, which shows the highest ECE. The highest figure of merit shifts to a higher temperature through a rise in the electric field due to the effect of the higher electric field on the phase transition to a higher temperature.

for BCZT sintered at 1450°C, the maximum figure of merit for electric fields of 10, 15, and 20 kV/cm occurs around 120°C; for electric fields of 25, 30 and 35 kV/cm, it occurs around 130°C; and for electric fields of 40, 45, and 50 kV/cm, it occurs around 140°C. These data show that an increase in the applied electric fields can increase the phase transformation temperature.

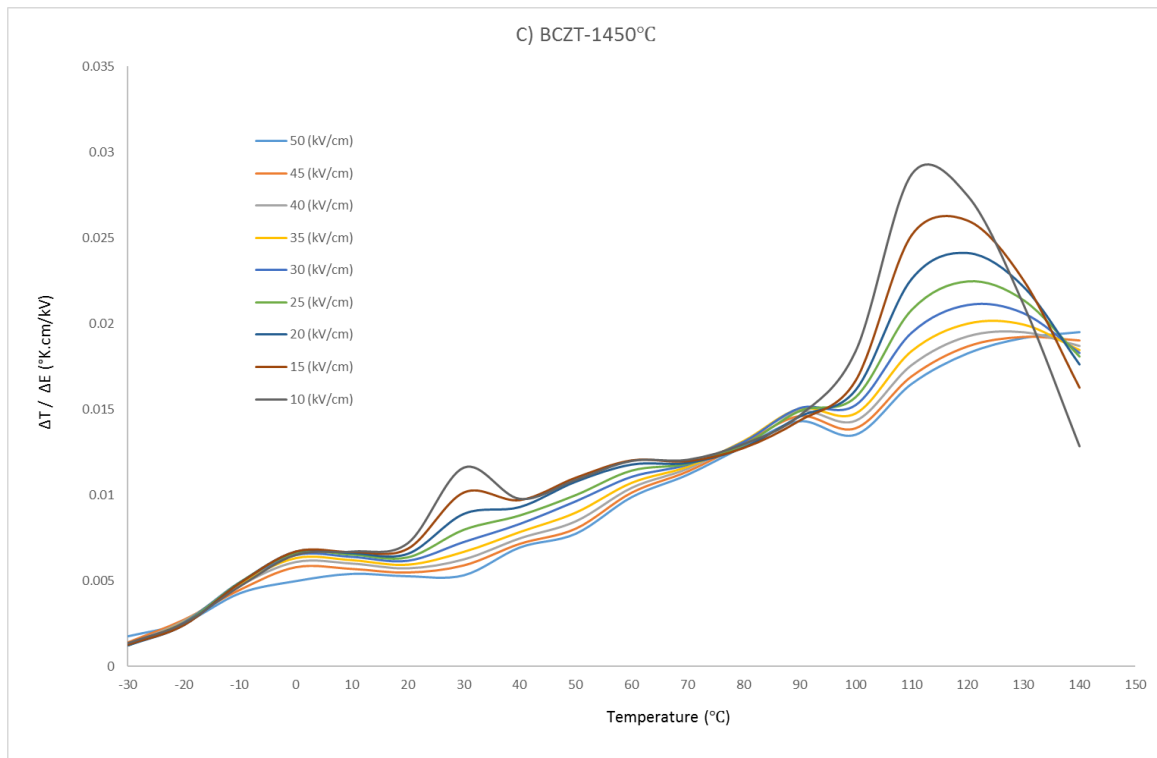


Figure 5-8: The ECE figure of merit as a function of temperature of pure BCZT sintered at 1450°C, and for a range of applied electric field values. (Pure BCZT sintered at 1400, 1425, 1475, and 1500°C in appendix II)

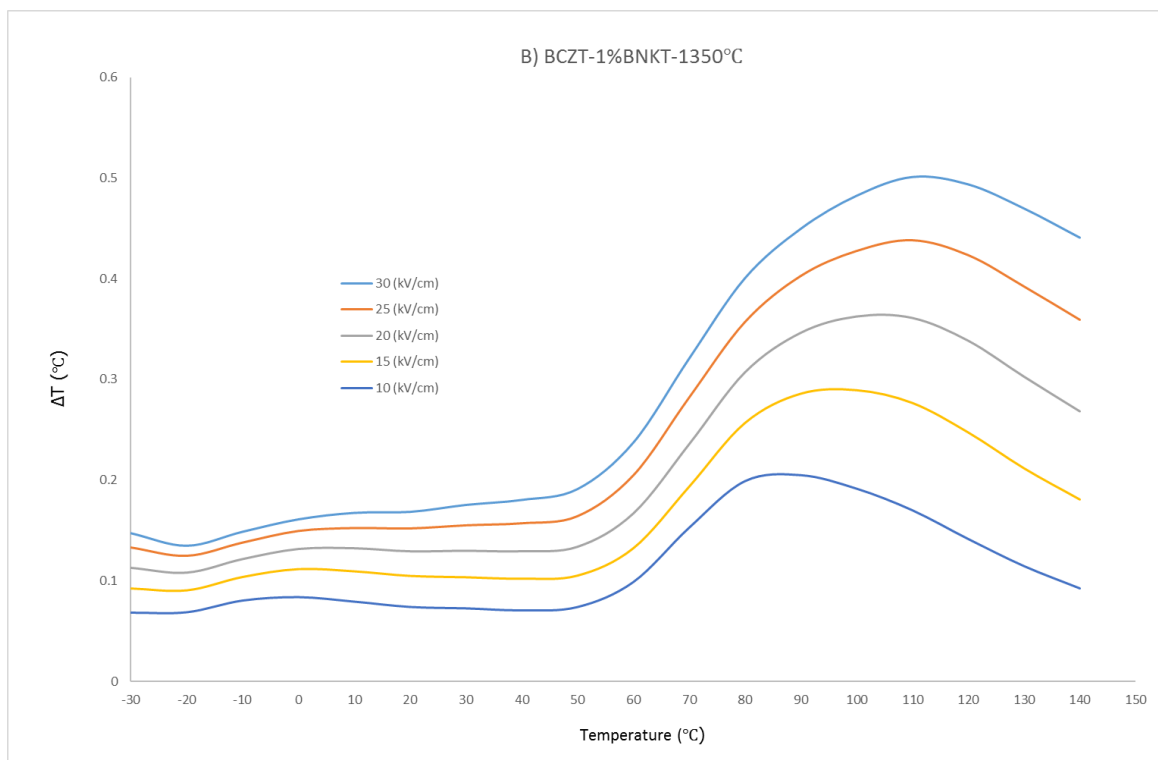
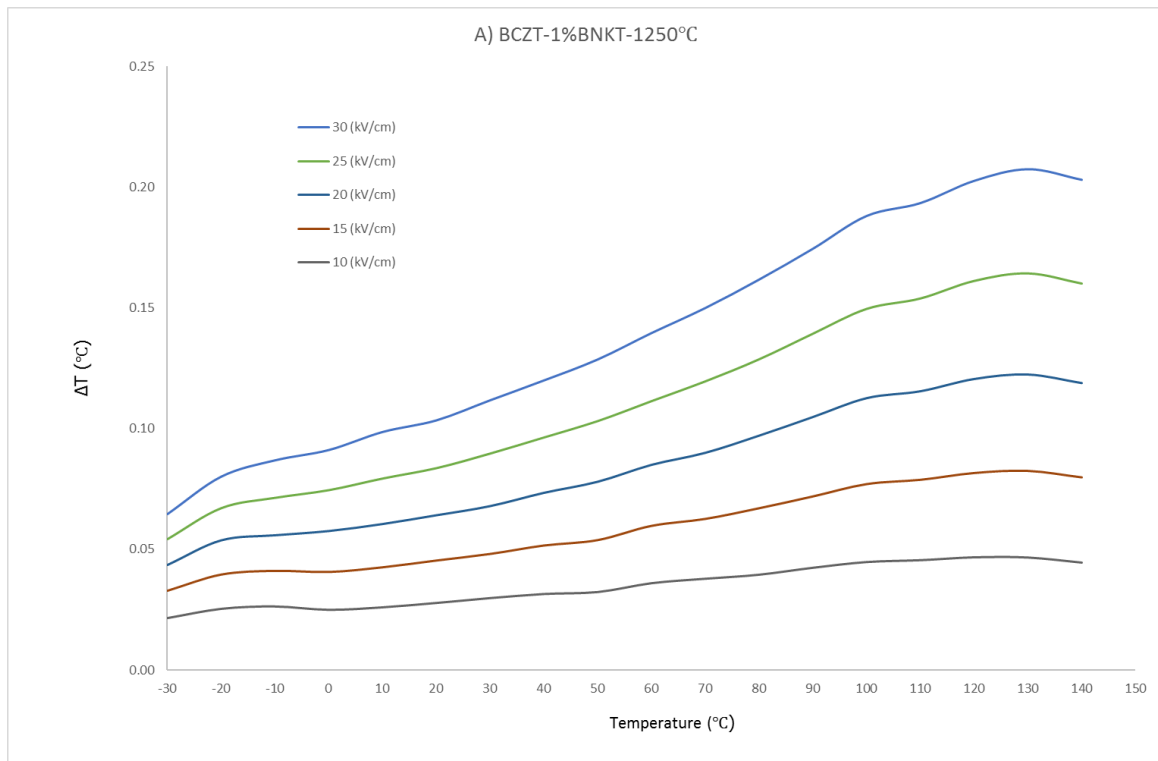
5.1.1.3 Using the indirect method to measure the ECE of BCZT-1% BNKT

Figure 5-9 shows the ECE of BCZT-1% BNKT sintered at 1250, 1350, 1450, and 1500 °C. The ECE increases with increasing measurement temperature for BCZT-1% BNKT sintered at 1250°C, and the highest ECE of around $\Delta T=0.2^{\circ}\text{C}$ was observed at 130°C and 30 kV/cm. Based on the relative permittivity-temperature of this composition, the highest relative permittivity is at 98.8°C. Above this temperature, the ECE is increased by a rise in the electric field and transferred into a higher temperature (130°C); after that, it decreases at 140°C. The relative density is around 95% at this compound, which is lower than the maximum relative density for this compound (96.5) and affect, the ECE.

The highest ECE is reached is $\Delta T=0.5^{\circ}\text{C}$ measured at 110°C and 30 kV/cm for BCZT-1% BNKT sintered at 1350°C. The Curie temperature for this compound is around 82°C, so the electric field transfers it to a higher temperature. This compound has a higher relative density compared to the compound sintered at 1250°C.

BCZT-1% BNKT sintered at 1450°C shows the highest ECE ($\Delta T=0.47^\circ\text{C}$) at 100°C and at 30 kV/cm, and above the Curie temperature (around 80°C). This shows that through a rise in the electric field, there is a shift in the phase transformation, from tetragonal to cubic. When the electric field increases, it causes the phase transformation to transfer to a higher temperature due to the effect of the electric field on the structure. In comparison with relative permittivity-temperature of this composition (Figure 4-26), the electric field causes the ferroelectric phase to be stable at a higher temperature than the Curie temperature through a change in the crystal structure and make it no centre symmetric. The relative density for this compound is around 93%, which is lower than samples sintered at 1350°C, so the highest ECE is decreased for this compound. However, compared to samples sintered at 1250°C, samples sintered at 1350°C have a higher ECE, which means that other factors such as polarisation switching may be significant. The higher sintering temperature for this sample causes the grain growth in the composition (Figure 4-22), which it makes switching the polarisation easier, which is one of the key points for a high ECE.

The behaviour of BCZT-1% BNKT samples sintered at 1450 and 1500°C are similar, but due to lower relative density (92.7%), the material sintered at the higher temperature exhibits $\Delta T=0.43^\circ\text{C}$ for 30 kV/cm at 110°C.



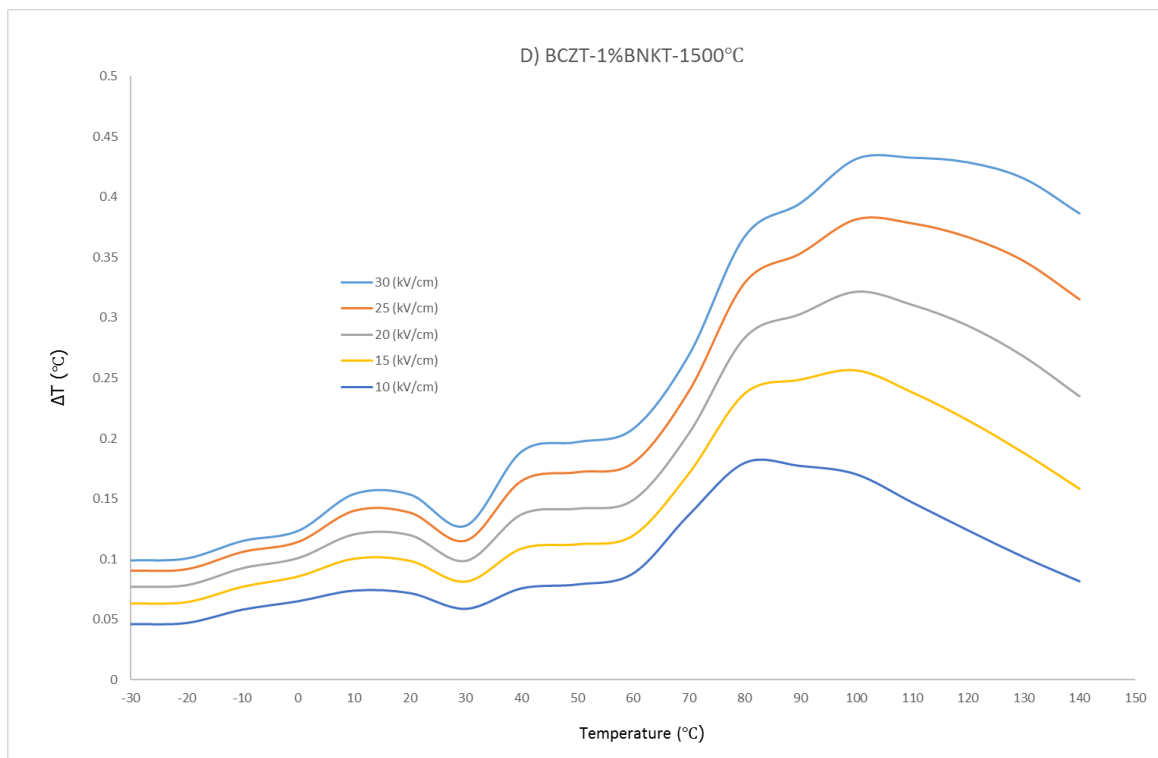
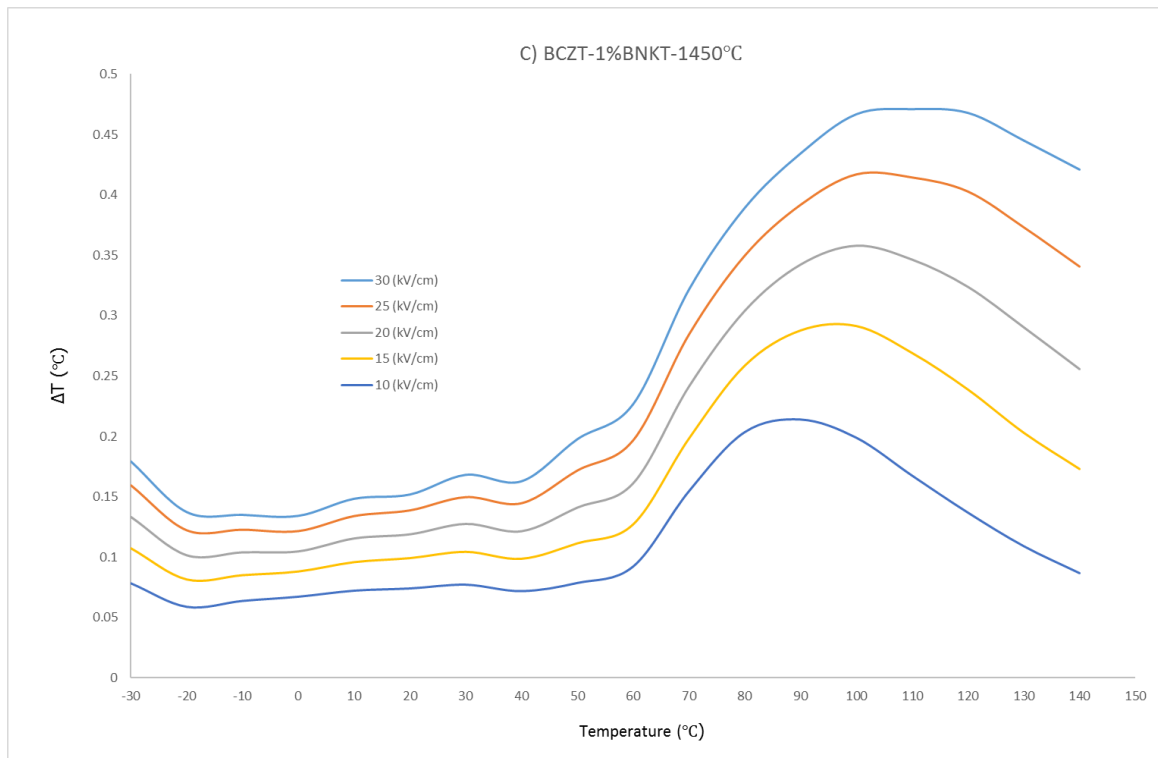
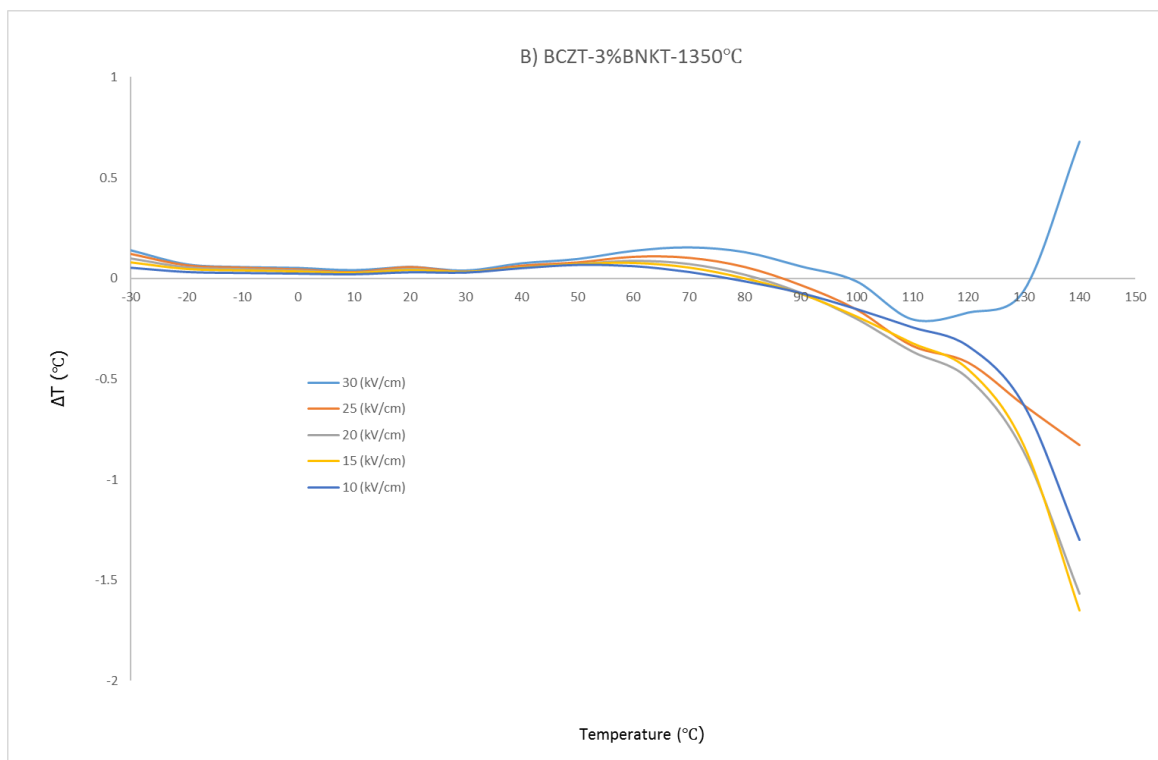
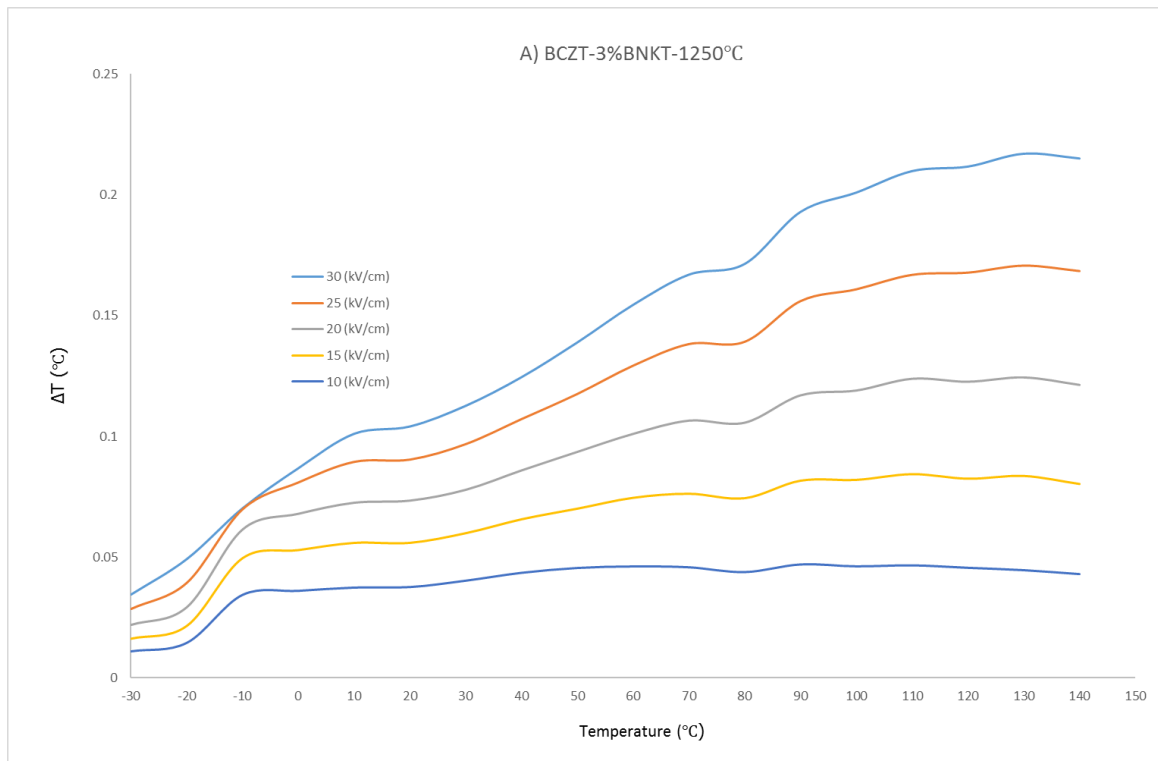


Figure 5-9: The ECE as a function of temperature and applied electric field for BCZT-1% BNKT ceramics sintered at A) 1250, B) 1350, C) 1450, and D) 1500°C. (The ECE figure of merit as a function of temperature and applied electric field for BCZT-1% BNKT ceramics sintered at A) 1250, B) 1350, C) 1450, and D) 1500°C in Appendix II)

5.1.1.4 Using the indirect method to measure the ECE of BCZT-3% BNKT

Figure 5-10 shows the ECE of BCZT-3% BNKT sintered at 1250, 1350, 1450, and 1500 °C. The BCZT-3% BNKT sintered at 1250°C shows the same behaviour as BCZT-1% BNKT sintered at 1250°C. The ECE has been increased for this compound and it reached $\Delta T=0.21^{\circ}\text{C}$ for 30 kV/cm at 130°C which is higher than the Curie temperature of around 80°C. The ECE has as wide a peak after the Curie temperature as a relaxor material. As explained previously, BCZT and BNKT did not diffuse into one structure; the ECE starts to decrease like a relaxor behaviour and not sharply, like a pure BCZT. The low magnitude of the ECE can be attributed to a lower grain size (2.2 μm) and more grain boundaries of this compound, in comparison with the pure BCZT, which makes the rotation of the domains more difficult, especially when the sintering temperature is low. BCZT-3% BNKT sintered at 1350°C shows $\Delta T=0.15^{\circ}\text{C}$ for 30 kV/cm at 70°C and after that, it reached to around $\Delta T=-1.65^{\circ}\text{C}$ for 15 kV/cm at 140°C. A more precise view of these peaks shows that the ECE does not increase with a rise in the electric field. The polarisation-electric loops were investigated at these temperatures and are presented in Figure 5-11 where it can be seen that the shapes of these loops are like a cross between banana and oval shapes. This usually happens when there is phase lag between the electric field and the polarisation due to the current leakage, the compound does not show the real response, which cannot be used for calculating the ECE. The phase lag can be due to the difficulty of domain-switching, which in this composition, happens between BNKT and BCZT grain due to different switching behaviour of each of them.

BCZT-3%BNKT sintered at 1450°C shows the highest ECE $\Delta T=0.31^{\circ}\text{C}$ at 90°C for 30 kV/cm and after that, it decreases until 110°C. The banana shape starts for the polarisation-electric field at around 110°C (not shown here), similarly to BCZT-3%BNKT sintered at 1350°C, so the ECE starts to increase sharply. The highest ECE of BCZT-3% BNKT sintered at 1500°C is $\Delta T=0.37^{\circ}\text{C}$ at 110°C for 30 kV/cm, and is higher than the Curie temperature, at around 76°C.



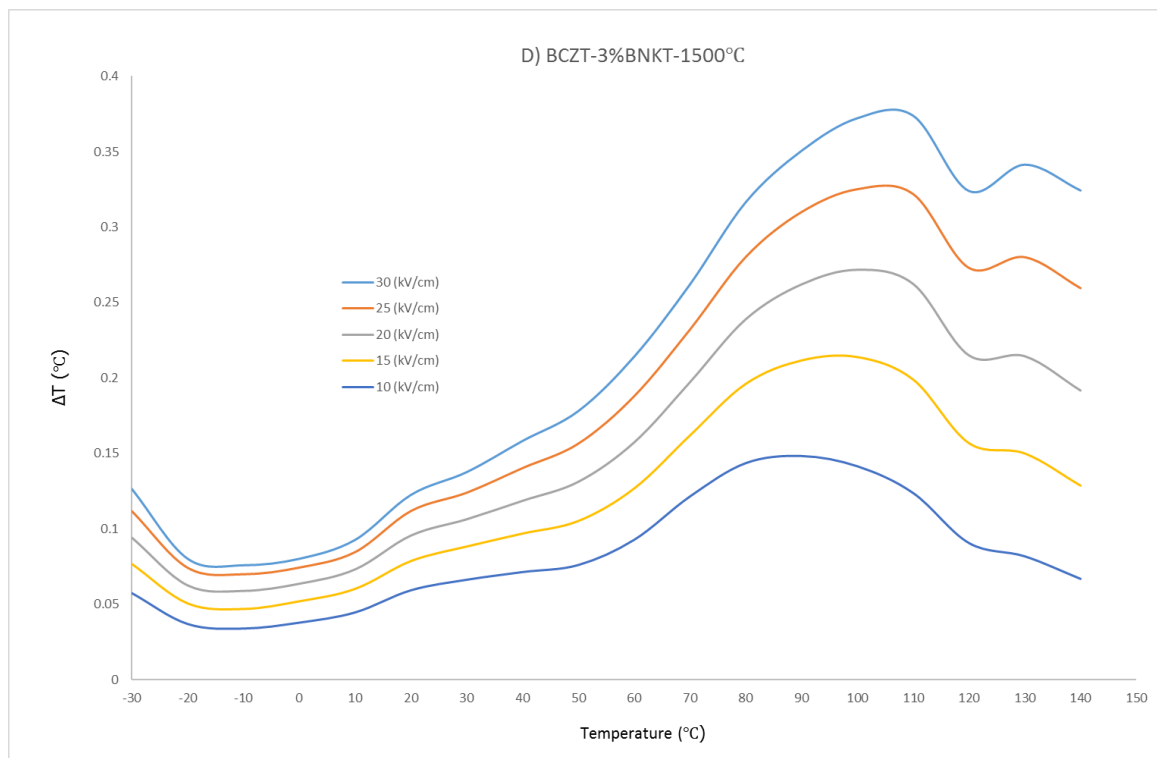
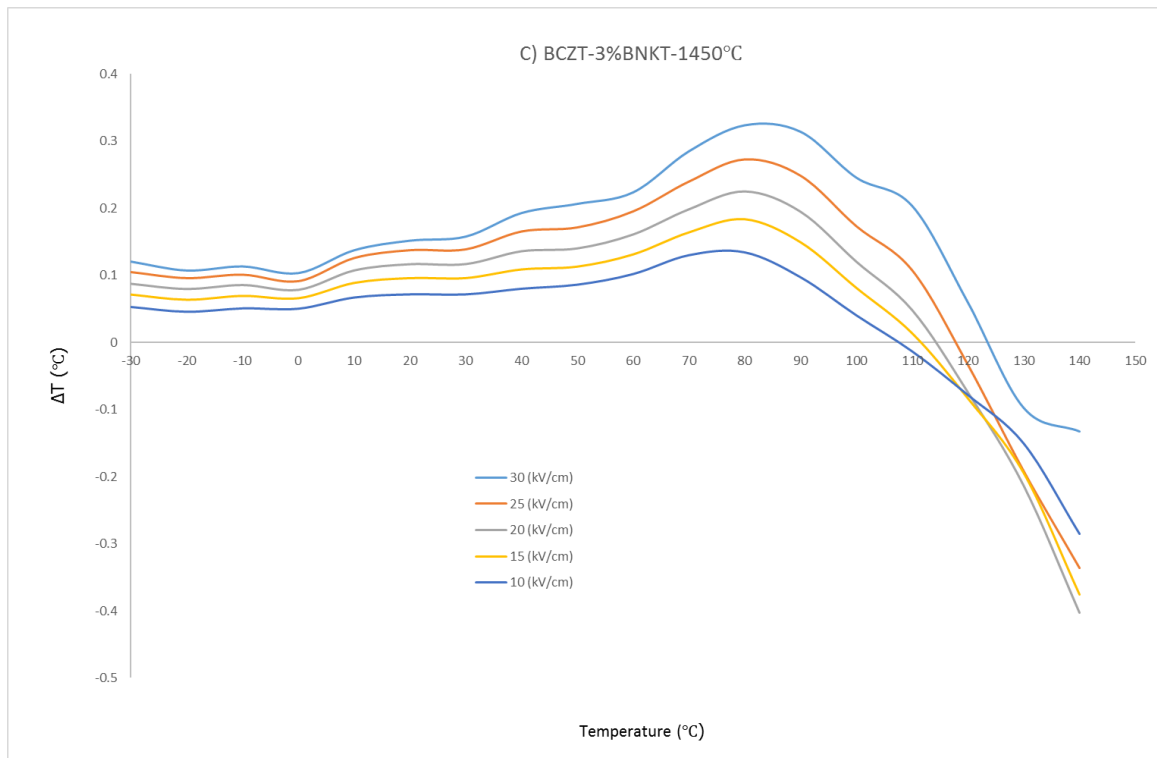


Figure 5-10: The ECE as a function of temperature and applied electric field for BCZT-3% BNKT ceramics sintered at A) 1250, B) 1350, C) 1450, and D) 1500°C. (The ECE figure of merit as a function of temperature and applied electric field for BCZT-3% BNKT ceramics sintered at A) 1250, B) 1350, C) 1450, and D) 1500°C in Appendix II)

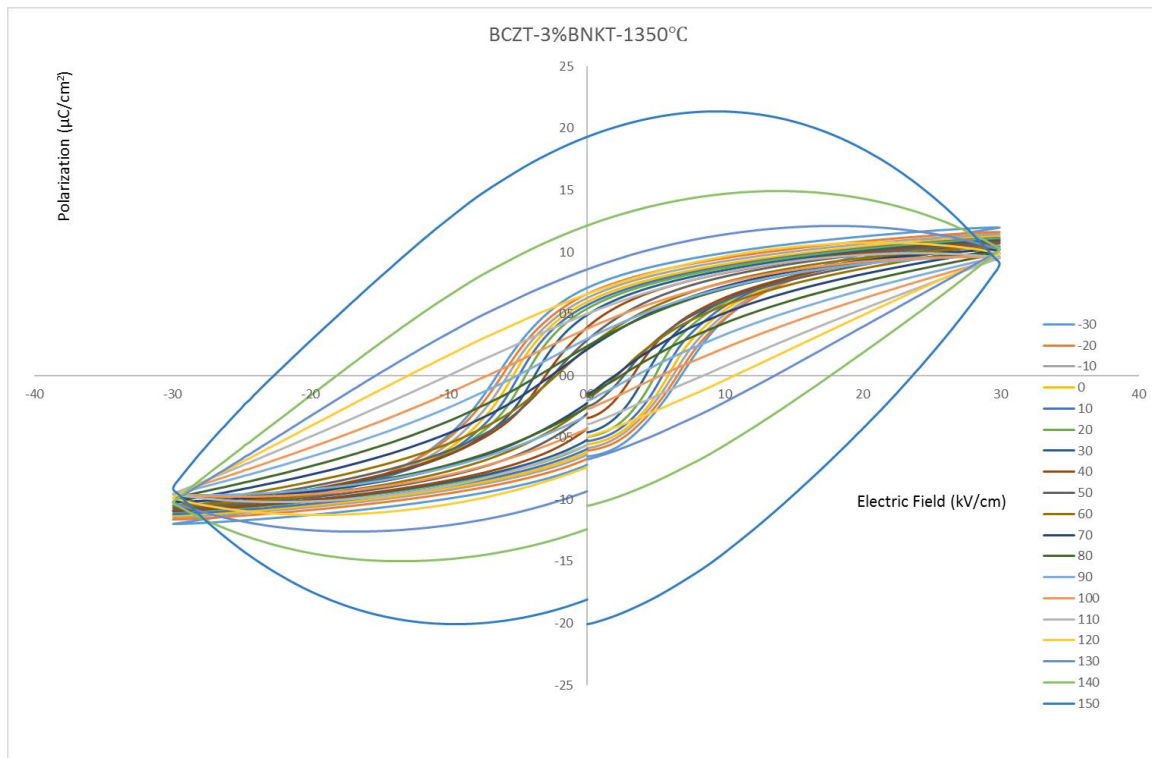


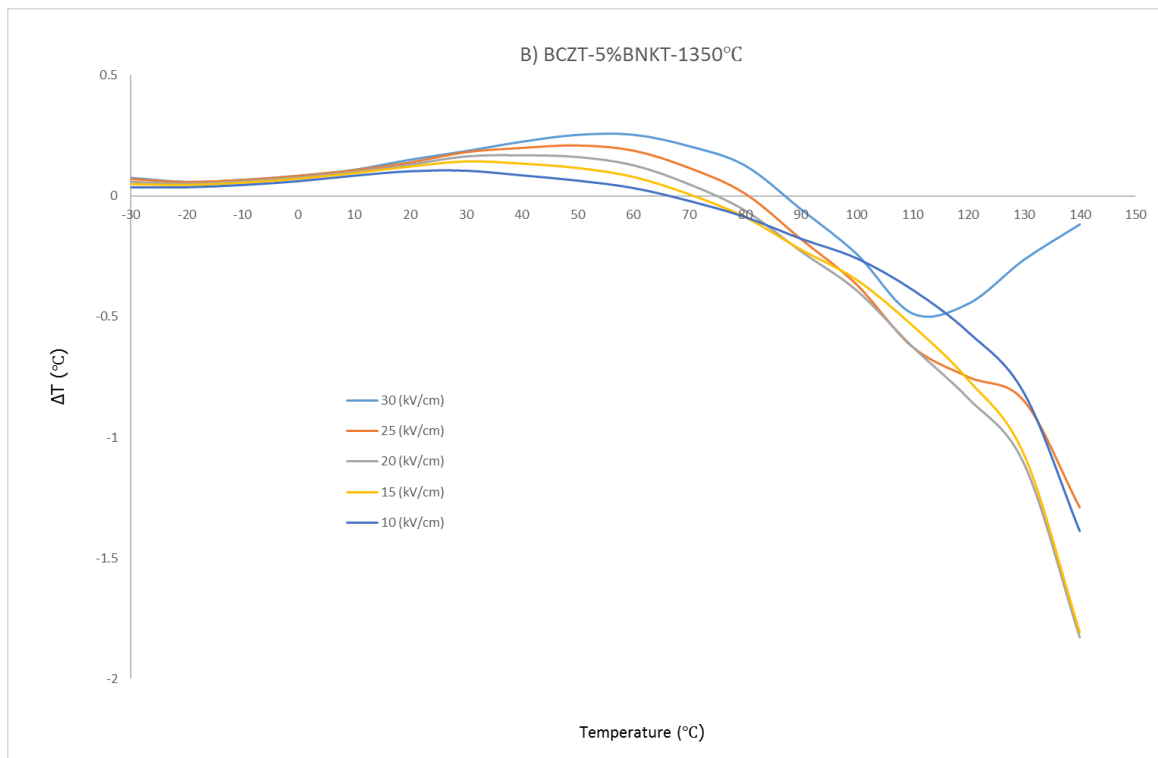
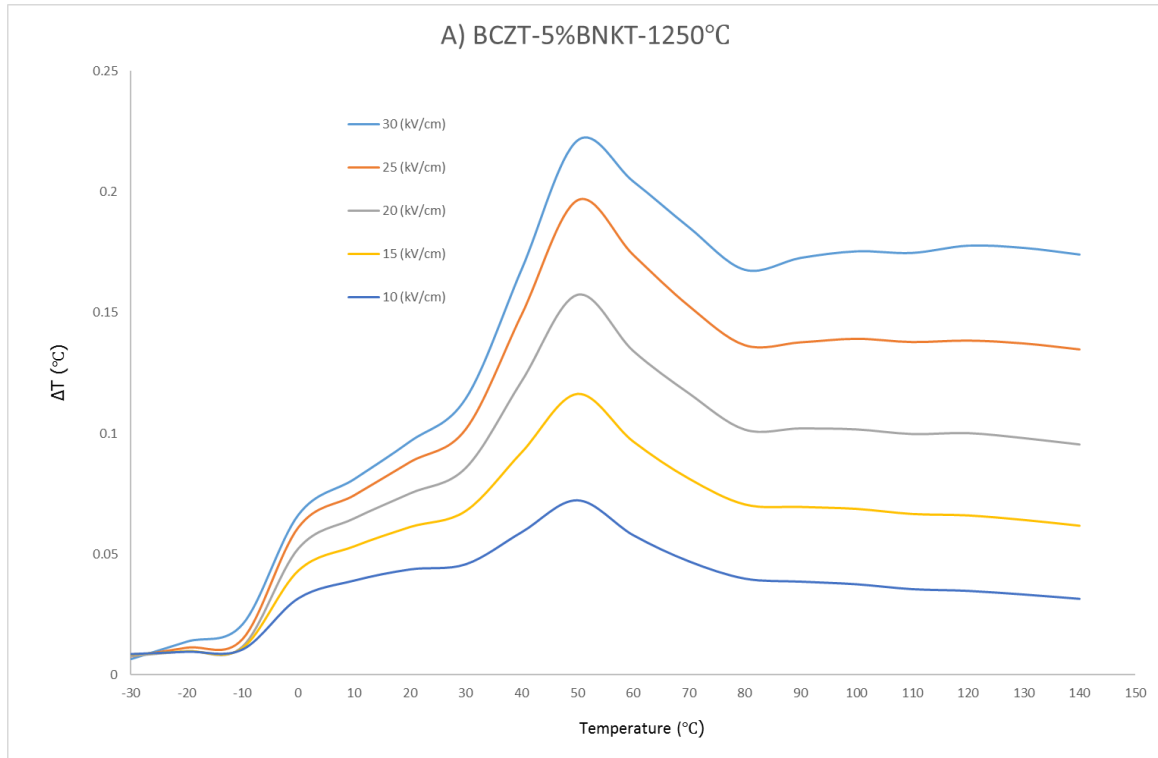
Figure 5-11: Polarisation-hysteresis loops of BCZT-3% BNKT, sintered at 1350°C and measured from -30 to 150°C.

5.1.1.5 Using the indirect method to measure the ECE of BCZT-5% BNKT

Figure 5-12 shows the ECE of BCZT-5% BNKT sintered at 1250, 1350, 1450, and 1500°C. The ECE of BCZT-5% BNKT sintered at 1250°C is about $\Delta T=0.22$ at 50°C for 30 kV/cm and after that, it decreases and become steady at $\Delta T=0.17$, and around 80 to 140°C for 30 kV/cm. This composition shows a steady ECE after the highest ECE, which is almost the same as the BCZT-1 and 3% BNKT sintered at the same temperature. This behaviour could be more practical than the sharp increases and decreases in the ECE, in spite of the high ECE.

BCZT-5% BNKT sintered at 1350°C shows the highest ECE ($\Delta T=0.25$) at 60°C for 30 kV/cm and after that, it starts to show banana and oval shapes of the polarisation-electric field loops, and this ECE is not acceptable. BCZT-5% BNKT sintered at 1450°C shows the ECE ($\Delta T=0.23$) at 90°C for 30 kV/cm and above the phase transformations to the cubic phase of this composition (64°C). The polarisation-electric field show a banana shape after 90°C. The ECE for BCZT-5% BNKT sintered at 1500°C starts to increase with a rise in the temperature, which shows the highest ECE $\Delta T=0.27$ °C at 130°C under 30 kV/cm, above

the Curie temperature at around 110°C. The change in the ECE usually follows the same method as relative permittivity, as can be seen for this composition (Figure 4-28).



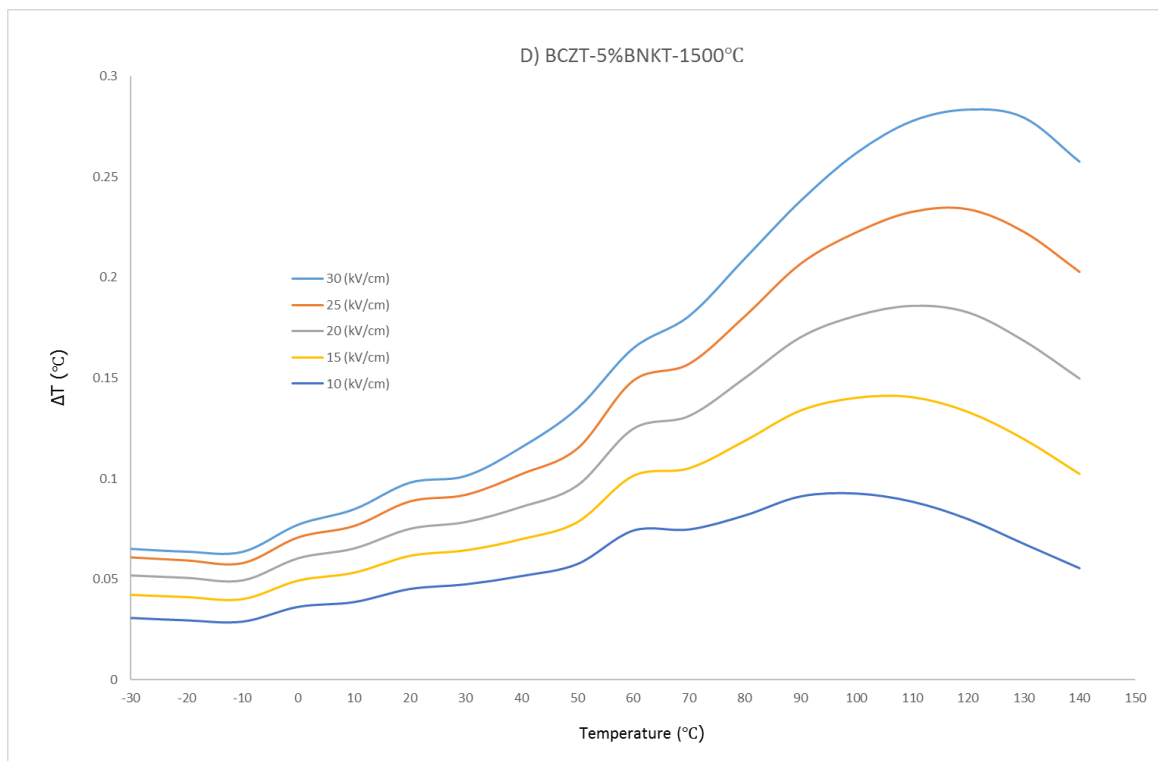
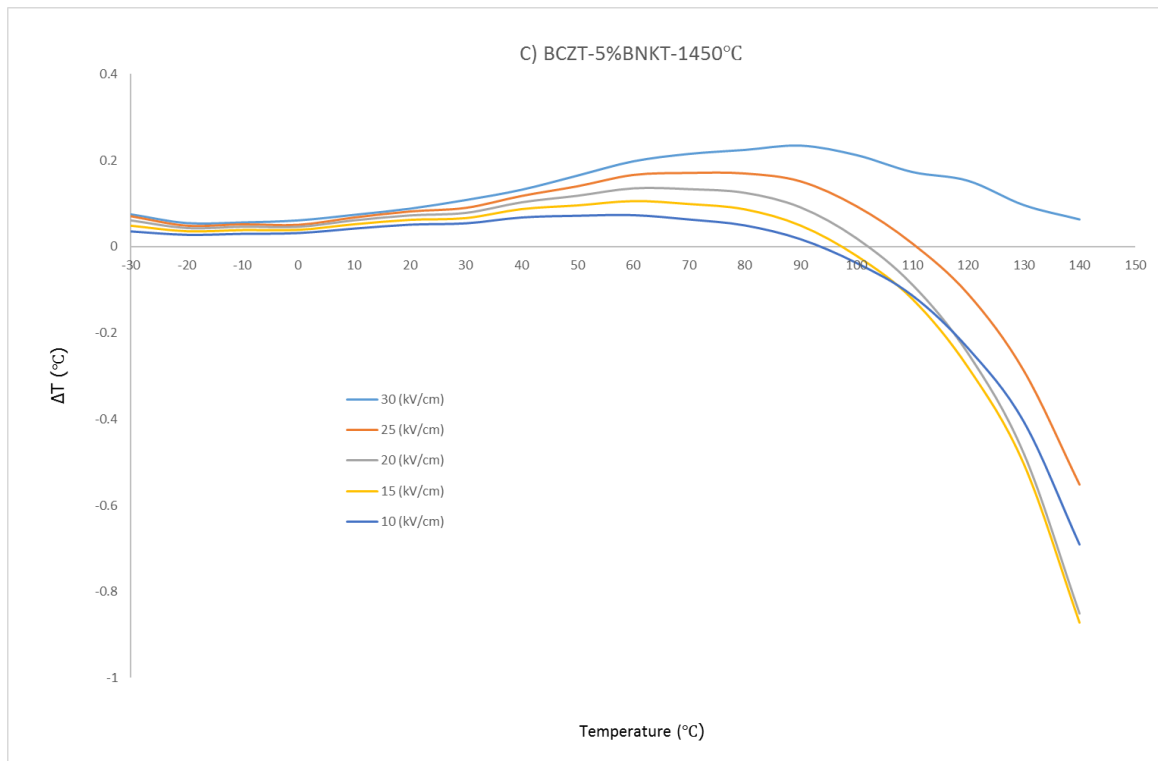


Figure 5-12: The ECE as a function of temperature and applied electric field for BCZT-5% BNKT ceramics sintered at A) 1250, B) 1350, C) 1450, and D) 1500°C. (The ECE figure of merit as a function of temperature and applied electric field for BCZT-5% BNKT ceramics sintered at A) 1250, B) 1350, C) 1450, and D) 1500°C in Appendix II)

5.1.2 Using the direct method to measure the ECE of BCZT-based materials

As explained in section 3.13, a jig was designed and constructed to enable the direct measurement of the ECE of the ceramic samples. Results produced using this equipment are reported below.

5.1.2.1 Pure BCZT

Figure 5-13 shows the ECE of the pure BCZT sintered between at 1450°C and measured from -30 to 125°C and 10, 20, and 30kV/cm. There were no ECE observations from -30 to -20°C; measurements were started from -20°C for a high electric field and went as high as 30kV/cm, and from 10°C for the lower electric field (10 and 20 kV/cm). It could be due to the low temperature which may make some difficulties for connections and measurements. One anomaly was observed for the pure BCZT at around 110 °C, near the Curie temperature (in the tetragonal-to-cubic transformation phase), based on the relative permittivity temperature in Figure 4-11. For the sample sintered at 1400°C and measured at 30kV/cm, ΔT started at around -30°C with 0.01°C, continued with a rise in the temperature to 0.4°C at 114.1°C, and then decreased to 0.35°C at 125°C. ΔT was increased by the rise in the electric field due to the higher electric field-induced polarisation change in the material. At the Curie temperature, there is a barrier between the state at which the ferroelectric material has polarisation, and its no-polarization state. In comparison with the temperature dependence of relative permittivity of BCZT (Figure 4-11), it is possible that this material will show polarisation at a higher Curie temperature under an electric field due to changes in the cubic structure to a non-centrosymmetric state. The highest polarisation change can happen in this state, so the highest entropy changes occur as well. For this reason, the highest ECE happens around the Curie temperature. As can be seen in Figure 5-1, there is a change in the heat capacity of the BCZT at around 100°C, which shows the latent heat due to the phase transformation between the tetragonal and cubic phases. The latent heat is due to the different entropy, lattice elastic energy, and spontaneous polarisation changes between these phases. When the electric field was applied, it caused the higher lattice deformation to take place, which resulted in a higher polarisation than the spontaneous polarisation. Domains can change from multi-state to single-state under an electric field, which leads to a higher polarisation. The E_c of the BCZT is quite low, around 2kV/cm, and the experiments were carried out at a higher electric fields, from 10 to 30kV/cm.

This implies that all the applied electric fields were higher than the minimum electric field for rotating the dipoles, and the ECE was increased because the higher electric field caused higher polarity, while the higher electric field caused a larger lattice elastic energy.

There was no observed difference between the ECE of the sintered BCZT at different sintering temperatures, while the highest EC for all of them were between 0.39 to 0.41°C at 30kV/cm. For the sample sintered at 1400, 1425, 1450, 1475, and 1500°C, the ECE reached $\Delta T=0.40, 0.39, 0.41, 0.41,$ and $0.39,$ respectively.

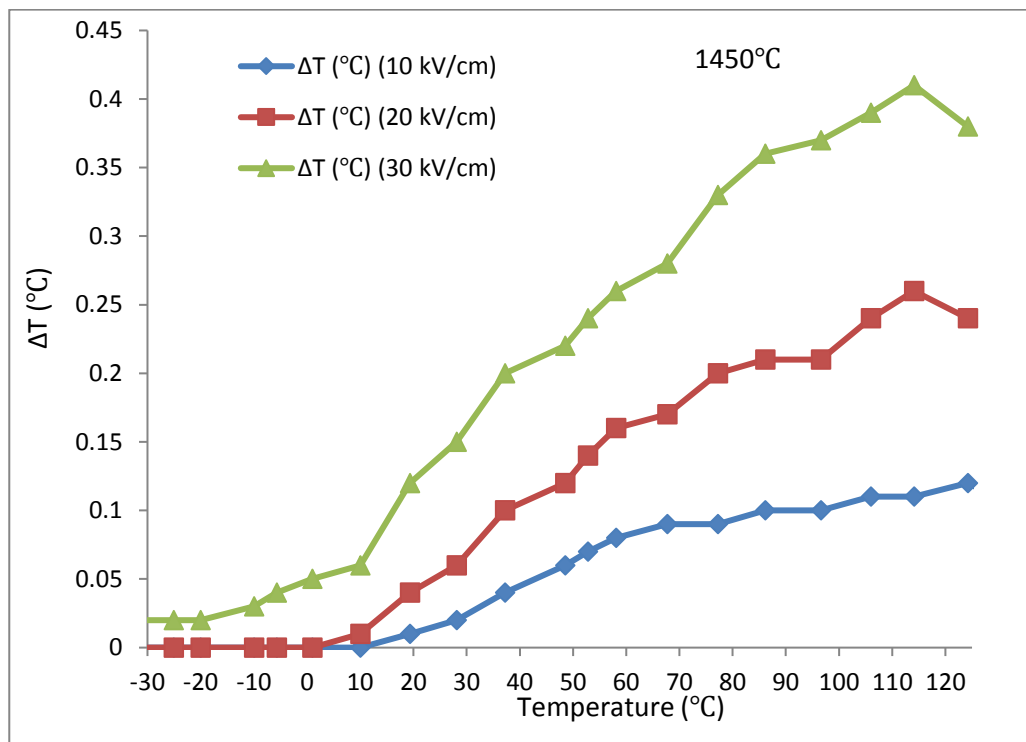


Figure 5-13: The ECE of the pure BCZT sintered at 1450°C measured between -30 and 125°C, using the direct method. (Pure BCZT sintered at 1400, 1425, 1475, and 1500°C in Appendix II)

Figure 5-14 shows the ECE figure of merit of pure BCZT sintered at 1450°C and measured between -30 and 125°C. As can be seen in the figure, the figure of merit increased until near the Curie temperature and after that, decreased. It shows that the highest value is observed near the Curie temperature. The figure of merit was lower for the lower electric field because the ECE was started at a higher temperature compared to the 30kV/cm electric field. The effect of the sintering temperature was negligible on the ECE figure of merit.

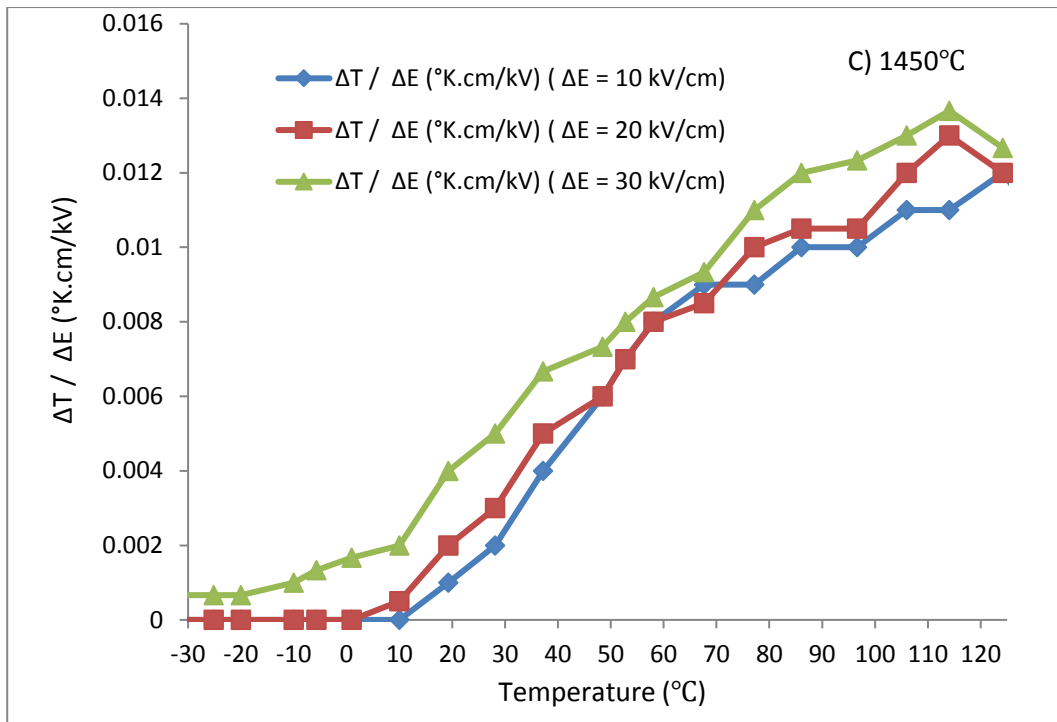


Figure 5-14: The ECE figure of merit of pure BCZT sintered at 1450°C and measured between -30 and 125°C (Pure BCZT sintered at 1400, 1425, 1475, and 1500°C in Appendix II).

5.1.2.2 BCZT-BNKT

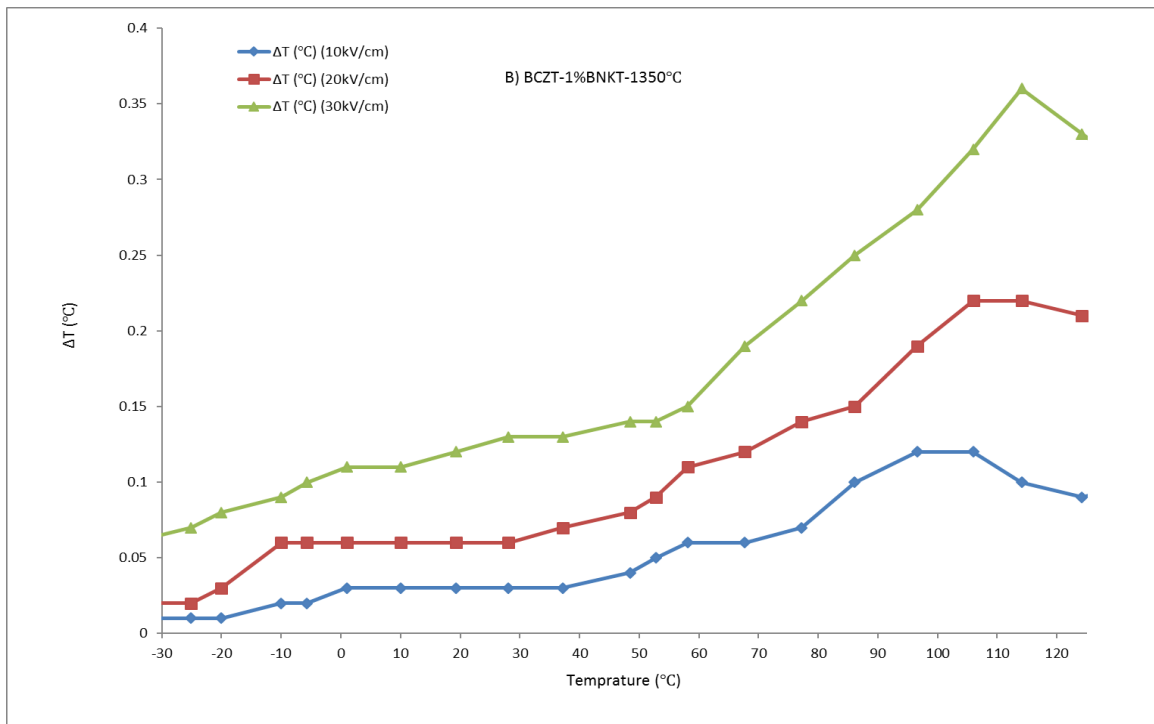
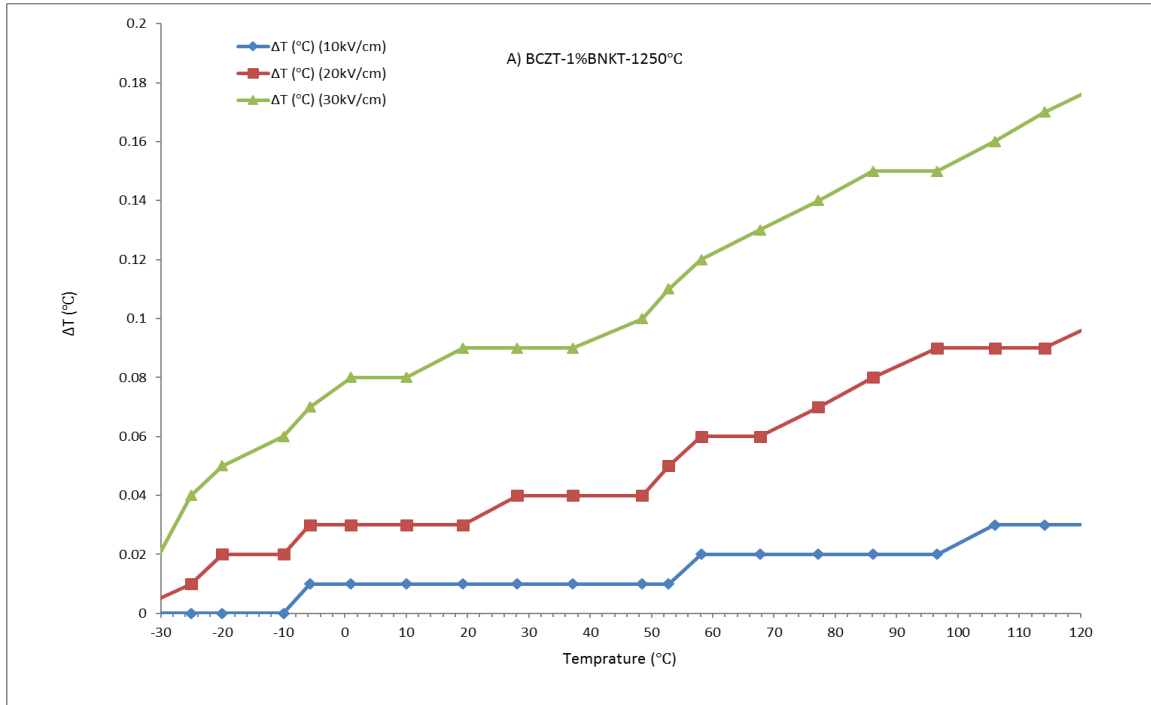
The effect of BNKT on the BCZT is discussed in section 4.2.1. This section explains the effect of this additive on the ECE of this composition measured using the direct method.

5.1.2.2.1 The ECE direct measurement of BCZT-1%BNKT

Figure 5-15 shows the ECE of the BCZT-1% BNKT sintered between 1250 and 1500°C, measured at -30 to 125°C and under three different electric fields. The ECE was reached at $\Delta T=0.17^\circ\text{C}$ around 114°C for the sample sintered at 1250°C. As can be seen, this was increased by a rise in the electric field, for the highest amount from $\Delta T=0.03^\circ\text{C}$ for 10kV/cm, $\Delta T=0.09^\circ\text{C}$ for 20kV/cm, and $\Delta T=0.17^\circ\text{C}$ for 30kV/cm. The results of the ECE from the direct measurement show the highest ECE for BCZT-1% BNKT sintered at 1250°C are at a temperature higher than the maximum relative permittivity (around 100°C) (Figure 4-26), and the same result has been achieved by the indirect method of ECE measurement.

In comparison with BCZT-1% BNKT sintered at 1250°C, BCZT-1% BNKT sintered at 1350°C shows a higher ECE and reached 0.36°C for 30 kV/cm at 114°C. BCZT-1% BNKT

sintered at 1450°C shows the highest ECE by direct measurement, of $\Delta T=0.32^{\circ}\text{C}$ at 96.6°C under 30 kV/cm. BCZT-1% BNKT sintered at 1500°C shows an ECE of $\Delta T=0.32^{\circ}\text{C}$ at 30 kV/cm and at around 114°C .



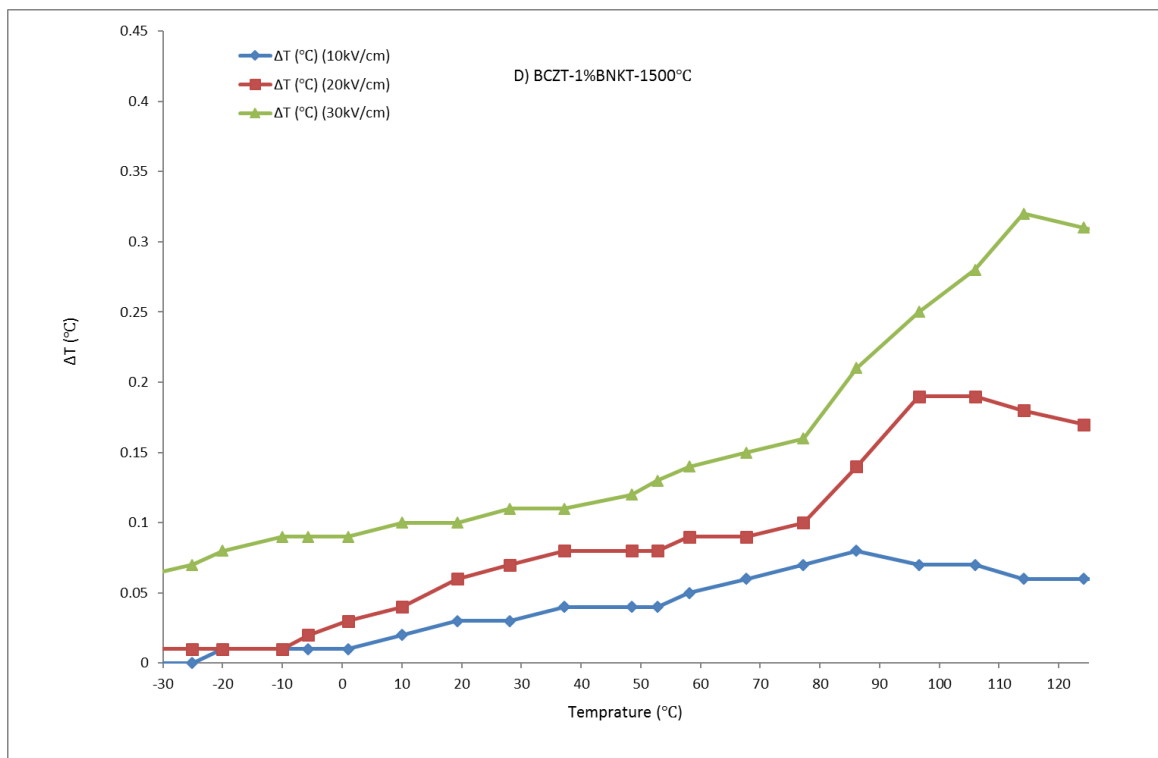
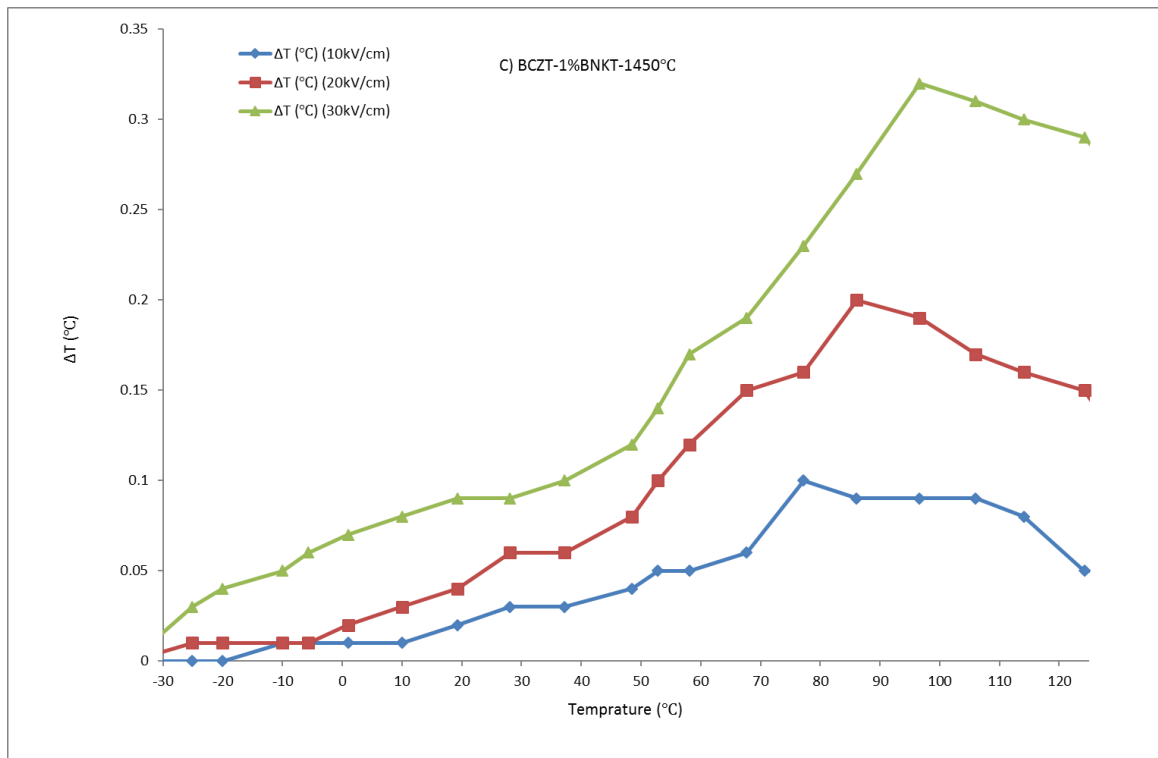


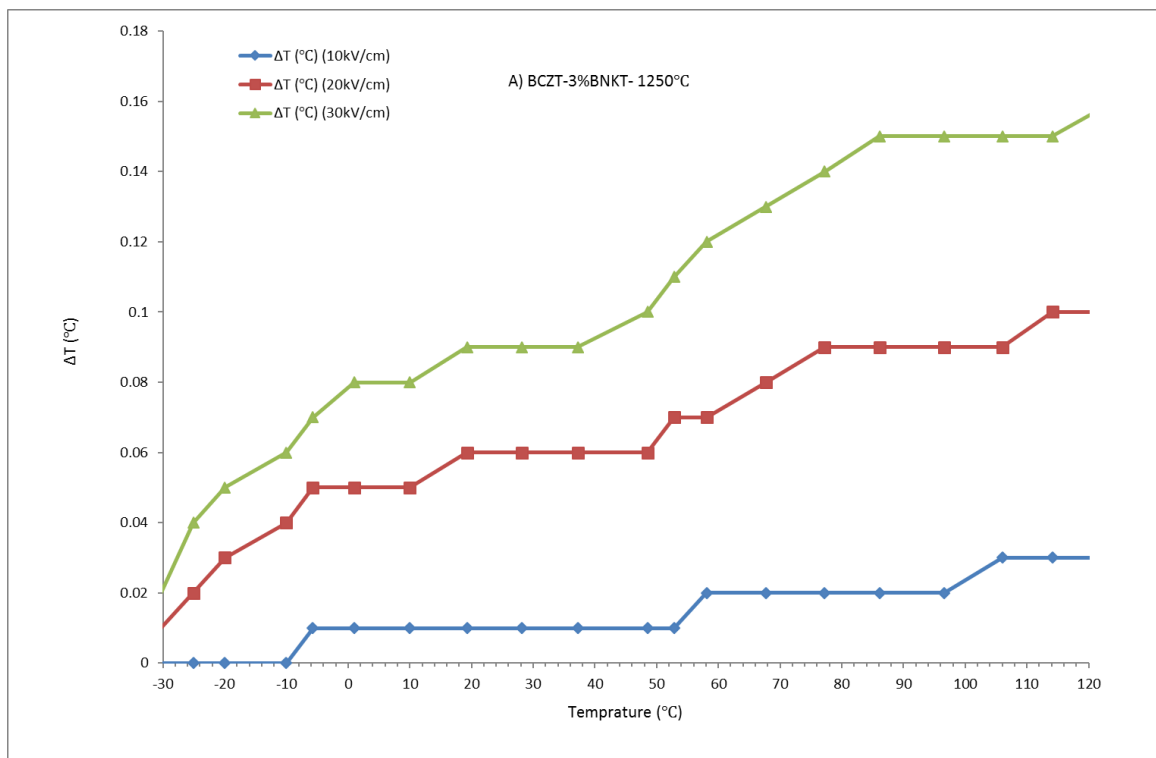
Figure 5-15: The ECE of the BCZT-1%BNKT sintered at A) 1250, B) 1350, C) 1450, and D) 1500°C measured between -30 and 125°C and at 10, 20, and 30 kV/cm.

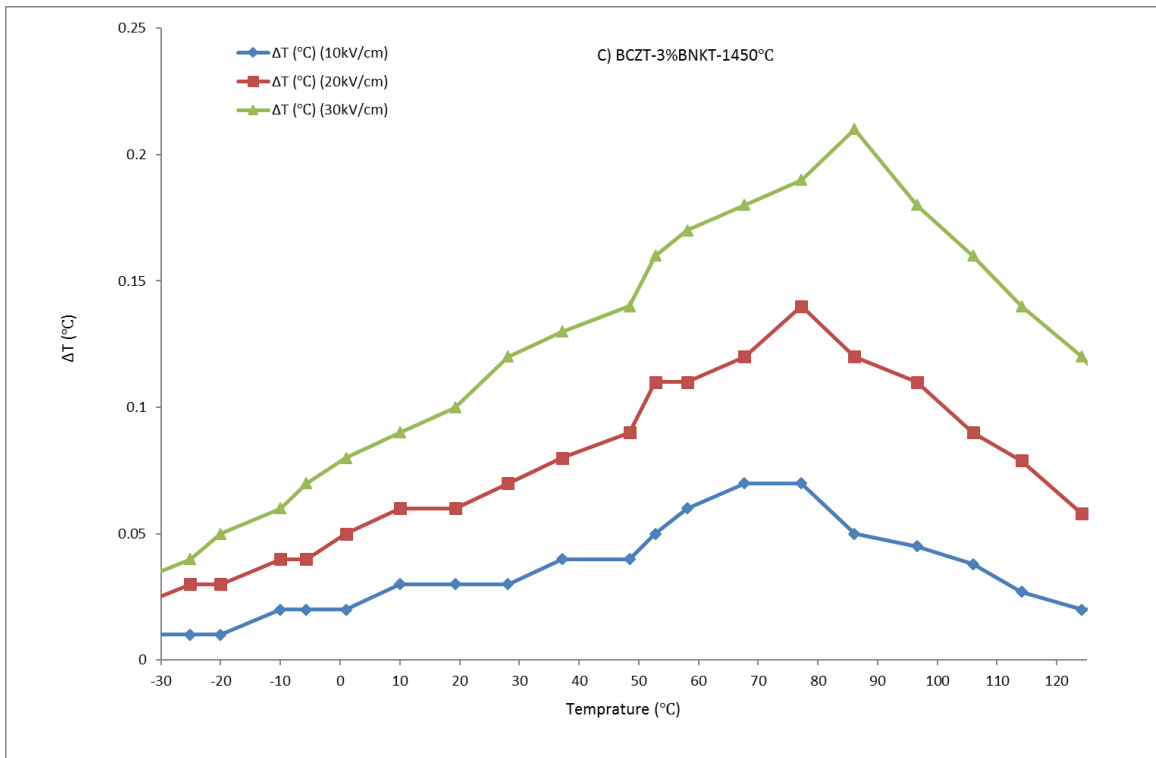
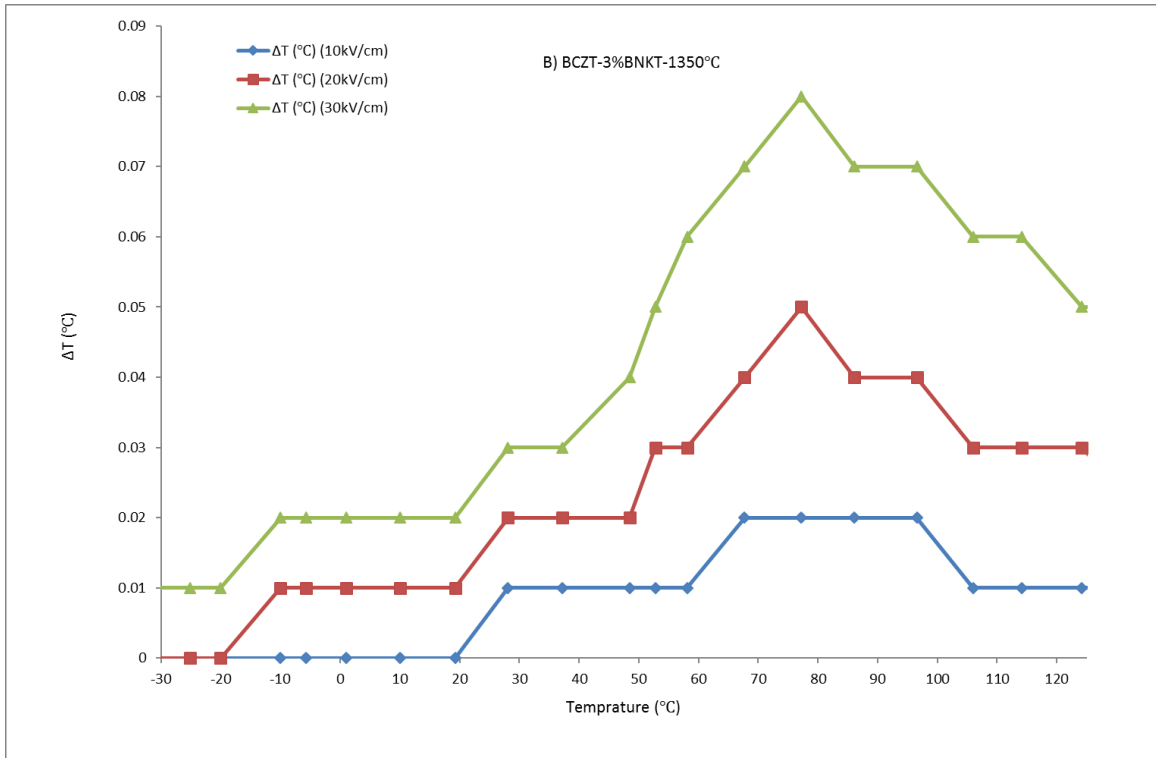
5.1.2.2.2 BCZT-3%BNKT

Figure 5-16 shows the ECE of BCZT-3%BNKT sintered at 1250, 1350, 1450, and 1500°C measured between -30 and 125°C and at 10, 20, and 30 kV/cm. BCZT-3% BNKT sintered at 1250°C reveals a low ECE due to the small grain size of 2.2µm, which leads to low polarisation and therefore a lower ECE. The highest ECE for this composition is $\Delta T=0.15^\circ\text{C}$ at 114°C for 30 kV/cm.

BCZT-3% BNKT sintered at 1350°C shows the highest $\Delta T=0.08$; the ECE is at around 77°C and under 30 kV/cm. Just as for the indirect method, the ECE measured by the direct method is low for this composition, while the ECE measured at a higher temperature is quite low, which the indirect method is unable to measure due to the current leakage. BCZT-3% BNKT sintered at 1450°C shows $\Delta T=0.21^\circ\text{C}$ at 86°C for 30 kV/cm, and the ECE is low for those parts, which the indirect method is unable to measure.

BCZT-3% BNKT sintered at 1500°C shows the highest ECE $\Delta T=0.24^\circ\text{C}$, at around 100°C.





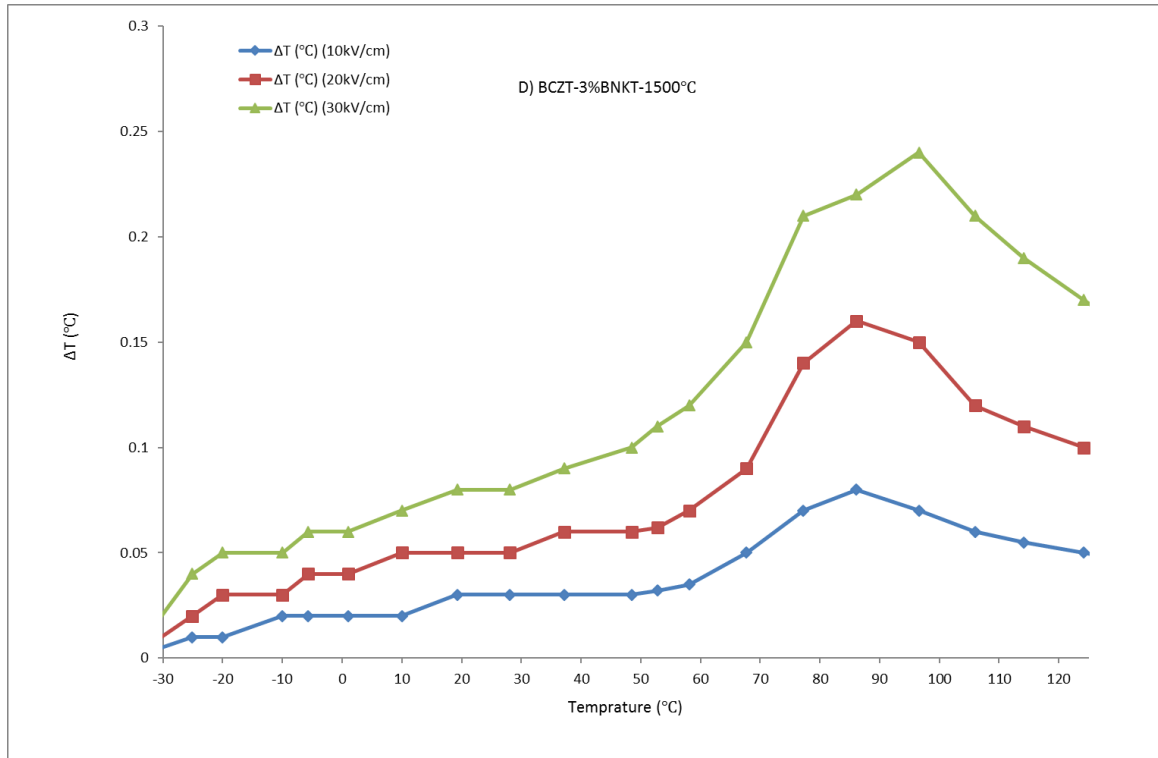
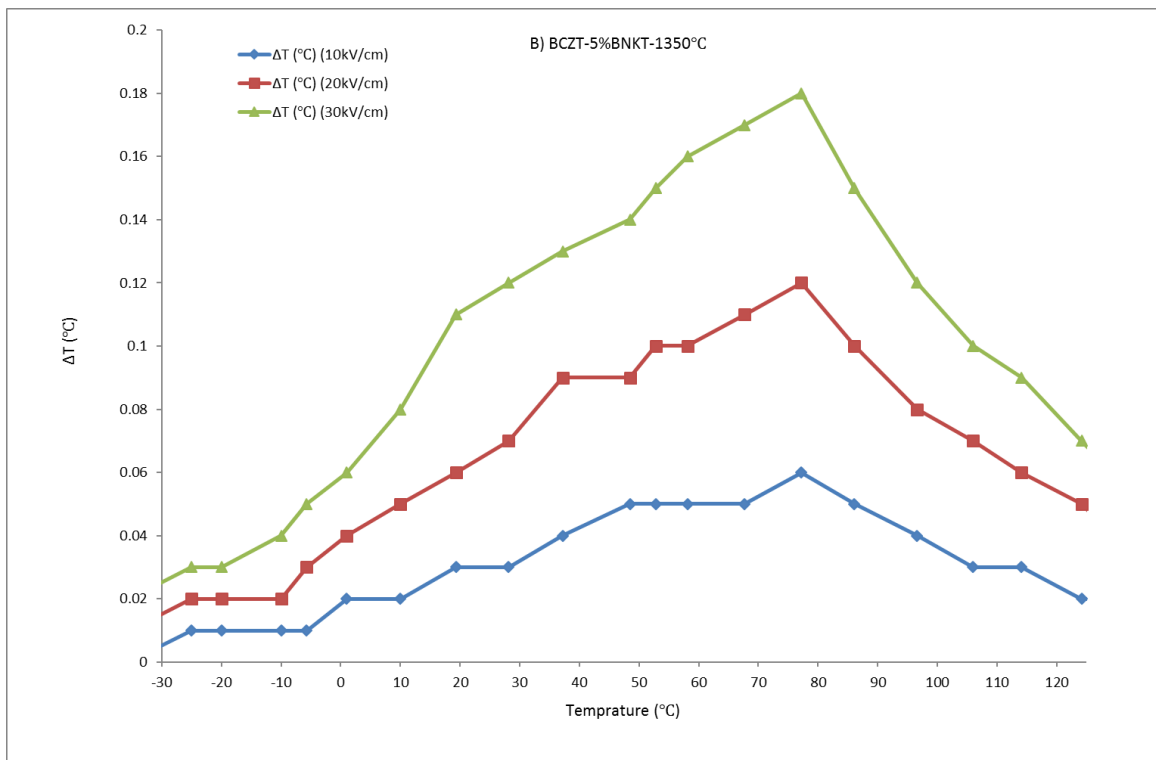
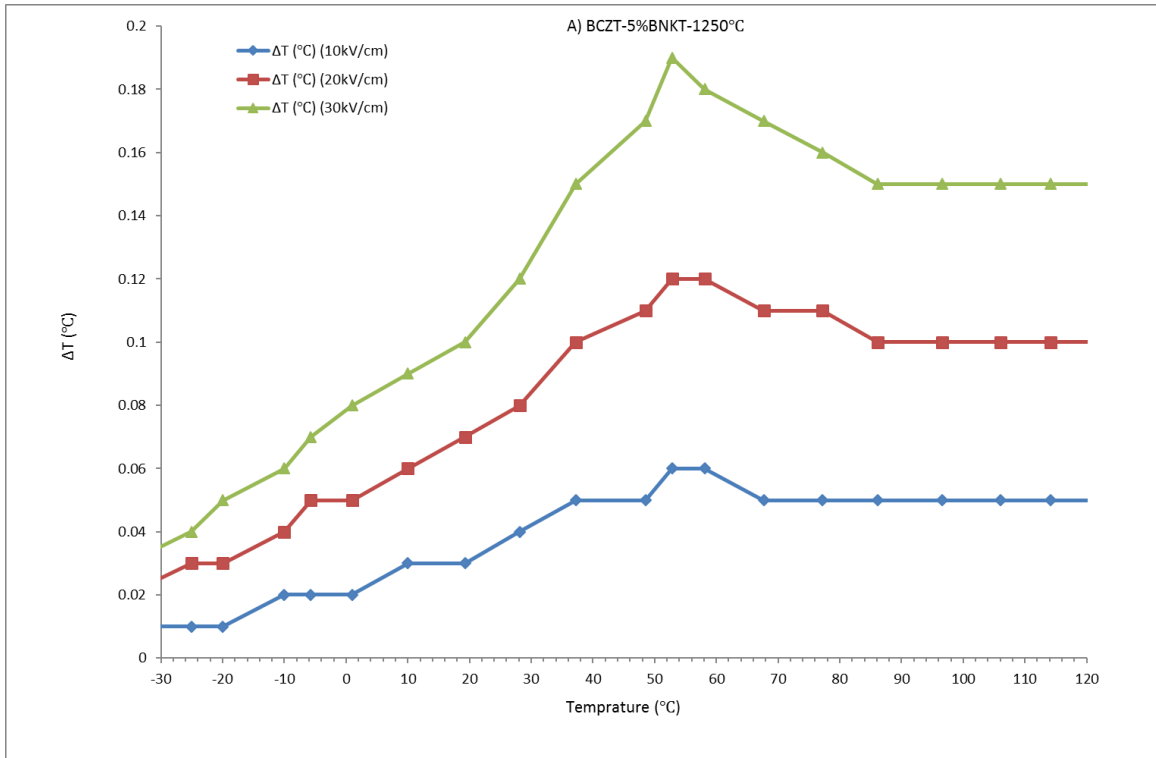


Figure 5-16: The ECE of the BCZT-3%BNKT sintered at A) 1250, B) 1350, C) 1450, and D) 1500°C measured between -30 and 125°C and at 10, 20, and 30 kV/cm.

5.1.2.2.3 BCZT-5%BNKT

Figure 5-17 shows the ECE of the BCZT-5% BNKT sintered at 1250, 1350, 1450, and 1500°C measured between -30 and 125°C and at 10, 20, and 30 kV/cm. BCZT-5% BNKT sintered at 1250°C shows the highest ECE ($\Delta T=0.19^{\circ}\text{C}$) at around 52.8°C for 30 kV/cm, and after that, it shows a lower ECE, but is quite steady. A direct measurement of BCZT-5% BNKT sintered at 1350°C shows the highest ECE ($\Delta T= 0.18^{\circ}\text{C}$) at around 78°C, which is higher than the phase transformation to cubic phase. BCZT-5% BNKT sintered at 1450°C shows the highest ECE ($\Delta T=0.18^{\circ}\text{C}$) at around 86°C, which is above the Curie temperature. In addition, BCZT -5% BNKT sintered at 1500°C shows the highest ECE ($\Delta T=0.20^{\circ}\text{C}$), at around 106°C.



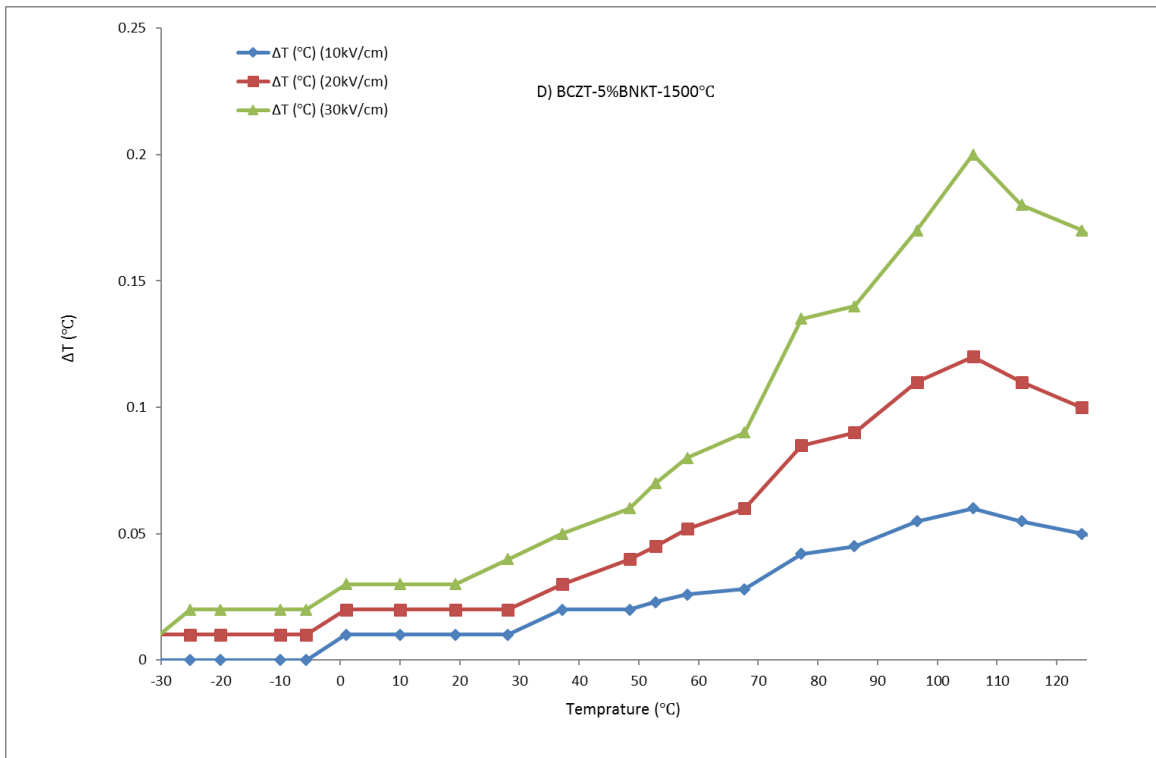
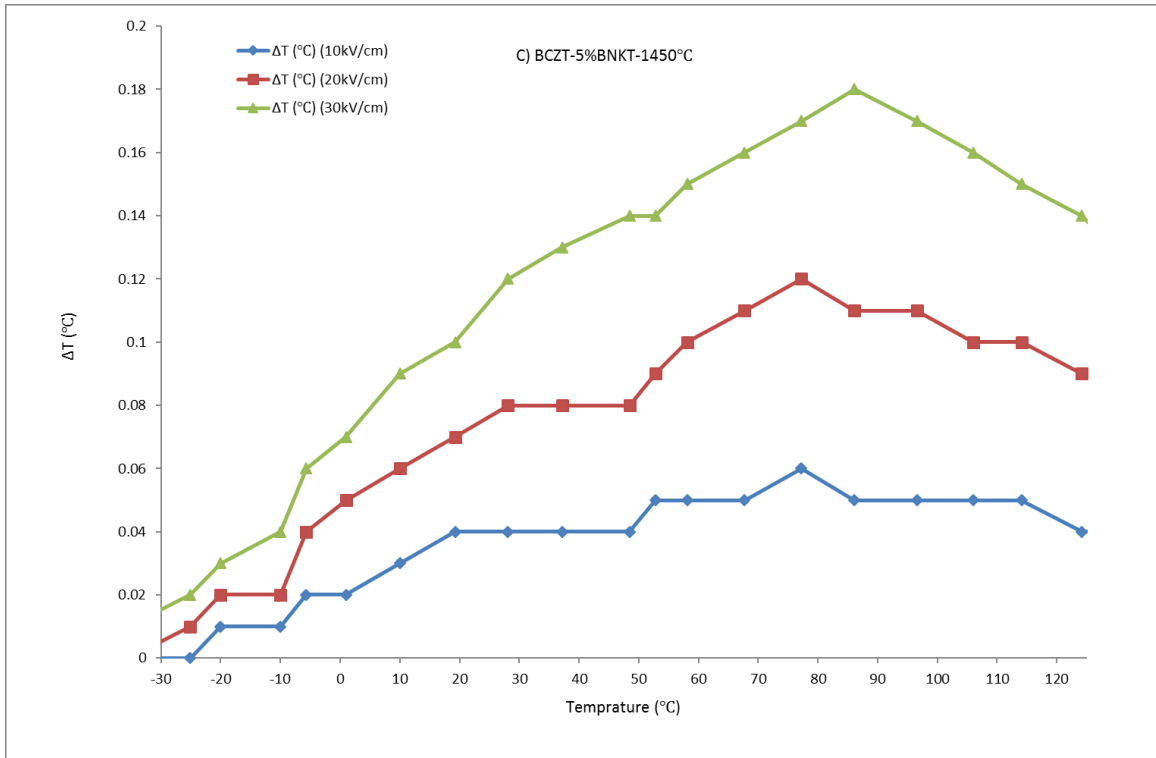


Figure 5-17: The ECE of the BCZT-5% BNKT sintered at A) 1250, B) 1350, C) 1450, and D) 1500°C measured between -30 and 125°C and at 10, 20, and 30 kV/cm by a direct method.

5.1.2.3 ECE comparison of BCZT- and BCZT-based ceramics

Table 5-1 offers a summary of the ECE of BCZT- and BCZT-based materials tested by direct and indirect methods. The pure BCZT sample sintered at 1450°C shows the highest value compared to the other sintering temperatures, for both the direct and indirect methods. As explained in section 4.2, the properties of BCZT have a direct relationship with its relative density, and 1450°C is the temperature that shows the highest relative density. A higher relative density causes less porosity, which acts as a clamp for the rotation of domains, and so leads to a higher ECE. The E_c of the BCZT is around 2 kV/cm for BCZT sintered at 1450°C based on the polarization-hysteresis loop at 20 and 30°C. For this reason, a low electric field can be used for the poling of this sample and saturation was obtained for the polarisation-electric loops.

The ECE figures of merit for BCZT sintered at 1400, 1425, 1450, 1475, and 1500°C are around 0.018, 0.017, 0.019, 0.017, and 0.018 (K. kV/cm), respectively due to almost similar relative density for the compound. It is worth noting that the figures of merit for higher applied electric fields have been selected for comparison, due to their higher ECE. A comparison between the results show that the ECE of BCZT sintered at 1450°C is higher than for the other samples ($\Delta T = 0.97^\circ\text{C}$ for 50kV/cm). The variation in the figure of merit is similar to that of the relative density of the samples (Figure 4-6), so relative density could be an important factor in achieving a good ECE. A low relative density means more porosity in the sample, and more porosity causes a reduction in the rotation speed of domains, which are in the opposite direction of the ECE due to the higher domain rotation speed, causing larger entropy change in EC materials and therefore a higher ECE. For this reason, one of the main factors that can be assumed for EC materials is relative density, and the process that can lead to more density in these materials [2].

The figure of merit for lower values of applied electric fields show that initial applied field leads to more polarisation [158] due to the low E_c in this compound (around 2 (kV/cm at RT)), which leads to a higher ECE. However, the ECE in low electric fields is quite low, which makes it unpractical.

A comparison of Table 5-1 and Table 2-7 shows that the ECE achieved for BCZT in this project is higher than that of some previous studies, and equal to that of other one. An ECE figure of merit of 0.014 K.cm/kV was achieved by Bai et al. [200] for a BCZT composition with 1200°C selected for calcination and 1400°C for sintering, while Patel et al. [206] obtained a 0.019 K.cm/kV of the ECE figure of merit for BCZT, with 1400°C (six hours) selected for calcination and 1450°C (four hours) for sintering. It is known that the calcination and sintering temperatures can affect other properties such as the k_p , d_{33} , relative density, so this could be one of the reasons for the different responses in the BCZT. As can be seen in Table 5-1, the ECE figure of merit has changed from 0.018 to 0.017 K.cm/kV, and then to 0.019, 0.017, and 0.018 K.cm/kV for the samples sintered from 1400 to 1500°C, respectively. The ECE figure of merit for BCZT sintered at 1400°C is close to the result obtained by Patel et al., but the optimisation in the fabrication process in this project has caused a rise in the ECE. The ECE figure of merit for BCZT samples measured by the direct method is 0.013, 0.013, 0.014, 0.014, and 0.013 K.cm/kV for samples sintered at 1400, 1425, 1450, 1475, and 1500°C respectively. The results of the direct method are lower than those of the indirect method as a non-adiabatic device has been used for measurement, which causes the ECE figure of merit for BCZT by the direct method to be almost 73% of that of the indirect method. However, the effect of the sintering temperature on the ECE is similar for both methods. In spite of the use of the non-adiabatic measurement device, the ECE figure of merit of this project is similar to that of Bai et al. of 0.014 K.cm/kV. Patel et al. also obtained the same ECE as this project, but with a higher calcination temperature.

The ECE figure of merit for BCZT-1% BNKT is 0.007, 0.016, 0.015, and 0.014 K.cm/kV for indirect method and 0.006, 0.012, 0.010, and 0.010 K.cm/kV for the direct method, with the samples sintered at 1250, 1350, 1450, and 1500°C, respectively. At the lowest sintering temperature for this composition (1250°C), the ECE and therefore the figure of merit is low, due to the low grain size (2 μm). After that, by raising the sintering temperature, the grain size increases (26, 33, and 35 μm for sintering temperatures of 1350, 1450, and 1500°C) and the relative density decreases (97, 93, and 92% for sintering temperatures of 1350, 1450, and 1500°C), which shows that the relative density has more of an effect on the ECE than the grain size. The ECE figure of merit reaches 0.016 K.cm/kV for 1350°C, which is lower than for pure BCZT (0.019 K.cm/kV for 1450°C), and is around 110°C, lower than for pure BCZT (140°C), therefore the results indicate that 1% of BNKT can be used for the lower working

temperature. Both the direct and indirect methods use the same method to obtain the ECE of BCZT-1% BNKT, and the direct method is only 75% of the indirect method.

The ECE figure of merit for BCZT-3% BNKT is 0.007, 0.005, 0.010, and 0.012 K.cm/kV for indirect method and 0.005, 0.002, 0.007, and 0.008 K.cm/kV for the direct method, with the samples sintered at 1250, 1350, 1450, and 1500°C, respectively. In general, the ECE of BCZT-3% BNKT is lower than for BCZT-1% BNKT and pure BCZT, due to its lower relative density and the lower grain size of these compounds. Also, the compound is more far from the MPB in comparison with pure BCZT and BCZT-1%BNKT.

The ECE figure of merit for BCZT-5% BNKT is 0.007, 0.007, 0.007, and 0.009 K.cm/kV using the indirect method, and 0.006, 0.006, 0.006 and 0.007 K.cm/kV for the direct method, with the samples sintered at 1250, 1350, 1450, and 1500°C, respectively. In general, the ECE of BCZT-5% BNKT is lower than BCZT-1 and 3%BNKT; it increases at 1500°C, but in general is similar for all the sintering temperatures. The lower relative density could be one of the main reasons for the lower ECE of this compound, while the higher ECE for the sample sintered at 1500°C can be attributed to the larger grain size. The results of the direct method are about 85% of those of the indirect method. The addition of BNKT to BCZT can divert the BCZT from the MPB, which is one of the main factors in whether ferroelectric materials will show a high ECE. In the MPB, the flattening energy barrier between two ferroelectric phases makes the rotation of the poles easier, and so leads to a higher ECE. The ECE is decreased by the addition of more BNKT to BCZT, which shows that more BNKT diverts the BCZT from the MPB.

Table 5-1: A summary of the ECE of BCZT- and BCZT-based materials using the direct and indirect methods.

Pure BCZT							
Sintering Temperature °C	1250	1300	1400	1425	1450	1475	1500
Relative density%	-	-	92	93.5	96.1	95.5	94.2
d_{33} pC/N	-	-	310	340	410	380	350
Grain Size (μm)	-	-	22	25	32	34	35
Temperature of Max ϵ_r °C	-	-	103.5	103	102.5	103	102
Maximum of EC (Indirect) °C	-	-	0.926	0.870	0.973	0.877	0.923
ΔE kV/cm	-	-	50	50	50	50	50
Indirect ECE figure of merit K.cm/kV	-	-	0.018	0.017	0.019	0.017	0.018
Temperature of maximum EC °C	-	-	140	130	140	140	140
Maximum of EC (Direct) °C	-	-	0.40	0.39	0.41	0.41	0.39
ΔE kV/cm	-	-	30	30	30	30	30
Direct ECE figure of merit K.cm/kV	-	-	0.013	0.013	0.014	0.014	0.013
Temperature of maximum EC °C	-	-	114	114	114	114	114
Spontaneous polarisation $\mu\text{C}/\text{cm}$ at RT	-	-	15.94	16.95	21.13	17.57	17.80
BCZT – 1% BNKT							
Sintering Temperature °C	1250	1350	1400	1425	1450	1475	1500
Relative density%	95	96	-	-	93	-	92
d_{33} pC/N	10	290	-	-	300	-	370
Grain Size (μm)	2	26	-	-	33	-	35
Temperature of Max ϵ_r °C	98.8	81.4	-	-	80.7	-	78.7
Maximum of EC (Indirect) °C	0.208	0.501	-	-	0.47	-	0.43
ΔE kV/cm	30	30	-	-	30	-	30
Indirect ECE figure of merit K.cm/kV	0.0068	0.0168	-	-	0.0157	-	0.0144
Temperature of maximum EC	130	110	-	-	110	-	110
Maximum of EC (Direct)	0.18	0.36	-	-	0.32	-	0.32
ΔE kV/cm	30	30	-	-	30	-	30
Direct ECE figure of merit K.cm/kV	0.006	0.012	-	-	0.010	-	0.010
Temperature of maximum EC °C	124	114	-	-	96.6	-	114.1
Spontaneous polarisation $\mu\text{C}/\text{cm}$ at RT	9.99	14.49	-	-	13.67	-	11.53
BCZT – 3% BNKT							
Sintering Temperature °C	1250	1350	1400	1425	1450	1475	1500
Relative density%	95	95	-	-	92	-	91
d_{33} pC/N	10	100	-	-	122.5	-	255
Grain Size (μm)	2.2	12	-	-	31	-	33
Temperature of Max ϵ_r °C	94.8	76.8	-	-	66.8	-	76.7
Maximum of EC (Indirect) °C	0.217	0.155	-	-	0.32	-	0.37
ΔE kV/cm	30	30	-	-	30	-	30
Indirect ECE figure of merit K.cm/kV	0.007	0.005	-	-	0.010	-	0.012
Temperature of maximum EC	130	70	-	-	80	-	110
Maximum of EC (Direct)	0.16	0.08	-	-	0.21	-	0.24

ΔE kV/cm	30	30	-	-	30	-	30
Direct ECE figure of merit K.cm/kV	0.005	0.002	-	-	0.007	-	0.008
Temperature of maximum EC	124	77.2	-	-	86	-	96
Spontaneous polarisation $\mu\text{C}/\text{cm}$ at RT	8.87	10.92	-		13.42	-	11.53
BCZT – 5% BNKT							
Sintering Temperature °C	1250	1350	1400	1425	1450	1475	1500
Relative density%	98	94	-	-	94	-	87
d_{33} pC/N	0	17.5	-	-	50	-	100
Grain Size (μm)	2.4	10	-	-	16	-	29
Temperature of Max ϵ_r °C	63.1	50.1	-	-	64	-	98.6
Maximum of EC (Indirect) °C	0.22	0.25	-	-	0.23	-	0.28
ΔE kV/cm	30	30			30		30
Indirect ECE figure of merit K.cm/kV	0.007	0.007	-	-	0.007	-	0.009
Temperature of maximum EC	50	60	-	-	90	-	130
Maximum of EC (Direct)	0.19	0.18	-	-	0.18	-	0.2
ΔE kV/cm	30	30			30		30
Direct ECE figure of merit K.cm/kV	0.006	0.006	-	-	0.006	-	0.007
Temperature of maximum EC	52	77	-	-	86	-	106
Spontaneous polarisation $\mu\text{C}/\text{cm}$ at RT	7.84	10.89	-	-	10.73	-	9.53

5.1.3 Indirect ECE measurements of BNT-BT based materials

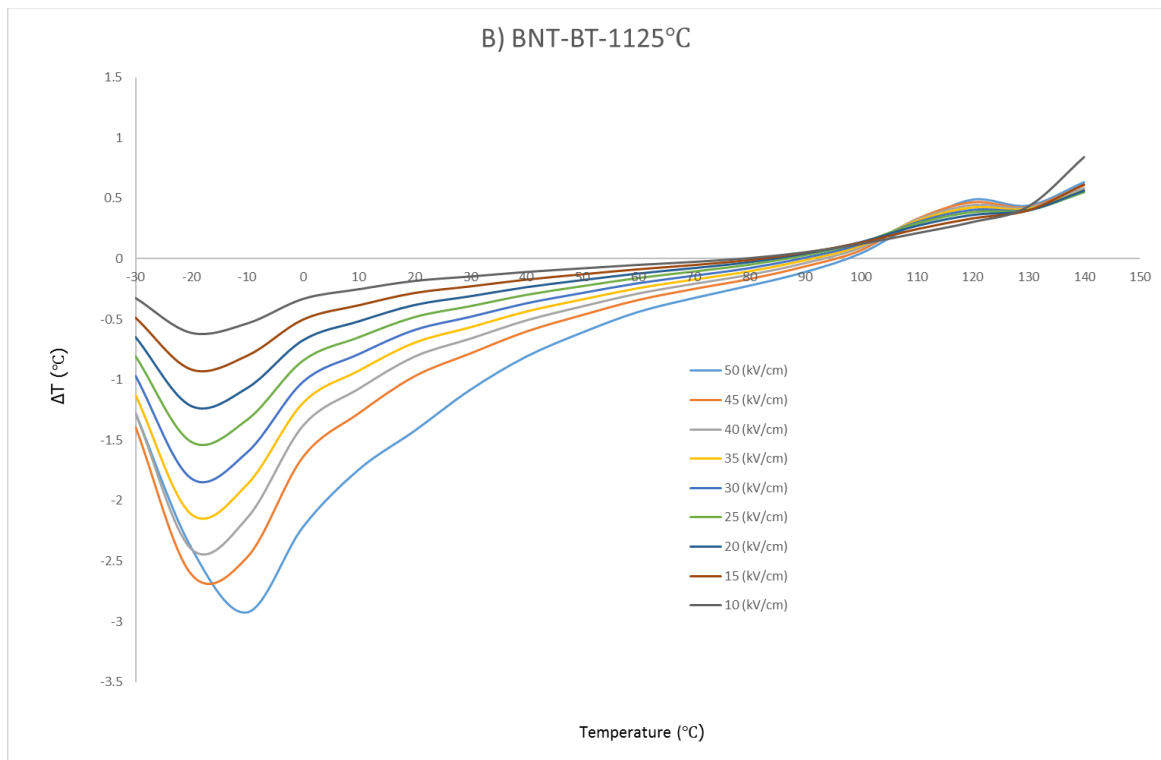
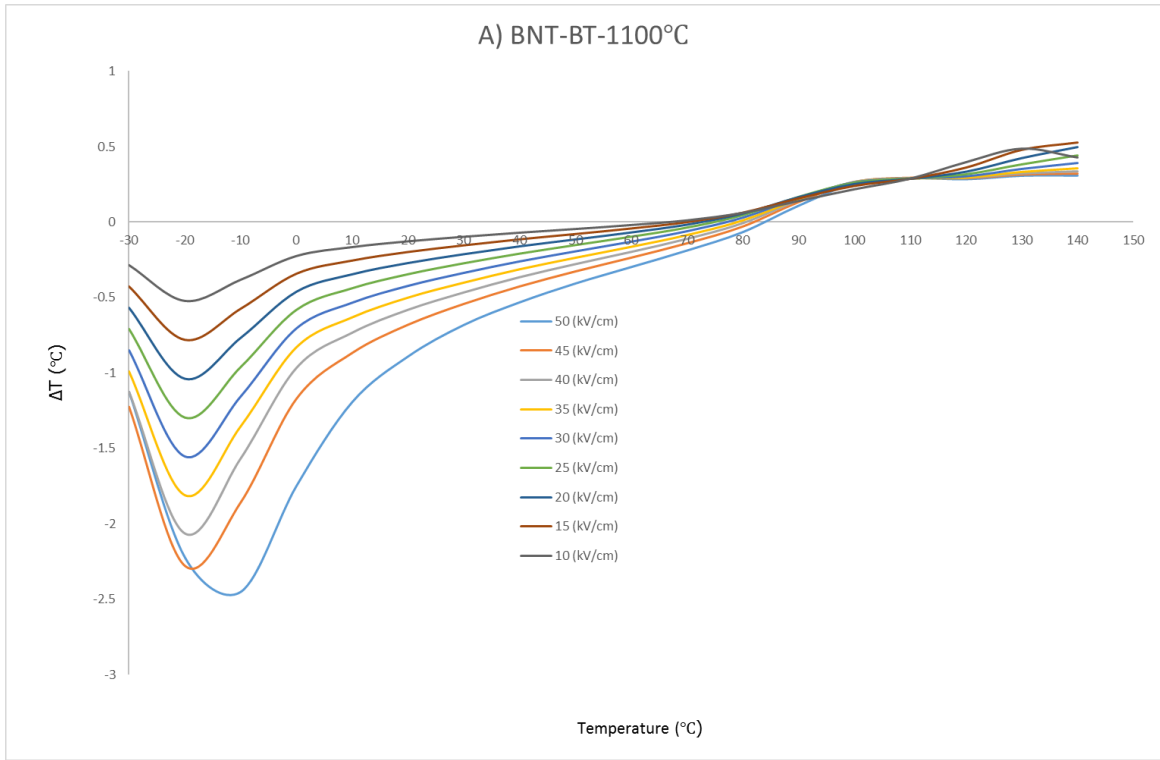
In this section, indirect measurements of sintered BNT-BT and BNT-BT-BF samples are reported and discussed.

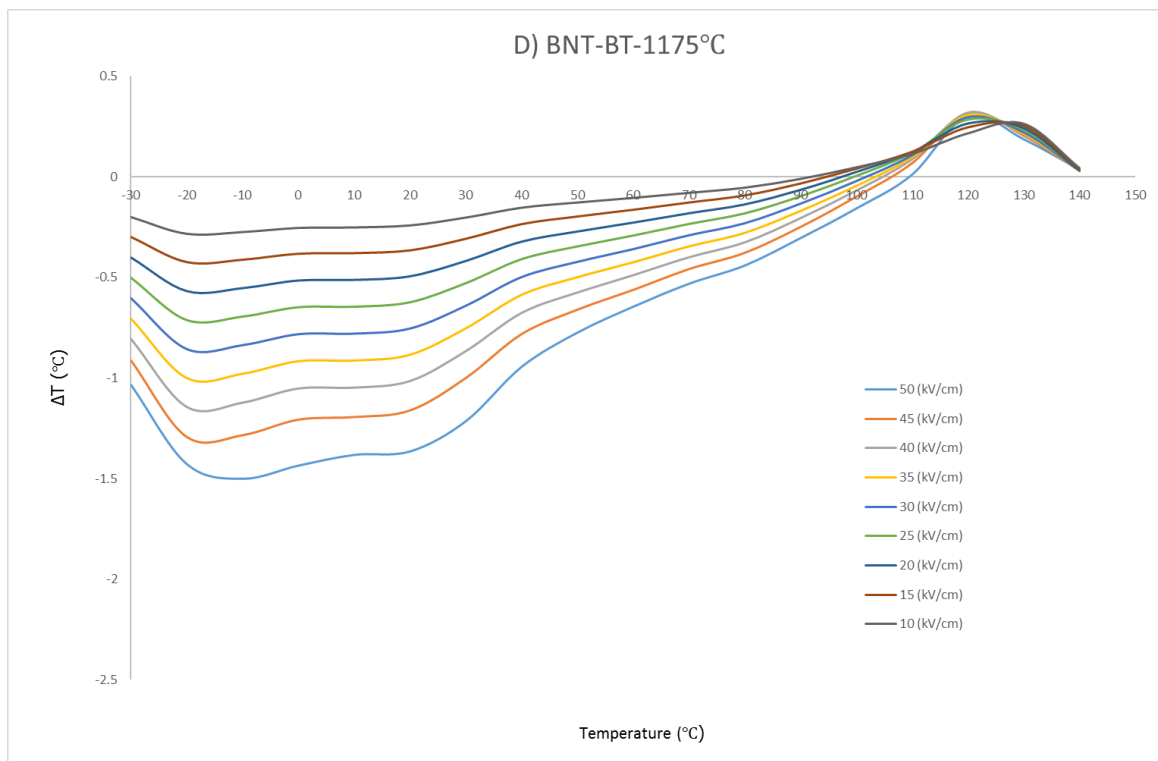
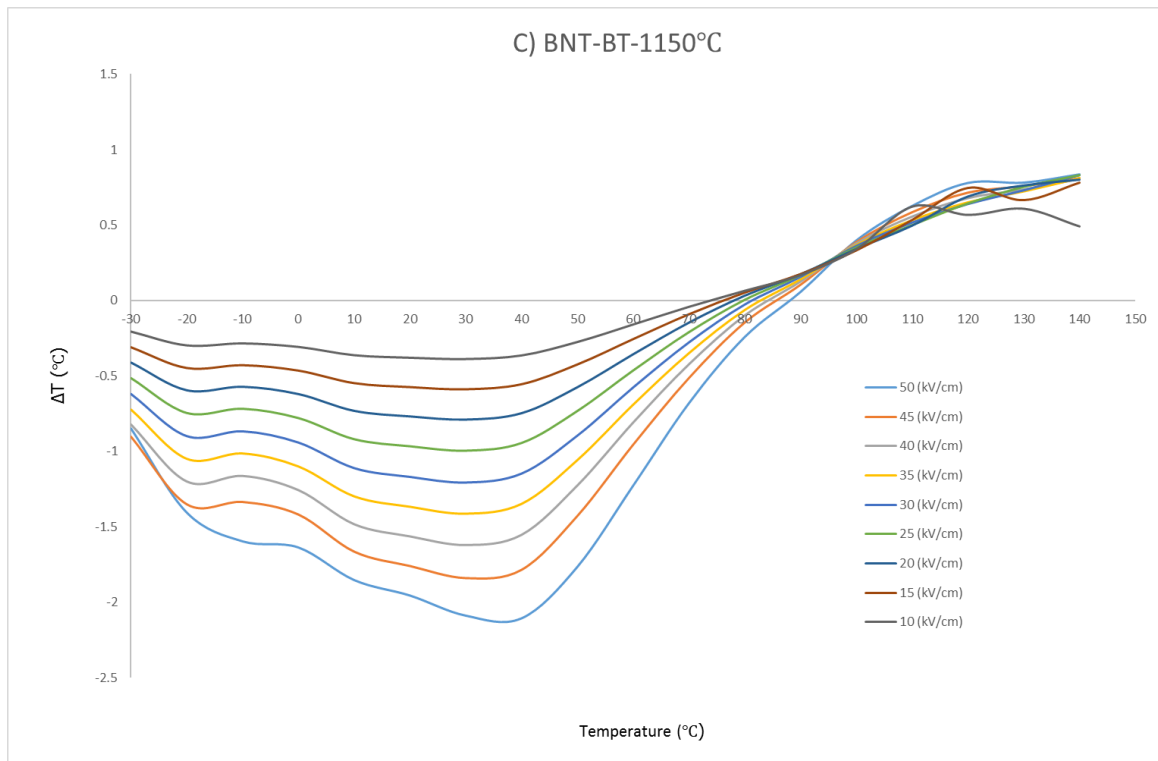
5.1.3.1 Indirect ECE measurement of pure BNT-BT

Figure 5-18 shows the ECE of BNT-BT sintered at 1100, 1125, 1150, 1175, and 1200°C measured between -30 to 125°C by the indirect method. The BNT-BT sample sintered at 1100°C shows the highest ECE ($\Delta T = -2.44^\circ\text{C}$) at around -10°C for 50 kV/cm. The ECE increases until -20 °C for the low electric field, after which the ECE decreases until around 80°C; then, it starts to show a positive ECE and it reaches around ($\Delta T = 0.35^\circ\text{C}$) at around 140°C for 50 (kV/cm). The BNT-BT sample sintered at 1125°C shows the highest ECE ($\Delta T = -2.92^\circ\text{C}$) at around -10°C for 50 kV/cm. The ECE increases for this sample until -20 °C, similarly to the BNT-BT sample sintered at 1100°C; after that, the ECE decreases until around 80°C, then it starts to show a positive ECE, and reaches around ($\Delta T = 0.63^\circ\text{C}$) at about 140°C for 50 kV/cm. The BNT-BT sample sintered at 1150°C shows the highest ECE ($\Delta T = -2.1^\circ\text{C}$) at around 40°C for 50 kV/cm. Then, the ECE is increased for this sample until 40°C; after that, the ECE decreases until about 80°C, and then it starts to show a positive ECE and reaches around ($\Delta T = 0.83^\circ\text{C}$) at about 140°C for 50 kV/cm. The BNT-BT sample sintered at 1175°C shows the highest ECE ($\Delta T = -1.50^\circ\text{C}$) at around -10°C for 50 kV/cm. The ECE was increased for this sample until about -20 °C and then, decreased until around 110°C; after that, it starts to show a positive ECE and reaches around ($\Delta T = 0.35^\circ\text{C}$) at about 140°C for 50 kV/cm. The BNT-BT sample sintered at 1200°C shows the highest ECE ($\Delta T = -1.30^\circ\text{C}$) at around -10°C for 50 kV/cm. The ECE increases for this sample until -20 °C, similarly to the BNT-BT sample sintered at 1175°C, and after that, the ECE is decreased until around 100°C; after that, it starts to show a positive ECE and reaches around ($\Delta T = 0.35^\circ\text{C}$) at about 140°C for 50 kV/cm.

All show the ECE as negative, which means that in adiabatic conditions, applying an electric field causes the entropy to increase, so the temperature decreases. The application of the electric field should align the dipoles in the direction of the applied electric field and decrease the entropy, but in the BNT-BT samples, it seems to have been increased. Figure 5-19 shows the polarisation-hysteresis loops of BNT-BT samples sintered at 1150°C measured from -30 to 150°C (the polarisation-electric loop has been

selected for some of the temperatures for more precise observation). The electric coercive field is decreased by a rise in the temperature, which reveals normal behaviour similar to most of the ferroelectric materials, but the remanant polarisation is increased until around 90°C and after that, decreases. There are two possible explanations for this: the first concerns the non-saturated hysteresis loop at a lower temperature, while the second is about the polarisation of the anti-ferroelectric phase, which also can be seen at room temperature and increase through a rise in the temperature. The loops show the saturated shape, which confirms that the electric field was sufficient for the samples. It has been proved that the anti-ferroelectric capacity exists in the BNT-BT at room temperature, as is explained in section 2.1.1.2.3.1. The anti-ferroelectric capacity starts to increase with a rise in the temperature and when the temperature reaches the ferroelectric-to-anti-ferroelectric transformation phase, it becomes the main phase in the structure. The anti-ferroelectric causes the contraction in the polarisation-electric field at high temperatures, as can be observed in Figure 5-19, and for the loops at 120 and 150°C. At these temperatures, the contraction can be observed for low electric fields, meaning that the applied electric field is not enough to align this phase, but with a higher electric field, this phase is aligned, so a normal loop can be observed for this composition. A rise in the polarisation due to a polarised anti-ferroelectric phase could be the reason for the negative ECE.





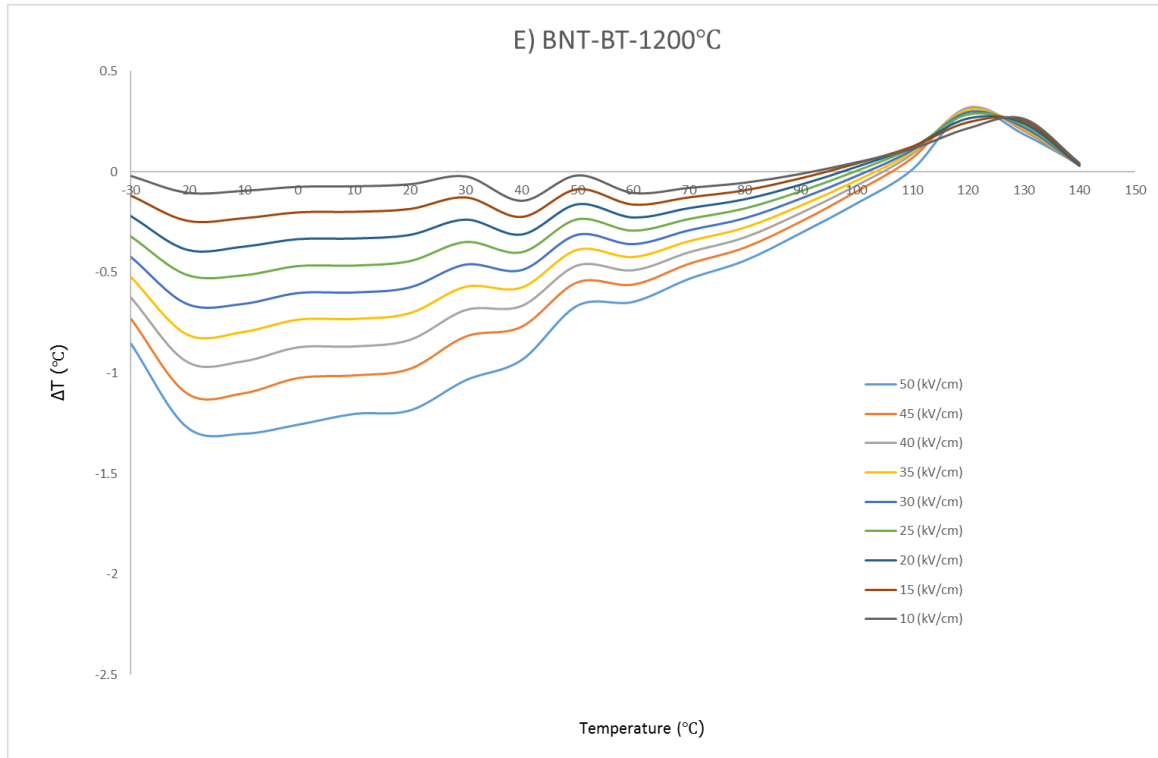


Figure 5-18: The ECE of BNT-BT sintered at A) 1100, B) 1125, C) 1150, D) 1175, and E) 1200°C measured between -30 and 140°C by the indirect method.

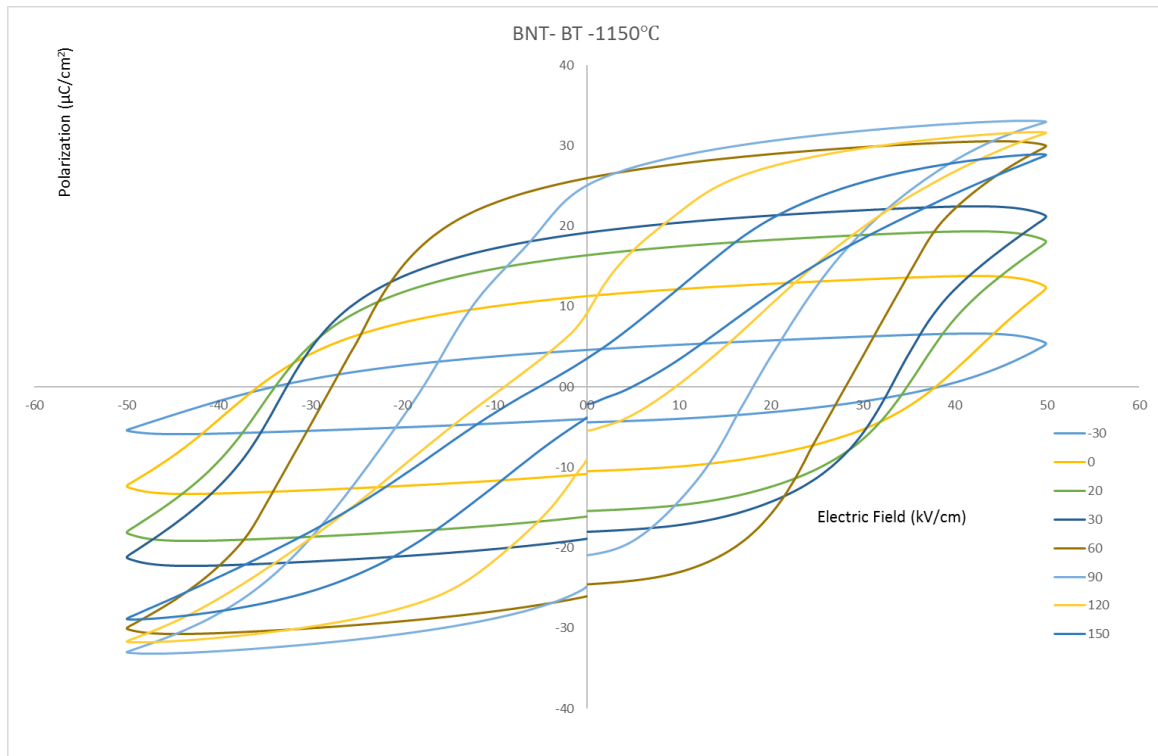
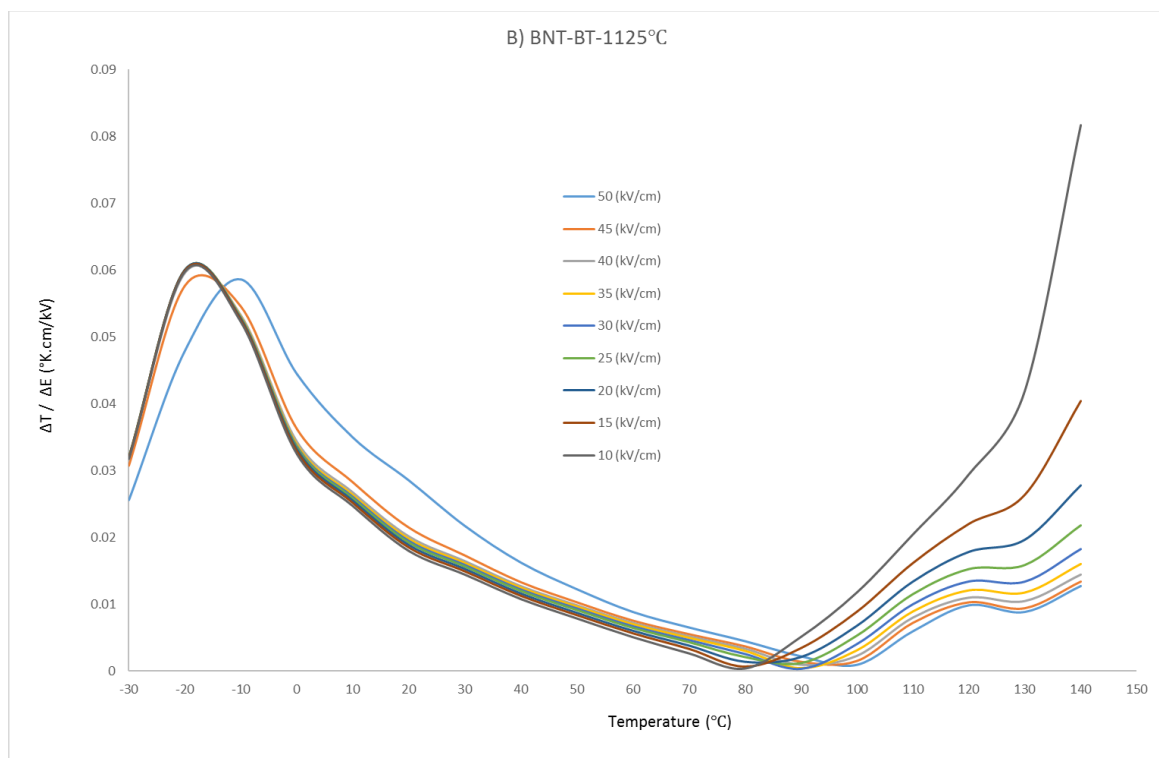
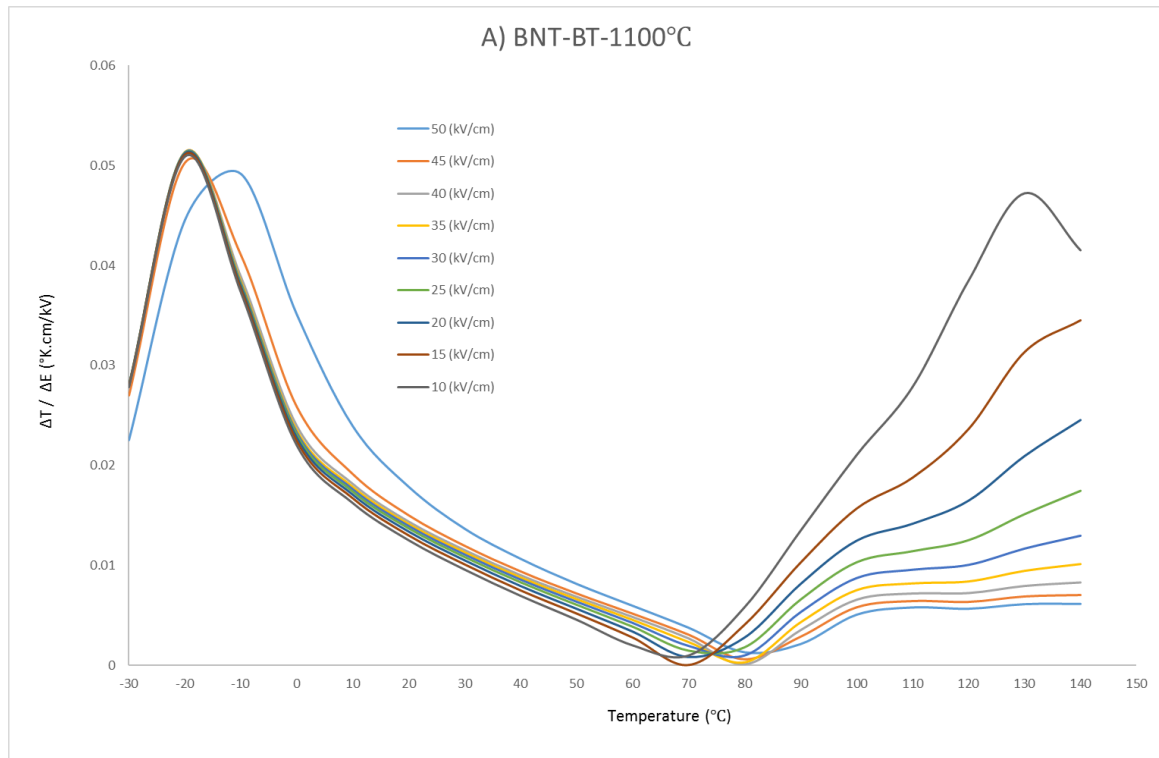
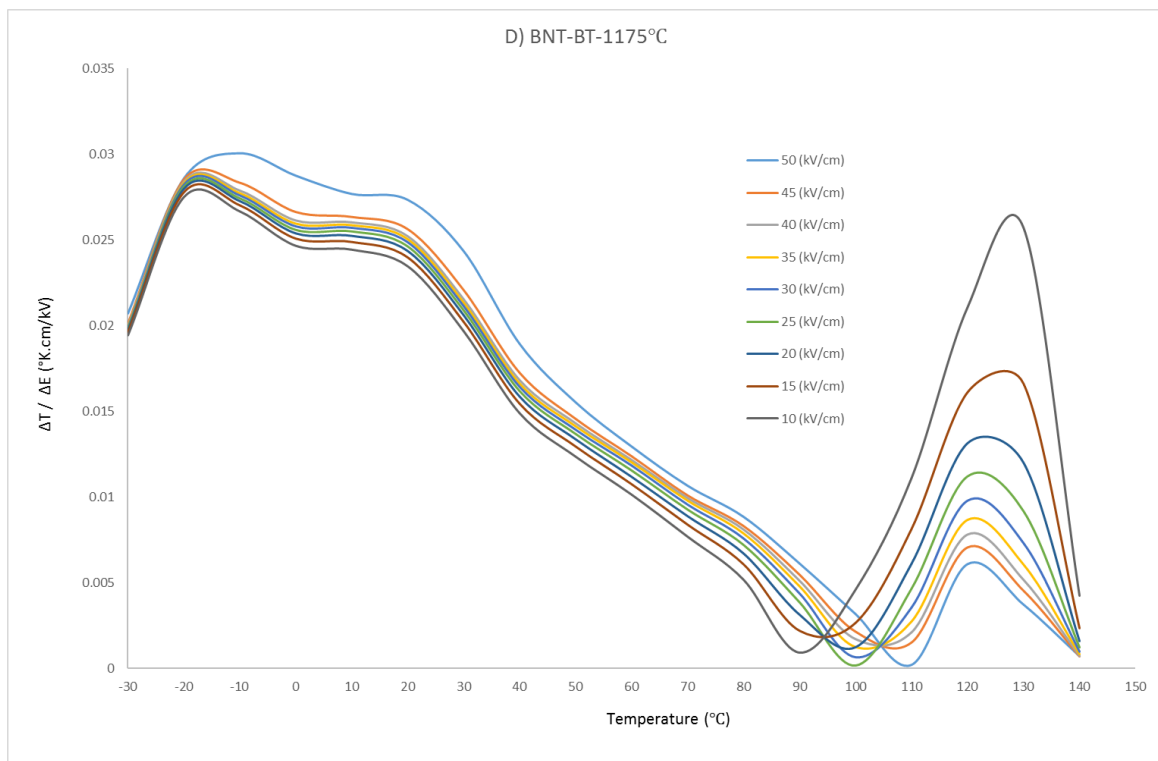
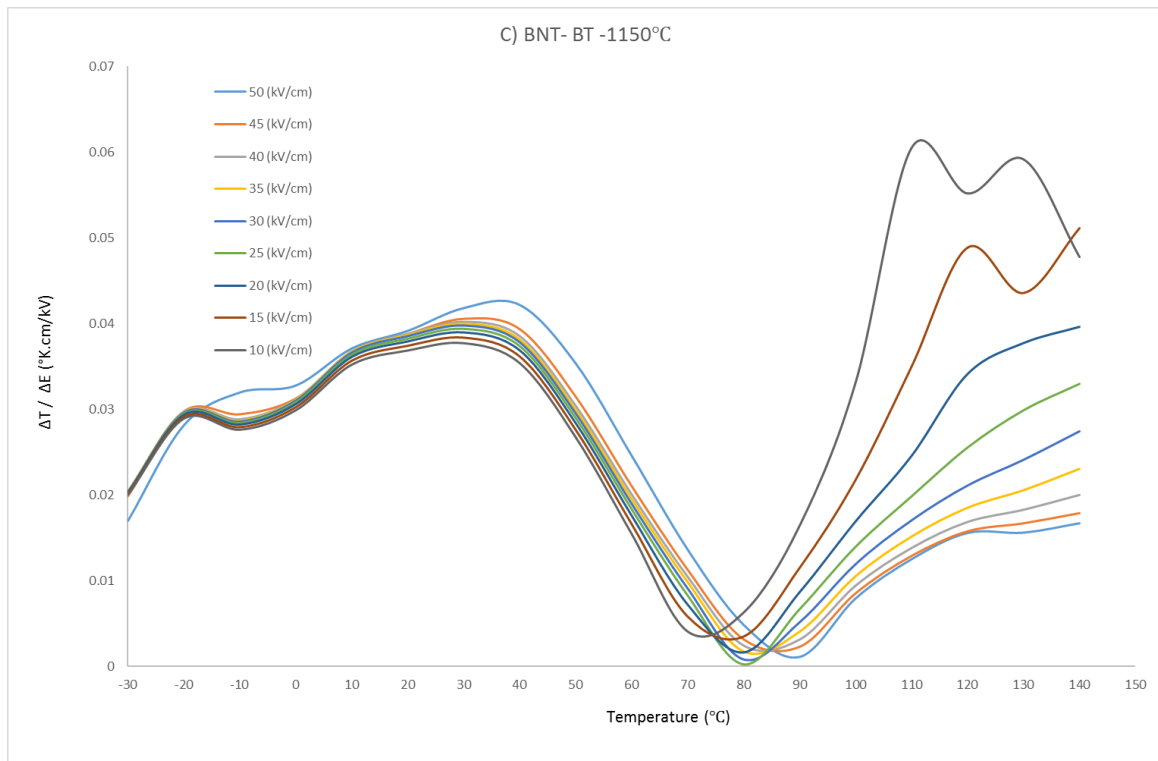


Figure 5-19: The polarisation-hysteresis loops of BNT-BT sintered at 1150°C measured from -30 to 150°C.

Figure 5-20 shows the ECE figure of merit of BNT-BT sintered at 1100, 1125, 1150, 1175, and 1200°C measured between -30 and 140°C by the indirect method. The BNT-BT samples

sintered at 1100, 1125, 1150, 1175, and 1200°C show the highest ECE figures of merit of 0.049, 0.058, 0.042, 0.030, and 0.026 K.cm/kV at -10, -10, 40, -10 and -10°C under 50 kV/cm, respectively.





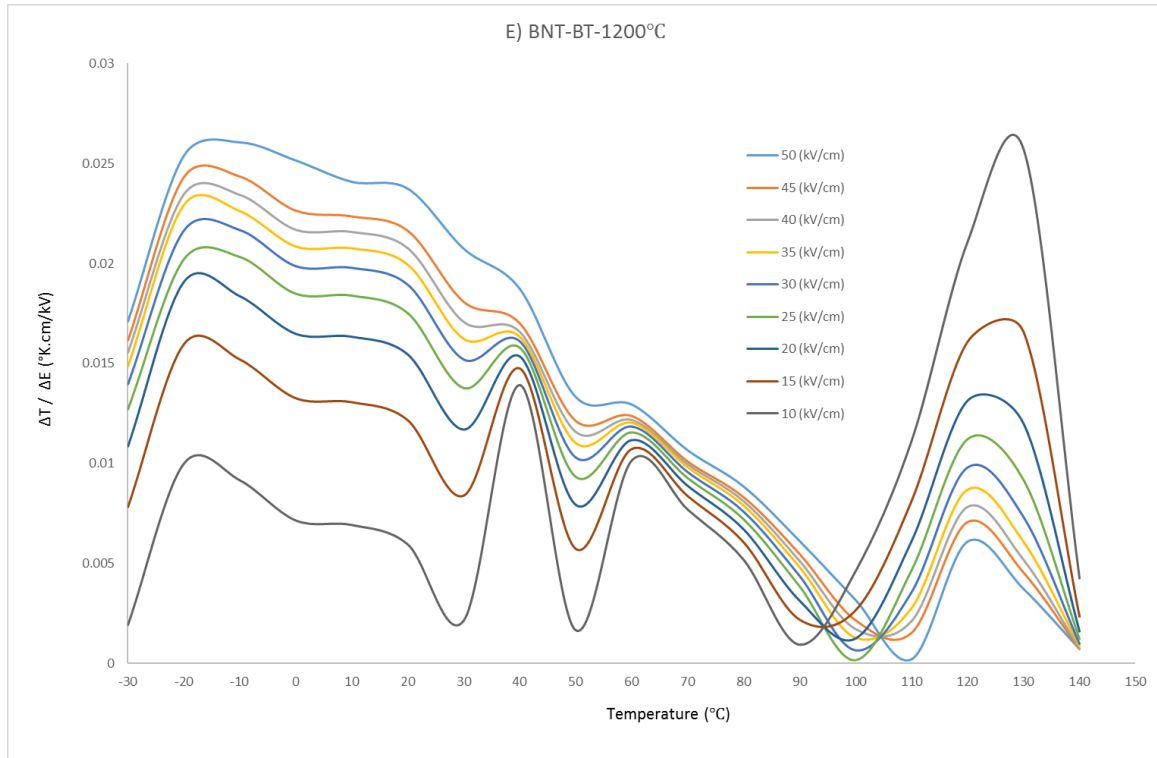
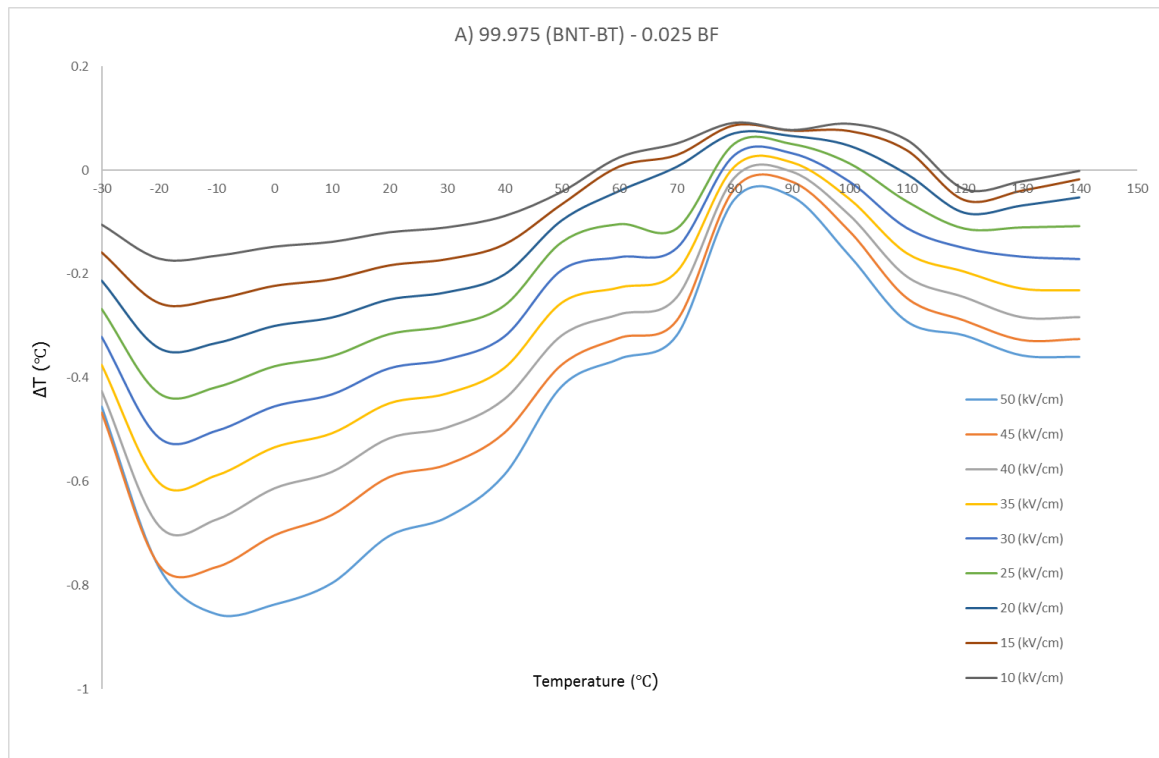


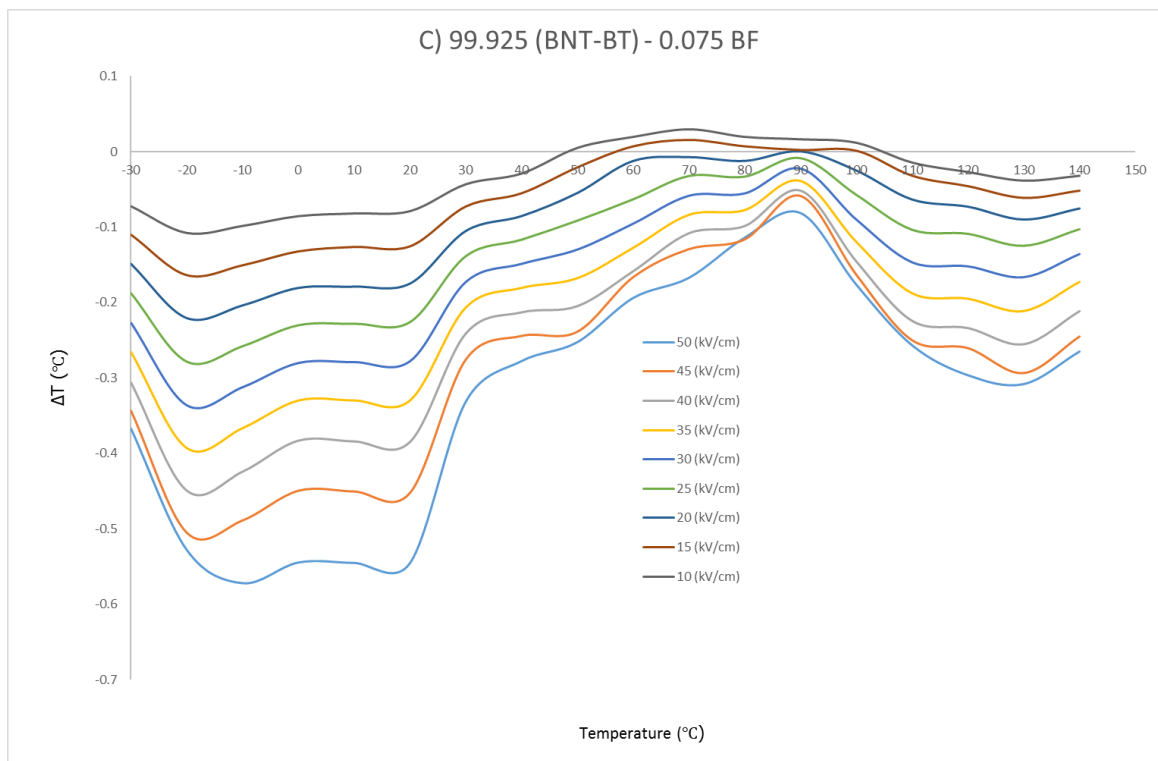
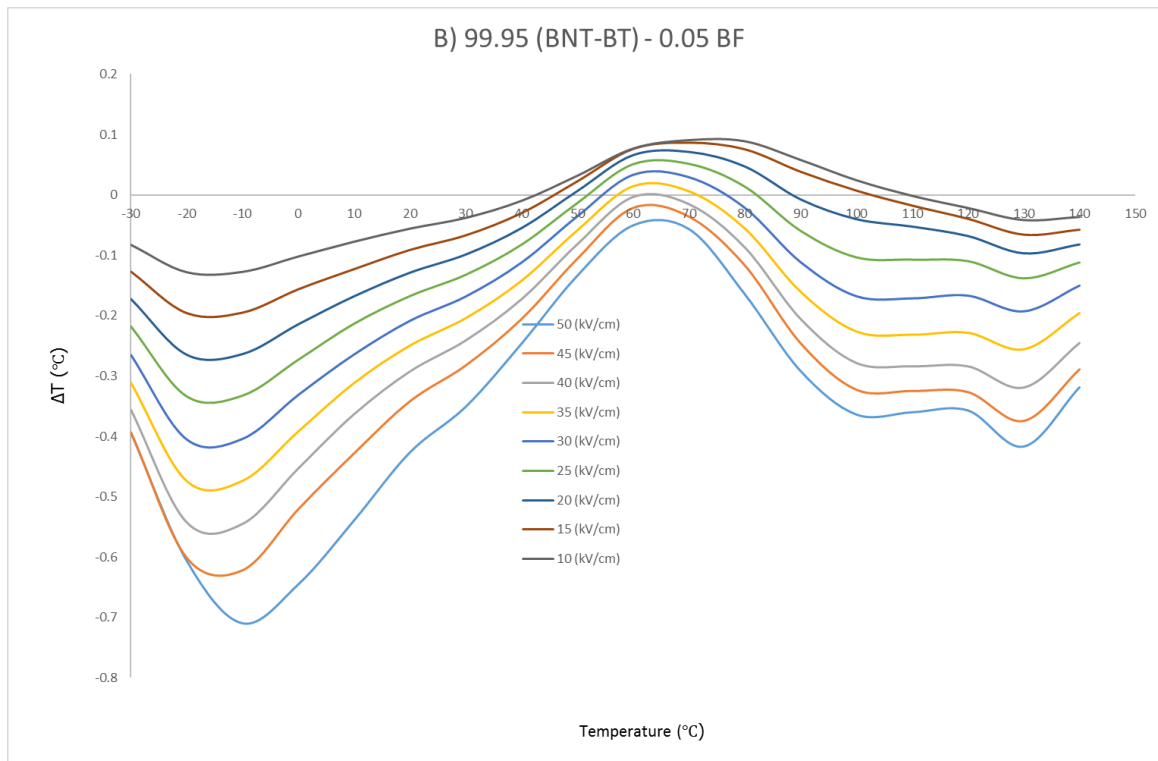
Figure 5-20: The ECE figures of merit of the BNT-BT samples sintered at A) 1100, B) 1125, C) 1150, D) 1175, and E) 1200°C measured between -30 and 140°C by the indirect method.

5.1.3.2 The indirect ECE measurements of BNT-BT-BF

Figure 5-21 shows the ECE of the (1-x) BNT-BT-x BF samples for x=0.025, 0.05, 0.075, and 0.1 measured between -30 and 140°C by the indirect method. 99.975 BNT-BT-0.025 BF shows the highest ECE ($\Delta T = -0.85^\circ\text{C}$) at around -10°C for 50 kV/cm. The ECE increases for this sample until -10°C and after that, it decreases until around 85°C; after that, it starts to increase and reaches around ($\Delta T = -0.35^\circ\text{C}$) at about 140°C for 50 kV/cm. 99.95 BNT-BT-0.05 BF shows the highest ECE ($\Delta T = -0.70^\circ\text{C}$) at around -20°C for 50 kV/cm. The ECE is increased for this sample until -10°C and then, the ECE decreases until around 70°C; after that, it starts to increase and it reaches around ($\Delta T = -0.41^\circ\text{C}$) at about 130°C for 50 kV/cm. 99.925 BNT-BT-0.075 BF shows the highest ECE ($\Delta T = -0.67^\circ\text{C}$) at around -20°C for 50 kV/cm. The ECE increases for this sample until -10°C and then, the ECE decreases until around 90°C; after that, it starts to increase and reaches around ($\Delta T = -0.3^\circ\text{C}$) at about 130°C for 50 kV/cm. 99.9 BNT-BT-0.1 BF shows the highest ECE ($\Delta T = -0.46^\circ\text{C}$) at around -20°C for 50 kV/cm. The ECE is increased for this sample until -10°C and after that, the ECE decreases until around 80°C, after which it starts to increase and reaches around ($\Delta T = -0.31^\circ\text{C}$) at about 130°C for 50 kV/cm. The ECE is decreased for the

composition containing BF and is further decreased by an addition of more BF to the BNT-BT. The addition of BF causes a diversion in the MPB of the BNT-BT, as is explained in section 4.3.1. A rotation of the dipoles is easier at the MPB due to the flattening of the energy barrier between the different phases, so the ECE decreases when the BF makes this diversion. Compared to BNT-BT, the ECE is more uniform at room temperature, and the temperature has been decreased to the point where the ECE reaches almost zero from around 70-90°C to 50-70°C, due to the effect of the BF in the reduction of depolarisation temperature, which can make it more practical for room temperature applications.





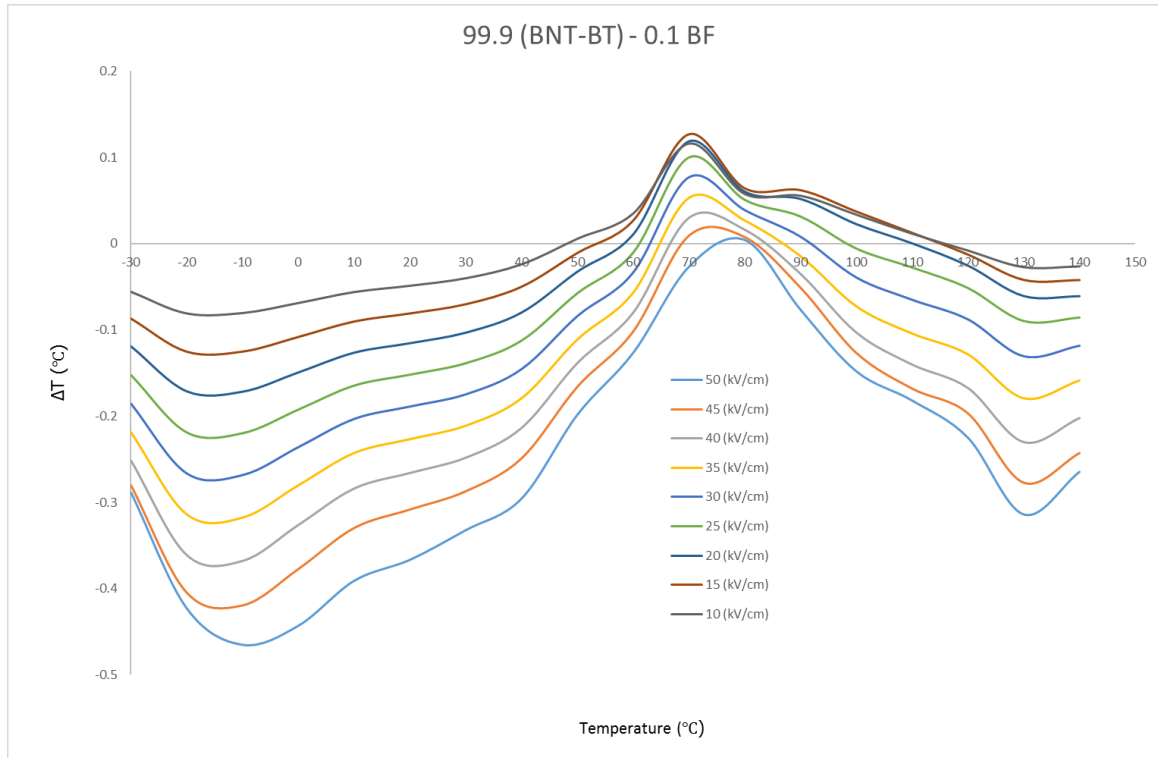
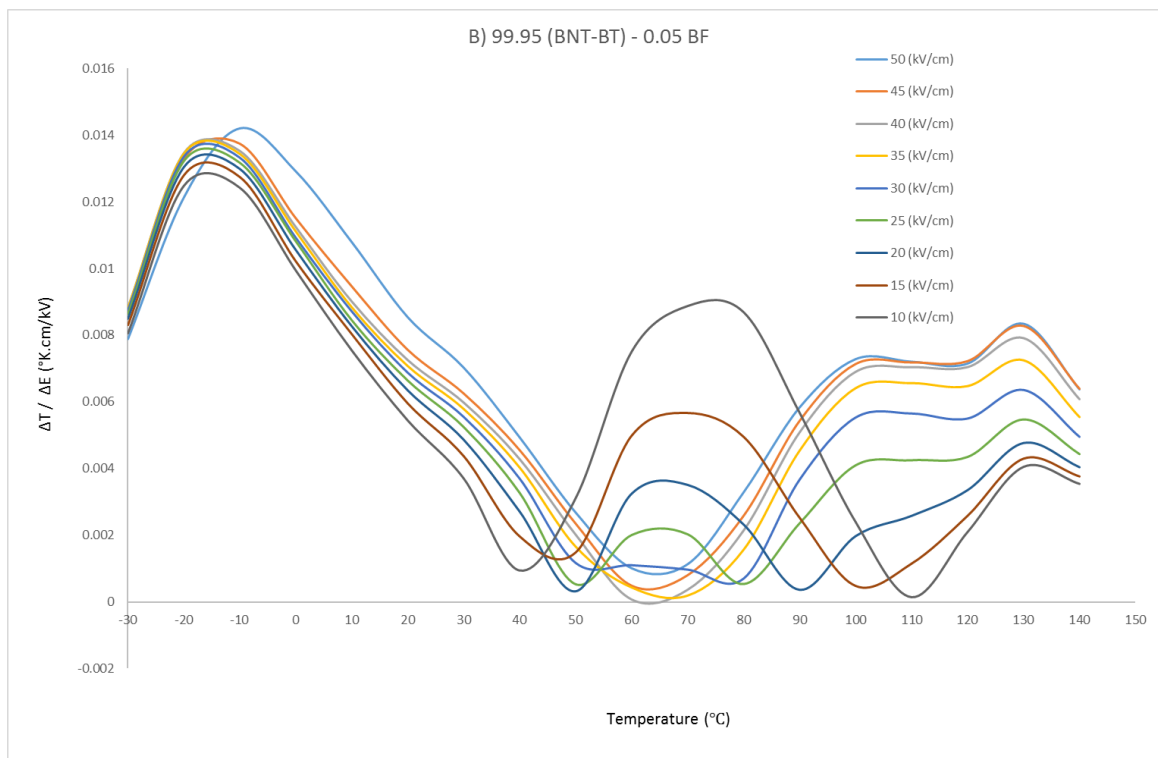
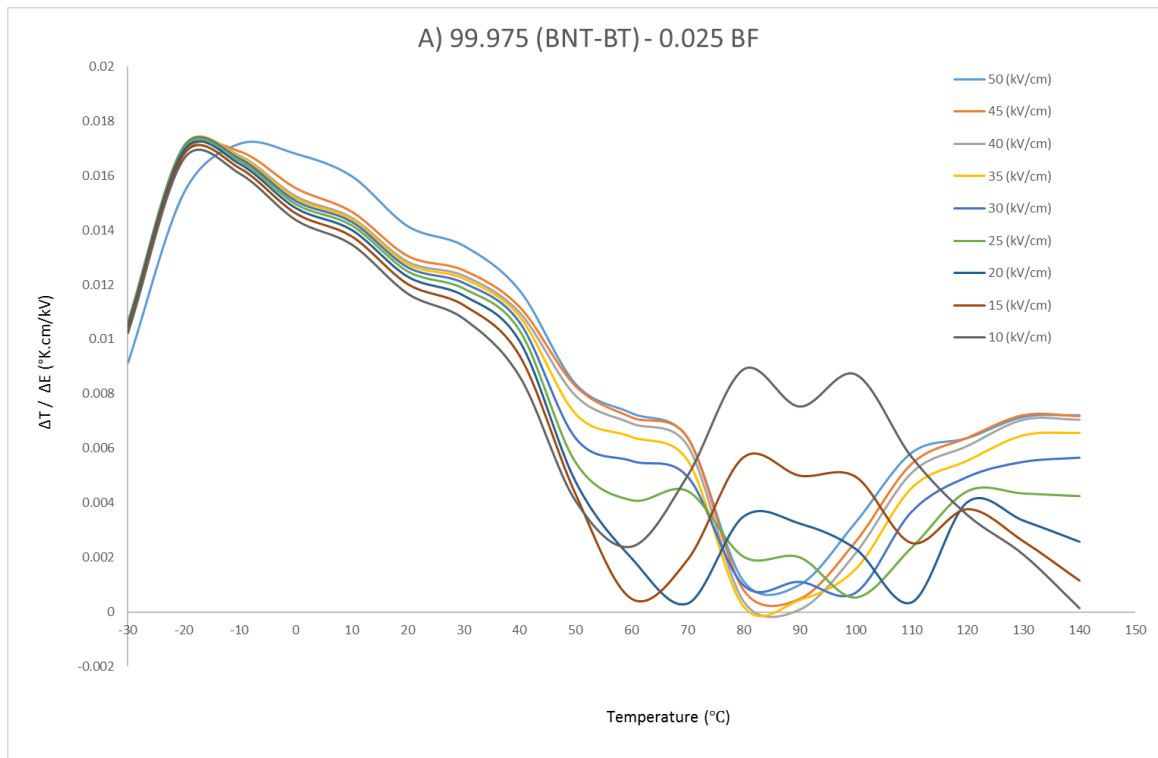


Figure 5-21: The ECE of the (1-x) BNT-BT-x BF samples for x A) 0.025, B) 0.05, C) 0.075, and D) 0.1 measured between -30 and 140°C by the indirect method.

Figure 5-22 shows the ECE figure of merit of the (1-x) BNT-BT-x BF samples for x=0.025, 0.05, 0.075, and 0.1 measured between -30 and 140°C by the indirect method. The (1-x) BNT-BT-x BF samples for x=0.025, 0.05, 0.075, and 0.1 show the highest ECE figures of merit of 0.017, 0.014, 0.011, and 0.009 K.cm/kV at -10°C for all of them, under 50 kV/cm, respectively. This shows that the addition of the BF to the BNT-BT decreases the ECE figure of merit.



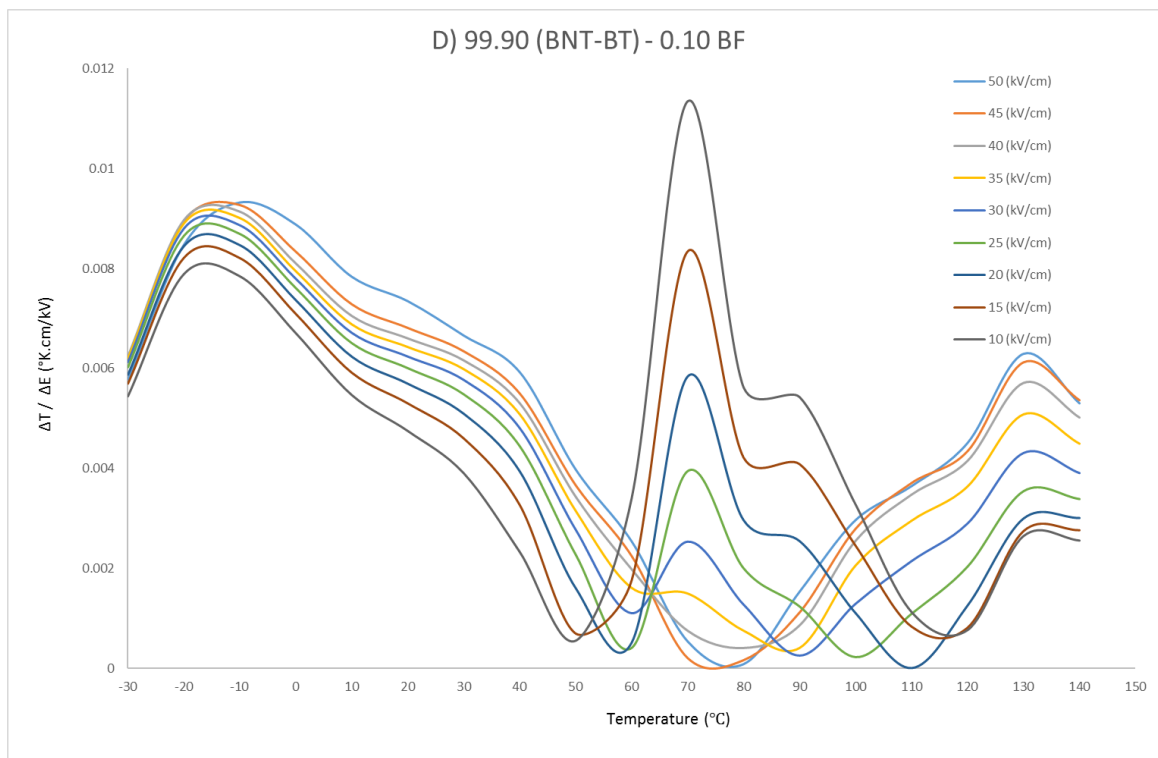
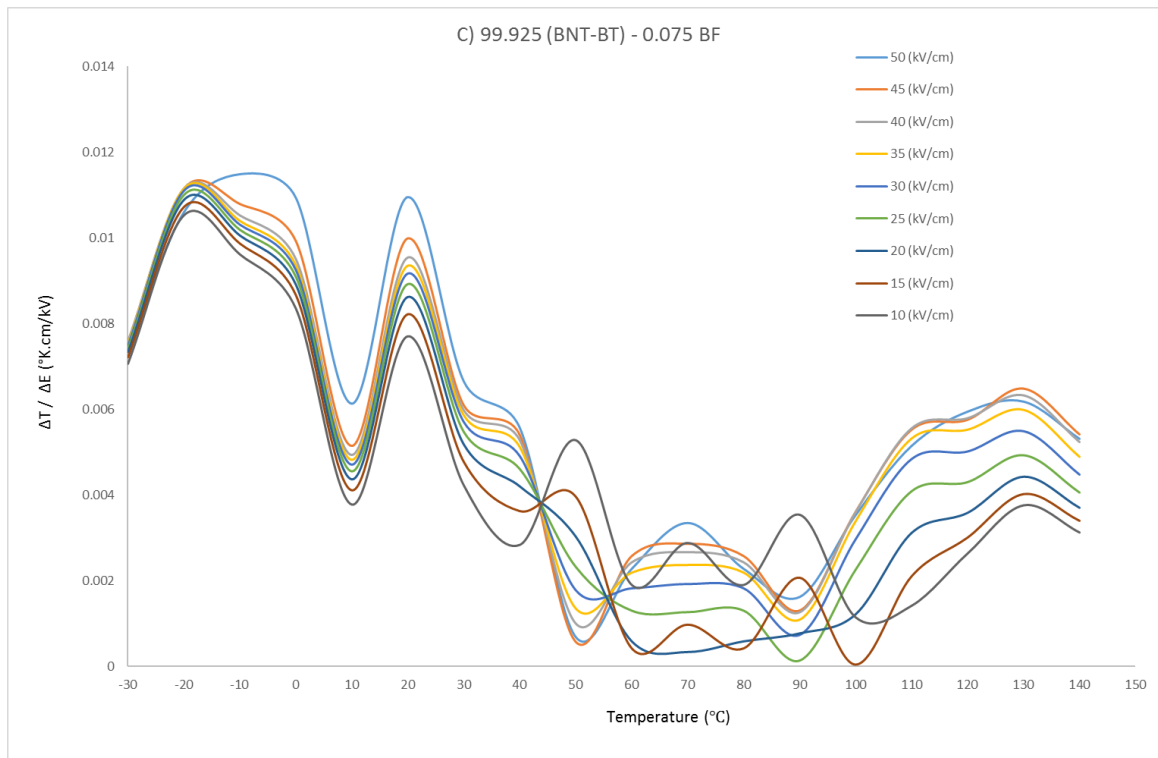


Figure 5-22: The ECE figures of merit of the (1-x) BNT-BT-x BF samples for x A) 0.025, B) 0.05, C) 0.075, and D) 0.1 measured between -30 and 140°C by the indirect method.

5.1.3.3 The indirect ECE measurement of BNT-BT deficient samples

Figure 5-23 shows the ECE of the BNT-BT deficient sample sintered at 1125°C and measured between -30 and 140°C by the indirect method. The BNT-BT deficient samples show the highest ECE ($\Delta T = -1.65^\circ\text{C}$) at around 0°C for 50 kV/cm. The ECE increases for this sample until 0°C and after that, the ECE decreases until around 60°C; then, it starts to show a positive ECE and reaches around ($\Delta T = 0.68^\circ\text{C}$) at about 110°C for 50 kV/cm. The ECE transfers to lower temperature compared to the BNT-BT due to the effect of the deficiency in the decrease of the depolarisation temperature. The ECE is decreased compared to pure BNT-BT, but it should be considered that the relative density decreases from 97 to 94% for this composition. It shows a higher ECE in comparison with the BNT-BT, with 95% of relative density (for the sample sintered at 1175°C).

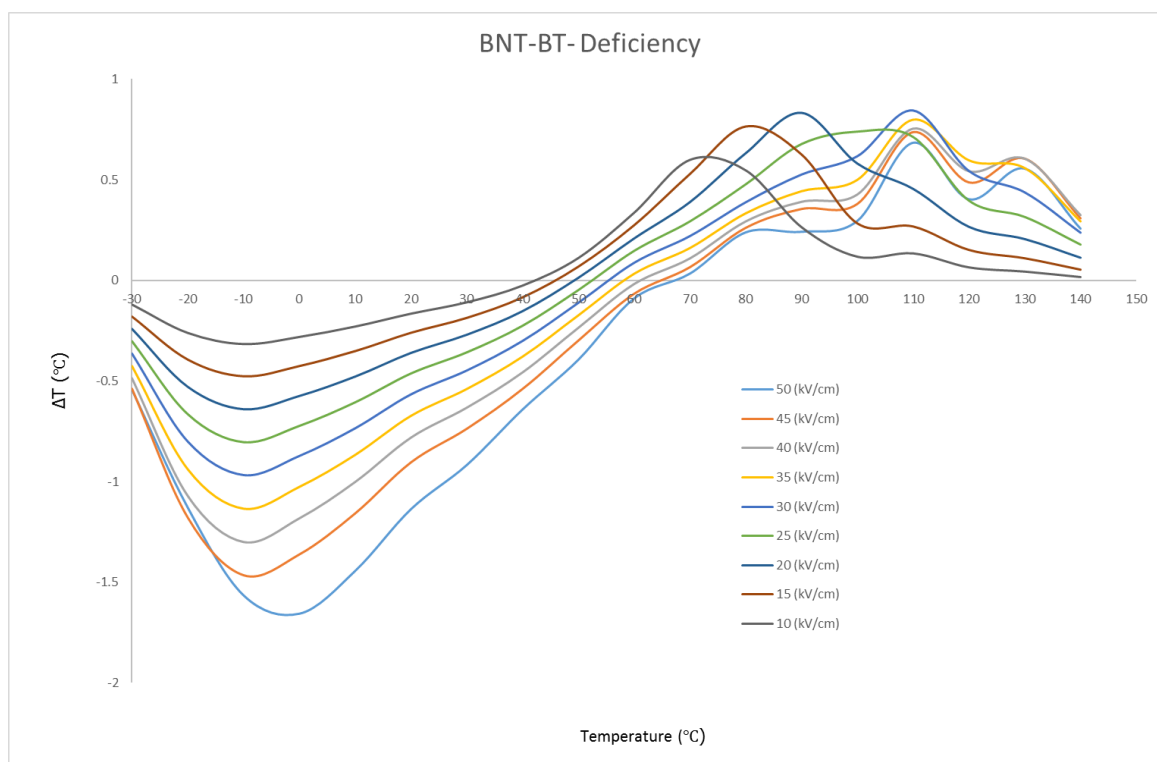


Figure 5-23: The ECE of the BNT-BT deficient samples sintered at 1125°C measured between -30 and 140°C by the indirect method.

Figure 4-24 shows the ECE figure of merit of the BNT-BT deficient samples sintered at 1125°C between -30 and 140°C by the indirect method. The highest ECE figure of merit is 0.031K.cm/kV at -10°C under 50 kV/cm.

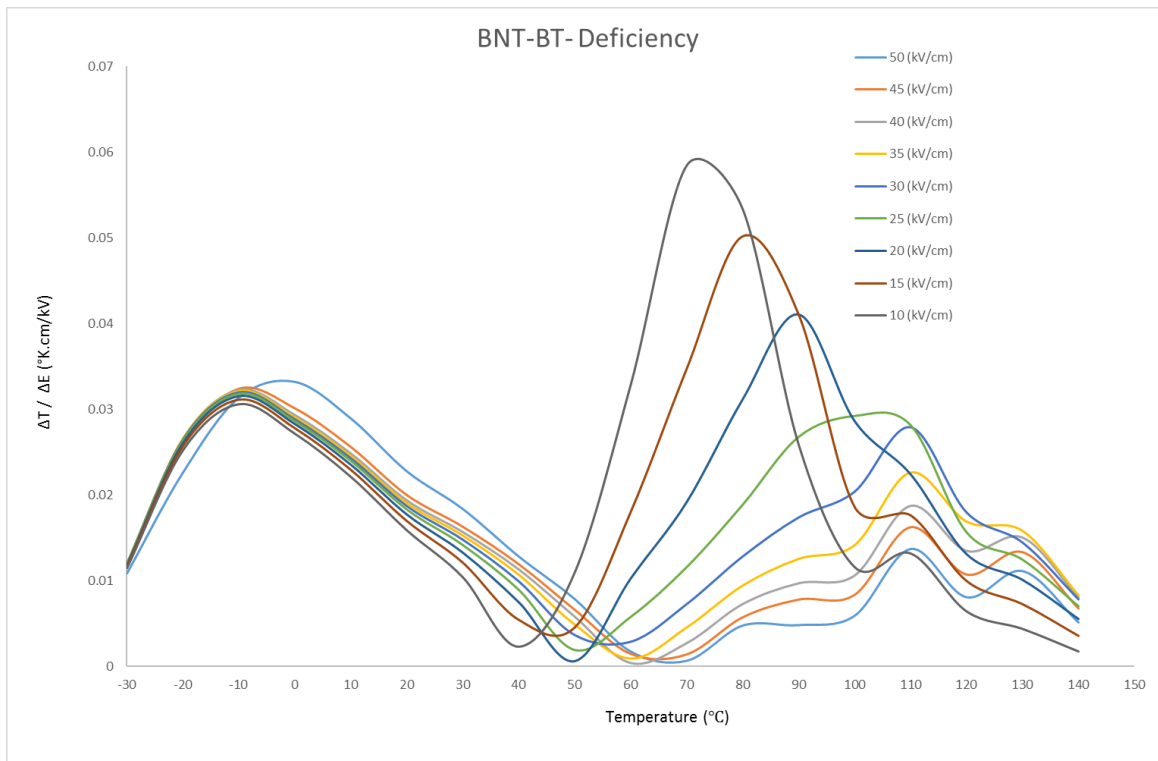


Figure 5-24: The ECE figure of merit of the BNT-BT deficient samples sintered at 1125°C measured between -30 and 140°C by the indirect method.

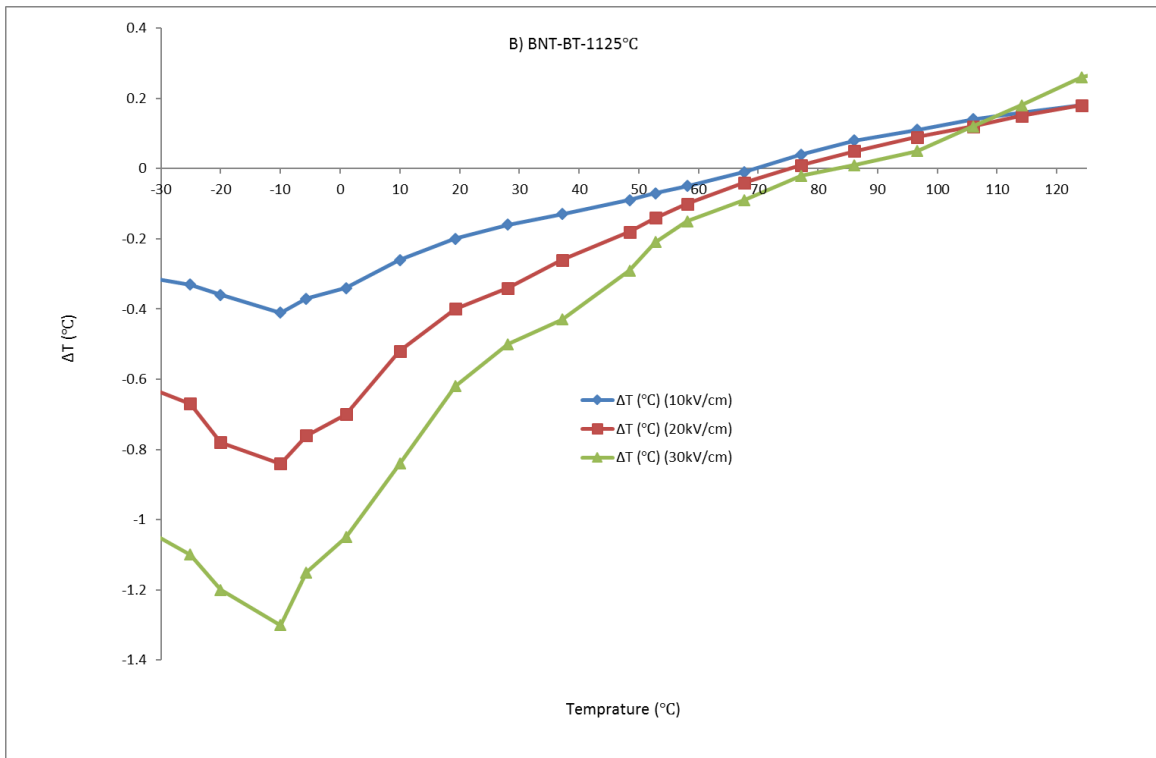
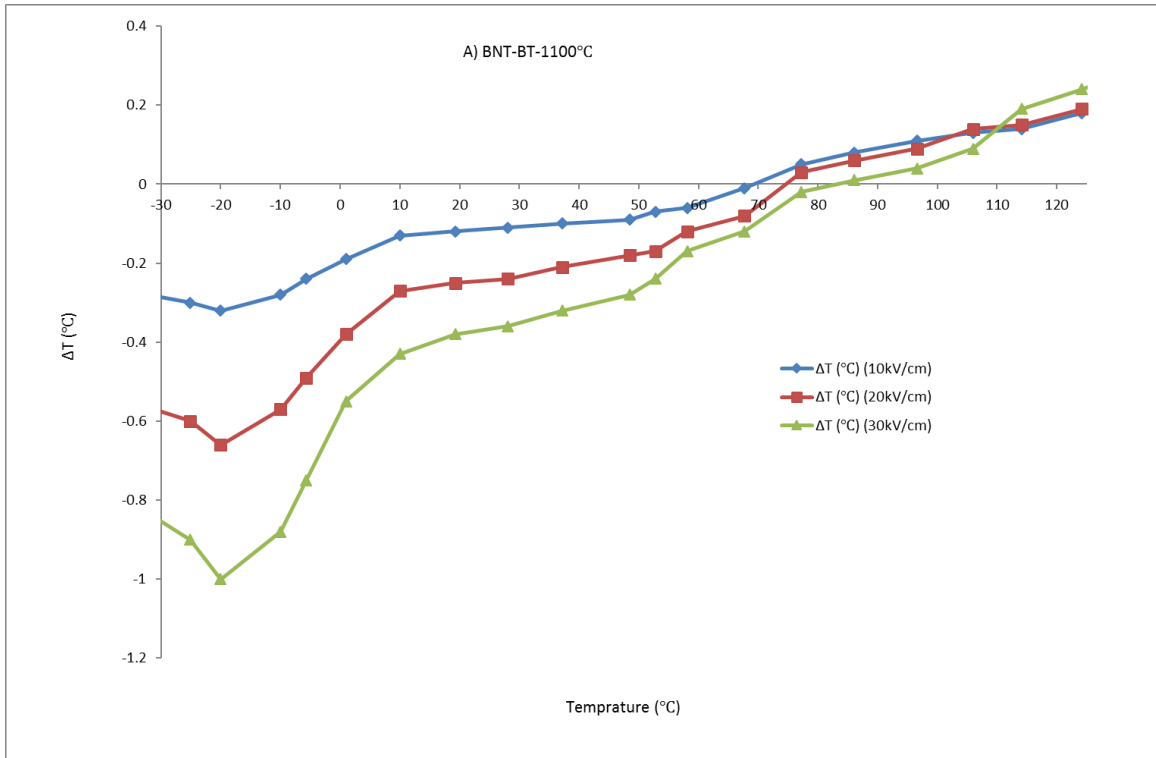
5.1.4 The direct ECE measurement of BNT-BT-based materials

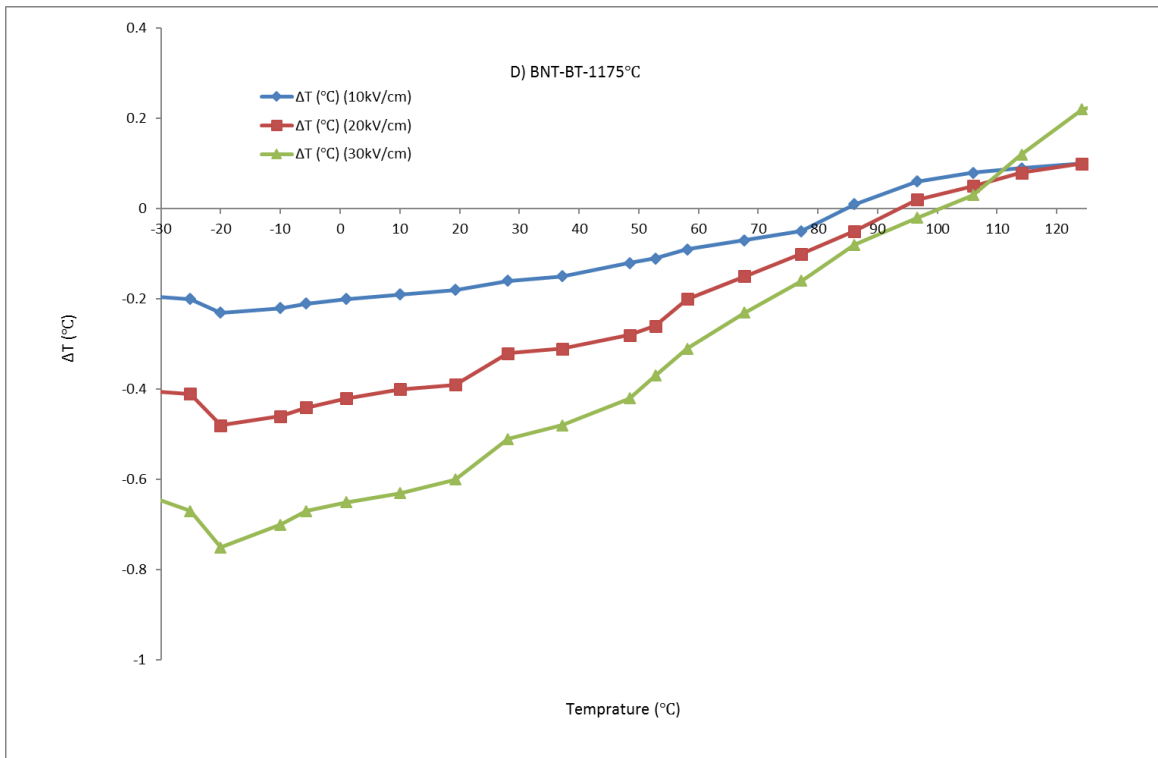
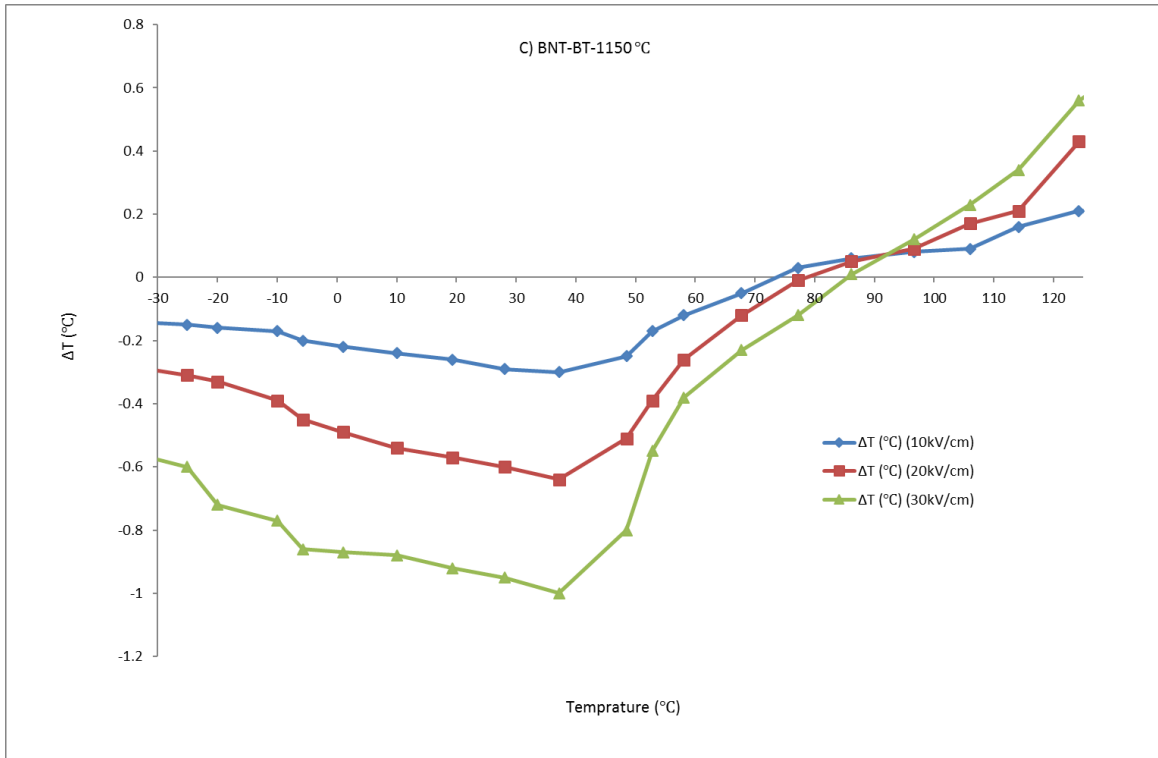
As explained in section 3.13, a device was designed to make the direct reading and after that, the ECE of the samples was measured and plotted for the BNT-BT-based materials.

5.1.4.1 The direct ECE measurement of pure BNT-BT

Figure 5-25 shows the ECE of the pure BNT-BT sintered at 1100, 1125, 1150, 1175, and 1200°C measured between -30 and 125°C by the direct method. As can be seen, the ECE of pure BNT-BT is increased by a rise in measurement temperature for all the samples and after that, it decreases to around 70-90°C, and then starts to show a positive ECE. The highest ECE of BNT-BT is $\Delta T = -1, -1.3, -1, -0.75,$ and -0.51°C at $-20, -10, 37, -20,$ and -20°C for samples sintered at 1100, 1125, 1150, 1175, and 1200°C, respectively, under 30 kV/cm. The ECE measured by the direct method shows a similar result to the indirect method, which confirms it, however, the measured ECE is lower than for the indirect method. As explained for BCZT, the direct method measurements are almost 75% of those of the indirect method due to the non-adiabatic nature of the device. In addition, as explained in section 2.3.2, the real ECE for relaxor materials is higher than the ECE measured by the indirect method, and the use of the

Maxwell relations. The direct ECE measurement of the BNT-BT sample shows almost 85 to 90% of the indirect method, which in comparison with BCZT, a normal ferroelectric, is closer to the indirect method. This difference confirms that the indirect method results in some diversion from the real ECE for relaxor materials. The Maxwell relations use only the primary pyroelectric coefficient to measure the ECE, and the formula does not contain the secondary pyroelectric coefficient, which is quite high for the relaxor materials, because of the electrostriction behaviour. It has also been shown that there are polar nano regions in this composition that show nonergodic behaviour, which results in a diversion in the Maxwell relation, which is defined for ergodic systems. For this reason, the indirect measurement leads to some deviation from the real ECE for those materials, and these experiments show that this is at least 10-15%. The E_c of the BNT-BT is about 37 kV/cm [10]; the value that is measured and used for the calculation of the indirect ECE at 30°C is around 50 kV/cm, while the maximum of the electric field is 30 kV/cm, used for the direct measurement. BNT-BT has an MPB of rhombohedral and tetragonal phases, while also possessing an anti-ferroelectric phase. This electric field does not lead to saturated polarisation in BNT-BT, so the weakly polar phase or anti-ferroelectric phase start to be reoriented through an application of the electric field (the samples were un-poled for the ECE measurements). A lower electric field than the coercive electric field cannot completely align the dipoles of these phases, so the entropy increases through an application of the electric field, and therefore the temperature decreases for this composition. The rise in temperature decreases the E_c for this composition, so the ECE starts to decrease until around 70 to 90°C. The reduction in the E_c causes the polarisation to reach the saturated state, so a rise in the temperature leads to a lower ECE. After that, there is an anti-ferroelectric phase in this composition, which causes a reduction in the polarisation and the ECE starts to show a positive effect.





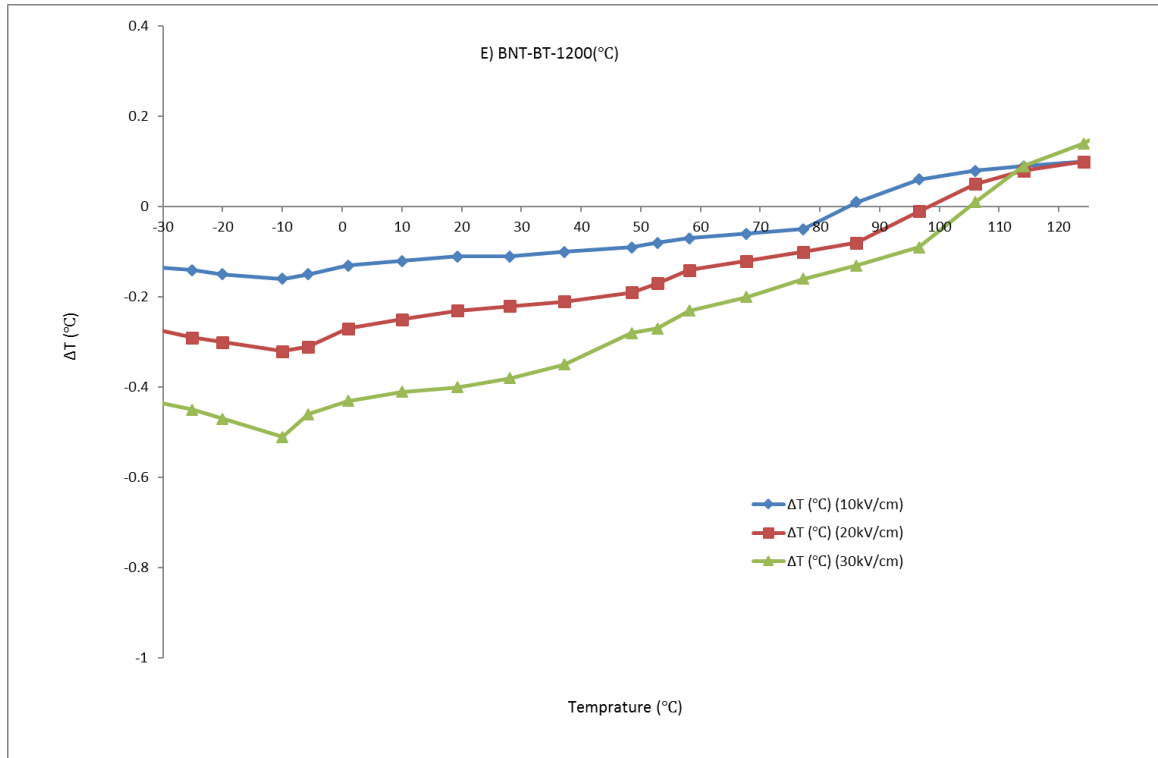
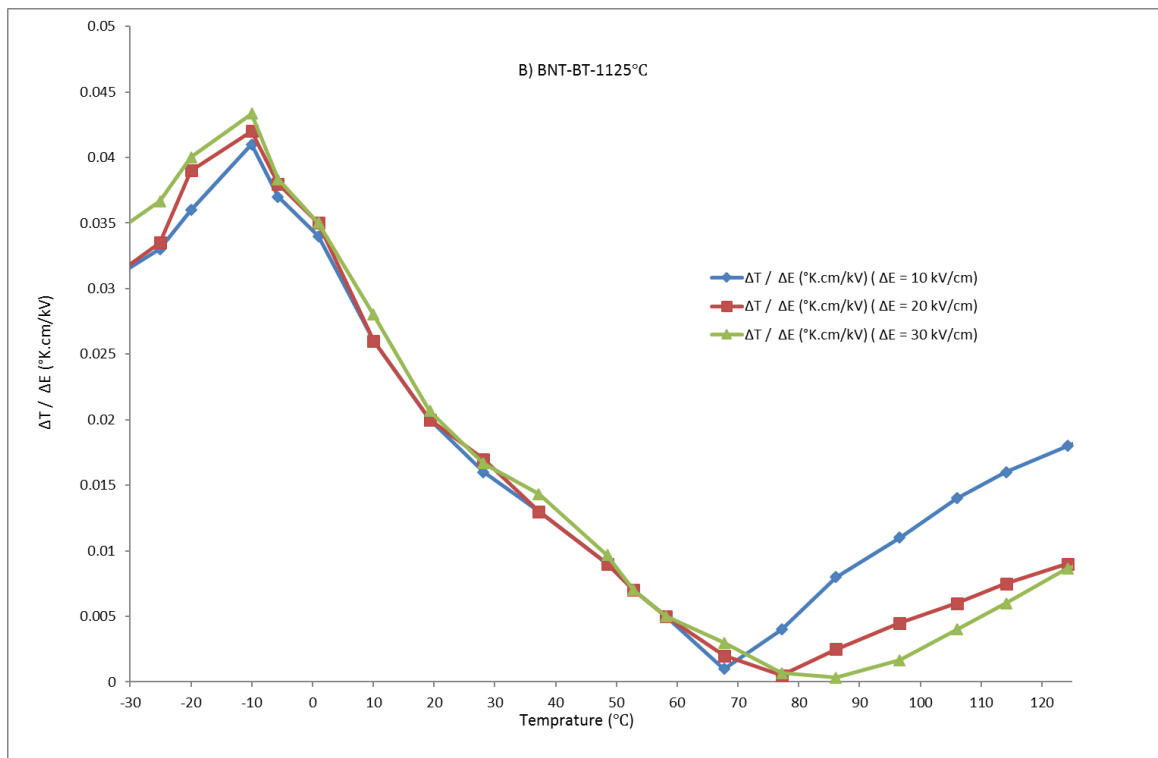
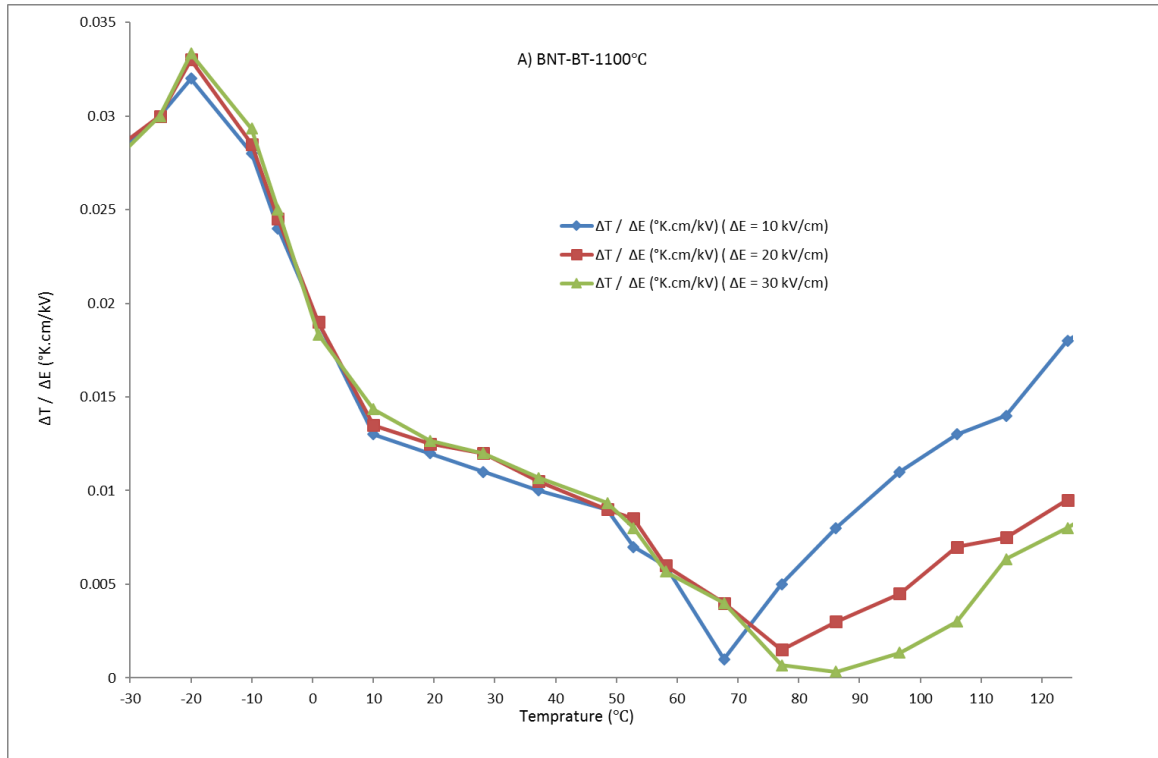
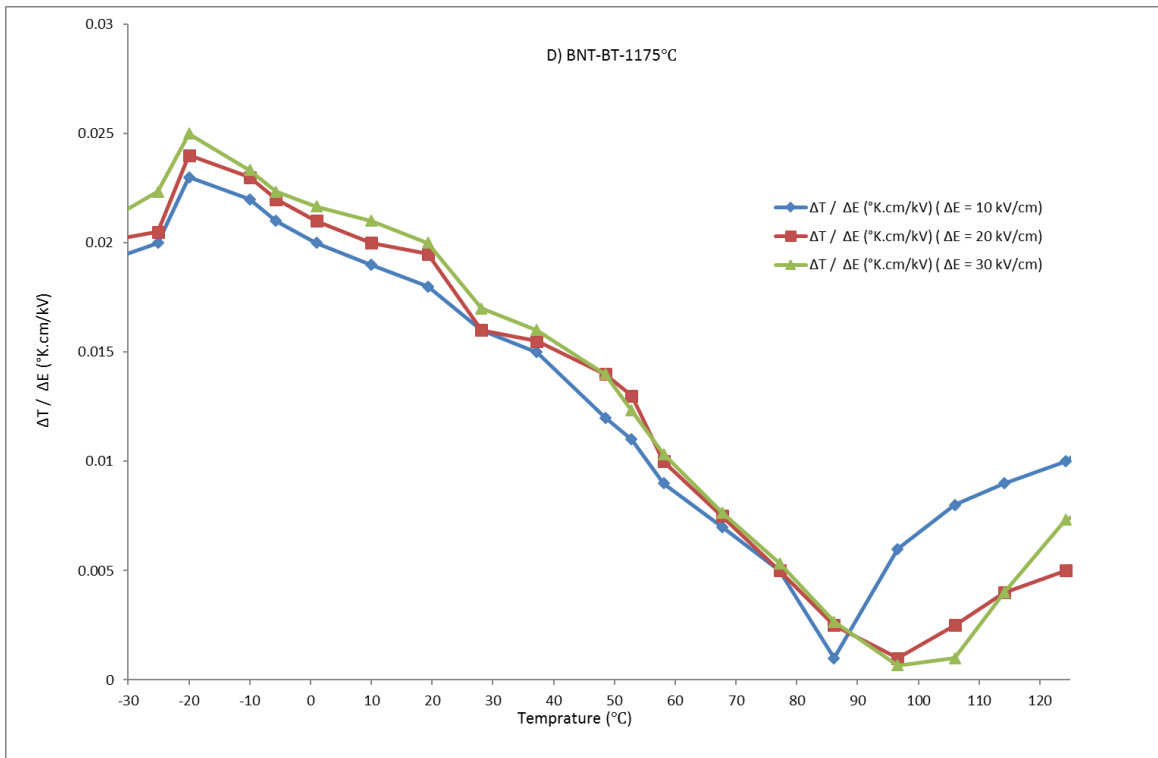
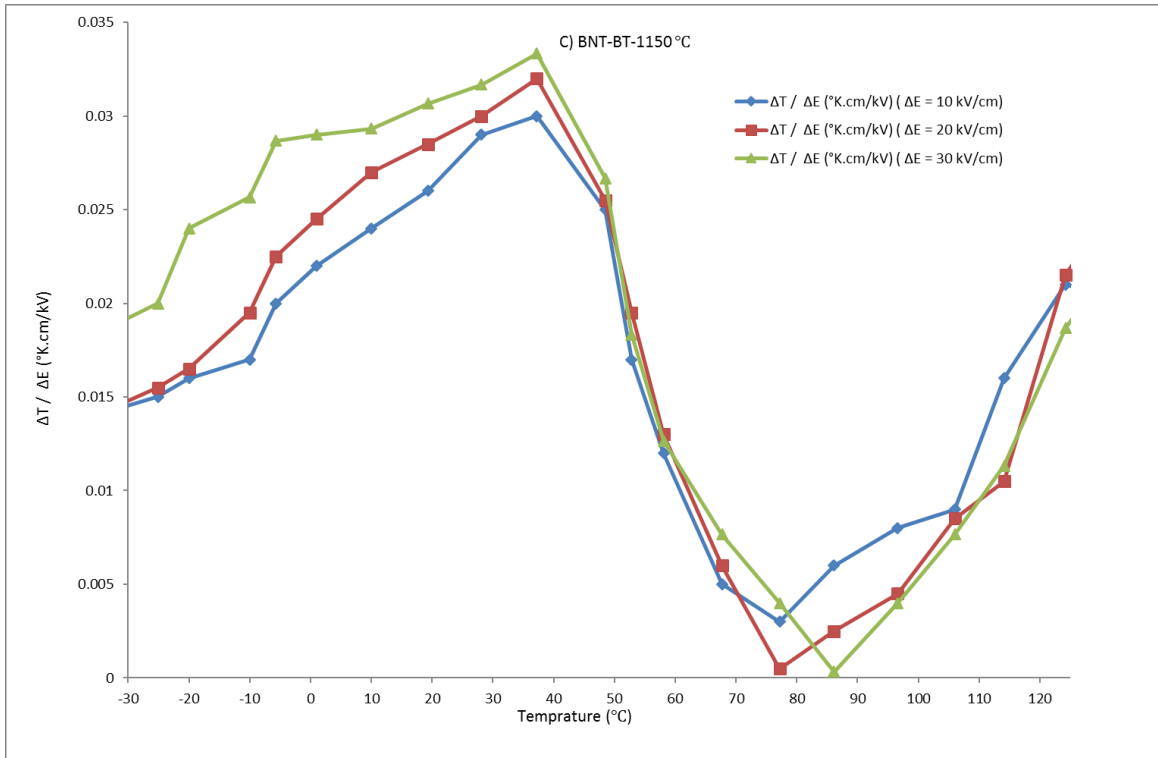


Figure 5-25: The ECE of the pure BNT-BT sintered at A) 1100, B) 1125, C) 1150, D) 1175, and E) 1200°C measured between -30 and 125°C by the direct method.

Figure 5-26 shows the ECE figure of merit of the pure BNT-BT sintered at 1100, 1125, 1150, 1175, and 1200°C between -30 and 125°C by the direct method. The highest ECE figure of merit is 0.033, 0.042, 0.033, 0.025, and 0.017 for samples sintered at 1100, 1125, 1145, 1175, and 1200°C, respectively, at 30 kV/cm. The best ECE figure of merit was observed in the BNT-BT sintered at 1125°C, which had the highest relative density. In addition, the ECE measured by the direct method shows the high ECE figure of merit, which makes it more practical for a future solid-state cooling system.





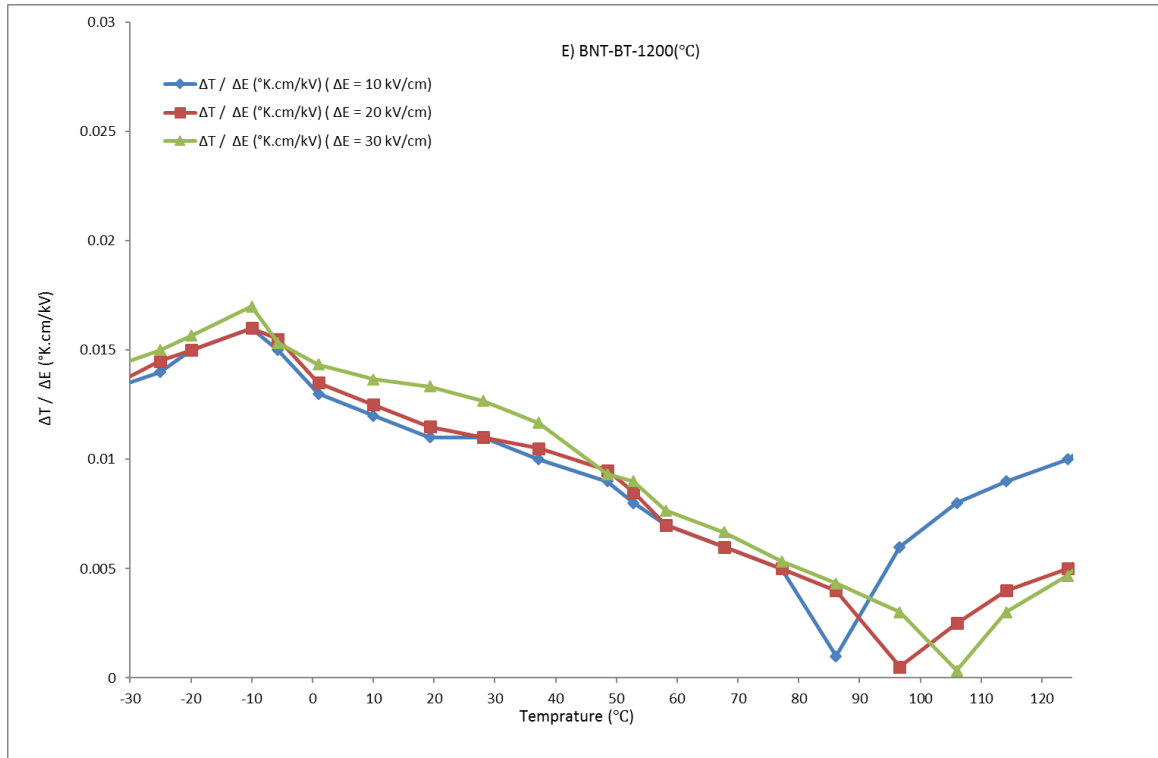
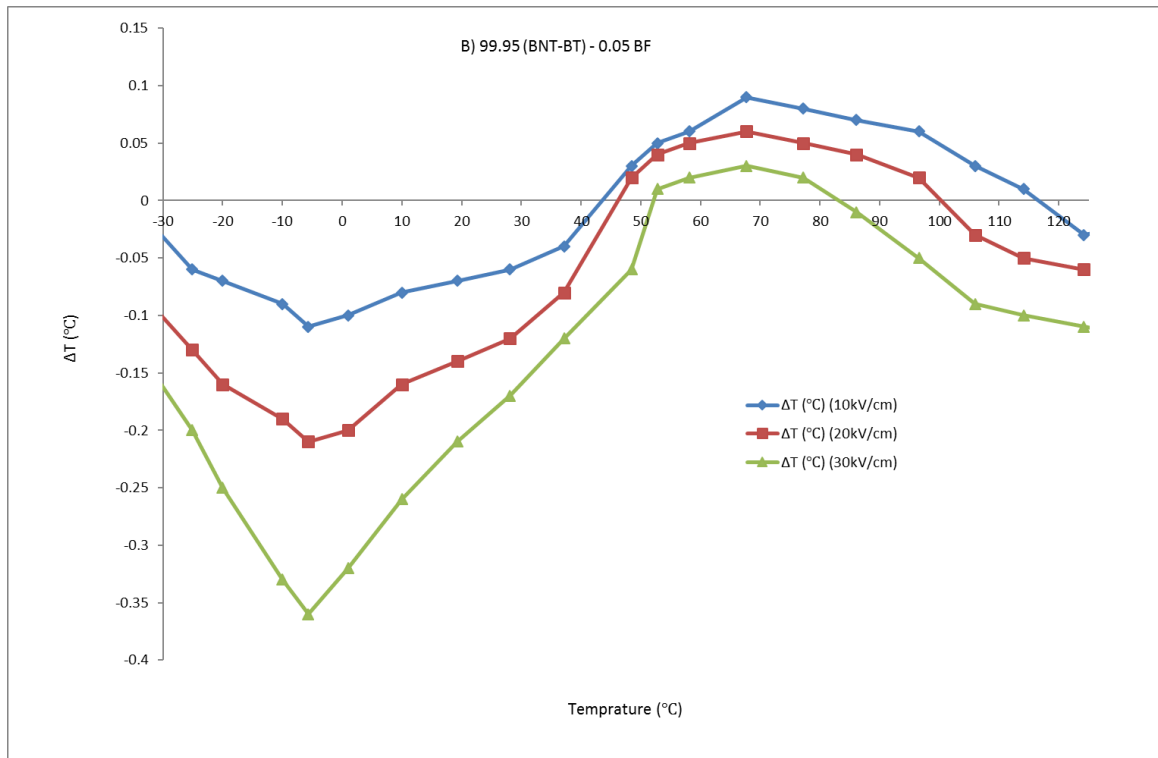
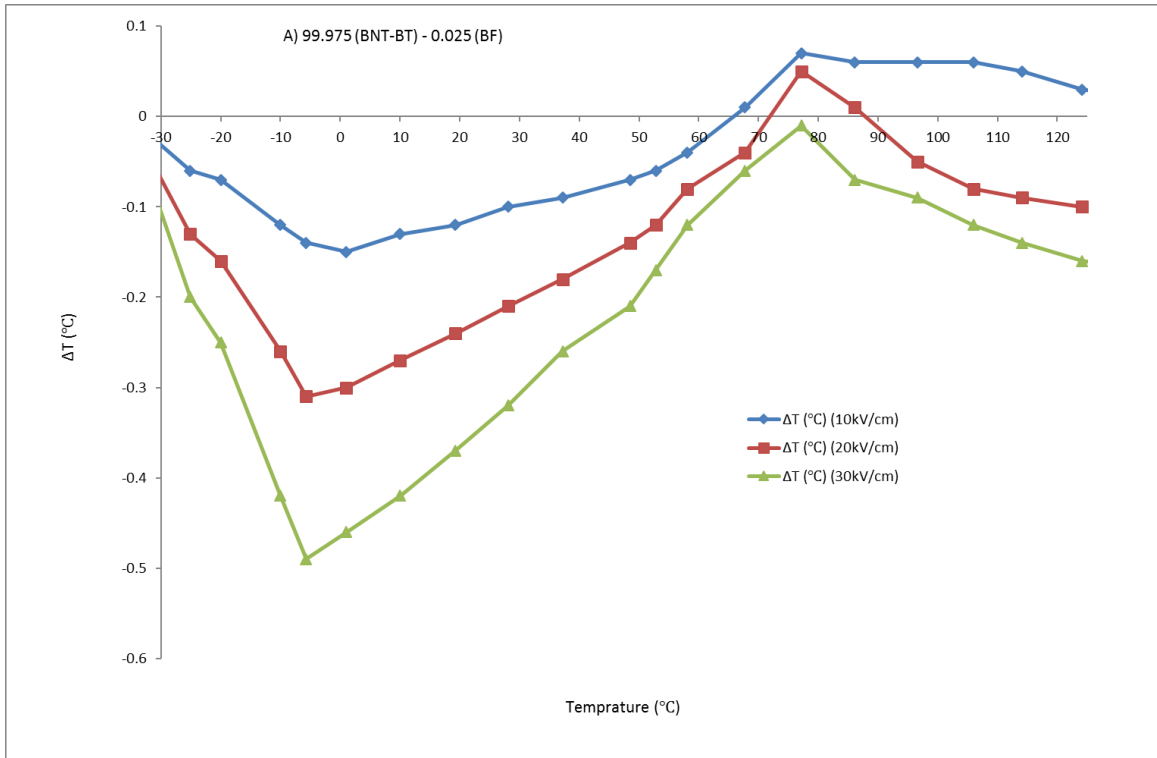


Figure 5-26: The ECE figure of merit of the pure BNT-BT sintered at A) 1100, B) 1125, C) 1150, D) 1175, and E) 1200°C measured between -30 and 125°C by the direct method.

5.1.4.2 The direct ECE measurement of BNT-BT-BF

Figure 4-27 shows the ECE of the (1-x) BNT-BT-x BF for x=0.025, 0.05, 0.075, and 0.1 between -30 and 125°C by the direct method. The addition of BF to BNT-BT decreased the depolarisation temperature, as explained in section 4.3.1, so the depolarisation temperature for BNT-BT samples including BF was decreased to a lower temperature. The highest ECE ($\Delta T = -0.49^\circ\text{C}$) for 0.975 (BNT-BT)-0.025 (BF) was observed at around -4.7°C at 30 kV/cm. In comparison with pure BNT-BT, the highest ECE decreases, which can be attributed to a diversion from the MBP due to the addition of BF. In addition, for the samples including the BF, the temperature at which the ECE changes from negative to positive decreases, compared to pure BNT-BT. Furthermore, adding more BF to BNT-BT causes the highest ECE decrease to $\Delta T = -0.36$, -0.31 , and -0.25°C at -5.7°C for 0.95 (BNT-BT) - 0.05 (BF), 0.925 (BNT-BT) - 0.075 (BF), and 0.9 (BNT-BT) - 0.1 (BF), respectively, at 30 kV/cm.



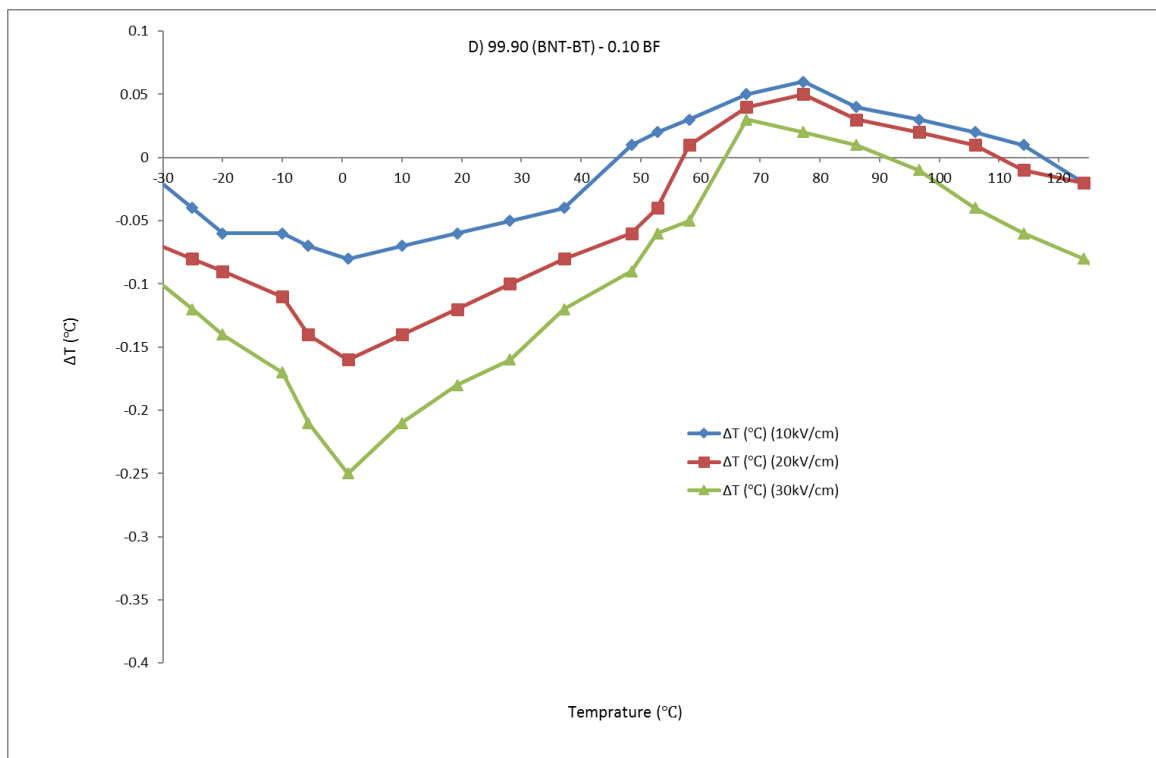
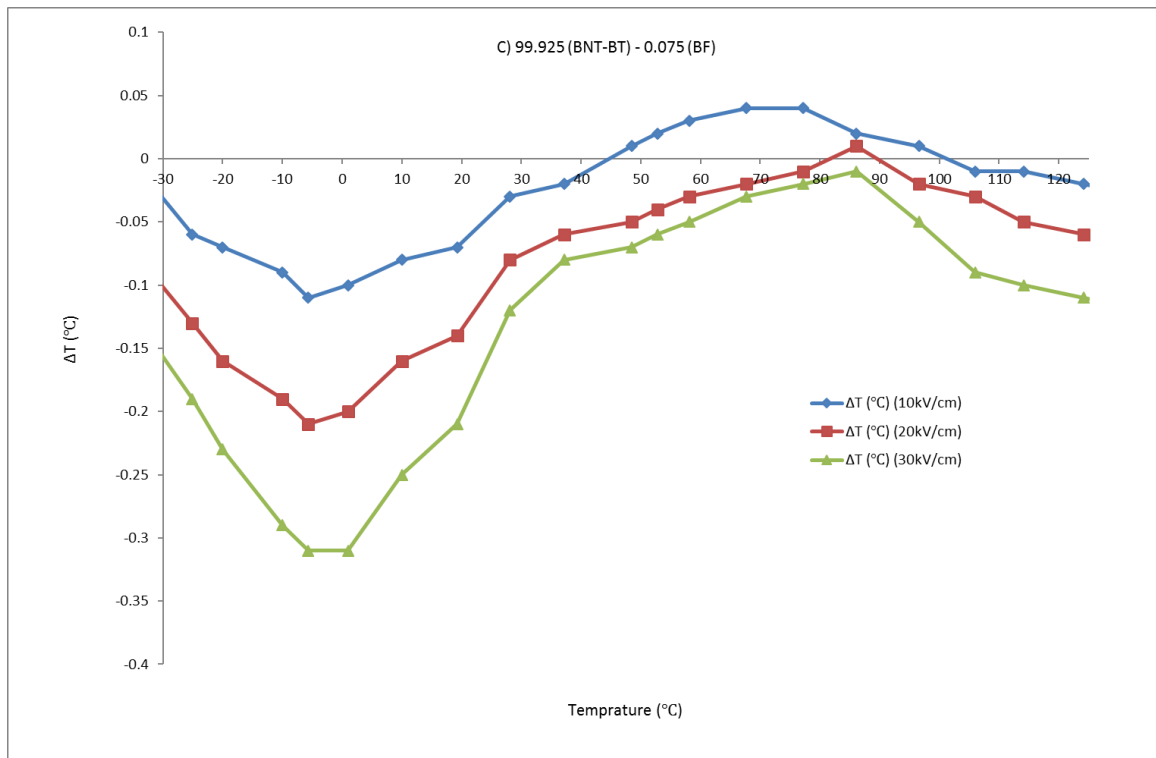
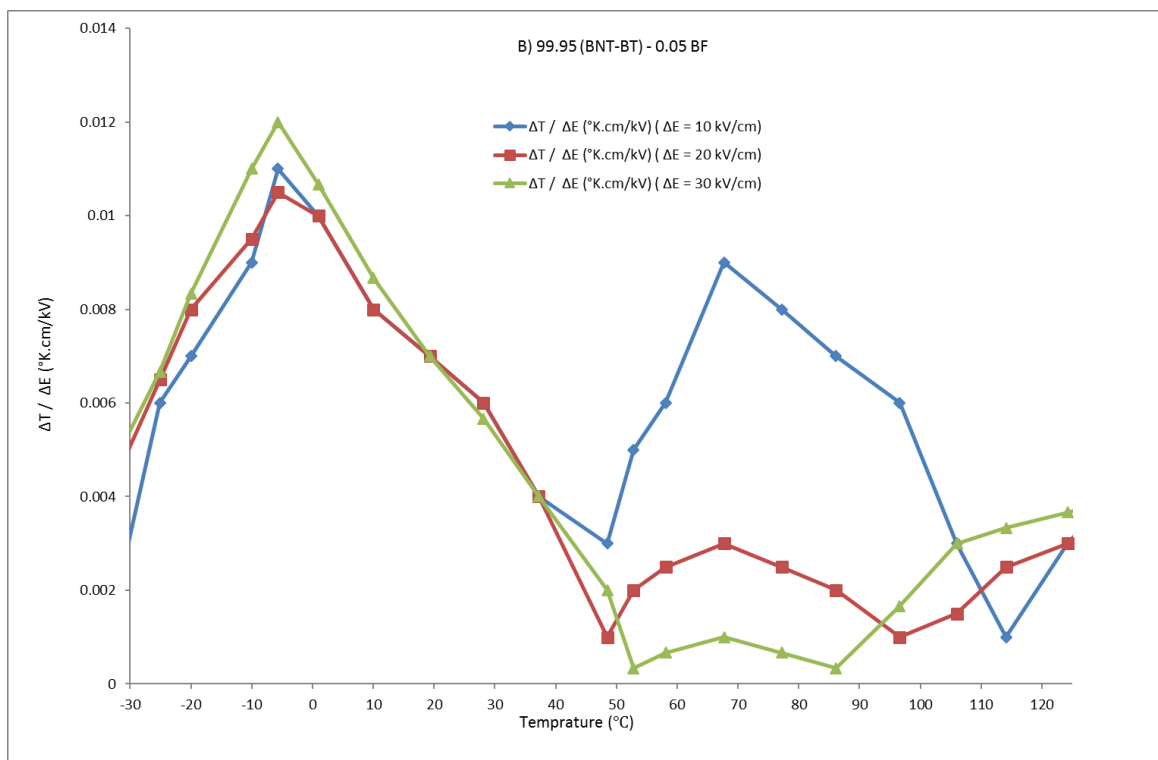
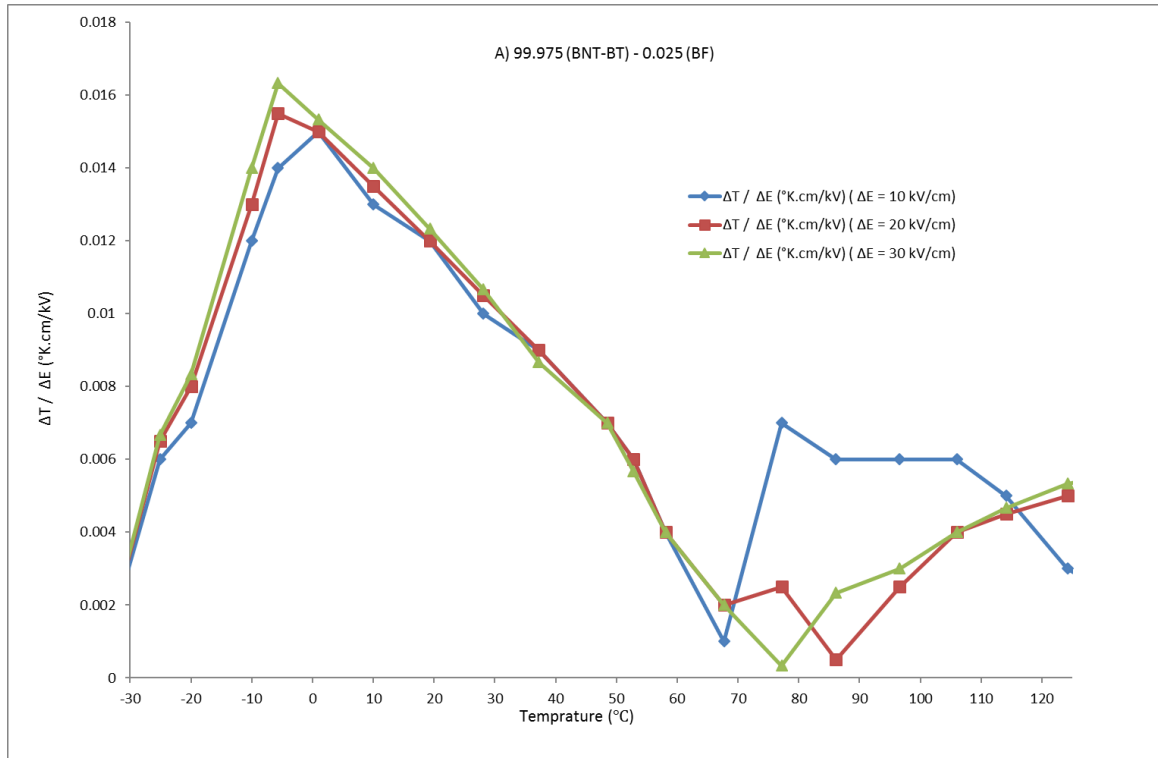


Figure 5-27: The ECE of the (1-x) BNT-BT-x BF for x A) 0.025, B) 0.05, C) 0.075, and D) 0.1 measured between -30 and 125°C by the direct method.

Figure 4-28 shows the ECE figure of merit of the (1-x) BNT-BT-x BF for x=0.025, 0.05, 0.075, and 0.1 between -30 and 125°C by the direct method. The highest ECE figures of merit

are 0.016, 0.012, 0.010, and 0.008 for (1-x) BNT-BT-x BF for x=0.025, 0.05, 0.075, and 0.1, respectively, at 30 kV/cm and -5.7°C. The addition of more BF to BNT-BT decreases the best ECE figure of merit for x=0.050, 0.075, and 0.1.



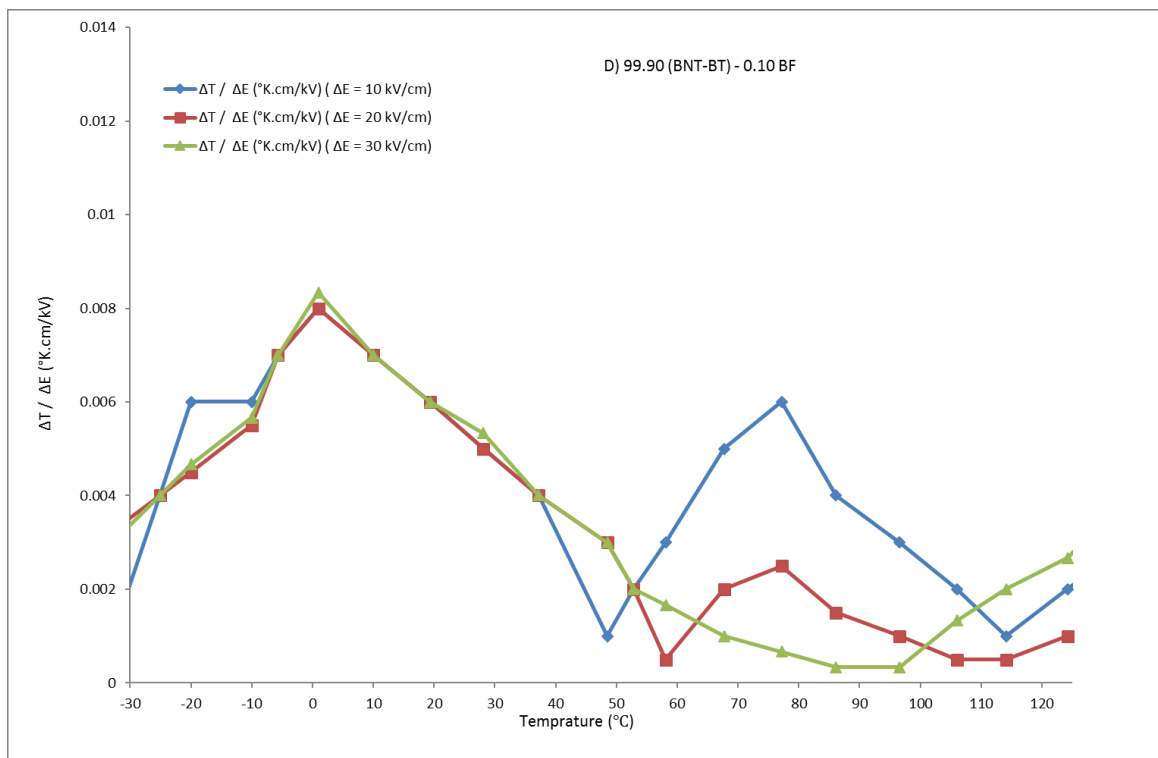
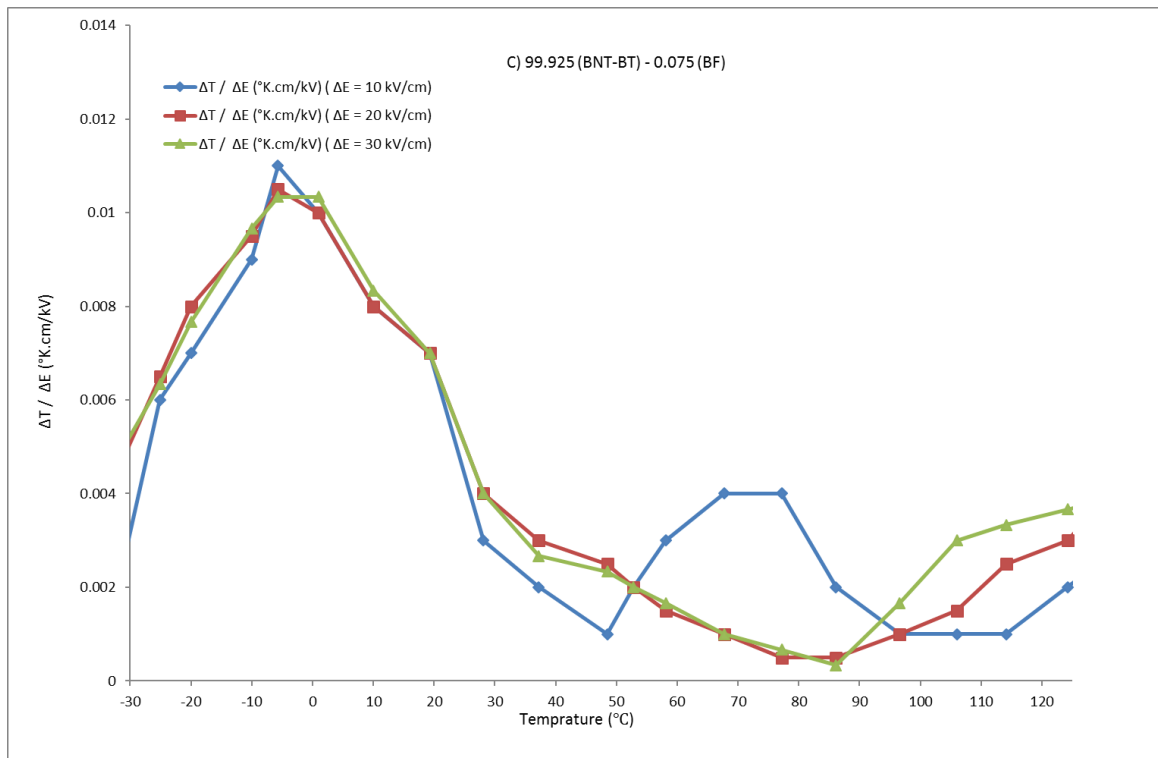


Figure 5-28: The ECE figure of merit of (1-x) BNT-BT-x BF for x A) 0.025, B) 0.05, C) 0.075, and D) 0.1 measured between -30 and 125°C by the direct method.

5.1.4.3 The direct ECE measurement of BNT-BT deficient samples

Figure 5-29 shows the ECE of the BNT-BT deficient samples, while Figure 5-30 shows the ECE figures of merit of BNT-BT deficient samples between -30 and 125°C, using the direct method. This composition shows the highest ECE $\Delta T = -0.77$ at 1°C for 30 kV/cm and the highest ECE figure of merit of 0.025 K.cm/kV.

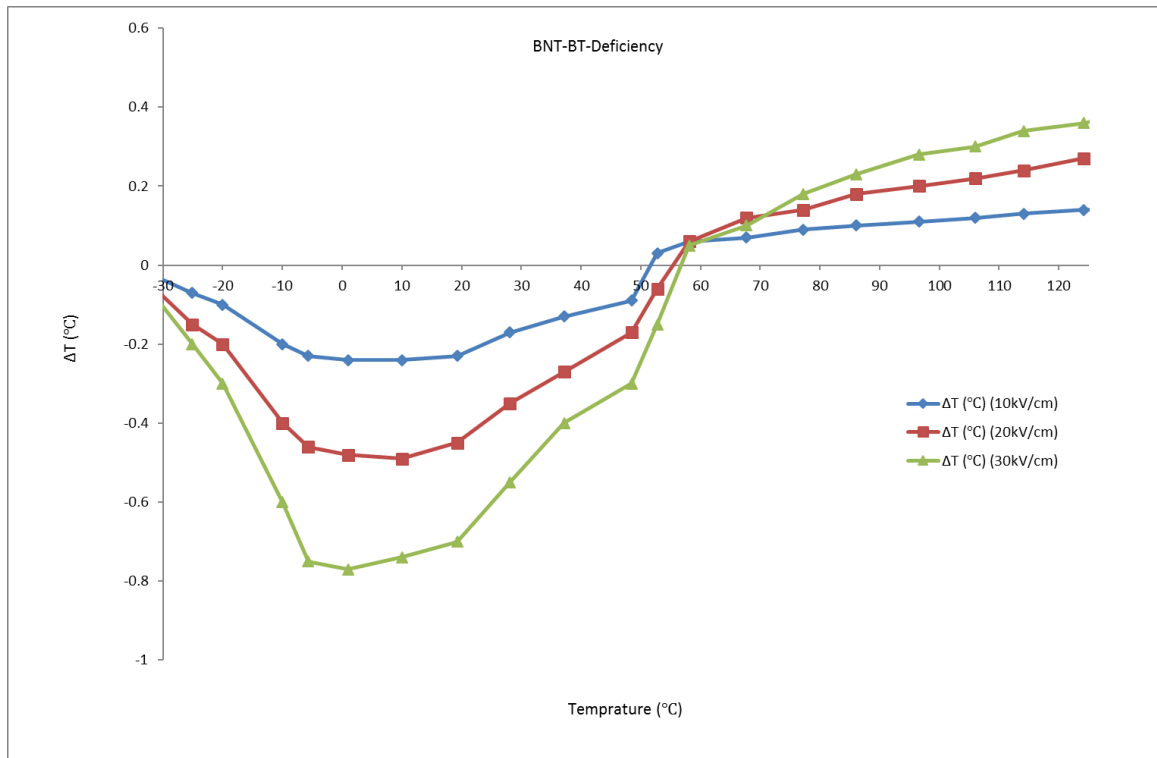


Figure 5-29: The ECE of BNT-BT deficient samples measured between -30 and 125°C by the direct method.

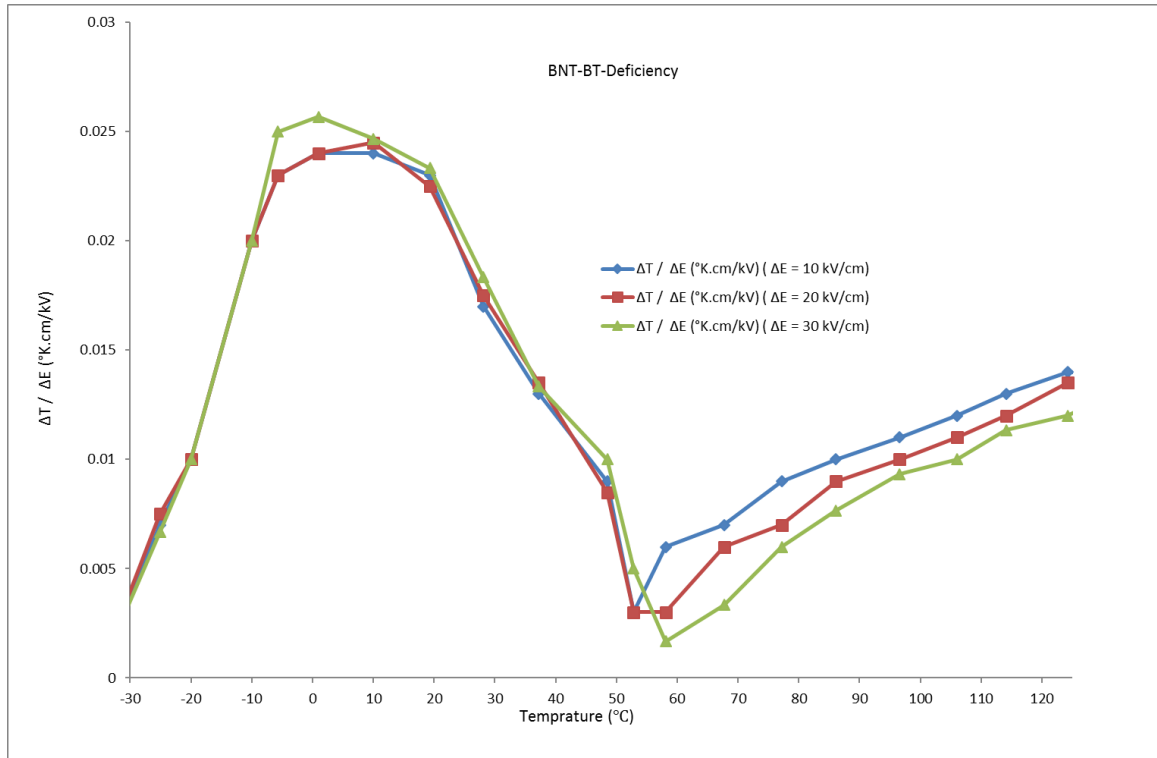


Figure 5-30: The ECE figure of merit of BNT-BT deficient samples measured between -30 to 125°C by the direct method.

5.1.4.4 ECE comparison of BNT-BT-based ceramics

Table 5-2 shows a summary of the ECE of BNT-BT and BNT-BT based materials using direct and indirect methods. The pure BNT-BT samples sintered at 1125°C show the highest ECE compared to the other sintering temperatures for both the direct and indirect methods, but it shows a sharp peak in a narrow temperature range, while the sample sintered at 1150°C shows a lower ECE at a broader temperature range. As explained in section 4.3, the properties of BNT-BT, similarly to BCZT, have a direct relationship with the relative density, and 1125 and 1150°C are the temperatures that show the highest relative density.

There are a number of differences between the shape and amount of the ECE for different sintering temperatures for BNT-BT. The highest ECE is increased by a rise in the relative density to 97% and reaches $\Delta T = -2.92^\circ\text{C}$. After that, through a reduction in the relative density, the ECE decreases to $\Delta T = -1.30^\circ\text{C}$ for samples sintered at 1200°C. The samples sintered at 1100 and 1125°C show quite a sharp peak where the highest ECE occurs, while for other sintering temperatures, the highest ECE exhibits broad peaks. The sample sintered at 1125°C has the highest relative density, but the grain size is 3.2

μm , which is lower than the sintered sample at 1150°C ($3.4 \mu\text{m}$). A higher grain size causes lower grain boundaries, which act as a clamp for the dipolar rotation and at a higher sintering temperature, the dipolar rotation is easier, and the ECE shows broader peaks.

A comparison of Table 5-2 and Table 2-6 shows that the ECE achieved in this project for BNT-BT is higher than that of previous studies, which equal $\Delta T = -2.92$ and -2.1°C for the samples sintered at 1125 and 1150°C . As an example of the results of other research, an ECE figure of merit of 0.017 K.cm/kV was achieved by Zheng et al. [190] for a BNT-BT composition, with 600°C (citrate method) selected for calcination and 1100°C for sintering. Uddin et al. [194] obtained $\Delta T = -2.1$ with an ECE figure of merit of 0.030 K.cm/kV for BNT-BT, and 800°C (sol-gel) was selected for calcination, and 1100°C for sintering.

It is known that the calcination and sintering temperature can affect other properties such as k_p , d_{33} , relative density, so could be one of the reasons for the different responses in the BNT-BT samples. As can be seen in Table 5-2, the ECE figure of merit has been changed from 0.049 to 0.058 K.cm/kV and then to 0.042 , 0.030 , and 0.026 K.cm/kV for samples sintered from 1100 to 1200°C , in 25°C increments, respectively. In this project, a two-step calcination process was selected, which can lead to a higher relative density in the sintered samples. A higher calcination temperature leads to a more uniform composition of grain boundaries, with the grains making the rotation of dipoles easier, and it could be the reason for the higher ECE of this project, compared to those of other researchers. The highest ECE figure of merit is 0.037 K.cm/kV among other researchers.

The highest ECE figure of merit for the BNT-BT samples measured by the direct method is 0.043 K.cm/kV for samples sintered at 1125°C . In previous research, the ECE of BNT-BT was only measured by the indirect method, while in this project, to measure it using the direct result, a reading device was designed and with it, the ECE of BNT-BT was measured. The results of the direct method are lower than for the indirect method, due to the use of the non-adiabatic device for measuring, which causes the ECE figure of merit for BNT-BT by the direct method to be almost 75-85% of the indirect method. However, the effect of the sintering temperature is similar for both methods, and they show the effect of the sintering temperature on the ECE. In spite of the non-adiabatic measurement device, the ECE figure of merit is still high, which makes it one of the best candidates for future solid-state cooling systems.

The ECE and ECE figures of merit are decreased for (1-x) BNT-BT-x BF (x=0.025, 0.050, 0.075, and 0.1). Only one study has been done on this composition, which increased the ECE of this composition for x=0.01. BF was separately added to BNT-BT after calcination, but in the previous study, the composition was prepared as a first step. This difference in fabrication can make a difference in the result due to the incomplete diffusion of BF to the BNT-BT structure, or the diffusion of bismuth and ferrite to the A and B sites, as explained in section 4.3.1.

A deficiency in the BNT-BT samples causes a reduction in the ECE, compared to the pure BNT-BT. As explained in section 2.1.1.2.3.1, this deficiency can increase the pyroelectric coefficient, but the application of an electric field reduces it, and for this reason, the ECE of this composition is lower than pure BNT-BT, but nevertheless has a high amount. In addition, it needs to be considered that the relative density is lower than for pure BNT-BT and compared to the pure BNT-BT (the sample sintered at 1175°C) with a higher relative density, it has a higher ECE.

Table 5-2: A summary of the ECE of BNT-BT and BNT-BT-based materials using the direct and indirect methods.

Pure BNT-BT					
Sintering Temperature °C	1100	1125	1150	1175	1200
Relative density%	94	97	96	95	93
d_{33} pC/N	115	165	155	145	120
Grain Size (μm)	2.5	3.2	3.4	3.8	4.1
Ferroelectric to anti ferroelectric temperature °C	110-128	110-128	106-128	110-128	110-128
Maximum of EC (Indirect) °C	-2.44	-2.92	-2.1	-1.5	-1.3
ΔE kV/cm	50	50	50	50	50
Indirect ECE figure of merit K.cm/kV	0.049	0.058	0.042	0.030	0.026
Temperature of maximum EC °C	-10	-10	40	-10	-10
Maximum of EC (Direct) °C	-1	-1.3	-1	-0.75	-0.51
ΔE kV/cm	30	30	30	30	30
Direct ECE figure of merit K.cm/kV	0.033	0.043	0.033	0.025	0.017
Temperature of maximum EC °C	-20	-10	37	-20	-20
Spontaneous polarisation $\mu\text{C}/\text{cm}$ at RT	21.10	25.08	24.01	23.30	20.68
(1-x) BNT-BT – x BF and BNT-BT with deficiency					
Composition	0.025	0.050	0.075	0.100	deficiency
Relative density%	93.2	92.84	92.7	92.4	94.22
d_{33} pC/N	95	75	70	30	70
Grain Size (μm)	6.5	6.7	7	7.2	1.7
Ferroelectric to anti ferroelectric temperature °C	100	85	79	74	82
Maximum of EC (Indirect) °C	-0.85	-0.70	-0.67	-0.46	-1.65
ΔE kV/cm	50	50	50	50	50
Indirect ECE figure of merit K.cm/kV	0.017	0.014	0.011	0.009	0.031
Temperature of maximum EC	-10	-10	-10	-10	-10
Maximum of EC (Direct) °C	-0.49	-0.36	-0.31	-0.25	-0.77
ΔE kV/cm	30	30	30	30	30
Direct ECE figure of merit K.cm/kV	0.016	0.012	0.010	0.008	0.025
Temperature of maximum EC °C	-5.7	-5.7	-5.7	-5.7	1
Spontaneous polarisation $\mu\text{C}/\text{cm}$ at RT	11.76	10.83	9.64	11.76	20.89

5.2 Discussion

In an attempt to investigate relationships between the measured ECE and other properties, selected data from Table 5.2 has been analysed further. Figures 5-31, 5-32 and 5-33 show the comparison between ECE and relative density, polarisation and d_{33} , respectively, for all samples including BCZT, BCZT-BNKT, BNT-BT, BNT-BT-BF and BNT-BT with deficiency. The BNT-BT samples show the highest ECE and as it can be seen that relative density has a larger effect for higher ECE. It is also interesting to note that although the data are clustered around specific compositions, the data for all the BNT-BT related samples (BNT-BT, BNT-BT-BF and BNT-BT with deficiency) could fit a general positive trend line for all the parameters (relative density, polarisation and d_{33}), whereas the ECE appears independent of the value of these parameters for the BCZT and BCZT-BNKT compositions. Thus, for the BNT-BT compositions, optimisation of the fabrication processes is necessary for achieving high ECE. Also, the BNT-BT samples show higher polarisation than other samples indicating that materials with higher polarisation have more polarisation change and so more ECE. The highest ECE in BNT-BT samples can be seen for the sample that it has the highest values of polarisation and relative density. For both BNT-BT and BCZT, the addition of additives causes a decrease in ECE and polarisation.

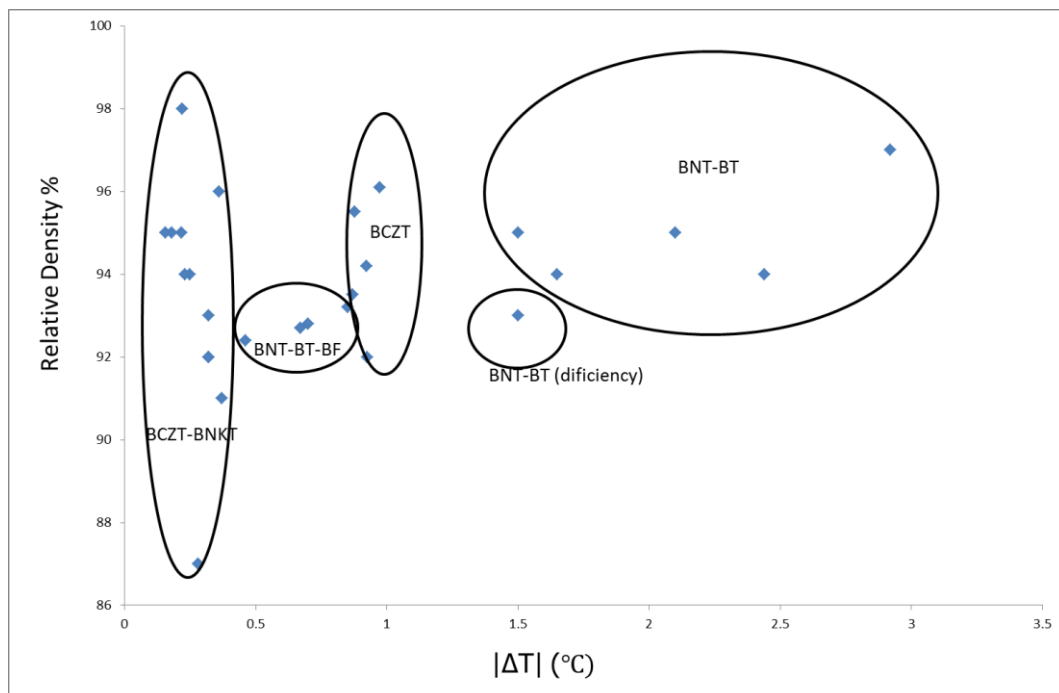


Figure 5-31: Comparison between ECE and relative density for all samples including BCZT, BCZT-BNKT, BNT-BT, BNT-BT-BF and BNT-BT with deficiency

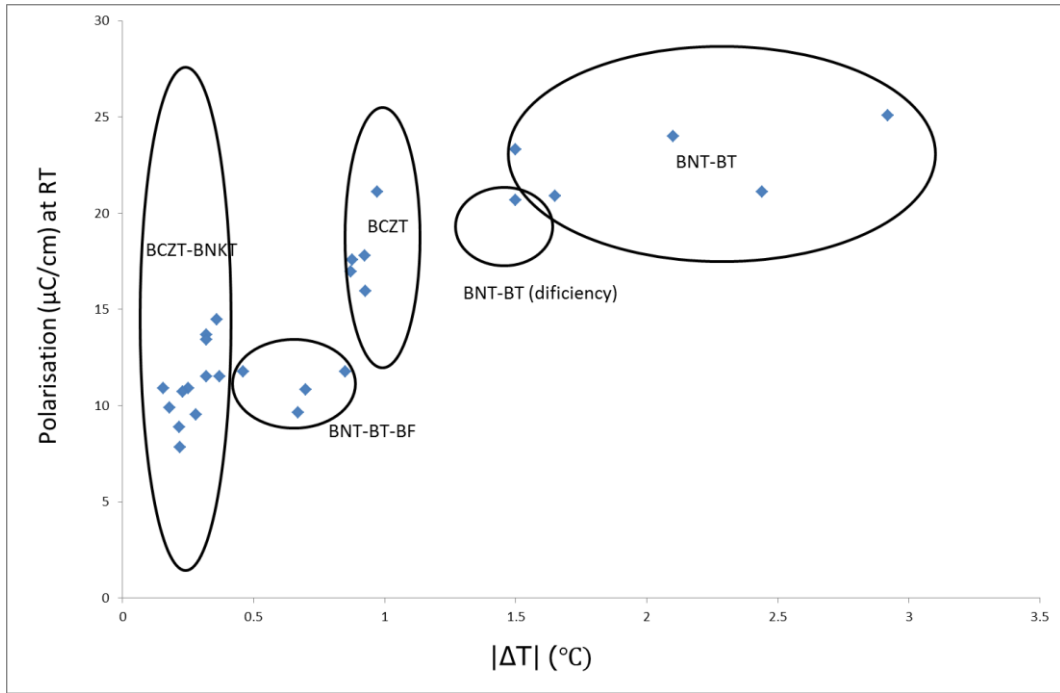


Figure 5-32: Comparison between ECE and polarisation for all samples including BCZT, BCZT-BNKT, BNT-BT, BNT-BT-BF and BNT-BT with deficiency

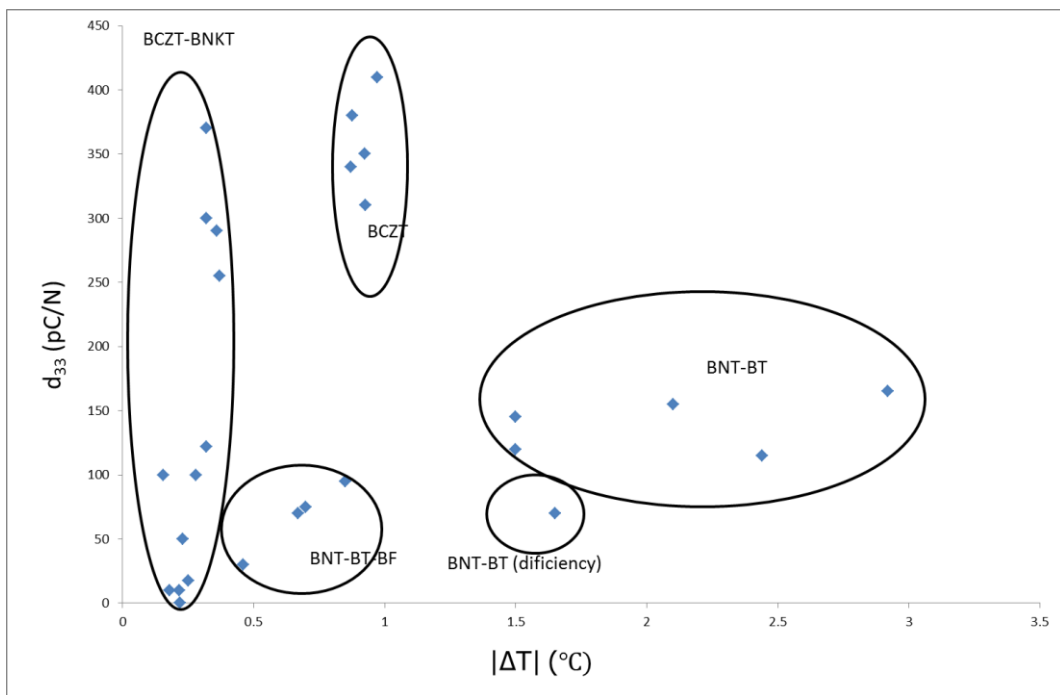


Figure 5-33: Comparison between ECE and d_{33} for all samples including BCZT, BCZT-BNKT, BNT-BT, BNT-BT-BF and BNT-BT with deficiency

Another factor is the grain size that should be considered. When grain size increase, the ECE increase for pure BNT-BT and BCZT and after the maximum relative density, grain size does not affect the ECE. It is the same for BNT-BT-BF samples, but for BCZT-BNKT samples, in spite of the relative density decrease, the ECE increase due to increase in the grain size.

Figure 5-34 shows the comparison between ECE and relative density for BCZT, BCZT-1, 3 and 5%BNKT samples. The ECE of samples depend on the relative density and it decreases with relative density reduction. There are some exceptions such as BCZT-3%BNKT, but, in general, relative density is one of the main factors. Also the plot show that the addition of BNKT causes ECE decrease and addition of more BNKT shows more decrease in the ECE. A comparison between Table 5-1 and 4-2 shows the importance of the optimisation of the processing. Similar to d_{33} , k_p and relative permittivity, ECE is dependent on the relative density and so any factor in the processing that increase the piezoelectric properties can have a positive effect on ECE as well.

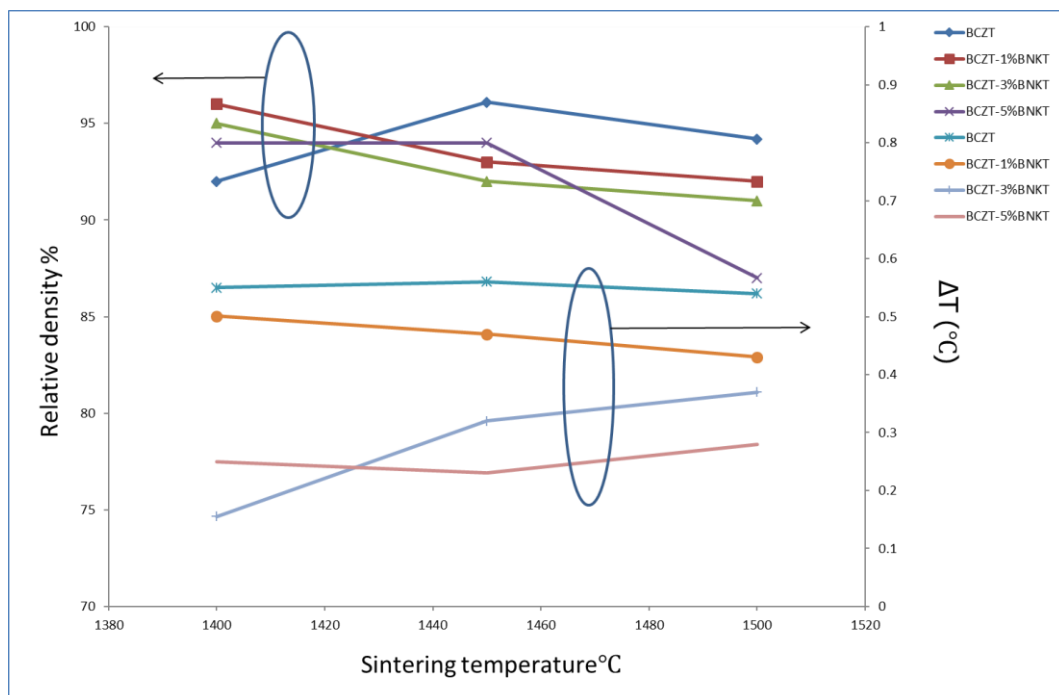


Figure 5-34: Comparison between ECE and relative density for BCZT, BCZT-1, 3 and 5%BNKT (ECE extracted of 30 kV/cm electric field for comparison)

Figure 5-35 shows the comparison between ECE and relative density for BNT-BT samples. As it can be seen, ECE follows relative density trend similar to BCZT samples. The ECE increases when relative density increases and shows the maximum at the maximum of relative density. A comparison between Table 4-3, 4-4, 4-4 and Table 5-2 show that the ECE follows the same route as piezoelectric properties. The two steps calcination of BNT- BT could increase the piezoelectric properties of this compound in comparison with previous research in Table 2-6 and it shows that it has the same effect on the ECE in comparison with previous research.

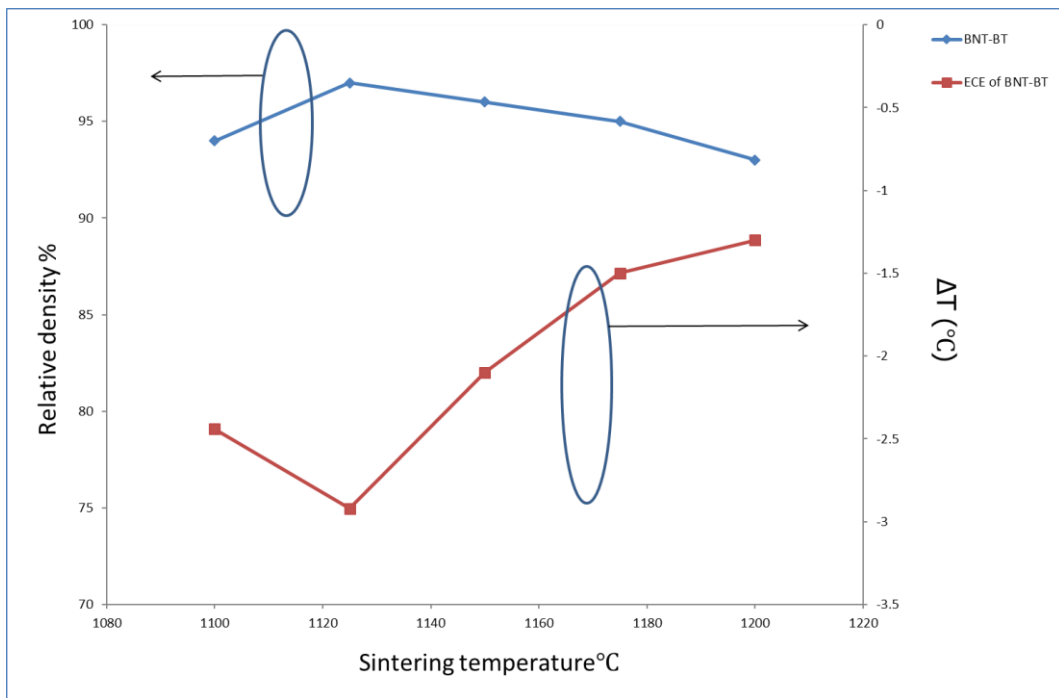


Figure 5-35: The comparison between ECE and relative density for BNT-BT

Chapter

6 Conclusions

The aims and objectives of this project were outlined in Section 2.5. It now remains to summarise the main outcomes of the work and the extent to which all the objectives have been achieved. The summary is divided into BCZT-based materials and then BNT-BT-based materials, and then some general comments as follows:

1- BCZT

1-1- Pure BCZT

- 1-1-1 BCZT powder was prepared by two different methods; firstly, from BaCO₃, ZrO₂, TiO₂ and CaCO₃ and secondly, from BCT and BZT; no difference was observed between the two methods. The powders were calcined at 1250°C for both methods.
- 1-1-3- Bulk samples were prepared via the uniaxial pressing method (90Mpa) and sintered at five different temperatures between 1400 and 1500°C, with increments of 25°C; the best properties were found at 1450°C, with a relative density of 96.1%, grain size of 32µm, piezoelectric charge coefficient (d₃₃) of 410 pC/N, and electromechanical coupling factor (k_p) of 46% .
- 1-1-4- Three anomalies were observed in the temperature dependence permittivity and dielectric loss of BCZT, which can be attributed to the rhombohedral to orthorhombic, orthorhombic to tetragonal, and tetragonal to cubic phase changes.
- 1-1-5- The best ECE ($\Delta T = 0.97$) was observed in the BCZT sample sintered at 1450°C, which shows its dependence on relative density.

1-2- BCZT-1, 3, and 5% BNKT

- 1-2-1- The effect of 1, 3, and 5% of BNKT was investigated on the BCZT composition sintered between 1250 to 1500°C, with a step size of 50°C, and as the relative density, grain size, d₃₃, and relative permittivity were measured.
- 1-2-2- The results show that by adding BNKT to BCZT, d₃₃, k_p and grain size decrease, while an increase in the amount of BNKT leads to a further reduction in them.
- 1-2-3- In the BCZT-1% BNKT, the d₃₃ is almost 90% of pure BCZT for the sample sintered at 1500°C, while the k_p is only decreased by 1%. The relative density is decreased by a rise in the sintering temperature, and

the relative permittivity at room temperature is higher than pure BCZT, which can make it practical for room temperature applications.

- 1-2-4- In the BCZT-3% BNKT, d_{33} is decreased to 255 for the sample sintered at 1500°C, and the k_p decreased by to 41%. The relative density decreases with a rise in the temperature, and the relative permittivity at room temperature is higher than for pure BCZT, especially for samples sintered at 1400°C for 3852.
- 1-2-5- In the BCZT-5% BNKT, the d_{33} decreases to 100 for samples sintered at 1500°C and the k_p reaches 26%, which can be attributed to a shift in the structure to cubic. The relative density was decreased with a rise in the sintering temperature, and the relative permittivity at room temperature is higher than for pure BCZT, especially for samples sintered at 1400°C with a value of 4222.
- 1-2-6- An addition of BNKT to BCZT decreased the ECE of this composition for all added amounts, except for the BCZT-1% BNKT sintered at 1350°C, which has a similar ECE figure of merit (0.017 K.cm/kV) to pure BCZT. The addition of BNKT can decrease the Curie temperature.

2- **BNT-BT**

2-1- **Pure BNT-BT**

2-1-1- BNT-BT has been calcined by two methods like BCZT; firstly, calcined from BNT and BT, and secondly, directly calcined from raw materials.

2-1-2- The existence of the pyrochlore phase and the remainder of the BT was observed in the XRD patterns of the BNT-BT calcined from raw materials. Therefore, the calcination of the BNT-BT from BNT and BT was selected to come to an understanding of the formation of BNT-BT and removing the secondary phases.

2-1-3- The results show that the pyrochlore phase that pertains to BNT formation is removed at 850°C, and that BNT with BT forms a solid solution at 1050°C.

2-1-4- The prepared pressed bulk samples were sintered between 1100 and 1200°C, with a step size of 25°C. The best properties were found at 1125°C with a relative density of 97%, grain size of 3.2µm, d_{33} of 165 pC/N, and k_p of 47%.

2-1-5- The BNT-BT shows a high ECE $\Delta T = -2.91$ and -2.1°C for the samples sintered at 1125 and 1150°C, respectively, under 50 kV/cm, which due to the two-step calcination process, is higher than the result obtained by previous researchers.

2-2- (1-x) BNT-BT-x BF

2-2-1- BiFeO₃ was calcined at 850°C for five hours. The XRD pattern shows a pure perovskite structure.

2-2-2- BF was added to BNT-BT for in different molar amounts of moles: 0.025, 0.05, 0.075, and 0.10.

2-2-3- Through a rise in the amount of BF from $x = 0$ to 0.1, a reduction can be seen in some of the properties, such as d_{33} (from 165 to 30 pC/N), relative permittivity at RT (1230 to 461), and k_p (47 to 14%); this could be due to the shift in the structure to cubic. An increase in the grain size can be seen and a reduction observed in the transformation from the ferroelectric to the anti-ferroelectric phase in the structure from around 120°C for pure BNT-BT to 74°C for 0.9 BNT-BT-0.1BF, which can be useful for room-temperature cooling systems.

2-2-4- The addition of the BF to the BNT-BT decreased the ECE of this composition for all samples, due to the diversion of the MPB for these compositions. The addition of BF can decrease the temperature of the highest ECE.

2-3- BNT-BT deficient samples

2-3-1- BNT samples with a deficiency were prepared by the same process as pure BNT and BNT-BT deficient samples and pure BNT-BT.

2-3-2- The general properties of the compound have been decreased for d_{33} to 70 pC/N, k_p (37%), the grain size of 1.7 µm, and the relative permittivity of 756 at RT.

2-3-3- A reduction can be observed in the transformation from the ferroelectric to anti-ferroelectric phase in the structure from around 120°C for pure

BNT-BT to 82°C for BNT-BT deficient samples, which can be useful for room-temperature cooling systems.

2-3-4- BNT-BT deficient samples show a high ECE $\Delta T = -1.65$ at -10°C under 50 kV/cm, and it has a lower relative density compared to pure BNT-BT, which leads to a lower ECE.

3- General Comments

Most ECE measurements are based on the indirect method, and there has been little research on direct methods with a focus on lead based materials. Direct measurements need changes in the existing equipment, which is not desirable. Also, a new design for adiabatic calorimetry is expensive. In this project, we designed a new device with high accuracy and low price. The ECE of different lead free materials were measured with direct method which is the main lack for lead free materials ECE measurements and comparative measurements were done of the direct and indirect ECE techniques.

The results of the direct method for BCZT based materials as a normal ferroelectric is almost 75% of the indirect method while for BNT- BT based materials is 85% of indirect method. As explained previously, the results for normal ferroelectric should be same for both direct and indirect methods method. The new device has almost 25% deviation for a normal ferroelectric material and almost 35-50% for relaxor materials with assuming that there is 50% difference between direct method and indirect method for relaxor ferroelectric. Possible origins of these discrepancies could arise from the equipment itself, the type of measurement and/or the materials being measured. The direct ECE measurements were done at a range of temperatures and, for this reason, the device was located in a large environment chamber to control the temperature. Due to big environment chamber, longer wires were need for connections with resulting increased conductivity losses. A thermistor was used to detect the temperature change of the samples which could contribute to in the measurement due to its heat capacity. The thermistor could absorb a part of the heat of the sample and this does not show the real response. In order to avoid this, the temperature change of the sample should be measured in adiabatic conditions to prevent heat transfer with environment. A new design would be needed to make a vacuum environment and transfer gas to the jig. This would, of course, be more costly.

The indirect method does not show the real ECE for the relaxor materials. With assuming the direct and indirect methods should be the same for a normal ferroelectric material, there is 10 to 15% different for a relaxor ferroelectric material via the indirect method. As mentioned previously, the indirect method is for ergodic systems, while BNT-BT shows non-ergodic behaviour and so the indirect method show discrepancy from the real ECE.

The results show that the results for the both methods are different for BCZT and BNT-BT based samples. A comparison between ECE of BCZT sintered at 1450°C and BNT-BT sintered at 1125°C show a difference of almost $|\Delta T|=2^\circ\text{C}$ under 50kV/cm. The ECE is mainly caused by polarisation and polarisation change and the polarisation of BCZT is almost 15-20 $\mu\text{C}/\text{cm}^2$ under 50kV/cm, while for BNT-BT is almost 20-30 $\mu\text{C}/\text{cm}^2$ under the same electric field and so more polarisation change. The E_c is 2 kV/cm for BCZT and it is 37 kV/cm for BNT-BT; so lower electric field aligns the dipoles in the BCZT materials and after that the polarisation change become slower, but higher electric field needs in the BNT-BT materials and so there is more polarisation change in the BNT-BT materials. As previously explained in section 2.1.1.2.3.1 and 4.3, BNT-BT has polar nano regions and so an electric field can form more polar nano regions and more polarisation change and it causes entropy increase and temperature decrease and it shows the negative ECE. In BCZT based materials, an electric field align the dipoles and so entropy decrease and temperature increase.

The results of BCZT and BNT-BT based materials show that there are three main factors affect the ECE of these materials. The first factor is the relative density and as it can be seen in Table 5-1 and 5-2, figure 5-31, 5-32 and 5-33 for both pure BCZT and BNT-BT, the maximum ECE is for the sample that shows the highest relative density. Also, BCZT-1%BNKT shows the maximum ECE at the maximum relative density similar to pure BCZT and BNT-BT. The lower porosities are in the sample with the maximum relative density that clamp the polarisation change in the samples and affect the ECE. Another factor that should be considered for ECE is the grain growth. The grain growth causes the lower grain boundaries that clamp the polarisation switching as it can be seen in BCZT-3 and 5%BNKT and the ECE increased by rise in the grain growth.

The addition of BNKT to BCZT and also BF to BNT-BT cause the MPB move and it affect the ECE for these compositions. It means the ECE decreases by adding more additive to pure BCZT and BNT-BT. So, the ECE show the highest ECE near MPB.

Our results show that the ECE is mainly related to the relative density (similar to piezoelectric properties), and that also grain growth can have an effect. The addition of additives causes changes in MPB and decreases ECE. However, addition can make a wide ECE rather than a sharp one. The results show that BNT-BT sintered at 1125 and 1150°C is one of the main candidates for cooling systems with high ECE.

Chapter

7 Future work and recommendations

Other lead free materials systems worth investigating include BNKT, BNT-BKT and BKT-BT. Other possible future work and recommendations can be summarised as follows:

1-1- Pure BCZT

1-1-1- BCZT could be calcined at temperatures such as 1300 and 1350°C, and also sintered at other temperatures, and the properties compared.

1-1-2- Differences in the type of preparation of BCZT from raw materials and other BCT and BZT methods should be investigated.

1-1-3- The effect of other additives such as Li could be investigated to see the piezoelectric and electrocaloric effect on this composition.

1-2- BCZT-BNKT

1-2-1- The prepared BCZT-1, 3, and 5% BNKT in this project was prepared from BCZT and BNKT powders. However, it could also be directly prepared from raw materials and after that, the results can be compared with those of this project.

1-2-2- BNKT could be added in other amounts, to study the dopant and diagram phases of these compounds and the ECEs.

2- Fabrication of BNT-BT

2-1- Pure BNT-BT

2-1-1- BNT-BT could be calcined at 1100°C and sintered at more temperatures, and the properties then compared.

2-1-2- The difference could be compared between BNT-BT prepared from raw materials and other methods from BNT and BT, and the effect on the ECE can be investigated.

2-2- BNT-BT-BF

2-2-1- BF could be added in other amounts, as the dopant and diagram phases investigated for these compounds.

2-2-2- BF can be added for the first step of mixing and not after calcination, and the effect on the ECE investigated.

2-3- Deficiencies in BNT-BT

Deficiencies can be applied to BNT-BT in different amount at the sodium and bismuth site, and the ECE investigated.

The lattice parameters can be calculated for the phases detected in the XRD patterns to investigate the effect of additives via changes in the lattice parameter. Based on the ionic radius of elements in the perovskite structure and the position of cations and anions in the structure, the lattice parameter can be calculated for a, b and c direction in the lattice.

How to apply EC materials to the cooling system is another important aspect of this project, and is necessary to make it more practical. It would also be useful to design a practical cooling system with these materials. As explained previously, the type of regenerator (solid, liquid, or gas) affects the efficiency of the cooling system. Another important aspect is the better application of the thermodynamic cycle, which can influence the efficiency. There has been some research on this subject, but most papers are based on modulation, and more tests and experiments are required to arrive at a final practical application.

References

1. United States Environmental Protection Agency, U.S.E.P., United States , <https://www.epa.gov/>
2. Correia, T. and Q. Zhang, *Electrocaloric Materials*. 2014: Springer.
3. Ožbolt, M., et al., *Electrocaloric vs. magnetocaloric energy conversion*. International Journal of Refrigeration, 2014. **37**: p. 16-27.
4. Ožbolt, M., et al., *Electrocaloric refrigeration: Thermodynamics, state of the art and future perspectives*. International Journal of Refrigeration, 2013.
5. Valant, M., *Electrocaloric materials for future solid-state refrigeration technologies*. Progress in Materials Science, 2012. **57**(6): p. 980-1009.
6. Radebaugh, R., et al., *Feasibility of electrocaloric refrigeration for the 4–15 K temperature range*. Cryogenics, 1979. **19**(4): p. 187-208.
7. Moulson, A.J. and J.M. Herbert, *Electroceramics: Materials, Properties, Applications*. 2003: Wiley.
8. Kao, K.C., *Dielectric phenomena in solids*. 2004: Academic press.
9. Safari, A. and E.K. Akdogan, *Piezoelectric and acoustic materials for transducer applications*. 2008: Springer.
10. Rodel, J., et al., *Perspective on the Development of Lead-free Piezoceramics*. Journal of the American Ceramic Society, 2009. **92**(6): p. 1153-1177.
11. Aksel, E. and J.L. Jones, *Advances in lead-free piezoelectric materials for sensors and actuators*. Sensors, 2010. **10**(3): p. 1935-1954.
12. Panda, P. and B. Sahoo, *PZT to Lead Free Piezo Ceramics: A Review*. Ferroelectrics, 2015. **474**(1): p. 128-143.
13. Seifert, K.T.P., *Lead-Free Piezoelectric Ceramics*. 2010, TU Darmstadt.
14. Shrout, T.R. and S.J. Zhang, *Lead-free piezoelectric ceramics: Alternatives for PZT?* Journal of Electroceramics, 2007. **19**(1): p. 113-126.
15. Liu, W. and X. Ren, *Large piezoelectric effect in Pb-free ceramics*. Physical Review Letters, 2009. **103**(25): p. 257602.
16. Maison, W., et al., *Phase content, tetragonality, and crystallite size of nanoscaled barium titanate synthesized by the catecholate process: effect of calcination temperature*. Journal of the European Ceramic Society, 2003. **23**(1): p. 127-132.
17. Naghib-zadeh, H., et al., *Low temperature sintering of barium titanate ceramics assisted by addition of lithium fluoride-containing sintering additives*. Journal of the European Ceramic Society, 2010. **30**(1): p. 81-86.
18. Varatharajan, R., et al., *Ferroelectric characterization studies on barium calcium titanate single crystals*. Materials characterization, 2000. **45**(2): p. 89-93.
19. Qian, X.S., et al., *Electrocaloric Materials: Giant Electrocaloric Response Over A Broad Temperature Range in Modified BaTiO₃ Ceramics (Adv. Funct. Mater. 9/2014)*. Advanced Functional Materials, 2014. **24**(9): p. 1336-1336.
20. Dong, L., D.S. Stone, and R.S. Lakes, *Enhanced dielectric and piezoelectric properties of xBaZrO₃-(1-x) BaTiO₃ ceramics*. Journal of Applied Physics, 2012. **111**(8): p. 084107.
21. Coondoo, I., et al., *Synthesis and characterization of lead-free 0.5 Ba (Zr_{0.2}Ti_{0.8}) O₃-0.5 (Ba_{0.7}Ca_{0.3}) TiO₃ ceramic*. Journal of Applied Physics, 2013. **113**(21): p. 214107.
22. Avrahami, Y. and H. Tuller, *Improved electromechanical response in rhombohedral BaTiO₃*. Journal of electroceramics, 2004. **13**(1-3): p. 463-469.

23. Bai, Y., G.-P. Zheng, and S.-Q. Shi, *Abnormal electrocaloric effect of Na_{0.5}Bi_{0.5}TiO₃-BaTiO₃ lead-free ferroelectric ceramics above room temperature*. Materials Research Bulletin, 2011. **46**(11): p. 1866.
24. Damjanovic, D., et al., *Elastic, dielectric, and piezoelectric anomalies and Raman spectroscopy of 0.5 Ba (Ti_{0.8}Zr_{0.2}) O₃-0.5 (Ba_{0.7}Ca_{0.3}) TiO₃*. Applied Physics Letters, 2012. **100**(19): p. 192907.
25. Haugen, A.B., et al., *Structure and phase transitions in 0.5 (Ba_{0.7}Ca_{0.3}TiO₃)-0.5 (BaZr_{0.2}Ti_{0.8}O₃) from -100° C to 150° C*. Journal of Applied Physics, 2013. **113**(1): p. 014103.
26. Singh, G., V. Tiwari, and P. Gupta, *Thermal stability of piezoelectric coefficients in (Ba_{1-x}Ca_x)(Zr_{0.05}Ti_{0.95}) O₃: A lead-free piezoelectric ceramic*. Applied Physics Letters, 2013. **102**(16): p. 162905.
27. Ye, S., J. Fuh, and L. Lu, *Structure and electrical properties of <001> textured (Ba_{0.85}Ca_{0.15})(Ti_{0.9}Zr_{0.1}) O₃ lead-free piezoelectric ceramics*. Applied Physics Letters, 2012. **100**(25): p. 252906.
28. Yi, J., et al., *Structure, dielectric, ferroelectric, and magnetic properties of (1-x) BiFeO_{3-x} (Ba_{0.85}Ca_{0.15})(Zr_{0.10}Ti_{0.90}) O₃ ceramics*. Materials Research Bulletin, 2015. **66**: p. 132-139.
29. Du, P., et al., *Optical temperature sensor based on upconversion emission in Er-doped ferroelectric 0.5 Ba (Zr_{0.2}Ti_{0.8}) O₃-0.5 (Ba_{0.7}Ca_{0.3}) TiO₃ ceramic*. Applied Physics Letters, 2014. **104**(15): p. 152902.
30. Benabdallah, F., et al., *Linking large piezoelectric coefficients to highly flexible polarization of lead free BaTiO₃-CaTiO₃-BaZrO₃ ceramics*. Journal of Applied Physics, 2011. **109**(12): p. 124116.
31. Gao, J., et al., *Microstructure basis for strong piezoelectricity in Pb-free Ba (Zr_{0.2}Ti_{0.8}) O₃-(Ba_{0.7}Ca_{0.3}) TiO₃ ceramics*. Applied Physics Letters, 2011. **99**(9): p. 092901.
32. Zhukov, S., et al., *Polarization dynamics across the morphotropic phase boundary in Ba (Zr_{0.2}Ti_{0.8}) O_{3-x} (Ba_{0.7}Ca_{0.3}) TiO₃ ferroelectrics*. Applied Physics Letters, 2013. **103**(15): p. 152904.
33. Wang, W., et al., *Piezoelectric properties of BaTiO₃-CaTiO₃-BaZrO₃ ceramics with compositions near the morphotropic phase boundary*. Ceramics International, 2014. **40**(9 Part B): p. 14907-14912.
34. Lu, S., et al., *Temperature driven nano-domain evolution in lead-free Ba (Zr_{0.2}Ti_{0.8}) O₃₋₅₀ (Ba_{0.7}Ca_{0.3}) TiO₃ piezoceramics*. Applied Physics Letters, 2014. **105**(3): p. 032903.
35. Tutuncu, G., et al., *Domain wall motion and electromechanical strain in lead-free piezoelectrics: Insight from the model system (1-x) Ba (Zr_{0.2}Ti_{0.8}) O_{3-x} (Ba_{0.7}Ca_{0.3}) TiO₃ using in situ high-energy X-ray diffraction during application of electric fields*. Journal of Applied Physics, 2014. **115**(14): p. 144104.
36. Ehmke, M.C., et al., *Phase coexistence and ferroelastic texture in high strain (1-x) Ba (Zr_{0.2}Ti_{0.8}) O_{3-x} (Ba_{0.7}Ca_{0.3}) TiO₃ piezoceramics*. Journal of Applied Physics, 2012. **111**(12): p. 124110.
37. Luo, B., et al., *Orientation-dependent piezoelectric properties in lead-free epitaxial 0.5 BaZr_{0.2}Ti_{0.8}O₃-0.5 Ba_{0.7}Ca_{0.3}TiO₃ thin films*. Applied Physics Letters, 2013. **103**(12): p. 122903.
38. Jeong, I.-K. and J. Ahn, *The atomic structure of lead-free Ba (Zr_{0.2}Ti_{0.8}) O₃-(Ba_{0.7}Ca_{0.3}) TiO₃ by using neutron total scattering analysis*. Applied Physics Letters, 2012. **101**(24): p. 242901.

39. Zhang, L., et al., *Phase transitions and the piezoelectricity around morphotropic phase boundary in Ba (Zr_{0.2}Ti_{0.8}) O_{3-x} (Ba_{0.7}Ca_{0.3}) TiO₃ lead-free solid solution*. Applied Physics Letters, 2014. **105**(16): p. 162908.
40. Gao, J., et al., *Major contributor to the large piezoelectric response in (1-x) Ba (Zr_{0.2}Ti_{0.8}) O_{3-x} (Ba_{0.7}Ca_{0.3}) TiO₃ ceramics: Domain wall motion*. Applied Physics Letters, 2014. **104**(25): p. 252909.
41. Wang, P., Y. Li, and Y. Lu, *Enhanced piezoelectric properties of (Ba_{0.85}Ca_{0.15})(Ti_{0.9}Zr_{0.1}) O₃ lead-free ceramics by optimizing calcination and sintering temperature*. Journal of the European Ceramic Society, 2011. **31**(11): p. 2005-2012.
42. Bai, Y., et al., *(Ba, Ca)(Zr, Ti) O₃ lead-free piezoelectric ceramics—The critical role of processing on properties*. Journal of the European Ceramic Society, 2015. **35**(13): p. 3445-3456.
43. Bharathi, P. and K. Varma, *Grain and the concomitant ferroelectric domain size dependent physical properties of Ba_{0.85}Ca_{0.15}Zr_{0.1}Ti_{0.9}O₃ ceramics fabricated using powders derived from oxalate precursor route*. Journal of Applied Physics, 2014. **116**(16): p. 164107.
44. Gao, J., et al., *Symmetry determination on Pb-free piezoceramic 0.5 Ba (Zr_{0.2}Ti_{0.8}) O_{3-0.5} (Ba_{0.7}Ca_{0.3}) TiO₃ using convergent beam electron diffraction method*. Journal of Applied Physics, 2014. **115**(5): p. 054108.
45. Singh, G., V. Sathe, and V. Tiwari, *Investigation of orthorhombic-to-tetragonal structural phase transition in (Ba_{1-x}Ca_x)(Zr_{0.05}Ti_{0.95}) O₃ ferroelectric ceramics using micro-Raman scattering*. Journal of Applied Physics, 2014. **115**(4): p. 044103.
46. Keeble, D.S., et al., *Revised structural phase diagram of (Ba_{0.7}Ca_{0.3}TiO₃)-(BaZr_{0.2}Ti_{0.8}O₃)*. Applied Physics Letters, 2013. **102**(9): p. 092903.
47. Ehmke, M.C., et al., *Reduction of the piezoelectric performance in lead-free (1-x) Ba (Zr_{0.2}Ti_{0.8}) O_{3-x} (Ba_{0.7}Ca_{0.3}) TiO₃ piezoceramics under uniaxial compressive stress*. Journal of Applied Physics, 2012. **112**(11): p. 114108.
48. Tian, Y., et al., *Phase transition behavior and electrical properties of lead-free (Ba_{1-x}Ca_x)(Zr_{0.1}Ti_{0.9}) O₃ piezoelectric ceramics*. Journal of Applied Physics, 2013. **113**(18): p. 184107.
49. Sindhu, M., et al., *Effect of Zr substitution on phase transformation and dielectric properties of Ba_{0.9}Ca_{0.1}TiO₃ ceramics*. Journal of Applied Physics, 2013. **114**(16): p. 164106.
50. Yao, S., et al., *High pyroelectricity in lead-free 0.5 Ba (Zr_{0.2}Ti_{0.8}) O_{3-0.5} (Ba_{0.7}Ca_{0.3}) TiO₃ ceramics*. Journal of Physics D: Applied Physics, 2012. **45**(19): p. 195301.
51. Chen, X., et al., *Low sintering temperature and high piezoelectric properties of Li-doped (Ba, Ca)(Ti, Zr) O₃ lead-free ceramics*. Journal of Alloys and Compounds, 2015.
52. Tan, C.K.I., K. Yao, and J. Ma, *Effects of LiF on the Structure and Properties of Ba_{0.85}Ca_{0.15}Zr_{0.1}Ti_{0.9}O₃ Lead-Free Piezoelectric Ceramics*. International Journal of Applied Ceramic Technology, 2013. **10**(4): p. 701-706.
53. Cui, Y., et al., *Lead-free (Ba_{0.85}Ca_{0.15})(Ti_{0.9}Zr_{0.1}) O₃-Y₂O₃ ceramics with large piezoelectric coefficient obtained by low-temperature sintering*. Journal of Materials Science: Materials in Electronics, 2013. **24**(2): p. 654-657.
54. Qiao, S., et al., *Effect of Ba_{0.85}Ca_{0.15}Ti_{0.90}Zr_{0.10}O₃ content on the microstructure and electrical properties of Bi_{0.51}(Na_{0.82}K_{0.18})_{0.50}TiO₃ ceramics*. Ceramics International, 2012. **38**(6): p. 4845-4851.

55. Wang, X., et al., *Dielectric Properties and Impedance Spectroscopy of MnCO₃-Modified (Ba_{0.85}Ca_{0.15})(Zr_{0.1}Ti_{0.9})O₃ Lead-Free Ceramics*. Journal of the American Ceramic Society, 2015.
56. Zhou, C., et al., *Triple-point-type morphotropic phase boundary based large piezoelectric Pb-free material—Ba (Ti_{0.8}Hf_{0.2})O₃-(Ba_{0.7}Ca_{0.3})TiO₃*. Applied Physics Letters, 2012. **100**(22): p. 222910.
57. Catalan, G. and J.F. Scott, *Physics and applications of bismuth ferrite*. Advanced Materials, 2009. **21**(24): p. 2463-2485.
58. Wu, J., G. Kang, and J. Wang, *Electrical behavior and oxygen vacancies in BiFeO₃/(Bi_{1/2}Na_{1/2})_{0.94}Ba_{0.06}]TiO₃ thin film*. Applied Physics Letters, 2009. **95**(19): p. 192901-192901-3.
59. Leontsev, S.O. and R.E. Eitel, *Dielectric and Piezoelectric Properties in Mn-Modified (1-x) BiFeO₃-xBaTiO₃ Ceramics*. Journal of the American Ceramic Society, 2009. **92**(12): p. 2957-2961.
60. Aksel, E. and J.L. Jones, *Phase Formation of Sodium Bismuth Titanate Perovskite During Solid-State Processing*. Journal of the American Ceramic Society, 2010. **93**(10): p. 3012-3016.
61. Tu, C., et al., *Phase coexistence and Mn-doping effect in lead-free ferroelectric (Na_{1/2}Bi_{1/2})TiO₃ crystals*. Applied Physics Letters, 2010. **96**(6): p. 062903-062903-3.
62. Aksel, E., et al., *Structure and properties of Fe-modified Na_{0.5}Bi_{0.5}TiO₃ at ambient and elevated temperature*. Physical Review B, 2012. **85**(2): p. 024121.
63. Beanland, R. and P.A. Thomas, *Imaging planar tetragonal sheets in rhombohedral Na_{0.5}Bi_{0.5}TiO₃ using transmission electron microscopy*. Scripta Materialia, 2011. **65**(5): p. 440-443.
64. Dorcet, V. and G. Trolliard, *A transmission electron microscopy study of the A-site disordered perovskite Na_{0.5}Bi_{0.5}TiO₃*. Acta Materialia, 2008. **56**(8): p. 1753-1761.
65. Jiang, X., et al., *Electrocaloric effect based on the depolarization transition in (1-x)Bi_{0.5}Na_{0.5}TiO₃-xKNbO₃ lead-free ceramics*. Ceramics International, 2014. **40**(2): p. 2627-2634.
66. Tan, X., et al., *The Antiferroelectric↔Ferroelectric Phase Transition in Lead-Containing and Lead-Free Perovskite Ceramics*. Journal of the American Ceramic Society, 2011. **94**(12): p. 4091-4107.
67. Aksel, E., et al., *Monoclinic crystal structure of polycrystalline Na_{0.5}Bi_{0.5}TiO₃*. Applied Physics Letters, 2011. **98**(15): p. 152901.
68. Spreitzer, M., M. Valant, and D. Suvorov, *Sodium deficiency in Na_{0.5}Bi_{0.5}TiO₃*. Journal of Materials Chemistry, 2007. **17**(2): p. 185-192.
69. Sinyavsky, Y.V., G. Lugansky, and N. Pashkov, *Electrocaloric refrigeration: Investigation of a model and prognosis of mass and efficiency indexes*. Cryogenics, 1992. **32**: p. 28-31.
70. Aksel, E., et al., *Structure and properties of La-modified Na_{0.5}Bi_{0.5}TiO₃ at ambient and elevated temperatures*. Journal of Applied Physics, 2012. **112**(5): p. 054111.
71. Chandrasekhar, M., *Synthesis and Characterizations of BNT-BT and BNT-BT-KNN Ceramics for Actuator and Energy Storage Applications*. Ceramics International, 2015.
72. Moharana, C., *Synthesis of low loss lead free piezoelectric BNT-BT ceramic*. 2009, National Institute of Technology, Rourkela.

73. Suchanicz, J., R. Poprawski, and S. Matyjasik, *Some properties of Na_{0.5}Bi_{0.5}TiO₃*. *Ferroelectrics*, 1997. **192**(1): p. 329-333.
74. Carter, J., et al., *Structure and ferroelectricity of nonstoichiometric (Na_{0.5}Bi_{0.5})TiO₃*. *Applied Physics Letters*, 2014. **104**(11): p. 112904.
75. Hu, D., et al., *Fabrication of [100]-oriented bismuth sodium titanate ceramics with small grain size and high density for piezoelectric materials*. *Journal of the European Ceramic Society*, 2014. **34**(5): p. 1169-1180.
76. Lei, N., et al., *Effect of lattice occupation behavior of Li⁺ cations on microstructure and electrical properties of (Bi_{1/2}Na_{1/2})TiO₃-based lead-free piezoceramics*. *Journal of Applied Physics*, 2011. **109**(5): p. 054102.
77. Shanmuga Sundari, S., B. Kumar, and R. Dhanasekaran, *Synthesis, dielectric and relaxation behavior of lead free NBT-BT ceramics*. *Ceramics International*, 2013. **39**(1): p. 555-561.
78. Saxena, K., *Synthesis and Characterisation of Lead Free Piezoelectric NBT-BT Ceramic*. 2010.
79. Abe, J., et al., *Influence of oxygen-partial pressure controlled sintering on physical properties of (Bi_{0.5}Na_{0.5}TiO₃)_{0.94}(BaTiO₃)_{0.06} ceramics*. 2005.
80. Luo, L., et al., *Raman spectroscopic study of Na_{1/2}Bi_{1/2}TiO₃-x% BaTiO₃ single crystals as a function of temperature and composition*. *Journal of Applied Physics*, 2011. **109**(11): p. 113507.
81. Jo, W., et al., *Evolving morphotropic phase boundary in lead-free (Bi_{1/2}Na_{1/2})TiO₃-BaTiO₃ piezoceramics*. *Journal of Applied Physics*, 2011. **109**(1): p. 014110.
82. Lidjici, H., et al., *XRD, Raman and electrical studies on the (1-x)(Na_{0.5}Bi_{0.5})TiO₃-xBaTiO₃ lead free ceramics*. *Journal of Alloys and Compounds*, 2015. **618**: p. 643-648.
83. Yao, J., et al., *Role of coexisting tetragonal regions in the rhombohedral phase of Na_{0.5}Bi_{0.5}TiO₃-xat.% BaTiO₃ crystals on enhanced piezoelectric properties on approaching the morphotropic phase boundary*. *Applied Physics Letters*, 2012. **100**(1): p. 012901.
84. Ge, W., et al., *Ultra-high electromechanical response in (1-x)(Na_{0.5}Bi_{0.5})TiO₃-xBaTiO₃ single-crystals via polarization extension*. *Journal of Applied Physics*, 2012. **111**(9): p. 093508.
85. Chen, C., et al., *Electric field and temperature-induced phase transition in Mn-doped Na_{1/2}Bi_{1/2}TiO₃-5.0 at.% BaTiO₃ single crystals investigated by micro-Raman scattering*. *Applied Physics Letters*, 2014. **104**(14): p. 142902.
86. Jo, W., et al., *On the phase identity and its thermal evolution of lead free (Bi_{1/2}Na_{1/2})TiO₃-6 mol% BaTiO₃*. *Journal of Applied Physics*, 2011. **110**(7): p. 074106.
87. Zheng, L., et al., *Complete set of material constants of 0.95 (Na_{0.5}Bi_{0.5})TiO₃-0.05 BaTiO₃ lead-free piezoelectric single crystal and the delineation of extrinsic contributions*. *Applied Physics Letters*, 2013. **103**(12): p. 122905.
88. Alonso-Sanjosé, D., et al., *Lead-Free Ferroelectric (Na_{1/2}Bi_{1/2})TiO₃-BaTiO₃ Thin Films in the Morphotropic Phase Boundary Composition: Solution Processing and Properties*. *Journal of the American Ceramic Society*, 2009. **92**(10): p. 2218-2225.
89. Maurya, D., et al., *Enhanced piezoelectricity and nature of electric-field induced structural phase transformation in textured lead-free piezoelectric Na_{0.5}Bi_{0.5}TiO₃-BaTiO₃ ceramics*. *Applied Physics Letters*, 2012. **100**(17): p. 172906.

90. Sapper, E., et al., *Influence of electric fields on the depolarization temperature of Mn-doped (1-x) Bi1/2Na1/2TiO3-xBaTiO3*. Journal of Applied Physics, 2012. **111**(1): p. 014105.
91. Simons, H., et al., *Domain fragmentation during cyclic fatigue in 94%(Bi1/2Na1/2) TiO3-6% BaTiO3*. Journal of Applied Physics, 2012. **112**(4): p. 044101.
92. Wang, S.-F., et al., *Structural stability and depolarization of manganese-doped (Bi0.5Na0.5) 1-xBaxTiO3 relaxor ferroelectrics*. Journal of Applied Physics, 2014. **116**(15): p. 154101.
93. Schneider, D., et al., *Anisotropy of ferroelectric behavior of (1-x) Bi1/2Na1/2TiO3-xBaTiO3 single crystals across the morphotropic phase boundary*. Journal of Applied Physics, 2014. **116**(4): p. 044111.
94. Ge, W., et al., *In-situ X-ray diffraction study of an electric field induced phase transition and giant strain in Na0.5Bi0.5TiO3-x% BaTiO3 lead-free single crystals*. physica status solidi (RRL)-Rapid Research Letters, 2011. **5**(9): p. 356-358.
95. Zhang, Q., et al., *Enhanced piezoelectric and ferroelectric properties in Mn-doped Na0.5Bi0.5TiO3-BaTiO3 single crystals*. Applied Physics Letters, 2009. **95**(10): p. 102904.
96. Park, J.-H., H.-Y. Lee, and S.-J.L. Kang, *Solid-state conversion of (Na1/2Bi1/2) TiO3-BaTiO3-(K1/2Na1/2) NbO3 single crystals and their piezoelectric properties*. Applied Physics Letters, 2014. **104**(22): p. 222910.
97. Luo, C., et al., *Crystallographic direction dependence of direct current field induced strain and phase transitions in Na0.5Bi0.5TiO3-x% BaTiO3 single crystals near the morphotropic phase boundary*. Applied Physics Letters, 2012. **101**(14): p. 141912.
98. Simons, H., et al., *Origin of large recoverable strain in 0.94 (Bi0.5Na0.5) TiO3-0.06 BaTiO3 near the ferroelectric-relaxor transition*. Applied Physics Letters, 2013. **102**(6): p. 062902.
99. Jo, W., et al., *Two-stage processes of electrically induced-ferroelectric to relaxor transition in 0.94 (Bi1/2Na1/2) TiO3-0.06 BaTiO3*. Applied Physics Letters, 2013. **102**(19): p. 192903.
100. Sapper, E., et al., *Electric-field-temperature phase diagram of the ferroelectric relaxor system (1-x) Bi1/2Na1/2TiO3-xBaTiO3 doped with manganese*. Journal of Applied Physics, 2014. **115**(19): p. 194104.
101. Groh, C., W. Jo, and J. Rödel, *Frequency and temperature dependence of actuating performance of Bi1/2Na1/2TiO3-BaTiO3 based relaxor/ferroelectric composites*. Journal of Applied Physics, 2014. **115**(23): p. 234107.
102. Craciun, F. and C. Galassi, *Smearing of induced ferroelectric transition and easy imprinting of different polarization configurations in relaxor ferroelectric (Na1/2Bi1/2) 1-xBaxTiO3*. Applied Physics Letters, 2013. **102**(16): p. 162902.
103. Craciun, F., C. Galassi, and R. Birjega, *Electric-field-induced and spontaneous relaxor-ferroelectric phase transitions in (Na1/2Bi1/2) 1-xBaxTiO3*. Journal of Applied Physics, 2012. **112**(12): p. 124106.
104. Zang, J., W. Jo, and J. Rödel, *Quenching-induced circumvention of integrated aging effect of relaxor lead lanthanum zirconate titanate and (Bi1/2Na1/2) TiO3-BaTiO3*. Applied Physics Letters, 2013. **102**(3): p. 032901.
105. Ge, W., et al., *Direct evidence of correlations between relaxor behavior and polar nano-regions in relaxor ferroelectrics: A case study of lead-free*

- piezoelectrics Na_{0.5}Bi_{0.5}TiO₃-x% BaTiO₃*. Applied Physics Letters, 2013. **103**(24): p. 241914.
106. Wang, D., et al., *Enhanced ferroelectric and piezoelectric properties in doped lead-free (Bi_{0.5}Na_{0.5})_{0.94}Ba_{0.06}TiO₃ thin films*. Applied Physics Letters, 2010. **97**(21): p. 212901-212901-3.
 107. Li, W., et al., *Orientation dependence on piezoelectric properties of Bi_{0.5}Na_{0.5}TiO₃-BaTiO₃-SrTiO₃ epitaxial thin films*. Applied Physics Letters, 2014. **104**(17): p. 172903.
 108. Meng, W., et al., *Two-step sintering and electrical properties of sol-gel derived 0.94 (Bi_{0.5}Na_{0.5})TiO₃-0.06 BaTiO₃ lead-free ceramics*. Journal of Materials Science: Materials in Electronics, 2011. **22**(12): p. 1841-1847.
 109. Xu, Q., et al., *Structure and electrical properties of (Na_{0.5}Bi_{0.5})_{1-x}Ba_xTiO₃ ceramics made by a citrate method*. Journal of Electroceramics, 2008. **21**(1-4): p. 617-620.
 110. Yan, Y., et al., *Fabrication and electrical properties of textured Na_{1/2}Bi_{1/2}TiO₃-BaTiO₃ ceramics by reactive-templated grain growth*. Journal of Electroceramics, 2008. **21**(1-4): p. 246-250.
 111. Ma, C., et al., *Domain structure-dielectric property relationship in lead-free (1-x)(Bi_{1/2}Na_{1/2})TiO₃-xBaTiO₃ ceramics*. Journal of Applied Physics, 2010. **108**(10): p. 104105.
 112. Guo, Y., M. Gu, and H. Luo, *Antiferroelectric Phase and Pyroelectric Response in (Na_yBi_z)Ti_{1-x}O₃ (1-x)-xBaTiO₃ Ceramics*. Journal of the American Ceramic Society, 2011. **94**(5): p. 1350-1353.
 113. Guo, Y., et al., *Composition-induced antiferroelectric phase and giant strain in lead-free (Na_yBi_z)Ti_{1-x}O₃ (1-x)-xBaTiO₃ ceramics*. Physical Review B, 2011. **83**(5): p. 054118.
 114. Sun, R., et al., *Pyroelectric properties of Mn-doped 94.6 Na_{0.5}Bi_{0.5}TiO₃-5.4 BaTiO₃ lead-free single crystals*. Journal of Applied Physics, 2014. **115**(7): p. 074101.
 115. Liu, Y., et al., *Effect of Sintering Temperature on Structural and Electrical Properties of Lead-free BNT-BT Piezoelectric Thick Films*. Ceramics International, 2015.
 116. Lidjici, H., et al., *The effects of sintering temperature and poling condition on the piezoelectric properties of 0.935(Bi_{0.5}Na_{0.5})TiO₃ - 0.065BaTiO₃ ceramics*. Sciences & Technologie B, 2010(32): p. 25-28.
 117. Sittiketkorn, P. and T. Bongkarn, *Effects of Sintering Temperature on Phase Formation, Microstructure and Dielectric Properties of BNT-BT Ceramics Prepared by Combustion Technique*. Ferroelectrics Letters Section, 2013. **40**(4-6): p. 77-84.
 118. Du, P., et al., *Photoluminescence and piezoelectric properties of Pr-doped NBT-xBZT ceramics Sensitive to structure transition*. Journal of Alloys and Compounds, 2013. **559**: p. 92-96.
 119. Datta, K., K. Roleder, and P. Thomas, *Enhanced tetragonality in lead-free piezoelectric (1-x)BaTiO₃-xNa_{1/2}Bi_{1/2}TiO₃ solid solutions where x=0.05-0.40*. Journal of Applied Physics, 2009. **106**(12): p. 123512.
 120. Chen, X., et al., *Microstructure, dielectric and ferroelectric properties of (1-x)(0.94 Bi_{0.5}Na_{0.5}TiO₃-0.06 BaTiO₃)-xBiFeO₃ lead-free ceramics synthesized via a high energy ball milling method*. Journal of alloys and compounds, 2010. **507**(2): p. 535-541.

121. Chen, X., et al., *Microstructure, dielectric and ferroelectric properties of 0.94Bi0.5Na0.5TiO3-0.06BaTiO3 (NBTB) and 0.05BiFeO3-0.95NBTB ceramics Effect of sintering atmosphere*. Journal of Alloys and Compounds, 2011. **509**(5): p. 1824-1829.
122. Niemann, R., et al., *Inapplicability of the Maxwell relation for the quantification of caloric effects in anisotropic ferroic materials*. International Journal of Refrigeration, 2014. **37**: p. 281-288.
123. Guyomar, D., et al., *Ferroelectric electrocaloric conversion in 0.75 (PbMg1/3Nb2/3O3)-0.25 (PbTiO3) ceramics*. Journal of Physics D: Applied Physics, 2006. **39**(20): p. 4491.
124. Maiwa, H. and S.-H. Kim, *Electrocaloric and pyroelectric properties of PZT and PMN-PNN-PZT thin films*. Ceramics International, 2013. **39**: p. S497-S500.
125. Sebald, G., et al., *Electrocaloric and pyroelectric properties of 0.75 Pb (Mg1/3Nb2/3) O3-0.25 PbTiO3 single crystals*. Journal of applied physics, 2006. **100**(12): p. 124112.
126. Dunne, L.J., et al., *Microscopic theory of the electrocaloric effect in the paraelectric phase of potassium dihydrogen phosphate*. Applied Physics Letters, 2008. **93**(12): p. 122906.
127. Suchanek, G. and G. Gerlach, *Electrocaloric cooling based on relaxor ferroelectrics*. Phase Transitions, Phase Transitions , 2015, **88**, p. 1-9.
128. Liu, Y., et al., *Giant mechanically-mediated electrocaloric effect in ultrathin ferroelectric capacitors at room temperature*. Applied Physics Letters, 2014. **104**(1): p. 012907.
129. Starkov, A., O. Pakhomov, and I. Starkov, *Solid-state cooler: new opportunities*. Ferroelectrics, 2012. **430**(1): p. 108-114.
130. Jia, Y. and Y.S. Ju, *A solid-state refrigerator based on the electrocaloric effect*. Applied Physics Letters, 2012. **100**(24): p. 242901.
131. Kar-Narayan, S. and N. Mathur, *Predicted cooling powers for multilayer capacitors based on various electrocaloric and electrode materials*. Applied Physics Letters, 2009. **95**(24): p. 242903.
132. Pakhomov, O., et al., *Thermodynamic estimation of cooling efficiency using an electrocaloric solid-state line*. Technical Physics, 2010. **55**(8): p. 1155-1160.
133. Perantie, J., et al., *Field-induced thermal response and irreversible phase transition enthalpy change in Pb (Mg 1/3 Nb 2/3) O 3-PbTiO 3*. Applied Physics Letters, 2009. **94**(10): p. 102903-102903-3.
134. Duncce, M., *Phase transitions and physical properties of BNT based solid solotions*, University of Latvia, Phd thesies, 2014.
135. Bai, Y., et al., *The giant electrocaloric effect and high effective cooling power near room temperature for BaTiO3 thick film*. Journal of applied physics, 2011. **110**(9): p. 094103.
136. Pirc, R., et al., *Electrocaloric effect in relaxor ferroelectrics*. Journal of Applied Physics, 2011. **110**(7): p. 074113.
137. Bai, Y., G.-P. Zheng, and S.-Q. Shi, *Kinetic electrocaloric effect and giant net cooling of lead-free ferroelectric refrigerants*. Journal of applied physics, 2010. **108**(10): p. 104102.
138. Prosandeev, S., I. Ponomareva, and L. Bellaiche, *Electrocaloric effect in bulk and low-dimensional ferroelectrics from first principles*. Physical Review B, 2008. **78**(5): p. 052103.

139. Bai, Y., et al., *Combined effects of diffuse phase transition and microstructure on the electrocaloric effect in Ba_{1-x}Sr_xTiO₃ ceramics*. Applied Physics Letters, 2013. **103**(16): p. 162902.
140. Liu, Y., et al., *Intrinsic electrocaloric effect in ultrathin ferroelectric capacitors*. Applied Physics Letters, 2012. **100**(19): p. 192902.
141. Beckman, S., et al., *Effective Hamiltonian methods for predicting the electrocaloric behavior of BaTiO₃*. Materials Letters, 2012. **89**: p. 254-257.
142. Valant, M., et al., *Electrocaloric temperature change constrained by the dielectric strength*. Materials Chemistry and Physics, 2012. **136**(2): p. 277-280.
143. Peng, B., H. Fan, and Q. Zhang, *A Giant Electrocaloric Effect in Nanoscale Antiferroelectric and Ferroelectric Phases Coexisting in a Relaxor Pb_{0.8}Ba_{0.2}ZrO₃ Thin Film at Room Temperature*. Advanced Functional Materials, 2013. **23**(23): p. 2987-2992.
144. Liu, Y., et al., *Giant electrocaloric effect in asymmetric ferroelectric tunnel junctions at room temperature*. Applied Physics Letters, 2014. **104**(8): p. 082901.
145. Starkov, A.S., O. Pakhomov, and I. Starkov, *Effect of thermal phenomena on a second-order phase transition in the Landau-Ginzburg model*. JETP letters, 2010. **91**(10): p. 507-511.
146. Anton, E.-M., et al., *Determination of depolarization temperature of (Bi_{1/2}Na_{1/2})TiO₃-based lead-free piezoceramics*. Journal of Applied Physics, 2011. **110**(9): p. 094108.
147. Liu, L., et al., *Theoretical investigation on polar dielectric with large electrocaloric effect as cooling devices*. Applied Physics Letters, 2011. **99**(18): p. 181908.
148. Ponomareva, I. and S. Lisenkov, *Bridging the macroscopic and atomistic descriptions of the electrocaloric effect*. Physical review letters, 2012. **108**(16): p. 167604.
149. Wang, J., et al., *DC electric field dependence for the dielectric permittivity in antiferroelectric and ferroelectric states*. Journal of Alloys and Compounds, 2014. **587**: p. 827-829.
150. Peräntie, J., et al., *Electric-field-induced dielectric and temperature changes in a(011)-oriented Pb(Mg_{1/3}Nb_{2/3})O₃-PbTiO₃ single crystal*. Physical Review B, 2010. **82**(13): p. 134119.
151. Lisenkov, S. and I. Ponomareva, *Intrinsic electrocaloric effect in ferroelectric alloys from atomistic simulations*. Physical Review B, 2009. **80**(14): p. 140102.
152. Liu, X.Q., et al., *Electrocaloric effects in spark plasma sintered Ba_{0.7}Sr_{0.3}TiO₃-based ceramics Effects of domain sizes and phase constitution*. Ceramics International, 2014.
153. Liu, X.Q., et al., *Enhanced Electrocaloric Effects in Spark Plasma-Sintered Ba_{0.65}Sr_{0.35}TiO₃-Based Ceramics at Room Temperature*. Journal of the American Ceramic Society, 2013. **96**(4): p. 1021-1023.
154. Gorzkowski, E., et al., *Glass-ceramics of barium strontium titanate for high energy density capacitors*. Journal of electroceramics, 2007. **18**(3-4): p. 269-276.
155. Zhang, L., et al., *Microstructure and energy-storage performance of BaO-B₂O₃-SiO₂ glass added (Na_{0.5}Bi_{0.5})TiO₃ thick films*. Journal of Materials Science: Materials in Electronics, 2013. **24**(10): p. 3830-3835.

156. Lu, S., et al., *Organic and inorganic relaxor ferroelectrics with giant electrocaloric effect*. Applied Physics Letters, 2010. **97**(16): p. 162904.
157. Lu, S.-G. and Q. Zhang, *Large electrocaloric effect in relaxor ferroelectrics*. Journal of Advanced Dielectrics, 2012. **2**(03).
158. Rožič, B., et al., *Influence of the critical point on the electrocaloric response of relaxor ferroelectrics*. Journal of Applied Physics, 2011. **110**(6): p. 064118.
159. Hamad, M.A., *Theoretical investigations on electrocaloric properties of relaxor ferroelectric 0.9 PbMg_{1/3}Nb_{2/3}O₃-0.1 PbTiO₃ thin film*. Journal of Computational Electronics, 2012. **11**(4): p. 344-348.
160. Peräntie, J., et al., *Electrocaloric properties in relaxor ferroelectric (1-x) Pb (Mg_{1/3}Nb_{2/3}) O₃-xPbTiO₃ system*. Journal of Applied Physics, 2013. **114**(17): p. 174105.
161. Luo, L., et al., *Pyroelectric and electrocaloric effect of <111>-oriented 0.9 PMN-0.1 PT single crystal*. Journal of Alloys and Compounds, 2011. **509**(32): p. 8149-8152.
162. Li, Q., et al., *Composition and temperature dependence of ferroelectric and pyroelectric properties of (1-x)[PMN-PT (65/35)]-xPZ (0 ≤ x ≤ 0.10) ceramics*. Materials Research Bulletin, 2014.
163. Singh, G. and V. Tiwari, *Electro-caloric effect in relaxor and ferroelectric compositions of Pb(Mg(1-x)₃Nb₂(1-x)₃Zrx)O₃ ceramics*. Journal of Alloys and Compounds, 2012. **523**: p. 30-35.
164. Zhang, J., et al., *Enhanced pyroelectric properties of Cax (Sr_{0.5}Ba_{0.5})_{1-x}Nb₂O₆ lead-free ceramics*. Applied Physics Letters, 2013. **102**(10): p. 102908.
165. Molin, C., et al., *Effect of dopants on the electrocaloric effect of 0.92 Pb (Mg_{1/3} Nb_{2/3}) O₃-0.08 PbTiO₃ ceramics*. Journal of the European Ceramic Society, 2015.
166. Yang, L., et al., *Novel polymer ferroelectric behavior via crystal isomorphism and the nanoconfinement effect*. Polymer, 2013. **54**(7): p. 1709-1728.
167. Shi, Y. and A. Soh, *Modeling of enhanced electrocaloric effect above the Curie temperature in relaxor ferroelectrics*. Acta Materialia, 2011. **59**(14): p. 5574-5583.
168. Xiao, D., et al., *Electrocaloric properties of (1-x) Pb (Mg_{1/3}Nb_{2/3}) O₃-xPbTiO₃ ferroelectric ceramics near room temperature*. Materials chemistry and physics, 1998. **57**(2): p. 182-185.
169. Wang, J., et al., *High room-temperature pyroelectric response of MgO-modified Pb_{0.99}(Zr_{0.95}Ti_{0.05})_{0.98}Nb_{0.02}O₃ ceramics*. Infrared Physics & Technology, 2013. **61**: p. 325-329.
170. Liu, Z., X. Li, and Q. Zhang, *Maximizing the number of coexisting phases near invariant critical points for giant electrocaloric and electromechanical responses in ferroelectrics*. Applied Physics Letters, 2012. **101**(8): p. 082904.
171. Upadhyay, S.K., et al., *Electro-caloric effect in lead-free Sn doped BaTiO₃ ceramics at room temperature and low applied fields*. Applied Physics Letters, 2014. **105**(11): p. 112907.
172. Luo, Z., et al., *Enhanced electrocaloric effect in lead-free BaTi_{1-x}Sn_xO₃ ceramics near room temperature*. Applied Physics Letters, 2014. **105**(10): p. 102904.
173. Li, X., et al., *Pyroelectric and electrocaloric materials*. Journal of Materials Chemistry C, 2013. **1**(1): p. 23-37.

174. Kar-Narayan, S., et al., *Direct electrocaloric measurements of a multilayer capacitor using scanning thermal microscopy and infra-red imaging*. Applied Physics Letters, 2013. **102**(3): p. 032903.
175. Sanlialp, M., et al. *Direct electrocaloric measurements using a differential scanning calorimeter*. in *Applications of Ferroelectric, International Symposium on Integrated Functionalities and Piezoelectric Force Microscopy Workshop (ISAF/ISIF/PFM), 2015 Joint IEEE International Symposium on the*. 2015. IEEE.
176. Asbani, B., et al., *Electrocaloric effect in Ba (0.2) Ca (0.8) Ti (0.95) Ge (0.05) O (3) determined by a new pyroelectric method*. Epl journal, 2015, 111 (5)
177. Kutnjak, Z., B. Rožič, and R. Pirc, *Electrocaloric Effect: Theory, Measurements, and Applications*. Wiley Encyclopedia of Electrical and Electronics Engineering, 2015.
178. Ivill, M., E. Ngo, and M.W. Cole, *Method and Characterization of Pyroelectric Coefficients for Determining Material Figures of Merit for Infrared (IR) Detectors*. 2013, DTIC Document, <http://www.dtic.mil/get-tr-doc/pdf?AD=ADA592778>
179. Crossley, S., et al., *Direct electrocaloric measurement of 0.9 Pb (Mg1/3Nb2/3) O3-0.1 PbTiO3 films using scanning thermal microscopy*. Applied Physics Letters, 2016. **108**(3): p. 032902.
180. Lu, S.G. and Q. Zhang, *Electrocaloric Materials for Solid-State Refrigeration*. Advanced Materials, 2009. **21**(19): p. 1983-1987.
181. Qiu, J. and Q. Jiang, *Effect of electric field on electrocaloric effect in Pb (Zr 1-x Ti x) O 3 solid solution*. Physics Letters A, 2008. **372**(48): p. 7191-7195.
182. Starkov, A. and O. Pakhomov, *Influence of the dynamic polarization of a ferroelectric material on the magnitude of its electrocaloric response*. Technical Physics Letters, 2010. **36**(1): p. 1-3.
183. Lu, S., et al., *Comparison of directly and indirectly measured electrocaloric effect in relaxor ferroelectric polymers*. Applied Physics Letters, 2010. **97**(20): p. 202901.
184. Bai, Y., G. Zheng, and S. Shi, *Direct measurement of giant electrocaloric effect in BaTiO 3 multilayer thick film structure beyond theoretical prediction*. Applied Physics Letters, 2010. **96**(19): p. 192902-192902-3.
185. Sebald, G., et al., *Electrocaloric properties of high dielectric constant ferroelectric ceramics*. Journal of the European Ceramic Society, 2007. **27**(13): p. 4021-4024.
186. Wang, J., et al., *Nonadiabatic direct measurement electrocaloric effect in lead-free Ba,Ca(Zr,Ti)O3*. Journal of Alloys and Compounds, 2013. **550**: p. 561-563.
187. Bai, Y., et al., *Entropy-change measurement of electrocaloric effect of BaTiO3 single crystal*. Physica status solidi (a), 2012. **209**(5): p. 941-944.
188. Kar-Narayan, S. and N. Mathur, *Direct and indirect electrocaloric measurements using multilayer capacitors*. Journal of Physics D: Applied Physics, 2010. **43**(3): p. 032002.
189. Geng, W., et al., *Giant Negative Electrocaloric Effect in Antiferroelectric La-Doped Pb (ZrTi) O3 Thin Films Near Room Temperature*. Advanced Materials, 2015.
190. Zheng, X.-C., et al., *Electro-caloric behaviors of lead-free Bi0.5Na0.5TiO3-BaTiO3 ceramics*. Journal of electroceramics, 2012. **28**(1): p. 20-26.
191. Zannen, M., et al., *Electrocaloric effect and luminescence properties of lanthanide doped (Na1/2Bi1/2) TiO3 lead free materials*. Applied Physics Letters, 2015. **107**(3): p. 032905.

192. Cao, W., et al., *Large electrocaloric response and high energy-storage properties over a broad temperature range in lead-free NBT-ST ceramics*. Journal of the European Ceramic Society, 2016. **36**(3): p. 593-600.
193. Cao, W., et al., *Enhanced electrocaloric effect in lead-free NBT-based ceramics*. Ceramics International, 2014.
194. Uddin, S., et al., *Unification of the negative electrocaloric effect in $\text{Bi}_{1/2}\text{Na}_{1/2}\text{TiO}_3\text{-BaTiO}_3$ solid solutions by $\text{Ba}_{1/2}\text{Sr}_{1/2}\text{TiO}_3$ doping*. Journal of Applied Physics, 2013. **114**(21): p. 213519.
195. Le Goupil, F., et al., *Electrocaloric enhancement near the morphotropic phase boundary in lead-free NBT-KBT ceramics*. Applied Physics Letters, 2015. **107**(17): p. 172903.
196. Tang, J., et al., *Influence of the composition-induced structure evolution on the electrocaloric effect in $\text{Bi}_{0.5}\text{Na}_{0.5}\text{TiO}_3$ -based solid solution*. Ceramics International, 2015.
197. Zheng, G.-P., et al., *Structural and electrocaloric properties of multiferroic- BiFeO_3 doped $0.94\text{Bi}_{0.5}\text{Na}_{0.5}\text{TiO}_3\text{-}0.06\text{BaTiO}_3$ solid solutions*. Journal of Alloys and Compounds, 2016. **663**: p. 249-255.
198. Li, Q., et al., *Large electrocaloric effect in $(\text{Bi}_{0.5}\text{Na}_{0.5})_{0.94}\text{Ba}_{0.06}\text{TiO}_3$ lead-free ferroelectric ceramics by La_2O_3 addition*. Materials Research Bulletin, 2016. **74**: p. 57-61.
199. Singh, G., V. Tiwari, and P. Gupta, *Electro-caloric effect in $(\text{Ba}_{1-x}\text{Ca}_x)(\text{Zr}_{0.05}\text{Ti}_{0.95})\text{O}_3$: A lead-free ferroelectric material*. Applied Physics Letters, 2013. **103**(20): p. 202903.
200. Bai, Y., X. Han, and L. Qiao, *Optimized electrocaloric refrigeration capacity in lead-free $(1-x)\text{BaZr}_{0.2}\text{Ti}_{0.8}\text{O}_3\text{-}x\text{Ba}_{0.7}\text{Ca}_{0.3}\text{TiO}_3$ ceramics*. Applied Physics Letters, 2013. **102**(25): p. 252904.
201. Singh, G., et al., *Electro-caloric effect in $0.45\text{BaZr}_{0.2}\text{Ti}_{0.8}\text{O}_3\text{-}0.55\text{Ba}_{0.7}\text{Ca}_{0.3}\text{TiO}_3$ single crystal*. Applied Physics Letters, 2013. **102**(8): p. 082902.
202. Sanlialp, M., et al., *Strong electrocaloric effect in lead-free $0.65\text{Ba}(\text{Zr}_{0.2}\text{Ti}_{0.8})\text{O}_3\text{-}0.35(\text{Ba}_{0.7}\text{Ca}_{0.3})\text{TiO}_3$ ceramics obtained by direct measurements*. Applied Physics Letters, 2015. **106**(6): p. 062901.
203. Kaddoussi, H., et al., *Room temperature electro-caloric effect in lead-free $\text{Ba}(\text{Zr}_{0.1}\text{Ti}_{0.9})_{1-x}\text{Sn}_x\text{O}_3$ ($x=0, x=0.075$) ceramics*. Solid State Communications, 2015. **201**: p. 64-67.
204. Ye, H.-J., et al., *Dielectric and electrocaloric responses of $\text{Ba}(\text{Zr}_{0.2}\text{Ti}_{0.8})\text{O}_3$ bulk ceramics and thick films with sintering aids*. Dielectrics and Electrical Insulation, IEEE Transactions on, 2015. **22**(3): p. 1501-1505.
205. Asbani, B., et al., *Lead-free $\text{Ba}_{0.8}\text{Ca}_{0.2}(\text{Zr}_x\text{Ti}_{1-x})\text{O}_3$ ceramics with large electrocaloric effect*. Applied Physics Letters, 2015. **106**(4): p. 042902.
206. Patel, S., A. Chauhan, and R. Vaish, *Electrocaloric Behavior and Temperature-Dependent Scaling of Dynamic Hysteresis of $\text{Ba}_{0.85}\text{Ca}_{0.15}\text{Ti}_{0.9}\text{Zr}_{0.1}\text{O}_3$ Ceramics*. International Journal of Applied Ceramic Technology, 2015.
207. Patel, S., P. Sharma, and R. Vaish, *Enhanced electrocaloric effect in $\text{Ba}_{0.85}\text{Ca}_{0.15}\text{Zr}_{0.1}\text{Ti}_{0.9-x}\text{Sn}_x\text{O}_3$ ferroelectric ceramics*. Phase Transitions, 2016: p. 1-12.
208. Patel, S., A. Chauhan, and R. Vaish, *Enhanced electrocaloric effect in Fe-doped $(\text{Ba}_{0.85}\text{Ca}_{0.15}\text{Zr}_{0.1}\text{Ti}_{0.9})\text{O}_3$ ferroelectric ceramics*. Applied Materials Today, 2015. **1**(1): p. 37-44.

209. Kim, Y.S. and J. Yoo, *Electrocaloric Effect of Lead-Free (Ba, Ca)(Zr, Ti) O₃ Ferroelectric Ceramic*. Journal of Electronic Materials, 2015. **44**(8): p. 2555-2558.
210. Kaddoussi, H., et al., *Indirect and direct electrocaloric measurements of (Ba 1-x Ca x)(Zr 0.1 Ti 0.9) O₃ ceramics (x= 0.05, x= 0.20)*. Journal of Alloys and Compounds, 2016.
211. Han, F., et al., *A systematic modification of the large electrocaloric effect within a broad temperature range in rare-earth doped BaTiO₃ ceramics*. Journal of Materials Chemistry C, 2016. **4**(9): p. 1842-1849.
212. Feng, Z., D. Shi, and S. Dou, *Large electrocaloric effect in highly (001)-oriented thin films*. Solid State Communications, 2011. **151**(2): p. 123-126.
213. Ye, H.-J., et al., *Giant electrocaloric effect in BaZr_{0.2}Ti_{0.8}O₃ thick film*. Applied Physics Letters, 2014. **105**(15): p. 152908.
214. Zhang, J., S. Alpay, and G. Rossetti, *Influence of thermal stresses on the electrocaloric properties of ferroelectric films*. Applied Physics Letters, 2011. **98**(13): p. 132907-132907-3.
215. Kesim, M., et al., *Enhanced electrocaloric and pyroelectric response from ferroelectric multilayers*. Applied Physics Letters, 2014. **105**(5): p. 052901.
216. Corkovic, S. and Q. Zhang, *Enhanced pyroelectric coefficient of antiferroelectric-ferroelectric bilayer thin films*. Journal of Applied Physics, 2009. **105**(6): p. 061610-061610-5.
217. Huang, K., et al., *Significant polarization variation near room temperature of Ba_{0.65}Sr_{0.35}TiO₃ thin films for pyroelectric energy harvesting*. Sensors and Actuators B: Chemical, 2012. **169**: p. 208-212.
218. Zheng, X.-C., et al., *Thermo-electrical energy conversions in Bi_{0.5}Na_{0.5}TiO₃-BaTiO₃ thin films prepared by sol-gel method*. Thin Solid Films, 2012. **522**: p. 125-128.
219. Dai, X., et al., *Influence of thermal strains on the electrocaloric and dielectric properties of ferroelectric nanoshells*. Journal of applied physics, 2009. **106**(3): p. 034103.
220. Zhou, C.-R. and L.-Y. Chai, *Dielectric and piezoelectric properties of Bi_{0.5}(Na_{0.82}K_{0.18})_{0.5}TiO₃-LiSbO₃ lead-free piezoelectric ceramics*. Bulletin of Materials Science, 2011. **34**(4): p. 933-936.
221. Nagata, H., et al., *Large piezoelectric constant and high Curie temperature of lead-free piezoelectric ceramic ternary system based on bismuth sodium titanate-bismuth potassium titanate-barium titanate near the morphotropic phase boundary*. Japanese Journal of Applied Physics, 2003. **42**(12R): p. 7401.
222. Dinh, T.H., et al., *Ergodicity and nonergodicity in La-doped Bi_{1/2}(Na_{0.82}K_{0.18})_{1/2}TiO₃ relaxors*. Journal of the Korean Physical Society, 2015. **66**(7): p. 1077-1081.
223. Pham, K.-N., et al., *Giant strain in Nb-doped Bi_{0.5}(Na_{0.82}K_{0.18})_{0.5}TiO₃ lead-free electromechanical ceramics*. Materials Letters, 2010. **64**(20): p. 2219-2222.
224. Yoon, S.O., et al., *Microwave dielectric properties of glass-Bi_{~2}Ti_{~2}O_{~7} ceramic composites*. Journal of Ceramic Processing Research, 2008. **9**(1): p. 34.
225. Shaobo, L. and L. Yanqiu, *Research on the electrocaloric effect of PMN/PT solid solution for ferroelectrics MEMS microcooler*. Materials Science and Engineering: B, 2004. **113**(1): p. 46-49.

Appendix I:

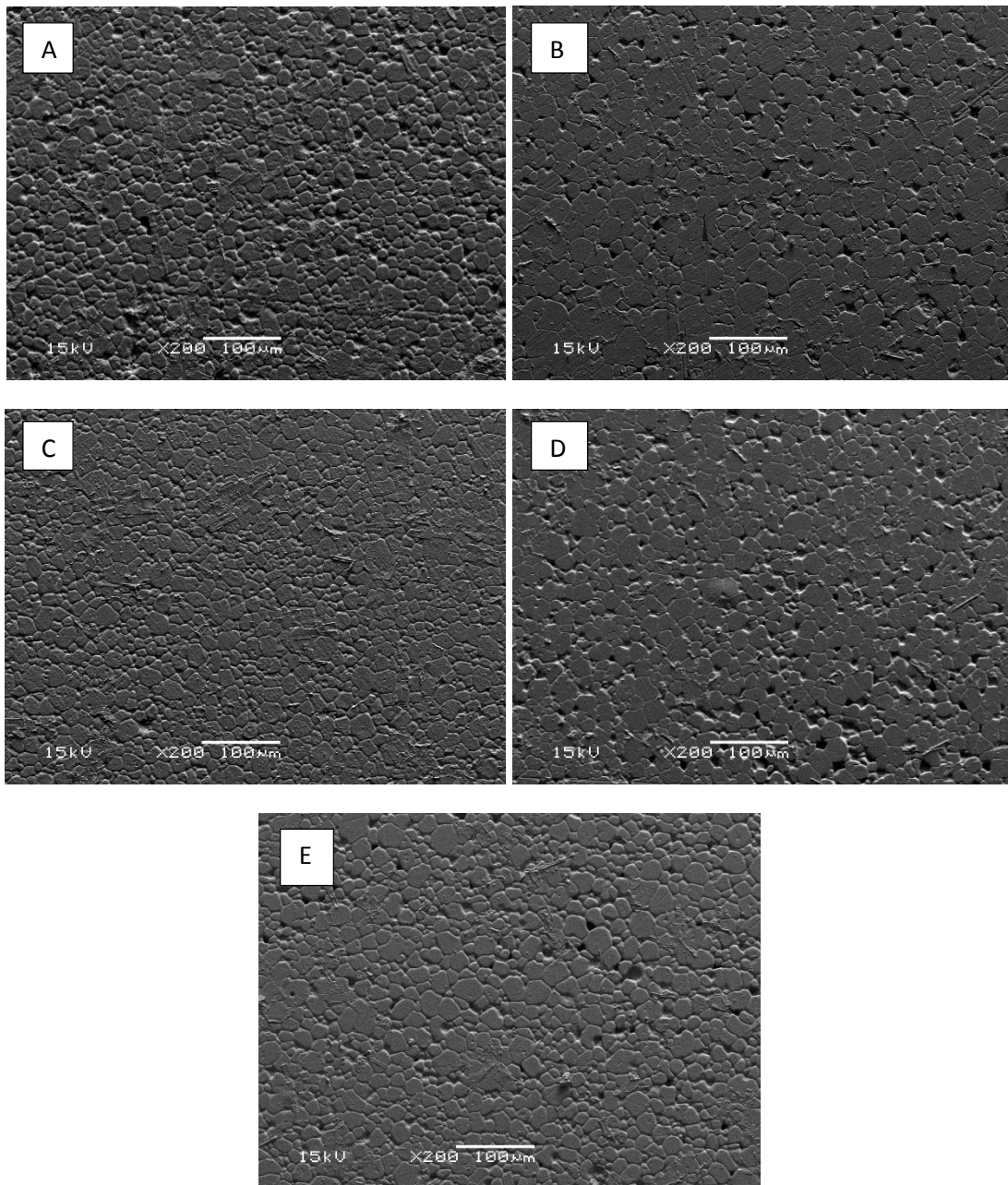


Figure I-1: : Low magnification SEM micrographs of the BCZT Samples sintered at a) 1400°C, B) 1425°C, C) 1450°C, D) 1475°C and E) 1500°C

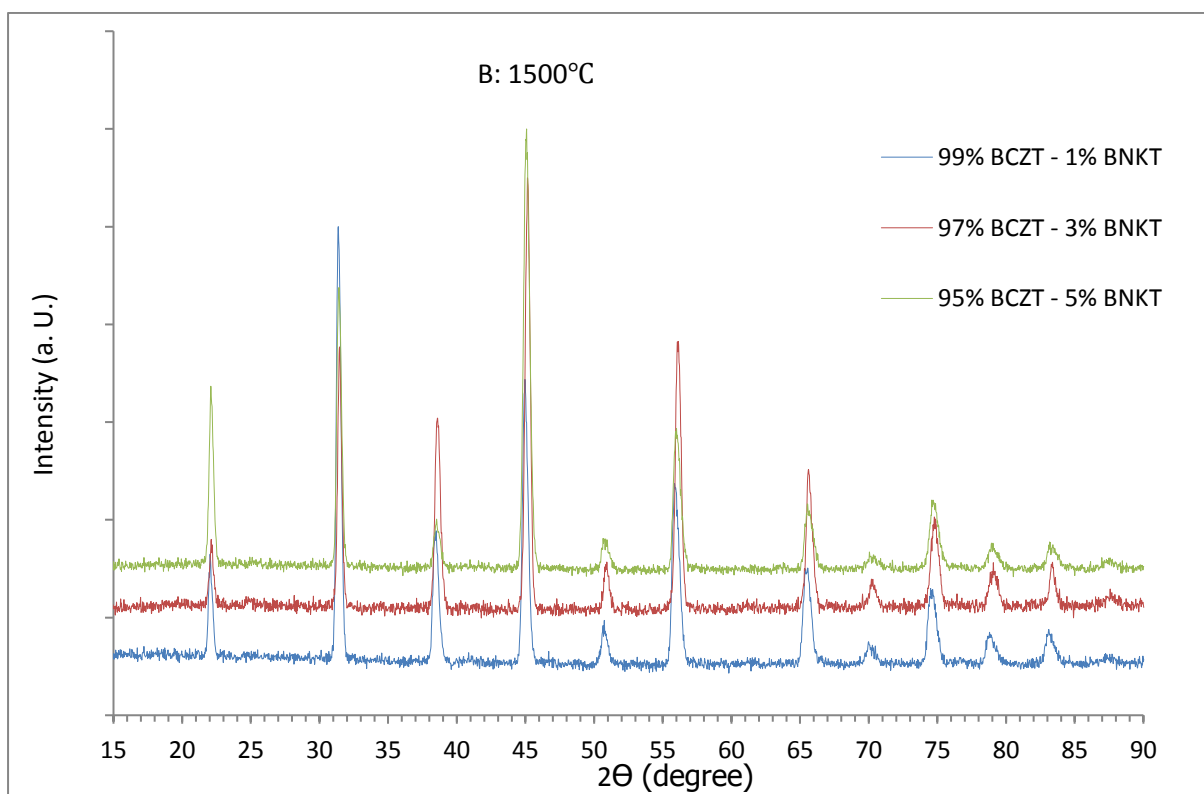
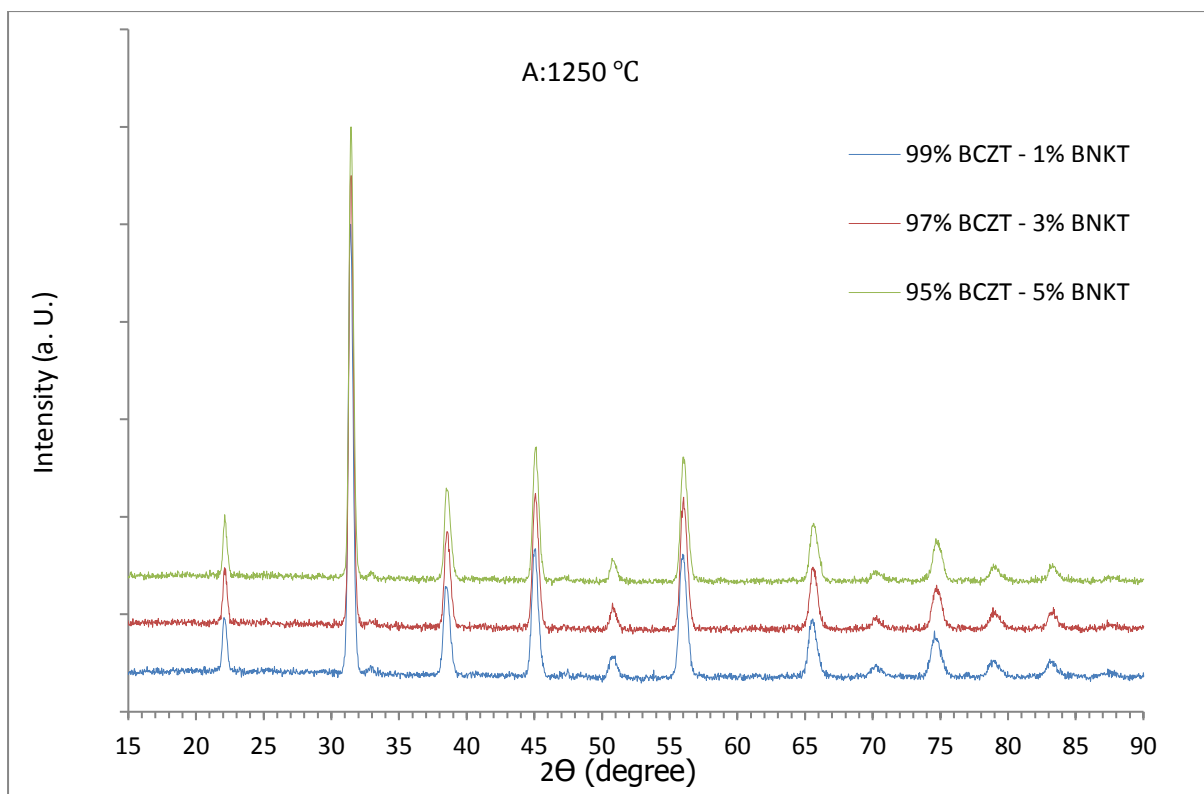


Figure I-2: The XRD Patterns of BCZT – 1, 3 and 5% BNKT at A) 1250°C, B) 1500°C sintered for 4 hours

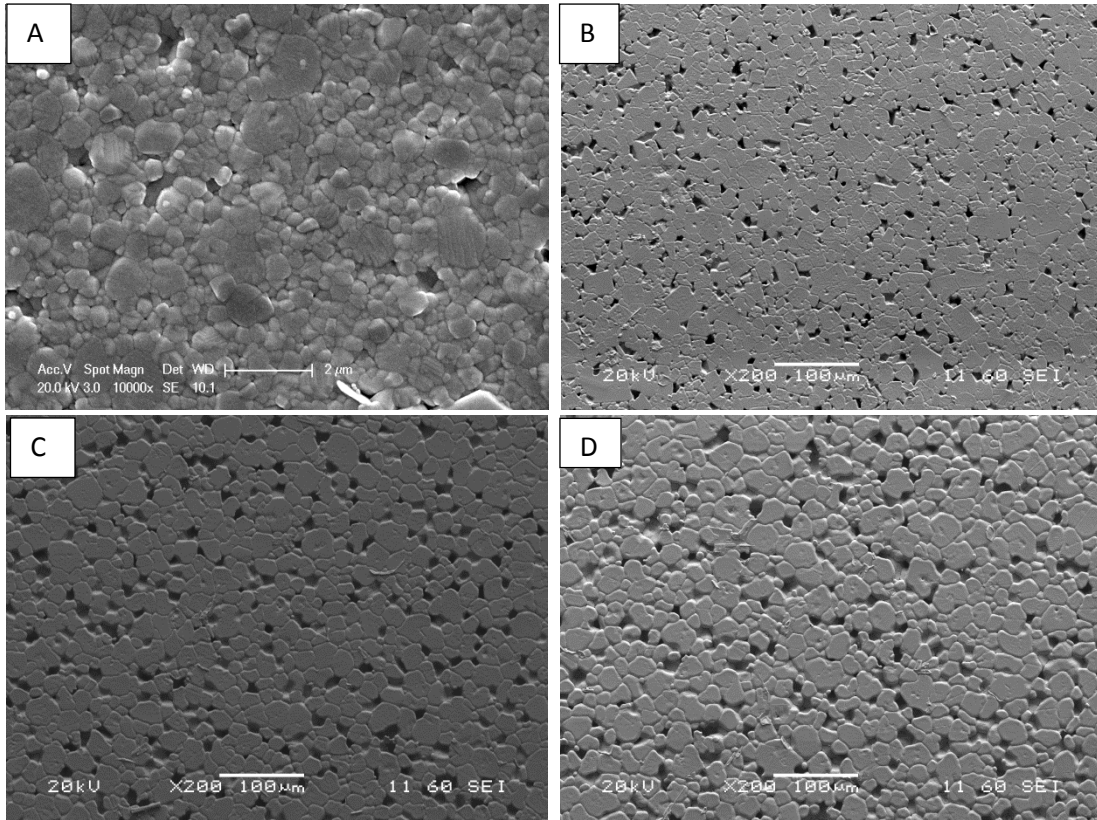


Figure I-3: SEM micrograph of the BCZT – 1% BNKT samples sintered at A) 1250°C (higher magnification) B) 1350°C, C) 1450°C and D) 1500°C.

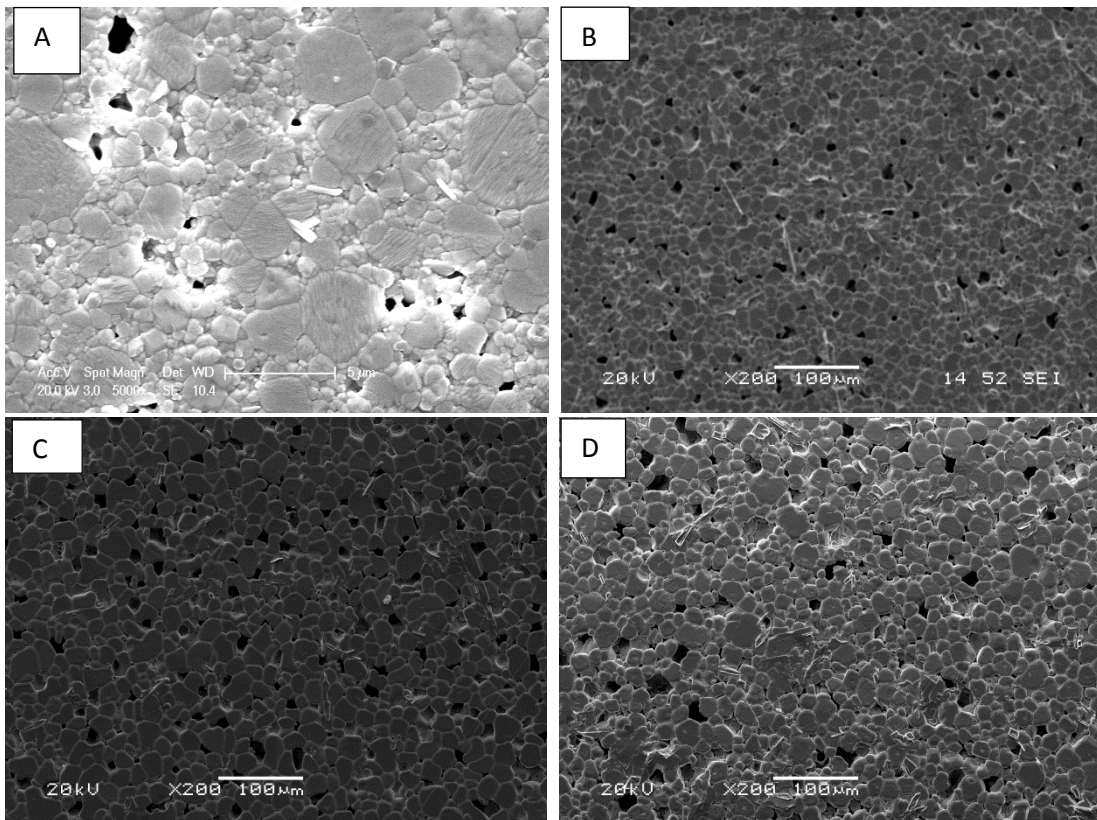


Figure I-4: SEM micrograph of the BCZT – 3% BNKT samples sintered at a) 1250°C, B) 1350°C, C) 1450°C and D) 1500°C

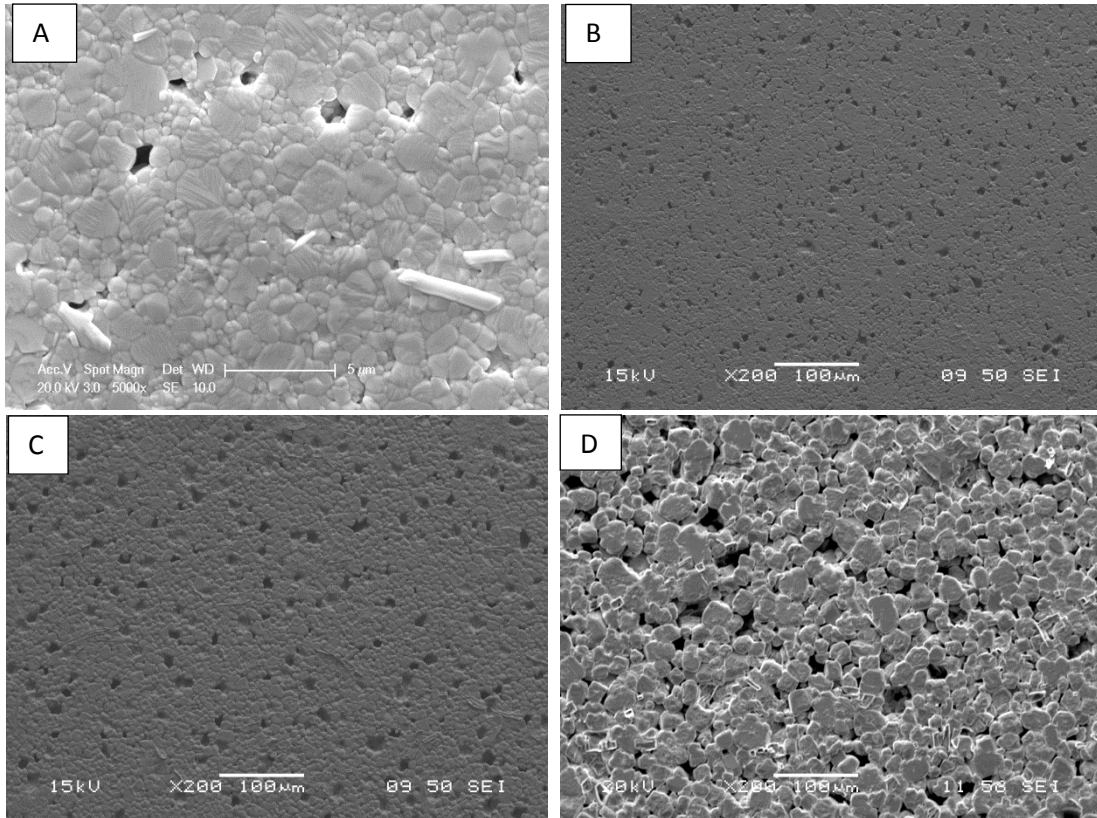


Figure I-5: SEM micrograph of the BCZT – 5% BNKT samples sintered at a) 1250°C, B) 1350°C, C) 1450°C and D) 1500°C

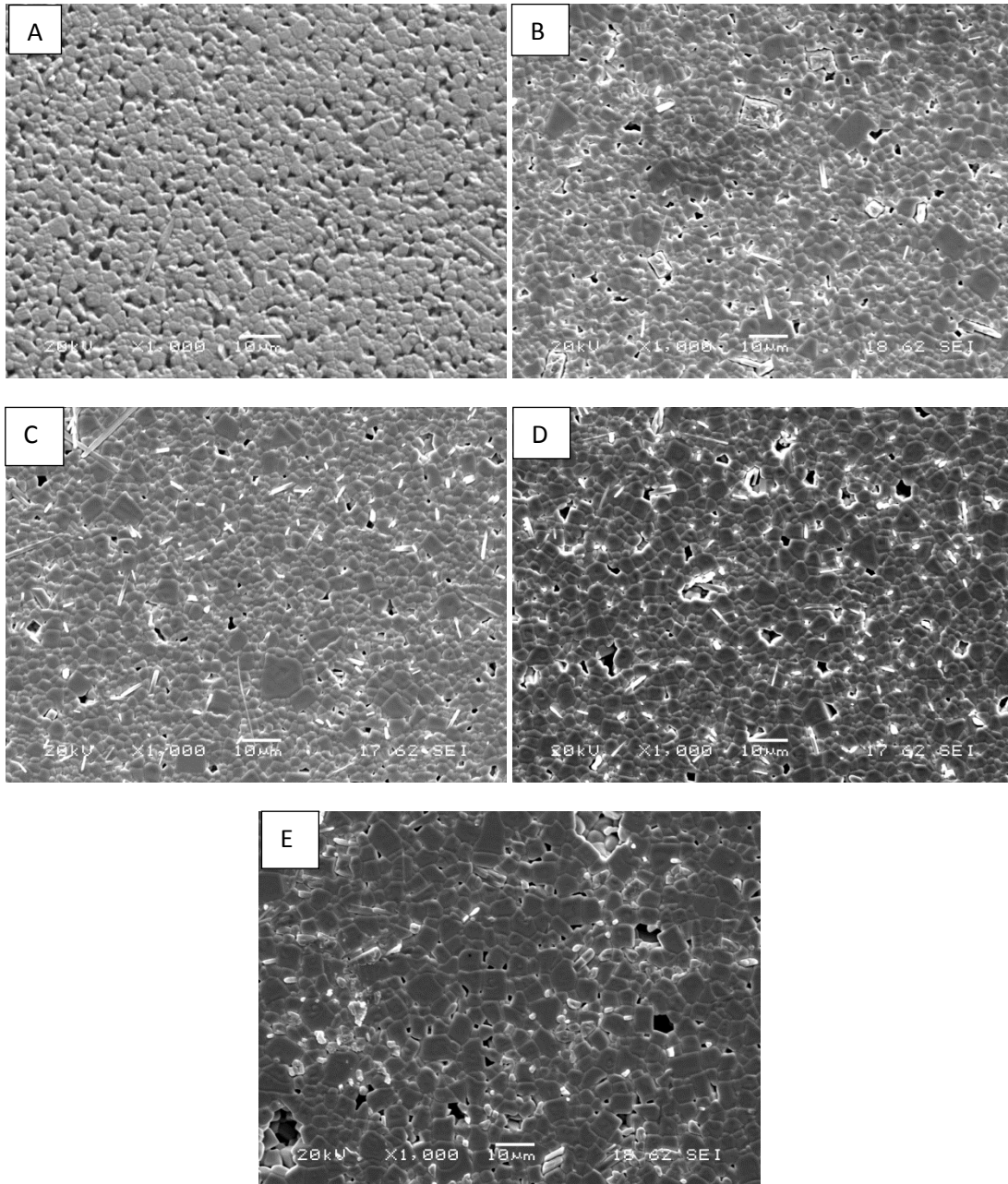


Figure I-6: SEM micrograph of the BNT – BT Samples sintered at a) 1100°C, B) 1125°C, C) 1150°C, D) 1175°C and E) 1200°C

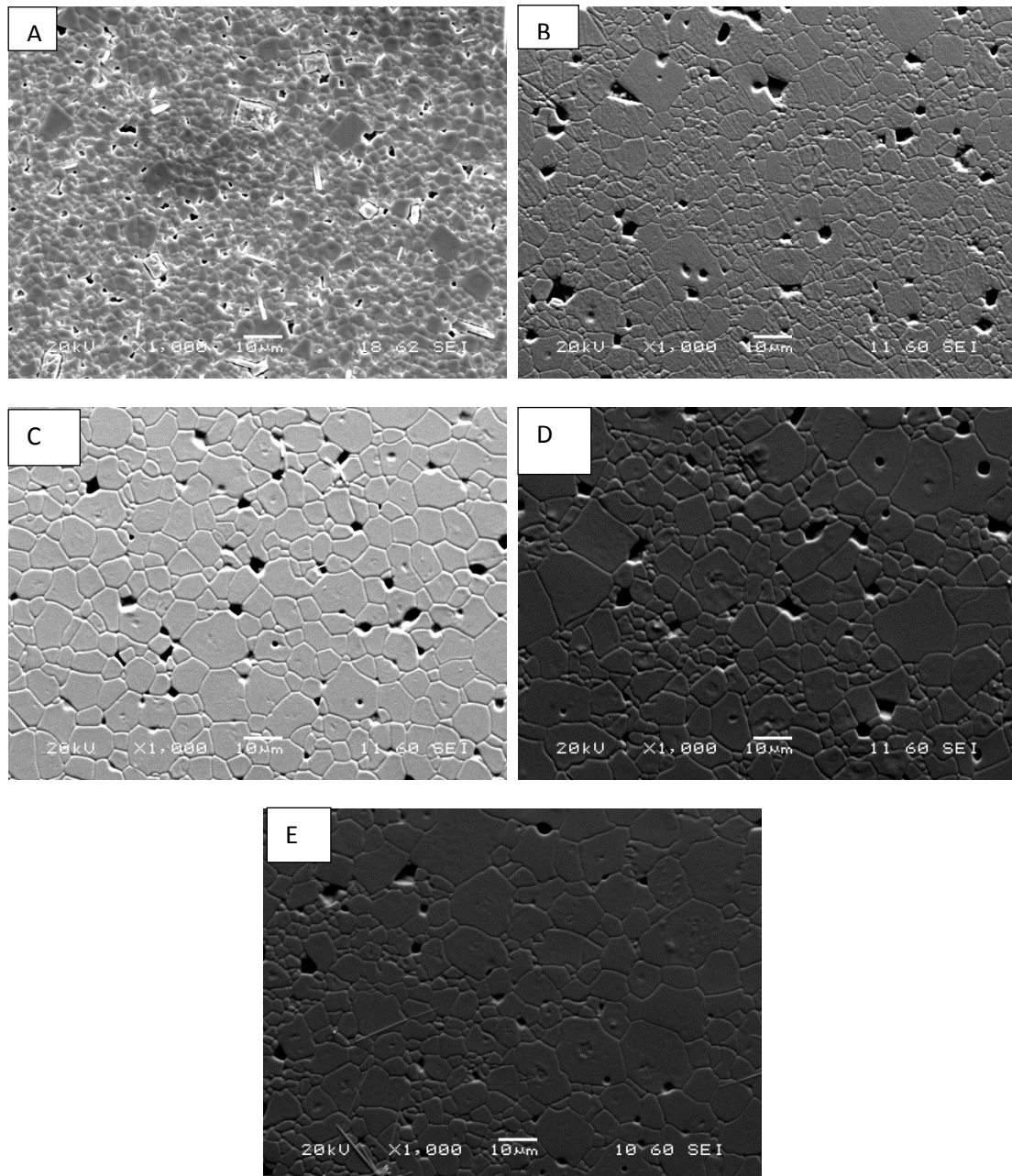


Figure I-7: SEM micrograph of the $(1-x)$ BNT – BT – x BF Samples sintered at 1125 °C at A) 0.000, B) 0.025, C) 0.050, D) 0.075 and E) 0.010 BF

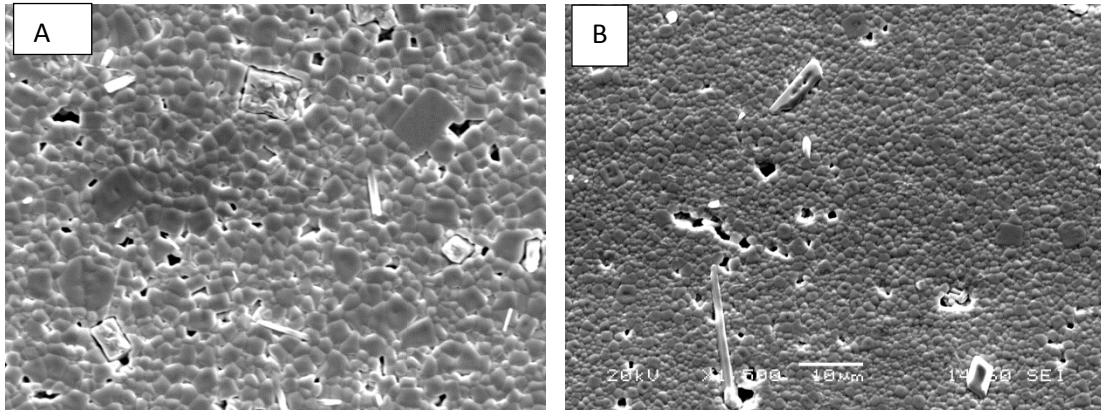
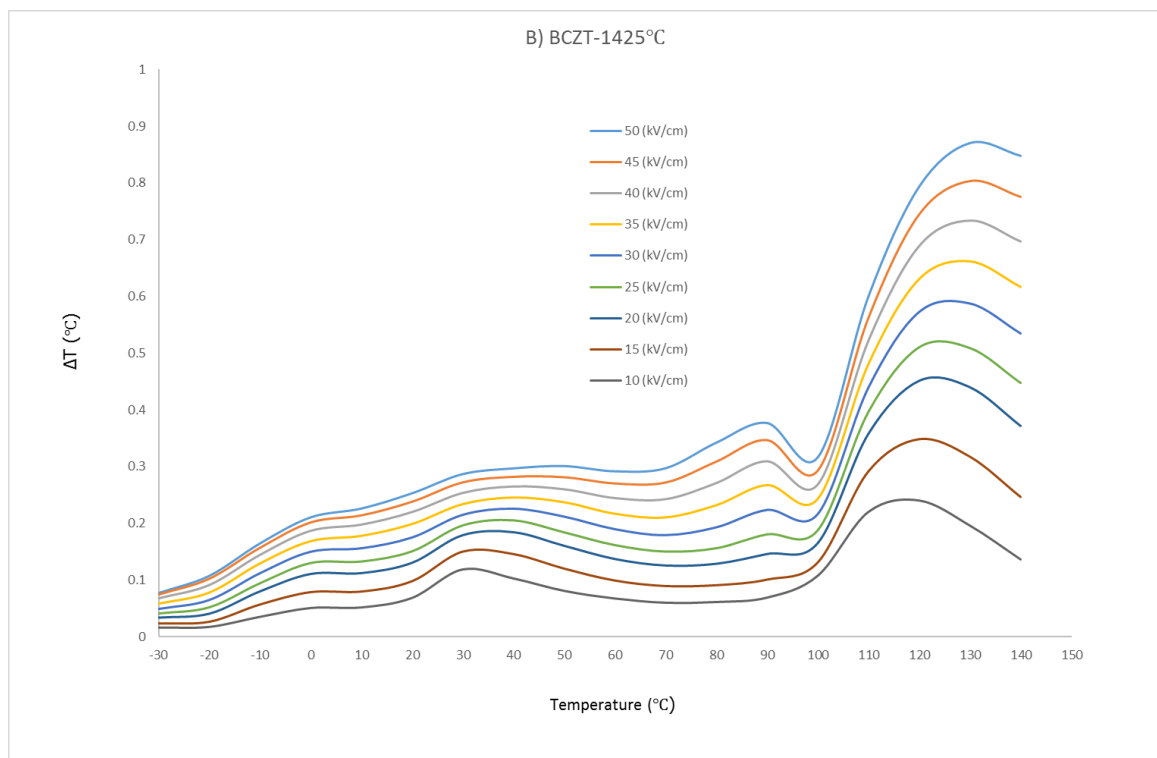
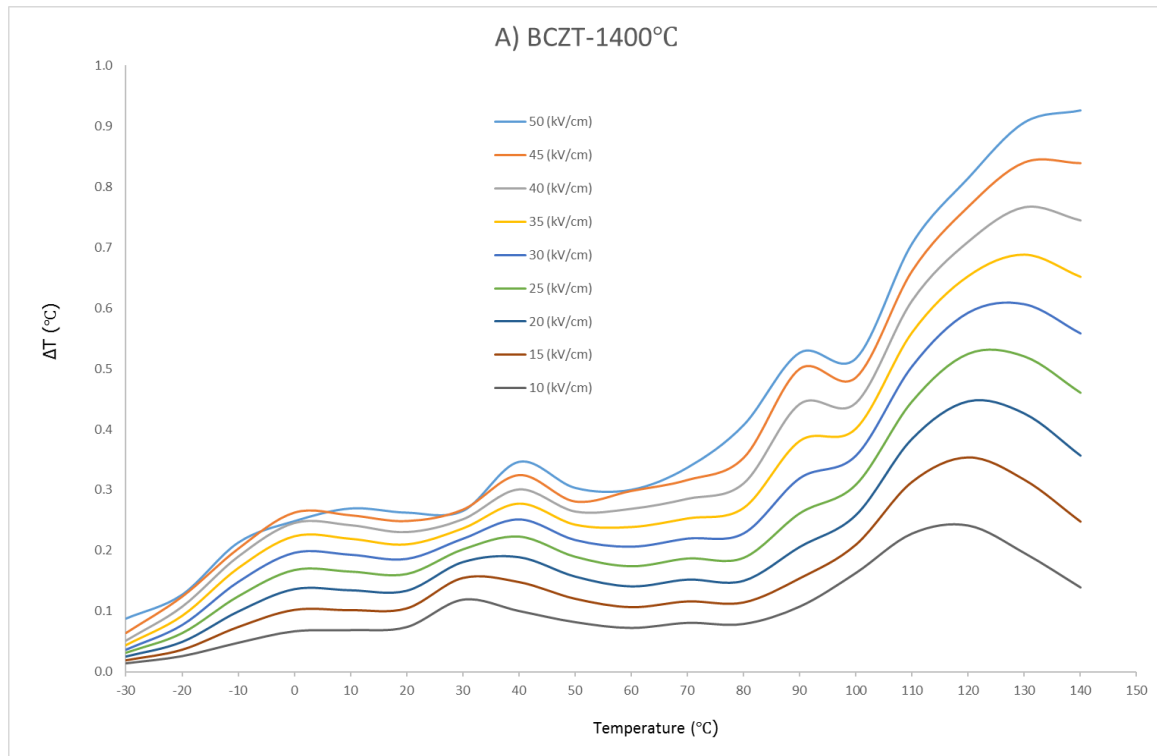
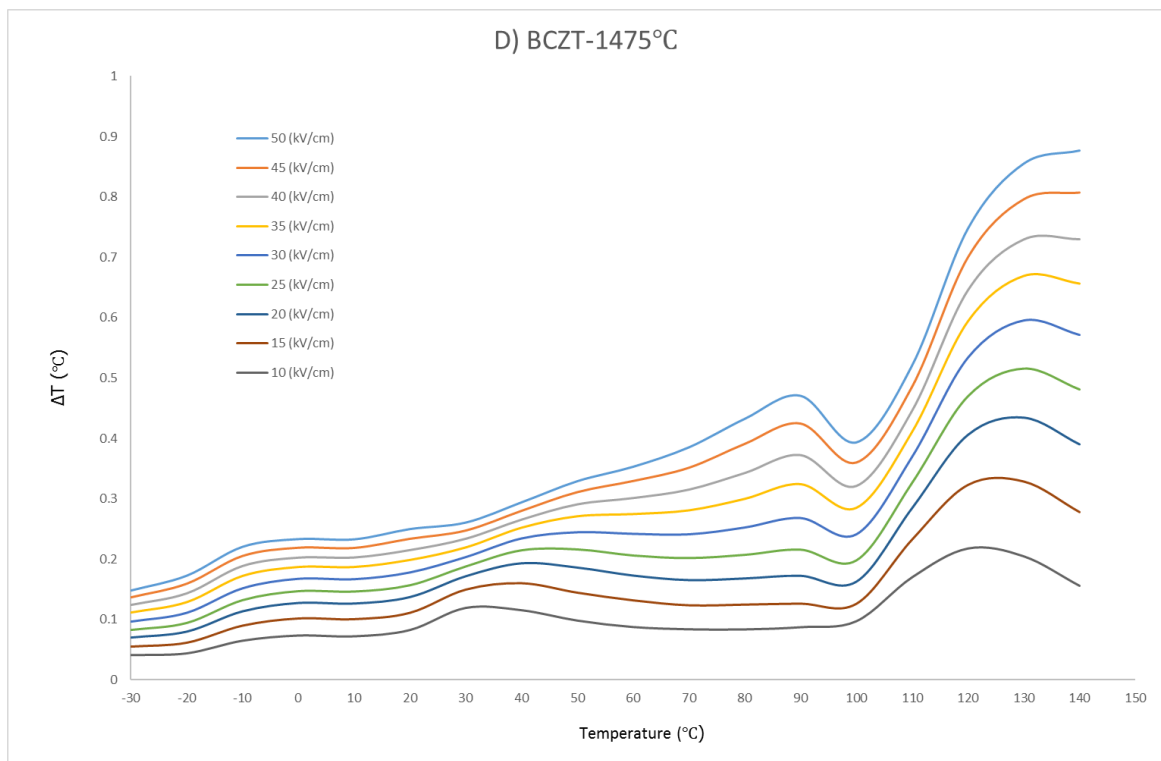
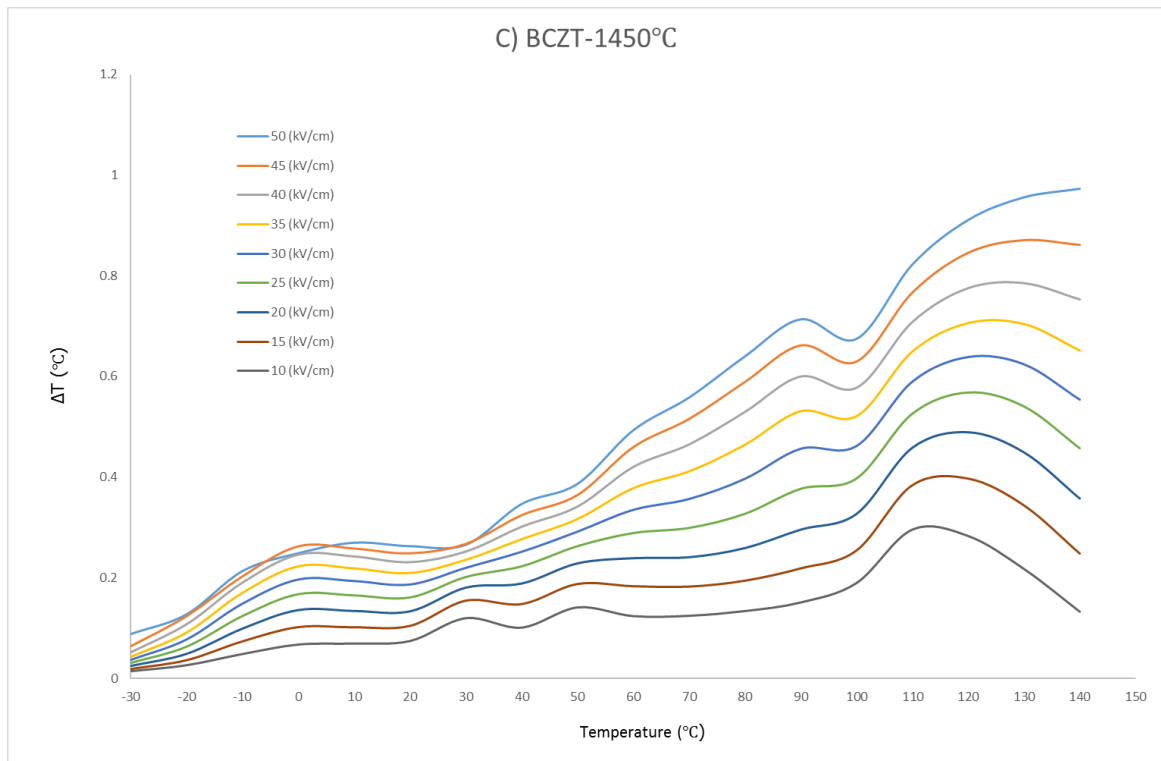


Figure I-8: SEM micrograph of the A) BNT - BT and B) BNT – BT deficiency Samples sintered at 1125 °C

Appendix II





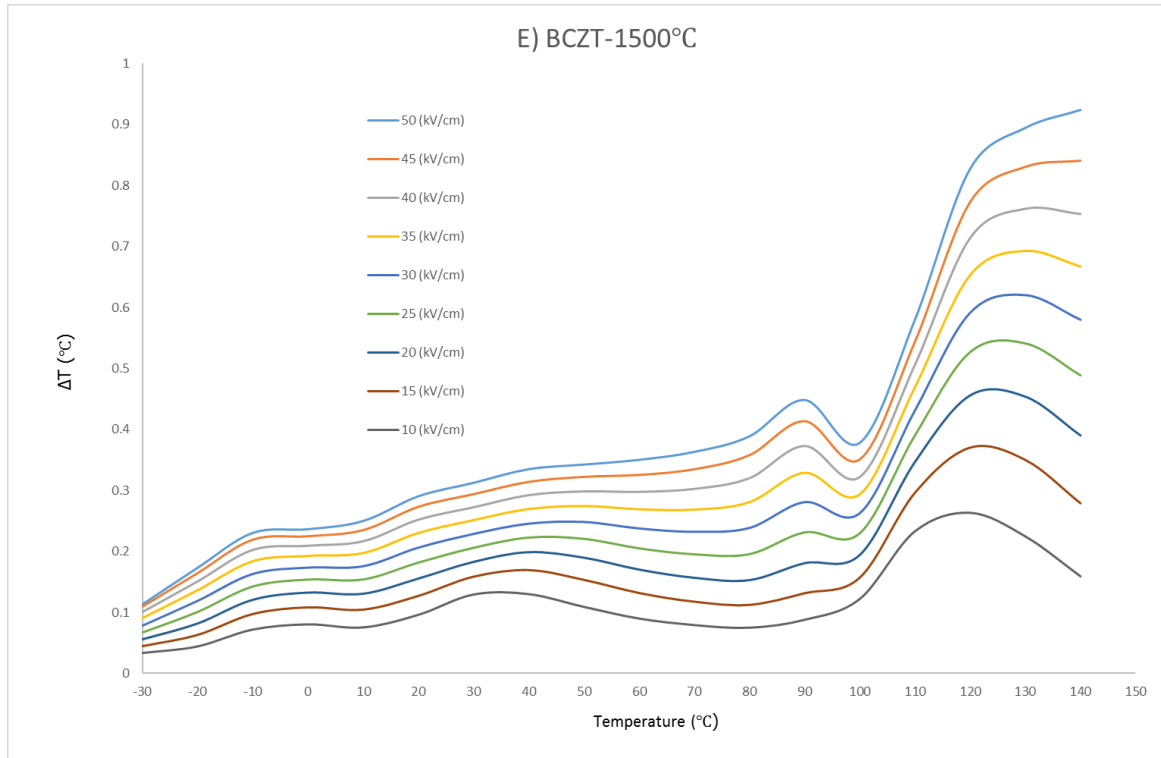
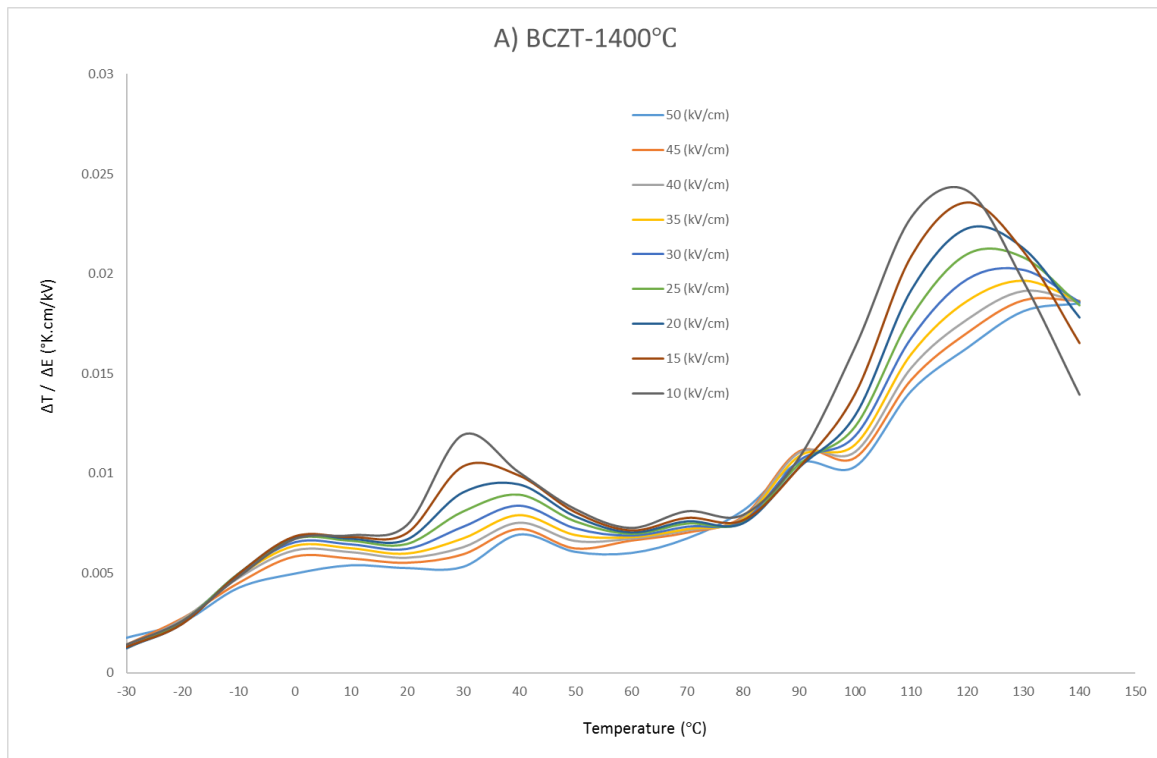
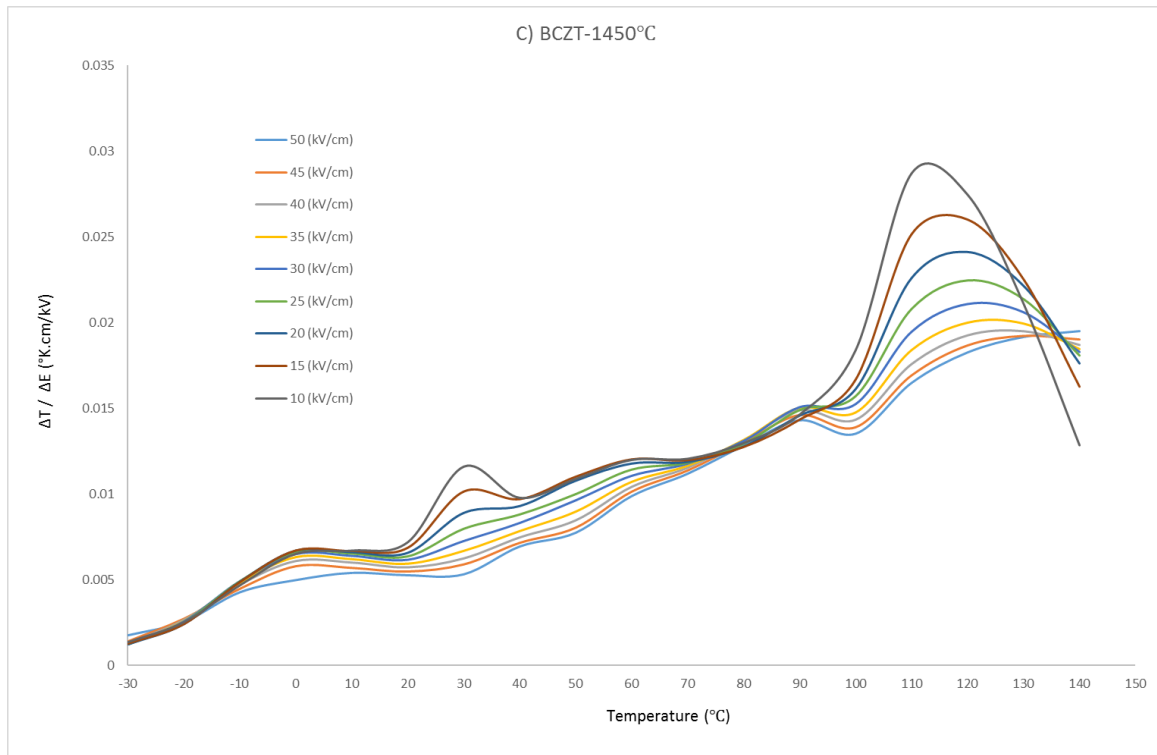
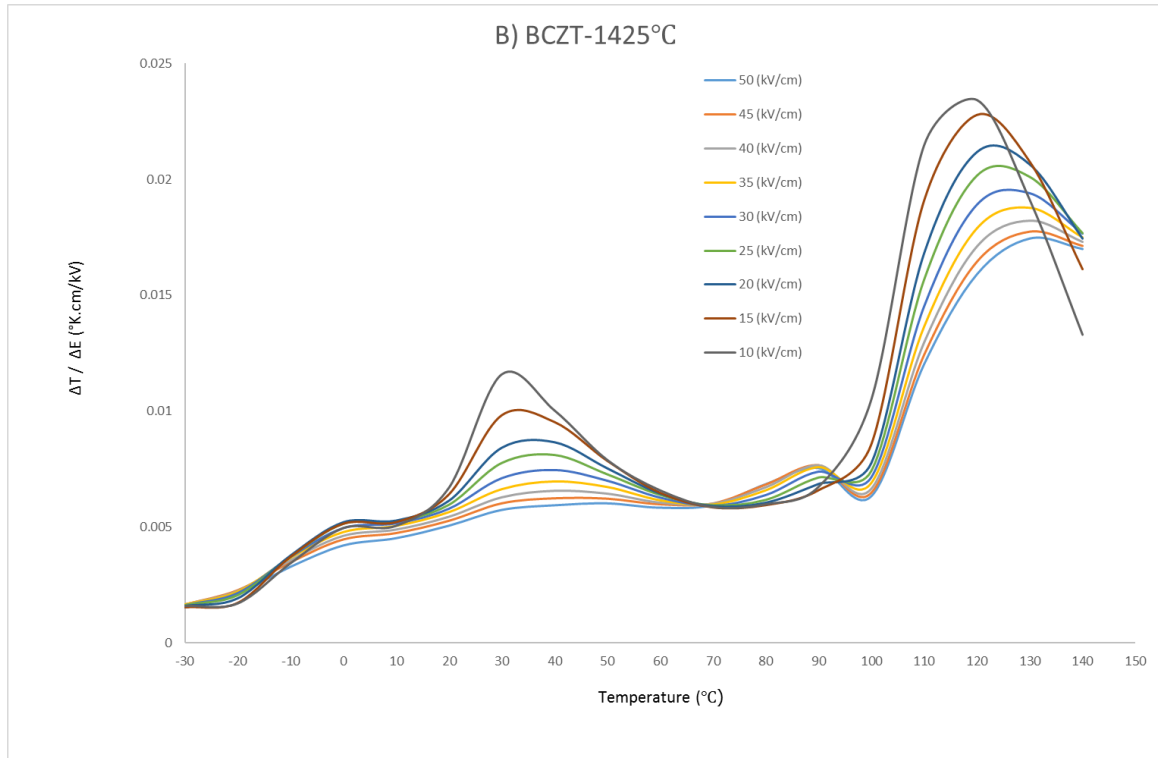


Figure II-1: The ECE of BCZT sintered at A) 1400, B) 1425, C) 1450, D) 1475, and E) 1500°C as a function of measurement temperature and for various applied electric field values.





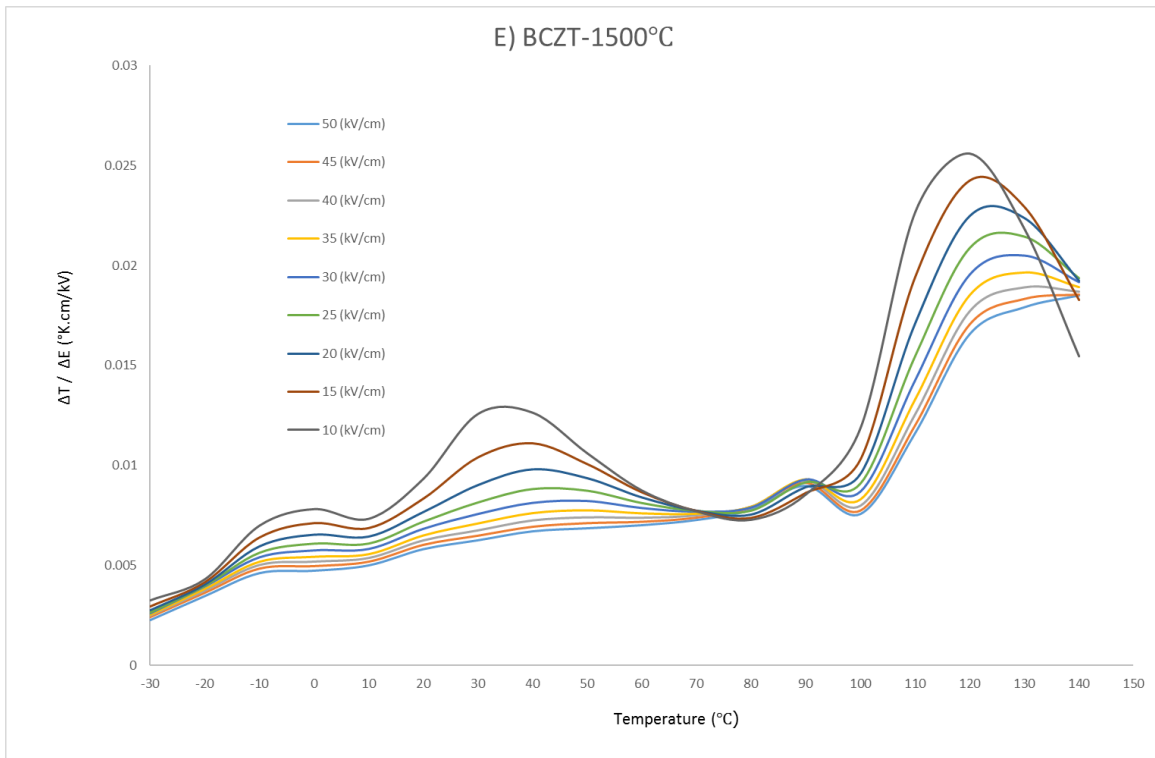
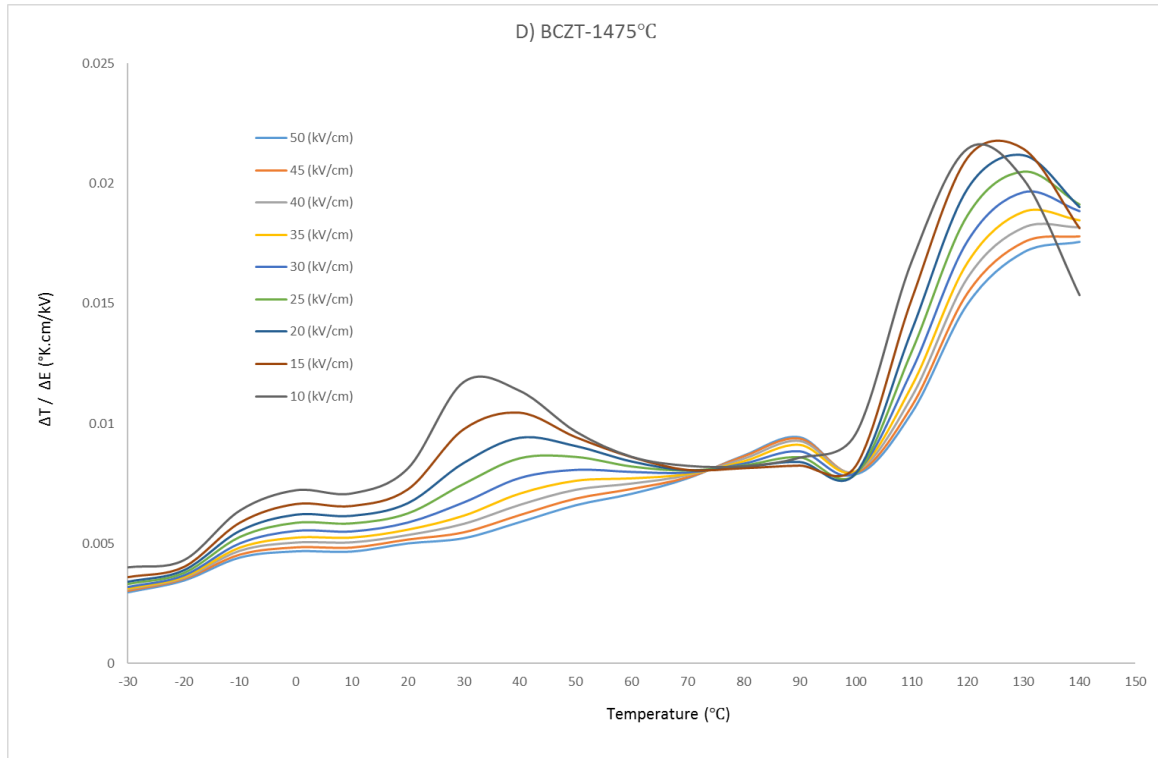
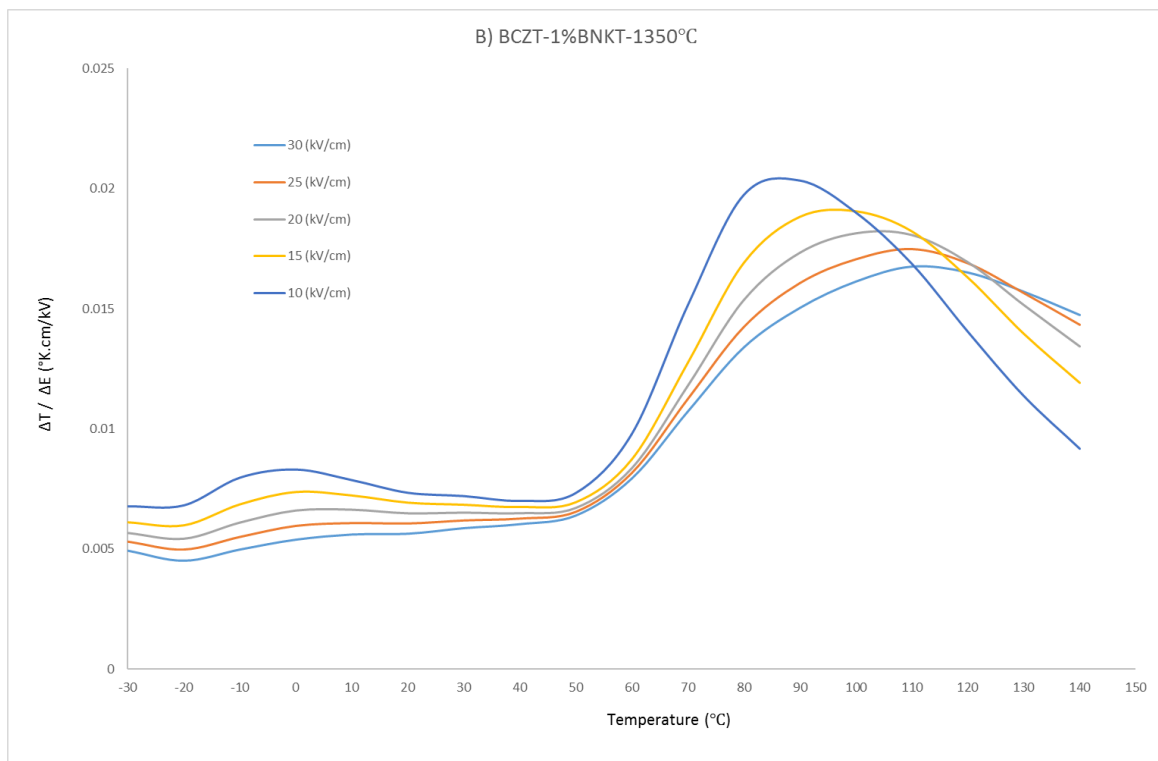
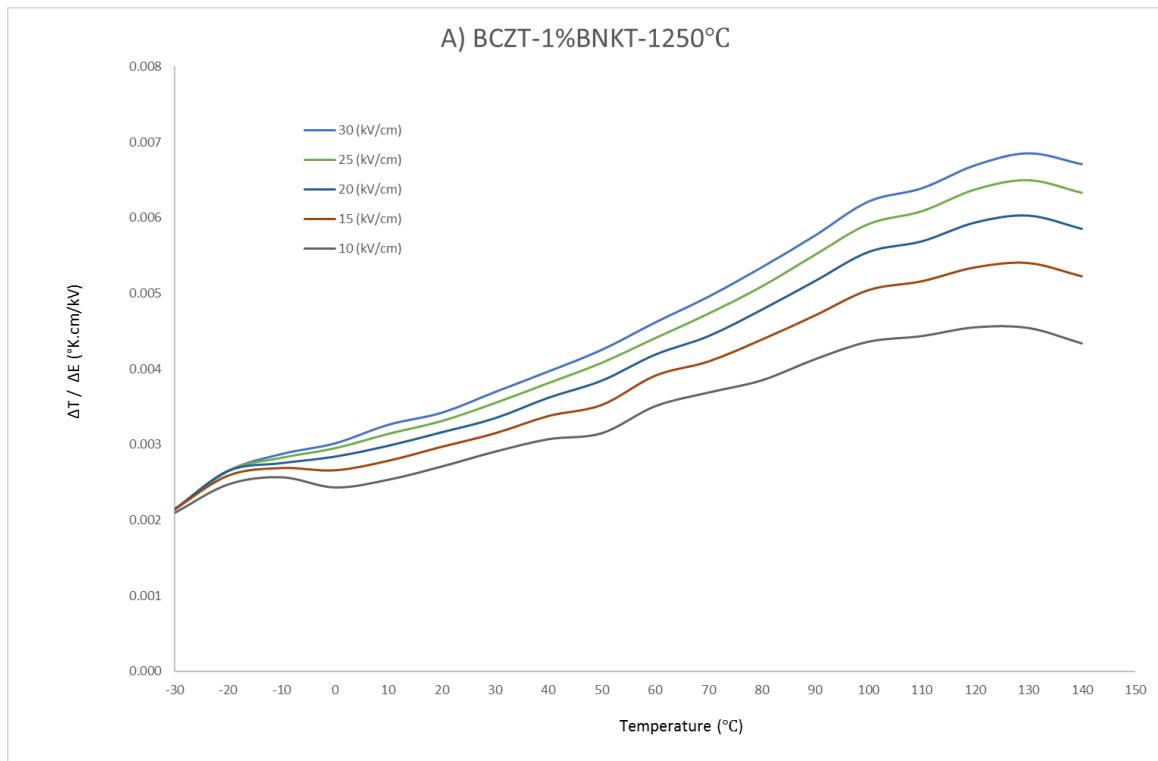


Figure II-2: The ECE figure of merit as a function of temperature of pure BCZT sintered at A) 1400, B) 1425, C) 1450, D) 1475, and E) 1500°C, and for a range of applied electric field values.



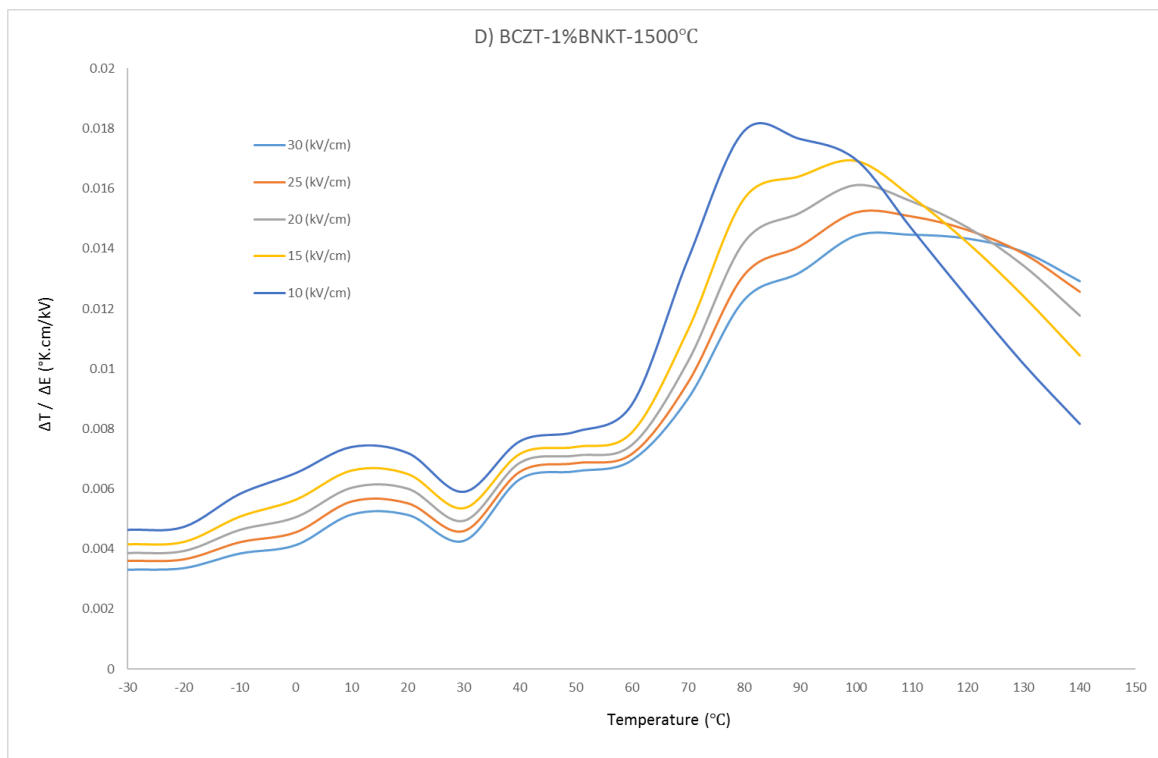
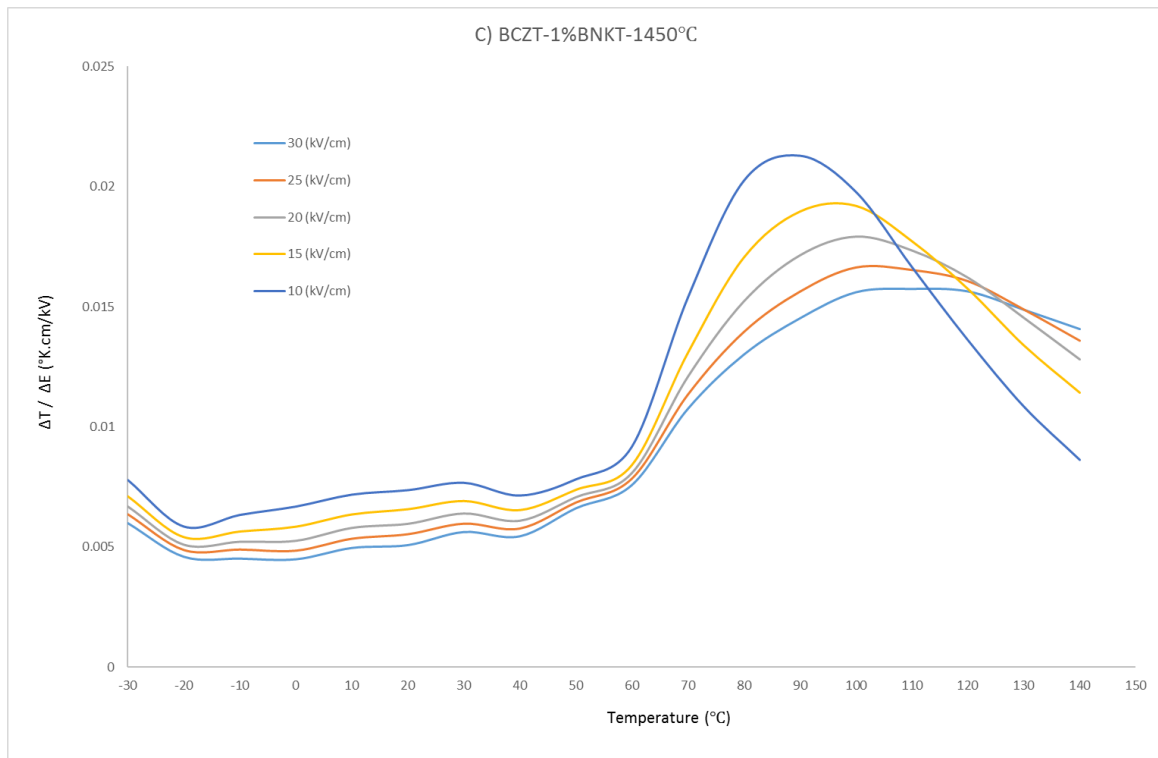
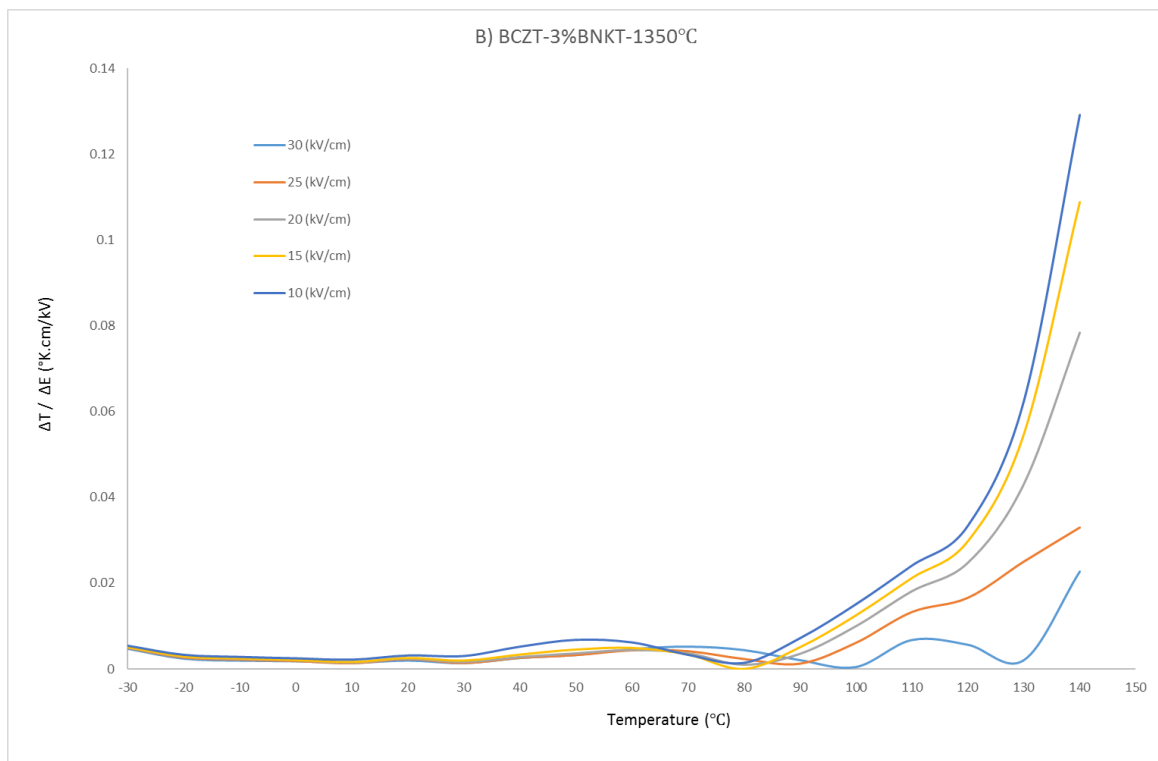
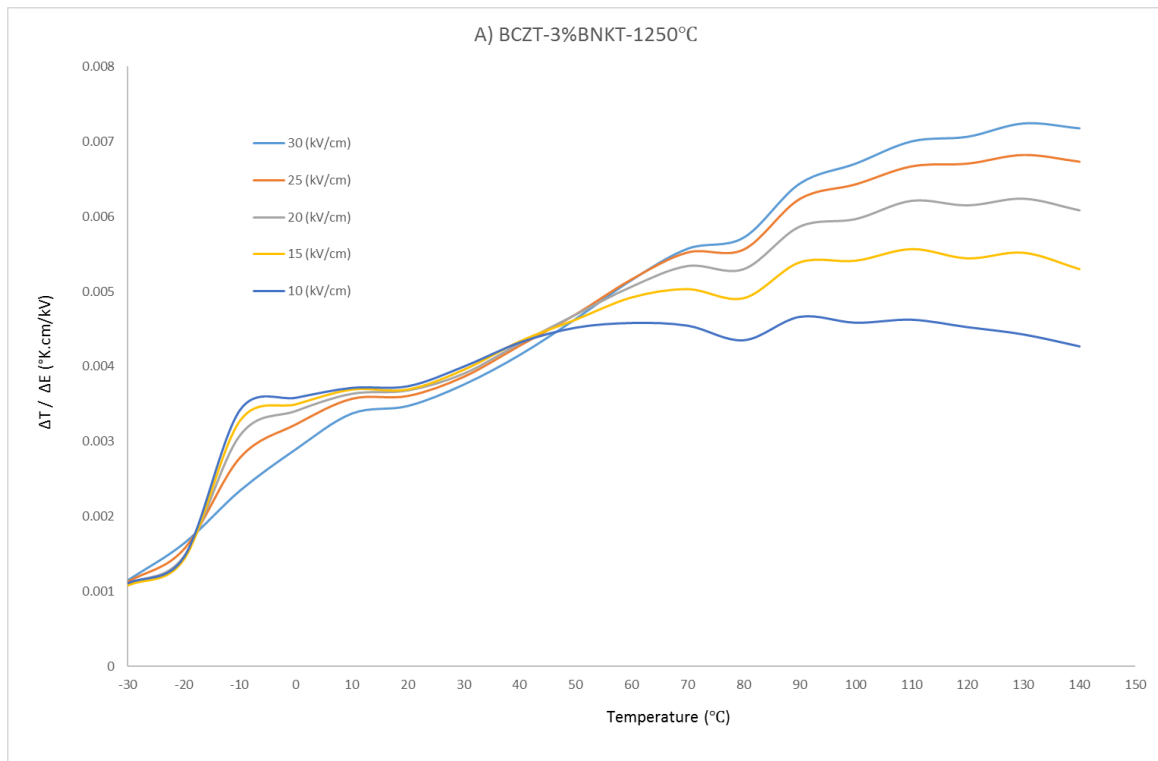


Figure II-3: The ECE figure of merit as a function of temperature of BCZT-1% BNKT, sintered at A) 1250, B) 1350, C) 1450, and D) 1500°C, and for a range of applied electric field values.



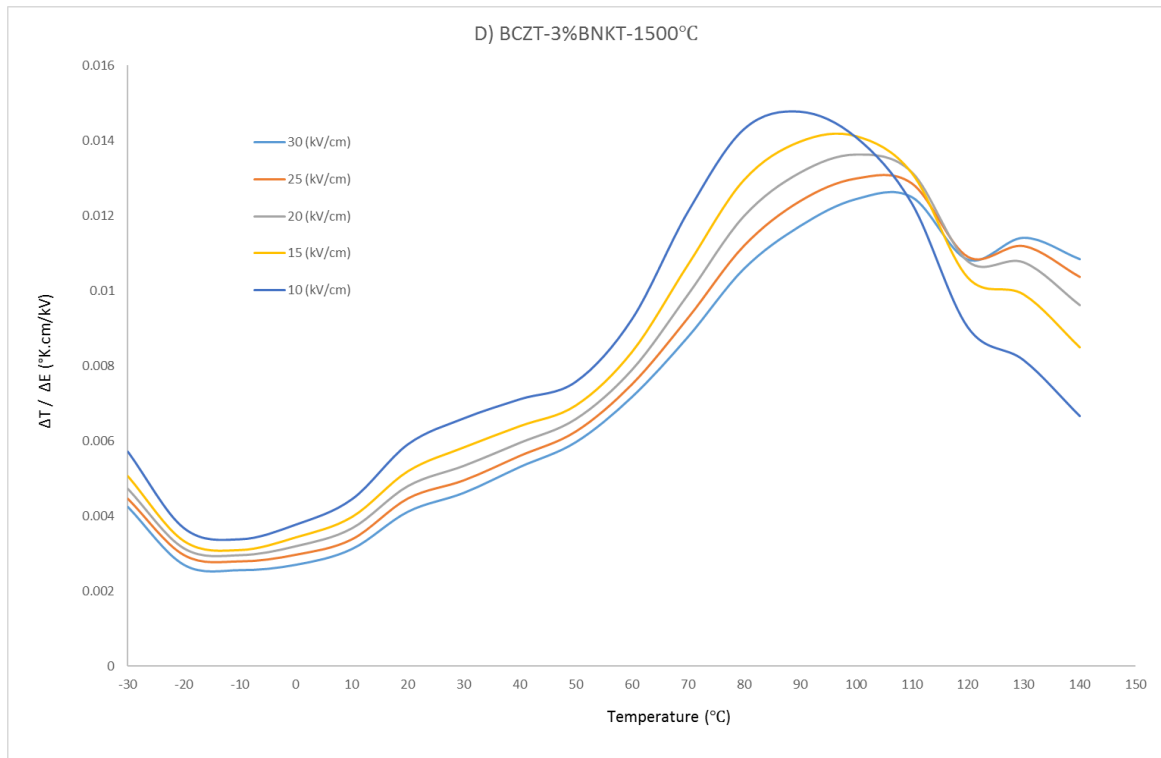
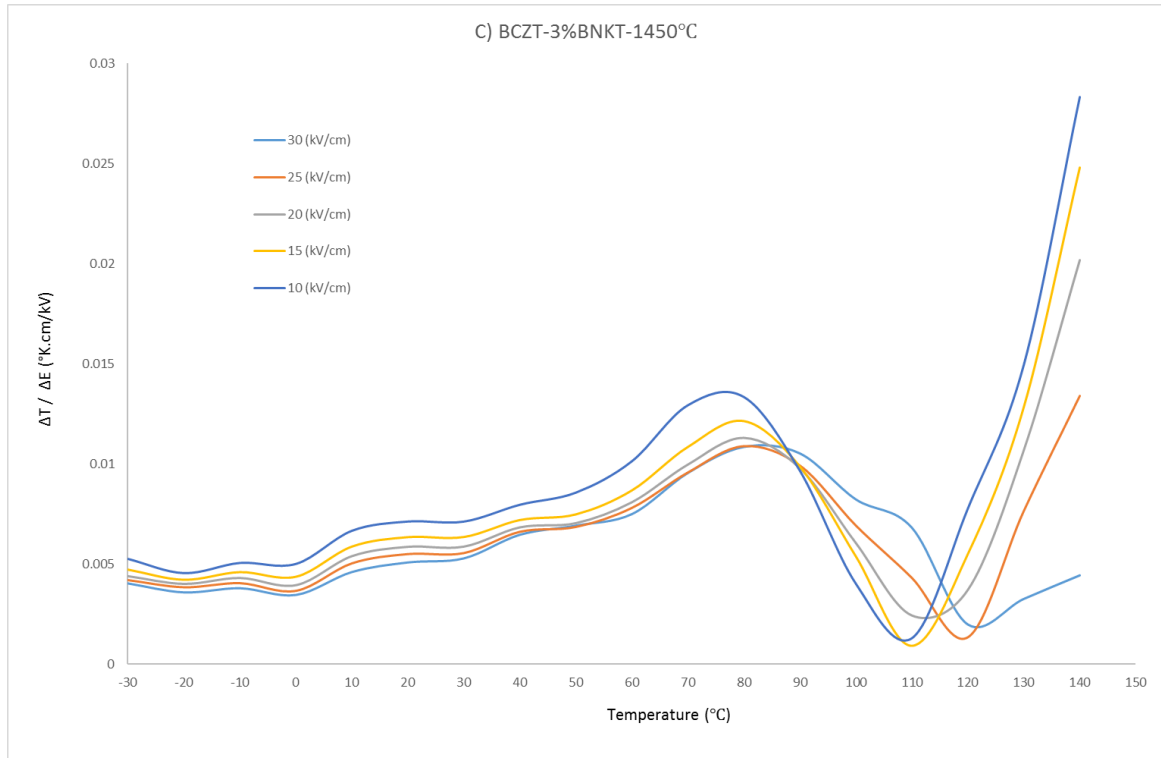
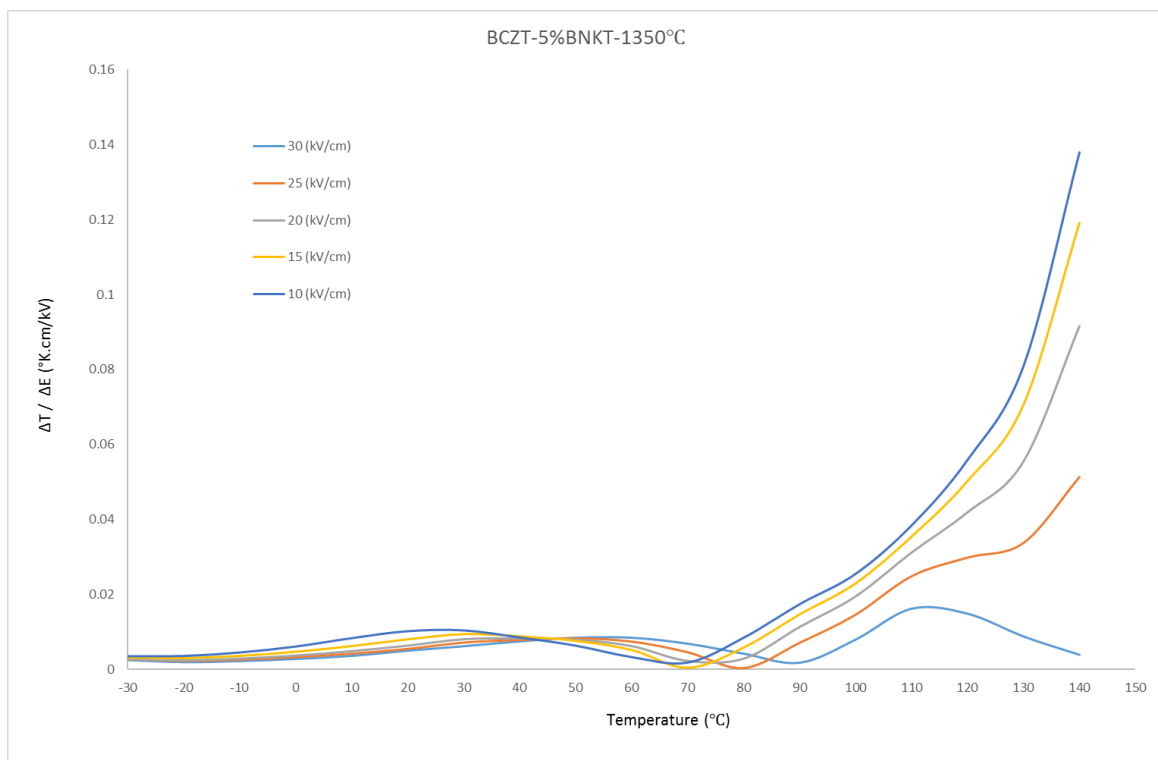
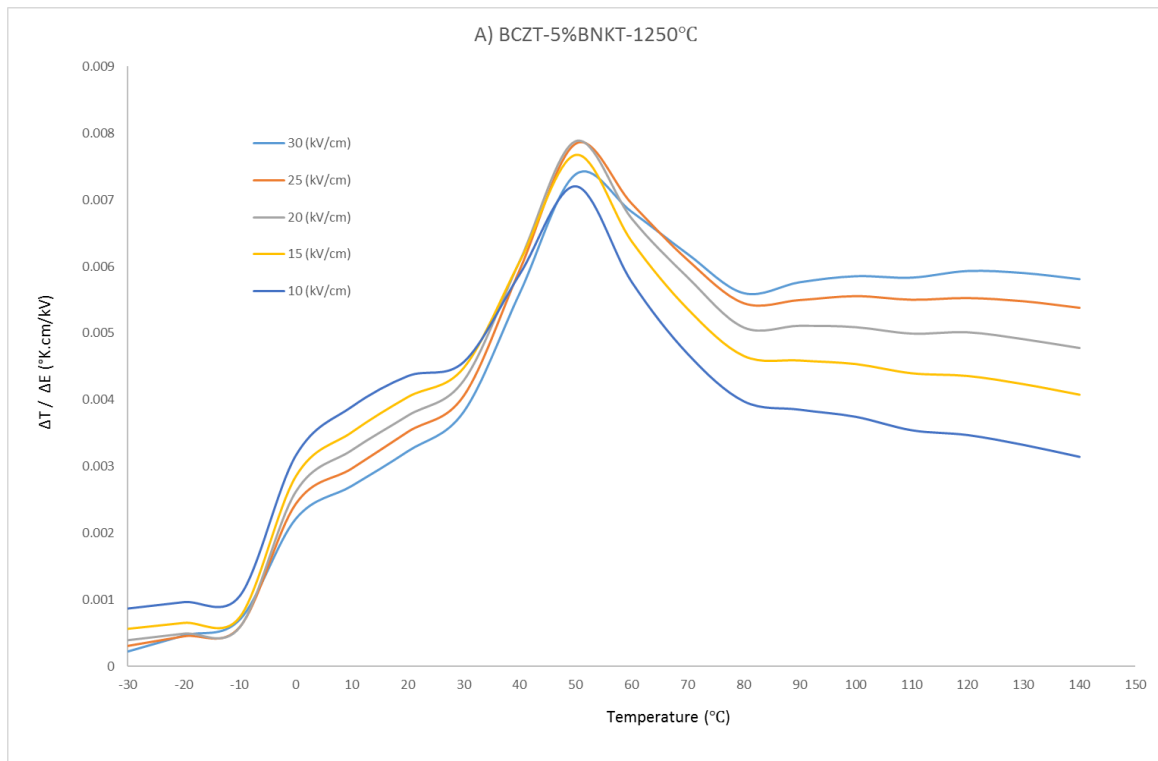


Figure II-4: The ECE figure of merit as a function of temperature of BCZT-3% BNKT, sintered at A) 1250, B) 1350, C) 1450, and D) 1500°C, and for a range of applied electric field values.



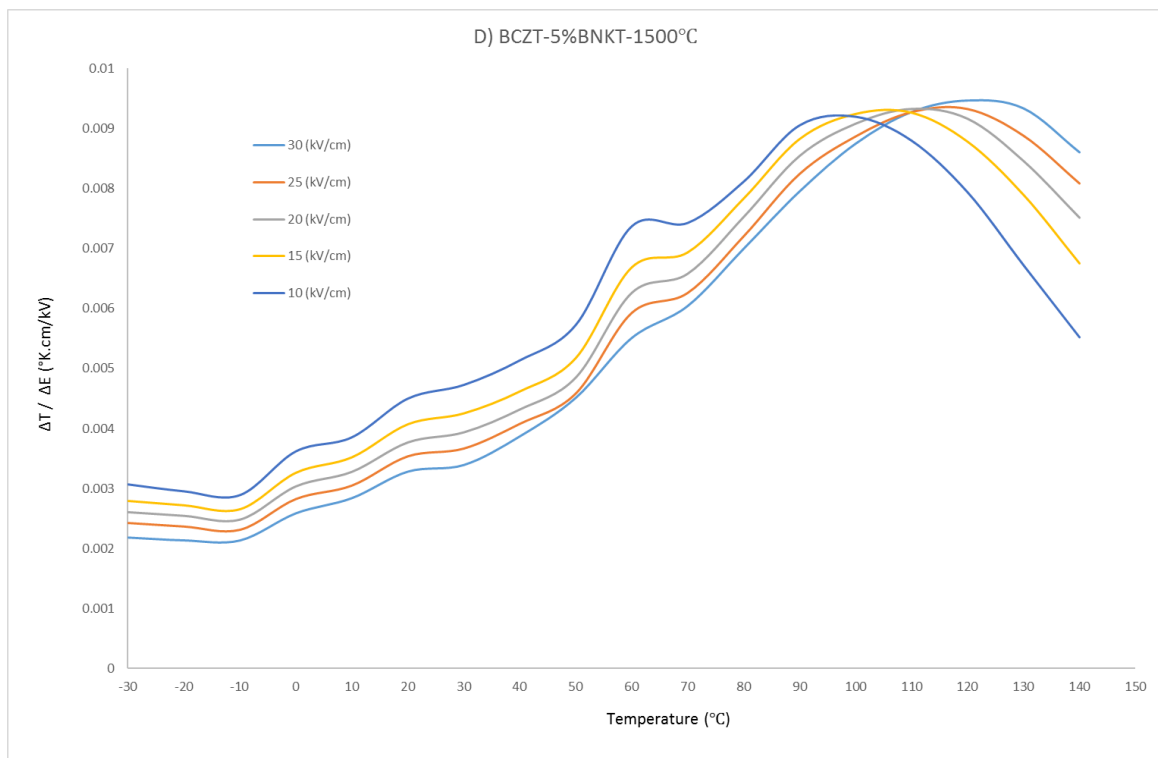
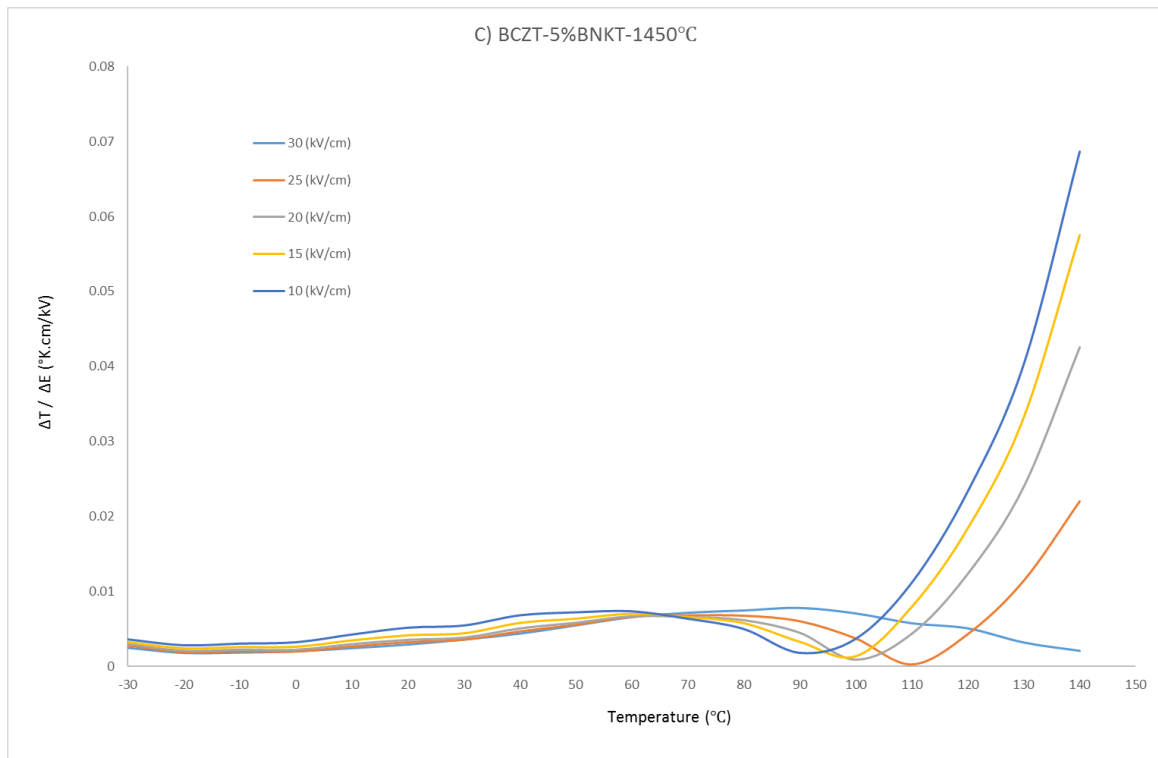
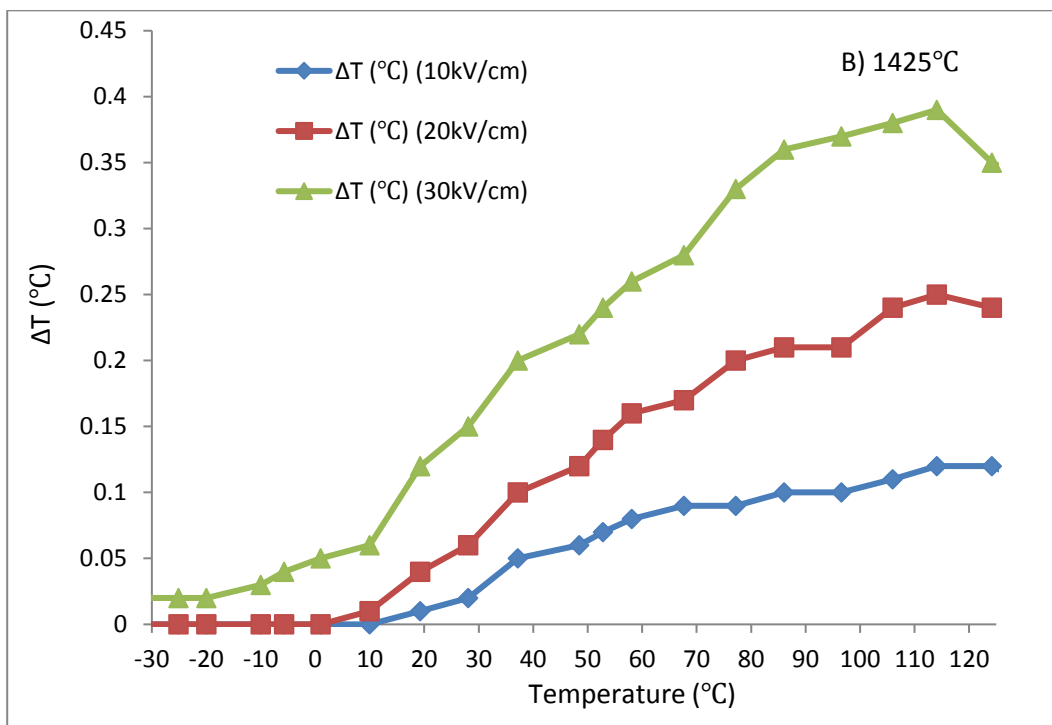
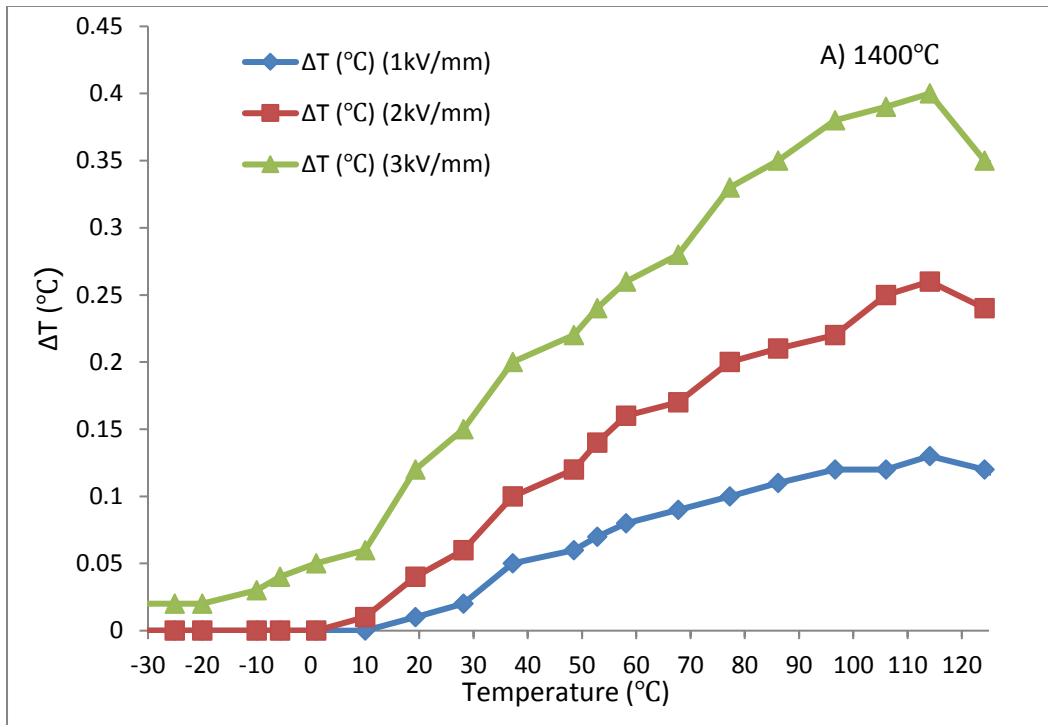
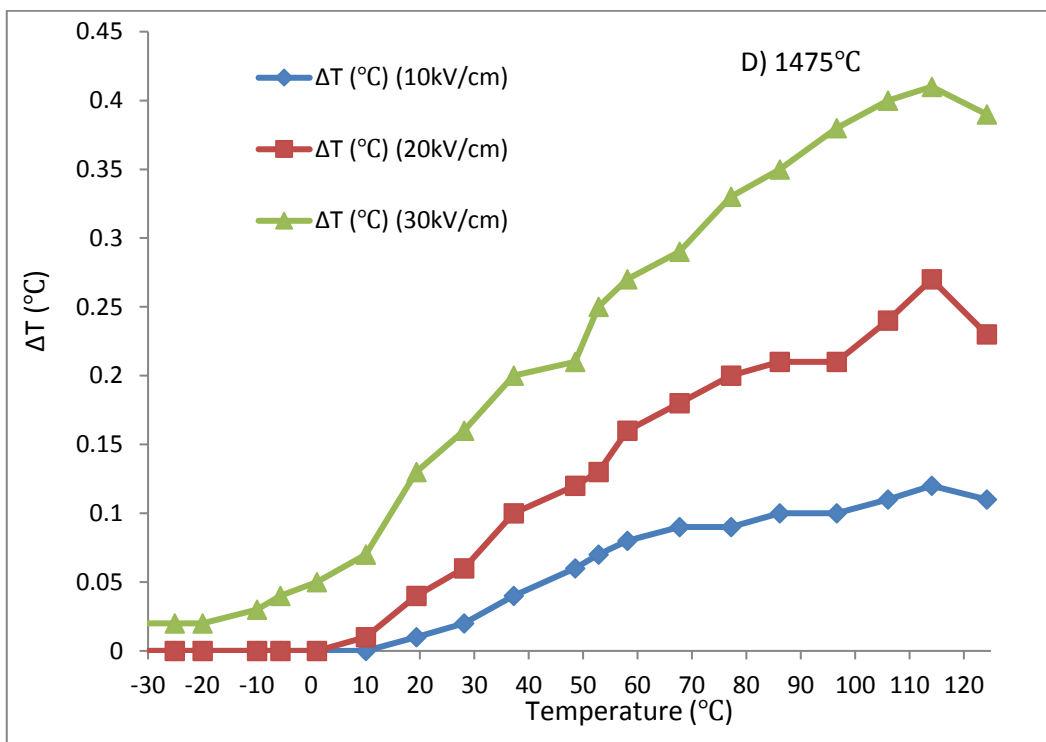
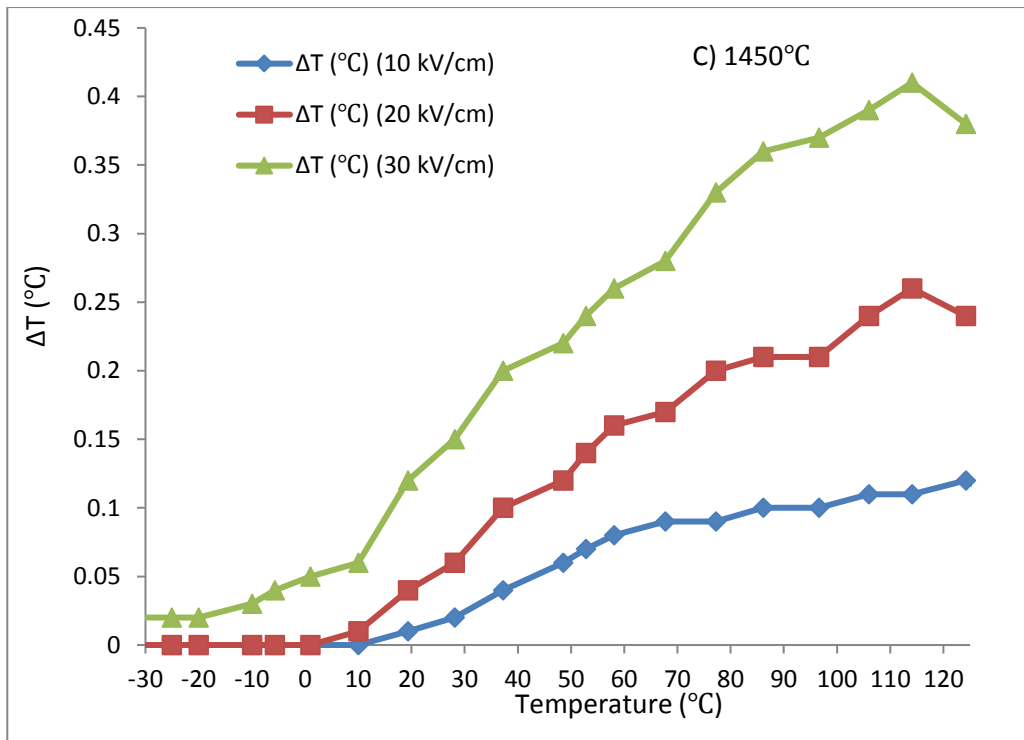


Figure II-5: The ECE figure of merit as a function of temperature of BCZT-5% BNKT, sintered at A) 1250, B) 1350, C) 1450, and D) 1500°C, and for a range of applied electric field values.





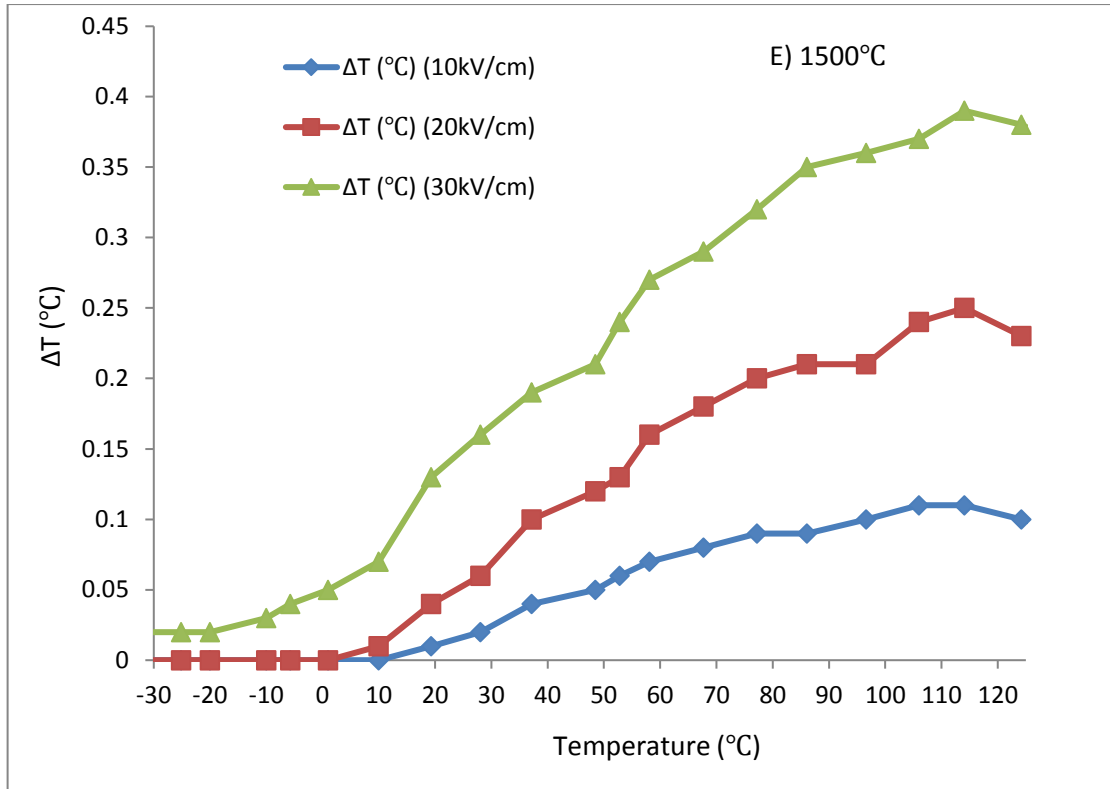
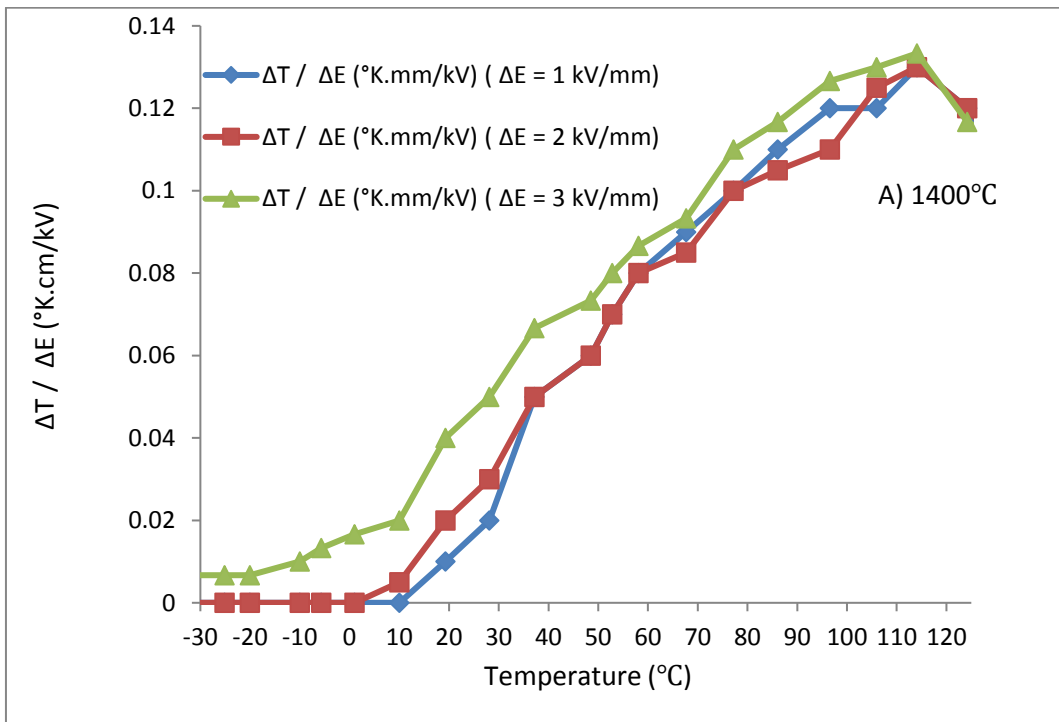
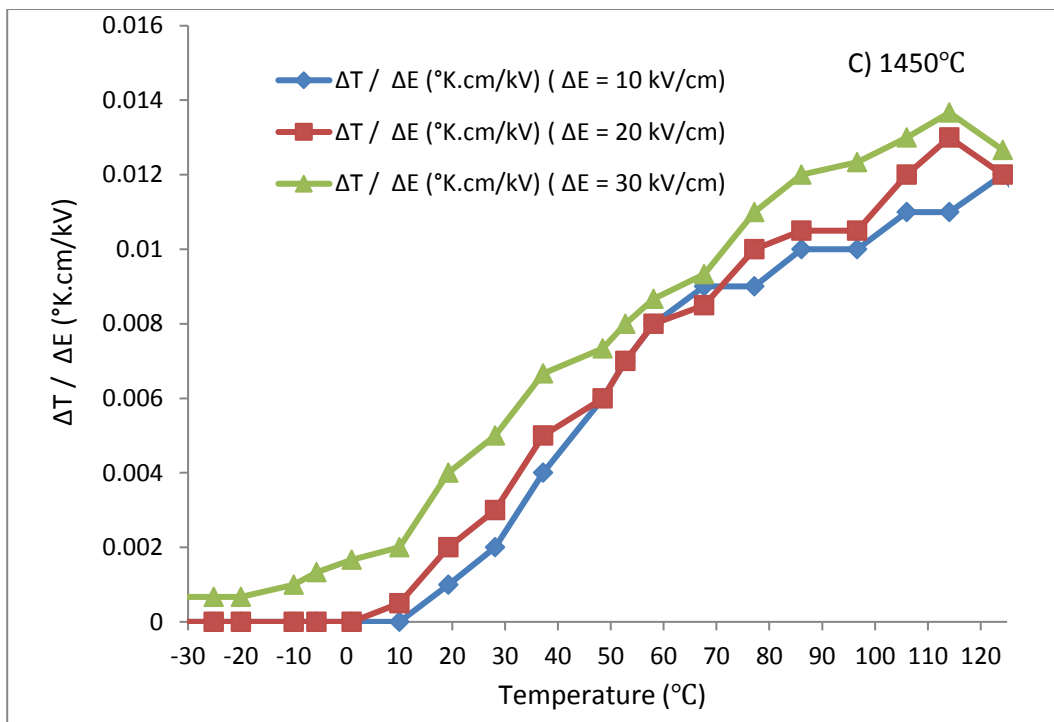
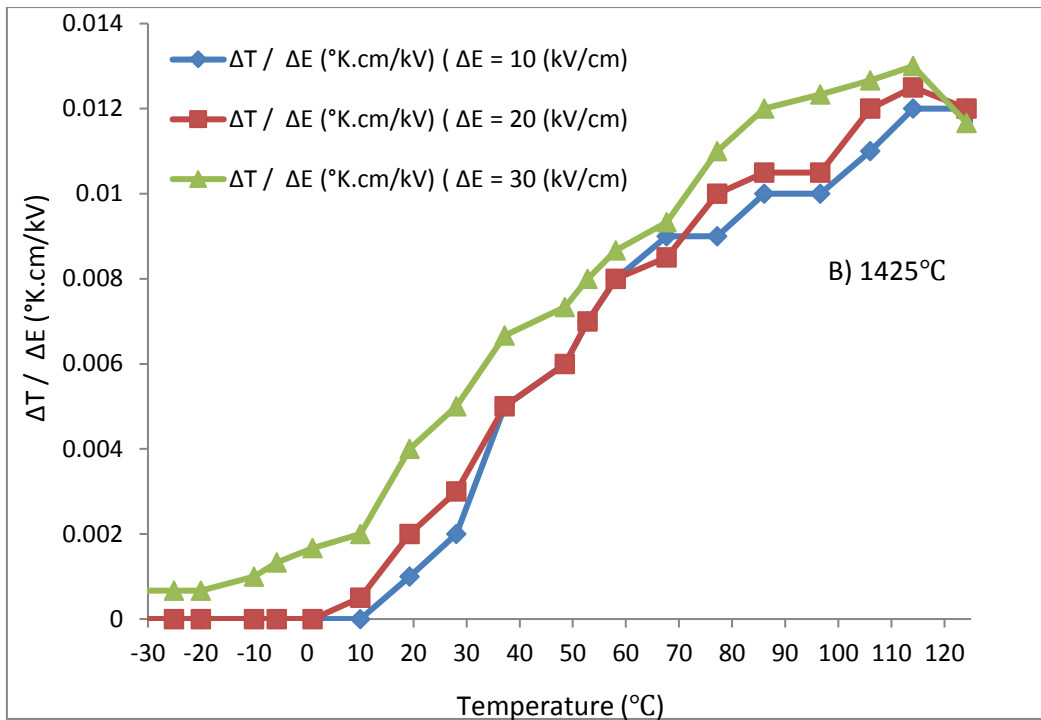


Figure II-6: The ECE of the pure BCZT sintered at 1400, 1425, 1450, 1475, and 1500°C measured between -50 and 150°C, using the direct method.





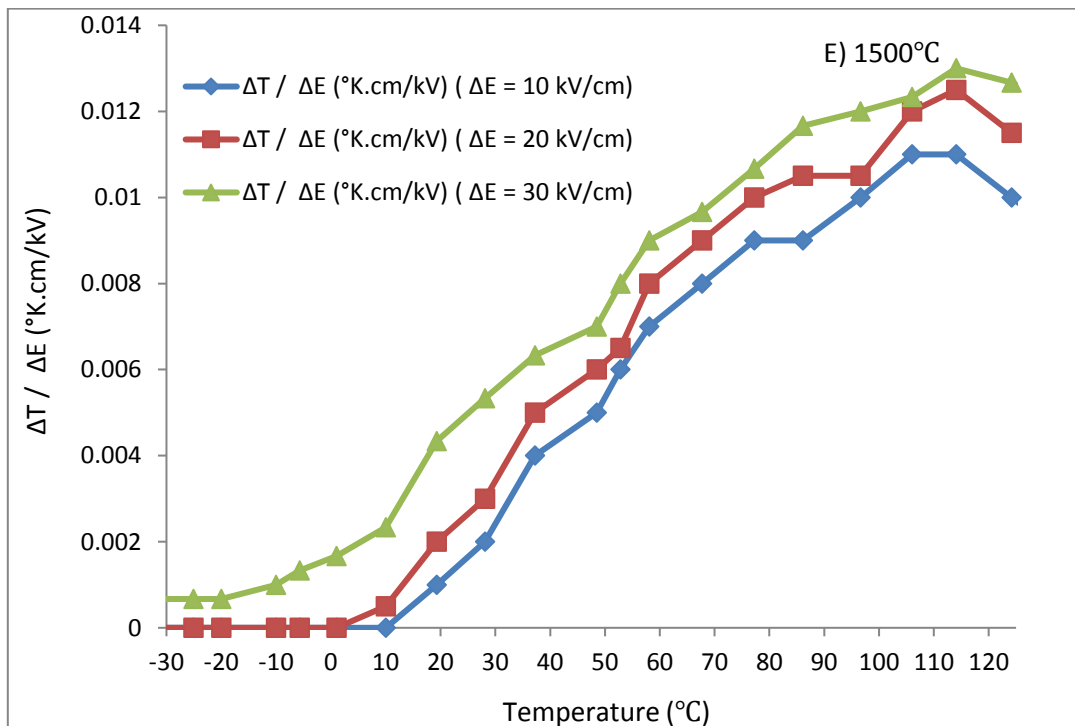
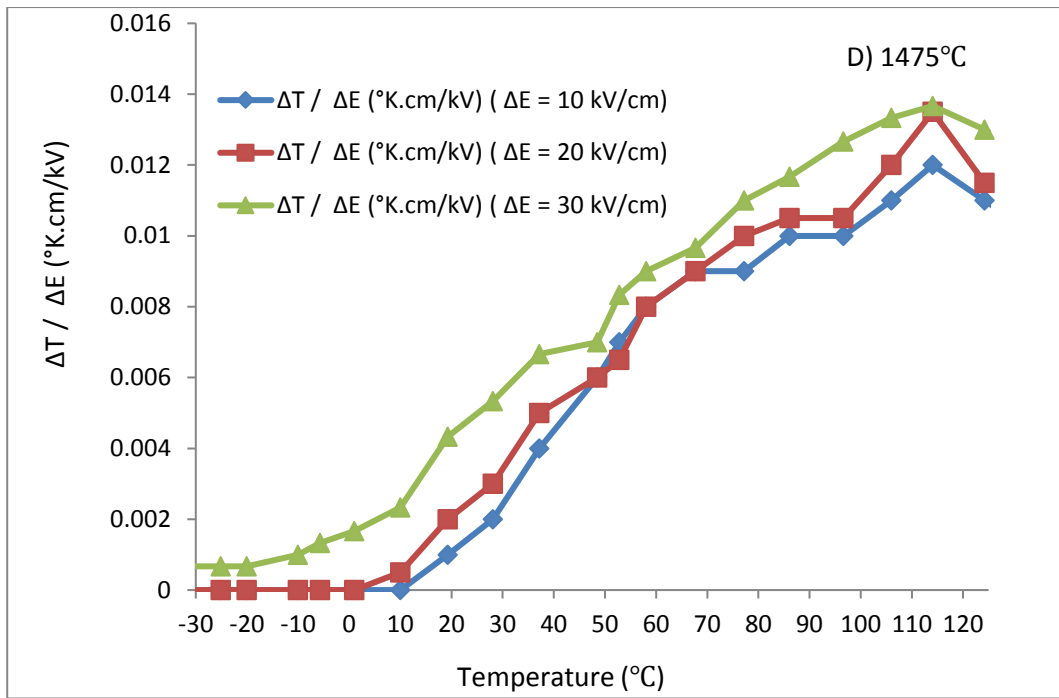
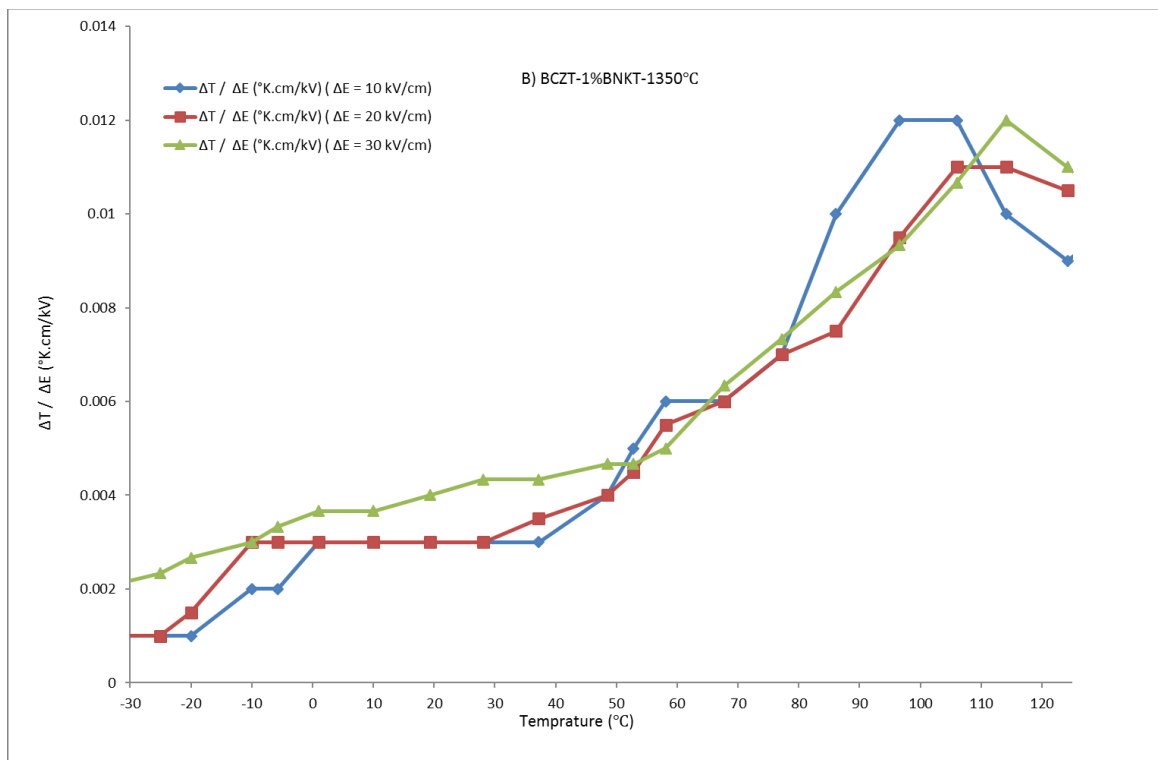
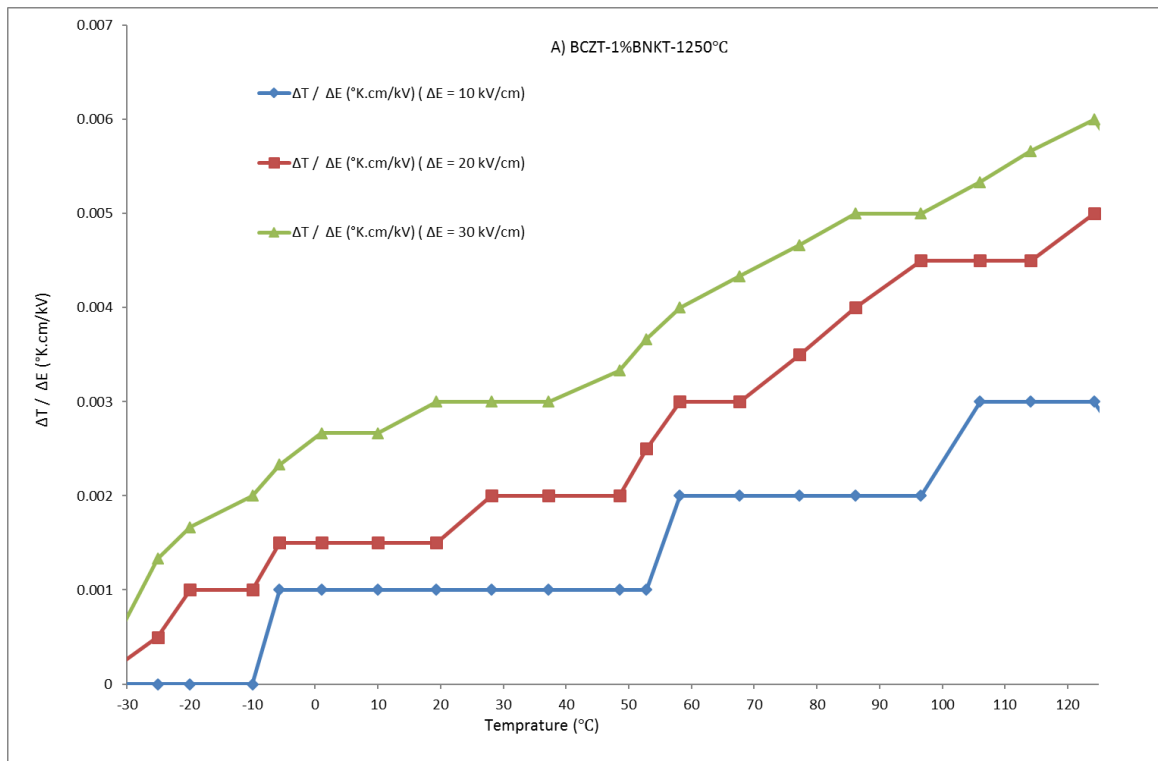


Figure II-7: The ECE figure of merit of pure BCZT sintered at A) 1400, B) 1425, C) 1450, D) 1475, and E) 1500°C and measured between -50 and 150°C.



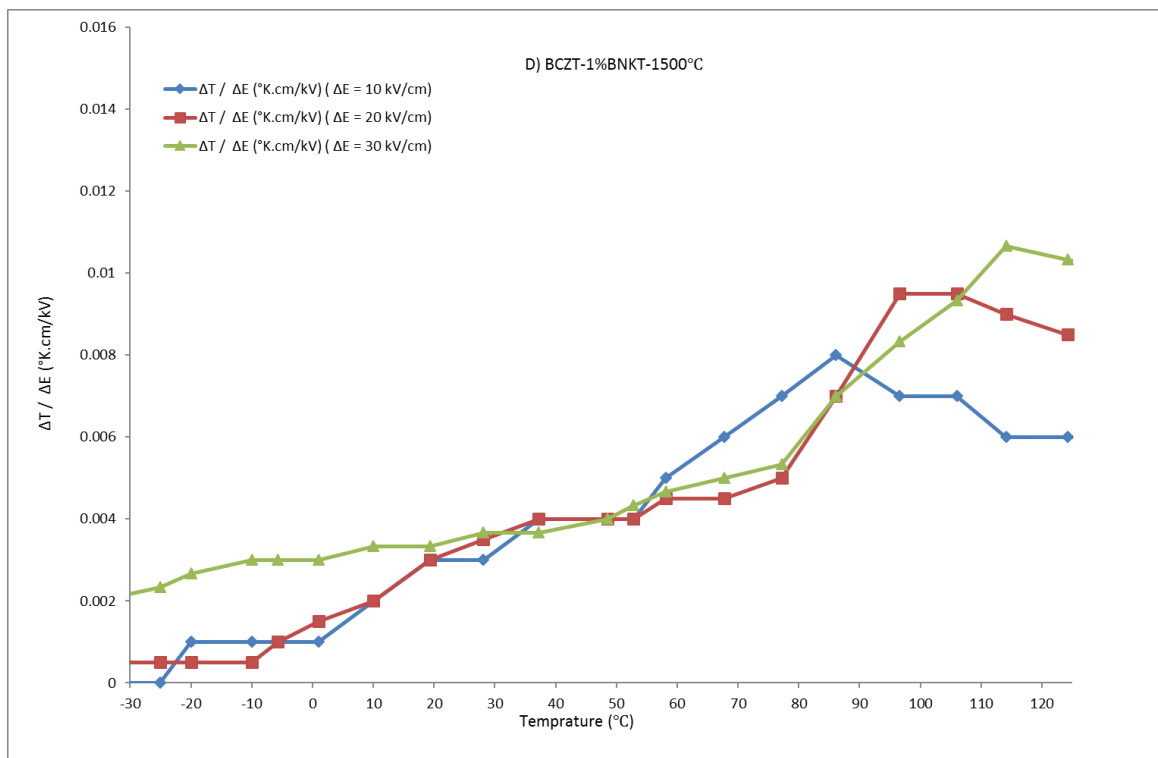
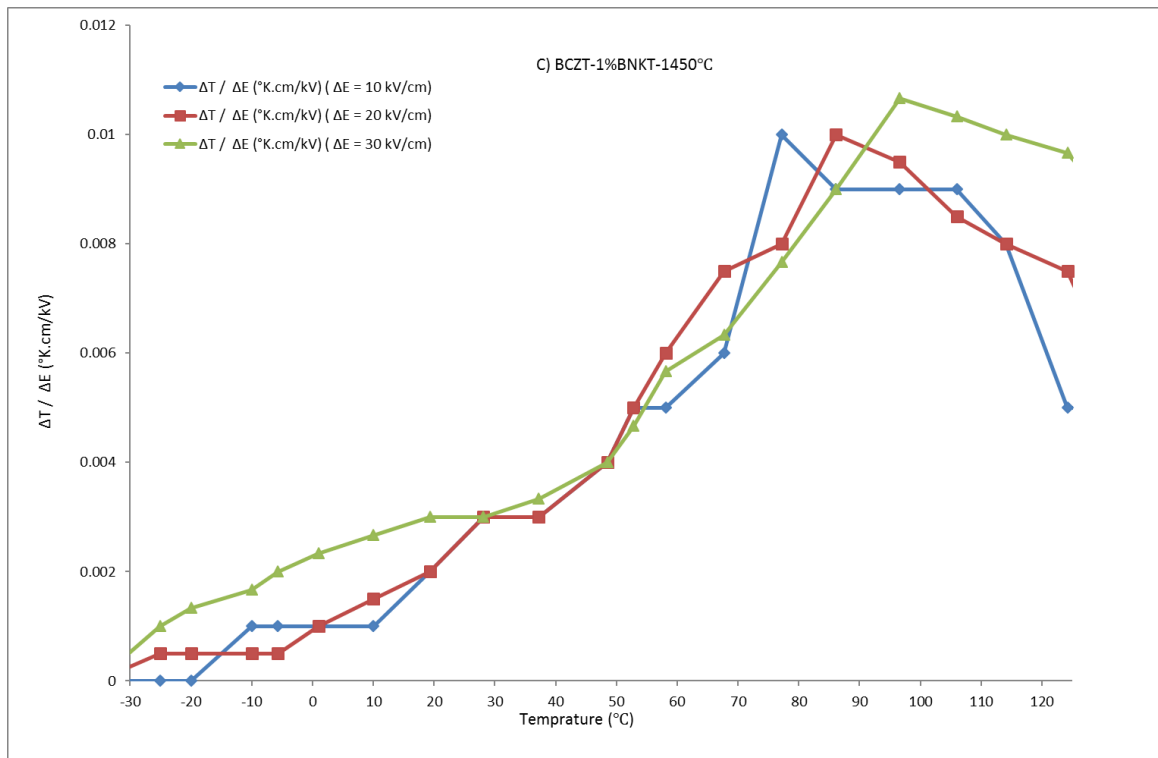
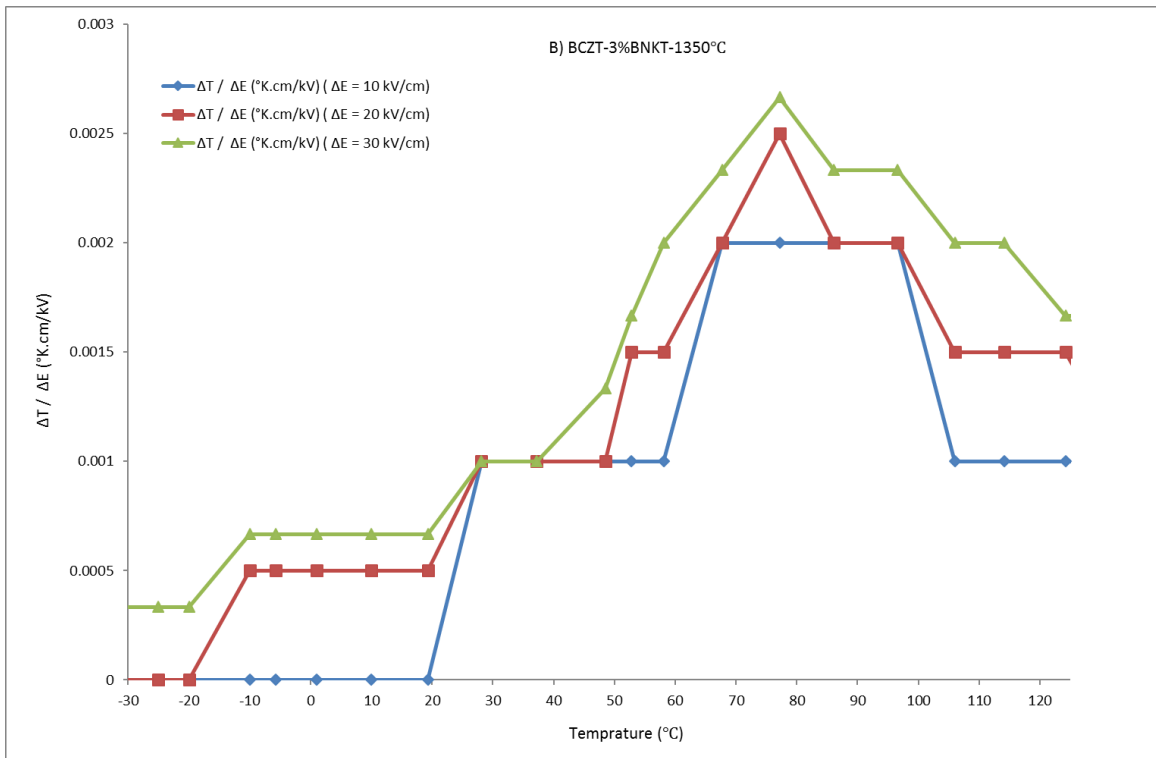
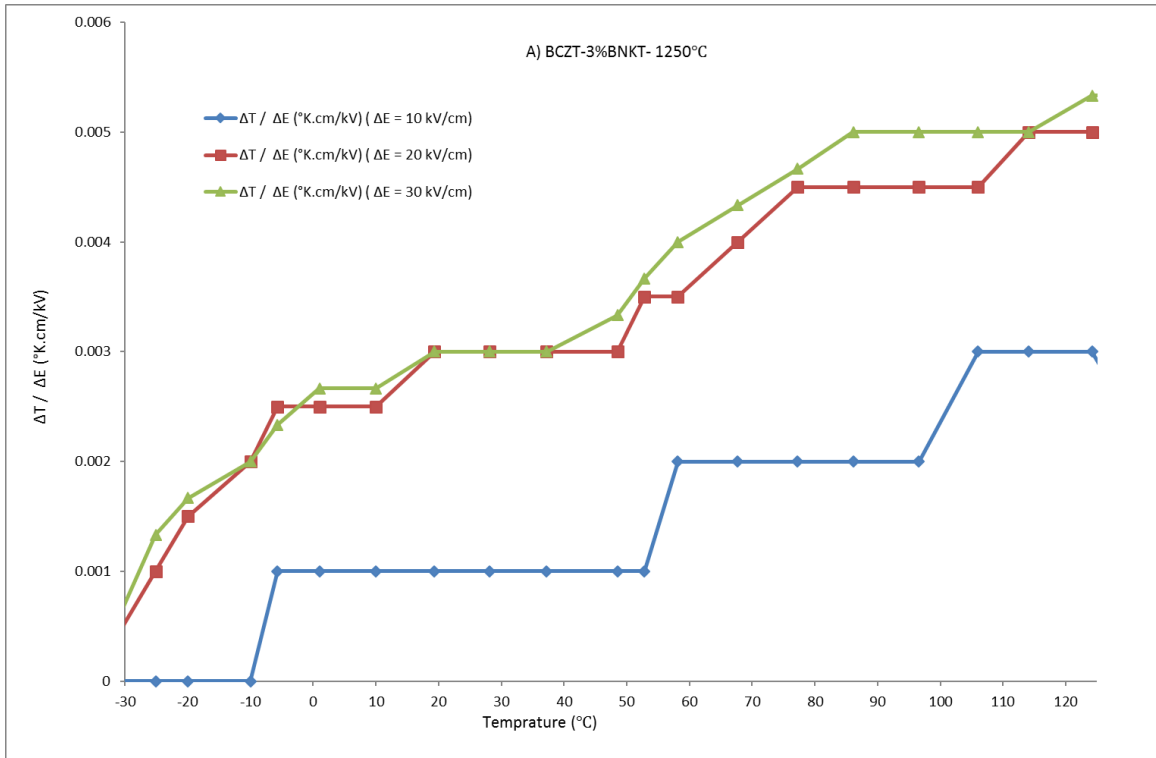


Figure II-8: The ECE figure of merit as a function of temperature of BCZT-1% BNKT, sintered at A) 1250, B) 1350, C) 1450, and D) 1500°C, and for a range of applied electric field values.



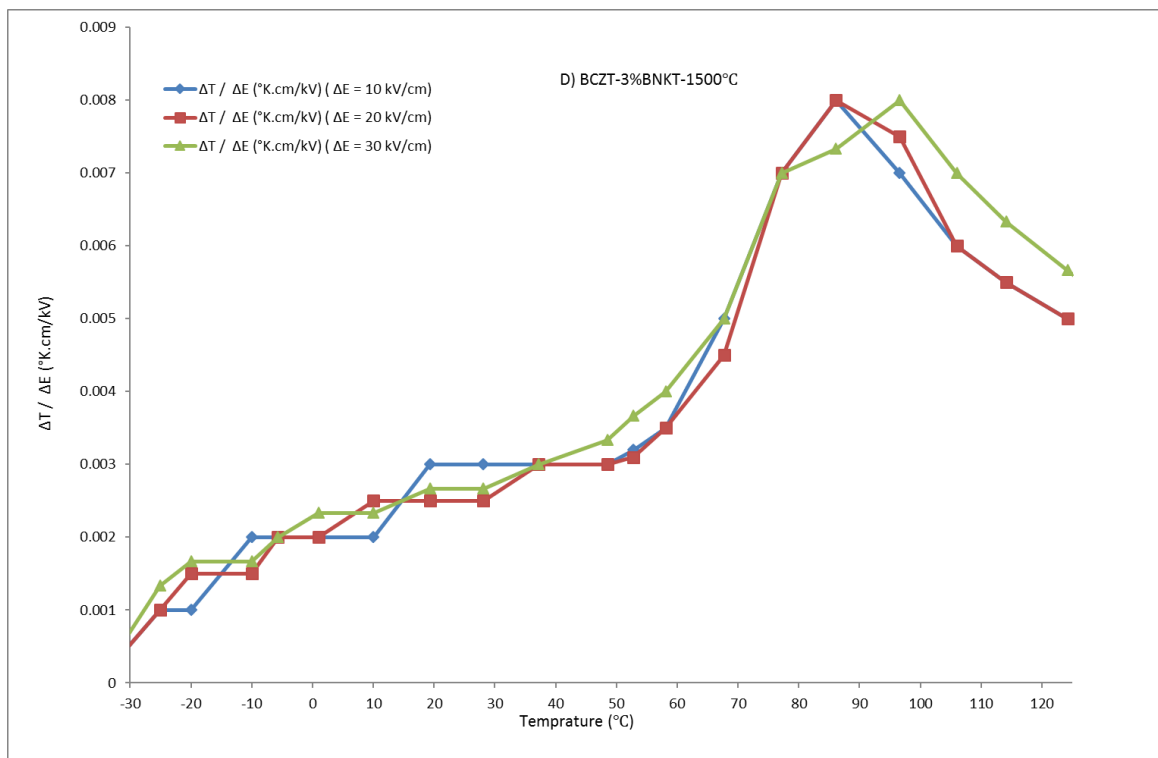
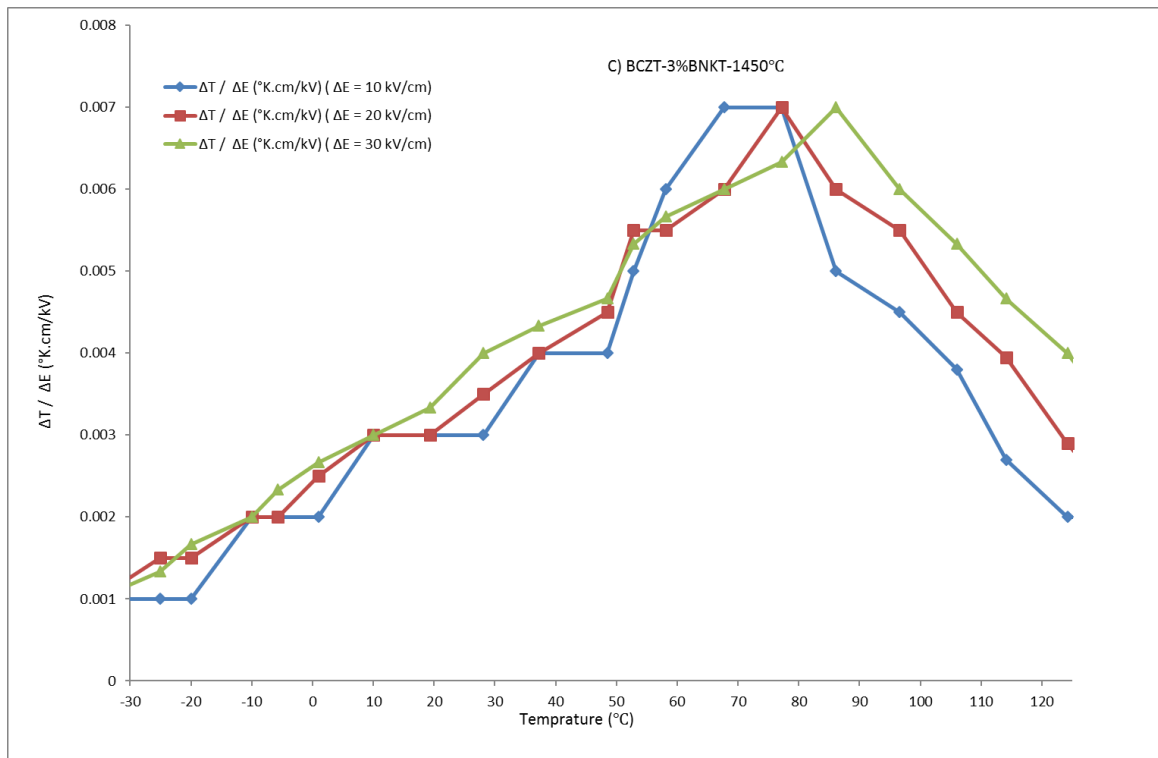
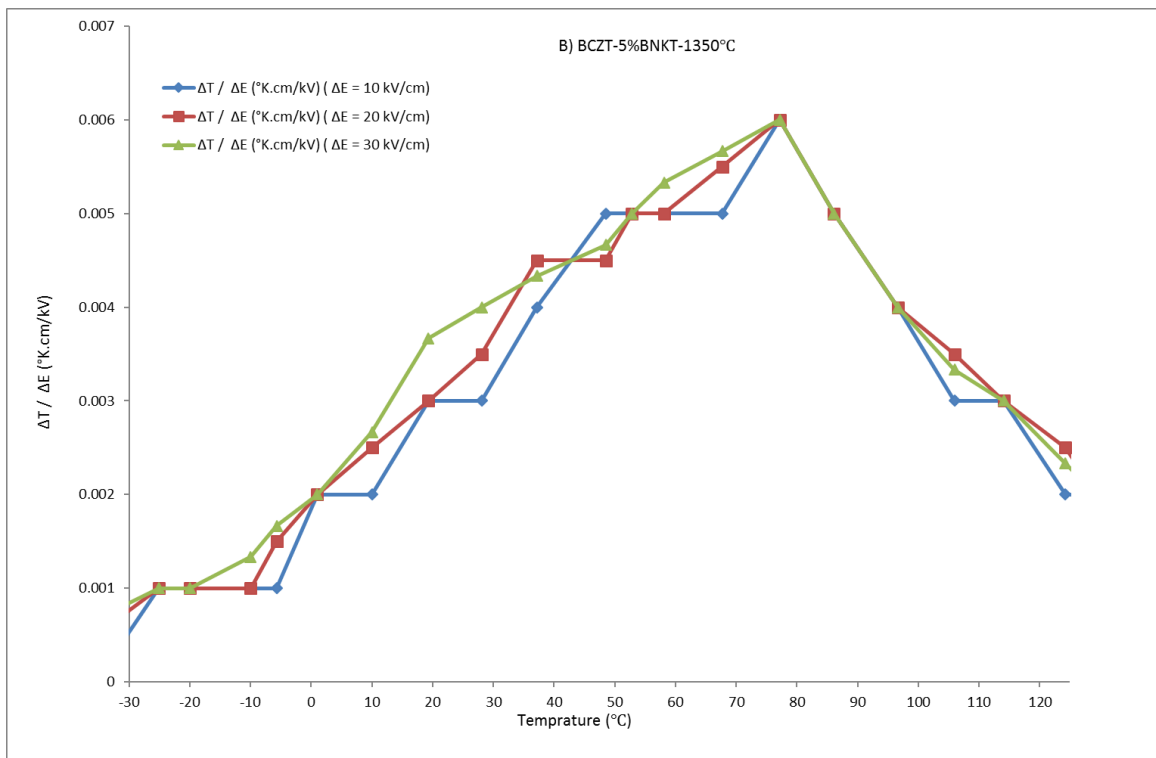
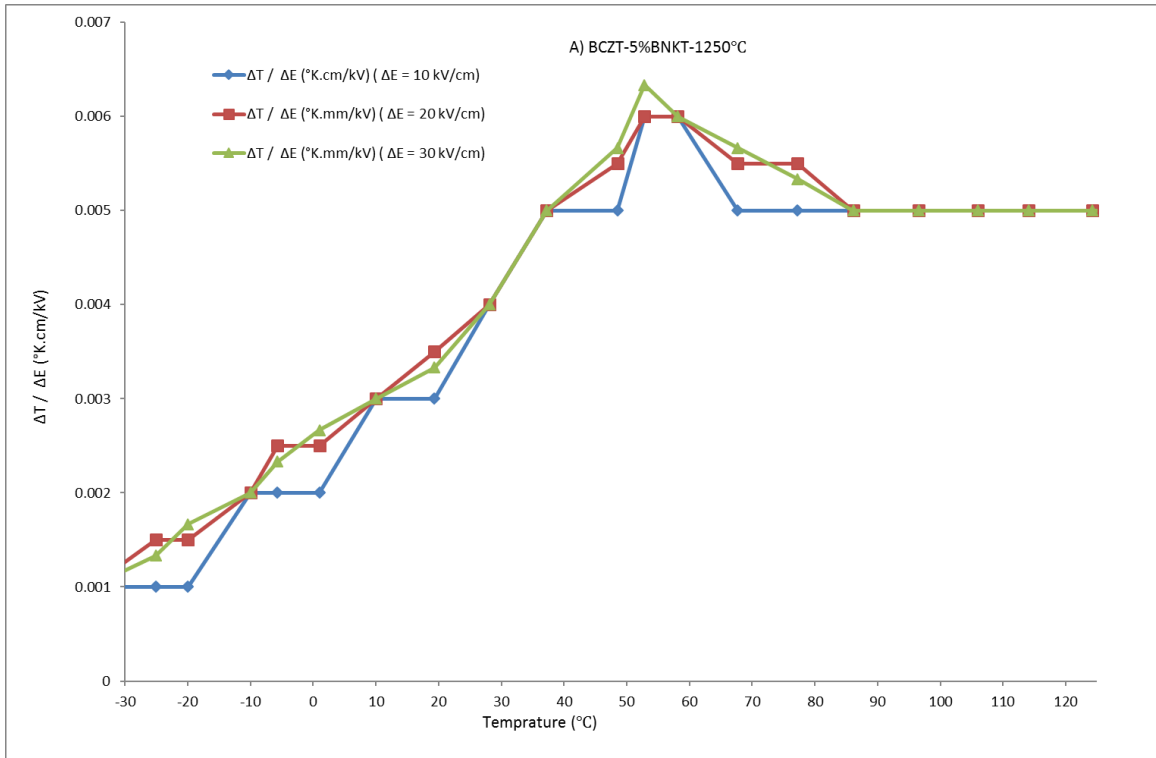


Figure II-9: The ECE figure of merit as a function of temperature of BCZT-3% BNKT, sintered at A) 1250, B) 1350, C) 1450, and D) 1500°C, and for a range of applied electric field values.



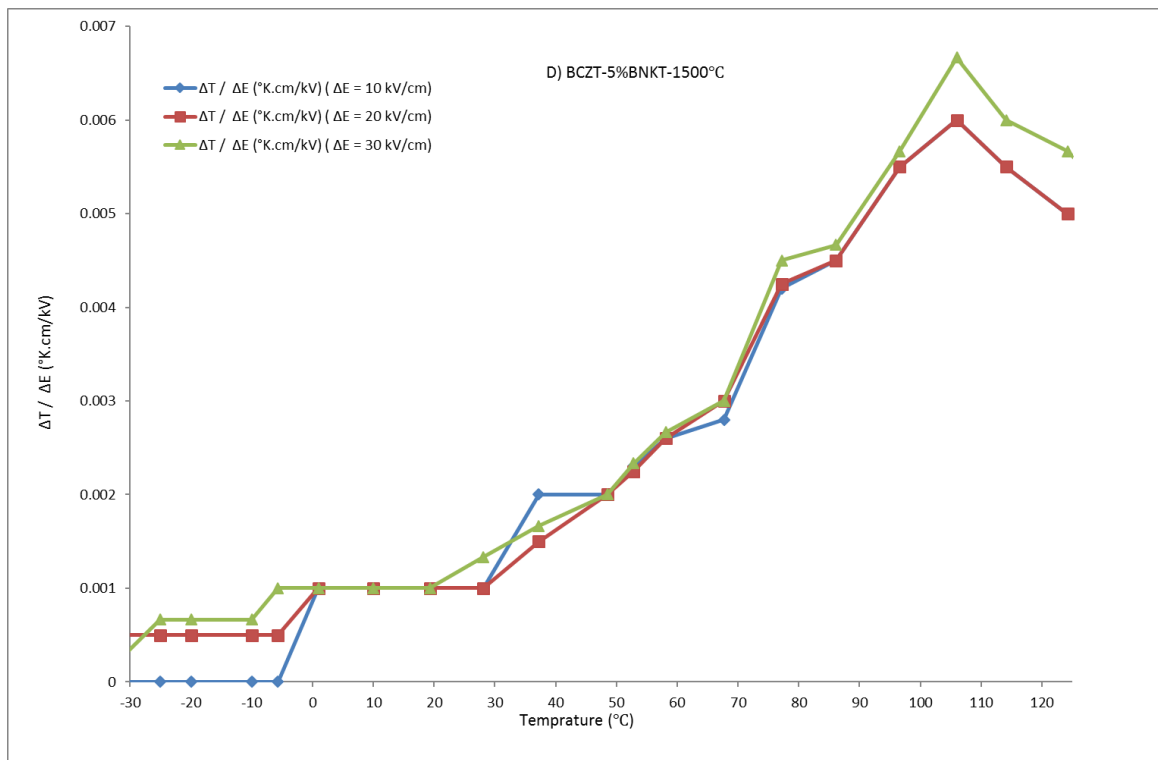
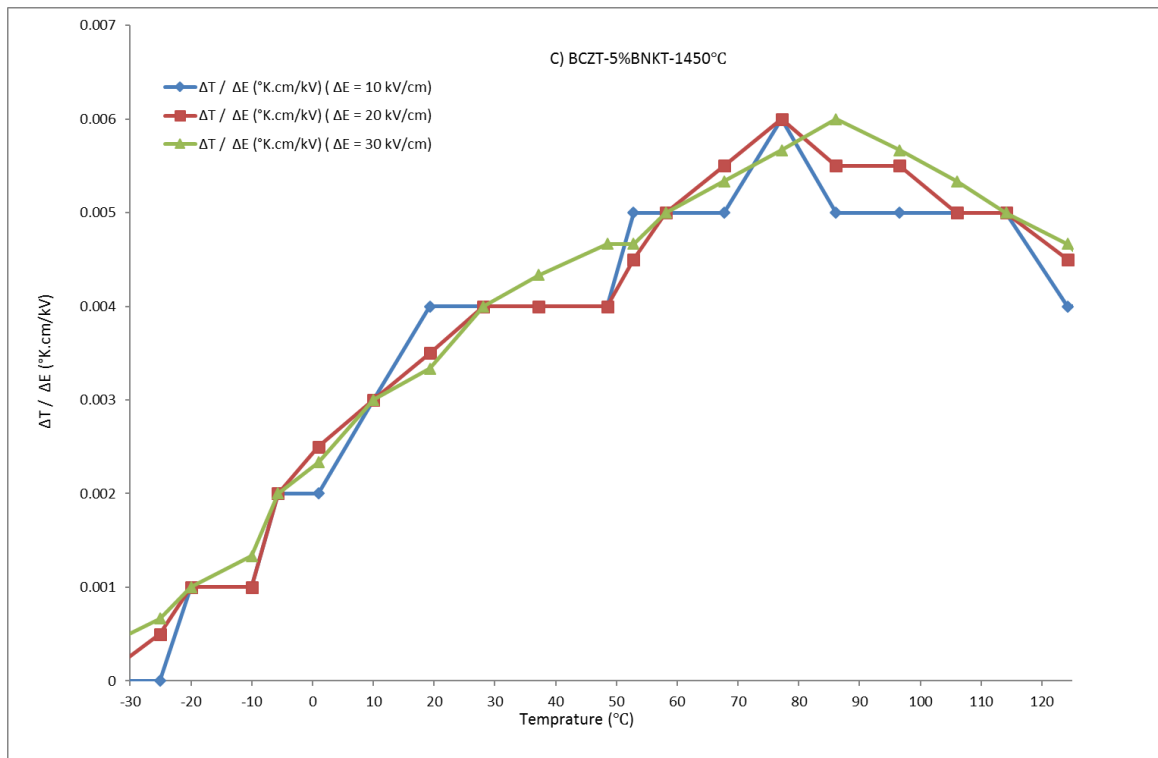


Figure II-10: The ECE figure of merit as a function of temperature of BCZT-5% BNKT, sintered at A) 1250, B) 1350, C) 1450, and D) 1500°C, and for a range of applied electric field values.